Subcellular Biochemistry 87

J. Robin Harris · Egbert J. Boekema
*Editors*

# Membrane Protein Complexes: Structure and Function

Springer

# Subcellular Biochemistry

Volume 87

**Series editor**
J. Robin Harris
University of Mainz, Mainz, Germany

The book series SUBCELLULAR BIOCHEMISTRY is a renowned and well recognized forum for disseminating advances of emerging topics in Cell Biology and related subjects. All volumes are edited by established scientists and the individual chapters are written by experts on the relevant topic. The individual chapters of each volume are fully citable and indexed in Medline/Pubmed to ensure maximum visibility of the work.



More information about this series at http://www.springer.com/series/6515

J. Robin Harris • Egbert J. Boekema
Editors

# Membrane Protein Complexes: Structure and Function

Springer

*Editors*
J. Robin Harris
Institute of Zoology
University of Mainz
Mainz, Germany

Egbert J. Boekema
Groningen Biomolecular Sciences and
Biotechnology Institute
University of Groningen
Groningen, The Netherlands

ISSN 0306-0225
Subcellular Biochemistry
ISBN 978-981-10-7756-2 ISBN 978-981-10-7757-9 (eBook)
https://doi.org/10.1007/978-981-10-7757-9

Library of Congress Control Number: 2018932357



Printed on acid-free paper

This Springer imprint is published by the registered company Springer Nature Singapore Pte Ltd. part of Springer Nature.
The registered company address is: 152 Beach Road, #21-01/04 Gateway East, Singapore 189721, Singapore

# Preface

This volume of the Subcellular Biochemistry series, devoted to membrane protein complexes, joins the related volume (Volume 83) of the series, entitled *Macromolecular Protein Complexes*. Further books in the series, devoted to the overall theme of *protein complex structure and function*, will duly follow.

As found for Volume 83, the selection of interesting chapter topics from the large range of membrane protein complexes currently being studied has inevitably been limited. Nevertheless, it is hoped that the chapters included in this book will provide a significant insight into this field of study. Unfortunately, during the ~12-month preparation period for this book, several of the initially commissioned contributions were withdrawn! The 14 remaining chapters included in the book are written by scientists actively involved in present-day research, utilizing X-ray crystallography, cryo-electron microscopy, and other biophysical and biochemical techniques to study membrane protein structure and function.

Both prokaryotic and eukaryotic membrane protein complexes are included in this book. Whilst space does not permit comment on all the chapters, it would be out of order to select just a few for discussion here. Rather, we recommend all these interesting chapters, the titles of which and authorship can be seen from the Contents List.

The study of membrane protein complexes has expanded greatly in recent years, from the more fundamental biochemical and biophysical aspects to more applied cellular and pharmacologically related topics of significance to agriculture, human, and animal medicine. Structural studies provide the fundamental data from which functional interpretations can be made.

Membrane receptors, enzymes, ion channels, and proton pumps are all included in this book, but the membrane-active toxins have been omitted as these were dealt with in Volume 51 (*Cholesterol Binding and Cholesterol Transport Proteins*) and Volume 83 of the series (*MACPF/CDC Proteins – Agents of Defence, Attack and Invasion*). However, both bacterial and plant photosystems are included.

We hope that the content of this book will complement the topics included in earlier volumes of the Subcellular Biochemistry series and be of broad interest and value to undergraduate and doctoral students, researchers, and academics within the

biological and biomedical sciences. The availability of e-books and e-chapters for the Subcellular Biochemistry series, for purchase and via institute online libraries, as well as the print copies of the books, increases the ease of access to this advanced scientific book series. The series is also indexed in PubMed.

Mainz, Germany J. Robin Harris
Groningen, The Netherlands Egbert J. Boekema

# Contents

# Chapter 1
# Bacterial Adhesion Pili


**Chelsea R. Epler Barbercheck, Esther Bullitt, and Magnus Andersson**

**Abstract** *Escherichia coli* bacterial cells produce multiple types of adhesion pili that mediate cell-cell and cell-host attachments. These pili (also called 'fimbriae') are large biopolymers that are comprised of subunits assembled via a sophisticated micro-machinery into helix-like structures that are anchored in the bacterial outer membrane. They are commonly essential for initiation of disease and thus provide a potential target for antibacterial prevention and treatment. To develop new therapeutics for disease prevention and treatment we need to understand the molecular mechanisms and the direct role of adhesion pili during pathogenesis. These helix-like pilus structures possess fascinating and unique biomechanical properties that have been thoroughly investigated using high-resolution imaging techniques, force spectroscopy and fluid flow chambers. In this chapter, we first discuss the structure of pili and the micro-machinery responsible for the assembly process. Thereafter, we present methods for measurement of the biomechanics of adhesion pili, including optical tweezers. Data demonstrate unique biomechanical properties of pili that allow bacteria to sustain binding during *in vivo* fluid shear forces. We thereafter summarize the current biomechanical findings related to adhesion pili and show that pili biomechanical properties are niche-specific. That is, the data suggest that there is an organ-specific adaptation of pili that facilitates infection of the bacteria's target tissue. Thus, pilus biophysical properties are an important part of *Escherichia coli* pathogenesis, allowing bacteria to overcome hydrodynamic challenges in diverse environments.

**Keywords** Fimbriae · Pilins · Pathogenesis · Virulence factors · Optical tweezers

C. R. Epler Barbercheck · E. Bullitt (✉)
Department of Physiology & Biophysics, Boston University School of Medicine, Boston, MA, USA
e-mail: crepler84@gmail.com; bullitt@bu.edu

M. Andersson
Department of Physics, Umeå University, Umeå, Sweden
e-mail: magnus.andersson@umu.se



J. R. Harris, E. J. Boekema (eds.), *Membrane Protein Complexes: Structure and Function*, Subcellular Biochemistry 87,
https://doi.org/10.1007/978-981-10-7757-9_1

## 1.1 Introduction

Adhesion pili expressed on the surface of pathogenic bacteria facilitate binding and sustained adherence of bacteria to target cells, see Fig. 1.1a. Pili, also called 'fimbriae', thus frequently provide an important first step during bacterial colonization: surface-tethered bacteria, attached via pili, are less susceptible to being washed away by natural cleansing mechanisms of the host. Indeed, pili are often an essential virulence factor (Roberts et al. 1994), and are commonly necessary for biofilm formation. In the 1980's the expression "No pili, no disease" was coined, based on clinical studies in which volunteers were fed bacteria with or without pili (Evans et al. 1978; Levine et al. 1979) that resulted in a greater than 85% increase of illness in those who ingested bacteria with CFA/I pili over those who ingested bacteria without pili. There are a large number of pilus types that support binding and sustained adhesion of bacteria, with variation due largely to adaptations that facilitate adhesion in the preferred environmental milieu of each bacterial strain. While some pili support additional functions (e.g., gliding motility of Type IV pili), the scope of this chapter includes only pili whose sole role in pathogenesis is adhesion, and in particular, those that are correlated with the pathogenesis of Gram-negative bacteria. This still encompasses a great many pilus types and bacterial strains, including Type 1 and P-pili expressed on uropathogenic *Escherichia coli* (UPEC) and CFA/I and many CS pili (coli surface; e.g., CS20) expressed on enterotoxigenic *Escherichia coli* (ETEC).

Pili specialized for adhesion are generally classified by their assembly pathways, described as either the chaperone-usher (Dodson et al. 1993) or the alternate chaperone-usher pathway (Soto and Hultgren 1999). As will be discussed below, the

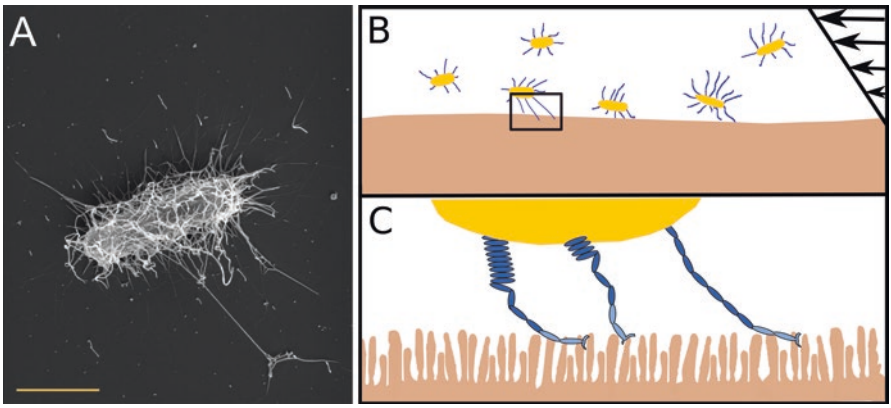


**Fig. 1.1** Conceptual model of bacteria attaching to intestinal epithelium (**a**) Scanning Electron Microscopy micrograph of an *E. coli* expressing multiple adhesion pili. Magnification bar is 1.0 µm. (**b**) Schematic of bacteria close to the intestinal epithelium and exposed to a gradient flow. (**c**) Bacteria attached to microvilli via pili that are partially uncoiled (left and middle) or completely uncoiled (right)

subunits that comprise the helical pilus filament (pilins and adhesins), along with their periplasmic chaperones and outer membrane ushers, are structurally similar for pili assembled by either pathway. The pathways were initially distinguished instead by a lack of sequence homology between the pilins (Sakellaris et al. 1996) and a lack of sequence homology between the C-terminal region of the chaperones (Zav'yalov et al. 1995; Busch and Waksman 2012), which is the site on the chaperone that interacts directly and specifically with adhesin and pilin subunits during transit across the periplasm. However, as each pilus type has its own usher protein, it is the usher protein sequence that is now used for designation of pili as chaperone/usher versus alternate chaperone/usher family members (Nuccio and Bäumler 2007), and the chaperone-usher and alternate chaperone-usher pathways (Soto and Hultgren 1999) are thought to represent convergent evolution (Sakellaris and Scott 1998). Biophysical properties of pili assembled by each pathway are discussed below.

All adhesion pili promote bacterial adhesion to target cells early in infection, see Fig. 1.1b, c. As the infection progresses, or when bacteria are in contact with inorganic surfaces, pilus expression often increases, leading to bacterium-bacterium interactions that promote biofilm formation (Mulvey et al. 1998). Aggregation of bacteria into a biofilm provides additional protection of bacteria from host cell defenses, thereby promoting increased colonization. For a review that includes the roles of a broad range of pili in biofilm formation, see (Otto 2014).

## 1.2 Structure of Pili

### *1.2.1 Pilus Biogenesis*

Adhesion pili are assembled at the outer membrane of Gram-negative bacteria, irrespective of whether they are members of the chaperone-usher pathway or the alternate chaperone-usher pathway. After translation of chaperone(s) and pilus structural proteins inside the cell, these proteins are targeted via their signal sequences to the bacterial inner membrane. As seen in Fig. 1.2, pilus-related proteins exit from the cytoplasm into the periplasm via the General Secretory Pathway through an inner membrane protein complex, Sec YEG. Upon secretion of adhesins and pilins into the periplasm, they are either picked up by their cognate chaperone, or are degraded in the periplasm by proteases (Kuehn et al. 1991; Jones et al. 1993). The structures of these adhesin and pilin subunits all include an immunoglobulin-like fold (Sauer et al. 1999), with one missing beta-strand (Fig. 1.3a). The lack of this beta-strand creates a hydrophobic groove that would cause protein aggregation if left unfilled. Amino acids on the chaperone surface act to fill the subunit's groove via "N-terminal complementation". The pilus subunits are thus protected from degradation by this chaperone/subunit interaction, allowing the chaperone/pilin complex to transit across the periplasm.

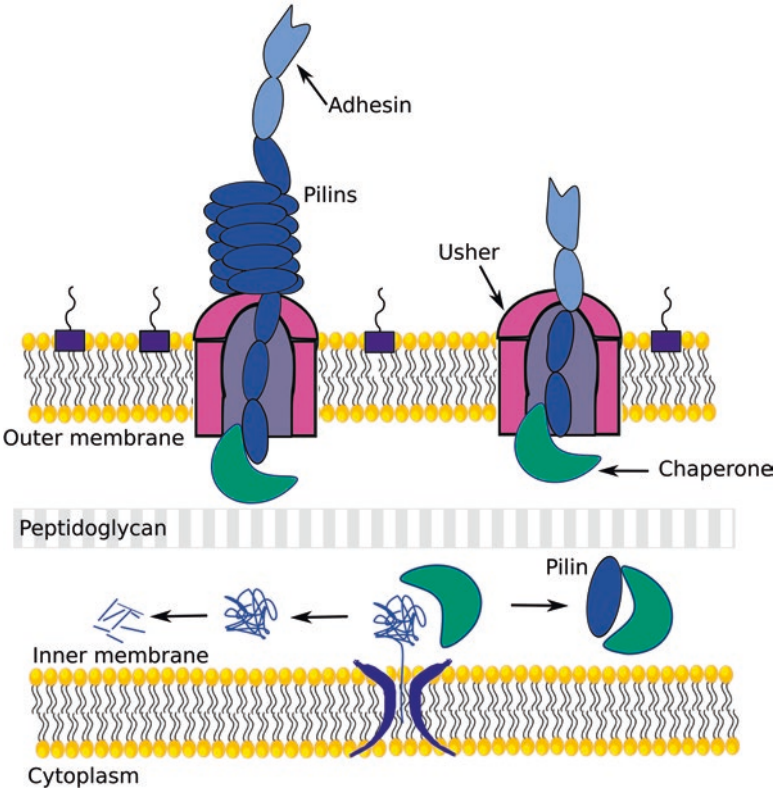


**Fig. 1.2** An illustration of the micro-machinery for assembling pili via the chaperone-usher or alternate chaperone-usher pathway. Pilin proteins are secreted from the cytoplasm via the General Secretory Pathway (dark blue), picked up by a chaperone protein (green) that transports pilins to the usher protein (pink) at the outer membrane. Misfolded protein is degraded in the periplasm. The subunits are assembled through the usher into a helical pilus filament (lipopolysaccharide (LPS), purple)

After transiting the periplasm, assembly of adhesins and pilins at the outer membrane is facilitated by binding to a pore-forming usher protein that spans the bacterial outer membrane. While the mechanism for assembly of the usher in the outer membrane is not well understood, its structure (Fig. 1.3b) has been determined alone (Thanassi et al. 1998) and in complex with its binding partners, the chaperone, adhesin, and pilins (Li et al. 2004; Nishiyama et al. 2005; Fronzes et al. 2008). From these data it has been determined that the usher includes a periplasmic binding site for the chaperone, a pore to the external milieu, and a plug domain that blocks the pore prior to pilus assembly. To begin assembly, the chaperone-adhesin complex docks to the usher, causing a conformational change in the usher that moves aside the plug domain that had been blocking the channel. This movement of the plug

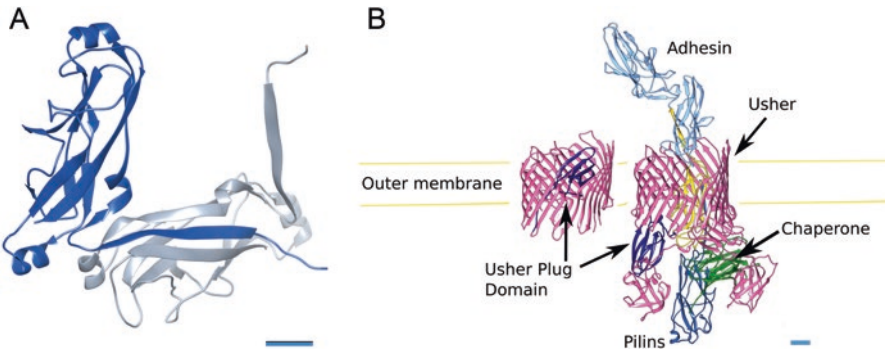


**Fig. 1.3** Pilin subunits and pilus assembly. (**a**) Two pilin subunits are shown, with the hydrophobic groove of the first subunit (gray) filled with the N-terminal extension of the second subunit (blue), as occurs in a mature pilus (from pdb 5flu, P-pili PapA (Hospenthal et al. 2016)). Scale bar 10 Å. (**b**) The transmembrane usher protein is the site of pilus assembly, located within the bacterial outer membrane. Shown on the left is the beta-barrel region of an usher (pink), with its plug domain (navy blue) blocking the pore prior to pilus assembly (pdb 3ohn; (Phan et al. 2011)). On the right, the macromolecular complex (pdb 4j3o; (Geibel et al. 2013)) shows the full usher with its plug now seen swung out from the pore and near the usher N-terminal domain, within the periplasm. The N-terminal domain helps stabilize incoming chaperone/pilin complexes while the chaperone binds to the usher C-terminal domain. The adhesin protein (sky blue) has already passed through the usher. It has an adhesin domain for binding at the tip and a pilin domain available for assembly of the subsequent pilin subunit (yellow). The second pilin (medium blue) has donated its N-terminal beta-strand to the yellow pilin, and the chaperone (green) is bound to the C-terminal domain of the usher, while continuing to protect the groove of the medium blue pilin. Scale bar, 10 Å

away from the pore by the binding of the chaperone/adhesin complex to the usher ensures that the adhesin is the first protein translocated through the usher's outer membrane pore. As a result, the adhesins are localized to the pilus tips, where they utilize their capacity as lectins (sugar-binding proteins) for attachment of bacteria to cell surface sugars present on their target cells (Roberts et al. 1994). First to transit through the usher, adhesins in Gram-negative bacteria have two distinct domains: a lectin domain and a pilin domain, such that the distal end of the protein binds to the host cell, and the proximal end is available to begin a chain of approximately 1000 pilin subunits that comprise the majority of the pilus filament.

A second role for the ternary usher/chaperone/adhesin complex is to prime the usher for active assembly of pilin subunits into the pilus structure (So and Thanassi 2006). To begin this phase of pilus assembly, the adhesin's pilin domain mimics the subsequently added pilins, which are assembled via a mechanism shown in Fig. 1.3 and described as "N-terminal exchange" (Choudhury et al. 1999; Sauer et al. 1999). During this exchange, the missing beta-strand in the pilin's IgG-like quaternary structure creates a groove that is filled during transit across the periplasm by amino acids on the chaperone surface. When released from the chaperone, the pilin's groove is subsequently complemented by the N-terminal beta-strand of the next incoming pilin as it is added to the growing pilus. There is no requirement for

external energy during pilus assembly (Jacob-Dubuisson et al. 1994), which instead utilizes these conformational changes to transition the filament's proteins from a high energy chaperone/pilin complex to the lower energy pilin/pilin complex in the assembling filament (Zavialov et al. 2005). Repeated binding of chaperone/pilin complexes and hand-off of additional pilin subunits produces the growing pilus filament. There is evidence that ushers may function as dimers, with assembly facilitated by passing of subunits from one usher's binding site through the second usher's pore (Li et al. 2004; Werneburg et al. 2015). To terminate pilus assembly, P-pili express a termination (or "anchor") pilin (Baga et al. 1987). However, in most pili there is no known anchor protein, and it is expected that pili continue elongating as long as there are pilins available to be added to the filament.

### *1.2.2 Quaternary Structure*

The ultrastructure of assembled pilus filaments, shown in Fig. 1.4, is a helical filament 7–8 nm in diameter that retains its connection to the usher protein in the bacterial outer membrane (see, e.g., reviews by Thanassi et al. 2012; Hospenthal et al. 2017). The pilus filament has between 3 and 3.5 subunits per turn of the helix and, while variable between types, the pitch of the helix in UPEC and ETEC pili is approximately 2.5 nm. Subunits are connected via a tongue-in-groove arrangement called 'donor strand exchange' (Choudhury et al. 1999; Sauer et al. 1999), and the helix can unwind to an extended thin fibrillar structure that is only the width of a single pilin subunit (Bullitt and Makowski 1995). Once extended, the new length can be 10 times the length of the original pilus structure. This unwinding occurs via disruption of the helix's non-covalent layer-to-layer interactions, which are strongest between the s and s + 3rd subunits (Fig. 1.4c), and is reversible.

### *1.2.3 Adhesins*

Located at the distal end of the pilus filament is the adhesin. As discussed above, the protein is comprised of two domains with the sugar binding, lectin domain at the tip. Thus the adhesin protein has about twice the molecular weight of the major pilin subunits. Due to its position at the very tip of the pilus filament the lectin domain of this subunit is available for binding to the target cell (Dodson et al. 2001). The adhesin is the most conserved subunit of the pilus structure, with precise specificity for sugars located on the target cell surface. The tip adhesin thereby defines the preferred microenvironmental niche of each bacterial strain. The second domain of the adhesin is pilin-like, comprised of an immunoglobulin-like fold with six beta-strands. A hydrophobic groove in the domain is available for a seventh strand, which is donated by the N-terminal amino acids of the first pilin subunit. Thus begins assembly of approximately 1000 pilin subunits, each subunit with a hydrophobic groove that is filled by the subsequent pilin during filament assembly.

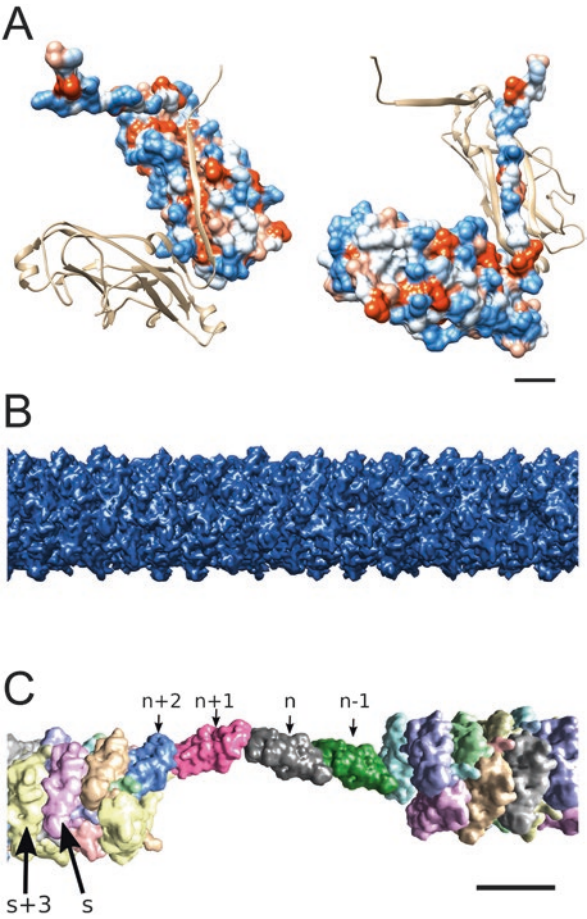


**Fig. 1.4** Pilus ultrastructure. (**a**) Pili assemble via a tongue-in-groove arrangement. Surface hydrophobicity of two adjacent pilin subunits shows that the groove of the $n^{th}$ subunit is highly hydrophobic (left), and the N-terminal beta-strand of the n + $1^{st}$ subunit has alternating hydrophobic amino acids to fit into the groove (right). Color scale: hydrophobic, red, to hydrophilic, blue. Scale bar 10 Å. (**b**) The assembled pilus filament is a helical filament with approximately 3.3 subunits per turn and a pitch of ~2.5 nm. (**c**) The pilus filament can unwind by disruption of layer-to-layer interactions, generally between the $n^{th}$ and n + $3^{rd}$ subunits, shown before disruption as s and s + 3. All panels: P-pili structure, adapted from pdb 5flu (Hospenthal et al. 2016)

## 1.3 Biophysical Properties of Pili

### *1.3.1 Measuring Biophysical Properties Using Force Measuring Optical Tweezers*

Bacterial pili are important virulence factors mediating adhesion of pathogenic bacteria to host tissue. Thus, understanding their structure and biomechanics is of great importance to enhance the knowledge of the adhesion process. Since pili are tiny polymers, a few nanometers wide and hundreds of nanometers long, sensitive techniques to measure the biophysical properties are needed. With the development of force spectroscopy techniques such as atomic force microscopy (AFM; see Fig. 1.1a) and optical tweezers (see Fig. 1.5a) it is now possible to perform strain measurements by applying tensile force to a pilus. These experiments provide force-extension data revealing structural and biomechanical information on the mechanisms of pilus responses to external forces (Fällman et al. 2004; Miller et al.

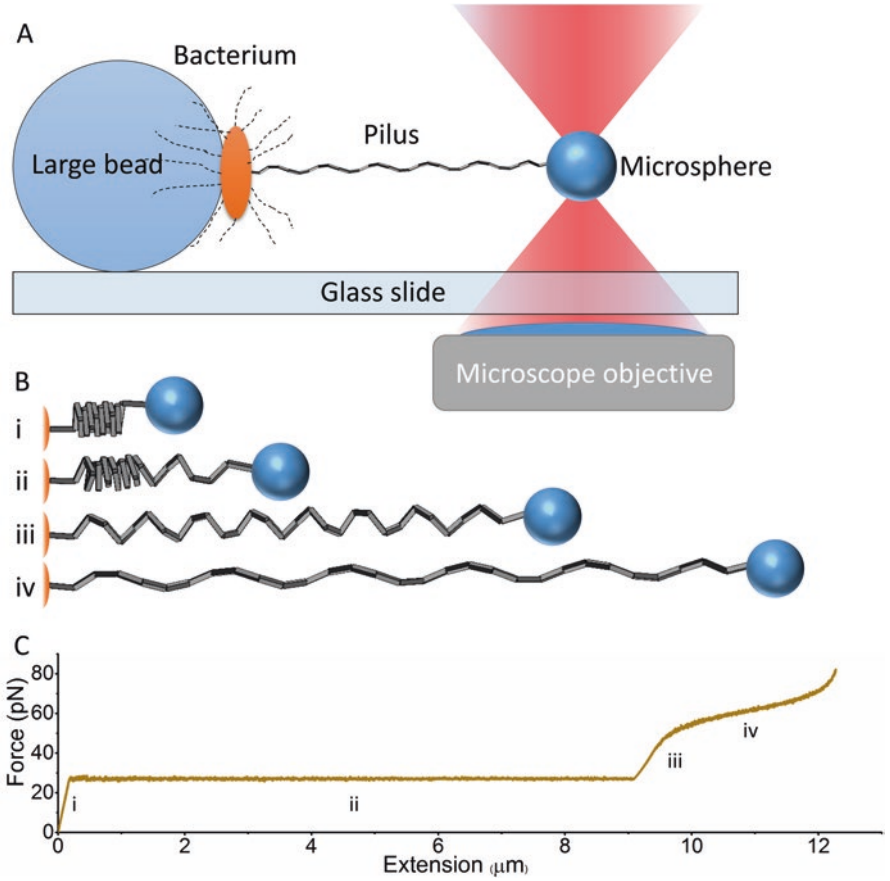


**Fig. 1.5** Illustration of how a measurement is performed using optical tweezers. Objects are not to scale. (**a**) schematic of a force-extension measurement of a pilus. A bacterium is attached to a ~10 μm microsphere coated with poly-L-lysine, which acts as a glue. The bacterium is drawn with pili; for representative purpose we depict the pilus under investigation in bold. The pilus is attached to a ~1 μm microsphere trapped in the focus of a stationary laser beam. By moving the glass slide using a piezo stage a force is applied to the pilus. (**b**) schematic showing different configurations of a pilus when exposed to tensile forces using optical tweezers. (*i*) No force applied, pilus is in its coiled configuration and the tip is attached to the microsphere. (*ii*) Bacterium and microsphere are separated and the pilus starts to uncoil sequentially. (*iii*) Pilus is uncoiled, no layers are connected. (*iv*) Overstretching of the pilus, head-to-tail bonds are stretched. (**c**) Monte Carlo simulation using the methodology presented in (Björnham et al. 2008) of a helix-like pilus with corresponding properties similar to a P-pilus. The force response is labeled to correlate to the configurations shown in panel B

2006). Optical tweezers have been used extensively to characterize pili, providing force resolution that is an order of magnitude higher than force measurements from AFM. The physical principle of optical tweezers is that any type of micrometer sized objects (inorganic as well as biological) can be trapped by a well-focused

laser light via transfer of light momentum (Ashkin et al. 1987). The technique has outstanding force and spatial resolution ($<10^{-12}$ N and <0.4 nm) and the ability to apply and measure dynamic and static forces. This technique has opened new doors to gain valuable structural and dynamic information. For example, force measurements can provide intrinsic characteristics of the pilus shaft and the pilus adhesin (Fällman et al. 2004; Björnham et al. 2009).

Pili force measurements can be realized by first trapping a bacterium using low laser power and then immobilizing the bacterium to a fixed surface, for example, a poly-L-lysine coated microsphere that in turn is immobilized to a cover slide, see Fig. 1.5a. For a detailed description of this process, see (Andersson et al. 2006a). A particle, such as a 1 μm polystyrene microsphere is thereafter trapped by the laser beam, with the trapping strength determined using the power spectrum calibration method (Berg-Sørensen and Flyvbjerg 2004). Thereafter, the microsphere is brought into contact with a pilus so that they adhere to each other. Then, by separating the bacterium and microsphere, as is shown in Fig. 1.5, and monitoring the position of the small bead in the trap, the pilus can be exposed to a well-calibrated force. The unwinding response of a helix-like pilus exposed to force is modelled in Fig. 1.5b. Force-extension experiments are used to measure the force response with high accuracy and evaluate the bio-mechanical and kinetic parameters of the pilus.

A typical force-extension response of a helix-like pilus is shown in Fig. 1.5c. The response is characteristic of helix-like pili since they show three distinct modes of response. For simplicity, we denote these regions i, ii and iii/iv. Region i shows a linear increasing force, similar to when extending a spring. Region ii shows an elongation-independent response. During this extension of the pilus, the force is constant and similar to plastic deformation, for example like extending Silly Putty®. However, in contrast to Silly Putty®, pilus unwinding is fully reversible: the pilus regains its original form when tension is released. This effect is a result of the quaternary structure of a pilus and can be described as sequential unzipping of shaft subunits as shown in Fig. 1.5b-ii, iii. In Region iii/iv the response initially increases linearly but the slope then changes. This change results from overstretching of the head-to-tail bonds (Fig. 1.5b-iv). This particular force response is seen when extending pili expressed by bacteria related to urinary tract infections for example, P, type 1, and F1C, (Fällman et al. 2004; Andersson et al. 2007; Castelain et al. 2011) but is also observed when extending pili expressed by enterotoxic bacteria, for example, CFA/I, CS20, and CS2 (Andersson et al. 2012; Mortezaei et al. 2015a, b).

To interpret force-extension data curves, physical models that describe the bio-mechanical responses of pili are needed. These models can provide information about the structure and its intrinsic properties such as energy levels and bond distances. A successful analytical model that describes the full extension of a helix-like pilus under tensile force is the sticky-chain model (Andersson et al. 2006b). The model is built upon a three-state energy landscape using two sets of rate equations, where each set can be solved analytically under steady-state conditions to predict the elongation of the chain. The predicted force-elongation dependence for unwinding shows excellent agreement with experimental data taken under steady-state conditions for numerous adhesion pili (Andersson et al. 2006b, 2007, 2012; Castelain

et al. 2009b, 2011). By using this model, parameters such as: bond opening length, energy levels and number of subunits in a pilus, can be estimated. In addition, the biomechanical properties of helix-like pili have also been successfully modelled using Monte Carlo simulations (Björnham et al. 2008), rigid multibody simulations (Zakrisson et al. 2015), and steered coarse-grained molecular dynamics simulations (Zhao et al. 2017). Both measurements and physical modelling are essential to improve our knowledge and to understand the intrinsic and molecular behaviour of adhesion organelles under *in vivo* conditions. However, to get the full picture we need to also understand the behaviour of the adhesin.

Bacterial adhesion is mediated by specific receptors located at the tip of the pili that bind to corresponding ligands that are expressed on membrane surfaces of host cells. When bacteria are attached to these host cells and exposed to fluid flow these receptor-ligand bonds are exposed to a tensile force. This force can act destructively on the bond lifetime (that is, the average length of time the receptor-ligand interaction remains intact) thus resulting in bond breaking and bacterial detachment. The lifetime of the receptor-ligand bond complex, involving weak noncovalent interactions, depends in turn directly on the type of bond and applied force. By applying known forces, the lifetime of adhesins can be tested on a single molecule level by repeated exposure of the bond to external forces, thus inducing a series of unbinding events (Rief and Grubmüller 2002). These events can be probed under either constant loads (Abbondanzieri et al. 2005) or by measuring the force at which the bond yields when the force is gradually increased (Merkel et al. 1999). In addition, the type of bond and its lifetime can be measured within flow chambers that provide a continuous fluid flow. Bacterial response to flow is determined by coating the surface of the flow chamber with ligands or host cells and measuring the length of time bacteria pause on the surface with increasing fluid flow.

These single molecule and flow chamber experiments were first applied to *E. coli* bacteria expressing type 1 pili, commonly correlated to urinary tract infections in the bladder, which bind through the adhesin protein FimH (Thomas et al. 2002; Forero et al. 2006; Kalas et al. 2017). Interestingly, these studies show that FimH is a shear-enhanced bond, implying that an applied force within a certain range *enhances* the strength of receptor-ligand interactions. That is, the lifetime of the bond initially grows with the applied force up to a certain characteristic threshold force, whereafter the bond exhibits normal slip behaviour (Isberg and Barnes 2002). This 'catch-bond' property thereby gives bacteria a shear-enhanced stick-and-roll adhesion behaviour when exposed to fluid flow, which is believed to give bacteria several advantages. For example, when the fluid flow is low the weak mode of adhesion may help bacteria to colonize new surfaces, whereas when the fluid flow is strong the shear-enhanced mode results in firm adhesion preventing bacterial detachment (Thomas 2008). This particular catch-bond property has also been shown for the CfaE adhesin at the tip of CFA/I pili, expressed on *E. coli* commonly related to diarrheal disease (Tchesnokova et al. 2010).

Type 1 and CFA/I pili show similarly shaped force-extension curves. Despite different magnitudes of force required to unwind them, both adhesins show catch-bond properties. Thus, with type 1 and CFA/I pili correlated to different pathophysiological niches, it is tempting to ask – How do these biomechanical properties of the shaft and adhesin relate to *in vivo* conditions?

### *1.3.2 Coevolution of the Helix-Like Structure and Its Adhesin?*

*In vivo*, bacteria are in general exposed to strong shear forces imposed by fluid flows such as expulsion of urine, mucosal secretions, blood flow, diarrhea, etc. These forces tend to act as natural defense mechanisms against colonization of pathogenic bacteria, washing away bacteria that are not strongly adhered. These fluidic flows cause drag forces, sometimes of considerable magnitude, which adherent bacteria must sustain to prevent being flushed away from the host. In particular, a bacterium attached to the surface of a host cell can be exposed to severe fluid drag forces with fast time dependent changes in both magnitude and directions originating from high fluid velocities (in the meters per second range) and the peristaltic reflex in, for example, the ureter and colon (Abrams 1997; Vogel et al. 2004; Jin et al. 2010), respectively. In order to manage these fluid forces it is believed that the biomechanics of bacterial pili are critically important and dependent on their biopolymer structure, which in turn is related to the properties of the pilus shaft and the tip adhesin (Forero et al. 2006; Zakrisson et al. 2013).

In general, biopolymers, such as pili, can have mechanical properties that can be related to a macroscopic 'understandable concept': they can be stiff, semi-flexible, or elastic. Helix-like pili, however, show a major attribute that distinguishes them from other known biopolymers, that is, they are elastic-perfectly-plastic. This implies that when exposed to tensile strain they initially show an elastic response that changes into a perfectly-plastic response that is also fully reversible. The force measured during the plastic response is constant with elongation, as seen in Fig. 1.5c-ii. The advantage for a bacterium attached to a surface with a pilus that can elongate under constant force has been investigated using numerical physical modelling (Zakrisson et al. 2012). It was found that unwinding of the pilus significantly reduces the force on the anchor point. This is seen in Fig. 1.6, showing the force on the anchor point for a cell that is exposed to increasing fluid flow velocity while tethered to a surface, via either a stiff polymer or a polymer with biomechanical properties similar to type 1 pili. If the cell is attached with a stiff polymer the force increases linearly with flow velocity, since the drag force is linearly proportional to velocity. However, when the cell is attached with pili, the force on the anchor point is similar to that of the stiff polymer for lower fluid velocities, since the required force needed for unwinding has not been reached. When the fluid velocity increases

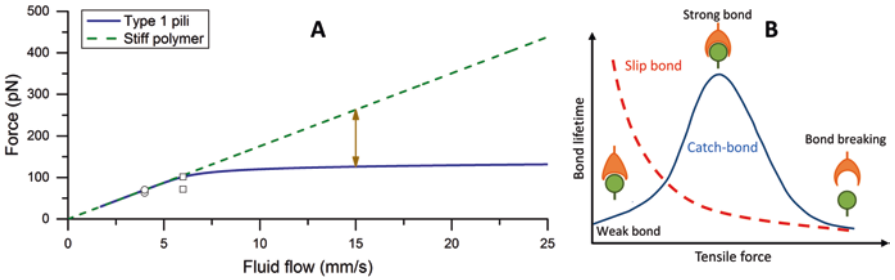


**Fig. 1.6** Relation between shaft biomechanics and properties of an adhesin. (**a**) The drag force as a function of flow for a bacterium attached to a surface with a stiff linker (dashed green) and a type 1 pilus (solid blue). (**b**) Schematic showing the difference between a slip-bond (red dashed curve) and catch-bond (solid blue curve) under tensile force. The lifetime of a slip-bond decreases with applied force whereas a catch-bond shows a short lifetime for low and high forces whereas a long lifetime for moderate forces

and the tensile force is higher than the unwinding force the pilus starts unwinding and the relative velocity of the pilus compared with the fluid velocity decreases, thus reducing the drag force. This reduction of external force on the anchor point is ~50% for flows >15 mm/s, and it is worth noting that unwinding also leads to an upper limit in the maximal force experienced by the receptor-ligand bond, ~120 pN for type 1 pili.

The significance of this constant force response in relation to the lifetime of the adhesin, which is positioned at the tip of the pilus, has been investigated using simulations. Miller et al. used Monte Carlo simulations to model an adhesin-receptor bond linked to three shafts (rods) with different biomechanical properties: stiff, semi-elastic, and uncoilable extensible rod similar to a pilus shaft (Miller et al. 2006). These simulations showed that the properties of the rods altered the lifetime of the receptor bond, that is, a bond linked to a rigid rod survived ~0.5 s, whereas this time increased to ~1 s for a semi-flexible rod and reached ~4 s when the rod could unwind. This was further investigated by Zakrisson et al. (Zakrisson et al. 2013), showing that unwinding is advantageous for a type 1 pili equipped with a FimH adhesin that is attached to a ligand. The work showed that even if the bacteria are exposed to very high flows, the shaft of the type 1 pilus can reduce the force experienced to a value similar to that of the critical force of FimH (~100 pN) and thereby prolong the adhesion lifetime. Thus, unwinding can significantly prolong the lifetime of the bacteria-host bond and it is therefore plausible that pili mechanics and adhesin-receptor interactions are optimized to each other, and that there are significant advantages for piliated bacteria in rapidly changing fluidic environments (Zakrisson et al. 2013).

### 1.3.3 *Relation Between Unwinding Force and* in vivo *Environment*

Bacteria can survive in very different environments since they sense and adapt to changes in the external environment by altering the expression of their genes for increased fitness (Rediers et al. 2005). When analyzing and clustering the unwinding force of pili according to their environment – intestinal, urinary tract, and respiratory tract – they clearly group into distinct force categories as seen in Fig. 1.7. The data indicate that pili commonly expressed by UPEC in the urinary tract require a twofold higher unwinding force (Andersson et al. 2007; Castelain et al. 2011) than that of pili expressed by ETEC in the intestine (Andersson et al. 2012; Mortezaei et al. 2015a, b). Moreover, unwinding of respiratory tract pili (Mu et al. 2002; Castelain et al. 2009a; Chen et al. 2011) requires a greater than fivefold force increase in comparison to intestinal pili. A comparison of the amino acids for ETEC expressing CS20 pili with the sequences of other pili shows that; even though CS20 is highly genetically similar to urinary tract pili they share more similar biomechanical properties with CS2 and CFA/I pili that are also expressed in the intestine (Mortezaei et al. 2015a). These data suggest that there is an organ-specific adaptation of pili mechanics, and that this mechanical function is an important part of *E. coli* pathogenesis, allowing bacteria to overcome hydrodynamic challenges in different environments. Also, these data show that a simple amino acid comparison of the major structural pilin proteins of different pili does not correlate with the pathophysiological niche of each *E. coli* strain.

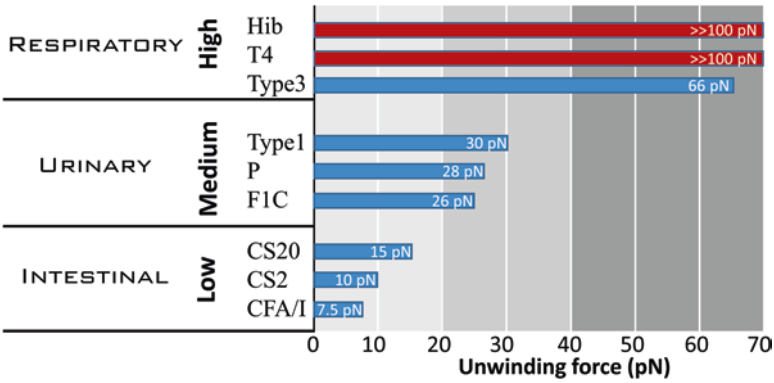


**Fig. 1.7** Clustering adhesion pili according to their niche environment. Environment where pili type is commonly found vs. the force required to unwind their helical structure. Red bars indicate that these pili have never been experimentally unwound

## 1.4 Conclusions

Each adhesion pilus type is anchored into the bacterial outer membrane via a pore-containing 'usher' protein. First through the usher is the adhesin subunit followed by pilin subunits in a top-down fashion. The adhesin works as a lectin to adhere bacteria to the hostcell's surface, with each adhesin binding to a specific surface-sugar target. Multiple pilin subunits (approximately 1000) are then added through the usher and linked to the growing pilus filament by donor strand exchange. Strong non-covalent subunit/subunit interactions produce a linear polymer of the major structural pilin subunits. Additional interactions between pilins allow the pilus filament to wind into its helical form, and also to reversibly unwind and rewind with changing velocity and direction of fluid flows in the host environment.

For progression of disease, each pilus type must retain sufficient structural integrity to sustain adhesion between the bacterium and its target cell under diverse environments. For example, P-pili expressed on UPEC are optimized for survival under fluid flow in the urinary tract, while CFA/I pili expressed on pathogenic ETEC are optimized to sustain binding in the more turbulent environment of the gut. This is demonstrated by the twofold lower unwinding force that is required by CFA/I pili due to the higher velocity and reversing directions of the fluid flow in the gut that could otherwise break the adhesin ligand interaction. Breaking of this interaction would cause the bacteria to be unable to colonize in their niche environment.

We have made a case here that there is an intimate relationship between the biophysical properties of pili and their preferred environmental milieu. Adhesion pili show biomechanical properties that appear to be optimized to overcome hydrodynamic challenges in different environments since they modulate the tensile force on the adhesin expressed at the tip of the biopolymer. These unique properties are a result of the assembly process where the micro-machinery organizes pilin subunits into a helix-like quaternary structure that can unwind in a sequential manner when tensile force is applied. Better understanding of both the adhesion and micro-machinery processes can therefore help us develop new therapeutics for disease prevention and treatment through disruption of pilus assembly or pilus-host interactions.

## References

Abbondanzieri EA, Greenleaf WJ, Shaevitz JW, Landick R, Block SM (2005) Direct observation of base-pair stepping by RNA polymerase. Nature 438:460–465. https://doi.org/10.1038/nature04268

Abrams P (1997) Urodynamics. Springer – Verlag, London

Andersson M, Fällman E, Uhlin BE, Axner O (2006a) Dynamic force spectroscopy of E. coli P pili. Biophys J 91:2717–2725. https://doi.org/10.1529/biophysj.106.087429

Andersson M, Fällman E, Uhlin BE, Axner O (2006b) A sticky chain model of the elongation and unfolding of Escherichia coli P pili under stress. Biophys J 90:1521–1534. https://doi.org/10.1529/biophysj.105.074674

Andersson M, Uhlin BE, Fällman E (2007) The biomechanical properties of E. coli pili for urinary tract attachment reflect the host environment. Biophys J 93:3008–3014. https://doi.org/10.1529/biophysj.107.110643

Andersson M, Björnham O, Svantesson M, Badahdah A, Uhlin BE, Bullitt E (2012) A structural basis for sustained bacterial adhesion: biomechanical properties of CFA/I pili. J Mol Biol 415:918–928

Ashkin A, Dziedzic JM, Yamane T (1987) Optical trapping and manipulation of single cells using infrared laser beams. Nature 330:769–771. https://doi.org/10.1038/330769a0

Baga M, Norgren M, Normark S (1987) Biogenesis of E. coli Pap pili: papH, a minor pilin subunit involved in cell anchoring and length modulation. Cell 49:241–251

Berg-Sørensen K, Flyvbjerg H (2004) Power spectrum analysis for optical tweezers. Rev Sci Instrum 75:594. https://doi.org/10.1063/1.1645654

Björnham O, Axner O, Andersson M (2008) Modeling of the elongation and retraction of Escherichia coli P pili under strain by Monte Carlo simulations. Eur Biophys J 37:381–391. https://doi.org/10.1007/s00249-007-0223-6

Björnham O, Nilsson H, Andersson M, Schedin S (2009) Physical properties of the specific PapG-galabiose binding in E. coli P pili-mediated adhesion. Eur Biophys J 38:245–254. https://doi.org/10.1007/s00249-008-0376-y

Bullitt E, Makowski L (1995) Structural polymorphism of bacterial adhesion pili. Nature 373:164–167

Busch A, Waksman G (2012) Chaperone-usher pathways: diversity and pilus assembly mechanism. Philos Trans R Soc B Biol Sci 367:1112–1122. https://doi.org/10.1098/rstb.2011.0206

Castelain M, Koutris E, Andersson M, Wiklund K, Björnham O, Schedin S, Axner O (2009a) Characterization of the biomechanical properties of T4 pili expressed by Streptococcus pneumoniae – a comparison between helix-like and open coil-like pili. Chem Phys Chem 10:1533–1540. https://doi.org/10.1002/cphc.200900195

Castelain M, Sjöström AE, Fällman E, Uhlin BE, Andersson M (2009b) Unfolding and refolding properties of S pili on extraintestinal pathogenic Escherichia coli. Eur Biophys J 39:1105–1115. https://doi.org/10.1007/s00249-009-0552-8

Castelain M, Ehlers S, Klinth JE, Lindberg S, Andersson M, Uhlin BE, Axner O (2011) Fast uncoiling kinetics of F1C pili expressed by uropathogenic Escherichia coli are revealed on a single pilus level using force-measuring optical tweezers. Eur Biophys J 40:305–316. https://doi.org/10.1007/s00249-010-0648-1

Chen F-J, Chan C-H, Huang Y-J, Liu K-L, Peng H-L, Chang H-Y, Liou G-G, Yew T-R, Liu C-H, Hsu KY, Hsu L (2011) Structural and mechanical properties of Klebsiella pneumoniae type 3 fimbriae. J Bacteriol 193:1718–1725. https://doi.org/10.1128/JB.01395-10

Choudhury D, Thompson A, Stojanoff V, Langermann S, Pinkner J, Hultgren SJ, Knight SD (1999) X-ray structure of the FimC-FimH chaperoneadhesin complex from uropathogenic Escherichia coli. Science 285:1061–1066. https://doi.org/10.1126/science.285.5430.1061

Dodson KW, Jacob-Dubuisson F, Striker RT, Hultgren SJ (1993) Outer-membrane PapC molecular usher discriminately recognizes periplasmic chaperone-pilus subunit complexes. Proc Natl Acad Sci USA 90:3670–3674

Dodson KW, Pinkner JS, Rose T, Magnusson G, Hultgren SJ, Waksman G (2001) Structural basis of the interaction of the pyelonephritic E. coli adhesin to its human kidney receptor. Cell 105:733–743

Evans DG, Satterwhite TK, Evans DJ, DuPont HL (1978) Differences in serological responses and excretion patterns of volunteers challenged with enterotoxigenic Escherichia coli with and without the colonization factor antigen. Infect Immun 19:883–888

Fällman E, Schedin S, Jass J, Andersson M, Uhlin BE, Axner O (2004) Optical tweezers based force measurement system for quantitating binding interactions: system design and application for the study of bacterial adhesion. Biosens Bioelectron 19:1429–1437. https://doi.org/10.1016/j.bios.2003.12.029

Forero M, Yakovenko O, Sokurenko EV, Thomas WE, Vogel V (2006) Uncoiling mechanics of Escherichia coli type I fimbriae are optimized for catch bonds. PLoS Biol 4:1509–1516. https://doi.org/10.1371/journal.pbio.0040298

Fronzes R, Remaut H, Waksman G (2008) Architectures and biogenesis of non-flagellar protein appendages in Gram-negative bacteria. EMBO J 27:2271–2280. https://doi.org/10.1038/emboj.2008.155

Geibel S, Procko E, Hultgren SJ, Baker D, Waksman G (2013) Structural and energetic basis of folded-protein transport by the FimD usher. Nature 496:243–246. https://doi.org/10.1038/nature12007

Hospenthal MK, Redzej A, Dodson K, Ukleja M, Frenz B, Rodrigues C, Hultgren SJ, DiMaio F, Egelman EH, Waksman G (2016) Structure of a chaperone-usher pilus reveals the molecular basis of rod uncoiling. Cell 164:269–278. https://doi.org/10.1016/j.cell.2015.11.049

Hospenthal MK, Costa TRD, Waksman G (2017) A comprehensive guide to pilus biogenesis in Gram-negative bacteria. Nat Rev Microbiol 15:365–379. https://doi.org/10.1038/nrmicro.2017.40. PMID: 28496159

Isberg RR, Barnes P (2002) Dancing with the host; flow-dependent bacterial adhesion. Cell 110:1–4

Jacob-Dubuisson F, Striker R, Hultgren SJ (1994) Chaperone-assisted self-assembly of pili independent of cellular energy. J Biol Chem 269:12447–12455

Jin Q, Zhang X, Li X, Wang J (2010) Dynamics analysis of bladder-urethra system based on CFD. Front Mech Eng China 5:336–340. https://doi.org/10.1007/s11465-010-0027-8

Jones CH, Pinkner JS, Nicholes AV, Slonim LN, Abraham SN, Hultgren SJ (1993) FimC is a periplasmic PapD-like chaperone that directs assembly of type 1 pili in bacteria. Proc Natl Acad Sci USA 90:8397–8401. PMID: 8104335. PMCID: PMC47363

Kalas V, Pinkner JS, Hannan TJ, Hibbing ME, Dodson KW, Holehouse AS, Zhang H, Tolia NH, Gross ML, Pappu RV, Janetka J, Hultgren SJ (2017) Evolutionary fine-tuning of conformational ensembles in FimH during host-pathogen interactions. Sci Adv 3:e1601944. https://doi.org/10.1126/sciadv.1601944

Kuehn MJ, Normark S, Hultgren SJ (1991) Immunoglobulin-like PapD chaperone caps and uncaps interactive surfaces of nascently translocated pilus subunits. Proc Natl Acad Sci 88:10586–10590

Levine MM, Nalin DR, Hoover DL, Bergquist EJ, Hornick RB, Young CR (1979) Immunity to enterotoxigenic Escherichia coli. Infect Immun 23:729–736

Li H, Qian L, Chen Z, Thibault D, Liu G, Liu T, Thanassi DG (2004) The outer membrane usher forms a twin-pore secretion complex. J Mol Biol 344:1397–1407. https://doi.org/10.1016/j.jmb.2004.10.008

Merkel R, Nassoy P, Leung A, Ritchie K, Evans E (1999) Energy landscapes of receptor-ligand bonds explored with dynamic force spectroscopy. Nature 397:50–53. https://doi.org/10.1038/16219

Miller E, Garcia T, Hultgren SJ, Oberhauser AF (2006) The mechanical properties of E. coli type 1 pili measured by atomic force microscopy techniques. Biophys J 91:3848–3856. https://doi.org/10.1529/biophysj.106.088989

Mortezaei N, Epler CR, Shao PP, Shirdel M, Singh B, McVeigh A, Uhlin BE, Savarino SJ, Andersson M, Bullitt E (2015a) Structure and function of enterotoxigenic Escherichia coli fimbriae from differing assembly pathways. Mol Microbiol 95:116–126. https://doi.org/10.1111/mmi.12847

Mortezaei N, Singh B, Zakrisson J, Bullitt E, Andersson M (2015b) Biomechanical and structural features of CS2 fimbriae of enterotoxigenic Escherichia coli. Biophys J 109:49–56. https://doi.org/10.1016/j.bpj.2015.05.022

Mu X-Q, Egelman EH, Bullitt E (2002) Structure and function of Hib pili from Haemophilus influenzae type b. J Bacteriol 184:4868. https://doi.org/10.1128/JB.184.17.4868

Mulvey MA, Lopez-Boado YS, Wilson CL, Roth R, Parks WC, Heuser J, Hultgren SJ (1998) Induction and evasion of host defenses by type 1- piliated uropathogenic Escherichia coli. Science 282:1494–1497. https://doi.org/10.1126/science.282.5393.1494

Nishiyama M, Horst R, Eidam O, Herrmann T, Ignatov O, Vetsch M, Bettendorff P, Jelesarov I, Grütter MG, Wüthrich K, Glockshuber R, Capitani G (2005) Structural basis of chaperone-subunit complex recognition by the type 1 pilus assembly platform FimD. EMBO J 24:2075–2086. https://doi.org/10.1038/sj.emboj.7600693

Nuccio S-P, Bäumler AJ (2007) Evolution of the chaperone/usher assembly pathway: fimbrial classification goes Greek. Microbiol Mol Biol Rev 71:551–575. https://doi.org/10.1128/MMBR.00014-07

Otto M (2014) Physical stress and bacterial colonization. FEMS Microbiol Rev 38:1250. https://doi.org/10.1111/1574-6976.12088

Phan G, Remaut H, Wang T, Allen WJ, Pirker KF, Lebedev A, Henderson NS, Geibel S, Volkan E, Yan J, Kunze MB, Pinkner JS, Ford B, Kay CWM, Li H, Hultgren SJ, Thanassi DG, Waksman G (2011) Crystal structure of the FimD usher bound to its cognate FimC-FimH substrate. Nature 474:49–53. https://doi.org/10.1038/nature10109

Rediers H, Rainey PB, Vanderleyden J, De Mot R (2005) Unraveling the secret lives of bacteria: use of in vivo expression technology and differential fluorescence induction promoter traps as tools for exploring niche-specific gene expression. Microbiol Mol Biol Rev 69:217–261. https://doi.org/10.1128/MMBR.69.2.217

Rief M, Grubmüller H (2002) Force spectroscopy of single biomolecules. ChemPhysChem 3:255–261. doi:10.1002/1439-7641(20020315)3:3<255::AID-CPHC255>3.0.CO;2-M

Roberts JA, Marklund BI, Ilver D, Haslam D, Kaack MB, Baskin G, Louis M, Mollby R, Winberg J, Normark S (1994) The gal(alpha 1-4)gal-specific tip adhesin of Escherichia Coli P-fimbriae is needed for pyelonephritis to occur in the normal urinary tract. Proc Natl Acad Sci U S A 91:11889–11893

Sakellaris H, Balding DP, Scott JR (1996) Assembly proteins of CS1 pili of enterotoxigenic Escherichia coli. Mol Microbiol 21:529–541

Sakellaris H, Scott JR (1998) New tools in an old trade: CS1 pilus morphogenesis. Mol Microbiol 30:681–687. https://doi.org/10.1046/j.1365-2958.1998.01088.x

Sauer F, Fütterer K, Pinkner JS, Dodson K, Hultgren SJ, Waksman G (1999) Structural basis of chaperone function and pilus biogenesis. Science 285:1058–1061. https://doi.org/10.1126/science.285.5430.1058

So SS, Thanassi DG (2006) Analysis of the requirements for pilus biogenesis at the outer membrane usher and the function of the usher C-terminus. Mol Microbiol 60:364–375. https://doi.org/10.1111/j.1365-2958.2006.05111.x

Soto GE, Hultgren SJ (1999) Bacterial adhesins: common themes and variations in architecture and assembly. J Bacteriol 181:1059–1071

Tchesnokova V, McVeigh AL, Kidd B, Yakovenko O, Thomas WE, Sokurenko EV, Savarino SJ (2010) Shear-enhanced binding of intestinal colonization factor antigen I of enterotoxigenic Escherichia coli. Mol Microbiol 76:489–502. https://doi.org/10.1111/j.1365-2958.2010.07116.x

Thanassi DG, Saulino ET, Hultgren SJ (1998) The chaperone/usher pathway: a major terminal branch of the general secretory pathway. Curr Opin Microbiol 1:223–231. https://doi.org/10.1016/S1369-5274(98)80015-5

Thanassi DG, Bliska JB, Christie PJ (2012) Surface organelles assembled by secretion systems of Gram-negative bacteria: diversity in structure and function. FEMS Microbiol Rev 36:1046–1082. https://doi.org/10.1111/j.1574-6976.2012.00342.x

Thomas WE (2008) Catch bonds in adhesion. Annu Rev Biomed Eng 10:39–57. https://doi.org/10.1146/annurev.bioeng.10.061807.160427

Thomas WE, Trintchina E, Forero M, Vogel V, Sokurenko EV (2002) Bacterial adhesion to target cells enhanced by shear force. Cell 109:913–923

Vogel A, Elmabsout B, Gintz D (2004) Modélisation du champ des vitesses de l'urine dans un bolus urétéral. Comptes Rendus Mécanique 332:737–742. https://doi.org/10.1016/j.crme.2004.03.017

Werneburg GT, Henderson NS, Portnoy EB, Sarowar S, Hultgren SJ, Li H, Thanassi DG (2015) The pilus usher controls protein interactions via domain masking and is functional as an oligomer. Nat Struct Mol Biol 22:540–546. https://doi.org/10.1038/nsmb.3044

Zakrisson J, Wiklund K, Axner O, Andersson M (2012) Helix-like biopolymers can act as dampers of force for bacteria in flows. Eur Biophys J 41:551–560. https://doi.org/10.1007/s00249-012-0814-8

Zakrisson J, Wiklund K, Axner O, Andersson M (2013) The shaft of the type 1 fimbriae regulates an external force to match the FimH catch bond. Biophys J 104:2137–2148. https://doi.org/10.1016/j.bpj.2013.03.059

Zakrisson J, Wiklund K, Servin M, Axner O, Lacoursière C, Andersson M (2015) Rigid multibody simulation of a helix-like structure – the dynamics of bacterial adhesion pili. Eur Biophys J 44(5):291–300. https://doi.org/10.1007/s00249-015-1021-1

Zav'yalov VP, Zav'yalova GA, Denesyuk AI, Gaestel M, Korpela T (1995) Structural and functional homology between periplasmic bacterial molecular chaperones and small heat shock proteins. FEMS Immunol Med Microbiol 11:265–272

Zavialov AV, Tischenko VM, Fooks LJ, Brandsdal BO, Aqvist J, Zav'yalov VP, Macintyre S, Knight SD (2005) Resolving the energy paradox of chaperone/usher-mediated fibre assembly. Biochem J 389:685–694. https://doi.org/10.1042/BJ20050426

Zhao X, Liu Y, Guo Z, Zhang Y, Li Y, Liu W (2017) Mechanical response and deformation mechanics of type IV pili investigated using steered coarse-grained molecular dynamics simulation. J Biomech 56:97. https://doi.org/10.1016/j.jbiomech.2017.03.013

# Chapter 2
# Microbial Rhodopsins

**Ivan Gushchin and Valentin Gordeliy**

**Abstract** Microbial rhodopsins (MRs) are a large family of photoactive membrane proteins, found in microorganisms belonging to all kingdoms of life, with new members being constantly discovered. Among the MRs are light-driven proton, cation and anion pumps, light-gated cation and anion channels, and various photoreceptors. Due to their abundance and amenability to studies, MRs served as model systems for a great variety of biophysical techniques, and recently found a great application as optogenetic tools. While the basic aspects of microbial rhodopsins functioning have been known for some time, there is still a plenty of unanswered questions. This chapter presents and summarizes the available knowledge, focusing on the functional and structural studies.

**Keywords** Bacteriorhodopsin · Ion pump · Ion channel · Photoactive proteins · X-ray crystallography · Optogenetics

## 2.1 Introduction

Microbial rhodopsins are a large family of photoactive membrane proteins found in bacteria, archaea, eukaryota and viruses (Ernst et al. 2014; Grote et al. 2014). The proteins are composed of seven transmembrane α-helices, labeled A to G, connected by three intracellular and three extracellular loops (Fig. 2.1). Whereas overall the microbial rhodopsin fold is very well conserved among the family members, the

I. Gushchin (✉)
Moscow Institute of Physics and Technology, Dolgoprudniy, Russia
e-mail: ivan.gushchin@phystech.edu

V. Gordeliy (✉)
Moscow Institute of Physics and Technology, Dolgoprudniy, Russia

University of Grenoble Alpes, CEA, CNRS, IBS, Grenoble, France

Institute of Complex Systems (ICS), ICS-6: Structural Biochemistry, Research Centre Jülich, Jülich, Germany
e-mail: valentin.gordeliy@ibs.fr



J. R. Harris, E. J. Boekema (eds.), *Membrane Protein Complexes: Structure and Function*, Subcellular Biochemistry 87,
https://doi.org/10.1007/978-981-10-7757-9_2

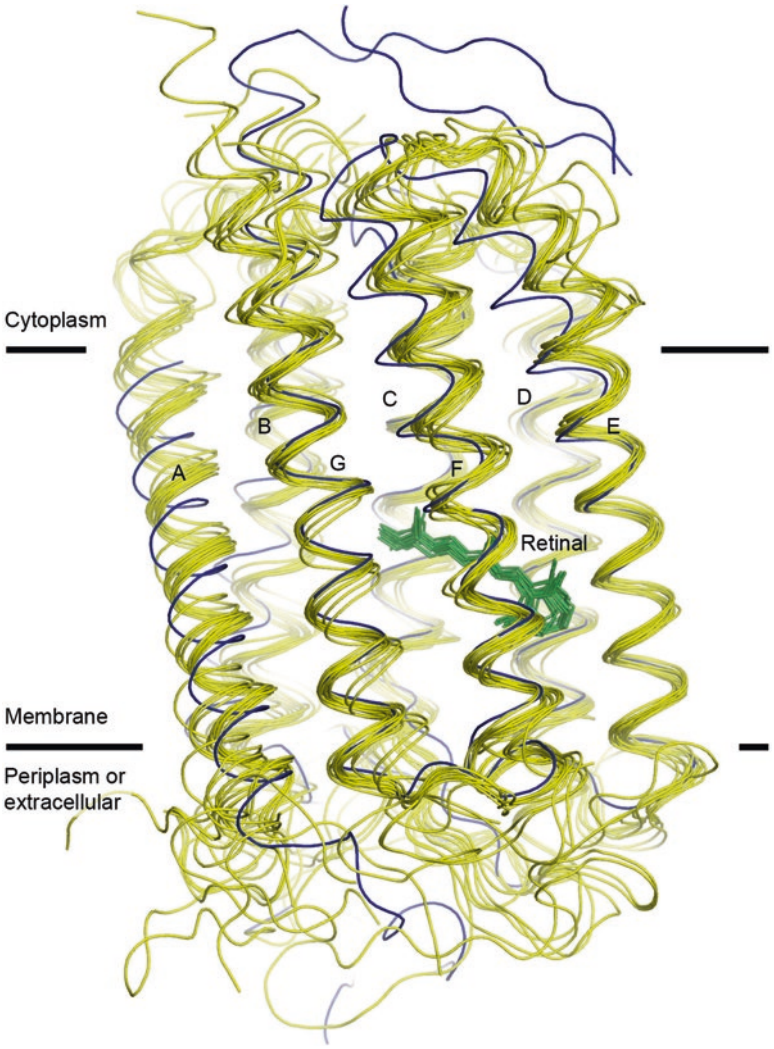


**Fig. 2.1** Superposition of known microbial rhodopsin structures. The retinal moieties are shown in green. Approximate membrane boundaries are shown using black lines. Channelrhodopsin structure (blue) differs the most from other proteins. Most variation is observed in the exposed loop regions and in the positions of the helices A and B

position of the helix A is relatively variable. Among the loops, the B-C loop is usually the longest one, and its conformation changes most among the different microbial rhodopsins. Microbial rhodopsins often form dimers, trimers, pentamers, hexamers and higher-order assemblies, such as purple membrane. In pumps and channels, the helices usually envelop a series of polar, often water-filled cavities, constituting the ion translocation pathway. In sensors, the pathway is often broken.

The unifying feature of microbial rhodopsins is the cofactor retinal residing in the middle of the protein (Fig. 2.1) that is covalently bound via a Schiff base to the side chain of a lysine residue of the helix G. The retinal imparts to the microbial rhodopsins the ability to utilize light for their photo-receptive function. Microbial rhodopsins reveal significant color adaptation, with absorption maxima of stable states ranging from 380/480 nm for histidine kinase rhodopsin I (Luck et al. 2012) to ~587 nm for natural channelrhodopsin Chrimson (Klapoetke et al. 2014) and 628 nm for evolved fluorescent protein (McIsaac et al. 2014).

In absence of illumination, the retinal Schiff base is protonated, and the retinal itself is usually in the all-*trans* conformation. For some of the proteins, so-called dark adaptation is observed, where retinal partially converts to 13-*cis* 15-*syn* conformation in the dark. Absorption of a light photon causes isomerization of the retinal and launches a series of thermally driven conformational transitions in the protein between its metastable states, called the photocycle. Conformational changes are usually accompanied by changes in the absorption spectrum, so the intermediate states are often referred to by their absorption maximum. However, it should be noted that some structural changes are spectrally silent, and also some metastable intermediates are in fact mixtures of several states with different absorption spectra (Chizhov et al. 1996). The intermediate states are labeled in alphabetical order, such as J, K, L, M, N and O. J, K and L are usually early intermediates observed on microsecond timescales. In M, the 13-*cis* retinal Schiff base is deprotonated, and the absorption maximum is significantly blue-shifted towards ~410 nm. Photocycles of some MRs lack the M state due to absence of protein acceptor residues in the vicinity of retinal. In N and O states, the Schiff base is reprotonated, but the protein has not completely relaxed into the ground state yet. Altogether, structural rearrangements during the photocycle result in ion translocation, opening of a channel, or generating a signal.

The first member of the microbial rhodopsins family, and the most studied to date, is the light-driven proton pump bacteriorhodopsin (BR) from *Halobacterium salinarum* (Lanyi 2004). It was discovered in 1971 as the major constituent of the *H.salinarum* purple membrane (Oesterhelt and Stoeckenius 1971). While *Hs*BR is the most studied microbial rhodopsin, many other proteins of this family have been identified. Soon after the discovery of *Hs*BR, a light-driven chloride pump was identified in the membrane of *H.salinarum*, dubbed halorhodopsin (Matsuno-Yagi and Mukohata 1977; Schobert and Lanyi 1982). Although no other ion pumping proteins were detected in *H. salinarum*, two light sensors with different functions were found: sensory rhodopsin I, responsible for both attractant and repellent responses (Hildebrand and Dencher 1975; Spudich and Spudich 1982; Bogomolni and Spudich 1982; Spudich and Bogomolni 1984), and sensory rhodopsin II, responsible for the repellent response and also known as phoborhodopsin (Takahashi et al. 1985; Tomioka et al. 1986; Wolff et al. 1986; Marwan and Oesterhelt 1987). Similar proteins were also found in other haloalkaliphilic archaea (Bivin and Stoeckenius 1986). Sometimes, as many as six different MR genes are found in a single organism (Fu et al. 2010).

The advent of metagenomics and sequencing of environmental samples that contained uncultivated bacteria marked a new era in microbial rhodopsin research. In 2000, a bacterial rhodopsin gene, coding for a functional protein, was discovered in a genomic fragment from a marine γ-proteobacteria, collected in Californian Monterey Bay (Béjà et al. 2000). Soon, it was demonstrated that the protein, dubbed proteorhodopsin, is indeed present in oceanic bacteria (Béjà et al. 2001). It also appeared that the proteins from this microbial rhodopsin subfamily were spectrally tuned to different habitats – that is, they absorbed light at different wavelengths in accordance with illumination available in the environment (Béjà et al. 2001). Since then, the proteorhodopsin genes were found to be distributed among divergent bacterial taxa (de la Torre et al. 2003; Bamann et al. 2014; Pinhassi et al. 2016), even as extreme as Siberian permafrost bacteria (Petrovskaya et al. 2010, 2015).

Besides proteorhodopsins, different kinds of sensory rhodopsins have been discovered in bacteria. *Salinibacter ruber* was found to possess a sensory rhodopsin I-like protein (Mongodin et al. 2005; Kitajima-Ihara et al. 2008) which passes the signal through its cognate transducer (Sudo et al. 2009), similarly to archaeal sensory rhodopsins. At the same time, *Anabaena* sensory rhodopsin is different in that its transducer is a soluble protein that dissociates upon illumination and affects gene expression directly (Vogeley et al. 2004). Finally, bacterial sodium (Inoue et al. 2013), chloride (Yoshizawa et al. 2014) and even sulfate (Niho et al. 2017) pumps have been now discovered.

The presence of microbial rhodopsins is not limited to bacteria and archaea as they were also found, for example, in fungi (Brown 2004; Waschuk et al. 2005), algae (Hegemann 2008) and giant viruses infecting unicellular eukaryotes (Yutin and Koonin 2012). Algal channelrhodopsins, which open a cation channel upon illumination, became of extreme importance in the recently developed field of optogenetics (Deisseroth 2011; Zhang et al. 2011) and were extensively modified to achieve some useful properties such as anion conduction (Berndt et al. 2014; Hayashi 2014; Wietek et al. 2014). Finally, enzyme-fused MRs such as algal histidine kinase rhodopsins have been identified (Kateriya et al. 2004; Luck et al. 2012).

Due to the richness and versatility of performed functions, and overall stability and easy expression, MRs have been studied very well, and have been the model membrane proteins for most of the biophysical techniques, including UV, visual and IR spectroscopy, electron microscopy, X-ray crystallography, NMR and AFM, as well as for various electrophysiology approaches. Below, we review the available functional and structural studies of currently known microbial rhodopsins, and describe briefly their application in optogenetics.

Comparison of the available structures is presented in the Fig. 2.1 and the corresponding information is summarized in the Table 2.1. The phylogenetic tree showing the relations between the important microbial rhodopsins and characteristic residues is presented in the Fig. 2.2.

**Table 2.1** Microbial rhodopsins, for which the atomistic structures have been determined

| Name of the protein | Abbreviation | PDB ID | Resolution, Å | References |
|---|---|---|---|---|
| Archaeal rhodopsins | | | | |
| Bacteriorhodopsin | BR, *Hs*BR | 1C3W | 1.55 | Luecke et al. (1999) |
| Archaerhodopsin 1 | aR-1 | 1UAZ | 3.4 | Enami et al. (2006) |
| Archaerhodopsin 2 | aR-2 | 2EI4 | 2.1 | Yoshimura and Kouyama (2008) |
| Deltarhodopsin 3 | dR-3 | 4FBZ | 2.7 | Zhang et al. (2013) |
| *Haloarcula marismortui* bacteriorhodopsin I | *Hm*BRI | 4PXK | 2.5 | Shevchenko et al. (2014) |
| Cruxrhodopsin-3 | cR-3 | 4L35 | 2.1 | Chan et al. (2014) |
| *Haloquadratum walsbyi* bacteriorhodopsin | *Hw*BR | 4QI1 | 1.85 | Hsu et al. (2015) |
| *Halobacterium salinarum* halorhodopsin | HR, *Hs*HR | 1E12 | 1.8 | Kolbe et al. (2000) |
| *Natronomonas pharaonis* halorhodopsin | *Np*HR | 3A7K | 2.0 | Kouyama et al. (2010) |
| *Natronomonas pharaonis* sensory rhodopsin II | *Np*SRII | 1H68 | 2.1 | Luecke et al. (2001) and Royant et al. (2001) |
| Bacterial rhodopsins | | | | |
| *Anabaena* sensory rhodopsin | ASR | 1XIO | 2.0 | Vogeley et al. (2004) |
| Xanthorhodopsin | XR | 3DDL | 1.9 | Luecke et al. (2008) |
| *Exiguobacterium sibiricum* rhodopsin | ESR | 4HYJ | 2.3 | Gushchin et al. (2013a) |
| Proteorhodopsin from Med12 | PR | 4JQ6 | 2.3 | Ran et al. (2013) |
| Proteorhodopsin from HOT75 | PR | 4KLY | 2.7 | Ran et al. (2013) |
| *Krokinobacter eikastus* rhodopsin 2 | KR2 | 4XTN | 1.45 | Gushchin et al. (2015) and Kato et al. (2015a) |
| *Nonlabens marinus* S1-08$^{T}$ chloride-pumping rhodopsin | NM-R3, ClR | 5G28, 5B2N | 1.57 | Hosaka et al. (2016) and Kim et al. (2016) |
| Thermophilic rhodopsin | TR | 5AZD | 2.8 | Tsukamoto et al. (2016) |
| Eukaryotic microbial rhodopsins | | | | |
| *Acetabularia* rhodopsin 2 | AR2 | 3AM6 | 3.2 | Wada et al. (2011) |
| Chimera of *Chlamydomonas reinhardtii* channelrhodopsins 1 and 2 | ChR | 3UG9 | 2.3 | Kato et al. (2012) |

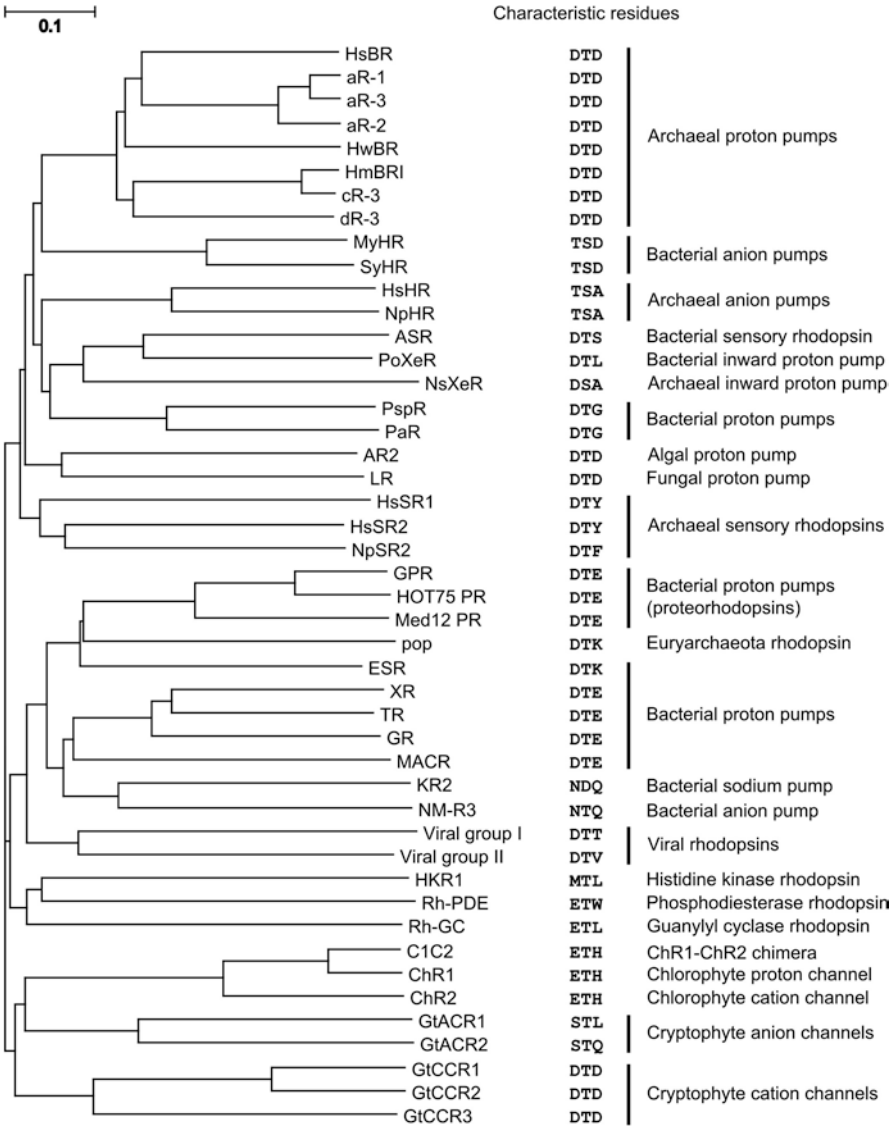


**Fig. 2.2** Phylogenetic tree of prominent microbial rhodopsins. Characteristic residues homologous to Asp-85 (proton acceptor), Thr-89 and Asp-96 (proton donor) in bacteriorhodopsin's helix C, are shown

## 2.2 Bacteriorhodopsin: Historical Perspective

Bacteriorhodopsin, the light-driven proton pump of *Halobacterium salinarum*, was discovered as the major constituent of its so-called purple membrane (Oesterhelt and Stoeckenius 1971). Due to its high abundance and ease of purification, BR can

be produced in large quantities. This property made it the model membrane protein, extensively used for development of numerous biophysical techniques. One of the first applications of bacteriorhodopsin was in providing evidence for the Mitchell's "chemiosmotic theory", according to which the proton gradient across the cell membrane can be utilized for ATP production (Racker and Stoeckenius 1974). Later, bacteriorhodopsin served as a model system for development of the electron microscopy techniques, which provided the first glimpse into its structure at the resolution of 7 Å (Henderson and Unwin 1975). After this, the resolution was gradually improved to almost-atomic (Henderson et al. 1990; Grigorieff et al. 1996).

At the same time, bacteriorhodopsin was extensively studied using different optical techniques such as UV-Visual (Lozier et al. 1975; Dencher and Wilms 1975), FTIR (Bagley et al. 1982) and resonance Raman (Braiman and Mathies 1982) spectroscopy. It was determined that upon absorption of a light photon the visual light absorption spectrum of bacteriorhodopsin undergoes a series of transformations, called the photocycle. Based on the absorption spectra, presence of several interconverting quasi-stable states, called K, L, M, N and O, was postulated (Chizhov et al. 1996). The spectrum of the M-state differs the most from the ground state spectrum as the retinal is in the 13-*cis* state and deprotonated in the M-state. Apart from the main photocycle, there are also states P and Q that can be induced by a second photon absorption. Finally, in the absence of illumination, thermal isomerization of the retinal from the all-*trans* to 13-*cis* 15-*syn* conformation is possible that gives rise to a so-called "dark" photocycle, which doesn't result in a proton translocation (Hofrichter et al. 1989).

While bacteriorhodopsin did not become the first membrane protein for which an X-ray crystallographic structure could be obtained (it was the *Rhodopseudomonas viridis* photosynthetic reaction center in 1985; Deisenhofer et al. 1985), experiments with it gave rise to a plethora of non-traditional crystallization techniques, where different lipidic phases are utilized as a crystallization media. Among them are crystallization in the lipidic cubic phase, the so-called *in meso* crystallization (Landau and Rosenbusch 1996; Pebay-Peyroula et al. 1997), crystallization from bicelles (Faham and Bowie 2002) and crystallization from vesicles (Takeda et al. 1998). Initially, these crystallization methods were considered too difficult for routine application. However, advent of automatization (Cherezov et al. 2004) and successful determination of the first non-rhodopsin GPCR structure (Cherezov et al. 2007) resulted in widespread adoption of *in meso* crystallization. More recently, BR was used to demonstrate suitability of steroid-based facial amphiphiles for membrane protein stabilization and crystallization (Lee et al. 2013). Amphipol-trapped or nanodisc-inserted BR could be successfully transferred to lipidic mesophase for traditional crystallization (Polovinkin et al. 2014; Nikolaev et al. 2017), as well as the closely related protein *Hw*BR solubilized using styrene–maleic acid (SMA) copolymers (Broecker et al. 2017). Finally, serial crystallography approaches have been tested using BR (Zander et al. 2015; Nogly et al. 2015), and its conformational changes were visualized using time-resolved serial femtosecond crystallography at an X-ray free electron laser (Nango et al. 2016).

Other structural techniques have also been applied to bacteriorhodopsin. Magic angle spinning NMR studies of $^{13}C$ labeled BR were used to get insight into protonation states of important aspartic acid residues (Engelhard et al. 1989). Neutron diffraction experiments on the deuterated BR samples provided information about the motions of BR helices during the photocycle (Dencher et al. 1989). Spin label attachment at the specific BR sites allowed probing of the microenvironment by the electron spin resonance technique (Altenbach et al. 1990). Finally, various atomic force microscopy (AFM) experiments have also been performed on BR. While simple AFM experiments corroborated the information about the BR packing in the purple membrane (Butt et al. 1990), advanced high-speed AFM allowed visualization of BR motion in the membrane and assembly of the highly-ordered hexagonal lattice (Shibata et al. 2010). Combination of AFM and single-molecule force spectroscopy revealed the unfolding pathways of bacteriorhodopsin (Oesterhelt et al. 2000).

Finally, BR and purple membranes have been extensively studied *in silico*. Simulations allowed construction of fully atomistic model of purple membrane (Baudry et al. 2001), deciphering of mechanisms of color tuning (Hayashi et al. 2001; Hoffmann et al. 2006) and conformational changes during the photocycle (Hayashi et al. 2002; Bondar et al. 2004; Grudinin et al. 2005). Finally, molecular dynamics simulations of purple membranes helped with interpretation of neutron scattering data (Wood et al. 2010).

## 2.3 Bacteriorhodopsin structure and function

Details of bacteriorhodopsin structural and functional studies have been excellently summarized in other reviews (Lanyi 2004, 2006; Hirai et al. 2009; Wickstrand et al. 2015). Here, we provide a short description of the available data.

The BR proton translocation pathway consists of three major checkpoints: the proton uptake site, the Schiff base region and the proton release region (Fig. 2.3). There is a general agreement on the mechanism of the proton pumping. In the ground state the proton is stored at the retinal Schiff base that makes a hydrogen bond to a proximal water molecule W402 (Fig. 2.4). W402 is also coordinated by the aspartates 85 and 212. The W402 cavity also contains two other water molecules. The cavity is blocked by the retinal at one side and by the Arg-82 side chain at the other. Absorption of the light photon by the retinal leads to isomerization of the retinal from the all-*trans* to 13-*cis* conformation. In this new position, the protonated state of the Schiff base is energetically unfavorable, and the proton transitions to the proton acceptor residue Asp-85.

After that, the proton needs to pass to the proton release group, consisting of the glutamates 194 and 204. In the ground state this is impossible because of the Arg-82 side chain. In the M-state this side chain turns away from the Schiff base, and the proton transfers to Glu-194/204, displacing another proton occupying that site, which goes in its turn into the bulk solvent.

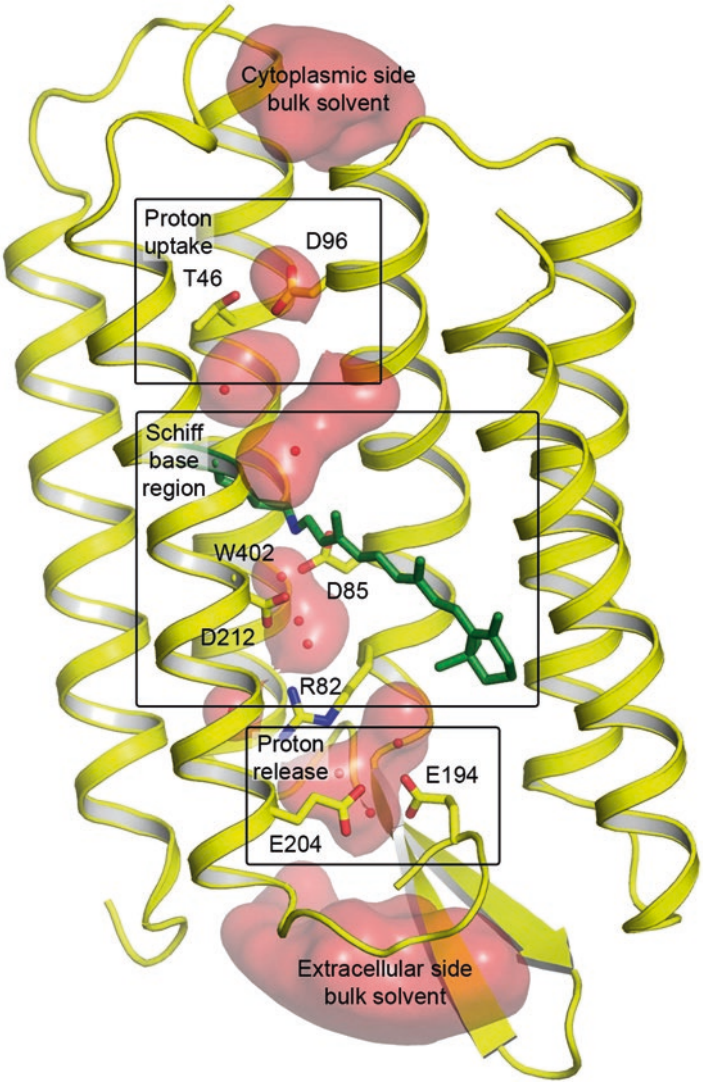


**Fig. 2.3** Structure of bacteriorhodopsin. Coordinates are taken from Luecke et al. (1999). Internal cavities are represented by the red surfaces. Crystallographically observed water molecules are shown as the red spheres. Helix F is hidden for clarity

As a next step the retinal is reprotonated with the proton stored at the proton uptake site on the Asp-96 side chain. Consequently, Asp-96 needs to be reprotonated from the cytoplasm, which can be possible due to a transient water molecule wire (Grudinin et al. 2005) or unlatching of the cytoplasmic side (Shibata et al. 2010; Wang et al. 2013b).

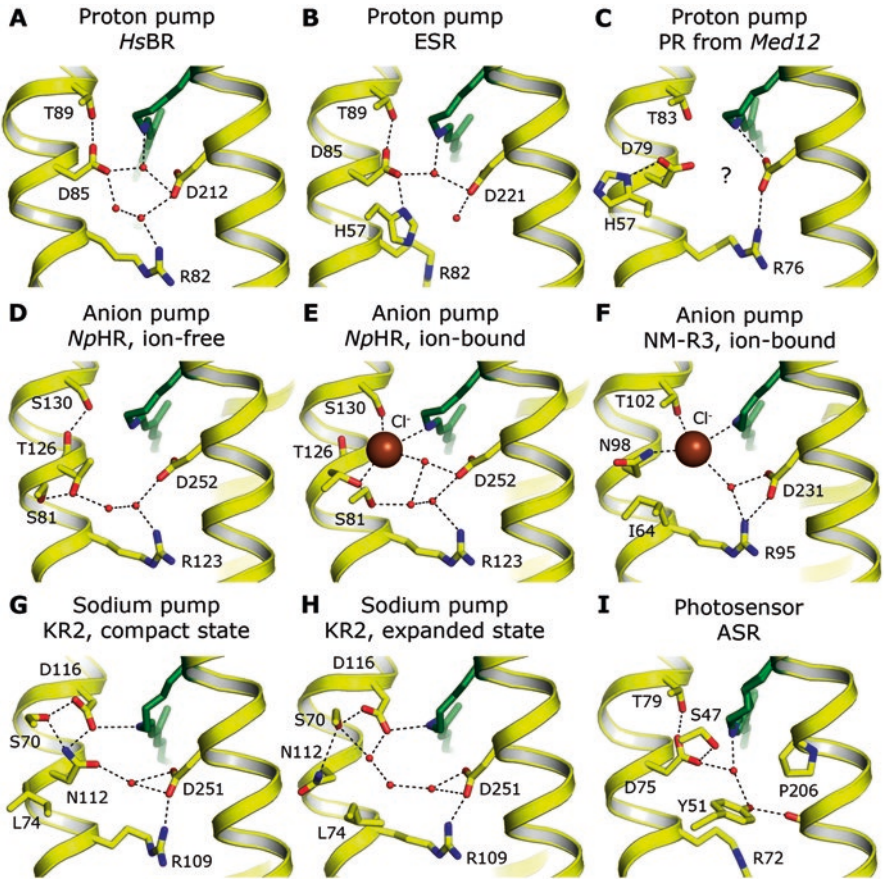


**Fig. 2.4** Schiff base environment in microbial rhodopsins. Positions of crystallographically resolved water molecules are shown using red particles. (**a**) *Halobacterium salinarum* bacteriorhodopsin (Luecke et al. 1999). (**b**) *Exiguobacterium sibiricum* rhodopsin (Gushchin et al. 2013a). (**c**) Proteorhodopsin from *Med12*. No ordered water molecules were observed at the resolution of 2.3 Å near the Schiff base (Ran et al. 2013). (**d**, **e**) Ion-free and ion-bound forms of *Natronomonas pharaonis* halorhodopsin (Kouyama et al. 2010; Kanada et al. 2011). (**f**) *Nonlabens marinus* rhodopsin 3 (Hosaka et al. 2016; Kim et al. 2016). (**g**, **h**) Compact and expanded conformations of pentameric KR2 (Gushchin et al. 2015). (**i**) *Anabaena* sensory rhodopsin (Vogeley et al. 2004)

Although these general points are agreed upon by most of the researchers, the details of the proton translocation mechanism and the associated conformational changes, in particular, are often disputed. For example, there are considerable differences in the crystallographic structures of the intermediate states published by different research groups (Hirai et al. 2009; Wickstrand et al. 2015). Although these differences might be a consequence of crystal twinning (Borshchevskiy et al. 2010) or unusual radiation sensitivity and consequent damage of BR crystals (Matsui et al. 2002; Borshchevskiy et al. 2011, 2014), their amplitude is also questioned, as the

electron microscopy studies, where the protein motions are supposedly less restrained by the environment, provide a picture of the larger-amplitude changes which are not observed in any of the crystallographic structures (Hirai and Subramaniam 2009). All these discrepancies are yet to be resolved.

## 2.4 Bacteriorhodopsin-Like Archaeal Rhodopsins

Besides *Halobacterium salinarum* bacteriorhodopsin (*Hs*BR), many other archaeal proton pumps have been described. Of note are archaerhodopsins 1 and 2, for which the atomic structures have been determined (Enami et al. 2006; Yoshimura and Kouyama 2008). Archaerhodopsin 3 from *Halorubrum sodomense* is used widely in optogenetics for neural silencing (Chow et al. 2010; Han et al. 2011) and measurement of membrane voltage (see below), and can be converted into light-gated proton channel (Inoue et al. 2015). Structure of deltarhodopsin from *Haloterrigena thermotolerans* revealed conserved proton pump features (Zhang et al. 2013). *Haloquadratum walsbyi* bacteriorhodopsin was used as a model protein to develop crystallization from styrene maleic acid polymer nanodiscs (Hsu et al. 2015; Broecker et al. 2017). Second microbial rhodopsin from *Haloquadratum walsbyi*, dubbed middle rhodopsin, was found to possess 11-*cis* retinal and revealed intermediate properties between those of bacteriorhodopsin and sensory rhodopsins (Sudo et al. 2011).

*Haloarcula marismortui* possesses a unique system of six rhodopsins (Fu et al. 2010), two of which, *Hm*BRI and *Hm*BRII, are proton pumps (Fu et al. 2013). *Hm*BRI can be expressed in *Escherichia coli* in large quantities and in fact can be used as a tag for production of other membrane proteins (Hsu et al. 2013). Structure of D94N mutant of *Hm*BRI revealed three additional inter-helical hydrogen bonds in the transmembrane region relative to *Hs*BR, and extended D-E loop, all of which appear to stabilize the protein. Similar structural elements are observed in the structure of cruxrhodopsin-3 from *Haloarcula vallismortis* (Chan et al. 2014).

## 2.5 Halorhodopsin

Halorhodopsins (HRs) are archaeal light-driven anion pumps, with *Halobacterium salinarum* halorhodopsin and *Natronomonas pharaonis* halorhodopsin being the best studied (Oesterhelt 1995; Essen 2002). Primarily, HRs are chloride pumps, and can also translocate some other anions, such as bromide, iodide and nitrate, but not sulfate (Bamberg et al. 1984; Duschl et al. 1990; Scharf and Engelhard 1994).

Spectroscopic and structural studies revealed that HRs bind several anion molecules in the ground state (Scharf and Engelhard 1994). The primary anion-binding site, relevant for translocation, is located in the retinal binding pocket (Kolbe et al. 2000; Gmelin et al. 2007; Kouyama et al. 2010; Schreiner et al. 2015). Consequently,

the bound anion serves as the counterion of the protonated retinal Schiff base whereas the proton acceptor residue, observed in proton pumps, is absent in HR (Fig. 2.4). Upon absorption of a light photon, HRs undergo a photocycle consisting of K, $L_1$, $L_2$, N and O intermediates (Hegemann et al. 1985; Oesterhelt et al. 1985; Chizhov and Engelhard 2001). However, the blue shifted M-like intermediate, corresponding to deprotonated retinylidene moiety, is lacking due to the absence of a proton acceptor residue.

Structural information about two halorhodopsins is currently available. *Hs*HR has a structure that is very similar to that of *Hs*BR (Kolbe et al. 2000). On the contrary, *Np*HR has an additional amphipathic α-helix at its N-terminus, and an extended B-C loop (Kouyama et al. 2010). Along with the ground state structures, those of $L_1$, azide-bound M-like, N, O and anion-free O-like, as well as 11-*cis* intermediates have also been determined (Gmelin et al. 2007; Kanada et al. 2011; Nakanishi et al. 2013; Kouyama et al. 2015; Chan et al. 2016). Upon absorption of a photon in the ground state, the all-*trans* retinal isomerizes into 13-*cis* conformation in $L_1$, while position of bound halide anion is virtually unchanged (Gmelin et al. 2007). In the $L_1$-$L_2$-N transitions, the ion moves first to Ser-130 and then to Ile-134, and the ion exit channel is formed. Then, the ion is released into the cytoplasm, and the channel closes. Finally, a new ion is taken up from the extracellular side (Kouyama et al. 2015).

Engineered *Np*HR found widespread use in optogenetics as a light-controlled inhibitor of neural activity due to its high expression level in mammalian neurons and low toxicity (Han and Boyden 2007; Gradinaru et al. 2008).

## 2.6 Sensory Rhodopsins

Sensory rhodopsins are the primary receptors of light in phototaxis signaling systems. While sensory rhodopsin I generates both an attractant response to 565 nm light and repellent to 370 nm light, sensory rhodopsin II (sometimes called phoborhodopsin) generates only a repellent signal to illumination with 480 nm light (Sasaki and Spudich 2008). Much more information is available for *Natronomonas pharaonis* SRII than for other sensory rhodopsins (Klare et al. 2004, 2011), and consequently we will focus on *Np*SRII.

Overall, in archaea and bacteria, phototaxis systems are very similar to chemotaxis systems. The difference is in the nature of the sensor. In chemotaxis systems, it is a homodimer of chemoreceptor proteins. The signal, binding of chemoattractant or chemorepellent, is generated by the extracellular domains of chemoreceptors, and then transmitted inside the cell by the transmembrane helices (Hazelbauer et al. 2008; Parkinson et al. 2015). In phototaxis systems, the photosensor and signal transducer are separate polypeptide chains that interact via their transmembrane domains and dimerize via transducers (Wegener et al. 2001; Gordeliy et al. 2002). The signal, illumination, is detected by sensory rhodopsin, which then passes it to the transmembrane part of a transducer protein (Gordeliy et al. 2002; Klare et al.

2004). In the cytoplasm, in both systems the signal passes through the HAMP domain to the kinase control module, which, in its turn, regulates the activity of the kinase CheA, phosphorylating the secondary response regulator CheY.

Interestingly, *Np*SRII, as well as *Np*SRI, is capable of pumping protons, albeit with poor efficiency (Bogomolni et al. 1994; Iwamoto et al. 1999; Sasaki and Spudich 1999; Schmies et al. 2000). This activity is inhibited upon binding of *Np*HtrII (Sudo et al. 2001; Schmies et al. 2001). Evidently, in the complex, opening of the cytoplasmic channel of *Np*SRII is hampered, and proton uptake kinetics is altered such that the reprotonation of the Schiff base is faster from the extracellular side (Sasaki and Spudich 2000). Mutation D75N, which eliminates the proton acceptor in *Np*SRII, inhibits the proton transport but does not affect signaling (Holterhues et al. 2011), while homologous mutation D73N in *Hs*SRII renders the sensor constitutively active but still able to respond to light (Spudich et al. 1997). Intriguingly, proton pump *Hs*BR can be converted into a sensor by just three mutations (Sudo and Spudich 2006). On the other hand, despite great efforts it has not been possible to change NpSRII into an efficient proton pump (Klare et al. 2002). Apparently, the requirements for an effective ion pump are much more demanding than those for a functional sensor.

Crystal structures are available for ground and active states of both individual *Np*SRII (Luecke et al. 2001; Royant et al. 2001; Edman et al. 2002; Gushchin et al. 2011b) and its 2:2 complex with transducer *Np*HtrII (Gordeliy et al. 2002; Moukhametzianov et al. 2006; Ishchenko et al. 2013, 2017). NMR studies provided the complementary information not only on the secondary structure, dynamics and topology of *Np*SRII (Etzkorn et al. 2007) but also on its structure (Gautier et al. 2010) and *Np*HtrII interface, E-F loop and conformational changes (Etzkorn et al. 2010). Finally, recent electron microscopy and modeling studies confirmed trimers-of-dimers arrangement of *Np*SRII/*Np*HtrII complexes, similar to what is observed for chemoreceptors (Orekhov et al. 2017). While in the ground state the structure of the receptor is almost the same as in the *Np*SRII/*Np*HtrII complex, in the active state the amplitude of the conformational changes is twice as large in a single *Np*SRII as in the 2:2 complex (Gushchin et al. 2011b). However, it should be noted that in crystal the amplitude of conformational changes in both cases may be affected by crystal contacts.

Absorption of a light photon and consequent *trans-cis* isomerization of the retinylidene chromophore of NpSRII initiates the photocycle, which takes about 1 second and is considerably slower than photocycles of light-driven pumps. The functionally important conformational step occurs during the M1→M2 transition, which leads to the signaling state (Wegener et al. 2000; Bordignon et al. 2007). During this transition, the signal is transferred through the interface comprising helices F and G to NpHtrII, resulting in a rotary motion and displacement of transmembrane helix TM2 (Wegener et al. 2001; Moukhametzianov et al. 2006; Gushchin et al. 2011b). Conformational changes in the helix F of *Np*SRII have also been observed using vibrational Stark effect (Mohrmann et al. 2016)

Interestingly, two different ground state structures of *Np*SRII-*Np*HtrII complex have been observed. In the structure that was determined first, the two *Np*SRII

molecules are significantly tilted, forming a V-like shape (Gordeliy et al. 2002). In the newer structure, the receptors are much more parallel, forming a U-like shape while rotating for 11° relative to the V-shape positions (Ishchenko et al. 2017). While the structure of *Np*SRII and its interface with *Np*HtrII is not affected by these differences, the arrangements of the transmembrane helices at the cytoplasmic side of *Np*HtrII are notably different. Even more interesting is that the TM helices occupy the intermediate position in the signaling-defective mutant G83F of *Np*HtrII. Similar conformational changes were recently observed in molecular dynamics studies (Nishikata et al. 2012) and implicated in transmembrane signaling by sensor histidine kinases (Molnar et al. 2014; Gushchin et al. 2017) and thus might also be related to signal transduction in the *Np*SRII-*Np*HtrII system (Gushchin and Gordeliy 2017).

The details of the signal transduction downstream of the membrane region are less well understood, in phototaxis systems as well as in two-component systems in general (Parkinson et al. 2015; Bhate et al. 2015; Zschiedrich et al. 2016). In *Np*HtrII, there are two HAMP domains (Parkinson 2010) separated by 2- or 4-heptad coiled coil inter-HAMP region (Gushchin et al. 2011a) that is similar to signaling helices of sensor histidine kinases (Anantharaman et al. 2006). The HAMP domain is organized as a symmetric homodimeric parallel coiled coil, where each protomer has two α-helices, AS1 and AS2, connected by a flexible linker segment (Bordignon et al. 2005; Doebber et al. 2008; Nishikata et al. 2010; Parkinson 2010; Etzkorn et al. 2010). Currently, there are several models of signal transduction through the HAMP domain (Parkinson 2010). For phototactic signal transducers, it was proposed that the HAMP domain of NpHtrII transduces the signal via switching between a compact and a highly dynamic state (Bordignon et al. 2005; Doebber et al. 2008) or acts as a mechanical joint (Hayashi et al. 2007). Fluorescent labeling studies, time-resolved EPR spectroscopy and molecular dynamics simulations revealed that the helices AS1 and AS2 move in opposite directions during signal transduction (Wang et al. 2012; Gushchin et al. 2013b; Klose et al. 2014). Finally, details of further propagation of the signal are less clear, although electron paramagnetic resonance studies and molecular dynamics simulations of full length signaling complexes (trimers of *Np*SRII-*Np*HtrII dimers) imply that the signaling mechanism is similar to that in bacterial chemoreceptors (Orban-Glaß et al. 2015; Orekhov et al. 2015).

## 2.7 *Anabaena* Sensory Rhodopsin

A new type of sensory rhodopsins (ASR) was discovered by Jung et al. (2003) in freshwater cyanobacterium *Anabaena (Nostoc)* sp. PCC7120. Crystal structure of ASR revealed an unusual hydrophilic cytoplasmic half-channel and a mixed population of 13-*cis* and all-*trans* retinal isomers, dominantly all-*trans* in the dark adapted form and under illumination with blue light, and shifted to dominantly 13-*cis* state under illumination with orange light (Vogeley et al. 2004). Detailed spectroscopic studies revealed that the protein is photochromic (Sineshchekov et al.

2005) and in fact the stable photoproduct of the all-*trans* form in ASR is 100% 13-*cis*, and that of the 13-*cis* form is 100% all-*trans* (Kawanabe et al. 2007). A more detailed discussion of spectroscopic properties of ASR can be found in following reviews (Kawanabe and Kandori 2009; Schapiro and Ruhman 2014). Finally, quantum mechanics simulations revealed that all photoisomerisations in ASR occur through unidirectional, counterclockwise 180° rotations of the ═C14─C15═ moiety with respect to the Lys-210-linked end of the chromophore axis, and thus ASR constitutes a light-driven molecular rotor (Strambi et al. 2010).

Interestingly, while most of microbial rhodopsin proton pumps are outward-directed, with the exception of xenorhodopsins, mutation D217E at the cytoplasmic side of ASR converted the protein into an inward proton pump (Kawanabe et al. 2009). Crystal structure of the mutant revealed rearrangements in the hydrogen bond network as well as in the backbone in the vicinity of retinal-binding Lys-210 (Dong et al. 2016).

While X-ray crystallographic structures of microbial rhodopsins and other membrane proteins are relatively common, NMR structures of membrane proteins are still scarce. ASR was the second microbial rhodopsin for which NMR structure has been determined (Wang et al. 2013a). *In situ* studies in *E. coli* membranes revealed site-specific structure perturbations in comparison with liposome data (Ward et al. 2015), and measurements of dipolar order parameter relaxation rates allowed probing the conformational dynamics of the receptor (Good et al. 2014).

Currently, the mechanism of ASR function is not fully clear. Irieda et al. (2012) observed direct regulation of gene expression by ASR: in the dark, but not under illumination, ASR repressed the expression of CRP reporter protein cloned under *cpcB* promoter. At the same time, ASR is accompanied by a 14 kDa soluble protein, called ASR transducer (ASRT), found in the same operon under the same promoter. Coexpression of ASR with ASRT increased the rate of the ASR photocycle, indicating the direct physical interaction between the two proteins, also confirmed by affinity enrichment chromatography and SPR measurements (Jung et al. 2003). ASRT was found to have a β-sandwich fold with partially disordered C-terminal α-helix and organize as a stable tetramer in crystal (Vogeley et al. 2007). Concomitantly with formation of the M-state upon photoactication of the all-*trans* form of ASR, ASRT dissociates from the protein (Kondoh et al. 2011). While no obvious DNA-binding motifs are evident in ASRT structure, it binds DNA fragments in 1:1 stoichiometry with micromolar affinity, and its C-terminus and loops between β-strands rearrange upon binding (Wang et al. 2011). ASRT was also found to interact with the promoter regions of *cpc*, *pec*, *kaiABC* and *asr* operons, both in vitro and in vivo (Kim et al. 2014).

## 2.8 Bacterial and Eukaryotic Proton Pumps

Advent of metagenomics and sequencing of environmental samples that contained uncultivated bacteria marked a new era in microbial rhodopsin research. Since the discovery of proteorhodopsin in 2000 (Béjà et al. 2000, 2001), a large variety of

bacterial proton pumps have been identified (Pinhassi et al. 2016). Besides proteorhodopsin (described below), there are numerous other notable examples. Xanthorhodopsin, a protein from eubacterium *Salinibacter ruber*, employs a second carotenoid, salinixanthin, acting as an antenna that transfers light to the retinal and extends the wavelength range of the pump (Balashov et al. 2005). *Gloeobacter violaceous* rhodopsin binds a similar carotenoid echinenone (Balashov et al. 2010). Distinct proton pumps were found in oceanic *Actinobacteria* and marine metagenomic samples (Sharma et al. 2008; Ghai et al. 2013). An unusual proton pump was identified in Siberian permafrost bacterium *Exiguobacterium sibiricum* (ESR, described below). Another proton pump, thermophilic rhodopsin, was identified in the extreme thermophilic bacterium *Thermus thermophilus* (Tsukamoto et al. 2013), followed by even more stable proton pump from *Rubrobacter xylanophilus* (Kanehara et al. 2017). Proteobacterial DTG rhodopsins with altered proton donor residues have also been found (Harris et al. 2015; Sudo and Yoshizawa 2016). Finally, while all of the above-mentioned proton pumps are outward-directed, xenorhodopsins have been recently identified as unique inward-directed proton pumps (Shevchenko et al. 2017; Ugalde et al. 2011; Inoue et al. 2016).

Retinal-based light-driven proton pumps are not limited to bacteria and archaea. Such pumps were also identified in fungi such as *Leptosphaeria* (Brown 2004; Waschuk et al. 2005) and alga *Acetabularia* (Tsunoda et al. 2006; Ernst et al. 2014). Structural and photochemical studies of *Acetabularia* rhodopsin 2 revealed mostly conserved mechanism of proton translocation (Wada et al. 2011; Kikukawa et al. 2011).

## 2.9 Proteorhodopsin

Proteorhodopsins are a diverse family of bacterial proton pumps identified first in marine proteobacteria and later found in all domains of life. Here, we provide a short description of key developments in the field. Further details were reviewed recently by (Bamann et al. 2014; Pinhassi et al. 2016).

The first bacterial rhodopsin gene was discovered in metagenomic DNA library from the Monterey Bay, California (Béjà et al. 2000). The protein was functionally expressed in *Escherichia coli* and bound retinal to from an active, light-driven proton pump. Soon thereafter, functional proteorhodopsin expression in native hosts has been confirmed, and the evidence of spectral adaptation to the wavelength of the environmentally available light has been presented (Béjà et al. 2001). Later, proteorhodopsin genes were found in many other bacteria (de la Torre et al. 2003), often living in extreme conditions such as Antarctic Sea ice (Koh et al. 2010), as well as in archaea and eukarya, evidently acquired via horizontal gene transfer (Frigaard et al. 2006; Slamovits et al. 2011).

*Pelagibacter ubique* from clade SAR11 was the first cultivatable bacterium for which functional proteorhodopsin expression was demonstrated both in autoclaved seawater and in its natural habitat in ocean (Giovannoni et al. 2005). However, in

that case, the bacteria did not reveal notable phototrophy. Later experiments showed that light stimulates growth of marine flavobacterium *Dokdonia* sp. Strain MED134 (Gómez-Consarnau et al. 2007) and of *Vibrio* strain AND4 during starvation (Gómez-Consarnau et al. 2010). Also, light-powering of engineered *Escherichia coli* cells with proteorhodopsin has been demonstrated (Walter et al. 2007; Martinez et al. 2007).

Overall, proteorhodopsins can be divided in two groups: the pigments absorbing green light (GPR, absorption maximum at approximately 525 nm), and those absorbing blue light (BPR, absorption maximum at approximately 490 nm), with the latter found deeper in the ocean, where green light is depleted (Man et al. 2003; Wang et al. 2003). While GPR and BPR show 20-30% sequence identity, the difference in the absorption spectra is mostly due to the residue at the position 105, leucine in GPR and glutamine in BPR (Ozaki et al. 2014).

Interestingly, proteorhodopsin's proton acceptor residue Asp-97 was found to have a relatively high $pK_a$ of ~7.68 (Dioumaev et al. 2002; Friedrich et al. 2002). This unusual $pK_a$ is explained by its hydrogen bonding to a neighboring histidine amino acid, His-75, not found in other microbial rhodopsins (Fig. 2.4) (Bergo et al. 2009; Hempelmann et al. 2011). Above that pH, proteorhodopsin acted as a traditional outward proton pump, however, below it PR changed the direction of pumping, and no M-like intermediate was observed (Friedrich et al. 2002; Lörinczi et al. 2009). No L-like intermediate was detected at any pH value (Friedrich et al. 2002; Váró et al. 2003).

For a long time, no structural information was available for proteorhodopsin. The first information came from atomic force microscopy, which revealed its seven-helical fold and unusual predominantly hexameric, but sometimes pentameric packing, in contrast to trimeric packing of bacterio- and halorhodopsins (Klyszejko et al. 2008). Solid-state and solution NMR studies confirmed the secondary structure of the pump, and, in particular, highlighted mobility of its E-F loop (Shi et al. 2009; Reckel et al. 2011; Yang et al. 2011). Finally, crystallographic structures of related pump ESR (Gushchin et al. 2013a) (discussed below) and proteorhodopsins *Med12*BPR and *HOT75*BPR (Ran et al. 2013) revealed the remaining details, including the cross-protomer interactions via His-75 and unusual helical break in the middle of the helix F, leading to significant mobility of its cytoplasmic side.

## 2.10 *Exiguobacterium Sibiricum* Rhodopsin

Along with BPR and GPR, *Exiguobacterium sibiricum* rhodopsin (ESR) is a particularly well-studied bacterial proton pump. Its gene was identified in the genome of the Gram-positive psychrotrophic bacterium *Exiguobacterium sibiricum* (Rodrigues et al. 2008), which inhabits Siberian permafrost soil and can withstand temperatures ranging from −5 to 40°C (Rodrigues et al. 2006). Currently, the role of ESR in its native host is not clear, however, the protein can be expressed heterologously in *Escherichia coli* and was shown to function in a wide pH range of 4.5–8.5

(Petrovskaya et al. 2010; Balashov et al. 2012). Functional studies of ESR are reviewed in (Petrovskaya et al. 2015)

Recent crystallographic structure of ESR revealed the elements common to all proteorhodopsins, as well as those particular to ESR (Gushchin et al. 2013a). While overall the secondary structures of all proton pumps are similar, there is an unusual structural element, first observed in ESR and later found in other PRs. The α-helical structure in the middle of its helix F is replaced by $3_{10}$- and π-helix-like elements that are stabilized by side chains of neighboring Trp-154 and Asn-224. This feature is characteristic for the proteorhodopsins family of proteins (Gushchin et al. 2013a) and is not found in bacterial proton pump xanthorhodopsin or archaeal pumps.

Similarly to other bacterial proton pumps, there is a histidine residue His-57 in the retinal's vicinity in ESR, tightly bound to the proton acceptor aspartate (Fig. 2.4). Consequently, the $pK_a$ of the proton acceptor group is notably higher in ESR relative to archaeal rhodopsins (Balashov et al. 2012). However, orientations of both histidine and Arg-82 gating residue in ESR are remarkably different from those in XR, BPR and GPR (Luecke et al. 2008; Gushchin et al. 2013a; Ran et al. 2013). His-57 points towards Arg-82, which is removed from the Schiff base region, and is in a conformation similar to that in the bacteriorhodopsin's M state (Lanyi 2004). Thus, Arg-82 is not coupled to the proton acceptor group and does not influence its $pK_a$ (Balashov et al. 2012), while the Asp-His pair can be accessed by water molecules from the bulk and might release the transported proton directly into the solvent (Gushchin et al. 2013a).

ESR's most unique feature is the cationic aminoacid lysine 96 in its proton uptake region (Gushchin et al. 2013a), contrary to aspartic and glutamic amino acids in other proton pumps (third characteristic residue in Fig. 2.2), but similar to proteorhodopsin genes in the metagenomic sequences of uncultured marine group II Euryarchaeota (Iverson et al. 2012). Reprotonation of the Schiff base in ESR is preceded by transient protonation of the ϵ-amino group of Lys-96 or a water molecule in its vicinity (Balashov et al. 2013), and the order of proton uptake and release by ESR is reversed relative to other proton pumps (Balashov et al. 2012; Dioumaev et al. 2013). The reason for this might be the adaptation to the wide range of pH (5.6–7.8) in the soil inhabited by *E. sibiricum,* because in the original proteorhodopsins, the vectoriality of proton pumping is inverted at acidic pH (Lörinczi et al. 2009).

## 2.11 Bacterial Cation Pumps

While microbial rhodopsins acting as anion or proton pumps have been known for a long time, the light-driven sodium pumps remained elusive. This elusiveness could have been rationalized by speculating that the positively charged protonated retinal Schiff base can displace a proton during its isomerization, and can displace an anion, pulling it by Coulombic attraction, but cannot move a cation as there is no suitable interaction.

Recently, a novel class of microbial rhodopsins, called NQ-rhodopsins, was described (Kwon et al. 2013). The name of the proteins comes from the fact that the retinal counterion position (D85 in bacteriorhodopsin) is occupied by asparagine (N) in this family, and proton uptake (D96 in bacteriorhodopsin) is occupied by glutamine (Q, Figs. 2.2 and 2.4). Despite these seemingly destructive substitutions the proteins were still able to pump protons (Kwon et al. 2013).

Soon thereafter, Inoue and colleagues (Inoue et al. 2013) found that KR2, rhodopsin 2 from *Krokinobacter eikastus* (now renamed to *Dokdonia eikasta*) and a member of the NQ-rhodopsins subfamily, is a light-driven sodium pump, which can pump protons in absence of sodium. Similarly to proton pumps, its photocycle consists of several intermediates (K, L, M and O), although there are slight differences probably explained by the fact that KR2 pumps preferably sodium and in its absence the turnover is slower and the pump is less efficient. The protein was also found to be very selective, pumping the $Li^+$ and $Na^+$ ions but not $K^+$, $Rb^+$ or $Cs^+$. Since then, similar pumps have been identified in other organisms: NM-R2 in *Nonlabens marinus* (Yoshizawa et al. 2014), GLR in *Gillisia limnaea* (Balashov et al. 2014), sodium pump in *Dokdonia* sp. PRO95 (Bertsova et al. 2015), IAR in *Indibacter alkaliphilus* (Li et al. 2015) and *Nd*R2 in *Nonlabens dokdonensis* (Zhao et al. 2017).

Dual $Na^+/H^+$ nature of the pumps received considerable attention. (Inoue et al. 2013) found that KR2 binds sodium ions with $K_d$ of ~11 mM in its ground state. Interestingly, disruption of sodium binding did not result in disruption of sodium translocation, and vice versa. This seeming paradox was later reconciled by crystallographic data: the sodium ion that binds to KR2 in the ground state is not the ion that is being translocated (Gushchin et al. 2015). In presence of $Na^+$ ions in solution, the KR2 photocycle is similar to that of proton pumps. The ion is uptaken from the medium in the M to O transition, and released on the other side of the protein during the relaxation to ground state. In absence of $Na^+$ ions, the photocycle is slowed down, and the protons are being transported (Inoue et al. 2013). Similar observations have been made for other pumps (Balashov et al. 2014; Li et al. 2015; Zhao et al. 2017). Finally, (Kato et al. 2015b) demonstrated that KR2 competitively uptakes $Na^+$ or $H^+$ upon decay of the M state, and the rate constant of $H^+$ uptake ($k_H$) is much larger than that of $Na^+$ uptake ($k_{Na}$) with a ratio $k_H/k_{Na}$ of $>10^3$. Thus, when concentrations of the ions are similar, protons will be transported preferentially, but at physiological sodium concentrations and neutral pH, the pump translocates sodium.

Several crystallographic structures of KR2 have been determined. (Kato et al. 2015a) elucidated the structure of monomeric KR2 at acidic pH 4.0 in blue state, and also the structure at pH of 7.5–8.5 by soaking the crystals, obtained at pH 4.0, in the solutions with pH 8.0–9.0. (Gushchin et al. 2015) determined the monomeric structure at acidic pH of 4.3 in blue state, and two different pentameric structures at pH 4.9 and 5.6, where most of the protein is in normal red ground state. Accompanied by mutagenesis studies, the structures revealed the ion uptake cavity, opened into the cytoplasm; positions of characteristic residues Asn-112 and Asp-116 in the retinal-binding pocket (Fig. 2.4); and the ion release cavity capped by unusual N-terminal α-helix (Gushchin et al. 2016). Compact and expanded conformations

of the Schiff base region in pentameric KR2 strongly resemble ion-free and ion-bound conformations of halorhodopsin (Fig. 2.4). (Gushchin et al. 2015) also observed sodium ions bound at the pentamerization interface. While there is a speculative possibility of binding a second carotenoid antenna by sodium pumps, similarly to XR (Luecke et al. 2008), recent study indicates that this is not the case (Bertsova et al. 2016).

Potentially, light-driven cation pumps would be a welcome addition to the repertoire of optogenetics tools. Application of KR2 for inhibition of spiking in neurons has been demonstrated by (Kato et al. 2015a). However, since KR2 and related pumps are outward-directed, and sodium concentration inside the studied cells is generally much lower than outside, either reversal of pump direction, or engineering of potassium pumps is highly desirable. Elucidation of KR2 structures allowed design of variants with $K^+$, and eventually, $Rb^+$ and $Cs^+$ pumping activity (Gushchin et al. 2015; Kato et al. 2015a; Konno et al. 2015). Search for novel pump variants requires high-throughput screening of significant number of mutants, to which end (Henrich et al. 2017) developed a combined nanodiscs and cell-free expression approach. For more in-depth discussions of sodium pump structures and functions we recommend specialized reviews (Gushchin et al. 2016; Kato et al. 2016).

## 2.12 Bacterial Anion Pumps

Soon after bacterial cation pumps, two different bacterial anion pumps have been discovered. Anion pumps of the first type, grouping close to bacterial cation pumps, were found in marine bacteria *Nonlabens marinus* and *Fulvimarina pelagi* (Yoshizawa et al. 2014; Inoue et al. 2014). Contrary to DTD or DTE motifs in proton pumps and NDQ in sodium pumps, in eubacterial anion pumps the characteristic residues are NTQ (asparagine, threonine and glutamine, Figs. 2.2 and 2.4). The pumping activity is the strongest for $Cl^-$ and $Br^-$, intermediate for $I^-$ and nitrates, and almost non-existent for sulfate ions. Anion pumps of the second type, *Mr*HR and *Sy*HR, are more similar to archaeal rhodopsins, and were found in cyanobacteria (Hasemi et al. 2016; Niho et al. 2017). In these proteins, the characteristic motif is TSD, and the selectivity profile is different from NTQ rhodopsins. *Mr*HR can pump $Cl^-$ and $Br^-$, but almost no $I^-$, nitrates or sulfates, and could be transformed into proton pump by a single mutation (Hasemi et al. 2016). *Sy*HR also pumps $Cl^-$ and $Br^-$ and almost no $I^-$ or nitrates. Surprisingly, it shows activity towards sulfates that is even higher than towards $Cl^-$ or $Br^-$, making it the first known microbial rhodopsin to transport divalent ions (Niho et al. 2017).

Despite the apparent differences in characteristic residues and pumping activities, the photocycles of bacterial anion pumps are similar to those of archaeal halorhodopsins in that the deprotonated Schiff base M-like intermediate is also lacking (Koua and Kandori 2015; Tsukamoto et al. 2017; Niho et al. 2017).

Recently, atomic structure of NTQ chloride pump NM-R3 from *Nonlabens marinus* has been deciphered (Hosaka et al. 2016; Kim et al. 2016). Overall, it is surprisingly similar to that of sodium pump KR2 (Gushchin et al. 2015), especially at the extracellular side, where a N-terminal α-helix is also observed and B-C loop has the same orientation. Interestingly, while NM-R3 is monomeric in crystal, its structure is closer to that of pentameric KR2, rather than monomeric one. The chloride ion binds near the retinal Schiff base, which is characteristically expanded, similarly to archaeal halorhodopsins and sodium pump KR2 (Fig. 2.4) (Gushchin et al. 2016).

## 2.13 Channelrhodopsins & Optogenetics

Channelrhodopsins (ChRs) were identified first as two microbial opsin-related genes in green alga *Chlamydomonas reinhardtii*. Channelrhodopsin-1 was characterized as a light-gated proton channel (Nagel et al. 2002), and Channelrhodopsin-2 was found to be a light-gated cation-selective channel (Nagel et al. 2003). Very soon, transmembrane part of ChR2 was employed for genetically targeted optical excitation and inhibition of neurons in cell cultures and living organisms (Boyden et al. 2005; Li et al. 2005; Nagel et al. 2005; Arenkiel et al. 2007; Petreanu et al. 2007). Consequently, ChR2 allowed precise millisecond-timescale noninvasive control of neuronal activity, which led to the birth of research field of optogenetics (Deisseroth 2011).

Several spectroscopic studies revealed highly unusual photocycle of channelrhodopsins with possible branching and slowly relaxing late intermediates, and uncovered the nature of conducting states (Hegemann et al. 2005; Bamann et al. 2008, 2010; Ernst et al. 2008; Ritter et al. 2008; Nikolic et al. 2009; Radu et al. 2009). Interestingly, it has been discovered that, in addition to being a light-gated cation channel, ChR2 is also a proton pump (Feldbauer et al. 2009).

Electron-crystallographic projection structure of ChR2 revealed that the protein is dimeric (Müller et al. 2011), whereas crystallization of ChR1-ChR2 chimera by (Kato et al. 2012) elucidated the details of the ion translocation pathway. Overall, ChR structure is notably different from those of other microbial rhodopsins, with its helix A occupying a unique position (Fig. 2.1). Finally, electron crystallography showed that illumination induces opposite motions of helices F and G, and also a displacement of helix B (Müller et al. 2015).

Aforementioned studies resulted in discovery of a number of important mutants of ChR2, such as E90Q, C128T and H134R. Later, even more elaborated versions, such as less-inactivating ChEF and ChIEF (Lin et al. 2009), Ca2+-permeable CatCh (Kleinlogel et al. 2011) and red-shifted ReaChR (Lin et al. 2013) have been engineered. Based on crystallographic structure, anion-conducting channels (Berndt et al. 2014; Wietek et al. 2014) or bistable variants of ChR2 (Berndt et al. 2016) have been created. Finally, in recent years, a number of naturally anion-conducting channelrhodopsins, along with new cation channels, have been discovered (Govorunova et al. 2015, 2016, 2017b).

For further details concerning the channelrhodopsins variants, function and applications, we address the reader to excellent reviews (Lórenz-Fonfría and Heberle 2014; Schneider et al. 2015; McIsaac et al. 2015; Wietek and Prigge 2016; Govorunova et al. 2017a). Optogenetics history and applications are described in (Adamantidis et al. 2015; Deisseroth 2015).

## 2.14 Rhodopsin-Based Enzymes

Along with light-driven ion pumps and light-gated ion channels, several light-modulated enzymes have been discovered. Generally, such proteins consist of the catalytic domain fused to microbial rhodopsin part, which controls its activity depending on illumination (Kateriya et al. 2004). Histidine kinase rhodopsin 1 from alga *Chlamydomonas reinhardtii* was characterized by (Luck et al. 2012) and found to be a bistable photochromic sensor (Penzkofer et al. 2014), where the retinal is converting between the protonated and deprotonated, and 13-*trans* and 13-*cis* states (Luck et al. 2015). Rhodopsin-guanylyl cyclase was discovered by (Avelar et al. 2014) in aquatic fungus *Blastocladiella emersonii* and was later shown to be an effective tool for optical control of cGMP signaling (Scheib et al. 2015; Gao et al. 2015). Finally, light-dependent cyclic nucleotide phosphodiesterase was found in choanoflagellate *Salpingoeca rosetta* by (Yoshida et al. 2017).

## 2.15 Rhodopsin-Based Voltage Indicators

In 2011 (Kralj et al. 2011) devised a new ingenious approach to optical recording of a cell's voltage by mutating green proteorhodopsin so that its fluorescence changed significantly with changing voltage. These new optogenetic tools were dubbed genetically encoded voltage indicators (GEVIs), and the approach was soon improved. First, a protein, Archaerhodopsin 3 (Arch), that could be expressed in plasma membrane of mammalian cells (Kralj et al. 2012) was found. Second, variants with improved brightness and voltage sensitivities have been evolved (Hochbaum et al. 2014; McIsaac et al. 2014; Flytzanis et al. 2014). Finally, FRET was used to further increase the sensitivity of the approach and extend the imaging color range of engineered sensors (Gong et al. 2014; Zou et al. 2014). The devised techniques were sensitive enough to record neural spikes in awake mice and flies with <1 ms precision (Gong et al. 2015).

Interestingly, (Maclaurin et al. 2013) found that the membrane voltage sensitivity of rhodopsin-based GEVIs fluorescence results not from the ground state, but rather from bias in the equilibrium in the M⇌N photocycle intermediate. Further elucidation of the voltage sensitivity mechanism allowed creation of more elaborated instruments. Measurements of kinetics of fluorescence changes allowed recording of absolute, rather than relative, membrane voltage (Hou et al. 2014).

Engineering of bistable mutants allowed development of "flash memory", where the membrane voltage can be recorded in the GEVI's state and accessed and rewritten at a later time (Venkatachalam et al. 2014).

Further information on GEVIs and their applications may be found in excellent reviews (Deisseroth and Schnitzer 2013; Cohen and Venkatachalam 2014; Gong 2015; Emiliani et al. 2015; Lin and Schnitzer 2016; Yang and St-Pierre 2016).

**Acknowledgements** The work was supported by the Russian Science Foundation research project 16-15-00242.

## References

Adamantidis A, Arber S, Bains JS et al (2015) Optogenetics: 10 years after ChR2 in neurons – views from the community. Nat Neurosci 18:1202–1212. https://doi.org/10.1038/nn.4106

Altenbach C, Marti T, Khorana HG, Hubbell WL (1990) Transmembrane protein structure: spin labeling of bacteriorhodopsin mutants. Science 248:1088–1092

Anantharaman V, Balaji S, Aravind L (2006) The signaling helix: a common functional theme in diverse signaling proteins. Biol Direct 1:25. https://doi.org/10.1186/1745-6150-1-25

Arenkiel BR, Peca J, Davison IG et al (2007) In vivo light-induced activation of neural circuitry in transgenic mice expressing channelrhodopsin-2. Neuron 54:205–218. https://doi.org/10.1016/j.neuron.2007.03.005

Avelar GM, Schumacher RI, Zaini PA et al (2014) A rhodopsin-guanylyl cyclase gene fusion functions in visual perception in a fungus. Curr Biol 24:1234–1240. https://doi.org/10.1016/j.cub.2014.04.009

Bagley K, Dollinger G, Eisenstein L et al (1982) Fourier transform infrared difference spectroscopy of bacteriorhodopsin and its photoproducts. Proc Natl Acad Sci U S A 79:4972–4976. PMC346807

Balashov SP, Imasheva ES, Boichenko VA et al (2005) Xanthorhodopsin: a proton pump with a light-harvesting carotenoid antenna. Science 309:2061–2064. https://doi.org/10.1126/science.1118046

Balashov SP, Imasheva ES, Choi AR et al (2010) Reconstitution of gloeobacter rhodopsin with echinenone: role of the 4-keto group. Biochemistry 49:9792–9799. https://doi.org/10.1021/bi1014166

Balashov SP, Petrovskaya LE, Lukashev EP et al (2012) Aspartate–histidine interaction in the retinal Schiff base counterion of the light-driven proton pump of Exiguobacterium sibiricum. Biochemistry 51:5748–5762. https://doi.org/10.1021/bi300409m

Balashov SP, Petrovskaya LE, Imasheva ES et al (2013) Breaking the carboxyl rule: lysine 96 facilitates reprotonation of the Schiff base in the photocycle of a retinal protein from Exiguobacterium sibiricum. J Biol Chem 288:21254–21265. https://doi.org/10.1074/jbc.M113.465138

Balashov SP, Imasheva ES, Dioumaev AK et al (2014) Light-driven Na+ pump from Gillisia limnaea: a high-affinity Na+ binding site is formed transiently in the photocycle. Biochemistry 53:7549–7561. https://doi.org/10.1021/bi501064n

Bamann C, Kirsch T, Nagel G, Bamberg E (2008) Spectral characteristics of the photocycle of channelrhodopsin-2 and its implication for channel function. J Mol Biol 375:686–694. https://doi.org/10.1016/j.jmb.2007.10.072

Bamann C, Gueta R, Kleinlogel S et al (2010) Structural guidance of the photocycle of channelrhodopsin-2 by an interhelical hydrogen bond. Biochemistry 49:267–278. https://doi.org/10.1021/bi901634p

Bamann C, Bamberg E, Wachtveitl J, Glaubitz C (2014) Proteorhodopsin. Biochim Biophys Acta 1837:614–625. https://doi.org/10.1016/j.bbabio.2013.09.010

Bamberg E, Hegemann P, Oesterhelt D (1984) Reconstitution of the light-driven electrogenic ion pump halorhodopsin in black lipid membranes. Biochim Biophys Acta 773:53–60. https://doi.org/10.1016/0005-2736(84)90549-2

Baudry J, Tajkhorshid E, Molnar F et al (2001) Molecular dynamics study of bacteriorhodopsin and the purple membrane. J Phys Chem B 105:905–918. https://doi.org/10.1021/jp000898e

Béjà O, Aravind L, Koonin EV et al (2000) Bacterial rhodopsin: evidence for a new type of phototrophy in the Sea. Science 289:1902–1906. https://doi.org/10.1126/science.289.5486.1902

Béjà O, Spudich EN, Spudich JL et al (2001) Proteorhodopsin phototrophy in the ocean. Nature 411:786–789. https://doi.org/10.1038/35081051

Bergo VB, Sineshchekov OA, Kralj JM et al (2009) His-75 in proteorhodopsin, a novel component in light-driven proton translocation by primary pumps. J Biol Chem 284:2836–2843. https://doi.org/10.1074/jbc.M803792200

Berndt A, Lee SY, Ramakrishnan C, Deisseroth K (2014) Structure-guided transformation of channelrhodopsin into a light-activated chloride channel. Science 344:420–424. https://doi.org/10.1126/science.1252367

Berndt A, Lee SY, Wietek J et al (2016) Structural foundations of optogenetics: determinants of channelrhodopsin ion selectivity. Proc Natl Acad Sci U S A 113:822–829. https://doi.org/10.1073/pnas.1523341113

Bertsova YV, Bogachev AV, Skulachev VP (2015) Proteorhodopsin from Dokdonia sp. PRO95 is a light-driven Na+-pump. Biochem Mosc 80:449–454. https://doi.org/10.1134/S0006297915040082

Bertsova YV, Arutyunyan AM, Bogachev AV (2016) Na+-translocating rhodopsin from Dokdonia sp. PRO95 does not contain carotenoid antenna. Biochem Mosc 81:414–419. https://doi.org/10.1134/S000629791604012X

Bhate MP, Molnar KS, Goulian M, DeGrado WF (2015) Signal transduction in histidine kinases: insights from new structures. Structure 23:981–994. https://doi.org/10.1016/j.str.2015.04.002

Bivin DB, Stoeckenius W (1986) Photoactive retinal pigments in haloalkaliphilic bacteria. J Gen Microbiol 132:2167–2177

Bogomolni RA, Spudich JL (1982) Identification of a third rhodopsin-like pigment in phototactic Halobacterium halobium. Proc Natl Acad Sci U S A 79:6250–6254

Bogomolni RA, Stoeckenius W, Szundi I et al (1994) Removal of transducer HtrI allows electrogenic proton translocation by sensory rhodopsin I. Proc Natl Acad Sci U S A 91:10188–10192

Bondar A-N, Elstner M, Suhai S et al (2004) Mechanism of primary proton transfer in bacteriorhodopsin. Structure 12:1281–1288. https://doi.org/10.1016/j.str.2004.04.016

Bordignon E, Klare JP, Doebber M et al (2005) Structural analysis of a HAMP domain. J Biol Chem 280:38767–38775. https://doi.org/10.1074/jbc.M509391200

Bordignon E, Klare JP, Holterhues J et al (2007) Analysis of light-induced conformational changes of Natronomonas pharaonis sensory rhodopsin II by time resolved electron paramagnetic resonance spectroscopy. Photochem Photobiol 83:263–272

Borshchevskiy V, Efremov R, Moiseeva E et al (2010) Overcoming merohedral twinning in crystals of bacteriorhodopsin grown in lipidic mesophase. Acta Crystallogr D Biol Crystallogr 66:26–32. https://doi.org/10.1107/S0907444909042838

Borshchevskiy VI, Round ES, Popov AN et al (2011) X-ray-radiation-induced changes in bacteriorhodopsin structure. J Mol Biol 409:813–825. https://doi.org/10.1016/j.jmb.2011.04.038

Borshchevskiy V, Round E, Erofeev I et al (2014) Low-dose X-ray radiation induces structural alterations in proteins. Acta Crystallogr D Biol Crystallogr 70:2675–2685. https://doi.org/10.1107/S1399004714017295

Boyden ES, Zhang F, Bamberg E et al (2005) Millisecond-timescale, genetically targeted optical control of neural activity. Nat Neurosci 8:1263–1268. https://doi.org/10.1038/nn1525

Braiman M, Mathies R (1982) Resonance Raman spectra of bacteriorhodopsin's primary photoproduct: evidence for a distorted 13-cis retinal chromophore. Proc Natl Acad Sci U S A 79:403–407

Broecker J, Eger BT, Ernst OP (2017) Crystallogenesis of membrane proteins mediated by polymer-bounded lipid nanodiscs. Structure 25:384–392. https://doi.org/10.1016/j.str.2016.12.004

Brown LS (2004) Fungal rhodopsins and opsin-related proteins: eukaryotic homologues of bacteriorhodopsin with unknown functions. Photochem Photobiol Sci 3:555–565. https://doi.org/10.1039/b315527g

Butt HJ, Downing KH, Hansma PK (1990) Imaging the membrane protein bacteriorhodopsin with the atomic force microscope. Biophys J 58:1473–1480. https://doi.org/10.1016/S0006-3495(90)82492-9

Chan SK, Kitajima-Ihara T, Fujii R et al (2014) Crystal structure of cruxrhodopsin-3 from Haloarcula vallismortis. PLoS ONE 9:e108362. https://doi.org/10.1371/journal.pone.0108362

Chan SK, Kawaguchi H, Kubo H et al (2016) Crystal structure of the 11-cis isomer of pharaonis halorhodopsin: structural constraints on interconversions among different isomeric states. Biochemistry 55:4092–4104. https://doi.org/10.1021/acs.biochem.6b00277

Cherezov V, Peddi A, Muthusubramaniam L et al (2004) A robotic system for crystallizing membrane and soluble proteins in lipidic mesophases. Acta Crystallogr D Biol Crystallogr 60:1795–1807. https://doi.org/10.1107/S0907444904019109

Cherezov V, Rosenbaum DM, Hanson MA et al (2007) High-resolution crystal structure of an engineered human β2-adrenergic G protein–coupled receptor. Science 318:1258–1265. https://doi.org/10.1126/science.1150577

Chizhov I, Engelhard M (2001) Temperature and halide dependence of the photocycle of halorhodopsin from natronobacterium pharaonis. Biophys J 81:1600–1612. https://doi.org/10.1016/S0006-3495(01)75814-6

Chizhov I, Chernavskii DS, Engelhard M et al (1996) Spectrally silent transitions in the bacteriorhodopsin photocycle. Biophys J 71:2329–2345. https://doi.org/10.1016/S0006-3495(96)79475-4

Chow BY, Han X, Dobry AS et al (2010) High-performance genetically targetable optical neural silencing by light-driven proton pumps. Nature 463:98–102. https://doi.org/10.1038/nature08652

Cohen AE, Venkatachalam V (2014) Bringing bioelectricity to light. Annu Rev Biophys 43:211–232. https://doi.org/10.1146/annurev-biophys-051013-022717

de la Torre JR, Christianson LM, Béjà O et al (2003) Proteorhodopsin genes are distributed among divergent marine bacterial taxa. Proc Natl Acad Sci U S A 100:12830–12835. https://doi.org/10.1073/pnas.2133554100

Deisenhofer J, Epp O, Miki K et al (1985) Structure of the protein subunits in the photosynthetic reaction centre of Rhodopseudomonas viridis at 3 Å resolution. Nature 318:618–624. https://doi.org/10.1038/318618a0

Deisseroth K (2011) Optogenetics. Nat Methods 8:26–29. https://doi.org/10.1038/nmeth.f.324

Deisseroth K (2015) Optogenetics: 10 years of microbial opsins in neuroscience. Nat Neurosci 18:1213–1225. https://doi.org/10.1038/nn.4091

Deisseroth K, Schnitzer MJ (2013) Engineering approaches to illuminating brain structure and dynamics. Neuron 80:568–577. https://doi.org/10.1016/j.neuron.2013.10.032

Dencher N, Wilms M (1975) Flash photometric experiments on the photochemical cycle of bacteriorhodopsin. Biophys Struct Mech 1:259–271. https://doi.org/10.1007/BF00535760

Dencher NA, Dresselhaus D, Zaccai G, Büldt G (1989) Structural changes in bacteriorhodopsin during proton translocation revealed by neutron diffraction. Proc Natl Acad Sci U S A 86:7876–7879

Dioumaev AK, Brown LS, Shih J et al (2002) Proton transfers in the photochemical reaction cycle of proteorhodopsin. Biochemistry 41:5348–5358. https://doi.org/10.1021/bi025563x

Dioumaev AK, Petrovskaya LE, Wang JM et al (2013) Photocycle of Exiguobacterium sibiricum rhodopsin characterized by low-temperature trapping in the IR and time-resolved studies in the visible. J Phys Chem B 117:7235–7253. https://doi.org/10.1021/jp402430w

Doebber M, Bordignon E, Klare JP et al (2008) Salt-driven equilibrium between two conformations in the HAMP domain from Natronomonas pharaonis: the language of signal transfer? J Biol Chem 283:28691–28701. https://doi.org/10.1074/jbc.M801931200

Dong B, Sánchez-Magraner L, Luecke H (2016) Structure of an inward proton-transporting Anabaena sensory rhodopsin mutant: mechanistic insights. Biophys J 111:963–972. https://doi.org/10.1016/j.bpj.2016.04.055

Duschl A, Lanyi JK, Zimányi L (1990) Properties and photochemistry of a halorhodopsin from the haloalkalophile, Natronobacterium pharaonis. J Biol Chem 265:1261–1267

Edman K, Royant A, Nollert P et al (2002) Early structural rearrangements in the photocycle of an integral membrane sensory receptor. Structure 10:473–482. https://doi.org/10.1016/S0969-2126(02)00736-0

Emiliani V, Cohen AE, Deisseroth K, Häusser M (2015) All-optical interrogation of neural circuits. J Neurosci 35:13917–13926. https://doi.org/10.1523/JNEUROSCI.2916-15.2015

Enami N, Yoshimura K, Murakami M et al (2006) Crystal structures of archaerhodopsin-1 and -2: common structural motif in archaeal light-driven proton pumps. J Mol Biol 358:675–685. https://doi.org/10.1016/j.jmb.2006.02.032

Engelhard M, Hess B, Emeis D et al (1989) Magic angle sample spinning carbon-13 nuclear magnetic resonance of isotopically labeled bacteriorhodopsin. Biochemistry 28:3967–3975. https://doi.org/10.1021/bi00435a051

Ernst OP, Murcia PAS, Daldrop P et al (2008) Photoactivation of channelrhodopsin. J Biol Chem 283:1637–1643. https://doi.org/10.1074/jbc.M708039200

Ernst OP, Lodowski DT, Elstner M et al (2014) Microbial and animal rhodopsins: structures, functions, and molecular mechanisms. Chem Rev 114:126–163. https://doi.org/10.1021/cr4003769

Essen L-O (2002) Halorhodopsin: light-driven ion pumping made simple? Curr Opin Struct Biol 12:516–522

Etzkorn M, Martell S, Andronesi OC et al (2007) Secondary structure, dynamics, and topology of a seven-helix receptor in native membranes, studied by solid-state NMR spectroscopy. Angew Chem Int Ed 46:459–462. https://doi.org/10.1002/anie.200602139

Etzkorn M, Seidel K, Li L et al (2010) Complex formation and light activation in membrane-embedded sensory rhodopsin II as seen by solid-state NMR spectroscopy. Structure 18:293–300. https://doi.org/10.1016/j.str.2010.01.011

Faham S, Bowie JU (2002) Bicelle crystallization: a new method for crystallizing membrane proteins yields a monomeric bacteriorhodopsin structure. J Mol Biol 316:1–6. https://doi.org/10.1006/jmbi.2001.5295

Feldbauer K, Zimmermann D, Pintschovius V et al (2009) Channelrhodopsin-2 is a leaky proton pump. Proc Natl Acad Sci U S A 106:12317–12322. https://doi.org/10.1073/pnas.0905852106

Flytzanis NC, Bedbrook CN, Chiu H et al (2014) Archaerhodopsin variants with enhanced voltage sensitive fluorescence in mammalian and caenorhabditis elegans neurons. Nat Commun 5:4894. https://doi.org/10.1038/ncomms5894

Friedrich T, Geibel S, Kalmbach R et al (2002) Proteorhodopsin is a light-driven proton pump with variable vectoriality. J Mol Biol 321:821–838

Frigaard N-U, Martinez A, Mincer TJ, DeLong EF (2006) Proteorhodopsin lateral gene transfer between marine planktonic bacteria and archaea. Nature 439:847–850. https://doi.org/10.1038/nature04435

Fu H-Y, Lin Y-C, Chang Y-N et al (2010) A novel six-rhodopsin system in a single Archaeon. J Bacteriol 192:5866–5873. https://doi.org/10.1128/JB.00642-10

Fu H-Y, Yi H-P, Y-H L, Yang C-S (2013) Insight into a single halobacterium using a dual-bacteriorhodopsin system with different functionally optimized pH ranges to cope with periplasmic pH changes associated with continuous light illumination. Mol Microbiol 88:551–561. https://doi.org/10.1111/mmi.12208

Gao S, Nagpal J, Schneider MW et al (2015) Optogenetic manipulation of cGMP in cells and animals by the tightly light-regulated guanylyl-cyclase opsin CyclOp. Nat Commun https://doi.org/10.1038/ncomms9046

Gautier A, Mott HR, Bostock MJ et al (2010) Structure determination of the seven-helix transmembrane receptor sensory rhodopsin II by solution NMR spectroscopy. Nat Struct Mol Biol 17:768–774. https://doi.org/10.1038/nsmb.1807

Ghai R, Mizuno CM, Picazo A et al (2013) Metagenomics uncovers a new group of low GC and ultra-small marine Actinobacteria. Sci Rep https://doi.org/10.1038/srep02471

Giovannoni SJ, Bibbs L, Cho J-C et al (2005) Proteorhodopsin in the ubiquitous marine bacterium SAR11. Nature 438:82–85. https://doi.org/10.1038/nature04032

Gmelin W, Zeth K, Efremov R et al (2007) The crystal structure of the L1 intermediate of halorhodopsin at 1.9 Å resolution. Photochem Photobiol 83:369–377. https://doi.org/10.1562/2006-06-23-RA-947

Gómez-Consarnau L, González JM, Coll-Lladó M et al (2007) Light stimulates growth of proteorhodopsin-containing marine Flavobacteria. Nature 445:210–213. https://doi.org/10.1038/nature05381

Gómez-Consarnau L, Akram N, Lindell K et al (2010) Proteorhodopsin phototrophy promotes survival of marine bacteria during starvation. PLoS Biol 8:e1000358. https://doi.org/10.1371/journal.pbio.1000358

Gong Y (2015) The evolving capabilities of rhodopsin-based genetically encoded voltage indicators. Curr Opin Chem Biol 27:84–89. https://doi.org/10.1016/j.cbpa.2015.05.006

Gong Y, Wagner MJ, Li JZ, Schnitzer MJ (2014) Imaging neural spiking in brain tissue using FRET-opsin protein voltage sensors. Nat Commun 5:3674. https://doi.org/10.1038/ncomms4674

Gong Y, Huang C, Li JZ et al (2015) High-speed recording of neural spikes in awake mice and flies with a fluorescent voltage sensor. Science 350:1361–1366. https://doi.org/10.1126/science.aab0810

Good DB, Wang S, Ward ME et al (2014) Conformational dynamics of a seven transmembrane helical protein Anabaena sensory rhodopsin probed by solid-state NMR. J Am Chem Soc 136:2833–2842. https://doi.org/10.1021/ja411633w

Gordeliy VI, Labahn J, Moukhametzianov R et al (2002) Molecular basis of transmembrane signalling by sensory rhodopsin II–transducer complex. Nature 419:484–487. https://doi.org/10.1038/nature01109

Govorunova EG, Sineshchekov OA, Janz R et al (2015) Natural light-gated anion channels: a family of microbial rhodopsins for advanced optogenetics. Science 349:647–650. https://doi.org/10.1126/science.aaa7484

Govorunova EG, Sineshchekov OA, Spudich JL (2016) Structurally distinct cation channelrhodopsins from cryptophyte algae. Biophys J 110:2302–2304. https://doi.org/10.1016/j.bpj.2016.05.001

Govorunova EG, Sineshchekov OA, Li H, Spudich JL (2017a) Microbial rhodopsins: diversity, mechanisms, and optogenetic applications. Annu Rev Biochem 86:845–872. https://doi.org/10.1146/annurev-biochem-101910-144233

Govorunova EG, Sineshchekov OA, Rodarte EM et al (2017b) The expanding family of natural anion channelrhodopsins reveals large variations in kinetics, conductance, and spectral sensitivity. Sci Rep 7:43358. https://doi.org/10.1038/srep43358

Gradinaru V, Thompson KR, Deisseroth K (2008) eNpHR: a Natronomonas halorhodopsin enhanced for optogenetic applications. Brain Cell Biol 36:129–139. https://doi.org/10.1007/s11068-008-9027-6

Grigorieff N, Ceska TA, Downing KH et al (1996) Electron-crystallographic refinement of the structure of bacteriorhodopsin. J Mol Biol 259:393–421. https://doi.org/10.1006/jmbi.1996.0328

Grote M, Engelhard M, Hegemann P (2014) Of ion pumps, sensors and channels – perspectives on microbial rhodopsins between science and history. Biochim Biophys Acta 1837:533–545. https://doi.org/10.1016/j.bbabio.2013.08.006

Grudinin S, Büldt G, Gordeliy V, Baumgaertner A (2005) Water molecules and hydrogen-bonded networks in bacteriorhodopsin – molecular dynamics simulations of the ground state and the M-intermediate. Biophys J 88:3252–3261. https://doi.org/10.1529/biophysj.104.047993

Gushchin I, Gordeliy VI, Grudinin S (2011a) Role of the HAMP domain region of sensory rhodopsin transducers in signal transduction. Biochemistry 50:574–580. https://doi.org/10.1021/bi101032a

Gushchin I, Reshetnyak A, Borshchevskiy V et al (2011b) Active state of sensory rhodopsin II: structural determinants for signal transfer and proton pumping. J Mol Biol 412:591–600. https://doi.org/10.1016/j.jmb.2011.07.022

Gushchin I, Chervakov P, Kuzmichev P et al (2013a) Structural insights into the proton pumping by unusual proteorhodopsin from nonmarine bacteria. Proc Natl Acad Sci U S A 110:12631–12636. https://doi.org/10.1073/pnas.1221629110

Gushchin I, Gordeliy V, Grudinin S (2013b) Two distinct states of the HAMP domain from sensory rhodopsin transducer observed in unbiased molecular dynamics simulations. PLoS ONE 8:e66917. https://doi.org/10.1371/journal.pone.0066917

Gushchin I, Gordeliy V (2017) Transmembrane signal transduction in two-component systems: piston, scissoring, or helical rotation? BioEssays 1700197. https://doi.org/10.1002/bies.201700197

Gushchin I, Shevchenko V, Polovinkin V et al (2015) Crystal structure of a light-driven sodium pump. Nat Struct Mol Biol 22:390–395. https://doi.org/10.1038/nsmb.3002

Gushchin I, Shevchenko V, Polovinkin V et al (2016) Structure of the light-driven sodium pump KR2 and its implications for optogenetics. FEBS J 283:1232–1238. https://doi.org/10.1111/febs.13585

Gushchin I, Melnikov I, Polovinkin V et al (2017) Mechanism of transmembrane signaling by sensor histidine kinases. Science https://doi.org/10.1126/science.aah6345

Han X, Boyden ES (2007) Multiple-color optical activation, silencing, and desynchronization of neural activity, with single-spike temporal resolution. PLoS ONE 2:e299. https://doi.org/10.1371/journal.pone.0000299

Han X, Chow BY, Zhou H et al (2011) A high-light sensitivity optical neural silencer: development and application to optogenetic control of non-human primate cortex. Front Syst Neurosci https://doi.org/10.3389/fnsys.2011.00018

Harris A, Ljumovic M, Bondar A-N et al (2015) A new group of eubacterial light-driven retinal-binding proton pumps with an unusual cytoplasmic proton donor. Biochim Biophys Acta 1847:1518–1529. https://doi.org/10.1016/j.bbabio.2015.08.003

Hasemi T, Kikukawa T, Kamo N, Demura M (2016) Characterization of a cyanobacterial chloride-pumping rhodopsin and its conversion into a proton pump. J Biol Chem 291:355–362. https://doi.org/10.1074/jbc.M115.688614

Hayashi S (2014) Silencing neurons with light. Science 344:369–370. https://doi.org/10.1126/science.1253616

Hayashi S, Tajkhorshid E, Pebay-Peyroula E et al (2001) Structural determinants of spectral tuning in retinal ProteinsBacteriorhodopsin vs sensory rhodopsin II. J Phys Chem B 105:10124–10131. https://doi.org/10.1021/jp011362b

Hayashi S, Tajkhorshid E, Schulten K (2002) Structural changes during the formation of early intermediates in the bacteriorhodopsin photocycle. Biophys J 83:1281–1297. https://doi.org/10.1016/S0006-3495(02)73900-3

Hayashi K, Sudo Y, Jee J et al (2007) Structural analysis of the phototactic transducer protein HtrII linker region from Natronomonas pharaonis. Biochemistry 46:14380–14390. https://doi.org/10.1021/bi701837n

Hazelbauer GL, Falke JJ, Parkinson JS (2008) Bacterial chemoreceptors: high-performance signaling in networked arrays. Trends Biochem Sci 33:9–19. https://doi.org/10.1016/j.tibs.2007.09.014

Hegemann P (2008) Algal sensory photoreceptors. Annu Rev Plant Biol 59:167–189. https://doi.org/10.1146/annurev.arplant.59.032607.092847

Hegemann P, Oesterhelt D, Steiner M (1985) The photocycle of the chloride pump halorhodopsin. I: azidecatalyzed deprotonation of the chromophore is a side reaction of photocycle intermediates inactivating the pump. EMBO J 4:2347–2350

Hegemann P, Ehlenbeck S, Gradmann D (2005) Multiple photocycles of channelrhodopsin. Biophys J 89:3911–3918. https://doi.org/10.1529/biophysj.105.069716

Hempelmann F, Hölper S, Verhoefen M-K et al (2011) His75−Asp97 cluster in green proteorhodopsin. J Am Chem Soc 133:4645–4654. https://doi.org/10.1021/ja111116a
Henderson R, Unwin PNT (1975) Three-dimensional model of purple membrane obtained by electron microscopy. Nature 257:28–32. https://doi.org/10.1038/257028a0
Henderson R, Baldwin JM, Ceska TA et al (1990) Model for the structure of bacteriorhodopsin based on high-resolution electron cryo-microscopy. J Mol Biol 213:899–929. https://doi.org/10.1016/S0022-2836(05)80271-2
Henrich E, Sörmann J, Eberhardt P et al (2017) From gene to function: cell-free electrophysiological and optical analysis of ion pumps in nanodiscs. Biophys J https://doi.org/10.1016/j.bpj.2017.03.026
Hildebrand E, Dencher N (1975) Two photosystems controlling behavioural responses of Halobacterium halobium. Nature 257:46–48. https://doi.org/10.1038/257046a0
Hirai T, Subramaniam S (2009) Protein conformational changes in the bacteriorhodopsin photocycle: comparison of findings from electron and X-ray crystallographic analyses. PLoS ONE 4:e5769. https://doi.org/10.1371/journal.pone.0005769
Hirai T, Subramaniam S, Lanyi JK (2009) Structural snapshots of conformational changes in a seven-helix membrane protein: lessons from bacteriorhodopsin. Curr Opin Struct Biol 19:433–439. https://doi.org/10.1016/j.sbi.2009.07.009
Hochbaum DR, Zhao Y, Farhi SL et al (2014) All-optical electrophysiology in mammalian neurons using engineered microbial rhodopsins. Nat Methods 11:825–833. https://doi.org/10.1038/nmeth.3000
Hoffmann M, Wanko M, Strodel P et al (2006) Color tuning in rhodopsins: the mechanism for the spectral shift between bacteriorhodopsin and sensory rhodopsin II. J Am Chem Soc 128:10808–10818. https://doi.org/10.1021/ja062082i
Hofrichter J, Henry ER, Lozier RH (1989) Photocycles of bacteriorhodopsin in light- and dark-adapted purple membrane studied by time-resolved absorption spectroscopy. Biophys J 56:693–706. PMC1280525
Holterhues J, Bordignon E, Klose D et al (2011) The signal transfer from the receptor NpSRII to the transducer NpHtrII is not hampered by the D75N mutation. Biophys J 100:2275–2282. https://doi.org/10.1016/j.bpj.2011.03.017
Hosaka T, Yoshizawa S, Nakajima Y et al (2016) Structural mechanism for light-driven transport by a new type of chloride ion pump, nonlabens marinus rhodopsin-3. J Biol Chem 291:17488–17495. https://doi.org/10.1074/jbc.M116.728220
Hou JH, Venkatachalam V, Cohen AE (2014) Temporal dynamics of microbial rhodopsin fluorescence reports absolute membrane voltage. Biophys J 106:639–648. https://doi.org/10.1016/j.bpj.2013.11.4493
Hsu M-F, T-F Y, Chou C-C et al (2013) Using Haloarcula marismortui bacteriorhodopsin as a fusion tag for enhancing and visible expression of integral membrane proteins in Escherichia coli. PLoS ONE 8:e56363. https://doi.org/10.1371/journal.pone.0056363
Hsu M-F, H-Y F, Cai C-J et al (2015) Structural and functional studies of a newly grouped haloquadratum walsbyi bacteriorhodopsin reveal the acid-resistant light-driven proton pumping activity. J Biol Chem 290:29567–29577. https://doi.org/10.1074/jbc.M115.685065
Inoue K, Ono H, Abe-Yoshizumi R et al (2013) A light-driven sodium ion pump in marine bacteria. Nat Commun 4:1678. https://doi.org/10.1038/ncomms2689
Inoue K, Koua FHM, Kato Y et al (2014) Spectroscopic study of a light-driven chloride ion pump from marine bacteria. J Phys Chem B 118:11190–11199. https://doi.org/10.1021/jp507219q
Inoue K, Tsukamoto T, Shimono K et al (2015) Converting a light-driven proton pump into a light-gated proton channel. J Am Chem Soc 137:3291–3299. https://doi.org/10.1021/ja511788f
Inoue K, Ito S, Kato Y et al (2016) A natural light-driven inward proton pump. Nat Commun https://doi.org/10.1038/ncomms13415
Irieda H, Morita T, Maki K et al (2012) Photo-induced regulation of the chromatic adaptive gene expression by Anabaena sensory rhodopsin. J Biol Chem 287:32485–32493. https://doi.org/10.1074/jbc.M112.390864

Ishchenko A, Round E, Borshchevskiy V et al (2013) Ground state structure of D75N mutant of sensory rhodopsin II in complex with its cognate transducer. J Photochem Photobiol B Biol 123:55–58. https://doi.org/10.1016/j.jphotobiol.2013.03.008

Ishchenko A, Round E, Borshchevskiy V et al (2017) New insights on signal propagation by sensory rhodopsin II/transducer complex. Sci Rep 7:41811. https://doi.org/10.1038/srep41811

Iverson V, Morris RM, Frazar CD et al (2012) Untangling genomes from metagenomes: revealing an uncultured class of marine Euryarchaeota. Science 335:587–590. https://doi.org/10.1126/science.1212665

Iwamoto M, Shimono K, Sumi M et al (1999) Light-induced proton uptake and release of pharaonis phoborhodopsin detected by a photoelectrochemical cell. J Phys Chem B 103:10311–10315. https://doi.org/10.1021/jp992168g

Jung K-H, Trivedi VD, Spudich JL (2003) Demonstration of a sensory rhodopsin in eubacteria. Mol Microbiol 47:1513–1522. https://doi.org/10.1046/j.1365-2958.2003.03395.x

Kanada S, Takeguchi Y, Murakami M et al (2011) Crystal structures of an O-like blue form and an anion-free yellow form of pharaonis halorhodopsin. J Mol Biol 413:162–176. https://doi.org/10.1016/j.jmb.2011.08.021

Kanehara K, Yoshizawa S, Tsukamoto T, Sudo Y (2017) A phylogenetically distinctive and extremely heat stable light-driven proton pump from the eubacterium Rubrobacter xylanophilus DSM 9941T. Sci Rep https://doi.org/10.1038/srep44427

Kateriya S, Nagel G, Bamberg E, Hegemann P (2004) "Vision" in single-celled algae. Physiology 19:133–137. https://doi.org/10.1152/nips.01517.2004

Kato HE, Zhang F, Yizhar O et al (2012) Crystal structure of the channelrhodopsin light-gated cation channel. Nature 482:369–374. https://doi.org/10.1038/nature10870

Kato HE, Inoue K, Abe-Yoshizumi R et al (2015a) Structural basis for Na+ transport mechanism by a light-driven Na+ pump. Nature 521:48–53. https://doi.org/10.1038/nature14322

Kato Y, Inoue K, Kandori H (2015b) Kinetic analysis of H+–Na+ selectivity in a light-driven Na+-pumping rhodopsin. J Phys Chem Lett 6:5111–5115. https://doi.org/10.1021/acs.jpclett.5b02371

Kato HE, Inoue K, Kandori H, Nureki O (2016) The light-driven sodium ion pump: a new player in rhodopsin research. BioEssays 38:1274–1282. https://doi.org/10.1002/bies.201600065

Kawanabe A, Kandori H (2009) Photoreactions and structural changes of Anabaena sensory rhodopsin. Sensors 9:9741–9804. https://doi.org/10.3390/s91209741

Kawanabe A, Furutani Y, Jung K-H, Kandori H (2007) Photochromism of Anabaena sensory rhodopsin. J Am Chem Soc 129:8644–8649. https://doi.org/10.1021/ja072085a

Kawanabe A, Furutani Y, Jung K-H, Kandori H (2009) Engineering an inward proton transport from a bacterial sensor rhodopsin. J Am Chem Soc 131:16439–16444. https://doi.org/10.1021/ja904855g

Kikukawa T, Shimono K, Tamogami J et al (2011) Photochemistry of Acetabularia rhodopsin II from a marine plant, Acetabularia acetabulum. Biochemistry 50:8888–8898. https://doi.org/10.1021/bi2009932

Kim SY, Yoon SR, Han S et al (2014) A role of Anabaena sensory rhodopsin transducer (ASRT) in photosensory transduction. Mol Microbiol 93:403–414. https://doi.org/10.1111/mmi.12635

Kim K, Kwon S-K, Jun S-H et al (2016) Crystal structure and functional characterization of a light-driven chloride pump having an NTQ motif. Nat Commun 7:12677. https://doi.org/10.1038/ncomms12677

Kitajima-Ihara T, Furutani Y, Suzuki D et al (2008) Salinibacter sensory rhodopsin. Sensory rhodopsin I-like protein from a eubacterium. J Biol Chem 283:23533–23541. https://doi.org/10.1074/jbc.M802990200

Klapoetke NC, Murata Y, Kim SS et al (2014) Independent optical excitation of distinct neural populations. Nat Methods 11:338–346. https://doi.org/10.1038/nmeth.2836

Klare JP, Schmies G, Chizhov I et al (2002) Probing the proton channel and the retinal binding site of Natronobacterium pharaonis sensory rhodopsin II. Biophys J 82:2156–2164

Klare JP, Gordeliy VI, Labahn J et al (2004) The archaeal sensory rhodopsin II/transducer complex: a model for transmembrane signal transfer. FEBS Lett 564:219–224. https://doi.org/10.1016/S0014-5793(04)00193-0

Klare JP, Bordignon E, Engelhard M, Steinhoff H-J (2011) Transmembrane signal transduction in archaeal phototaxis: the sensory rhodopsin II-transducer complex studied by electron paramagnetic resonance spectroscopy. Eur J Cell Biol 90:731–739. https://doi.org/10.1016/j.ejcb.2011.04.013

Kleinlogel S, Feldbauer K, Dempski RE et al (2011) Ultra light-sensitive and fast neuronal activation with the Ca2+-permeable channelrhodopsin CatCh. Nat Neurosci 14:513–518. https://doi.org/10.1038/nn.2776

Klose D, Voskoboynikova N, Orban-Glass I et al (2014) Light-induced switching of HAMP domain conformation and dynamics revealed by time-resolved EPR spectroscopy. FEBS Lett 588:3970–3976. https://doi.org/10.1016/j.febslet.2014.09.012

Klyszejko AL, Shastri S, Mari SA et al (2008) Folding and assembly of proteorhodopsin. J Mol Biol 376:35–41. https://doi.org/10.1016/j.jmb.2007.11.030

Koh EY, Atamna-Ismaeel N, Martin A et al (2010) Proteorhodopsin-bearing bacteria in Antarctic Sea ice. Appl Environ Microbiol 76:5918–5925. https://doi.org/10.1128/AEM.00562-10

Kolbe M, Besir H, Essen L-O, Oesterhelt D (2000) Structure of the light-driven chloride pump halorhodopsin at 1.8 Å resolution. Science 288:1390–1396. https://doi.org/10.1126/science.288.5470.1390

Kondoh M, Inoue K, Sasaki J et al (2011) Transient dissociation of the transducer protein from Anabaena sensory rhodopsin concomitant with formation of the M state produced upon photoactivation. J Am Chem Soc 133:13406–13412. https://doi.org/10.1021/ja202329u

Konno M, Kato Y, Kato HE et al (2015) Mutant of a light-driven sodium ion pump can transport cesium ions. J Phys Chem Lett 7:51–55. https://doi.org/10.1021/acs.jpclett.5b02385

Koua FHM, Kandori H (2015) Light-induced structural changes during early photo-intermediates of the eubacterial Cl− pump Fulvimarina rhodopsin observed by FTIR difference spectroscopy. RSC Adv 6:383–392. https://doi.org/10.1039/C5RA19363J

Kouyama T, Kanada S, Takeguchi Y et al (2010) Crystal structure of the light-driven chloride pump halorhodopsin from Natronomonas pharaonis. J Mol Biol 396:564–579. https://doi.org/10.1016/j.jmb.2009.11.061

Kouyama T, Kawaguchi H, Nakanishi T et al (2015) Crystal structures of the L1, L2, N, and O states of pharaonis halorhodopsin. Biophys J 108:2680–2690. https://doi.org/10.1016/j.bpj.2015.04.027

Kralj JM, Hochbaum DR, Douglass AD, Cohen AE (2011) Electrical spiking in Escherichia coli probed with a fluorescent voltage-indicating protein. Science 333:345–348. https://doi.org/10.1126/science.1204763

Kralj JM, Douglass AD, Hochbaum DR et al (2012) Optical recording of action potentials in mammalian neurons using a microbial rhodopsin. Nat Methods 9:90–95. https://doi.org/10.1038/nmeth.1782

Kwon S-K, Kim BK, Song JY et al (2013) Genomic makeup of the marine flavobacterium nonlabens (Donghaeana) dokdonensis and identification of a novel class of rhodopsins. Genome Biol Evol 5:187–199. https://doi.org/10.1093/gbe/evs134

Landau EM, Rosenbusch JP (1996) Lipidic cubic phases: a novel concept for the crystallization of membrane proteins. Proc Natl Acad Sci U S A 93:14532–14535

Lanyi JK (2004) Bacteriorhodopsin. Annu Rev Physiol 66:665–688. https://doi.org/10.1146/annurev.physiol.66.032102.150049

Lanyi JK (2006) Proton transfers in the bacteriorhodopsin photocycle. Biochim Biophys Acta 1757:1012–1018. https://doi.org/10.1016/j.bbabio.2005.11.003

Lee SC, Bennett BC, Hong W-X et al (2013) Steroid-based facial amphiphiles for stabilization and crystallization of membrane proteins. Proc Natl Acad Sci U S A 110:E1203–E1211. https://doi.org/10.1073/pnas.1221442110

Li X, Gutierrez DV, Hanson MG et al (2005) Fast noninvasive activation and inhibition of neural and network activity by vertebrate rhodopsin and green algae channelrhodopsin. Proc Natl Acad Sci U S A 102:17816–17821. https://doi.org/10.1073/pnas.0509030102

Li H, Sineshchekov OA, da Silva GFZ, Spudich JL (2015) In vitro demonstration of dual light-driven Na+/H+ pumping by a microbial rhodopsin. Biophys J 109:1446–1453. https://doi.org/10.1016/j.bpj.2015.08.018

Lin MZ, Schnitzer MJ (2016) Genetically encoded indicators of neuronal activity. Nat Neurosci 19:1142–1153. https://doi.org/10.1038/nn.4359

Lin JY, Lin MZ, Steinbach P, Tsien RY (2009) Characterization of engineered channelrhodopsin variants with improved properties and kinetics. Biophys J 96:1803–1814. https://doi.org/10.1016/j.bpj.2008.11.034

Lin JY, Knutsen PM, Muller A et al (2013) ReaChR: a red-shifted variant of channelrhodopsin enables deep transcranial optogenetic excitation. Nat Neurosci 16:1499–1508. https://doi.org/10.1038/nn.3502

Lórenz-Fonfría VA, Heberle J (2014) Channelrhodopsin unchained: structure and mechanism of a light-gated cation channel. Biochim Biophys Acta 1837:626–642. https://doi.org/10.1016/j.bbabio.2013.10.014

Lörinczi É, Verhoefen M-K, Wachtveitl J et al (2009) Voltage- and pH-dependent changes in vectoriality of photocurrents mediated by wild-type and mutant proteorhodopsins upon expression in Xenopus oocytes. J Mol Biol 393:320–341. https://doi.org/10.1016/j.jmb.2009.07.055

Lozier RH, Bogomolni RA, Stoeckenius W (1975) Bacteriorhodopsin: a light-driven proton pump in Halobacterium halobium. Biophys J 15:955–962. https://doi.org/10.1016/S0006-3495(75)85875-9

Luck M, Mathes T, Bruun S et al (2012) A photochromic Histidine Kinase Rhodopsin (HKR1) that is bimodally switched by ultraviolet and blue light. J Biol Chem 287:40083–40090. https://doi.org/10.1074/jbc.M112.401604

Luck M, Bruun S, Keidel A et al (2015) Photochemical chromophore isomerization in histidine kinase rhodopsin HKR1. FEBS Lett 589:1067–1071. https://doi.org/10.1016/j.febslet.2015.03.024

Luecke H, Schobert B, Richter H-T et al (1999) Structure of bacteriorhodopsin at 1.55 Å resolution. J Mol Biol 291:899–911. https://doi.org/10.1006/jmbi.1999.3027

Luecke H, Schobert B, Lanyi JK et al (2001) Crystal structure of sensory rhodopsin II at 2.4 Angstroms: insights into color tuning and transducer interaction. Science 293:1499–1503. https://doi.org/10.1126/science.1062977

Luecke H, Schobert B, Stagno J et al (2008) Crystallographic structure of xanthorhodopsin, the light-driven proton pump with a dual chromophore. Proc Natl Acad Sci U S A 105:16561–16565. https://doi.org/10.1073/pnas.0807162105

Maclaurin D, Venkatachalam V, Lee H, Cohen AE (2013) Mechanism of voltage-sensitive fluorescence in a microbial rhodopsin. Proc Natl Acad Sci U S A 110:5939–5944. https://doi.org/10.1073/pnas.1215595110

Man D, Wang W, Sabehi G et al (2003) Diversification and spectral tuning in marine proteorhodopsins. EMBO J 22:1725–1731. https://doi.org/10.1093/emboj/cdg183

Martinez A, Bradley AS, Waldbauer JR et al (2007) Proteorhodopsin photosystem gene expression enables photophosphorylation in a heterologous host. Proc Natl Acad Sci U S A 104:5590–5595. https://doi.org/10.1073/pnas.0611470104

Marwan W, Oesterhelt D (1987) Signal formation in the halobacterial photophobic response mediated by a fourth retinal protein (P480). J Mol Biol 195:333–342

Matsui Y, Sakai K, Murakami M et al (2002) Specific damage induced by X-ray radiation and structural changes in the primary photoreaction of bacteriorhodopsin. J Mol Biol 324:469–481

Matsuno-Yagi A, Mukohata Y (1977) Two possible roles of bacteriorhodopsin; a comparative study of strains of Halobacterium halobium differing in pigmentation. Biochem Biophys Res Commun 78:237–243. https://doi.org/10.1016/0006-291X(77)91245-1

McIsaac RS, Engqvist MKM, Wannier T et al (2014) Directed evolution of a far-red fluorescent rhodopsin. Proc Natl Acad Sci U S A 111:13034–13039. https://doi.org/10.1073/pnas.1413987111
McIsaac RS, Bedbrook CN, Arnold FH (2015) Recent advances in engineering microbial rhodopsins for optogenetics. Curr Opin Struct Biol 33:8–15. https://doi.org/10.1016/j.sbi.2015.05.001
Mohrmann H, Kube I, Lórenz-Fonfría VA et al (2016) Transient conformational changes of sensory rhodopsin II investigated by vibrational stark effect probes. J Phys Chem B 120:4383–4387. https://doi.org/10.1021/acs.jpcb.6b01900
Molnar KS, Bonomi M, Pellarin R et al (2014) Cys-scanning disulfide crosslinking and Bayesian modeling probe the transmembrane signaling mechanism of the histidine kinase, PhoQ. Structure 22:1239–1251. https://doi.org/10.1016/j.str.2014.04.019
Mongodin EF, Nelson KE, Daugherty S et al (2005) The genome of Salinibacter ruber: convergence and gene exchange among hyperhalophilic bacteria and archaea. Proc Natl Acad Sci U S A 102:18147–18152. https://doi.org/10.1073/pnas.0509073102
Moukhametzianov R, Klare JP, Efremov R et al (2006) Development of the signal in sensory rhodopsin and its transfer to the cognate transducer. Nature 440:115–119. https://doi.org/10.1038/nature04520
Müller M, Bamann C, Bamberg E, Kühlbrandt W (2011) Projection structure of channelrhodopsin-2 at 6 Å resolution by electron crystallography. J Mol Biol 414:86–95. https://doi.org/10.1016/j.jmb.2011.09.049
Müller M, Bamann C, Bamberg E, Kühlbrandt W (2015) Light-induced helix movements in channelrhodopsin-2. J Mol Biol 427:341–349. https://doi.org/10.1016/j.jmb.2014.11.004
Nagel G, Ollig D, Fuhrmann M et al (2002) Channelrhodopsin-1: a light-gated proton channel in green algae. Science 296:2395–2398. https://doi.org/10.1126/science.1072068
Nagel G, Szellas T, Huhn W et al (2003) Channelrhodopsin-2, a directly light-gated cation-selective membrane channel. Proc Natl Acad Sci U S A 100:13940–13945. https://doi.org/10.1073/pnas.1936192100
Nagel G, Brauner M, Liewald JF et al (2005) Light activation of channelrhodopsin-2 in excitable cells of Caenorhabditis elegans triggers rapid behavioral responses. Curr Biol 15:2279–2284. https://doi.org/10.1016/j.cub.2005.11.032
Nakanishi T, Kanada S, Murakami M et al (2013) Large deformation of helix F during the photoreaction cycle of pharaonis halorhodopsin in complex with azide. Biophys J 104:377–385. https://doi.org/10.1016/j.bpj.2012.12.018
Nango E, Royant A, Kubo M et al (2016) A three-dimensional movie of structural changes in bacteriorhodopsin. Science 354:1552–1557. https://doi.org/10.1126/science.aah3497
Niho A, Yoshizawa S, Tsukamoto T et al (2017) Demonstration of a light-driven SO42–transporter and its spectroscopic characteristics. J Am Chem Soc 139:4376–4389. https://doi.org/10.1021/jacs.6b12139
Nikolaev M, Round E, Gushchin I et al (2017) Integral membrane proteins can be crystallized directly from nanodiscs. Cryst Growth Des 17:945–948. https://doi.org/10.1021/acs.cgd.6b01631
Nikolic K, Grossman N, Grubb MS et al (2009) Photocycles of channelrhodopsin-2. Photochem Photobiol 85:400–411. https://doi.org/10.1111/j.1751-1097.2008.00460.x
Nishikata K, Fuchigami S, Ikeguchi M, Kidera A (2010) Molecular modeling of the HAMP domain of sensory rhodopsin II transducer from Natronomonas pharaonis. Biophysics 6:27–36
Nishikata K, Ikeguchi M, Kidera A (2012) Comparative simulations of the ground state and the M-intermediate state of the sensory rhodopsin II–transducer complex with a HAMP domain model. Biochemistry 51:5958–5966. https://doi.org/10.1021/bi300696b
Nogly P, James D, Wang D et al (2015) Lipidic cubic phase serial millisecond crystallography using synchrotron radiation. IUCrJ 2:168–176. https://doi.org/10.1107/S2052252514026487
Oesterhelt D (1995) Structure and function of halorhodopsin. Isr J Chem 35:475–494. https://doi.org/10.1002/ijch.199500044
Oesterhelt D, Stoeckenius W (1971) Rhodopsin-like protein from the purple membrane of Halobacterium halobium. Nature 233:149–152. https://doi.org/10.1038/10.1038/newbio233149a0

Oesterhelt D, Hegemann P, Tittor J (1985) The photocycle of the chloride pump halorhodopsin. II: quantum yields and a kinetic model. EMBO J 4:2351–2356

Oesterhelt F, Oesterhelt D, Pfeiffer M et al (2000) Unfolding pathways of individual bacteriorhodopsins. Science 288:143–146. https://doi.org/10.1126/science.288.5463.143

Orban-Glaß I, Voskoboynikova N, Busch KB et al (2015) Clustering and dynamics of phototransducer signaling domains revealed by site-directed spin labeling electron paramagnetic resonance on SRII/HtrII in membranes and nanodiscs. Biochemistry 54:349–362. https://doi.org/10.1021/bi501160q

Orekhov PS, Klose D, Mulkidjanian AY et al (2015) Signaling and adaptation modulate the dynamics of the photosensoric complex of Natronomonas pharaonis. PLoS Comput Biol 11:e1004561. https://doi.org/10.1371/journal.pcbi.1004561

Orekhov P, Bothe A, Steinhoff H-J et al (2017) Sensory rhodopsin I and sensory rhodopsin II form trimers of dimers in complex with their cognate transducers. Photochem Photobiol 93:796–804. https://doi.org/10.1111/php.12763

Ozaki Y, Kawashima T, Abe-Yoshizumi R, Kandori H (2014) A color-determining amino acid residue of proteorhodopsin. Biochemistry 53:6032–6040. https://doi.org/10.1021/bi500842w

Parkinson JS (2010) Signaling mechanisms of HAMP domains in chemoreceptors and sensor kinases. Annu Rev Microbiol 64:101–122. https://doi.org/10.1146/annurev.micro.112408.134215

Parkinson JS, Hazelbauer GL, Falke JJ (2015) Signaling and sensory adaptation in Escherichia coli chemoreceptors: 2015 update. Trends Microbiol 23:257–266. https://doi.org/10.1016/j.tim.2015.03.003

Pebay-Peyroula E, Rummel G, Rosenbusch JP, Landau EM (1997) X-ray structure of bacteriorhodopsin at 2.5 angstroms from microcrystals grown in lipidic cubic phases. Science 277:1676–1681. https://doi.org/10.1126/science.277.5332.1676

Penzkofer A, Luck M, Mathes T, Hegemann P (2014) Bistable retinal Schiff base photodynamics of Histidine Kinase Rhodopsin HKR1 from Chlamydomonas reinhardtii. Photochem Photobiol 90:773–785. https://doi.org/10.1111/php.12246

Petreanu L, Huber D, Sobczyk A, Svoboda K (2007) Channelrhodopsin-2–assisted circuit mapping of long-range callosal projections. Nat Neurosci 10:663–668. https://doi.org/10.1038/nn1891

Petrovskaya LE, Lukashev EP, Chupin VV et al (2010) Predicted bacteriorhodopsin from Exiguobacterium sibiricum is a functional proton pump. FEBS Lett 584:4193–4196. https://doi.org/10.1016/j.febslet.2010.09.005

Petrovskaya LE, Balashov SP, Lukashev EP et al (2015) ESR – a retinal protein with unusual properties from Exiguobacterium sibiricum. Biochem Mosc 80:688–700

Pinhassi J, DeLong EF, Béjà O et al (2016) Marine bacterial and archaeal ion-pumping rhodopsins: genetic diversity, physiology, and ecology. Microbiol Mol Biol Rev 80:929–954. https://doi.org/10.1128/MMBR.00003-16

Polovinkin V, Gushchin I, Sintsov M et al (2014) High-resolution structure of a membrane protein transferred from amphipol to a lipidic mesophase. J Membr Biol 247:997–1004. https://doi.org/10.1007/s00232-014-9700-x

Racker E, Stoeckenius W (1974) Reconstitution of purple membrane vesicles catalyzing light-driven proton uptake and adenosine triphosphate formation. J Biol Chem 249:662–663

Radu I, Bamann C, Nack M et al (2009) Conformational changes of channelrhodopsin-2. J Am Chem Soc 131:7313–7319. https://doi.org/10.1021/ja8084274

Ran T, Ozorowski G, Gao Y et al (2013) Cross-protomer interaction with the photoactive site in oligomeric proteorhodopsin complexes. Acta Crystallogr D Biol Crystallogr 69:1965–1980. https://doi.org/10.1107/S0907444913017575

Reckel S, Gottstein D, Stehle J et al (2011) Solution NMR structure of proteorhodopsin. Angew Chem Int Ed 50:11942–11946. https://doi.org/10.1002/anie.201105648

Ritter E, Stehfest K, Berndt A et al (2008) Monitoring light-induced structural changes of channelrhodopsin-2 by UV-visible and fourier transform infrared spectroscopy. J Biol Chem 283:35033–35041. https://doi.org/10.1074/jbc.M806353200

Rodrigues DF, Goris J, Vishnivetskaya T et al (2006) Characterization of Exiguobacterium isolates from the Siberian permafrost. Description of Exiguobacterium sibiricum sp. nov. Extremophiles 10:285–294. https://doi.org/10.1007/s00792-005-0497-5

Rodrigues DF, Ivanova N, He Z et al (2008) Architecture of thermal adaptation in an Exiguobacterium sibiricum strain isolated from 3 million year old permafrost: a genome and transcriptome approach. BMC Genomics 9:547. https://doi.org/10.1186/1471-2164-9-547

Royant A, Nollert P, Edman K et al (2001) X-ray structure of sensory rhodopsin II at 2.1-Å resolution. Proc Natl Acad Sci U S A 98:10131–10136. https://doi.org/10.1073/pnas.181203898

Sasaki J, Spudich JL (1999) Proton circulation during the photocycle of sensory rhodopsin II. Biophys J 77:2145–2152. https://doi.org/10.1016/S0006-3495(99)77055-4

Sasaki J, Spudich JL (2000) Proton transport by sensory rhodopsins and its modulation by transducer-binding. Biochim Biophys Acta 1460:230–239. https://doi.org/10.1016/S0005-2728(00)00142-0

Sasaki J, Spudich JL (2008) Signal transfer in Haloarchaeal sensory rhodopsin – transducer complexes. Photochem Photobiol 84:863–868. https://doi.org/10.1111/j.1751-1097.2008.00314.x

Schapiro I, Ruhman S (2014) Ultrafast photochemistry of Anabaena sensory rhodopsin: experiment and theory. Biochim Biophys Acta 1837:589–597. https://doi.org/10.1016/j.bbabio.2013.09.014

Scharf B, Engelhard M (1994) Blue halorhodopsin from Natronobacterium pharaonis: wavelength regulation by anions. Biochemistry 33:6387–6393. https://doi.org/10.1021/bi00187a002

Scheib U, Stehfest K, Gee CE et al (2015) The rhodopsin–guanylyl cyclase of the aquatic fungus Blastocladiella emersonii enables fast optical control of cGMP signaling. Sci Signal 8:rs8. https://doi.org/10.1126/scisignal.aab0611

Schmies G, Lüttenberg B, Chizhov I et al (2000) Sensory rhodopsin II from the haloalkaliphilic natronobacterium pharaonis: light-activated proton transfer reactions. Biophys J 78:967–976. https://doi.org/10.1016/S0006-3495(00)76654-9

Schmies G, Engelhard M, Wood PG et al (2001) Electrophysiological characterization of specific interactions between bacterial sensory rhodopsins and their transducers. Proc Natl Acad Sci U S A 98:1555–1559. https://doi.org/10.1073/pnas.031562298

Schneider F, Grimm C, Hegemann P (2015) Biophysics of channelrhodopsin. Annu Rev Biophys 44:167–186. https://doi.org/10.1146/annurev-biophys-060414-034014

Schobert B, Lanyi JK (1982) Halorhodopsin is a light-driven chloride pump. J Biol Chem 257:10306–10313

Schreiner M, Schlesinger R, Heberle J, Niemann HH (2015) Structure of halorhodopsin from Halobacterium salinarum in a new crystal form that imposes little restraint on the E–F loop. J Struct Biol 190:373–378. https://doi.org/10.1016/j.jsb.2015.04.010

Sharma AK, Zhaxybayeva O, Papke RT, Doolittle WF (2008) Actinorhodopsins: proteorhodopsin-like gene sequences found predominantly in non-marine environments. Environ Microbiol 10:1039–1056. https://doi.org/10.1111/j.1462-2920.2007.01525.x

Shevchenko V, Gushchin I, Polovinkin V et al (2014) Crystal structure of Escherichia coli-expressed Haloarcula marismortui bacteriorhodopsin I in the trimeric form. PLoS ONE 9:e112873. https://doi.org/10.1371/journal.pone.0112873

Shevchenko V, Mager T, Kovalev K et al (2017) Inward H+ pump xenorhodopsin: mechanism and alternative optogenetic approach. Sci Adv 3:e1603187. https://doi.org/10.1126/sciadv.1603187

Shi L, Lake EMR, Ahmed MAM et al (2009) Solid-state NMR study of proteorhodopsin in the lipid environment: secondary structure and dynamics. Biochim Biophys Acta 1788:2563–2574. https://doi.org/10.1016/j.bbamem.2009.09.011

Shibata M, Yamashita H, Uchihashi T et al (2010) High-speed atomic force microscopy shows dynamic molecular processes in photoactivated bacteriorhodopsin. Nat Nanotechnol 5:208–212. https://doi.org/10.1038/nnano.2010.7

Sineshchekov OA, Trivedi VD, Sasaki J, Spudich JL (2005) Photochromicity of Anabaena sensory rhodopsin, an atypical microbial receptor with a cis-retinal light-adapted form. J Biol Chem 280:14663–14668. https://doi.org/10.1074/jbc.M501416200

Slamovits CH, Okamoto N, Burri L et al (2011) A bacterial proteorhodopsin proton pump in marine eukaryotes. Nat Commun 2:183. https://doi.org/10.1038/ncomms1188

Spudich JL, Bogomolni RA (1984) Mechanism of colour discrimination by a bacterial sensory rhodopsin. Nature 312:509–513. https://doi.org/10.1038/312509a0

Spudich EN, Spudich JL (1982) Control of transmembrane ion fluxes to select halorhodopsin-deficient and other energy-transduction mutants of Halobacterium halobium. Proc Natl Acad Sci U S A 79:4308–4312

Spudich EN, Zhang W, Alam M, Spudich JL (1997) Constitutive signaling by the phototaxis receptor sensory rhodopsin II from disruption of its protonated Schiff base–Asp-73 interhelical salt bridge. Proc Natl Acad Sci U S A 94:4960–4965

Strambi A, Durbeej B, Ferré N, Olivucci M (2010) Anabaena sensory rhodopsin is a light-driven unidirectional rotor. Proc Natl Acad Sci U S A 107:21322–21326. https://doi.org/10.1073/pnas.1015085107

Sudo Y, Spudich JL (2006) Three strategically placed hydrogen-bonding residues convert a proton pump into a sensory receptor. Proc Natl Acad Sci U S A 103:16129–16134. https://doi.org/10.1073/pnas.0607467103

Sudo Y, Yoshizawa S (2016) Functional and photochemical characterization of a light-driven proton pump from the Gammaproteobacterium Pantoea vagans. Photochem Photobiol 92:420–427. https://doi.org/10.1111/php.12585

Sudo Y, Iwamoto M, Shimono K et al (2001) Photo-induced proton transport of pharaonis phoborhodopsin (sensory rhodopsin II) is ceased by association with the transducer. Biophys J 80:916–922. https://doi.org/10.1016/S0006-3495(01)76070-5

Sudo Y, Okada A, Suzuki D et al (2009) Characterization of a signaling complex composed of sensory rhodopsin I and its cognate transducer protein from the Eubacterium Salinibacter ruber. Biochemistry 48:10136–10145. https://doi.org/10.1021/bi901338d

Sudo Y, Ihara K, Kobayashi S et al (2011) A microbial rhodopsin with a unique retinal composition shows both sensory rhodopsin II and bacteriorhodopsin-like properties. J Biol Chem 286:5967–5976. https://doi.org/10.1074/jbc.M110.190058

Takahashi T, Tomioka H, Kamo N, Kobatake Y (1985) A photosystem other than PS370 also mediates the negative phototaxis of Halobacterium halobium. FEMS Microbiol Lett 28:161–164

Takeda K, Sato H, Hino T et al (1998) A novel three-dimensional crystal of bacteriorhodopsin obtained by successive fusion of the vesicular assemblies. J Mol Biol 283:463–474. https://doi.org/10.1006/jmbi.1998.2103

Tomioka H, Takahashi T, Kamo N, Kobatake Y (1986) Flash spectrophotometric identification of a fourth rhodopsin-like pigment in Halobacterium halobium. Biochem Biophys Res Commun 139:389–395. https://doi.org/10.1016/S0006-291X(86)80003-1

Tsukamoto T, Inoue K, Kandori H, Sudo Y (2013) Thermal and spectroscopic characterization of a proton pumping rhodopsin from an extreme thermophile. J Biol Chem 288:21581–21592. https://doi.org/10.1074/jbc.M113.479394

Tsukamoto T, Mizutani K, Hasegawa T et al (2016) X-ray crystallographic structure of thermophilic rhodopsin implications for high thermal stability and optogenetic function. J Biol Chem 291:12223–12232. https://doi.org/10.1074/jbc.M116.719815

Tsukamoto T, Yoshizawa S, Kikukawa T et al (2017) Implications for the light-driven chloride ion transport mechanism of nonlabens marinus rhodopsin 3 by its photochemical characteristics. J Phys Chem B 121:2027–2038. https://doi.org/10.1021/acs.jpcb.6b11101

Tsunoda SP, Ewers D, Gazzarrini S et al (2006) H+-pumping rhodopsin from the marine alga Acetabularia. Biophys J 91:1471–1479. https://doi.org/10.1529/biophysj.106.086421

Ugalde JA, Podell S, Narasingarao P, Allen EE (2011) Xenorhodopsins, an enigmatic new class of microbial rhodopsins horizontally transferred between archaea and bacteria. Biol Direct 6:52. https://doi.org/10.1186/1745-6150-6-52

Váró G, Brown LS, Lakatos M, Lanyi JK (2003) Characterization of the photochemical reaction cycle of proteorhodopsin. Biophys J 84:1202–1207. https://doi.org/10.1016/S0006-3495(03)74934-0

Venkatachalam V, Brinks D, Maclaurin D et al (2014) Flash memory: photochemical imprinting of neuronal action potentials onto a microbial rhodopsin. J Am Chem Soc 136:2529–2537. https://doi.org/10.1021/ja411338t

Vogeley L, Sineshchekov OA, Trivedi VD et al (2004) Anabaena sensory rhodopsin: a photochromic color sensor at 2.0 Å. Science 306:1390–1393. https://doi.org/10.1126/science.1103943

Vogeley L, Trivedi VD, Sineshchekov OA et al (2007) Crystal structure of the Anabaena sensory rhodopsin transducer. J Mol Biol 367:741–751. https://doi.org/10.1016/j.jmb.2006.11.074

Wada T, Shimono K, Kikukawa T et al (2011) Crystal structure of the eukaryotic light-driven proton-pumping rhodopsin, Acetabularia rhodopsin II, from marine alga. J Mol Biol 411:986–998. https://doi.org/10.1016/j.jmb.2011.06.028

Walter JM, Greenfield D, Bustamante C, Liphardt J (2007) Light-powering Escherichia coli with proteorhodopsin. Proc Natl Acad Sci U S A 104:2408–2412. https://doi.org/10.1073/pnas.0611035104

Wang W-W, Sineshchekov OA, Spudich EN, Spudich JL (2003) Spectroscopic and photochemical characterization of a deep ocean proteorhodopsin. J Biol Chem 278:33985–33991. https://doi.org/10.1074/jbc.M305716200

Wang S, Kim SY, Jung K-H et al (2011) A eukaryotic-like interaction of soluble Cyanobacterial sensory rhodopsin transducer with DNA. J Mol Biol 411:449–462. https://doi.org/10.1016/j.jmb.2011.06.002

Wang J, Sasaki J, Tsai A, Spudich JL (2012) HAMP domain signal relay mechanism in a sensory rhodopsin-transducer complex. J Biol Chem 287:21316–21325. https://doi.org/10.1074/jbc.M112.344622

Wang S, Munro RA, Shi L et al (2013a) Solid-state NMR spectroscopy structure determination of a lipid-embedded heptahelical membrane protein. Nat Methods 10:1007–1012. https://doi.org/10.1038/nmeth.2635

Wang T, Sessions AO, Lunde CS et al (2013b) Deprotonation of D96 in bacteriorhodopsin opens the proton uptake pathway. Structure 21:290–297. https://doi.org/10.1016/j.str.2012.12.018

Ward ME, Wang S, Munro R et al (2015) In situ structural studies of Anabaena sensory rhodopsin in the E. coli membrane. Biophys J 108:1683–1696. https://doi.org/10.1016/j.bpj.2015.02.018

Waschuk SA, Bezerra AG, Shi L, Brown LS (2005) Leptosphaeria rhodopsin: bacteriorhodopsin-like proton pump from a eukaryote. Proc Natl Acad Sci U S A 102:6879–6883. https://doi.org/10.1073/pnas.0409659102

Wegener A-A, Chizhov I, Engelhard M, Steinhoff H-J (2000) Time-resolved detection of transient movement of helix F in spin-labelled pharaonis sensory rhodopsin II. J Mol Biol 301:881–891. https://doi.org/10.1006/jmbi.2000.4008

Wegener AA, Klare JP, Engelhard M, Steinhoff HJ (2001) Structural insights into the early steps of receptor-transducer signal transfer in archaeal phototaxis. EMBO J 20:5312–5319. https://doi.org/10.1093/emboj/20.19.5312

Wickstrand C, Dods R, Royant A, Neutze R (2015) Bacteriorhodopsin: would the real structural intermediates please stand up? Biochim Biophys Acta 1850:536–553. https://doi.org/10.1016/j.bbagen.2014.05.021

Wietek J, Prigge M (2016) Enhancing channelrhodopsins: an overview. In: Kianianmomeni A (ed) Optogenetics. Springer, New York, pp 141–165

Wietek J, Wiegert JS, Adeishvili N et al (2014) Conversion of channelrhodopsin into a light-gated chloride channel. Science 344:409–412. https://doi.org/10.1126/science.1249375

Wolff EK, Bogomolni RA, Scherrer P et al (1986) Color discrimination in halobacteria: spectroscopic characterization of a second sensory receptor covering the blue-green region of the spectrum. Proc Natl Acad Sci U S A 83:7272–7276

Wood K, Tobias DJ, Kessler B et al (2010) The low-temperature inflection observed in neutron scattering measurements of proteins is due to methyl rotation: direct evidence using isotope labeling and molecular dynamics simulations. J Am Chem Soc 132:4990–4991. https://doi.org/10.1021/ja910502g

Yang HH, St-Pierre F (2016) Genetically encoded voltage indicators: opportunities and challenges. J Neurosci 36:9977–9989

Yang J, Aslimovska L, Glaubitz C (2011) Molecular dynamics of proteorhodopsin in lipid bilayers by solid-state NMR. J Am Chem Soc 133:4874–4881. https://doi.org/10.1021/ja109766n

Yoshida K, Tsunoda SP, Brown LS, Kandori H (2017) A unique choanoflagellate enzyme rhodopsin exhibits light-dependent cyclic nucleotide phosphodiesterase activity. J Biol Chem 292:7531–7541. https://doi.org/10.1074/jbc.M117.775569

Yoshimura K, Kouyama T (2008) Structural role of bacterioruberin in the trimeric structure of archaerhodopsin-2. J Mol Biol 375:1267–1281. https://doi.org/10.1016/j.jmb.2007.11.039

Yoshizawa S, Kumagai Y, Kim H et al (2014) Functional characterization of flavobacteria rhodopsins reveals a unique class of light-driven chloride pump in bacteria. Proc Natl Acad Sci U S A 111:6732–6737. https://doi.org/10.1073/pnas.1403051111

Yutin N, Koonin EV (2012) Proteorhodopsin genes in giant viruses. Biol Direct 7:34. https://doi.org/10.1186/1745-6150-7-34

Zander U, Bourenkov G, Popov AN et al (2015) MeshAndCollect: an automated multi-crystal data-collection workflow for synchrotron macromolecular crystallography beamlines. Acta Crystallogr D Biol Crystallogr 71:2328–2343

Zhang F, Vierock J, Yizhar O et al (2011) The microbial opsin family of optogenetic tools. Cell 147:1446–1457. https://doi.org/10.1016/j.cell.2011.12.004

Zhang J, Mizuno K, Murata Y et al (2013) Crystal structure of deltarhodopsin-3 from Haloterrigena thermotolerans. Proteins Struct Funct Bioinf 81:1585–1592. https://doi.org/10.1002/prot.24316

Zhao H, Ma B, Ji L et al (2017) Coexistence of light-driven Na+ and H+ transport in a microbial rhodopsin from Nonlabens dokdonensis. J Photochem Photobiol B Biol 172:70–76. https://doi.org/10.1016/j.jphotobiol.2017.05.004

Zou P, Zhao Y, Douglass AD et al (2014) Bright and fast multicoloured voltage reporters via electrochromic FRET. Nat Commun 5:4625. https://doi.org/10.1038/ncomms5625

Zschiedrich CP, Keidel V, Szurmant H (2016) Molecular mechanisms of two-component signal transduction. J Mol Biol 428:3752–3775. https://doi.org/10.1016/j.jmb.2016.08.003

# Chapter 3
# The Structural Basis for the Extraordinary Energy-Transfer Capabilities of the Phycobilisome


**Dvir Harris, Shira Bar-Zvi, Avital Lahav, Itay Goldshmid, and Noam Adir**

**Abstract** Light absorption is the initial step in the photosynthetic process. In all species, most of the light is absorbed by dedicated pigment-protein complexes called light harvesting complexes or antenna complexes. In the case of cyanobacteria and red-algae, photosynthetic organisms found in a wide variety of ecological niches, the major antenna is called the Phycobilisome (PBS). The PBS has many unique characteristics that sets it apart from the antenna complexes of other organisms (bacteria, algae and plants). These differences include the type of light absorbing chromophores, the protein environment of the chromophores, the method of assembly and association and the intercellular location with respect to the photosynthetic reaction centers (RCs). Since the final goal of all antenna complexes is the same – controlled absorption and transfer of the energy of the sun to the RCs, the unique structural and chemical differences of the PBS also require unique energy transfer mechanisms and pathways. In this review we will describe in detail the structural facets that lead to a mature PBS, followed by an attempt to understand the energy transfer properties of the PBS as they have been measured experimentally.

**Keywords** Phycobilisome (PBS) · Light absorption · Light harvesting complex (LHC) · Chromophore · Reaction centre (RC) · Photosystem (PS) · Excitation energy transfer · Oxygenic photosynthesis · Self-assembly · Cyanobacteria · Protein structure

D. Harris · S. Bar-Zvi · A. Lahav · I. Goldshmid · N. Adir (✉)
The Schulich Faculty of Chemistry, Technion – Israel Institute of Technology, Haifa, Israel
e-mail: sgoitay4@campus.technion.ac.il; noam@ch.technion.ac.il



J. R. Harris, E. J. Boekema (eds.), *Membrane Protein Complexes: Structure and Function*, Subcellular Biochemistry 87,
https://doi.org/10.1007/978-981-10-7757-9_3

## 3.1 Introduction

The absorption of light by the Phycobilsome (PBS), the major photosynthetic light harvesting complex (LHC) in cyanobacteria and red algae (Adir 2005; Glazer 1989; Grossman et al. 2001; Marx et al. 2014; Watanabe and Ikeuchi 2013) is the driving force for a large proportion of the primary production on earth. These species can be found in all aquatic and terrestrial habitats, in deserts that experience high light-fluencies to depths of lake and oceanic water columns with reduced penetration of visible light (Samsonoff and MacColl 2001; Flombaum et al. 2013). In plants, green algae and most non-oxygenic photosynthetic bacteria, LHCs have evolved to spatially exist within the same confined intracellular compartment as the photochemical reaction centers (RC) – the thylakoid membrane (Cheng and Fleming 2009; Cogdell et al. 2004; Croce and van Amerongen 2013; van Amerongen and Croce 2013; Hohmann-Marriott and Blankenship 2011; Kouril et al. 2011). In some organisms, the RC tightly binds internal antenna pigments that are a permanent facet of the structure, resulting in a photosystem (PS) that can function independently of additional LHCs. However, obtaining efficient solar energy conversion (SEC) at low light conditions requires the binding of additional independent LHCs to the PS. The dimensions of the photosynthetic membrane limit the dimensions of these LHCs, and thus to increase the light harvesting capabilities, the chromophores are hydrophobic chlorophylls, and the packing of pigments bound to each unit is quite high, with typical distances of <1 nm between chromophores. In contrast, the PBS is found outside the membrane, attached to the stromal surface of the RCs. The PBS size is thus only limited by the spacing between membranes, and it appears that in these organisms the spacing between membranes may indeed be determined by the size of the PBS. Having both the LHCs and PS in the membrane facilitates inter-complex interactions and requires specific peripheral chromophores in both to facilitate efficient inter-component energy transfer (ET) between adjacent LHCs and between LHCs adjacent to a PS. The relatively loose binding of LHCs to the PS and the fluid nature of the membrane then affords the potential for control over the flow of energy from LHCs to RCs. We have today high-resolution three-dimensional structures of almost all of the transmembrane LHCs and RC, and lower resolution structures and/or biochemical evidences for the fashion of the organization of LHCs onto the RC. In the case of the two oxygenic photosynthetic RCs, Photosystem II (PSII) and Photosystem I (PSI), the distance between the closest LHC pigments to the site of photochemical charge separation is kept quite large, with many intervening absorption/emission steps. Since the PBS is not constrained by the membrane thickness, it assembles into huge complexes with dimensions that can reach 80 × 50 × 12 nm. Electron microscopy images of various PBS containing strains have also revealed that the thylakoid membranes are almost completely covered with PBSs (Samsonoff and MacColl 2001), with the PBS representing a large proportion of protein content within the cyanobacterial cell. These observations indicate that a fraction of the PBS units can sit directly above the RC, and may be able to transfer energy in a single step. Unlike the chlorophyll based transmembrane

LHCs, the PBS utilize linear tetrapyrrole chromophores, covalently bound to the soluble protein subunits. The large size and concentration of PBS permits a much less dense packing of chromophores, with center to center distances exceeding 20 Å. Thus it would appear that the fashion by which energy transfer pathways within the PBS are quite different to those of the transmembrane LHCs. In the PBS, ET would appear to occur via many independent absorption/emission steps, with only a single final jump from the PBS to the RC. In the transmembrane-type LHCs, each complex serves as a single absorbing/emitting unit, with ET over major distances between LHCs, and between LHCs to the internal PS antenna chromophores. One might expect the loose packing of the PBS chromophores to decrease the overall ET efficiency, however *in vivo* and *in vitro* measurements show similar, almost unity efficiency. The goal of this review is to describe the structural characteristics that allow this phenomenon to exist. In addition, we will describe the unique methods of protection from over-excitation of the RC as well as the mechanism for balancing PSII/PSI photochemistry in the PBS containing organisms.

## 3.2 PBS Assembly Affords Efficient Energy Transfer in Different Geometries

Phycobiliproteins (PBP) are the major building blocks of the PBS. Each PBP binds 1–3 tetrapyrrole bilin-type chromophores. The chromophores are produced within the cells by the activities of heme oxidases. When cleaved, the heme backbone would tend to remain in a closed configuration, cyclohelical form with generally poor conjugation between adjacent double bonds. This leads to strong absorption in the UV with much less significant absorption in the visible region. Nevertheless, when incorporated into a protein environment, the bilins are stretched almost to their maximum length, with protein-induced twisting that results in almost conserved ZZZasa geometry. When positioned correctly, their ability to both strongly absorb light in the range of 500–680 nm as well as avoid non-radiative relaxation (either as heat or conformational changes) is enhanced. The bilins are thus well suited to harvest solar energy in a wide range of the visible spectrum that is not covered by chlorophyll *a,* the major pigment of the RCs. To avoid binding instability of the bilins, resulting from the solubility of the PBPs and bilin linearity, the bilins are covalently bound to the PBP via specific thio-ether bonds with conserved cysteine residues. Bond formation is catalyzed by a specific class of lyases (Scheer and Zhao 2008).

The phycobilisome can be generally divided into two main domains: the core domain (2–5 inner cylinders) and the rod domain (6–8 cylinders surrounding the core domain). The most basic assembly of PBPs is typically called a monomer in the literature, despite actually being a heterodimer made of one α subunit and one β subunit (Fig. 3.1a). Monomers self-assemble into trimers, which in turn self-assemble into hexamers (mostly due to formation of interactions between the face

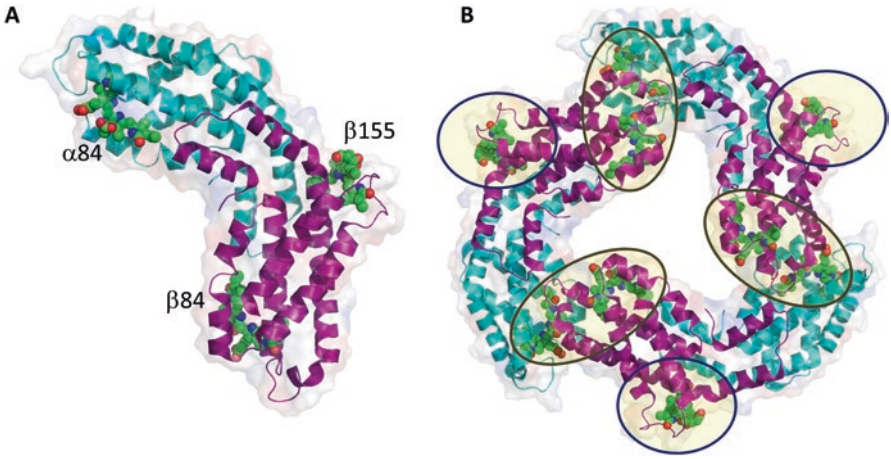


**Fig. 3.1 Phycobiliprotein assembly.** (**a**) The lowest level of assembly of all phycobiliproteins (PBP) is the monomer. Here, a PC monomer (coordinates from PDB code 3O18) is depicted in cartoon representation with the α subunit in cyan in the back and β subunit in purple in front. Three phycocyanoblilin chromophores are presented in atomic space filling representation in CPK colors, and named after the cysteine residue to which they are covalently bound (APC, PE and PEC contain less or more chromophores, not shown). **(b)** The second level of assembly of all PBPs is obtained by self-assembly of three monomers. Here, the PC trimeric assembly creates 3 pairs of coupled PCBs (colored in CPK and circled by brown oval) in the inner circumference of the trimer. The 3 β155 PCBs (colored in CPK and circled by dark blue oval) are positioned in the outer circumference of the trimer. All molecular graphics obtained using Pymol (The PyMOL Molecular Graphics System, Version 1.8 Schrödinger, LLC)

formed by the ring of α subunits in the trimers) and finally into either rod or core cylinders (formed via interactions β-β interface of the hexamers), depending on the PBP variant present. Trimerization brings chromophores found in adjacent monomers into closer proximity (~20 Å center to center). Within the rod and core cylinder assemblies one can also find a second class of proteins called "linker proteins" (LPs), which are mostly non-chromophorylated (Tandeau de Marsac 2003; Liu et al. 2005). It was recently suggested (Marx et al. 2014) that LPs may have an additional role; Based on volume calculations, it was deduced that rod LPs are relatively condensed and may be confined to a single hexamer and therefore do not necessarily physically/structurally "link" adjacent hexamers, but rather have a tuning effect and assist in energy propagation within the complex. This hypothesis was very recently supported by empirical findings (Chang et al. 2015).

The size, constitution and arrangement of the PBS is species-specific. Each form of PBS can contain 6–8 rod cylinders, with each cylinder containing 2–4 hexamers. Rods will always contain the PBP called phycocyanin (PC, $\lambda_{max}$ = 620 nm) that are found adjacent to the core. However, in addition the rods may contain other PBPs that expand the cross section for absorption: phycoerythrin (PE; $\lambda_{max}$ = 560 nm) or phycoerythrocyanin (PEC; $\lambda_{max}$ = 575 nm). PE or PEC are always assembled onto the PC hexamers and are distal to the core. The PBS core consists of 2–5 cylinders,

each cylinder containing 1–2 hexamers of the lowest energy absorbing PBP unit, called allophycocyanin (APC; $\lambda_{max}$ = 652 nm).

PC and APC bind the same chromophore called phycocyanobilin (PCB). While the APC monomer binds 2 PCB molecules covalently attached to Cys84 of both the α and β subunits, the PC monomer binds 3 PCB molecules. Two PCB molecules are bound at the same positions as described for APC while an additional PCB is bound to Cys155 (for numbering of residues see ref. (Apt and Grossman 1993)). At the trimeric level, both α84 and β84 are found in the inner circumference of the trimer, with PC having its β155 chromophore located at the outer circumference of the trimer (Fig. 3.1b). In their monomeric forms, both PC and APC have similar absorption and emission characteristics. However, the APC trimer absorbs maximally with a bathochromic shift of about 30 nm as compared to PC (MacColl 2004). This major shift in absorption might suggest the formation of an exitonically coupled pair of chromophores (Holzwarth et al. 1990; Csatorday et al. 1984). Excitonic coupling infers a strong overlap of the excited states, which necessitates physical proximity (5–10 Å) and the necessary intervening milieu. PC has the identical α84 and β84 PCBs bound at the same positions and with similar configurations, yet there is no shift in absorption upon trimerization. The nearest distance between the PCBs in both APC and PC is ~20 Å center-to-center which is thought to be too big of a gap to allow for strong coupling. Thus, if there is indeed coupling involved in the bathochromic shift, it must be due to the differences in the surroundings of the PCBs in APC in comparison to PC. We have suggested that stronger coupling may exist in APC by the unique multiple shell surroundings of the chromophore pair (McGregor et al. 2008). In the shell immediately surrounding the APC PCBs there is a more hydrophobic pocket, which is encircled by a second, highly polar/charged shell. This exceptional encapsulation of the chromophore pair does not exist in PC, and is lost when APC is monomerized.

Two core basal cylinders typically assemble onto the membrane surface while the rest of the core cylinders are assembled on top of the basal layer. The basal layer cylinders contain minor APC subunits that have been shown to serve as the terminal emitters (referred to as ApcE and ApcD). The width of the two basal APC core cylinders matches in dimension that of a single Photosystem II dimer within the membrane. These cylinders are the most likely to propagate energy transfer between the PBS and the RCs thanks to the strong overlap of the emission of the terminal emitters and the absorption of chlorophyll *a* found in PSII, as will be discussed later.

Elucidation of the PBS structure and assembly has been a major goal of many research groups for the past 50 years. Extensive efforts have been made throughout the years to determine the elaborate structure of the PBS and the exact way in which each subunit interacts with each other in the process of efficient energy transfer. Individual PBP structures were mostly determined using X-ray crystallography, however the overall complex has yet to be determined using this technique. The biggest success in this aspect was achieved using transmission electron microscopy (TEM) of isolated PBS complexes (Gantt and Conti 1966; Bryant et al. 1976; Tandeau de Marsac and Cohen-Bazire 1977; Arteni et al. 2009). In their native environment, attached to the stromal side of the membrane, it was suggested that the

protein dense environment in the intramembrane space contributes to maintaining the assembled complexes (Gantt and Lipschultz 1972; Zilinskas and Glick 1981). Various studies have produced micrographs of negatively stained, isolated PBS (Glazer 1989; Anderson and Toole 1998) while other studies yielded much less ordered aggregations. However, *in situ* membrane associated PBS investigations are rather scarce and these show very tightly arranged complexes (Liu et al. 2008).

Upon cell rupture in typical low ionic strength buffer solutions, much of the PBS is released from the cell. The released PBS has been shown to rapidly disassemble under these conditions, typically to the level of trimers (Yamanaka et al. 1978). Preserving complex intactness by external means is thus required and the use of high concentrations of buffered phosphate ions (>0.75 M) yield the best result. It has been proposed that the high salt concentration imitates the dense protein environment in the stroma (Stagg et al. 2007). The high phosphate requirement is an obstacle in the EM sample preparation procedure, which entails removal of the concentrated salts prior to TEM staining. Therefore, it is quite possible that this procedure has an effect on the resulting image.

One method of coping with this shortcoming is to eliminate the phosphate buffer as fast possible before negatively staining the sample so that the complex will have as little time to disassemble. This was done quite successfully by Chang et al. (2015), producing a detailed image by 3D reconstitution of the intact PBS and a PBS in complex with PSII, and also located most of the LPs. LPs are more difficult to structurally analyze as they are located with the cylinder rings, but are lost upon isolation. All but one high-resolution X-ray structure of PBPs are either devoid of the linkers, or if present, are situated on symmetry axes in a fashion that averages out their contribution to the diffraction pattern.

Alternative methods have been developed to try and visualize as accurately as possible the ‘native’ form of the PBS, aiming to assign the role of each subunit, and thereby obtain an overall mode-of-action of each of the sub-components. Recent findings have suggested that the canonical PBS structure might not be the only form of assembly that affords efficient energy transfer, in essence there may be more than one “right” way to assemble the PBS complex. This hypothesized flexibility in structure functionality is best demonstrated through the use of the cross-linking (CL) stabilization. CL stabilization of the PBS was developed to overcome the aforementioned instability of the isolated PBS complex in the absence of high ionic strength buffer. Covalent cross linking was obtained by use of the general reagent glutaraldehyde (GA) on the PBS isolated in high concentration phosphate buffer (HPB). Since GA is a quite short cross-linker (7.5 Å between its functional groups) and the concentrations of both the GA and the PBS were reduced in HPB solution, CL occurs mostly in an intra-complex fashion, thus eliminating the potential for inter-complex artifacts and retaining the ‘native’ PBS architecture. Following CL, the stabilized PBS can be transferred to low salt conditions, enabling better use of various techniques which require low salt, such as crystallization, purification by chromatography, negative-stained TEM and non-stained cryo-TEM. This procedure has helped us to demonstrate functional intactness of the intact PBS with clear energy transfer from PC to the terminal core emitters, ApcD and ApcE, without the

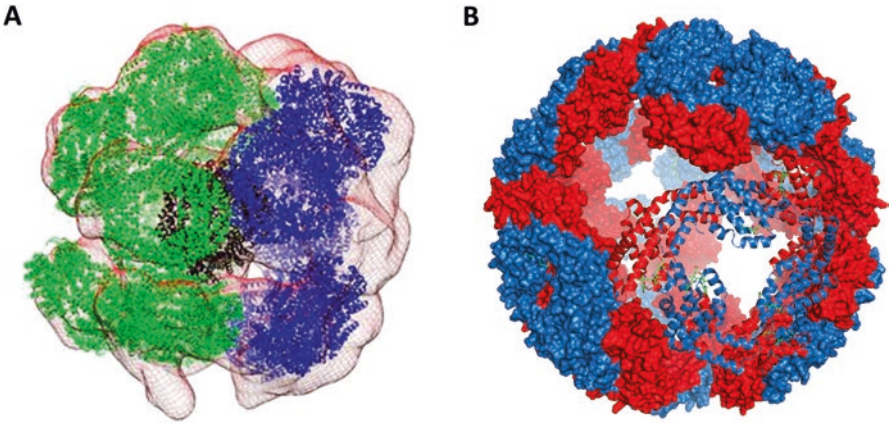


**Fig. 3.2 Phycobiliproteins unorthodox assemblies**. (**a**) Stuffed-ball like structure as obtained from cryo-TEM micrographs of cross-linked stabilized PBS complexes from *T. vulcanus* (adapted from David et al. 2014). The center of the ball contains a single hexamer in black, surrounded by dome-like assembly made of 5 hexamers (blue) and 8 hexamers (green) were fit into six elongated protrusions connected to the dome. (**b**) Structure of ApcD (blue) and ApcB (yellow) compose 8 α/β trimers which form a cage-like assembly in the crystal lattice (PDB code 4PO5) as described in Peng et al. (2014). All trimers are shown in surface representation except for the outward facing trimer that is in cartoon representation

presence of HPB (David et al. 2014). Various studies in our lab have produced functional cross linked PBSs in low salt buffer from different cyanobacterial species: the thermophilic *Thermosynechococcus vulcanus* (Tv), the mesophilic *Synechocystis* sp. PCC 6803 (Syn) and the chlorophyll *d* containing *Acaryochloris marina* (Am). While the cross-linked PBSs were indeed completely functioning in energy transfer from PC to the terminal APC emitters, both negatively stained TEM and single particle reconstruction by cryo-TEM showed that the TvPBS was not in their accepted "native" fan-like form; TvPBS exhibited an open globular structure instead of the accepted fan-like structure (Fig. 3.2a). Each of the proposed hexameric units of PC is connected to the cap of the structure which was proposed to contain APC, although the low resolution did not afford clear identification of the different components.

This same material, cross-linked stabilized TvPBS in low salt was also crystallized. The crystal structure of this was solved to 2.4 Å (PDB code: 4N6S), and surprisingly showed that the crystal packing forces had altered the PBS structure. The crystal contains infinitely elongated rods, very much the same as found previously for *T. vulcanus* trimers or rods (David et al. 2011). However, unlike these previously determined crystal structures, the PBS crystals showed energy transfer from PC to APC by confocal microscopy. In addition, mass spectrometry analysis of solubilized crystals showed the presence of all of the core components. We hypothesized that the core components are randomly distributed within the crystal structure and therefore did not contribute to the electron density. The structure was solved with a single PC monomer in the asymmetric unit.

The main and surprising conclusion from both the globular and rod-like cross-link stabilized PBS altered complexes was that the energy transfer, which was assumed to be highly dependent on the elaborate and precise assembly of the whole complex, was in fact seemingly independent and quite un-affected by the apparent massive structure alteration. This functional sturdiness might be a result of the threefold symmetry of all PBPs, which affords strong coupling in multiple directions. Recent investigations of the rod-core interface using cross-linking coupled to mass spectrometry have proposed a PC/APC interface, which was used to build a model of the rod-core interaction (Tal et al. 2014). It was suggested that the rod is oriented perpendicular to the core, entirely covering the core hexamers with its own circumference. It was also found that the PC chromophore closest to the interface (β84) and the nearest APC chromophores are about 30 Å away. Although remote, the energy transfer is highly efficient and ultra-fast (~psec scale), much faster than typically measured for such long-distance transfer. We therefore infer that the PBPs can assemble in many different interface types which afford efficient long-range energy transfer. While the typically accepted mechanism for long range (>10 Å) energy transfer is based on the model of Förster Resonance Energy Transfer (FRET), the almost unitary efficiency and fast kinetics of energy transfer between the rod PC and core APC would appear to indicate that some form of excitonic coupling, perhaps mediated by the protein environment, exits here.

Unlike the APC core components, in which all of the chromophores are embedded within the protein environment, as found closer to the internal circumference of the PBP disks, PC, PEC and PE all have additional chromophores, that are found on the outer circumference of the disks, and are less embedded with the protein matrix. In isolated monomeric or trimeric form, the peripheral chromophores have been shown to have the highest energy absorption (MacColl 1998). However, when the PBS is assembled, and organized within the crowded intercellular milieu (as mentioned above), these chromophores may actually be brought into close proximity to one another and the assembly could tune their absorption/emission properties to values that might promote inter-complex energy transfer. The case of *A. marina* PBS is a unique example of such organization. Electron micrographs show the PBS to be rod-like structures with a repetitive structure spread throughout the thylakoid membrane in a near-crystalline array (Chen et al. 2009). The AmPBS was hypothesized to be composed of 3 PC hexamers and 1 PC/APC heterohexamer by spectroscopic characteristics and by Western blot protein identification. This PBS is lacking a conventional terminal emitter. While rod or core components of other cyanobacteria are easily isolated, our lab encountered great difficulties in isolating the hypothesized “heterohexamer”, comprised of both PC and APC, which was originally determined and isolated by (Hu et al. 1998; Marquardt et al. 1997). While accurate identification by LC-MS/MS of PC was published since (Chan et al. 2007), APC isolation or identification by LC-MS/MS appears to be more difficult and has not been reported. While the isolated AmPBS appears to perform normal PC to APC energy transfer, in our analysis, the amount of the APC component is nearly undetectable, and well below the 1:7 APC:PC ratio of the hypothesized model. We have hypothesized that the APC component may indeed be only a single monomer within

the terminal trimer (and not a full APC trimer). It would be difficult to differentiate between such an assembly, as it would be somewhat homologous to that of the ApcD components of the regular PBS forms, in which a single copy of ApcD replaces a single copy of ApcA, forming a hetero-trimer. In order to assure efficient energy transfer within the *in situ* organized AmPBS assembly, it is possible that the AmPBS transfers energy efficiently laterally, from rod to rod in competition with internal energy transfer, within the rod. Since not every rod will be situated ideally above an RC, the lateral transfer mechanism would facilitate transfer to a rod that is situated optimally, and from there energy will be transferred to the RC.

The concept of lateral energy transfer in PBPs has already been applied in a semi-synthetic assembly (Eisenberg et al. 2014). Here, it was shown that isolated TvPC could be made to spontaneously assemble into nanowires when placed on a glass substrate, exhibiting long range energy transfer through hundreds of aligned trimers. Energy transfer was achieved over 2 μm from the area of excitation. It was suggested that this might be at least partially a result of long range excitonic coupling. We therefore suggest that the highly packed environment (Fig. 3.3) could

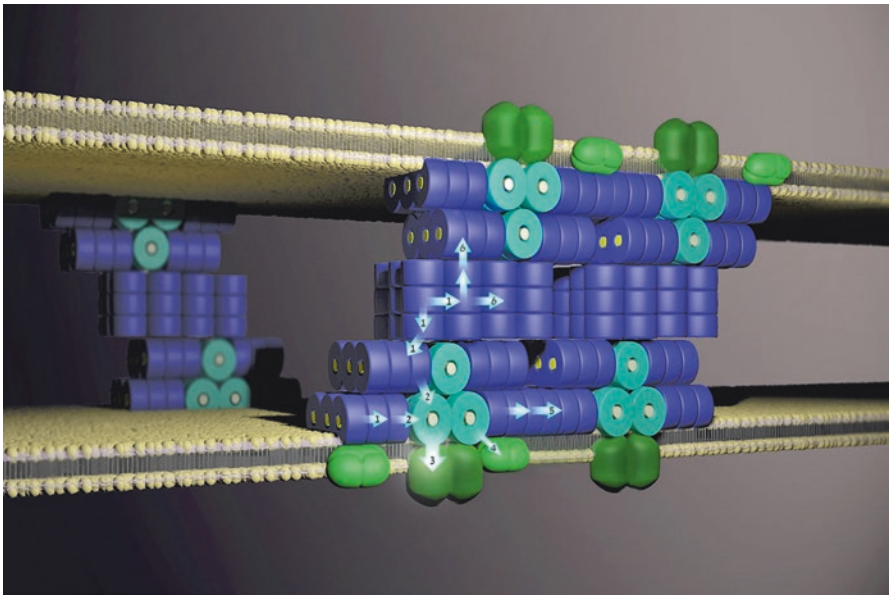

**Fig. 3.3 Schematic representation of thylakoid membranes with respect to PBS abundance in the stroma.** PBS core basal cylinders sit on top of a PSII dimer (dark green). The rods are positioned perpendicularly to the cores, having their circumferences covering the core cylinders. The rods can interact with their distal ends with a trimeric PSI complex (bright green). The core cylinders may be in contact with either a PSII dimer and/or a PSI trimer (as demonstrated in the closest PBS core assembly). Excitation energy transfer (EET) is depicted in white arrows and the direction of energy flow is denoted by numbers: *1*. Intra-rod intra-PBS EET, *2*. EET from rods to core. *3*. EET from PBS to PSII. *4*. EET from PBS to PSI. *5*. Inter-rod EET, between adjacent PBS on the same membrane. *6*. Inter-molecular EET between PBSs, between PBSs on different membranes

facilitate energy flow not only internally in a single PBS complex, but also in an inter-complex fashion between closely associated PBSs. Moreover, we would advocate looking at the whole thylakoid membrane stroma as the true form of the PBS antenna instead of the view of each PBS serving as an independent antenna. In essence, following the initial photon absorption at any one chromophore site, energy transfer can occur within the absorbing element (rod or core cylinder), between rods (lateral transfer) or even between rods that belong to PBS attached to adjacent membranes (*see* Arteni et al. 2008).

Unlike core trimers made up of ApcA/ApcB monomers (the most prevalent APC component, hereafter called APC660 due to its maximal 660 nm fluorescence emission wavelength), the core possesses the aforementioned terminal emitters ApcD and ApcE, that emit at ~680 nm fluorescence emission wavelength. As mentioned above, ApcD is an α-subunit like homolog. ApcE however is much larger with molecular weights of between ~70–120 kDa, depending on the size of the PBS – from bicylindrical to pentacylindrical cores. In addition to its α-subunit domain, ApcE has multiple additional loops. It has been suggested that these additional ApcE loops perform a physical "linking" function for the entire core substructure, and have a tethering effect to PSII (Liu et al. 2005; Zhao et al. 2005; Lundell et al. 1981). Much like all other rod and rod-core LPs, the hydrophobic nature of ApcE is a major hurdle in its study. When trying to isolate it in low salt conditions precipitation occurs and therefore its structure could not be resolved as a whole (same as other LPs). Some success was achieved when only segments of LPs were expressed (Tang et al. 2015; Gao et al. 2011). Due to the highly symmetric nature of the PBP assemblies, however, the contribution of the LPs to the diffraction is averaged out, and the LPs position does not appear in the electron density maps; only a single X-ray structure of the complex between an APC trimer and the small core linker ($L_c$) exists (David et al. 2011, 2014; Reuter et al. 1999; Chang et al. 1996; Contreras-Martel et al. 2001). Recently, a high resolution crystal structure of ApcD was obtained (Peng et al. 2014), however not in its native environment as part of an $(ApcA/ApcB)_2(ApcD/ApcB)$ trimer. The crystal structure revealed that the unique protein environment of ApcD, coupled with a normal ApcB subunit confers a strong effect on the PCB chrmophore, making it highly planer. The high degree of planarity is suggested to increase the conjugation of the PCB chromophores, inducing the strong red-shift. This situation is apparently different in the case of ApcE α-subunit domain. Here, the trimer is a (ApcA/ApcB)(ApcE/ApcB)(ApcA/ApcF) trimer, where ApcF is a homolog of ApcB. The trimer is assembled in a fashion that brings the ApcE and ApcF from adjacent monomers in proximity. The PCB chromophore of ApcE is bound such that its position within the binding pocket is different than in ApcA (McGregor et al. 2008) and combined with the unique surrounding imparted by the ApcF subunit most likely creates a stronger red-shift inducing coupling. A modified ApcE-type construct expressed in *E. coli* was recently described (Miao et al. 2016) and in this construct the PCB was not covalently bound to the protein, and the result was an even greater red-shift, absorbing >700 nm.

Other suggested effects on the terminal emitter photophysical characteristics include possible π-π interaction between the D ring of the PCB and a nearby Tryptophan side chain (50), and the fact the PCB of ApcE adopts the rare ZZZssa geometry (which is typical for bilin chromophores in phytochromes and cyanobacteriochromes), which is known to induce >650 nm maximum in absorbance (Tang et al. 2015).

This redshifted characteristic of the APC680s creates a superb overlap between the emission of the APC680 with the absorption cross-section of chlorophyll *a*, the major chromophores in cyanobacterial RCs (MacColl 2004). The distance between the APC680 chromophores and the nearest chlorophyll molecules is even further than the minimal 20 Å separation in the case of the chromophore pair and the 30 Å separation in the case of rod-core interface, and is most likely on the order of 40 Å. As demonstrated in Fig. 3.4, the possible β155- β155 distance between adjacent rods may compete well with all of these distances, enabling lateral energy flow. It should be noted that Peng et al. (2014) also produced a very interesting spherical cage-like ultra-structure in the crystal lattice (Fig. 3.2b). This is a rather unique assembly within structural realm of PBPs X-ray endeavors and may provide additional evidence for the unorthodox nature of the PBPs to cross-interact.

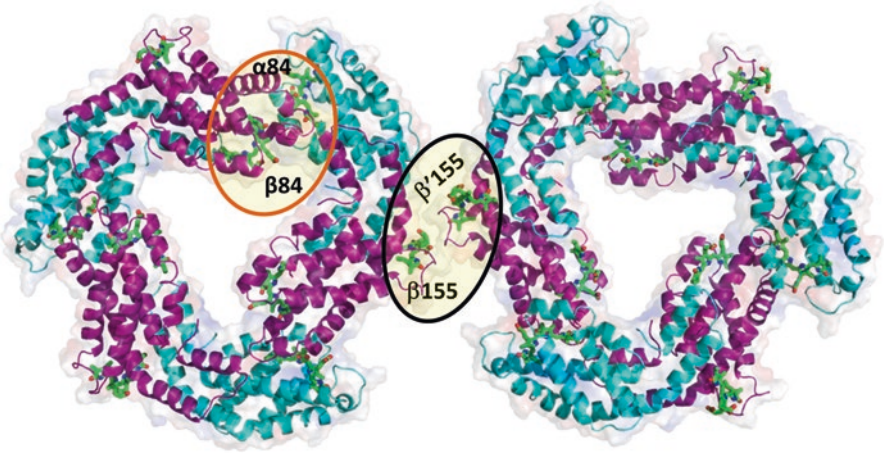


**Fig. 3.4 β155 promotes lateral energy flow.** 2 PC trimers (PDB code 3O18) are shown positioned in opposite orientations, mimicking two rods of neighboring PBSs. Internally coupled PCBs (α84 and β84, circled by orange oval) in the inner circumference of the trimer have about the same center-to-center separation (~20 Å) as the externally coupled PCBs (β155 and β '155, encircled by black oval) are suggestively positioned in high proximity in the outer circumference of each trimer, possibly creating a viable route for inter-complex energy propagation

## 3.3 The Final Step: Energy Transfer to Reaction Centers or Energy Dissipation

Once absorbed, the energy must be transferred swiftly to its final destination, to avoid alternative dissipative routes by other mechanisms, such as fluorescence or heat. On the other hand, photosynthetic systems have been shown to be optimized to certain regimes of light intensity and quality, and thus shifting the energy flow from productive energy flow (leading to charge separation) or dissipation (preventing photoinhibition) is a necessary prerequisite of the overall system. One of the major questions that has been addressed by many studies over the years is the major target for the absorbed energy. It should be noted that in both cyanobacteria and red algae, the ratio of PSI:PSII is not approximately equimolar, as it is in plants and green algae. The ratio can change, depending on the light intensity and quality, but it has been typically found to be between 2:1 and 10:1 (Fraser et al. 2013; Sonoike et al. 2001; Kawamura et al. 1979). One of the reasons for this disparity has been the suggested importance of cyclic electron flow driven by PSI (Munekage et al. 2004), but also due to the size and efficiency of the PBS. The amount of PBS appears to be rather invariant, covering the stromal surface of the thylakoid membrane. Since the major pigment of the accessory internal antennas of both PSII and PSI is chlorophyll *a* (except for only a few organisms which contain red-shifted major pigment such as chlorophyll *d* in *A. marina*), it is quite reasonable to assume that energy transfer to both photosystems is possible. It has been shown that the PBS can associate with PSII functionally through interactions with ApcE, and thus it has typically been assumed that the PBS mostly serves as an antenna to PSII. If indeed most of the PBS energy flows into the PSII RC, it would explain how significantly fewer PSII complexes can provide sufficient electron flow (via the cytochrome b6/f complexes) to the more prevalent PSI. This can also be rationalized by the need to ensure sufficient excitation of PSII which has a small internal bed of pigments (only 35 chlorophyll *a* molecules per RC) as opposed to PSI (which have nearly 100 chlorophyll *a* molecules per RC). The aforementioned covering of the stromal side of the thylakoid membrane will certainly lead to the state of close contact between the PBS and PSII, but will also allow contact with PSI. Interestingly, a unique rod-like PBS found in association with pseudo-tetrameric PSI was isolated from *Anabaena* sp. PCC 7120 (Watanabe et al. 2014). This unique rod-like PBS contains the only variant of the rod-core linker, CpcG3, which has a highly hydrophobic C-terminal domain (out of four different CpcGs in the genome). It was suggested that this hydrophobic C-terminal of CpcG serves as an anchor in the membrane, placing the end of the rod on the periphery of the PSI tetramer. Liu and co-workers have identified a "mega-complex" in *Synechocystis* sp. PCC 6803, by also applying cross-linking stabilization, *in vivo* (Liu et al. 2013). This "mega-complex", which is comprised of a PBS, a PSII dimer and a PSI trimer, has a molecular mass of over 7.5 MDa (as depicted in Fig. 3.3). The *in vivo* cross linking approach can yield functional PBS structures which transfer energy to the reaction center successfully (David et al. 2014; Papageorgiou 1977). Although being able to transfer energy to

both photosystems, it was clearly demonstrated that while PBS-PSII energy transfer was extremely swift (faster than maximal resolution of measuring device), the PBS-PSI energy transfer was rather slow. It was suggested that unlike the tight and fine-tuned PBS-PSII interaction, the PBS-PSI energy transfer rate could be either a result of spillover from PSII, loose interaction interface between, PBS and PSI, or due to the stabilizing cross-linking reagent.

In natural environments the abiotic environment changes constantly. To sustain photosynthetic life, the structure and function of the PBS antenna must react to these changes. The reaction to changes in light quantity (intensity) or quality (wavelength) may be swift and reversible, or slow and more permanent. We can describe these changes as "short term" acclimation processes like state transitions and non-photochemical quenching and "long term" processes like PBS degradation and chromatic acclimation.

### *3.3.1 State Transitions*

State transitions enable redistribution of absorbed light between photosystems, according to changing light quality and intensity. This process provides photosynthetic organisms with the ability to acclimate to changing environmental conditions. The phenomenon was first described in green and red algae (Murata 1969; Bonaventura and Myers 1969) in the 1960s. State transition allows excitation energy reallocation between PSI and PSII to support efficient energy flow through the photosynthetic apparatus. Moreover, differential energy transfers to either PSI or PSII by phycobilisomes have also been shown to be induced by changes in osmolality (Stamatakis and Papageorgiou 2001).

The extent of state transition differs between photosynthetic organisms. Much of the work in this field was performed using the green alga Chlamydomonas reinhardtii, an organism in which state transition plays a prominent role in photosynthesis (Rochaix et al. 2012). Although components of the photosynthetic apparatus differ between green algae and cyanobacteria (Hohmann-Marriott and Blankenship 2011), the concept of state transition remains similar. When illumination is such that it leads to excess excitation of PSII, transition from state 1 to state 2, a state favoring excitation of PSI, occurs. When PSI is excited in excess, transition from state 2 to state 1, favoring excitation of PSII, occurs.

In cyanobacteria state transition is often measured using dark vs. low light conditions as opposed to the red vs. far red light protocol used commonly for algae and plants There are a number of chlorophyll fluorescence-based tools for detecting state transition in cyanobacteria. State transition was shown to effect the slow (tens of seconds) "S to M" transition in fluorescence rise kinetics, for example (Kana et al. 2012). The major tool for detecting state transition is measurements of 77 K chlorophyll fluorescence spectra (Krause and Weis 1984; Walters and Horton 1991; Demmig and Bjorkman 1987). The samples are exposed to a specific light-state prior to freezing in liquid nitrogen. Low temperature detection resolves the PSI

fluorescence component that cannot be observed at room temperature. Shifts in the relative intensity of the PSI and PSII peaks record the distribution of excitation energy between the photosystems.

State transitions in cyanobacteria are likely to be prompted by changes in redox state of electron carriers between PSII and PSI. This was shown by Mullineaux and Allen, who, in their experiment, used various chemical and illumination treatments to modify the redox state of the electron transport chain. They found that state transitions occur in response to change in the redox state of the plastoquinone pool and therefore concluded that they are controlled by the redox state of plastoquinone or a closely associated electron carrier (Mullineaux and Allen 1990).

Two mechanisms of state transition have been proposed: the first involving phycobilisomes, in which case phycobilisomes transfer energy differentially to either photosystem according to light conditions (Van Thor et al. 1998); the second mechanism involves energy transfer between reaction center chlorophylls, and is described as the spillover of energy from PSII directly to PSI (Federman et al. 2000). Diffusion of phycobilisomes between photosystems was shown, using the Fluorescence Recovery After Photobleaching (FRAP) method, to be required for phycobilisome-dependent state transitions (Joshua and Mullineaux 2004). However, this matter is still debated, and it has also been reported that illumination used in the FRAP method may cause excitonic decoupling of phycobilisomes from the reaction centers and possibly even detachment from the thylakoid membrane (Tamary et al. 2012).

A random mutagenesis approach used by Emlyn-Jones and coworkers identified genes essential for state transition in cyanobacteria. State transition deficient mutants all appeared to have one defective gene – rpaC. These mutants are locked in state 1 (Emlyn-Jones et al. 1999). The only documented phenotype of rpaC deletion mutants is lack of state transitions, a phenotype expressed uniquely under low light intensities and wavelengths relevant to phycobilisomes. This led Mullineaux and Emlyn-Jones to conclude that state transitions in cyanobacteria are only physiologically important under low light, allowing optimization of light absorption by the photosystems (Mullineaux and Emlyn-Jones 2005). Dong et al. (2009) described the phycobilisome terminal core emitter protein, ApcD, as being essential for both state transition and protection against photodamage under high light conditions. ApcD is required for direct energy transfer from phycobilisomes to PSI (Dong et al. 2009). Mutants lacking ApcD were unable to perform state transitions and were more sensitive to photoinhibition when grown under green light, which is preferentially absorbed by phycobilisomes. This effect is likely due to an inability to redirect light to PSI through transition to state 2.

Evidence for the structural basis of state transition can be drawn from the analysis of *in vivo* cross-linking and LC-MS results. The aforementioned megacomplex formed in cyanobacteria by phycobilisomes, PSII and PSI (Liu et al. 2013) could be a source of part of the state transition mechanism. Beyond the structural implications discussed above, time resolved fluorescence spectroscopy measurements indicate that energy transfer occurs from the attached phycobilisome core to both photosystems. Energy transfer rates to PSI are slower than to PSII. Modulations of this structure may provide a basis for the state transition phenomenon.

### 3.3.2 Non Photochemical Quenching

Fluorescence quenching terminology was developed for higher plants where it is defined as a decline in the maximal fluorescence ($F_m$) following transition from dark to light (Krause and Weis 1991). Fluorescence quenching is composed of a number of components; state transition, discussed above, being one of them.

While state transition is a dark/low light phenomenon, non-photochemical quenching (NPQ) takes place under excess light conditions. Under these conditions the risk of photoinhibitory damage increases (Keren and Krieger-Liszkay 2011; Tikkanen et al. 2014). With NPQ the risk is mitigated by releasing a larger fraction of the absorbed light energy as heat (Papageorgiou and Govindjee 2011; Horton 2012). Different mechanisms were proposed for the NPQ phenomenon in the plant and algae, including the effect of pH, carotenoid de-epoxidation and the involvement of the PsbS protein (Li et al. 2009; Campbell et al. 1998). In cyanobacteria, where PsbS and antenna carotenoids are missing, NPQ reacts differently and is driven by different mechanisms. In cyanobacteria $F_M$ fluorescence in the dark adapted state, $F_{M\text{-dark}}$, is low (Wu and Krogmann 1997). Under actinic illumination higher $F_M$ levels can be measured. Exposure to high light intensity will result in reduced $F_M'$ values, or NPQ.

A major factor in cyanobacterial NPQ is the existence of the orange carotenoid protein (OCP). It was originally isolated as a soluble carotenoid protein by Krogmann and coworkers (Holt and Krogmann 1981; Wu and Krogmann 1997). The protein binds a single 3′-hydroxyechinenone carotenoid molecule. A mutant in which the gene coding for OCP was disrupted was found to be unable to perform NPQ (Wilson et al. 2006). State transition was not affected by this mutation. Biochemical analysis suggested that this soluble protein is associated with the PBS (Wilson et al. 2006). The structure and function of OCP were reviewed in detail for the past decade (Kirilovsky 2015; Kirilovsky and Kerfeld 2016; Kerfeld and Kirilovsky 2013). Recently, the structure of the active form of the N-terminal domain of the OCP binding a carotenoid chromophore was determined (Leverenz et al. 2015). It was inferred that upon high light irradiation, the OCP undergoes a significant structural change that modifies its characteristics from its inactive ($OCP^O$) state to its active state ($OCP^R$) by physically separating its N-terminal and the C-terminal domains. This separation causes the carotene molecule to disconnect from its association with the C-terminal domain and shift 12 Å deeper into a designated cavity within the now quenching-active N-terminal domain (Fig. 3.5a). Following these findings, a structural model for the PBS-$OCP^R$ interaction was suggested (Harris et al. 2016). By coupling of a cross-linking reaction (Fig. 3.5b) with LC-MS/MS analysis in addition to mutational analyses, it was concluded that the N-terminal domain of the OCP burrows into the terminal emitters' hexamer within a basal core cylinder, causing assembly alterations to the PBS (Fig. 3.5c). In this model scope is limited to a protein-protein interaction, therefore the exact nature of the quenching mechanism could not be deducted – it is not yet clear whether the carotenoid serves as a quenching pair to a PBS' bilin, or perhaps the PBS-$OCP^R$ interaction affects a nearby bilin, turning its energy propagation mode into a quench-

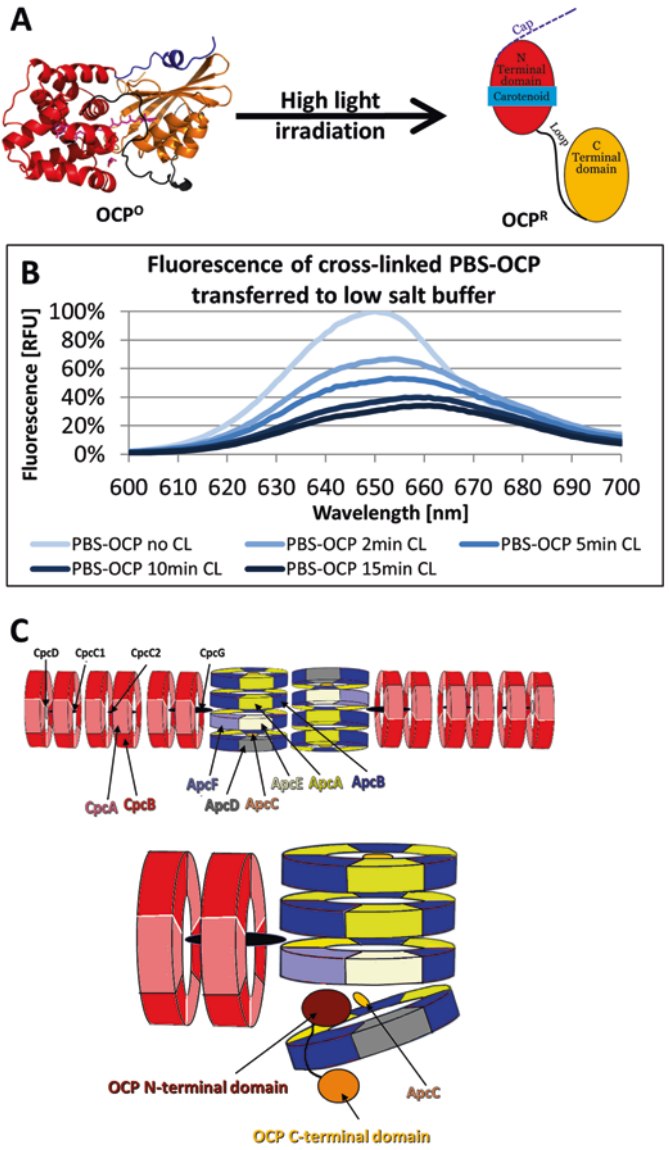


**Fig. 3.5** OCP-related NPQ mechanism of *Synechocystis* pcc sp. 6803 PBS. (**a**) OCP photo-induced transition. Following high-light irradiation, the OCP (depicted in cartoon representation, PDB code 3MG1) is converted by white light illumination from its inactive $OCP^O$ state to the active $OCP^R$ state. This transition is characterized by separation of the N-terminal (red) and the C-terminal (orange) domains which are still connected by a flexible loop (black). This separation causes the 3-hECN chromophore (cyan) to shift 12 Å deeper into the N-terminal domain from its original inter-domain location. (**b**) Fluorescence of time-dependent cross-linking of PBS-OCP complex in low salt buffer. As the cross-linking reaction proceeds further (by extending the reaction time), more significant quenching of fluorescence is observed (which can be attributed to enhanced stability of the PBS-OCP interaction), with a small redshift in the fluorescence

ing mode. However, it was clearly demonstrated that PBS assembly is altered, thus possibly favoring a specific energy propagation pathway towards the affected APC680 hexamer. This alteration suggests once more that structural adaptability is a virtue for the PBS function. While OCP clearly plays an important role, additional mechanisms were proposed for the NPQ phenomenon.

Although highly efficient, the OCP-dependent photoprotection mechanism is a relatively slow process. Recent work (Gwizdala et al. 2016) has suggested that the PBS has an additional NPQ mechanism, helping it to overcome high light stress with quick response, prior to OCP activation. It was proposed that this NPQ mechanism, called blinking for the presence of random and reversible metastable dark states of nanoscale emitters, is sufficient to avoid highly deleterious effects by reducing the intensities at merely 2% from $F_m$. Blinking was similarly demonstrated to effect mostly the core components of the PBS.

In addition, Tamary and co-workers suggested a heat dissipation mechanism based on small structural and functional alterations of the PBS structure (Tamary et al. 2012).

### *3.3.3 PBS Degradation*

As described above, the metabolic investment in the size and amount of PBS found lining the thylakoid membrane is great. A large proportion of the biosynthesis of new proteins that occurs within dividing cells is dedicated towards new PBS complexes. The sheer quantity of PBS complexes demonstrates its importance to the cell – driving all of photosynthesis (both PSII and PSI) which in turn provides the energy needed for all cellular processes. As indicated above, short-term mechanisms can provide better energy distribution as well as avoiding some aspects of over-excitation. In some environmental conditions, cells are exposed to additional forms of stress (extreme temperature changes, nutrient availability, etc.) to which over excitation can occur under conditions that inhibit protective mechanisms. Under some of these extreme conditions cyanobacteria disassemble and degrade their PBS. This physiological behavior would most likely be a "last-resort" mechanism, since it diminishes the very source of energy cells need for survival. The most studied condition in this respect is nitrogen limitation. The initial observation was that non-diazotrophic cyanobacteria lose their typical blue-green color under nitrogen limitation (Allen and Smith 1969). Originally named "nitrogen bleaching", it was found to be caused by a decrease in the concentration of the PC component of

**Fig. 3.5** (continued) maximum (which can be attributed to enhanced PBS assembly integrity). (**c**) PBS bottom view (from the thylakoid membrane looking up) and the suggested model of PBS-OCP interaction. The N-terminal domain of $OCP^R$ penetrates into the terminal emitters' hexamer of the basal core cylinder, causing structural rearrangement within the PBS core. The C-terminal domain is left outside the complex volume available for interaction with FRP for fluorescence recovery upon relaxation in irradiation conditions (For more details, *see* Leverenz et al. 2015)

the PBS. The change in cellular pigmentation could be reversed by the re-addition of nitrogen compounds to the growth media (Baier et al. 2001). The process of PBS breakdown and recovery following nitrogen supplementation, its kinetic properties and molecular control mechanisms, have been subjected to intensive research conducted with different cyanobacterial strains (Baier et al. 2001; Collier and Grossman 1992, 1994; Elmorjani and Herdman 1987; Gilbert et al. 1996; Gorl et al. 1998; Krasikov et al. 2012; Lau et al. 1977; Sauer et al. 2001; Schwarz and Grossman 1998). The common feature reported in these studies was a massive, regulated breakdown of PBS on a time scale of a few hours to 2 days following nitrogen step-down. The first step of the response to nitrogen limitation is the disassembly of the PBS. Disassembly is initiated by the expression of the NblA (non-bleaching A) protein. Activation of the NblA degradation pathway is itself under the control of the response regulator NblR (Schwarz and Grossman 1998). The NblA protein is a small (~7 kDa) polypeptide that has no intrinsic proteolytic activity and it was thus proposed to serve as a molecular disassemblase (Dines et al. 2008; Baier et al. 2001; Collier and Grossman 1994). The NblA monomer has a helix-loop-helix motif which dimerizes into an open, four-helical bundle (Dines et al. 2008) and it was suggested that this structure allows NblA to interact with the phycobilisome via "structural mimicry" due to similarity in structural motifs found in all phycobiliproteins. NblA was found to be present in close association with PBS complexes *in vivo* and the current hypothesis is that its function is in tagging the PBS complex for degradation (Sendersky et al. 2014), possibly through the action of the Clp protease complex (Baier et al. 2014).

The amino acids released by the degradation of PBS can be used directly, or catabolically to provide nitrogen (and in some cases sulfur) to the cell (Boussiba and Richmond 1980). On the one hand, this reserve of critical nutrients can assist the cell in its survival long-term survival. However the reuse of internal stores, requires energy input as well, indicating that a delicate balance between PBS disassembly and photosynthetic rates must be maintained. For this reason, the nitrogen-bleaching mechanism is quite slow (days). Maintaining normal rates of photosynthesis, without the concomitant use of its energy-rich and reduced products, as well as reactive oxygen species, could lead to further internal damage to the cell (Schwarz and Forchhammer 2005). As the metabolic processes decrease due to lack of nitrogen, there is a shift to a metabolic state that drives the degradation of proteins, chlorophyll (reaction centers) and other components not absolutely essential for survival (Schwarz and Grossman 1998). As the PBS complexes are disassembled, the amount of excitation energy transferred to active reaction centers diminishes, reducing the stress on the cell. It has recently been shown that under a combination of nitrogen limitation and low light growth conditions, the rate of PBS disassembly and degradation is also reduced, supporting the suggestion that avoidance of over-excitation is indeed more critical to the cell than the actual lack of nitrogen (Salomon et al. 2013).

### 3.3.4 Chromatic Acclimation

An additional acclimation mechanism used by some cyanobacterial species is the synthesis of different PBPs or their associated chromophores to match the ambient illumination wavelengths. This phenomenon is referred to as complementary chromatic acclimation (CCA). Cyanobacteria capable of CCA must perceive the wavelengths of absorbed light, and respond by induction of signal transduction pathways, which lead to synthesis of the relevant PBPs and linker polypeptides (Kehoe and Gutu 2006; Grossman 1990). Regulation of the mechanisms of CCA has recently been further elucidated, with the identification of genes involved in the process as well as their mode of action (Shukla et al. 2012; Bezy et al. 2011; Gutu et al. 2013).

The prominent phycobiliproteins involved in the process are PC and two types of PE, PEI and PEII. PC accumulates in cultures grown under red light, while PE accumulates in cultures grown under green light. Not all cyanobacterial species expressing both PC and PE genes are capable of CCA, and the mechanism also requires expression of structural and regulatory genes for this purpose (Kehoe and Gutu 2006). Initially, three groups of responses to shifts between green and red light were identified in cyanobacteria expressing both PC and PE. In Group I, PC and PE content do not change in response to light wavelength; Group II exhibits a partial response to changing light wavelength, regulating only synthesis of PE; Group III, to which most cyanobacteria expressing both PC and PE belong, exhibits a more comprehensive response, showing differential accumulation of either PC or PE in accordance with light wavelength (Demarsac and Houmard 1988). More recent work on CCA has shown that it includes response to a wider range of wavelengths. Response to blue and green light, common among the marine cyanobacterial species *Synechococcus*, does not involve changes in the phycobiliprotein composition of the PBS rods, but rather of the chromophores associated with PEII (Gutu and Kehoe 2012). The PBS structure of cyanobacteria from hot spring bacterial mats was shown to be able to adjust to far red light (Gan et al. 2014).

Chromatic acclimation is controlled by photoreceptors, rather than by photosynthesis. Group III chromatic acclimation is regulated by two light-responsive pathways: Rca and Cgi (Demarsac and Houmard 1988). The Rca system regulates transcription under red light conditions (transcription of PC related genes and repression of PE related genes). It is controlled by the phytochrome-class photoreceptor RcaE, that has been suggested to act as a kinase in red light and phosphatase in green light. The Cgi system also operates under red light conditions, by post-transcriptionally repressing PE related genes, apparently via transcription attenuation, a process in which the translation initiation factor IF3 has been suggested to take part. Group II chromatic acclimation is controlled by a phytochrome-class photoreceptor-based two-component system, CcaS/R, which is capable of sensing both red and green light (Bezy et al. 2011; Gutu et al. 2013; Gutu and Kehoe 2012). Type 4 chromatic acclimation is still only poorly understood, however, progress has been made, beginning with the identification of MpeZ, an enzyme involved in ligation and isomerization of one of the PEII-linked chromophores (Shukla et al. 2012).

## 3.4 Conclusions

The exceptional energy transfer efficiency demonstrated by the PBS might be further explained by the lateral energy flow between adjacently associated PBSs, mostly through rod-rod interactions. This lateral process may assist in avoiding bottle-necks in intra-molecular energy transfer. Such an efficient, protein-rich antenna should therefore be accompanied by multiple adaptation mechanisms (Fig. 3.6), helping the organism to overcome stressful conditions which may lead eventually to cell death.

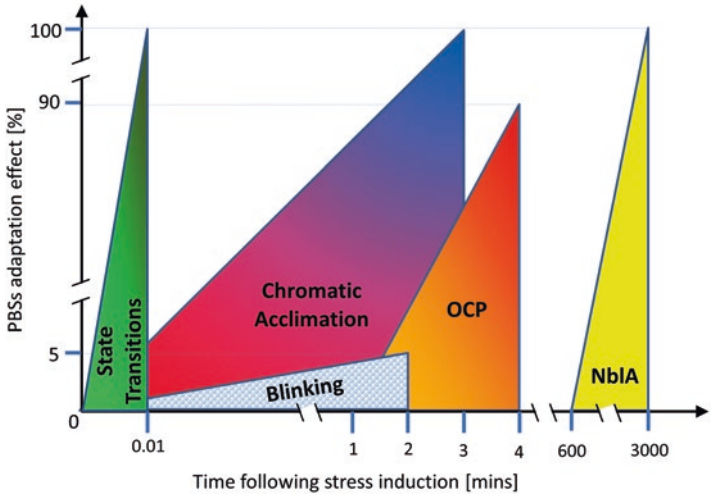


**Fig. 3.6 Short and long-term modifications to Phycobilisome activity**. Schematic illustration of the different mechanisms which modify energy transfer from the PBS to photosystems. Each triangle represents the adaptation process and the height of the triangle (along the non-linear Y axis) represents the strength of effect. The non-linear X axis shows the approximate response time following initiation of the relevant stress, either due to low light quality changes (state transitions), high irradiation fluencies (Blinking or OCP) or nitrogen starvation (NblA). The strength of effect on the PBS is determined by either decreasing the efficiency of EET (Blinking or OCP) or by protein degradation (NblA) or changing the efficiency of EET between photosystems (state transitions)

## References

Adir N (2005) Elucidation of the molecular structures of components of the phycobilisome: reconstructing a giant. Photosynth Res 85(1):15–32

Allen MM, Smith AJ (1969) Nitrogen chlorosis in blue-green algae. Arch Mikrobiol 69(2):114–120

Anderson LK, Toole CM (1998) A model for early events in the assembly pathway of cyanobacterial phycobilisomes. Mol Microbiol 30(3):467–474

Apt KE, Grossman AR (1993) Genes encoding phycobilisome linker polypeptides on the plastid genome of Aglaothamnion neglectum (Rhodophyta). Photosynth Res 35(3):235–245. https://doi.org/10.1007/BF00016555

Arteni AA, Liu LN, Aartsma TJ, Zhang YZ, Zhou BC, Boekema EJ (2008) Structure and organization of phycobilisomes on membranes of the red alga Porphyridium cruentum. Photosynth Res 95(2–3):169–174

Arteni AA, Ajlani G, Boekema EJ (2009) Structural organisation of phycobilisomes from Synechocystis sp. strain PCC6803 and their interaction with the membrane. Biochim Biophys Acta 1787(4):272–279

Baier K, Nicklisch S, Grundner C, Reinecke J, Lockau W (2001) Expression of two nblA-homologous genes is required for phycobilisome degradation in nitrogen-starved Synechocystis sp. PCC6803. FEMS Microbiol Lett 195(1):35–39

Baier A, Winkler W, Korte T, Lockau W, Karradt A (2014) Degradation of phycobilisomes in Synechocystis sp. PCC6803: evidence for essential formation of an NblA1/NblA2 heterodimer and its codegradation by A Clp protease complex. J Biol Chem 289(17):11755–11766. https://doi.org/10.1074/jbc.M113.520601

Bezy RP, Wiltbank L, Kehoe DM (2011) Light-dependent attenuation of phycoerythrin gene expression reveals convergent evolution of green light sensing in cyanobacteria. Proc Natl Acad Sci U S A 108(45):18542–18547. https://doi.org/10.1073/pnas.1107427108

Bonaventura C, Myers J (1969) Fluorescence and oxygen evolution from Chlorella pyrenoidosa. Biochim Biophys Acta 189(3):366–383

Boussiba S, Richmond AE (1980) C-phycocyanin as a storage protein in the blue-green-alga Spirulina-platensis. Arch Microbiol 125(1-2):143–147. https://doi.org/10.1007/Bf00403211

Bryant DA, Glazer AN, Eiserling FA (1976) Characterization and structural properties of the major biliproteins of Anabaena sp. Arch Microbiol 110(1):61–75

Campbell D, Hurry V, Clarke AK, Gustafsson P, Oquist G (1998) Chlorophyll fluorescence analysis of cyanobacterial photosynthesis and acclimation. Microbiol Mol Biol Rev 62(3):667–683

Chan YW, Nenninger A, Clokie SJ, Mann NH, Scanlan DJ, Whitworth AL, Clokie MR (2007) Pigment composition and adaptation in free-living and symbiotic strains of Acaryochloris marina. FEMS Microbiol Ecol 61(1):65–73. https://doi.org/10.1111/j.1574-6941.2007.00320.x

Chang WR, Jiang T, Wan ZL, Zhang JP, Yang ZX, Liang DC (1996) Crystal structure of R-phycoerythrin from Polysiphonia urceolata at 2.8 Å resolution. J Mol Biol 262(5):721–731

Chang L, Liu X, Li Y, Liu CC, Yang F, Zhao J, Sui SF (2015) Structural organization of an intact phycobilisome and its association with photosystem II. Cell Res 25(6):726–737. https://doi.org/10.1038/cr.2015.59

Chen M, Floetenmeyer M, Bibby TS (2009) Supramolecular organization of phycobiliproteins in the chlorophyll d-containing cyanobacterium Acaryochloris marina. FEBS Lett 583(15):2535–2539

Cheng YC, Fleming GR (2009) Dynamics of light harvesting in photosynthesis. Annu Rev Phys Chem 60:241–262. https://doi.org/10.1146/annurev.physchem.040808.090259

Cogdell RJ, Gardiner AT, Roszak AW, Law CJ, Southall J, Isaacs NW (2004) Rings, ellipses and horseshoes: how purple bacteria harvest solar energy. Photosynth Res 81(3):207–214

Collier JL, Grossman AR (1992) Chlorosis induced by nutrient deprivation in Synechococcus sp. strain PCC 7942: not all bleaching is the same. J Bacteriol 174(14):4718–4726

Collier JL, Grossman AR (1994) A small polypeptide triggers complete degradation of light-harvesting phycobiliproteins in nutrient-deprived cyanobacteria. EMBO J 13(5):1039–1047

Contreras-Martel C, Martinez-Oyanedel J, Bunster M, Legrand P, Piras C, Vernede X, Fontecilla-Camps JC (2001) Crystallization and 2.2 a resolution structure of R-phycoerythrin from Gracilaria chilensis: a case of perfect hemihedral twinning. Acta Crystallogr D Biol Crystallogr 57(Pt 1):52–60

Croce R, van Amerongen H (2013) Light-harvesting in photosystem I. Photosynth Res 116(2–3):153–166. https://doi.org/10.1007/s11120-013-9838-x

Csatorday K, MacColl R, Csizmadia V, Grabowski J, Bagyinka C (1984) Exciton interaction in allophycocyanin. Biochemistry 23(26):6466–6470

David L, Marx A, Adir N (2011) High-resolution crystal structures of trimeric and rod phycocyanin. J Mol Biol 405(1):201–213. https://doi.org/10.1016/j.jmb.2010.10.036

David L, Prado M, Arteni AA, Elmlund DA, Blankenship RE, Adir N (2014) Structural studies show energy transfer within stabilized phycobilisomes independent of the mode of rod-core assembly. Biochim Biophys Acta 1837(3):385–395. https://doi.org/10.1016/j.bbabio.2013.12.014

Demarsac NT, Houmard J (1988) Complementary chromatic adaptation – physiological conditions and action spectra. Methods Enzymol 167:318–328

Demmig B, Bjorkman O (1987) Comparison of the effect of excessive light on chlorophyll fluorescence (77K) and photon yield of $O_2$ evolution in leaves of higher plants. Planta 171(2):171–184. https://doi.org/10.1007/BF00391092

Dines M, Sendersky E, David L, Schwarz R, Adir N (2008) Structural, functional, and mutational analysis of the NblA protein provides insight into possible modes of interaction with the phycobilisome. J Biol Chem 283(44):30330–30340

Dong C, Tang A, Zhao J, Mullineaux CW, Shen G, Bryant DA (2009) ApcD is necessary for efficient energy transfer from phycobilisomes to photosystem I and helps to prevent photoinhibition in the cyanobacterium Synechococcus sp. PCC 7002. Biochim Biophys Acta 1787(9):1122–1128. https://doi.org/10.1016/j.bbabio.2009.04.007

Eisenberg I, Yochelis S, Ben-Harosh R, David L, Faust A, Even-Dar N, Taha H, Haegel NM, Adir N, Keren N, Paltiel Y (2014) Room temperature biological quantum random walk in phycocyanin nanowires. Phys Chem Chem Phys. https://doi.org/10.1039/c4cp00345d

Elmorjani K, Herdman M (1987) Metabolic control of phycocyanin degradation in the cyanobacterium synechocystis Pcc 6803 – a glucose effect. J Gen Microbiol 133:1685–1694

Emlyn-Jones D, Ashby MK, Mullineaux CW (1999) A gene required for the regulation of photosynthetic light harvesting in the cyanobacterium Synechocystis 6803. Mol Microbiol 33(5):1050–1058

Federman S, Malkin S, Scherz A (2000) Excitation energy transfer in aggregates of photosystem I and photosystem II of the cyanobacterium Synechocystis sp. PCC 6803: can assembly of the pigment-protein complexes control the extent of spillover? Photosynth Res 64(2–3):199–207. https://doi.org/10.1023/A:1006485823403

Flombaum P, Gallegos JL, Gordillo RA, Rincon J, Zabala LL, Jiao N, Karl DM, Li WK, Lomas MW, Veneziano D, Vera CS, Vrugt JA, Martiny AC (2013) Present and future global distributions of the marine Cyanobacteria Prochlorococcus and Synechococcus. Proc Natl Acad Sci U S A 110(24):9824–9829. https://doi.org/10.1073/pnas.1307701110

Fraser JM, Tulk SE, Jeans JA, Campbell DA, Bibby TS, Cockshutt AM (2013) Photophysiological and photosynthetic complex changes during iron starvation in Synechocystis sp. PCC 6803 and Synechococcus elongatus PCC 7942. PLoS One 8(3):e59861. https://doi.org/10.1371/journal.pone.0059861

Gan F, Zhang S, Rockwell NC, Martin SS, Lagarias JC, Bryant DA (2014) Extensive remodeling of a cyanobacterial photosynthetic apparatus in far-red light. Science 345(6202):1312–1317. https://doi.org/10.1126/science.1256963

Gantt E, Conti SF (1966) Phycobiliprotein localization in algae. Brookhaven Symp Biol 19:393–405

Gantt E, Lipschultz CA (1972) Phycobilisomes of Porphyridium cruentum. I. Isolation. J Cell Biol 54:313–324

Gao X, Zhang N, Wei TD, HN S, Xie BB, Dong CC, Zhang XY, Chen XL, Zhou BC, Wang ZX, JW W, Zhang YZ (2011) Crystal structure of the N-terminal domain of linker L(R) and the assembly of cyanobacterial phycobilisome rods. Mol Microbiol 82(3):698–705. https://doi.org/10.1111/j.1365-2958.2011.07844.x

Gilbert SM, Allison GG, Rogers LJ, Smith AJ (1996) Expression of genes involved in phycocyanin biosynthesis following recovery of Synechococcus PCC 6301 from nitrogen starvation, and the effect of gabaculine on cpcBa transcript levels. FEMS Microbiol Lett 140(1):93–98

Glazer AN (1989) Light guides. Directional energy transfer in a photosynthetic antenna. J Biol Chem 264(1):1–4

Gorl M, Sauer J, Baier T, Forchhammer K (1998) Nitrogen-starvation-induced chlorosis in Synechococcus PCC 7942: adaptation to long-term survival. Microbiology 144(Pt 9):2449–2458. https://doi.org/10.1099/00221287-144-9-2449

Grossman AR (1990) Chromatic adaptation and the events involved in phycobilisome biosynthesis. Plant Cell Environ 13(7):651–666. https://doi.org/10.1111/j.1365-3040.1990.tb01081.x

Grossman AR, Bhaya D, He Q (2001) Tracking the light environment by cyanobacteria and the dynamic nature of light harvesting. J Biol Chem 276(15):11449–11452

Gutu A, Kehoe DM (2012) Emerging perspectives on the mechanisms, regulation, and distribution of light color acclimation in cyanobacteria. Mol Plant 5(1):1–13. https://doi.org/10.1093/mp/ssr054

Gutu A, Nesbit AD, Alverson AJ, Palmer JD, Kehoe DM (2013) Unique role for translation initiation factor 3 in the light color regulation of photosynthetic gene expression. Proc Natl Acad Sci U S A 110(40):16253–16258. https://doi.org/10.1073/pnas.1306332110

Gwizdala M, Berera R, Kirilovsky D, van Grondelle R, Kruger TP (2016) Controlling light harvesting with light. J Am Chem Soc 138(36):11616–11622. https://doi.org/10.1021/jacs.6b04811

Harris D, Tal O, Jallet D, Wilson A, Kirilovsky D, Adir N (2016) Orange carotenoid protein burrows into the phycobilisome to provide photoprotection. Proc Natl Acad Sci U S A 113(12):E1655–E1662. https://doi.org/10.1073/pnas.1523680113

Hohmann-Marriott MF, Blankenship RE (2011) Evolution of photosynthesis. Annu Rev Plant Biol 62:515–548. https://doi.org/10.1146/annurev-arplant-042110-103811

Holt TK, Krogmann DW (1981) A carotenoid-protein from cyanobacteria. Biochim Biophys Acta 637:408–414

Holzwarth AR, Bittersmann E, Reuter W, Wehrmeyer W (1990) Studies on chromophore coupling in isolated phycobiliproteins. III. Picosecond excited state kinetics and time-resolved fluorescence spectra of different allophycocyanins from Mastigocladus laminosus. Biophys J 57(1):133–145

Horton P (2012) Optimization of light harvesting and photoprotection: molecular mechanisms and physiological consequences. Philos Trans R Soc Lond Ser B Biol Sci 367(1608):3455–3465. https://doi.org/10.1098/rstb.2012.0069

Hu Q, Ishikawa T, Inoue Y, Iwasaki I, Miyashita H, Kurano N, Miyachi S, Iwaki M, Itoh S, Marquardt J, Morschel E (1998) Heterogeneity of chlorophyll D-binding photosystem I reaction centers from the photosynthetic prokaryote Acaryochloris marina. Photosynthesis: mechanisms and effects. In: Proceedings of the International Congress on photosynthesis, 11th, Budapest, August 17–22, 1998, 1:437–440

Joshua S, Mullineaux CW (2004) Phycobilisome diffusion is required for light-state transitions in cyanobacteria. Plant Physiol 135(4):2112–2119. https://doi.org/10.1104/pp.104.046110

Kana R, Kotabova E, Komarek O, Sediva B, Papageorgiou GC, Govindjee PO (2012) The slow S to M fluorescence rise in cyanobacteria is due to a state 2 to state 1 transition. Biochim Biophys Acta 1817(8):1237–1247. https://doi.org/10.1016/j.bbabio.2012.02.024

Kawamura M, Mimuro M, Fujita Y (1979) Quantitative relationship between two reaction centers in the photosynthetic system of blue-green algae. Plant Cell Physiol 20:697–705

Kehoe DM, Gutu A (2006) Responding to color: the regulation of complementary chromatic adaptation. Annu Rev Plant Biol 57:127–150. https://doi.org/10.1146/annurev.arplant.57.032905.105215

Keren N, Krieger-Liszkay A (2011) Photoinhibition: molecular mechanisms and physiological significance. Physiol Plant 142(1):1–5. https://doi.org/10.1111/j.1399-3054.2011.01467.x
Kerfeld CA, Kirilovsky D (2013) Structural, mechanistic and genomic insights into OCP-mediated photoprotection. Adv Bot Res 65:1–26. https://doi.org/10.1016/B978-0-12-394313-2.00001-9
Kirilovsky D (2015) Modulating energy arriving at photochemical reaction centers: orange carotenoid protein-related photoprotection and state transitions. Photosynth Res 126(1):3–17. https://doi.org/10.1007/s11120-014-0031-7
Kirilovsky D, Kerfeld CA (2016) Cyanobacterial photoprotection by the orange carotenoid protein. Nat Plants 2(12):16180. https://doi.org/10.1038/nplants.2016.180
Kouril R, Oostergetel GT, Boekema EJ (2011) Fine structure of granal thylakoid membrane organization using cryo electron tomography. Biochim Biophys Acta 1807(3):368–374. https://doi.org/10.1016/j.bbabio.2010.11.007
Krasikov V, Aguirre von Wobeser E, Dekker HL, Huisman J, Matthijs HC (2012) Time-series resolution of gradual nitrogen starvation and its impact on photosynthesis in the cyanobacterium Synechocystis PCC 6803. Physiol Plant 145(3):426–439. https://doi.org/10.1111/j.1399-3054.2012.01585.x
Krause GH, Weis E (1984) Chlorophyll fluorescence as a tool in plant physiology: II. Interpretation of fluorescence signals. Photosynth Res 5(2):139–157. https://doi.org/10.1007/BF00028527
Krause GH, Weis E (1991) Chlorophyll fluorescence and photosynthesis: the basics. Annu Rev Plant Biol 42:313–349
Lau RH, MacKenzie MM, Doolittle WF (1977) Phycocyanin synthesis and degradation in the blue-green bacterium Anacystis nidulans. J Bacteriol 132(3):771–778
Leverenz RL, Sutter M, Wilson A, Gupta S, Thurotte A, Bourcier de Carbon C, Petzold CJ, Ralston C, Perreau F, Kirilovsky D, Kerfeld CA (2015) A 12 A carotenoid translocation in a photoswitch associated with cyanobacterial photoprotection. Science 348(6242):1463–1466. https://doi.org/10.1126/science.aaa7234
Li Z, Wakao S, Fischer BB, Niyogi KK (2009) Sensing and responding to excess light. Annu Rev Plant Biol 60:239–260. https://doi.org/10.1146/annurev.arplant.58.032806.103844
Liu LN, Chen XL, Zhang YZ, Zhou BC (2005) Characterization, structure and function of linker polypeptides in phycobilisomes of cyanobacteria and red algae: an overview. Biochim Biophys Acta 1708(2):133–142
Liu LN, Aartsma TJ, Thomas JC, Lamers GE, Zhou BC, Zhang YZ (2008) Watching the native supramolecular architecture of photosynthetic membrane in red algae: topography of phycobilisomes and their crowding, diverse distribution patterns. J Biol Chem 283(50):34946–34953
Liu H, Zhang H, Niedzwiedzki DM, Prado M, He G, Gross ML, Blankenship RE (2013) Phycobilisomes supply excitations to both photosystems in a megacomplex in cyanobacteria. Science 342(6162):1104–1107. https://doi.org/10.1126/science.1242321
Lundell DJ, Williams RC, Glazer AN (1981) Molecular architecture of a light-harvesting antenna. In vitro assembly of the rod substructures of Synechococcus 6301 phycobilisomes. J Biol Chem 256(7):3580–3592
MacColl R (1998) Cyanobacterial phycobilisomes. J Struct Biol 124(2–3):311–334
MacColl R (2004) Allophycocyanin and energy transfer. Biochim Biophys Acta 1657(2–3):73–81
Marquardt J, Senger H, Miyashita H, Miyachi S, Moerschel E (1997) Isolation and characterization of biliprotein aggregates from Acaryochloris marina, a Prochloron-like prokaryote containing mainly chlorophyll d. FEBS Lett 410(2,3):428–432
Marx A, David L, Adir N (2014) Piecing together the phycobilisome. In: Hohmann-Marriott MF (ed) The structural basis of biological energy generation, Advances in photosynthesis and respiration, vol 39. Springer, Dordrecht, pp 59–76
McGregor A, Klartag M, David L, Adir N (2008) Allophycocyanin trimer stability and functionality are primarily due to polar enhanced hydrophobicity of the phycocyanobilin binding pocket. J Mol Biol 384(2):406–421
Miao D, Ding WL, Zhao BQ, Lu L, Xu QZ, Scheer H, Zhao KH (2016) Adapting photosynthesis to the near-infrared: non-covalent binding of phycocyanobilin provides an extreme spectral

red-shift to phycobilisome core-membrane linker from Synechococcus sp. PCC7335. Biochim Biophys Acta 1857(6):688–694. https://doi.org/10.1016/j.bbabio.2016.03.033

Mullineaux CW, Allen JF (1990) State 1-State 2 transitions in the cyanobacterium Synechococcus 6301 are controlled by the redox state of electron carriers between photosystems I and II. Photosynth Res 23(3):297–311. https://doi.org/10.1007/BF00034860

Mullineaux CW, Emlyn-Jones D (2005) State transitions: an example of acclimation to low-light stress. J Exp Bot 56(411):389–393

Munekage Y, Hashimoto M, Miyake C, Tomizawa K, Endo T, Tasaka M, Shikanai T (2004) Cyclic electron flow around photosystem I is essential for photosynthesis. Nature 429(6991):579–582. https://doi.org/10.1038/nature02598

Murata N (1969) Control of excitation transfer in photosynthesis. I. Light-induced change of chlorophyll a fluorescence in Porphyridium cruentum. Biochim Biophys Acta 172(2):242–251

Papageorgiou GC (1977) Photosynthetic activity of diimidoester-modified cells, permeaplasts, and cell-free membrane fragments of the blue-green alga Anacystis nidulans. Biochim Biophys Acta 461(3):379–391

Papageorgiou GC, Govindjee (2011) Photosystem II fluorescence: slow changes – scaling from the past. J Photochem Photobiol B 104(1–2):258–270. https://doi.org/10.1016/j.jphotobiol.2011.03.008

Peng PP, Dong LL, Sun YF, Zeng XL, Ding WL, Scheer H, Yang X, Zhao KH (2014) The structure of allophycocyanin B from Synechocystis PCC 6803 reveals the structural basis for the extreme redshift of the terminal emitter in phycobilisomes. Acta Crystallogr D Biol Crystallogr 70(Pt 10):2558–2569. https://doi.org/10.1107/S1399004714015776

Reuter W, Wiegand G, Huber R, Than ME (1999) Structural analysis at 2.2 A of orthorhombic crystals presents the asymmetry of the allophycocyanin-linker complex, AP.LC7.8, from phycobilisomes of Mastigocladus laminosus. Proc Natl Acad Sci U S A 96(4):1363–1368

Rochaix JD, Lemeille S, Shapiguzov A, Samol I, Fucile G, Willig A, Goldschmidt-Clermont M (2012) Protein kinases and phosphatases involved in the acclimation of the photosynthetic apparatus to a changing light environment. Philos Trans R Soc Lond Ser B Biol Sci 367(1608):3466–3474. https://doi.org/10.1098/rstb.2012.0064

Salomon E, Bar-Eyal L, Sharon S, Keren N (2013) Balancing photosynthetic electron flow is critical for cyanobacterial acclimation to nitrogen limitation. BBA-Bioenergetics 1827(3):340–347. https://doi.org/10.1016/j.bbabio.2012.11.010

Samsonoff WA, MacColl R (2001) Biliproteins and phycobilisomes from cyanobacteria and red algae at the extremes of habitat. Arch Microbiol 176(6):400–405

Sauer J, Schreiber U, Schmid R, Volker U, Forchhammer K (2001) Nitrogen starvation-induced chlorosis in Synechococcus PCC 7942. Low-level photosynthesis as a mechanism of long-term survival. Plant Physiol 126(1):233–243

Scheer H, Zhao KH (2008) Biliprotein maturation: the chromophore attachment. Mol Microbiol 68(2):263–276

Schwarz R, Forchhammer K (2005) Acclimation of unicellular cyanobacteria to macronutrient deficiency: emergence of a complex network of cellular responses. Microbiol-Sgm 151:2503–2514. https://doi.org/10.1099/mic.0.27883-0

Schwarz R, Grossman AR (1998) A response regulator of cyanobacteria integrates diverse environmental signals and is critical for survival under extreme conditions. Proc Natl Acad Sci U S A 95(18):11008–11013

Sendersky E, Kozer N, Levi M, Garini Y, Shav-Tal Y, Schwarz R (2014) The proteolysis adaptor, NblA, initiates protein pigment degradation by interacting with the cyanobacterial light-harvesting complexes. Plant J 79(1):118–126. https://doi.org/10.1111/tpj.12543

Shukla A, Biswas A, Blot N, Partensky F, Karty JA, Hammad LA, Garczarek L, Gutu A, Schluchter WM, Kehoe DM (2012) Phycoerythrin-specific bilin lyase-isomerase controls blue-green chromatic acclimation in marine Synechococcus. Proc Natl Acad Sci U S A 109(49):20136–20141. https://doi.org/10.1073/pnas.1211777109

Sonoike K, Hihara Y, Ikeuchi M (2001) Physiological significance of the regulation of photosystem stoichiometry upon high light acclimation of Synechocystis sp. PCC 6803. Plant Cell Physiol 42(4):379–384

Stagg L, Zhang SQ, Cheung MS, Wittung-Stafshede P (2007) Molecular crowding enhances native structure and stability of alpha/beta protein flavodoxin. Proc Natl Acad Sci U S A 104(48):18976–18981

Stamatakis K, Papageorgiou GC (2001) The osmolality of the cell suspension regulates phycobilisome-to-photosystem I excitation transfers in cyanobacteria. Biochim Biophys Acta 1506(3):172–181

Tal O, Trabelcy B, Gerchman Y, Adir N (2014) Investigation of phycobilisome subunit interaction interfaces by coupled cross-linking and mass spectrometry. J Biol Chem 289(48):33084–33097. https://doi.org/10.1074/jbc.M114.595942

Tamary E, Kiss V, Nevo R, Adam Z, Bernat G, Rexroth S, Rogner M, Reich Z (2012) Structural and functional alterations of cyanobacterial phycobilisomes induced by high-light stress. Biochim Biophys Acta 1817(2):319–327. https://doi.org/10.1016/j.bbabio.2011.11.008

Tandeau de Marsac N (2003) Phycobiliproteins and phycobilisomes: the early observations. Photosynth Res 76:197–205

Tandeau de Marsac N, Cohen-Bazire G (1977) Molecular composition of cyanobacterial phycobilisomes. Proc Natl Acad Sci U S A 74:1635–1639

Tang K, Ding WL, Hoppner A, Zhao C, Zhang L, Hontani Y, Kennis JT, Gartner W, Scheer H, Zhou M, Zhao KH (2015) The terminal phycobilisome emitter, LCM: a light-harvesting pigment with a phytochrome chromophore. Proc Natl Acad Sci U S A 112(52):15880–15885. https://doi.org/10.1073/pnas.1519177113

Tikkanen M, Mekala NR, Aro EM (2014) Photosystem II photoinhibition-repair cycle protects photosystem I from irreversible damage. Biochim Biophys Acta 1837(1):210–215. https://doi.org/10.1016/j.bbabio.2013.10.001

van Amerongen H, Croce R (2013) Light harvesting in photosystem II. Photosynth Res 116(2–3):251–263. https://doi.org/10.1007/s11120-013-9824-3

Van Thor JJ, Mullineaux CW, Matthijs HCP, Hellingwerf KJ (1998) Light harvesting and state transitions in cyanobacteria. Bot Acta 111:430–443

Walters RG, Horton P (1991) Resolution of components of non-photochemical chlorophyll fluorescence quenching in barley leaves. Photosynth Res 27(2):121–133. https://doi.org/10.1007/BF00033251

Watanabe M, Ikeuchi M (2013) Phycobilisome: architecture of a light-harvesting supercomplex. Photosynth Res 116:265–276. https://doi.org/10.1007/s11120-013-9905-3

Watanabe M, Semchonok DA, Webber-Birungi MT, Ehira S, Kondo K, Narikawa R, Ohmori M, Boekema EJ, Ikeuchi M (2014) Attachment of phycobilisomes in an antenna-photosystem I supercomplex of cyanobacteria. Proc Natl Acad Sci U S A 111(7):2512–2517. https://doi.org/10.1073/pnas.1320599111

Wilson A, Ajlani G, Verbavatz JM, Vass I, Kerfeld CA, Kirilovsky D (2006) A soluble carotenoid protein involved in phycobilisome-related energy dissipation in cyanobacteria. Plant Cell 18(4):992–1007. https://doi.org/10.1105/tpc.105.040121

Wu YP, Krogmann DW (1997) The orange carotenoid protein of Synechocystis PCC 6803. Biochim Biophys Acta 1322(1):1–7

Yamanaka G, Glazer AN, Williams RC (1978) Cyanobacterial phycobilisomes. Characterization of the phycobilisomes of Synechococcus sp. 6301. J Biol Chem 253(22):8303–8310

Zhao KH, Su P, Bohm S, Song B, Zhou M, Bubenzer C, Scheer H (2005) Reconstitution of phycobilisome core-membrane linker, LCM, by autocatalytic chromophore binding to ApcE. Biochim Biophys Acta 1706(1–2):81–87

Zilinskas BA, Glick RE (1981) Noncovalent intermolecular forces in phycobilisomes of Porphyridium cruentum. Plant Physiol 68(2):447–452

# Chapter 4
# Bacterial Mechanosensitive Channels


**Tim Rasmussen and Akiko Rasmussen**

**Abstract** Mechanosensitive (MS) channels protect bacteria against hypo-osmotic shock and fulfil additional functions. Hypo-osmotic shock leads to high turgor pressure that can cause cell rupture and death. MS channels open under these conditions and release unspecifically solutes and consequently the turgor pressure. They can recognise the raised pressure via the increased tension in the cell membrane. Currently, a better understanding how MS channels can sense tension on molecular level is developing because the interaction of the lipid bilayer with the channel is being investigated in detail. The MS channel of large conductance (MscL) and of small conductance (MscS) have been distinguished and studied in molecular detail. In addition, larger channels were found that contain a homologous region corresponding to MscS so that MscS represents a family of channels. Often several members of this family are present in a species. The importance of this family is underlined by the fact that members can be found not only in bacteria but also in higher organisms. While MscL and MscS have been studied for years in particular by electrophysiology, mutagenesis, molecular dynamics, X-ray crystallography and other biophysical techniques, only recently more details are emerging about other members of the MscS-family.

**Keywords** Mechanosensitive channels · Lipid-protein interaction · Hypo-osmotic shock · Channel mechanism · Bacterial stress response

## 4.1 Introduction

Bacteria as single celled organisms have to be able to adapt to drastic and rapid changes in their environment. Maintaining a favourable pH value and composition of solutes in the cytosol that allows a functional metabolism is a major challenge for

T. Rasmussen (✉) · A. Rasmussen
Institut für Biochemie, Rudolf-Virchow-Zentrum, Universität Würzburg, Würzburg, Germany
e-mail: tim.rasmussen@uni-wuerzburg.de



J. R. Harris, E. J. Boekema (eds.), *Membrane Protein Complexes: Structure and Function*, Subcellular Biochemistry 87,
https://doi.org/10.1007/978-981-10-7757-9_4

life. The turgor pressure allows bacteria to keep the cell shape and permits cell growth. However, a sudden drop of solute concentrations in the surrounding fluid will drive water through the membrane into the cell so that the pressure very quickly reaches dangerous levels. MS channels prevent cell lysis because they release unspecifically solutes so that no more water is osmotically driven into the cell. Nevertheless, the release of solutes disrupts cell homeostasis and causes the membrane potential to collapse. Their opening must be carefully regulated and it is thought that the presence of different kind of MS channels allows for a graded response tailored to the severity of the hypo-osmotic shock.

The patch-clamp technique played a decisive role in the understanding of channels as a whole but also triggered the discovery of MS channels in bacteria. In 1987 Kung and co-workers applied this technique to giant protoplasts obtained from *Escherichia coli* cells and saw stepwise currents when they employed pressure over the membrane (Martinac et al. 1987). It was directly recognised that these activities could be caused by channels that sense and respond to the osmolarity in the surrounding fluid. Electrophysiology (e.-phys.) is still the best way to study the function of MS channels (Box 4.1). Membrane protein extracts from *E. coli* were

**Box 4.1: Electrophysiological (e.-phys.) Characterisation of MS Channels**

Single molecule functional properties can be obtained by recording the electrical current through MS channels after activation by a stimulus. This has been done predominately for MS channels with the patch-clamp technique (Blount et al. 1999) but also with a planar lipid setup (Pliotas et al. 2015) and with a droplet bilayer interface setup (Najem et al. 2015). A narrow pipette tip with a sealing excised membrane patch (inside-out mode) is usually used in the patch-clamp technique. The circuit is closed by connecting the solution inside the pipette with a bath in which the pipette is immersed. Bacterial cells are too small for patching with the pipette. For this reason bacteria are grown in the presence of cephalexin which inhibits cell division so that long "snakes" are formed. Then the cell wall is destroyed with lysozyme in presence of EDTA and large protoplasts are formed which can be patched. Purified MS channels reconstituted in liposomes can also be used for patching. The "sucrose method" of reconstitution (Battle et al. 2009) is easier in comparison to the classical "dehydration/rehydration method" but seems to be more restricted what lipids can be used. Once a GΩ seal of the membrane patch in the pipette tip is formed, MS channels can be activated by applying suction on the patch through the pipette and currents are recorded (see Box Fig. 4.1). The height of the step in the recording provides the conductivity (using Ohm's

(continued)

**Box 4.1** (continued)
law) of the channel and with this information of the pore size. Sometimes subconducting states are observed that represent transient states between the closed and the fully open states. MS gating depends directly on the tension in the membrane but only indirectly on the pressure in the pipette. Thus, thresholds for gating are often reported as the ratio of the pressure to gate MscL relative to MscS ($P_L$:$P_S$) or its inverse. This is easier than to determine the tension. The $P_L$:$P_S$ ratio is an important molecular property which often changes when a mutation is introduced. Another characteristic of a channel is its open dwell time which is for example shorter for *E. coli* MscL wild type (WT) than MscS WT. If the current is measured dependent on the applied voltage (I-V curves), cation/anion preference and rectification of the channel can be determined. Another property is the adaptation behaviour of MscS which was only revealed by e.-phys. experiments.

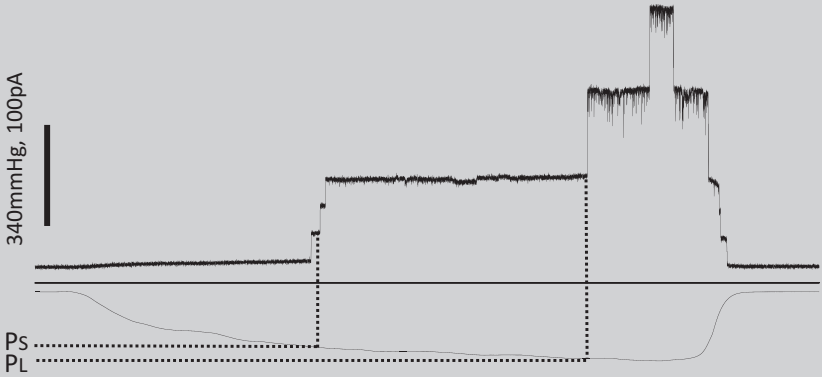


**Box Fig. 4.1** E.-phys. trace for a mutant of EcMscS (small steps) and EcMscL WT (large steps). The applied pressure as suction on the patch is shown in the lower trace

reconstituted into liposomes and then characterised by electrophysiology; a MS channel of unspecific large conductance of ≈3 nS (MscL) and a slightly anionic specific channel of smaller conductance of ≈1 nS (MscS) were distinguished (Sukharev et al. 1993). This study also showed that these activities are caused by different proteins. The discovery of the genes for MscL (Sukharev et al. 1994) and MscS (Levina et al. 1999) opened up the field of bacterial MS channel research.

This chapter will give a general overview over the field and will focus on some recent developments. It cannot be comprehensive and will instead also refer to other reviews that provide further opportunities to obtain a complete understanding of the present knowledge of this class of channels (Perozo and Rees 2003; Booth et al. 2007a; Corry and Martinac 2008; Haswell et al. 2011; Naismith and Booth 2012; Iscla and Blount 2012; Wilson et al. 2013; Kocer 2015).

## 4.2 Mechanosensitive Channel of Large Conductance (MscL)

Although MscL creates the largest pore upon activation of about 30 Å diameter, it is encoded by the smallest gene among the known bacterial MS channels. MscL from *E. coli* (EcMscL) consists of 136 amino acids resulting in a molecular mass of 15 kDa. In comparison to other MS channels, MscL is a robust protein and is readily purified. Thus, it is perhaps not surprising that the first crystal structure of a MS channel was obtained from *Mycobacterium tuberculosis* MscL (MtMscL; Chang et al. 1998; Steinbacher et al. 2007). This first structure as well as later structures (Li et al. 2015) showed that MscL forms a homopentameric complex, but a tetrameric structure was also described (Liu et al. 2009). Each subunit contributes two transmembrane (TM) helices and a C-terminal cytosolic helix to the complex (Fig. 4.1). Re-analysis of the original data also resolved a short N-terminal helix which is presumably lying on the cytosolic membrane surface (Steinbacher et al. 2007); beforehand it was suggested to face inwards and form a second gate (Sukharev et al. 2001a, b). TM1 is predominantly coating the pore while TM2 is more exposed to the surrounding membrane. TM1 is roughly co-aligned to TM2 of the next subunit (TM2'). In contrast to MscS, the pore in MscL is lined by hydrophilic residues except for the hydrophobic seal at L17 and V21 (numbering for MtMscL; L19 and V23 for EcMscL) where TM1 helices contact each other. The pore is funnel-shaped, contracting from the periplasmic side to the hydrophobic seal at the cytosolic side of the membrane domain. The hydrophobic seal is almost completely closed so that this first structure of MtMscL is thought to represent the closed conformation of the channel (Chang et al. 1998; Steinbacher et al. 2007). The narrow and hydrophobic pore remaining in this region is not expected to conduct (Gullingsrud et al. 2001; Anishkin et al. 2010). Introduction of hydrophilic/charged moieties in this region sensitively changes the ability to open, causing Gain-Of-Function (GOF) phenotypes (i.e. requires lower tension to open the channel) or even enables the channel to open without applied tension (Ou et al. 1998; Yoshimura et al. 1999; Bartlett et al. 2004). Even modifications on only one subunit of the pentameric complex had a drastic effect (Birkner et al. 2012; Mika et al. 2013).

How does MscL open? To address this question Perozo and co-workers systematically mutated MscL in 55 positions of the membrane domain to cysteine residues, one at the time, and labelled the purified channels with a spin label (Perozo et al.

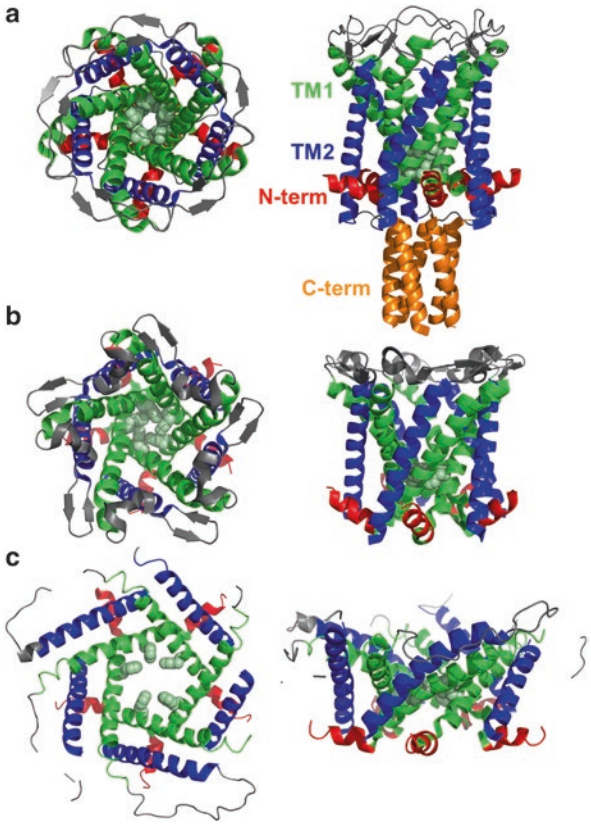


**Fig. 4.1** Structure of MscL. The crystal structures of MtMscL in the closed conformation (**a**; PDB: 2OAR), MaMscL in the closed conformation (**b**; PDB: 4Y7K), and in the expanded intermediate conformation (**c**; PDB: 4Y7J) are shown (Chang et al. 1998; Steinbacher et al. 2007; Li et al. 2015). Views from the periplasmic side (left images) and within the membrane plane (right images) are given. The N-terminal amphipathic helix (red), TM1 (green), TM2 (blue), and the C-terminal cytosolic helix (orange) are highlighted. Residues of the hydrophobic seal, L17 and V21 for MtMscL and F23 for MaMscL, are depicted as spheres. MaMscL does not have a C-terminal helix and the fused protein is not shown. The closed structures show the funnel shaped pore predominately lined by TM1 contracting towards the hydrophobic seal. Comparison of the closed and intermediate conformation reveals that TM1 and 2 stay antiparallel and that the hydrophobic membrane domain thins. Loops between TM1 and 2 become disordered upon expansion

2002a). After reconstitution of MscL into liposomes Continuous Wave- Electron Spin Resonance (CW-ESR) spectra were recorded. The mobility of the spin label and access to the membrane or water bulk phase can be deduced (Hubbell et al. 2000). Lysophosphocholine (LPC) has been shown to trigger opening of MS channels even when no external tension is applied to the membrane. This was related to its curvature-inducing properties (Perozo et al. 2002b). LPC was used to obtain ESR data of MscL in the open conformation and a model was suggested (Perozo et al. 2002a). The TM helices lean into the membrane which allows an iris-like opening

of the pore to take place. The open model is therefore much flatter within the membrane and the pore is 25 Å wide, explaining the high conductance observed in patch-clamp experiments. A theoretical study combined with mutagenesis experiments came to a similar model for opening that predicted tilting of the TM helices (Sukharev et al. 2001a, b). However, both models proposed opposite rotation of TM1 upon activation which leaves completely different side chains within the pore for the open state. Systematic cysteine mutagenesis and modification with the positively charged modifier 2-(trimethylammonium)ethylmethanethiosulfonate (MTSET) of the TM helices led to phenotypes that agreed with a clockwise rotation of TM1 and thus supports the ESR model of the open structure (Bartlett et al. 2004). A thorough single-molecule FRET study provided more experimental data of structural changes upon opening (Wang et al. 2014). A pore size of 28 Å was determined and a helix-tilt model for opening of the channel confirmed.

Crystal structures of completely open MscL are still not available but intermediate states were recently trapped providing good evidence for the opening transition (Liu et al. 2009; Li et al. 2015). A truncated MscL from *Staphylococcus aureus* without the C-terminal cytosolic helix (SaMscL[CΔ26]) showed an intermediate state on the trajectory to the open form because the pore was still not sufficiently wide for conductance (Liu et al. 2009). However, the structural changes agreed well with the model for the open MscL from the ESR study. In comparison to the closed structure, the antiparallel TM1 and TM2' stay together and seem to form a rigid unit while the helices lean more around the central axis. Surprisingly, a tetrameric instead of a pentameric complex was seen which seems also to be present for full-length SaMscL in solution. Further evidence for variability of the oligomeric state of MscL was found indentifying tetramers, pentamers and even hexamers (Gandhi et al. 2011). However, *in vivo* cross linking experiments on double cysteine mutants suggested that the native state is pentameric and that depending on the detergent used for extraction and purification other oligomeric state can be obtained *in vitro* (Dorwart et al. 2010; Iscla et al. 2011). While this casted doubts about the physiological relevance of the tetrameric structure, it was astounding to see that different stable oligomeric states are accessible to MscL and detergent exchange can reversibly change it (Dorwart et al. 2010). A comprehensive study by native mass spectrometry of more than 50 conditions showed that not only detergents and lipids influence the oligomeric state but also the temperature (Reading et al. 2015).

In the light of these doubts, further manifestation of the suggested conformational changes upon opening came from an excellent structural study on MscL from the archaea *Methanosarcina acetivorans* (MaMscL; Li et al. 2015). The pentameric state was stabilised *in vitro* by fusion to a pentameric soluble protein which also promoted crystallisation. Structures of a closed and an extended intermediate conformation were obtained. The pivoting of the helices observed for the tetrameric MscL was confirmed here for the pentameric oligomer but additional interesting structural features were revealed. The periplasmic loop between TM1 and 2 forms a ω-shaped loop and short β-hairpin in the closed structure which extends to an unstructured loop in the intermediate conformation in a spring-like fashion (Li et al. 2015). Mutations in this loop showed how important this structural feature is for

modulating the gating transition (Blount et al. 1996; Ou et al. 1998; Tsai et al. 2005; Yang et al. 2013). It was suggested that disruption of hydrogen-bonds in the closed conformation leads to a GOF phenotype while other mutations also can cause a Loss-Of-Function (LOF; higher pressure is required to open the channel). Deletion of six residues in the loop prevents opening while replacement with six alanine residues or proteolytic digest of the loop leads to GOF (Ajouz et al. 2000; Li et al. 2015). Furthermore, the short N-terminal helix was highlighted as a sliding and rotating membrane anchor that limits opening by mechanical coupling to the TM1-TM2' pair (Li et al. 2015).

E.-phys. experiments revealed that MscL has not only an open and closed state but several subconducting intermediate states (Sukharev et al. 1999; Anishkin et al. 2005). Suggestions for the structure of these intermediates were first provided by modelling (Sukharev et al. 2001a, b; Bilston and Mylvaganam 2002; Kong et al. 2002; Colombo et al. 2003; Louhivuori et al. 2010) and later by the above mentioned crystal structures (Liu et al. 2009; Li et al. 2015). In a technically challenging study the mutation EcMscL G22C in the seal region was introduced subunit-wise in mixture with WT subunits and it was possible to separate the different mixed complexes (Birkner et al. 2012). The authors concluded that close-open transitions are asymmetrical though it is not clear if the heterogenic complexes itself induced this asymmetric behaviour and if the same would happen in a homo-oligomeric complex. Intersubunit cross linking experiments of single cysteine mutants in the N-terminal region indicated temporal asymmetric conformations (Shapovalov et al. 2003; Iscla et al. 2007). Mutation of V15C in MtMscL led to the trapping in a subconducting state which was not sensitive to tension anymore (Shapovalov et al. 2003). Asymmetric transitions were also indicated by molecular dynamics simulations (Bilston and Mylvaganam 2002; Kong et al. 2002; Colombo et al. 2003; Louhivuori et al. 2010).

Whichever transition pathway MscL takes, it is clear that it forms an enormous pore of about 30 Å in diameter once it is completely open (Cruickshank et al. 1997; Sukharev et al. 1999; Wang et al. 2014). It has been shown that even small proteins up to a size of 6.5 kDa are able to pass (van den Bogaart et al. 2007). If the gating of MscL could be more easily manipulated, it could have immense biotechnological potential as "nano valve", for example for the specific delivery of drugs (Fig. 4.2). Exactly this was achieved by Koçer et al. with a photo switch located at the hydrophobic seal of MscL (Koçer et al. 2005; Koçer et al. 2007). The mutant G22C (numbering for EcMscL) allowed the specific location of the dyes in the hydrophobic seal. Transition to a charged form by illumination with UV light causes MscL to open. It was even possible to obtain a reversible switch which turns back to an uncharged form (causing closing) with visible light. Structural changes upon light activation could be monitored using partial spin labelling and ESR spectroscopy which showed that maximal changes were observed with at least 3 photo switches in the pore (Yilmaz et al. 2015). Charge dependent opening has also been realised by pH changes with an attached pH-dependent moiety on G22C (Koçer et al. 2006). A pH dependence of gating has already been reported earlier for the mutant G22H, though not in complete absence of applied tension (Yoshimura et al. 1999). In an

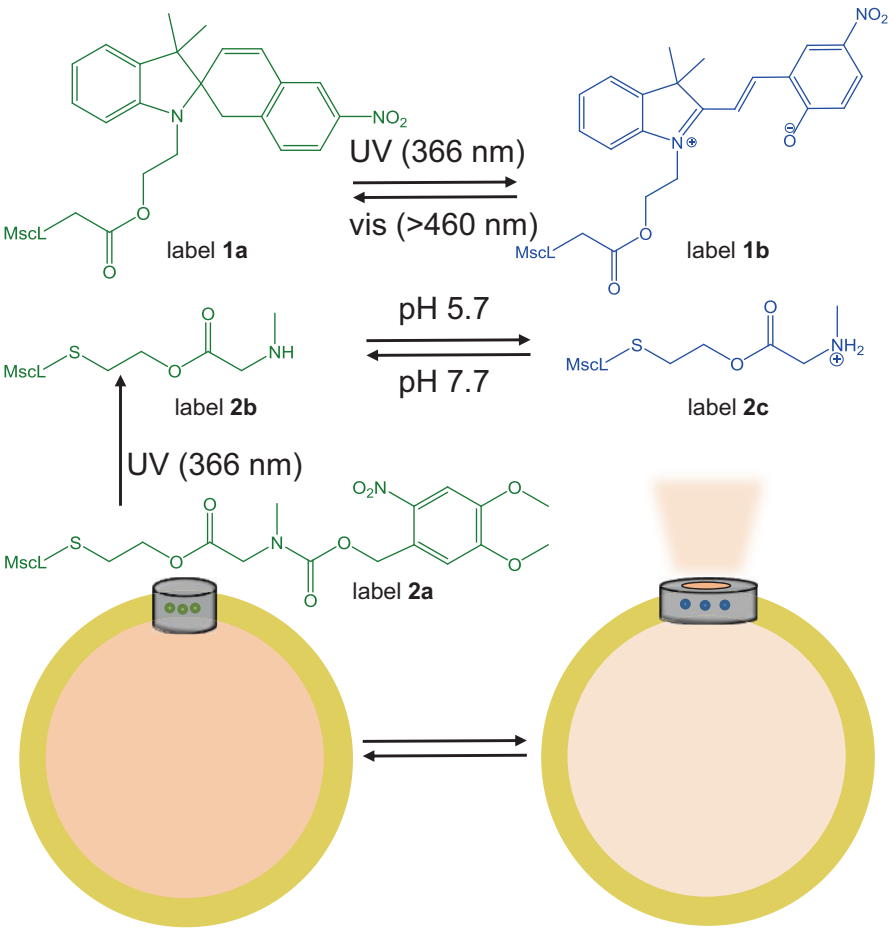


**Fig. 4.2** Application of MscL as a "nano valve". MscL has the potential to be used as a "nano valve" because its large pore allows the passage of a wide range of compounds, even small proteins. Reconstituted into liposomes, drugs could be delivered to specific sites in the body. Modification of MscL at the seal (e.g. G22C) with the shown labels allows the gating by a specific stimulus at the desired place due to the change of these labels from an uncharged (green) to a charged (blue) form. The label **1a** can be switched on by UV-light to **1b** and switched off again with visible light (Koçer et al. 2005). MscL can be gated by lowering the pH by changing label **2b**–**2c** (Koçer et al. 2006). Control can even be further increased by photo-protecting this group (label **2a** is activated to **2b** by UV-light)

attempt to allow gating by a magnetic field, superparamagnetic $CoFe_2O_4$ nanoparticles were introduced to the pore of MscL (Nakayama et al. 2015). While a magnetic field facilitated gating, tension changes were still required in this system. More recently it was revealed that position G26 instead of G22 is more efficient for "nano valve" modifications because more stable openings can be achieved (Iscla et al. 2013). In a different effort to use MscL as "nano valve" in medical applications,

MscL was expressed in mammalian cells and the passage of usually impermeable compounds was enabled (Doerner et al. 2012).

MS channels are bacterial stress response systems and should therefore be potential targets for antibacterial drugs. Only very recently this was convincingly demonstrated in a high throughput screen evaluating MscL as target (Iscla et al. 2014). Surprisingly, a number of known antibiotics were identified as "hits" which had already other established targets. MscL increased the potency of streptomycin which in turn increased the activity of MscL in e.-phys. experiments. It was concluded that this antibiotic can activate MscL and probably uses the channel as entrance gate to the cell to reach its molecular target, the ribosome. In a rational drug design effort, *in silico* docking studies with MscL as target identified ligands affecting the channel (Iscla et al. 2015). One of these compounds, 1,3,5-tris[(1E)-2′-(4″-benzoic acid)vinyl]benzene, promises to be a novel antibiotic: It proved to be effective at low concentrations against methicillin-resistant *Staphylococcus aureus* (MRSA) in an *in vivo* model while it is non-toxic to human cells at similar concentrations. This compound enhanced the activity of MscL in e.-phys. experiments.

## 4.3 Mechanosensitive Channel of Small Conductance (MscS)

MscS is evolutionary and structurally distinct from MscL so that their similar function might be based on completely different mechanisms. MscS from *E. coli* (EcMscS) consists of 286 amino acids with a subunit mass of 31 kDa. MscS forms homoheptameric complexes though crosslinking experiments indicated that archaeal homologues from *Thermoplasma volcanium* may form homopentamers (Löw et al. 2013). Two tryptophan residues in the cytosolic domain of EcMscS are important for complex stability but can be replaced by other aromatic amino acids (Rasmussen et al. 2007). Monomers and dimers can sometimes be seen as dissociation products (Rasmussen et al. 2007, 2010, 2015). In addition, it has not been possible to obtain the heptameric complex *in vitro* from dissociated subunits so far, while for MscL this was used to produce heterocomplexes (Yilmaz et al. 2015).

The first crystal structure of EcMscS was solved by the Rees group in 2002 (Bass et al. 2002; Steinbacher et al. 2007). Two TM helices (TM1 and 2) outline the so called "sensor paddle" for each subunit (Fig. 4.3). A third TM from all 7 subunit together enclose the central pore (TM3a) which after a kink at residue G113 strays outwards on the cytosolic side (TM3b) to extend to a large lantern shaped cytosolic domain enclosing a vestibule. This domain has side portals between a region that forms a continuous band of β-sheets around the complex (β-domain) and a further compact region of α-helices and β-sheets (αβ-domain) (Fig. 4.3). At the C-terminus a further portal to the vestibule is shaped by a β-barrel. In common with MscL, a hydrophobic seal can be seen towards the cytosolic side of the membrane domain consisting of residues L105 and L109 (numbering for EcMscS). It is even less geometrically occluded than in MscL and was therefore first seen as an open structure. However, molecular dynamics simulations suggested that it is still narrow and

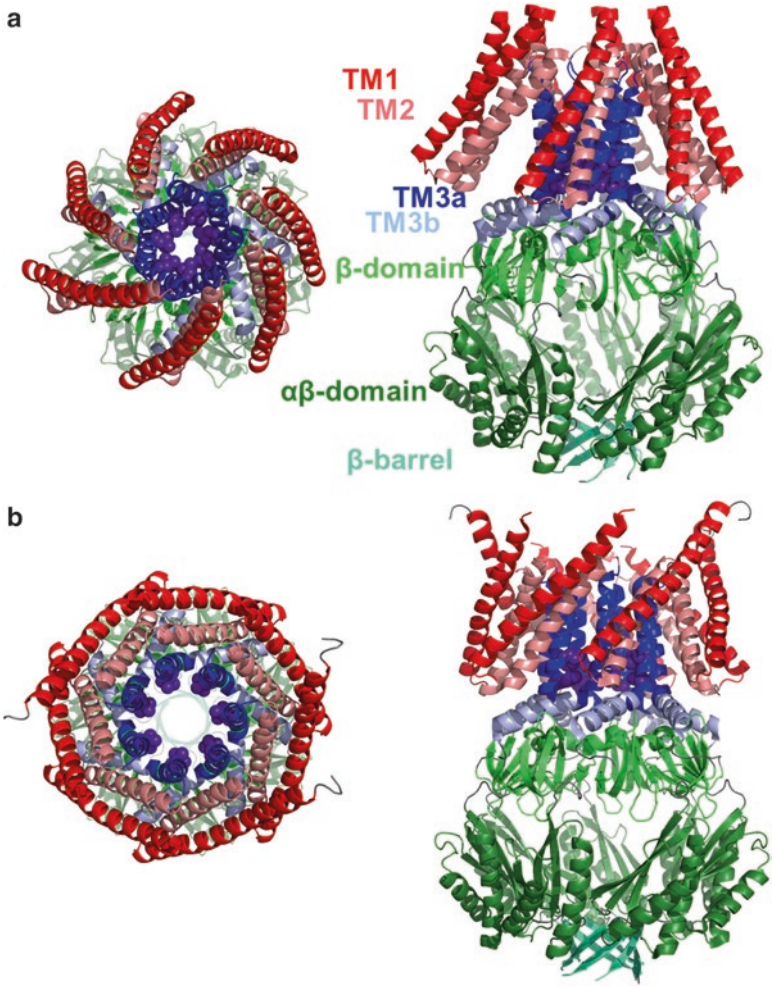


**Fig. 4.3** Structure of MscS. The crystal structures of EcMscS WT in the closed conformation (**a**; PDB: 2OAU) and the spin-labelled mutant EcMscS D67C in the open conformation (**b**; PDB: 5AJI) are shown (Bass et al. 2002; Steinbacher et al. 2007; Pliotas et al. 2015). Views from the periplasmic side (left images) and within the membrane (right images) are provided. The membrane domain is represented by the sensor paddle (TM1: red and TM2: pink) and the kinked TM3 (TM3a: blue and TM3b: light-blue). Residues of the hydrophobic seal, L105 and L109, are represented as purple spheres. The cytosolic vestibule is shown in green with its β-domain, αβ-domain and β-barrel

hydrophobic enough that no stable water column is formed, resulting in a "vapour lock" that keeps the channel closed (Anishkin and Sukharev 2004; Anishkin et al. 2010). The pore stays fairly narrow and hydrophobic towards the periplasm (Rasmussen et al. 2015) until the N-terminal end of TM3a at residue G90 where it extends to a flat funnel. The kink in TM3 prevents the sensor paddles from lying flat

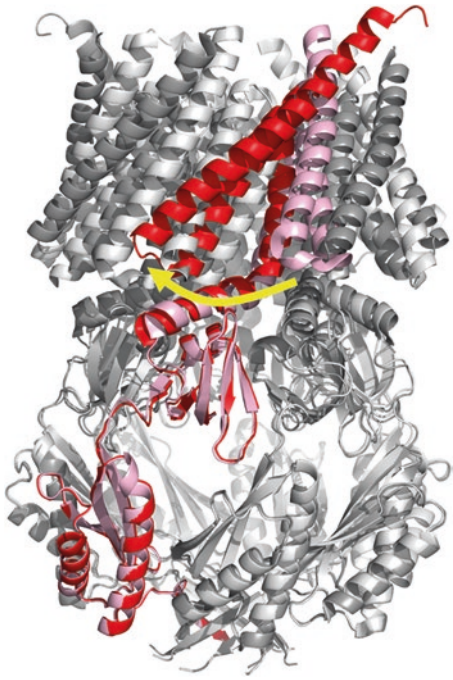

**Fig. 4.4** Movement of the sensor paddle upon activation in MscS. Crystal structures of the open and closed conformations (the same as in Fig. 4.3) aligned to visualise the changes. One subunit is marked (closed structure: pink; open structure: red). It can be seen that the sensor paddle in the closed structure is on top of TM3b of the neighbouring subunit and makes a rotational movement around the central complex axis to lie on top of TM3b of the same subunit in the open conformation. Hardly any changes are seen for the cytosolic domain

on the core of the complex. A rough triangle from the N-terminal end of TM3a to the C-terminal end of TM3b' of the next subunit is drawn. Thus, pockets are present between the paddles and TM3 and the overall shape of the membrane domain is a cone. The N-terminus of MscS, about the first 25 residues, is located in the periplasm but its structure is unknown because no crystal structure could resolve this region so far. The latest crystal structure resolved data from residue 17 and showed that TM1 starts already at Q21 preceded by a loop (Pliotas et al. 2015). A tryptophan residue in this region, W16, influences gating as shown by the increase of the gating threshold if it is modified by mutagenesis (Rasmussen et al. 2007). One could speculate that this effect is caused if W16 is located at the water-membrane interface where tryptophan residues often "anchor" membrane proteins (Killian and von Heijne 2000).

The first open crystal structure of MscS was produced from the EcMscS mutant A106V (Wang et al. 2008). The TM3a helices are pulled apart and straightened towards the central axis which widens the pore. The largest conformational change is seen for the sensor paddles which make a rotational motion around the central axis in comparison to the closed structure (Fig. 4.4). Consequently, the sensor paddles are more tilted relative to the central axis and their tips now contact the end of TM3b from the same subunit. This rotational movement causes also the TM3a helices to rotate which elegantly moves the large side chains of the seal residues L105 and L109 out of the way. Changes within the pore were also measured by fluorescence spectroscopy using L105 W as probe confirming the hydrophilic change (Rasmussen et al. 2010) and a change in pore properties was also observed after

reconstitution (Rasmussen et al. 2015). A conserved glycine – alanine pattern seems to act like a thread on TM3a which was revealed by mutagenesis and electrophysiology (Edwards et al. 2005). As a consequence of the outward movement, gaps between TM3a helices in the pore wall appear when MscS opens. During the opening, the side chain of A110 on TM3a has to cross over the side chain of L115 on TM3b which was suggested to form a kinetic barrier for the transition between open and closed states (Wang et al. 2008). In contrast to the membrane domain, hardly any structural differences in the cytosolic domain can be seen between the open and closed conformations. A fluorescence study, using Förster Resonance Energy Transfer (FRET) for distance measurements, contradicts this because distance changes were found (Machiyama et al. 2009). The decrease in FRET efficiency upon addition of the channel opener LPC suggested that the cytosolic domain swells upon opening.

The crystal structures from *E. coli* implied that the side portals are the conducting pathways into the vestibule from the cytosol rather than the narrow central β-barrel (Bass et al. 2002; Wang et al. 2008). A structural and functional comparison with MscS from *Thermoanaerobacter tengcongensis* (TtMscS) provided a better understanding concerning the pathways and the ion selectivity (Zhang et al. 2012). The structure of TtMscS is in general very similar to the closed structure of EcMscS. However, because of larger side chains F157, M243 and W246 in TtMscS (compared to A158, G244 and Q247 in EcMcsS) the portal diameter is much smaller and presumably non-conducting. In contrast, smaller side chains of T272 and L276 in comparison to the homologous M273 and F277 in EcMscS widen the pore in the β-barrel. Thus it was suspected that the β-barrel instead of the portals is the main conducting pathway in TsMscS. EcMscS shows a weak anion selectivity in e.-phys. experiments (Martinac et al. 1987; Sukharev et al. 1993; Sukharev 2002) which is more pronounced in TsMscS (Zhang et al. 2012). MscS-like channels from plants showed anion selectivity too (Falke et al. 1988; Qi et al. 2004; Maksaev and Haswell 2012) while a homologue from archaea is cation selective (Kloda and Martinac 2001a). A different electrostatic surface potential in the β-barrel was seen in the TsMscS structure in comparison to MscS which was suggested as reason for the difference in selectivity. A chimera construct where the last C-terminal residues of EcMscS were introduced in TsMscS showed almost no anion selectivity similar to EcMscS WT. The opposite construct of EcMscS with the C-terminus of TsMscS showed more anion selectivity than EcMscS WT but not as much as TsMscS. It was reasoned that in the latter chimera unspecific conductance through the portals beside the selective conductance through the β-barrel would lead to a mixed phenotype. An additional mutation reduced the radius of the portals in this chimera and resulted in a stronger anion selectivity which supported their interpretation (Zhang et al. 2012). In addition, for EcMscS it also has been reported that negatively charged residues inside the vestibule close to the portals are important for the anion selectivity because the selectivity is reduced by the mutations E187R or E227A (Cox et al. 2013). In summary, charged residues at different locations close to the openings of the vestibule are likely to contribute to the ion selectivity while no indication have been found that pore residues influence the selectivity (Edwards et al. 2008).

All crystal structures of MscS obtained from different species, some with mutations and using different detergents, are either similar to the first closed or first open structure described above (Bass et al. 2002; Wang et al. 2008; Pliotas et al. 2012; Zhang et al. 2012; Lai et al. 2013; Pliotas et al. 2015). This may imply that these are inherently important conformations for this channel, *i.e.* the closed and open state in the activation cycle, despite the fact that these structures were obtained from solubilised MscS not embedded in the membrane. However, we know at least of one additional state of MscS from adaptation in e.-phys. experiments; if pressure is kept on a patch for a prolonged duration, MscS enters a non-conducting state (Fig. 4.5) (Sukharev et al. 1997; Koprowski and Kubalski 1998; Levina et al. 1999). Furthermore, *desensitised* and *inactivated* states were distinguished: The former can enter the open state again, with a pulse of high saturating pressure, while the latter cannot (Akitake et al. 2007). Hence in this chapter beside the specific terms *desensitisation* and *inactivation*, the superordinate term *adaptation* is used if the process is not specified. The inactivated state needs a long recovery of a few minutes without tension to allow reactivation (Koprowski and Kubalski 1998). The molecular basis for these states is not well established and remains controversial. Co-solvents that are excluded from the protein surface enhanced the adaptation kinetics if they were added to the cytosolic side of the patch in e.-phys. experiments (Grajkowski et al. 2005). This hinted that the adapted state had a more compact cytosolic domain. Application of controlled pressure ramps in patch-clamp experiments revealed that far fewer MscS channels reach the open state if a slow instead of a fast pressure ramp is applied, indicating that the adapted state is directly populated from the closed state (Akitake et al. 2005). The authors proposed that the sprayed out sensor paddles, as seen in the first crystal structure, represent the adapted state while the real closed state has the paddles neatly aligned to the pore forming TM3 helices. This paddle adjustment would act like a dashpot allowing bacteria to distinguish between a slow and fast osmotic downshock. It should be emphasised that in this model the occluded crystal structures (Bass et al. 2002; Zhang et al. 2012; Lai et al. 2013) represent not the closed but the adapted state. This model has further been developed by the Sukharev group by using extrapolated-motion dynamics (EMD) simulations and e.-phys. experiments. To allow for alignment of the paddles to TM3, there is no kink of TM3 at G113 in this model for the open state while a kink at a different place, G121, is seen for the closed state (Akitake et al. 2007; Anishkin et al. 2008a, b). Mutants that stabilised helicity at G113 (G113A or G113E) showed less of the inactivated state in e.-phys. experiments and it was therefore concluded that the kink at this position is indicative for the inactivated state while the mutation Q112G which promotes flexibility in this region had the opposite effect (Akitake et al. 2007). Increasing flexibility at G121 by introduction of the mutation A120G caused fast desensitisation and inactivation while G121A stabilised the open state and decreased adaptation. To clarify which adapted state the proposed kink at G121 is associated with, a double mutant was constructed, G113A/G120G, which indeed showed fast desensitisation but slow inactivation. The mutant G113A/G121A was stabilised in the open state so that even after complete release of pressure from the patch the channel stayed open for a

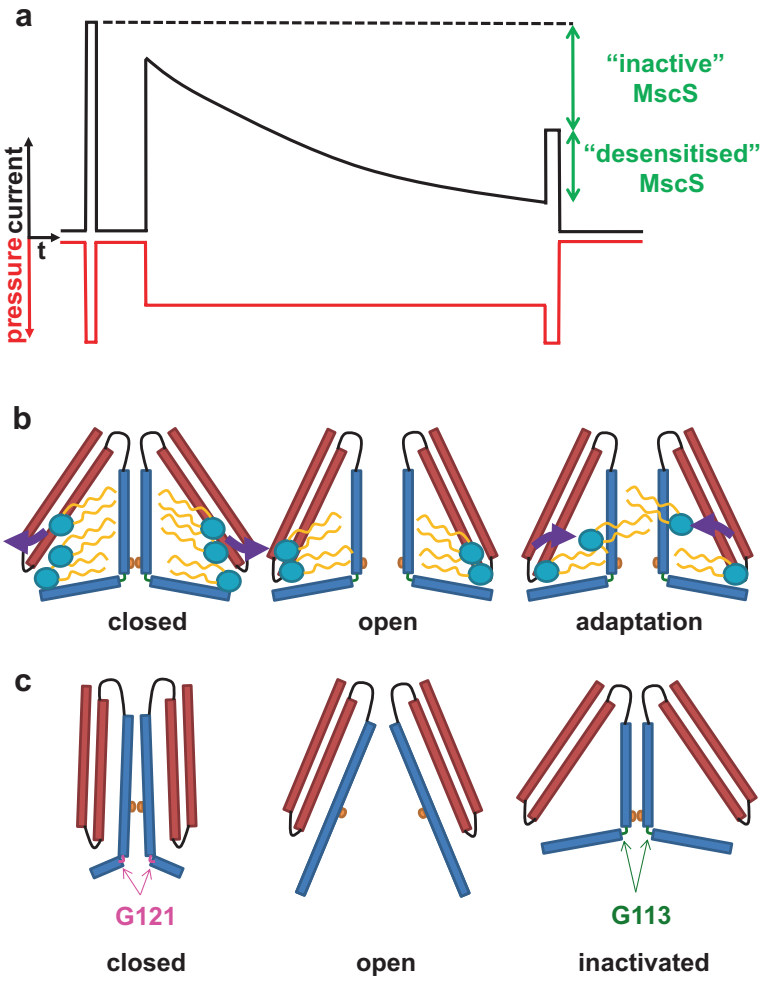


**Fig. 4.5** Adaptation of MscS. (A) Schematic e.-phys. experiment of a population of MscS channels. The current trace (black) shows that if a constant sub-saturating pressure is applied, MscS changes to a non-conductive adapted state over time. The pressure profile applied to the patch (red) has also saturating pressure spikes. The spike in the beginning establishes how many channels can be opened in total which is indicated by the dotted line. The spike at the end shows that only a fraction of channels can be returned into the open state by pressure saturation (*desensitised* MscS) while the remaining fraction needs a long recovery of about 3 min before the channels can be opened again (*inactivated* MscS) (Akitake et al. 2007). Additional probing pressure spikes can be introduced, for example to resolve the kinetic of recovery from the inactivated state after release of the constant sub-saturating pressure. (B) Model for MscS activation based on the crystal structures and the experimental evidence that the pockets are filled with lipids (Pliotas et al. 2015). Lipid extraction from the pockets triggers opening. Fenestrations seen in the open crystal structures led to the proposal that lipid penetration into the pore could be responsible for adaptation (Rasmussen 2016; Zhang et al. 2016). (C) Model for MscS activation based on theoretical EMD and e.-phys. studies (Akitake et al. 2007). No pockets between the paddles (red) and TM3 (blue) are present. The closed state has a kink at G121 while the open state has no kink at all. A kink at G113, resembling the closed crystal structure, was in this model associated to the inactivated state

period of ≈3 min. Further mutational analysis of position G113 showed no correlation of adaptation and the propensity to form α-helices of the amino acid used to replace G113 (Edwards et al. 2008). It was also found that G101D and A102P in TM3a cause loss of desensitisation, which does not correlate with the EMD model. In summary, the EMD model suggests different structures for the closed and open states compared to the conformational states seen in the crystal structures. The inactivated state was related to the non-conductive state seen in crystal structures, while the structure of the desensitised state was not specified but related to a kink at G121. It was also not specified how the structure of the cytosolic domain would change in the open state with the completely stretched TM3 helix. Another model for adaptation was put forward with the first open crystal structure: Because the glycine-alanine "knobs and holes" on TM3a (Edwards et al. 2005) are disentangled during opening, they could re-engage in the wrong way when coming together again and cause adaptation (Wang et al. 2008). This model was supported by mutational studies of residues on TM3a. A further model for adaptation of MscS is discussed below in Sect. 5.

A third structural model for closed and open states of MscS was obtained from spin-labelling and ESR spectroscopic data which were used to constrain MD simulations (Vásquez et al. 2008a, b). This structural model agrees with neither the EMD model nor with the crystal structures. A detailed comparison of the three alternative structural models is described elsewhere (Naismith and Booth 2012). While the crystal structures were criticised because MscS is not embedded in the membrane and lattice packing effects could occur, the EMD model is disputed because no experimental structural evidence validates these simulations. Concerning the ESR model, the spectroscopic data provided only weak 3-dimensional constraints, as no distances by spin-spin interactions were measured. Pulsed electron-electron double resonance (PELDOR) studies were initiated to provide clarification concerning the structures of the MscS states (Pliotas et al. 2012; Ward et al. 2014). It is possible to measure distances between spin labels with PELDOR which was used to test the alternative structural models. MscS solubilised in DDM resulted in distances which were only compatible with the open crystal structure but not with the ESR or EMD model (Pliotas et al. 2012). This showed that lattice effects are not relevant in the crystal structures of MscS. Furthermore, MscS reconstituted in nanodiscs or bicelles provided distances in agreement with the crystal structures (Ward et al. 2014). These data support the correctness of the crystal structures as functionally relevant states of MscS, because it is well established that MscS can be solubilised and reconstituted without substantially changing its functional characteristics in e.-phys. experiments (Sukharev 2002; Battle et al. 2009; Nomura et al. 2012).

## 4.4 MscS-Family

Already in the 1990s' the e.-phys. characterisation of *E. coli* protoplasts provided evidence that more MS channels than MscL and MscS are present. According to their small conductance, they were termed MS channels of "mini" conductance,

MscM (Cui et al. 1995; Berrier et al. 1996). The relation of the *kefA* gene to MS channel activity (Cui et al. 1995) allowed the identification of the *mscS* gene and the MscS-family as a whole by homology searches (Levina et al. 1999). Knock-out mutants showed that mainly *mscL* and *mscS* are responsible for osmo protection in *E. coli*. KefA was characterised as MS channel regulated by the extracellular potassium concentration and therefore renamed MscK (Li et al. 2002). MscK showed a similar conductance and a slight anion preference than MscS in e.-phys. experiments, but is activated at a lower pressure threshold and does not display adaptation. Functional characterisation of the other four orthologues of MscS in *E. coli* was far more difficult and only described recently (Schumann et al. 2010; Edwards et al. 2012). YbdG was shown to be partially responsible for the MscM activity but an e.-phys. characterisation was only possible for the functional mutant V229A (Schumann et al. 2010). YbdG is a low abundance MS channel that is activated at low tensions. Thus, it was suggested that it is functional at mitigating a small hypo-osmotic shock which does not require activation of MscS or MscL. The *E. coli* Δ7 strain (MJF641), where all suspected MS genes were deleted, was instrumental to characterise the remaining three MS channels, YjeP, YbiO, and YnaI (Edwards et al. 2012). Overexpression of the corresponding genes in the Δ7 background allowed the e.-phys. characterisation which showed that YjeP is the main contributor to the MscM activity while the activities of YbiO and YnaI were not previously described. Overexpression of these channels provides protection against osmotic downshock. This proved that all MscS-like genes found in *E. coli* encode functional MS channels.

At the amino acid sequence level, MscS is the smallest common core unit in the MscS-family which represents the C-terminal part of the larger family members (Table 4.1). Two additional TM helices N-terminal to the sensor paddle helices are predicted for YbdG and YnaI while eight additional TM helices are indicated for YbiO, YjeP and MscK. Furthermore, extended periplasmic domains are predicted for YjeP and MscK. In general, the size of the cytosolic domain, *i.e.* the length of the encoded region, is similar within the family except for YbdG which has a ~50 amino acid insertion (Schumann et al. 2010). The MscS homologue from *Corynebacterium glutamicum*, MscCG, has a ~250 amino acid C-terminal extension beyond the common cytosolic domain which seems to be specific for *Corynebacteriaceae* (Becker et al. 2013). Surprisingly, a fourth TM helix was predicted by topology analysis for this domain. Some other MscS-like channels from different organisms and their function is discussed below in Sect. 6.

Biochemical characterisation showed that all family members from *E. coli* form heptameric complexes (Schumann et al. 2010; Edwards et al. 2012). No crystal structures are presently available for any other family members except MscS itself. However, a low resolution 13 Å cryo-electron microscopy and single particle analysis of *E. coli* YnaI provided a first glimpse on structural features of a larger family member (Böttcher et al. 2015). Overall, the cytosolic domain agrees well with the crystal structures of MscS (Fig. 4.6). The electron density for the membrane domain indicates that the pore-lining helices are positioned similar to the TM3a helices in the closed MscS structures. In addition, pockets are resolved which agree with the

**Table 4.1** MS channels in *E. coli*

| MS channel | TM helices | Amino acids | e.-phys. characteristics | | | Number of channels /cell | Protection in downshock Expression | | References |
|---|---|---|---|---|---|---|---|---|---|
| | | | Conductance (nS) | Pressure threshold $P_L$:$P_X$ | Ion selectivity $P_{Cl}$:$P_K$ | | Native | High | |
| MscL | 2 | 136 | 3 | 1 | ≈1 | 560 | ✓ | ✓ | Sukharev et al. (1994) and Hase et al. (1995) |
| MscS | 3 | 286 | 1.25 | 1.59 ± 0.04 | 1.2–3 | 610 | ✓ | ✓ | Levina et al. (1999), Sukharev (2002) and Edwards et al. (2005) |
| YbdG | 3 + 2 | 415 | 0.3[a] | n.r. | n.r. | 51 | ✗ | ✓ | Schumann et al. (2010) |
| YnaI | 3 + 2 | 343 | 0.1 | 1.05 ± 0.02 | n.r. | 31 | ✗ | ✓ | Edwards et al. (2012) |
| YbiO | 3 + 8 | 741 | 1 | 1.21 ± 0.03 | n.r. | 0 | ✗ | ✓ | Edwards et al. (2012) |
| MscK | 3 + 8 | 1120 | 0.875 | 1.87 ± 0.07 | <1 < MscS | 106 | ✗ | ✓ | Li et al. (2002, 2007) |
| YjeP | 3 + 8 | 1107 | 0.3 | 1.64 ± 0.07 | n.r. | 63 | ✗ | ✓ | Edwards et al. (2012) |

Functional and basic structural details are given. The number of TM helices for the larger MscS-like channels are predicted from hydrophobicity plots. The pressure threshold ($P_L$:$P_X$) is given as pressure ratio for EcMscL WT relative to the corresponding MscS-like channel. Numbers of channels per cell were calculated from data for growth in a complete MOPS-based medium given by Li et al. (2014) assuming a pentameric complex for MscL and heptameric complexes for MscS-like channels. Protection in osmotic downshock experiments is indicated for native and high expression levels

[a]For the mutant YbdG V229A; n.r. = not reported

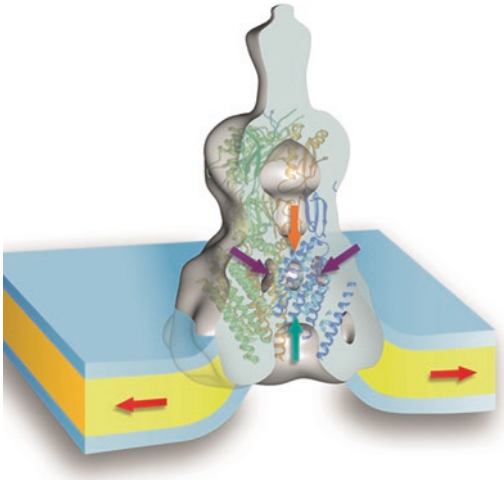

**Fig. 4.6** Structure of YnaI. The electron density of YnaI (grey envelop; EMDB: 3035) was determined by cryo-EM and single particle analysis (Böttcher et al. 2015). The overlaid crystal structure of MscS (coloured ribbon; PDB: 2OAU) shows that the cytosolic domains are very similar. The central pore has two constrictions: The constriction towards the vestibule (orange arrow) agrees with the hydrophobic seal seen in MscS and an additional constriction is shown towards the periplasm (cyan arrow). Off-centre pockets (purple arrows) agree with the pockets seen in MscS and fluorescence experiments showed that they are accessible to lipids. The overall shape of the membrane domain implies that the sensor paddles in YnaI are extended by the two predicted TM helices retaining a cone-shaped membrane domain in comparison to MscS. Therefore, lipid extraction from the pockets or a local membrane bending could be the basis for tension sensing in YnaI. Note that in this figure the cytosol is above the membrane and the periplasm below

pockets between TM3 and the paddles in MscS. Extra electron density in comparison to MscS implies that the sensor paddles are extended by the two additional N-terminal TM helices predicted from the sequence.

## 4.5 How Can MS Channels Sense Stress?

MS channels do not directly sense the pressure in the cell, but the resulting tension in the membrane (Gustin et al. 1988; Sokabe et al. 1991; Moe and Blount 2005). This led to the force-from-lipid principle which proposed that the changes in the surrounding membrane trigger directly conformational changes in the MS channel for activation (Martinac et al. 1990; Anishkin et al. 2014; Teng et al. 2015). In contrast, several eukaryotic MS channels experience force *via* tethering to the cytoskeleton (Hayakawa et al. 2008; Grillet et al. 2009). MscL and MscS were purified and reconstituted into artificial membranes and shown to be active, proving that no additional cofactors or other proteins were required to sense the tension change in the

membrane (Sukharev et al. 1993, 1994; Sukharev 2002). Despite this knowledge it was difficult to study the lipid-protein interaction experimentally and only a few studies addressed them until recently (Powl et al. 2003; Yoshimura et al. 2004; Powl et al. 2005a, b, 2007, 2008; Nomura et al. 2006). Significantly, structural studies by X-ray crystallography often do not resolve lipid molecules because of the temporary nature of interaction and the fact that the structures were obtained from detergent-solubilised samples. Thus, only one structure of MS channels so far resolved aliphatic chains which could originate from lipids (Pliotas et al. 2015).

Attempts to fill this gap of knowledge were tried by using other experimental methods, in parallel to application of theoretical MD simulations. The population of open channels relative to closed ones were determined in e-phys. experiments in dependence of the applied tension. Data of these experiments could be fitted to a simple two state model which follows the Bolzmann statistic (Sukharev et al. 1999). The steepness was related to the change of area that the channel occupies in the membrane in the open and closed states ($\Delta A$). Some experimental uncertainty is introduced because the tension has to be derived from the pressure and the patch geometry applying the Laplace law. The latest determination for MscL estimates $\Delta A \approx 20$ nm$^2$ which agrees fairly well with structural models for MscL (Chiang et al. 2004). For MscS values between 8.4 and 18 nm$^2$ were published which are considerably larger than expected from the crystal structures (Sukharev 2002; Akitake et al. 2005; Belyy et al. 2010; Kamaraju et al. 2010). This was taken to suggest that the assignment of the states seen in all of the crystal structures as closed and open were wrong (Anishkin et al. 2008a). Recently an alternative explanation was put forward that the model needs to be adapted due to the interaction of MscS with lipids which is explained below (Pliotas et al. 2015). Another recent study determined $\Delta A = 7.8$ nm$^2$ for MscS in protoplasts as well as in azolectin liposomes and no such discrepancy to the open and closed crystal structures was seen because of the way $\Delta A$ was estimated from the structures (Shaikh et al. 2014).

Previously it was proposed that $\Delta A$ could be not the only energetic driving force for gating of MS channels. Elastic changes of the membrane close to the protein complex could contribute too (Phillips et al. 2009). For MscL a drastic change in the thickness of the hydrophobic domain between the closed and open state is proposed. Thus a hydrophobic mismatch between this protein region and the hydrophobic core of the membrane could be important for gating. Fluorescence experiments illustrated that the hydrophobic surfaces are matched in the closed state (Powl et al. 2003). A thinning membrane under tension (Goulian et al. 1998; Neder et al. 2010) would drive the activation of MscL because the hydrophobic region of MscL is thinner in the open state. Indeed, e.-phys. experiments displayed a change of gating if MscL was reconstituted into membranes of different thicknesses (Perozo et al. 2002b; Nomura et al. 2012). For MscS a different modulation of the proximal membrane has been suggested; theoretical studies concluded that the cone-shape of the membrane domain could induce a local bending of the membrane surrounding the complex (Sotomayor and Schulten 2004; Phillips et al. 2009; Pliotas et al. 2015). A change of this bending could drive activation because the cone shape in the open

crystal structures is less pronounced. It was suggested that the contribution to gating by the local bending of the membrane could be substantial in contrast to the global bending (Bavi et al. 2016b).

In addition to this membrane bending, a recent study showed that the pockets between the paddles and TM3 in EcMscS are filled with lipids (Pliotas et al. 2015). Mutant forms of MscS which had a single tryptophan residue within the pockets were used as fluorescence probes. The purified complex was reconstituted into membranes with brominated lipids. The bromine is located on the hydrophobic fatty acid tails and quenches the fluorescence of tryptophan if it is in collisional distance to the tryptophan (Kasha 1952). Thus, only short range interactions are reported in contrast to often long range interactions seen with FRET. This has the advantage that real contact sites of the lipids on the protein can be localised (Carney et al. 2006). In addition, tryptophan is a small fluorescence probe and often does not disturb the protein context. The bromine as quencher induces only a subtle change of the lipid and membranes consisting of these lipids, which behave in a similar manner to membranes containing unsaturated lipids (Wiener and White 1991). Fluorescence intensities of these mutant MscS forms reconstituted into brominated lipids are compared with reconstitutions into normal non-brominated lipids. These experiments showed strong quenching for several residues within the pockets of MscS which indicates lipid penetration into these pockets (Pliotas et al. 2015). Furthermore, mass spectroscopy of the solubilised native complexes showed that lipids are associated with the complex (Pliotas et al. 2015). This finding agreed with earlier ICP-MS results quantifying lipid within the complex (Rasmussen et al. 2010). The above mentioned crystal structure which showed aliphatic chains in the pockets and MD simulations further substantiated lipid localisation in the pockets (Pliotas et al. 2015). These MD simulations also proposed that fewer lipids interact with the open form in comparison with the closed form. Thus, it was suggested that the lipid extraction from the pockets by increased tension triggers activation. Fluorescence experiments showed that LPC also accesses the pockets. This new model explains the activation of MscS by LPC with the smaller hydrophobic volume of LPC filling less of the pockets while space available for head groups stays the same.

The EM structure of YnaI shows pockets similar to MscS. Therefore, these pockets could have a similar function in tension sensing as proposed for MscS. However, the additional TM helices in YnaI might obscure access of lipids to the pockets (Booth et al. 2011). Hence, fluorescence experiments were performed for YnaI in the same way as described for MscS. The residues were selected by sequence alignment with MscS. A similar degree of quenching was seen in YnaI compared to MscS suggesting that these pockets in YnaI are accessible to lipids (Böttcher et al. 2015). Furthermore, although the helices are not resolved in the structure, the electron density suggests that the additional TM helices are also tilted relative to the central axis, extending the senor paddles. This would imply that the membrane around YnaI could be bent as was suggested for MscS (Fig. 4.6). Tension sensing mechanisms proposed for MscS, local membrane bending and lipid intercalation, could therefore be conserved in YnaI (Böttcher et al. 2015).

In summary, extraction of lipids from the pockets and local membrane bending were proposed as important factors of tension sensing in MscS on the basis of the crystal structures while the expansion of the area of the complex plays only a limited role. In contrast, the model of Sukharev is based on ΔA, driving gating, and EMD structural models, assuming the crystal structures were not the relevant open and closed forms. For MscL it is likely that ΔA and the hydrophobic mismatch could play important roles in tension sensing. However, in addition, the N-terminal helix of MscL was identified as crucial structural feature for tension sensing and lipid-protein interaction. It serves as a membrane anchor and guides the opening movement (Iscla et al. 2008). Structural studies showed clearly that the movement of this helix and the TM helices are coupled (Li et al. 2015). Recently it was suggested that not only the N-terminal helix guides the opening movement but that lipids actively pull it (Bavi et al. 2016a). This was advocated as general principle of MS channel sensing with a similar role for TM3b in MscS.

Based on the lipid-protein interactions a new model for adaption of MscS has recently been put forward (Rasmussen 2016; Zhang et al. 2016). In the crystal structures of the open MscS fenestrations between the pore-forming TM3a helices can be seen. It was suggested that lipid molecules can leak into the pore through this fenestrations and block it (Fig. 4.5). Some further experimental results support this model: MD simulations as well as fluorescence quenching of L105W indicate some access of lipids to the pore (Pliotas et al. 2015). There might be some lipid dependence of adaptation because MscS reconstituted into liposomes showed a slightly lower degree of adaptation than MscS in protoplasts (Sukharev 2002; Battle et al. 2009). Mutations were described within TM3a, G101D, A102P and A102G, which affect adaptation (Edwards et al. 2008; Wang et al. 2008). However, the mutations at G113 and G121 does not seem to support this model because they are far away from the fenestrations (Akitake et al. 2007; Edwards et al. 2008). In relation to this model it is intriguing to see that in the eukaryotic MS channel TRAAK lipids were blocking the pore through fenestrations in the closed state (Brohawn et al. 2014a). Further details concerning the lipid-protein interaction, force-from-lipid principle and tension sensing can be found in several reviews (Yoshimura and Sokabe 2010; Booth et al. 2011; Naismith and Booth 2012; Iscla and Blount 2012; Teng et al. 2015; Battle et al. 2015; Brohawn 2015; Rasmussen 2016; Zhang et al. 2016).

## 4.6 How Do MS Channels Protect Against Hypo-osmotic Shock and What Else Can They Do?

The fact that *E. coli* possess seven different functional MS channels directly poises the question why so many are required. Osmotic downshock experiments established that these channels really protect bacteria against this stress, but showed that in *E. coli* MscL and MscS are predominantly responsible for protection (Levina et al. 1999). It is likely that the redundancy can partly be explained by the advantage

of a graded response; a smaller osmotic shock provides only enough stimuli to open a smaller pore (MscS). Yet the disturbance of homeostasis is not as dramatic as for the formation of a very large pore (MscL) which only opens close to the lytic pressure. Downshock experiments showed that YbdG can protect against a mild hypoosmotic shock, evident in a background where MscL, MscS and MscK are deleted (Schumann et al. 2010).

The osmotic downshock assay is a good qualitative assay to test the function and the abundance of MS channel in a population of bacterial cells (Booth et al. 2007b; Booth 2014). However, the process and outcome of these shocks on individual cell level is complex. Time resolved shock experiments using stopped-flow equipment showed that cells swell within 30–50 ms and MS channels gate in 150–200 ms (Boer et al. 2011) while the intrinsic ability of MS channels to respond to tension is within a few μs faster (Shapovalov and Lester 2004). Lysis continues to take place for at least 20 min after shock (Levina et al. 1999; Bialecka-Fornal et al. 2015). Cell death can manifest itself with different outcomes. While some cells loose the entire cell content and form empty "ghosts", other cells loose only part of their content or form blebs (Reuter et al. 2014; Bialecka-Fornal et al. 2015). Furthermore, the rate of osmotic change is relevant to the degree of cell death. With a refined single cell based assay it was also possible to show that the minor MS channels in *E. coli* have the ability to protect at native expression levels if the shock is slow (Bialecka-Fornal et al. 2015). High resolution single cell imaging showed that cells expand by up to 15% of its volume for about 30 s after an osmotic downshock and slowly decrease the cell volume afterwards and can even shrink below the pre-shock volume (Buda et al. 2016). The recovery is significantly slower than the *in vitro* response of the MS channels. Mathematical modelling of the volume change suggested that solute efflux is rate limiting for the recovery. Upon MS channel opening, first water influx is increased until the pressure reverses the direction of flow with water and solute efflux (Buda et al. 2016). It should be noted that the kinetics seen in this study are quite different from the stopped-flow experiments described above (Boer et al. 2011).

The outcome of a hypo-osmotic shock depends not only on the molecular properties of the channels, as for example conductivity and activation threshold, but also on the expression levels of these channels in the individual cell. E.-phys. experiments estimated the number of MscL complexes between 4 and 100 per cell (Blount et al. 1999; Stokes et al. 2003) while for radiolabelling 50 MscL complexes were counted (Häse et al. 1997). A more recent study using Western blots and single cell fluorescence microscopy found a much higher number, 300–1000 MscL per cell (Bialecka-Fornal et al. 2012). Considering the fact that a single MscL channel could deplete the entire ion pool of the cell within 1–10 s (Steinbacher et al. 2007; Booth 2014), the question why so many channels are found in the cell arises. A potential answer is that the kinetics of response is important and a high number of channels allow faster release of pressure (Booth 2014). A genome wide study by ribosome

profiling in *E. coli* confirmed the high numbers for MscL (~500 channels) and also showed high numbers for MscS (400–600 channels), while numbers for the remaining MscS-family members were much lower (Li et al. 2014)(Table 4.1). Recently, a linear relationship between survival and channel numbers was established (van den Berg et al. 2016). It was demonstrated that at least 100 channels of MscL or MscS are required to protect the cell when only one type of MS channel is present. The above mentioned single cell fluorescence microscopy study revealed that the number of MscL channels can substantially vary from cell-to-cell (Bialecka-Fornal et al. 2012). Consistently, variability in the volume change upon shock was observed (Buda et al. 2016). The interesting possibility was raised that this variability is a population survival strategy where a subset of cells with high numbers are able to survive harsh shocks while the majority of cells enjoy the lower metabolic burden of lower channel numbers (Bialecka-Fornal et al. 2012).

Beside *E. coli*, analysis of genome sequences showed that bacteria often contain a single gene for *mscL* but several genes for *mscS* family members (Pivetti et al. 2003). Homologues from other prokaryotes than *E. coli* which have been characterised are listed in Table 4.2. The cell wall-less mycoplasma have usually a *mscL* gene while *mscS* is absent (Booth and Blount 2012). Some bacteria living in a marine environment have no gene for MscL which was related to their halophilic life style (Nakamaru et al. 1999; Bucarey et al. 2012). Furthermore, the food born pathogen *Campylobacter jejuni* has no *mscL* gene while its two MscS homologues were implicated in the pathogenicity (Kakuda et al. 2012). Almost all *Vibrio* species have no *mscL* gene while *Vibrio cholerae* has a copy and it was advocated that this could provide adaptation to its pathogenic niche (Booth and Blount 2012; Rowe et al. 2013). In *Bacillus subtilis* the spore protein SpoVAC, non-related to MscL or MscS, has been shown to be mechanosensitive and the ability to protect in osmotic downshocks (Velásquez et al. 2014) despite the fact that functional MscL and MscS homologues have been described in this bacterium (Moe et al. 1998; Wahome and Setlow 2008; Hoffmann et al. 2008). SpoVAC probably releases calcium dipicolinic acid during spore germination. It is not clear yet if its mechanosensation is important for the function *in vivo* or not. In general, channels could be accidental MS channels if they show a ΔA between their active conformations. Beyond the bacterial kingdom, *mscL* and *mscS* are widespread in archea. *MscS* and *mscK* can be found in protozoa while *mscL* is absent (Prole and Taylor 2013). *MscL* is found in some fungi and oomycetes while *mscS* homologues are distributed in plants. *Arabidopsis thaliana* for example has ten *mscS*-like genes which have been extensively studied, localised in different compartments fulfilling different functions; for a recent review see (Hamilton et al. 2015). In contrast, *mscL* and *mscS* seem to be absent from animals (Pivetti et al. 2003; Balleza and Gómez-Lagunas 2009).

**Table 4.2** Characterisation of MS channels from prokaryotes

| MS channel | Species | e.-phys. characterisation | | Comment | References |
|---|---|---|---|---|---|
| | | Conductance (nS) | Ion selectivity ($P_{Cl}$:$P_K$) | | |
| MscL | *Erwinia carotovora* | 4.1 ± 0.3 | ≈1 | $P_L$:$P_S$ = 1.5 | Moe et al. (1998) |
| | *Haemophilus influenza* | 4.0 ± 0.2 | ≈1 | $P_L$:$P_S$ = 1.5 | Moe et al. (1998) |
| | *Pseudomonas fluorescence* | 3.7 ± 0.1 | ≈1 | $P_L$:$P_S$ = 1.5 | Moe et al. (1998) |
| | *Vibrio cholerae* | 2.75 | ≈1 | $P_L$:$P_S$ = 2.1 (in V.c. membr.) | Rowe et al. (2013) |
| | *Rhizobium etli* | 3.3 | ≈1 | $P_L$:$P_S$ = 1.34 ± 0.6; protection in downshock in *E. coli* | Balleza et al. (2010) |
| | *Synechocystis PCC 6803* | 3.6 ± 0.3 | ≈1 | $P_L$:$P_S$ = 3; osmo regulation | Moe et al. (1998) and Nanatani et al. (2014) |
| | *Mycobacterium tuberculosis* | ≈ 3–4 | ≈1 | X-ray structure; PL:PS depend on phosphatidyl-inositol presence | Chang et al. (1998), Moe et al. (2000) and Zhong and Blount (2013) |
| | *Clostridium perfringens* | 4.9 ± 0.2 | ≈1 | $P_L$:$P_S$ = 1.5 | Moe et al. (1998) |
| | *Bacillus subtilis* | 3.6 ± 0.1 | ≈1 | $P_L$:$P_S$ = 1.5; protection in downshock | Moe et al. (1998), Wahome and Setlow (2008) and Hoffmann et al. (2008) |
| | *Staphylococcus aureus* | n.r. | ≈1 | X-ray structure of tetramer; biochemical characterisation; "flickery" activity in e.-phys. of mutants | Moe et al. (1998), Liu et al. (2009), Dorwart et al. (2010) and Iscla et al. (2011) |
| | *Lactococcus lactis* | 2.0 ± 0.3 | ≈1 | Protects in downshock; main MS channel in *L. lactis* | Folgering et al. (2005) |
| | *Methanosarcina acetivorans* | 0.2–0.3 | n.r. | X-ray structure | Li et al. (2015) |
| MscS | *Helicobacter pylori* | n.r. | n.r. | X-ray structure | Lai et al. (2013) |
| MscSP | *Silicibacter pomeroyi* | 1.04 | 1.4 | $P_L$:$P_S$ = 1.28 (reconst); no adaptation in e.-phys. | Petrov et al. (2013) |

| | | | | | |
|---|---|---|---|---|---|
| MscS | *Vibrio cholerae* | 0.87 | ≈1 | $P_L$:$P_S$ = 2.1 (in *V.cholera* membr.); shows adaptation | Rowe et al. (2013) |
| Cjj0263 | *Campylobacter jejuni* | n.r. | n.r. | Protection in downshock; involved in host colonisation | Kakuda et al. (2012) |
| Cjj1025 | *Campylobacter jejuni* | n.r. | n.r. | Involved in host colonisation | Kakuda et al. (2012) |
| MscS | *Thermoanaerobacter tengcongensis* | 0.134 | 8.7 | X-ray structure | Zhang et al. (2012) |
| MscCG | *Corynebacterium glutamicum* | 0.33–0.34 | 0.3 | Glutamate efflux; no adaptation in e.-phys.; $P_L$:$P_S \approx 2$ | Börngen et al. (2010), Becker et al. (2013), Yamashita et al. (2013) and Nakayama et al. (2013) |
| YkuT | *Bacillus subtilis* | n.r. | n.r. | Protection in downshock | Wahome and Setlow (2008) and Hoffmann et al. (2008) |
| YncB | *Lactococcus lactis* | 0.87 ± 0.07 | ≈1 | Shows desensitisation; protects in downshock in *E. coli* | Folgering et al. (2005) |
| MscMJLR | *Methanococcus jannaschii* | 2 | 0.2 | No adaptation in e.-phys. | Kloda and Martinac (2001a, b) |
| MscMJ | *Methanococcus jannaschii* | 0.27 | 0.16 | No adaptation in e.-phys. | Kloda and Martinac (2001b) |
| Ss-bCNGa | *Synechocystis PCC 6803* | n.r. | n.r. | Protection in downshock | Malcolm et al. (2012b) |
| Se-bCNG | *Synechococcus elongatus PCC 7942* | n.r. | n.r. | MscS homologue but no MS activity found (also for bCNG from several other species) | Caldwell et al. (2010) and Malcolm et al. (2012a, b) |
| SpoVAC | *Bacillus subtilis* | 0.11–0.15 | n.r. | Spore germination protein; no relation to MscL or MscS, protects in downshock | Velásquez et al. (2014) |

MS channels from prokaryotes are listed which have been functionally or structurally characterised. Data for MS channels from *E. coli* are given in Table 4.1

Evolution of *mscL* has been constrained while *mscS* has developed into a diverse superfamily of channels where often additional parts where fused, especially to the N-terminus but also to the C-terminus of the core unit (Malcolm and Maurer 2012; Cox et al. 2015; Booth et al. 2015). This led probably also to a diversification of function in the MscS family. It was discussed above that all family members in *E. coli* are mechanosensitive and that different channels are beneficial during a graded response to osmotic stress. However, for YjeP it was shown that there is a potential link to the phosphatidyl ethanolamine synthesis (Dowhan 2013). Recently, an interaction between the cytosolic domain of MscS with the cell division protein FtsZ was demonstrated (Koprowski et al. 2015). FtsZ is not only involved in cell division but also cell wall synthesis and it seems that MscS contributes to the latter function by mitigating cell wall damage. The above mentioned MscS homologue in *C. glutamicum*, MscCG, has been shown to facilitate glutamate efflux (Nakamura et al. 2007; Becker et al. 2013). bCNG channels have a C-terminal cyclic adenosine mono phosphate (cAMP) binding domain and have been shown to gate in response to cyclic nucleotides instead of membrane tension (Caldwell et al. 2010). However, one homologue from *Synechocystis PCC 6803*, Ss-bCNGa, provided protection in downshock experiments (Malcolm et al. 2012b) and some truncated homologues, where the CNG-domain was removed, showed limited protection (Malcolm et al. 2012a). Some MscS-family members, predominately from fungi, have EF calcium binding domains which seems to protect cells from hypo-osmotic shock by regulation of the intracellular calcium concentration (Nakayama et al. 2012; Malcolm and Maurer 2012; Nakayama and Iida 2014).

## 4.7 Conclusions

MscL and the MscS-family are fascinating stress response systems for a fundamental challenge to bacteria, the change of osmolality in their environment. They are also crucial model systems for MS channels in general since several eukaryotic channels were recently proven to be gated directly by membrane tension (Berrier et al. 2013; Brohawn et al. 2014b; Syeda et al. 2016). Despite progress we are still struggling to measure quantitatively contributions from different proposed tension sensing mechanisms and to appreciate their importance. In addition, methods to link experimental structural data to the different functional states of MscS are still desired. The journey to explore the structural and functional diversity of the MscS family just started! Furthermore, development of MscL as “nano valve” and as antimicrobial drug target will show its impact in the coming years.

## References

Ajouz B, Berrier C, Besnard M et al (2000) Contributions of the different extramembranous domains of the mechanosensitive ion channel MscL to its response to membrane tension. J Biol Chem 275:1015–1022

Akitake B, Anishkin A, Sukharev S (2005) The "dashpot" mechanism of stretch-dependent gating in MscS. J Gen Physiol 125:143–154

Akitake B, Anishkin A, Liu N, Sukharev S (2007) Straightening and sequential buckling of the pore-lining helices define the gating cycle of MscS. Nat Struct Mol Biol 14:1141–1149

Anishkin A, Sukharev S (2004) Water dynamics and dewetting transitions in the small mechanosensitive channel MscS. Biophys J 86:2883–2895

Anishkin A, Chiang C-S, Sukharev S (2005) Gain-of-function mutations reveal expanded intermediate states and a sequential action of two gates in MscL. J Gen Physiol 125:155–170

Anishkin A, Akitake B, Sukharev S (2008a) Characterization of the resting MscS: modeling and analysis of the closed bacterial mechanosensitive channel of small conductance. Biophys J 94:1252–1266

Anishkin A, Kamaraju K, Sukharev S (2008b) Mechanosensitive channel MscS in the open state: modeling of the transition, explicit simulations, and experimental measurements of conductance. J Gen Physiol 132:67–83

Anishkin A, Akitake B, Kamaraju K et al (2010) Hydration properties of mechanosensitive channel pores define the energetics of gating. J Phys Condens Matter 22:454120

Anishkin A, Loukin SH, Teng J, Kung C (2014) Feeling the hidden mechanical forces in lipid bilayer is an original sense. Proc Natl Acad Sci U S A 111:7898–7905

Balleza D, Gómez-Lagunas F (2009) Conserved motifs in mechanosensitive channels MscL and MscS. Eur Biophys J 38:1013–1027

Balleza D, Gómez-Lagunas F, Quinto C (2010) Cloning and functional expression of an MscL ortholog from rhizobium etli: characterization of a mechanosensitive channel. J Membr Biol 234:13–27

Bartlett JL, Levin G, Blount P (2004) An in vivo assay identifies changes in residue accessibility on mechanosensitive channel gating. Proc Natl Acad Sci U S A 101:10161–10165

Bass RB, Strop P, Barclay M, Rees DC (2002) Crystal structure of Escherichia coli MscS, a voltage-modulated and mechanosensitive channel. Science 298:1582–1587

Battle AR, Petrov E, Pal P, Martinac B (2009) Rapid and improved reconstitution of bacterial mechanosensitive ion channel proteins MscS and MscL into liposomes using a modified sucrose method. FEBS Lett 583:407–412

Battle AR, Ridone P, Bavi N et al (2015) Lipid-protein interactions: lessons learned from stress. Biochim Biophys Acta 1848:1744–1756

Bavi N, Cortes DM, Cox CD et al (2016a) The role of MscL amphipathic N terminus indicates a blueprint for bilayer-mediated gating of mechanosensitive channels. Nat Commun 7:11984

Bavi O, Cox CD, Vossoughi M et al (2016b) Influence of global and local membrane curvature on mechanosensitive ion channels: a finite element approach. Membr (Basel) 6:14

Becker M, Börngen K, Nomura T et al (2013) Glutamate efflux mediated by Corynebacterium glutamicum MscCG, Escherichia coli MscS, and their derivatives. Biochim Biophys Acta 1828:1230–1240

Belyy V, Kamaraju K, Akitake B et al (2010) Adaptive behavior of bacterial mechanosensitive channels is coupled to membrane mechanics. J Gen Physiol 135:641–652

Berrier C, Besnard M, Ajouz B et al (1996) Multiple mechanosensitive ion channels from Escherichia coli, activated at different thresholds of applied pressure. J Membr Biol 151:175–187

Berrier C, Pozza A, de Lacroix de Lavalette A et al (2013) The purified mechanosensitive channel TREK-1 is directly sensitive to membrane tension. J Biol Chem 288:27307–27314

Bialecka-Fornal M, Lee HJ, DeBerg HA, Gandhi CS, Phillips R (2012) Single-cell census of mechanosensitive channels in living bacteria. PLoS One 7:e33077

Bialecka-Fornal M, Lee HJ, Phillips R (2015) The rate of osmotic downshock determines the survival probability of bacterial mechanosensitive channel mutants. J Bacteriol 197:231–237
Bilston LE, Mylvaganam K (2002) Molecular simulations of the large conductance mechanosensitive (MscL) channel under mechanical loading. FEBS Lett 512:185–190
Birkner JP, Poolman B, Koçer A (2012) Hydrophobic gating of mechanosensitive channel of large conductance evidenced by single-subunit resolution. Proc Natl Acad Sci U S A 109:12944–12949
Blount P, Sukharev SI, Schroeder MJ et al (1996) Single residue substitutions that change the gating properties of a mechanosensitive channel in Escherichia coli. Proc Natl Acad Sci U S A 93:11652–11657
Blount P, Sukharev SI, Moe PC et al (1999) Mechanosensitive channels of bacteria. Methods Enzymol 294:458–482
Boer M, Anishkin A, Sukharev S (2011) Adaptive MscS gating in the osmotic permeability response in E. coli: the question of time. Biochemistry 50:4087–4096
Booth I (2014) Bacterial mechanosensitive channels: progress towards an understanding of their roles in cell physiology. Curr Opin Microbiol 18:16–22
Booth IR, Blount P (2012) The MscS and MscL families of mechanosensitive channels act as microbial emergency release valves. J Bacteriol 194:4802–4809
Booth IR, Edwards MD, Black S et al (2007a) Mechanosensitive channels in bacteria: signs of closure? Nat Rev Microbiol 5:431–440
Booth IR, Edwards MD, Black S et al (2007b) Physiological analysis of bacterial mechanosensitive channels. Methods Enzymol 428:47–61
Booth IR, Rasmussen T, Edwards MD et al (2011) Sensing bilayer tension: bacterial mechanosensitive channels and their gating mechanisms. Biochem Soc Trans 39:733–740
Booth IR, Miller S, Müller A, Lehtovirta-Morley L (2015) The evolution of bacterial mechanosensitive channels. Cell Calcium 57:140–150
Börngen K, Battle AR, Möker N et al (2010) The properties and contribution of the Corynebacterium glutamicum MscS variant to fine-tuning of osmotic adaptation. Biochim Biophys Acta 1798:2141–2149
Böttcher B, Prazak V, Rasmussen A et al (2015) The structure of YnaI implies structural and mechanistic conservation in the MscS family of mechanosensitive channels. Structure 23:1705–1714
Brohawn SG (2015) How ion channels sense mechanical force: insights from mechanosensitive K2P channels TRAAK, TREK1, and TREK2. Ann N Y Acad Sci 1352:20–32
Brohawn SG, Campbell EB, MacKinnon R (2014a) Physical mechanism for gating and mechanosensitivity of the human TRAAK K+ channel. Nature 516:126–130
Brohawn SG, Su Z, MacKinnon R (2014b) Mechanosensitivity is mediated directly by the lipid membrane in TRAAK and TREK1 K + channels. Proc Natl Acad Sci 111:3614–3619
Bucarey SA, Penn K, Paul L et al (2012) Genetic complementation of the obligate marine actinobacterium Salinispora tropica with the large mechanosensitive channel gene mscL rescues cells from osmotic downshock. Appl Environ Microbiol 78:4175–4182
Buda R, Liu Y, Yang J et al (2016) Dynamics of Escherichia coli 's passive response to a sudden decrease in external osmolarity. Proc Natl Acad Sci 113:E5838–E5846
Caldwell DB, Malcolm HR, Elmore DE, Maurer JA (2010) Identification and experimental verification of a novel family of bacterial cyclic nucleotide-gated (bCNG) ion channels. Biochim Biophys Acta 1798:1750–1756
Carney J, East JM, Mall S et al (2006) Fluorescence quenching methods to study lipid-protein interactions. Curr Protoc Protein Sci Chapter 19:Unit 19.12
Chang G, Spencer R, Lee A et al (1998) Structure of the MscL homolog from mycobacterium tuberculosis: a gated mechanosensitive ion channel. Science 282:2220–2226
Chiang C-S, Anishkin A, Sukharev S (2004) Gating of the large mechanosensitive channel in situ: estimation of the spatial scale of the transition from channel population responses. Biophys J 86:2846–2861

Colombo G, Marrink SJ, Mark AE (2003) Simulation of MscL gating in a bilayer under stress. Biophys J 84:2331–2337
Corry B, Martinac B (2008) Bacterial mechanosensitive channels: experiment and theory. Biochim Biophys Acta 1778:1859–1870
Cox C, Nomura T, Ziegler C et al (2013) Selectivity mechanism of the mechanosensitive channel MscS revealed by probing channel subconducting states. Nat Commun 4:2137
Cox C, Nakayama Y, Nomura T, Martinac B (2015) The evolutionary "tinkering"of MscS-like channels: generation of structural and functional diversity. Pflugers Arch 467:3–13
Cruickshank CC, Minchin RF, Le Dain AC, Martinac B (1997) Estimation of the pore size of the large-conductance mechanosensitive ion channel of Escherichia coli. Biophys J 73:1925–1931
Cui C, Smith DO, Adler J (1995) Characterization of mechanosensitive channels in Escherichia coli cytoplasmic membrane by whole-cell patch clamp recording. J Membr Biol 144:31–42
Doerner JF, Febvay S, Clapham DE (2012) Controlled delivery of bioactive molecules into live cells using the bacterial mechanosensitive channel MscL. Nat Commun 3:990
Dorwart MR, Wray R, Brautigam CA et al (2010) S. aureus MscL is a pentamer in vivo but of variable stoichiometries in vitro: implications for detergent-solubilized membrane proteins. PLoS Biol 8:e1000555
Dowhan W (2013) A retrospective: use of Escherichia coli as a vehicle to study phospholipid synthesis and function. Biochim Biophys Acta 1831:471–494
Edwards MD, Li Y, Kim S et al (2005) Pivotal role of the glycine-rich TM3 helix in gating the MscS mechanosensitive channel. Nat Struc. Mol Biol 12:113–119
Edwards MD, Bartlett W, Booth IR (2008) Pore mutations of the Escherichia coli MscS channel affect desensitization but not ionic preference. Biophys J 94:3003–3013
Edwards MD, Black S, Rasmussen T et al (2012) Characterization of three novel mechanosensitive channel activities in Escherichia coli. Channels 6:272–281
Falke LC, Edwards KL, Pickard BG, Misler S (1988) A stretch-activated anion channel in tobacco protoplasts. FEBS Lett 237:141–144
Folgering JHA, Moe PC, Schuurman-Wolters GK et al (2005) Lactococcus lactis uses MscL as its principal mechanosensitive channel. J Biol Chem 280:8784–8792
Gandhi CS, Walton TA, Rees DC (2011) OCAM: a new tool for studying the oligomeric diversity of MscL channels. Protein Sci 20:313–326
Goulian M, Mesquita ON, Fygenson DK et al (1998) Gramicidin channel kinetics under tension. Biophys J 74:328–337
Grajkowski W, Kubalski A, Koprowski P (2005) Surface changes of the mechanosensitive channel MscS upon its activation, inactivation, and closing. Biophys J 88:3050–3059
Grillet N, Kazmierczak P, Xiong W et al (2009) The mechanotransduction machinery of hair cells. Sci Signal 2:pt5
Gullingsrud J, Kosztin D, Schulten K (2001) Structural determinants of MscL gating studied by molecular dynamics simulations. Biophys J 80:2074–2081
Gustin M, Zhou X, Martinac B, Kung C (1988) A mechanosensitive ion channel in the yeast plasma membrane. Science 242:762–765
Hamilton ES, Schlegel AM, Haswell ES (2015) United in diversity: mechanosensitive ion channels in plants. Annu Rev Plant Biol 66:113–137
Hase CC, Le Dain AC, Martinac B (1995) Purification and functional reconstitution of the recombinant large mechanosensitive ion channel (MscL) of Escherichia coli. J Biol Chem 270:18329–18334
Häse CC, Minchin RF, Kloda A, Martinac B (1997) Cross-linking studies and membrane localization and assembly of radiolabelled large mechanosensitive ion channel (MscL) of Escherichia coli. Biochem Biophys Res Commun 232:777–782
Haswell ES, Phillips R, Rees DC (2011) Mechanosensitive channels: what can they do and how do they do it? Structure 19:1356–1369
Hayakawa K, Tatsumi H, Sokabe M (2008) Actin stress fibers transmit and focus force to activate mechanosensitive channels. J Cell Sci 121:496–503

Hoffmann T, Boiangiu C, Moses S, Bremer E (2008) Responses of Bacillus subtilis to hypotonic challenges: physiological contributions of mechanosensitive channels to cellular survival. Appl Environ Microbiol 74:2454–2460

Hubbell WL, Cafiso DS, Altenbach C (2000) Identifying conformational changes with site-directed spin labeling. Nat Struct Biol 7:735–739

Iscla I, Blount P (2012) Sensing and responding to membrane tension: the bacterial MscL channel as a model system. Biophys J 103:169–174

Iscla I, Levin G, Wray R, Blount P (2007) Disulfide trapping the mechanosensitive channel MscL into a gating-transition state. Biophys J 92:1224–1232

Iscla I, Wray R, Blount P (2008) On the structure of the N-terminal domain of the MscL channel: helical bundle or membrane interface. Biophys J 95:2283–2291

Iscla I, Wray R, Blount P (2011) The oligomeric state of the truncated mechanosensitive channel of large conductance shows no variance in vivo. Protein Sci 20:1638–1642

Iscla I, Eaton C, Parker J et al (2013) Improving the design of a MscL-based triggered nanovalve. Biosensors 3:171–184

Iscla I, Wray R, Wei S et al (2014) Streptomycin potency is dependent on MscL channel expression. Nat Commun 5:4891

Iscla I, Wray R, Blount P et al (2015) A new antibiotic with potent activity targets MscL. J Antibiot (Tokyo) 68:453–462

Kakuda T, Koide Y, Sakamoto A, Takai S (2012) Characterization of two putative mechanosensitive channel proteins of Campylobacter jejuni involved in protection against osmotic downshock. Vet Microbiol 160:53–60

Kamaraju K, Gottlieb PA, Sachs F, Sukharev S (2010) Effects of GsMTx4 on bacterial mechanosensitive channels in inside-out patches from giant spheroplasts. Biophys J 99:2870–2878

Kasha M (1952) Collisional perturbation of spin-orbital coupling and the mechanism of fluorescence quenching. A visual demonstration of the perturbation. J Chem Phys 20:71

Killian JA, von Heijne G (2000) How proteins adapt to a membrane–water interface. Trends Biochem Sci 25:429–434

Kloda A, Martinac B (2001a) Structural and functional differences between two homologous mechanosensitive channels of Methanococcus jannaschii. EMBO J 20:1888–1896

Kloda A, Martinac B (2001b) Molecular identification of a mechanosensitive channel in archaea. Biophys J 80:229–240

Koçer A (2015) Mechanisms of mechanosensing – mechanosensitive channels, function and re-engineering. Curr Opin Chem Biol 29:120–127

Koçer A, Walko M, Meijberg W, Feringa BL (2005) A light-actuated nanovalve derived from a channel protein. Science 309:755–758

Koçer A, Walko M, Bulten E et al (2006) Rationally designed chemical modulators convert a bacterial channel protein into a pH-sensory valve. Angew Chem Int Ed 45:3126–3130

Koçer A, Walko M, Feringa BL (2007) Synthesis and utilization of reversible and irreversible light-activated nanovalves derived from the channel protein MscL. Nat Protoc 2:1426–1437

Kong Y, Shen Y, Warth TE, Ma J (2002) Conformational pathways in the gating of Escherichia coli mechanosensitive channel. Proc Natl Acad Sci U S A 99:5999–6004

Koprowski P, Kubalski A (1998) Voltage-independent adaptation of mechanosensitive channels in Escherichia coli protoplasts. J Membr Biol 164:253–262

Koprowski P, Grajkowski W, Balcerzak M et al (2015) Cytoplasmic domain of MscS interacts with cell division protein FtsZ: a possible non-channel function of the mechanosensitive channel in Escherichia coli. PLoS One 10:e0127029

Lai J, Poon Y, Kaiser J, Rees D (2013) Open and shut: crystal structures of the dodecylmaltoside solubilized mechanosensitive channel of small conductance from Escherichia coli and Helicobacter at 4.4 Å and 4.1 Å resolutions. Protein Sci 22:502–509

Levina N, Tötemeyer S, Stokes NR et al (1999) Protection of Escherichia coli cells against extreme turgor by activation of MscS and MscL mechanosensitive channels: identification of genes required for MscS activity. EMBO J 18:1730–1737

Li Y, Moe PC, Chandrasekaran S et al (2002) Ionic regulation of MscK, a mechanosensitive channel from Escherichia coli. EMBO J 21:5323–5330
Li C, Edwards MD, Jeong H et al (2007) Identification of mutations that alter the gating of the Escherichia coli mechanosensitive channel protein, MscK. Mol Microbiol 64:560–574
Li G-W, Burkhardt D, Gross C, Weissman JS (2014) Quantifying absolute protein synthesis rates reveals principles underlying allocation of cellular resources. Cell 157:624–635
Li J, Guo J, Ou X et al (2015) Mechanical coupling of the multiple structural elements of the large-conductance mechanosensitive channel during expansion. Proc Natl Acad Sci U S A 112:10726–10731
Liu Z, Gandhi CS, Rees DC (2009) Structure of a tetrameric MscL in an expanded intermediate state. Nature 461:120–124
Louhivuori M, Risselada HJ, van der Giessen E, Marrink SJ (2010) Release of content through mechano-sensitive gates in pressurized liposomes. Proc Natl Acad Sci U S A 107:19856–19860
Löw C, Yau YH, Pardon E et al (2013) Nanobody mediated crystallization of an archeal mechanosensitive channel. PLoS One 8:e77984
Machiyama H, Tatsumi H, Sokabe M (2009) Structural changes in the cytoplasmic domain of the mechanosensitive channel MscS during opening. Biophys J 97:1048–1057
Maksaev G, Haswell ES (2012) MscS-Like10 is a stretch-activated ion channel from Arabidopsis thaliana with a preference for anions. Proc Natl Acad Sci U S A 109:19015–19020
Malcolm HR, Maurer JA (2012) The mechanosensitive channel of small conductance (MscS) superfamily: not just mechanosensitive channels anymore. Chembiochem 13:2037–2043
Malcolm HR, Elmore DE, Maurer JA (2012a) Mechanosensitive behavior of bacterial cyclic nucleotide gated (bCNG) ion channels: insights into the mechanism of channel gating in the mechanosensitive channel of small conductance superfamily. Biochem Biophys Res Commun 417:972–976
Malcolm HR, Heo Y-Y, Caldwell DB et al (2012b) Ss-bCNGa: a unique member of the bacterial cyclic nucleotide gated (bCNG) channel family that gates in response to mechanical tension. Eur Biophys J 41:1003–1013
Martinac B, Buechner M, Delcour AH et al (1987) Pressure-sensitive ion channel in Escherichia coli. Proc Natl Acad Sci 84:2297–2301
Martinac B, Adler J, Kung C (1990) Mechanosensitive ion channels of E. coli activated by amphipaths. Nature 348:261–263
Mika JT, Birkner JP, Poolman B, Koçer A (2013) On the role of individual subunits in MscL gating: “all for one, one for all?”. FASEB J 27:882–892
Moe P, Blount P (2005) Assessment of potential stimuli for mechano-dependent gating of MscL: effects of pressure, tension, and lipid headgroups. Biochemistry 44:12239–12244
Moe PC, Blount P, Kung C (1998) Functional and structural conservation in the mechanosensitive channel MscL implicates elements crucial for mechanosensation. Mol Microbiol 28:583–592
Moe PC, Levin G, Blount P (2000) Correlating a protein structure with function of a bacterial mechanosensitive channel. J Biol Chem 275:31121–31127
Naismith JH, Booth IR (2012) Bacterial mechanosensitive channels – MscS: evolution’s solution to creating sensitivity in function. Annu Rev Biophys 41:157–177
Najem JS, Dunlap MD, Rowe ID et al (2015) Activation of bacterial channel MscL in mechanically stimulated droplet interface bilayers. Sci Rep 5:13726
Nakamaru Y, Takahashi Y, Unemoto T, Nakamura T (1999) Mechanosensitive channel functions to alleviate the cell lysis of marine bacterium, Vibrio alginolyticus, by osmotic downshock. FEBS Lett 444:170–172
Nakamura J, Hirano S, Ito H, Wachi M (2007) Mutations of the Corynebacterium glutamicum NCgl1221 gene, encoding a mechanosensitive channel homolog, induce L-glutamic acid production. Appl Environ Microbiol 73:4491–4498
Nakayama Y, Iida H (2014) Organellar mechanosensitive channels involved in hypo-osmoregulation in fission yeast. Cell Calcium 56:467–471

Nakayama Y, Yoshimura K, Iida H (2012) Organellar mechanosensitive channels in fission yeast regulate the hypo-osmotic shock response. Nat Commun 3:1020
Nakayama Y, Yoshimura K, Iida H (2013) Electrophysiological characterization of the mechanosensitive channel MscCG in Corynebacterium glutamicum. Biophys J 105:1366–1375
Nakayama Y, Mustapić M, Ebrahimian H et al (2015) Magnetic nanoparticles for "smart liposomes". Eur Biophys J 44:647–654
Nanatani K, Shijuku T, Akai M et al (2014) Characterization of the role of a mechanosensitive channel in osmotic down shock adaptation in Synechocystis sp PCC 6803. Channels 7:238–242
Neder J, West B, Nielaba P, Schmid F (2010) Coarse-grained simulations of membranes under tension. J Chem Phys 132:115101
Nomura T, Sokabe M, Yoshimura K (2006) Lipid-protein interaction of the MscS mechanosensitive channel examined by scanning mutagenesis. Biophys J 91:2874–2881
Nomura T, Cranfield CG, Deplazes E et al (2012) Differential effects of lipids and lyso-lipids on the mechanosensitivity of the mechanosensitive channels MscL and MscS. Proc Natl Acad Sci U S A 109:8770–8775
Ou X, Blount P, Hoffman RJ, Kung C (1998) One face of a transmembrane helix is crucial in mechanosensitive channel gating. Proc Natl Acad Sci 95:11471–11475
Perozo E, Rees DC (2003) Structure and mechanism in prokaryotic mechanosensitive channels. Curr Opin Struct Biol 13:432–442
Perozo E, Cortes DM, Sompornpisut P et al (2002a) Open channel structure of MscL and the gating mechanism of mechanosensitive channels. Nature 418:942–948
Perozo E, Kloda A, Cortes DM, Martinac B (2002b) Physical principles underlying the transduction of bilayer deformation forces during mechanosensitive channel gating. Nat Struct Biol 9:696–703
Petrov E, Palanivelu D, Constantine M et al (2013) Patch-clamp characterization of the MscS-like Mechanosensitive Channel from Silicibacter pomeroyi. Biophys J 104:1426–1434
Phillips R, Ursell T, Wiggins P, Sens P (2009) Emerging roles for lipids in shaping membrane-protein function. Nature 459:379–385
Pivetti CD, Yen M-R, Miller S et al (2003) Two families of mechanosensitive channel proteins. Microbiol Mol Biol Rev 67:66–85
Pliotas C, Ward R, Branigan E et al (2012) Conformational state of the MscS mechanosensitive channel in solution revealed by pulsed electron-electron double resonance (PELDOR) spectroscopy. Proc Natl Acad Sci U S A 109:E2675–E2682
Pliotas C, Dahl ACE, Rasmussen T et al (2015) The role of lipids in mechanosensation. Nat Struct Mol Biol 22:991–998
Powl AM, East JM, Lee AG (2003) Lipid-protein interactions studied by introduction of a tryptophan residue: the mechanosensitive channel MscL. Biochemistry 42:14306–14317
Powl AM, East JM, Lee AG (2005a) Heterogeneity in the binding of lipid molecules to the surface of a membrane protein: hot spots for anionic lipids on the mechanosensitive channel of large conductance MscL and effects on conformation. Biochemistry 44:5873–5883
Powl AM, Wright JN, East JM, Lee AG (2005b) Identification of the hydrophobic thickness of a membrane protein using fluorescence spectroscopy: studies with the mechanosensitive channel MscL. Biochemistry 44:5713–5721
Powl AM, East JM, Lee AG (2007) Different effects of lipid chain length on the two sides of a membrane and the lipid annulus of MscL. Biophys J 93:113–122
Powl AM, East JM, Lee AG (2008) Anionic phospholipids affect the rate and extent of flux through the mechanosensitive channel of large conductance MscL. Biochemistry 47:4317–4328
Prole DL, Taylor CW (2013) Identification and analysis of putative homologues of mechanosensitive channels in pathogenic protozoa. PLoS One 8:e66068
Qi Z, Kishigami A, Nakagawa Y et al (2004) A mechanosensitive anion channel in Arabidopsis thaliana mesophyll cells. Plant Cell Physiol 45:1704–1708
Rasmussen T (2016) How do mechanosensitive channels sense membrane tension? Biochem Soc Trans 44:1019–1025

Rasmussen A, Rasmussen T, Edwards MD et al (2007) The role of tryptophan residues in the function and stability of the mechanosensitive channel MscS from Escherichia coli. Biochemistry 46:10899–10908

Rasmussen T, Edwards MD, Black SS et al (2010) Tryptophan in the pore of the mechanosensitive channel MscS: assessment of pore conformations by fluorescence spectroscopy. J Biol Chem 285:5377–5384

Rasmussen T, Rasmussen A, Singh S et al (2015) Properties of the Mechanosensitive Channel MscS pore revealed by tryptophan scanning mutagenesis. Biochemistry 54:4519–4530

Reading E, Walton TA, Liko I et al (2015) The effect of detergent, temperature, and lipid on the oligomeric state of MscL constructs: insights from mass spectrometry. Chem Biol 22:593–603

Reuter M, Hayward NJ, Black SS et al (2014) Mechanosensitive channels and bacterial cell wall integrity: does life end with a bang or a whimper? J R Soc Interface 11:20130850

Rowe I, Elahi M, Huq A, Sukharev S (2013) The mechanoelectrical response of the cytoplasmic membrane of Vibrio cholerae. J Gen Physiol 142:75–85

Schumann U, Edwards MD, Rasmussen T et al (2010) YbdG in Escherichia coli is a threshold-setting mechanosensitive channel with MscM activity. Proc Natl Acad Sci U S A 107:12664–12669

Shaikh S, Cox CD, Nomura T, Martinac B (2014) Energetics of gating MscS by membrane tension in azolectin liposomes and giant spheroplasts. Channels 8:321–326

Shapovalov G, Lester HA (2004) Gating transitions in bacterial ion channels measured at 3 microns resolution. J Gen Physiol 124:151–161

Shapovalov G, Bass R, Rees DC, Lester HA (2003) Open-state disulfide crosslinking between Mycobacterium tuberculosis mechanosensitive channel subunits. Biophys J 84:2357–2365

Sokabe M, Sachs F, Jing ZQ (1991) Quantitative video microscopy of patch clamped membranes stress, strain, capacitance, and stretch channel activation. Biophys J 59:722–728

Sotomayor M, Schulten K (2004) Molecular dynamics study of gating in the mechanosensitive channel of small conductance MscS. Biophys J 87:3050–3065

Steinbacher S, Bass R, Strop P, Rees DC (2007) Structures of the prokaryotic mechanosensitive channels MscL and MscS. In: Benos DG, Simon SA (eds) Current topics in membranes, mechanosensitive ion channels, part A, vol 58. Elsevier, Amsterdam, pp 1–24

Stokes NR, Murray HD, Subramaniam C et al (2003) A role for mechanosensitive channels in survival of stationary phase: regulation of channel expression by RpoS. Proc Natl Acad Sci U S A 100:15959–15964

Sukharev S (2002) Purification of the small mechanosensitive channel of Escherichia coli (MscS): the subunit structure, conduction, and gating characteristics in liposomes. Biophys J 83:290–298

Sukharev SI, Martinac B, Arshavsky VY, Kung C (1993) Two types of mechanosensitive channels in the Escherichia coli cell envelope: solubilization and functional reconstitution. Biophys J 65:177–183

Sukharev SI, Blount P, Martinac B et al (1994) A large-conductance mechanosensitive channel in E. coli encoded by mscL alone. Nature 368:265–268

Sukharev SI, Blount P, Martinac B, Kung C (1997) Mechanosensitive channels of Escherichia coli: the MscL gene, protein, and activities. Annu Rev Physiol 59:633–657

Sukharev SI, Sigurdson WJ, Kung C, Sachs F (1999) Energetic and spatial parameters for gating of the bacterial large conductance mechanosensitive channel, MscL. J Gen Physiol 113:525–540

Sukharev S, Betanzos M, Chiang CS, Guy HR (2001a) The gating mechanism of the large mechanosensitive channel MscL. Nature 409:720–724

Sukharev S, Durell SR, Guy HR (2001b) Structural models of the MscL gating mechanism. Biophys J 81:917–936

Syeda R, Florendo MN, Cox CD et al (2016) Piezo1 channels are inherently mechanosensitive. Cell Rep 17:1739–1746

Teng J, Loukin S, Anishkin A, Kung C (2015) The force-from-lipid (FFL) principle of mechanosensitivity, at large and in elements. Pflügers. Arch Eur J Physiol 467:27–37

Tsai I-J, Liu Z-W, Rayment J et al (2005) The role of the periplasmic loop residue glutamine 65 for MscL mechanosensitivity. Eur Biophys J 34:403–412
van den Berg J, Galbiati H, Rasmussen A et al (2016) On the mobility, membrane location and functionality of mechanosensitive channels in Escherichia coli. Sci Rep 6:32709
van den Bogaart G, Krasnikov V, Poolman B (2007) Dual-color fluorescence-burst analysis to probe protein efflux through the mechanosensitive channel MscL. Biophys J 92:1233–1240
Vásquez V, Sotomayor M, Cordero-Morales J et al (2008a) A structural mechanism for MscS gating in lipid bilayers. Science 321:1210–1214
Vásquez V, Sotomayor M, Cortes DM et al (2008b) Three-dimensional architecture of membrane-embedded MscS in the closed conformation. J Mol Biol 378:55–70
Velásquez J, Schuurman-Wolters G, Birkner JP et al (2014) Bacillus Subtilis spore protein SpoVAC functions as a mechanosensitive channel. Mol Microbiol 92:813–823
Wahome PG, Setlow P (2008) Growth, osmotic downshock resistance and differentiation of Bacillus Subtilis strains lacking mechanosensitive channels. Arch Microbiol 189:49–58
Wang W, Black SS, Edwards MD et al (2008) The structure of an open form of an E. coli mechanosensitive channel at 3.45 a resolution. Science 321:1179–1183
Wang Y, Liu Y, Deberg HA et al (2014) Single molecule FRET reveals pore size and opening mechanism of a mechano-sensitive ion channel. Elife 3:e01834
Ward R, Pliotas C, Branigan E et al (2014) Probing the structure of the mechanosensitive channel of small conductance in lipid bilayers with pulsed electron-electron double resonance. Biophys J 106:834–842
Wiener M, White S (1991) Transbilayer distribution of bromine in fluid bilayers containing a specifically brominated analog of dioleoylphosphatidylcholine. Biochemistry 30:6997–7008
Wilson MME, Maksaev G, Haswell EES (2013) MscS-like mechanosensitive channels in plants and microbes. Biochemistry 52:5708–5722
Yamashita C, Hashimoto K-I, Kumagai K et al (2013) L-Glutamate Secretion by the N-Terminal Domain of the Corynebacterium glutamicum NCgl1221 mechanosensitive channel. Biosci Biotechnol Biochem 77:1008–1013
Yang L-M, Zhong D, Blount P (2013) Chimeras reveal a single lipid-interface residue that controls MscL channel kinetics as well as mechanosensitivity. Cell Rep 3:520–527
Yilmaz D, Dimitrova AI, Walko M, Kocer A (2015) Study of light-induced MscL gating by EPR spectroscopy. Eur Biophys J 44:557–565
Yoshimura K, Sokabe M (2010) Mechanosensitivity of ion channels based on protein-lipid interactions. J R Soc Interface 7(Suppl 3):S307–S320
Yoshimura K, Batiza A, Schroeder M et al (1999) Hydrophilicity of a single residue within MscL correlates with increased channel mechanosensitivity. Biophys J 77:1960–1972
Yoshimura K, Nomura T, Sokabe M (2004) Loss-of-function mutations at the rim of the funnel of mechanosensitive channel MscL. Biophys J 86:2113–2120
Zhang X, Wang J, Feng Y et al (2012) Structure and molecular mechanism of an anion-selective mechanosensitive channel of small conductance. Proc Natl Acad Sci U S A 109:18180–18185
Zhang XC, Liu Z, Li J (2016) From membrane tension to channel gating: a principal energy transfer mechanism for mechanosensitive channels. Protein Sci 25:1954–1964
Zhong D, Blount P (2013) Phosphatidylinositol is crucial for the mechanosensitivity of Mycobacterium tuberculosis MscL. Biochemistry 52:5415–5420

# Chapter 5
# Monoamine Oxidases


**Dale E. Edmondson and Claudia Binda**

**Abstract** Monoamine oxidases A and B (MAO A and B) are mammalian flavoenzymes bound to the outer mitochondrial membrane. They were discovered almost a century ago and they have been the subject of many biochemical, structural and pharmacological investigations due to their central role in neurotransmitter metabolism. Currently, the treatment of Parkinson's disease involves the use of selective MAO B inhibitors such as rasagiline and safinamide. MAO inhibition was shown to exert a general neuroprotective effect as a result of the reduction of oxidative stress produced by these enzymes, which seems to be relevant also in non-neuronal contexts. MAOs were successfully expressed as recombinant proteins in *Pichia pastoris*, which allowed a thorough biochemical and structural characterization. These enzymes are characterized by a globular water-soluble main body that is anchored to the mitochondrial membrane through a C-terminal α-helix, similar to other bitopic membrane proteins. In both MAO A and MAO B the enzyme active site consists of a hydrophobic cavity lined by residues that are conserved in the two isozymes, except for few details that determine substrate and inhibitor specificity. In particular, human MAO B features a dual-cavity active site whose conformation depends on the size of the bound ligand. This article provides a comprehensive and historical review of MAOs and the state-of-the-art of these enzymes as membrane drug targets.

**Keywords** Monoamine oxidase · Flavin · Neurotransmitter · Neurodegeneration · Inhibitor · Drug design · Oxidative stress

D. E. Edmondson
Department of Biochemistry, Emory University, Atlanta, GA, USA
e-mail: deedmon@emory.edu

C. Binda (✉)
Department of Biology and Biotechnology, University of Pavia, Pavia, Italy
e-mail: claudia.binda@unipv.it



J. R. Harris, E. J. Boekema (eds.), *Membrane Protein Complexes: Structure and Function*, Subcellular Biochemistry 87,
https://doi.org/10.1007/978-981-10-7757-9_5

## Abbreviations

| | |
|---|---|
| EPR | electron paramagnetic resonance |
| GFP | green fluorescence protein |
| MAO | monoamine oxidase |
| MPTP | 1-metil 4-fenil 1,2,3,6-tetraidro-piridina |
| ROS | reactive oxygen species |

## 5.1 The Monoamine Oxidases (MAOs): A Historical Perspective from 60 Years of Research

The initial discovery of mammalian MAOs was published almost 90 years ago (Hare 1928) where she observed a tyramine oxidase activity in rabbit liver. In addition to tyramine, the enzyme was found to catalyze the oxidative degradation of a number of neurologically important amine substrates including dopamine, norepinephrine, epinephrine, serotonin, and phenethylamine. The electron acceptor for the oxidation of these important primary amines is $O_2$ which is reduced directly to $H_2O_2$ (Fig. 5.1).

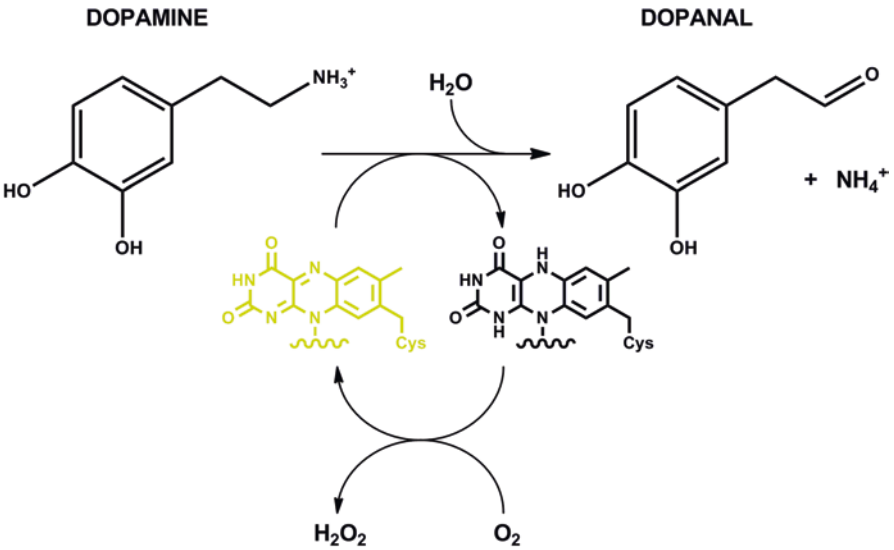


**Fig. 5.1** Chemical reaction catalyzed by MAOs. Dopamine is showed as an example of neurotransmitter substrate. Other physiological substrates are epinephrine, norepinephrine, phenylethylamine, tyramine, serotonin. Substrate specificity is tissue-dependent although in general phenylethylamine is preferentially metabolized by MAO B and serotonin by MAO A (Edmondson et al. 2009). The flavin cofactor (in yellow) undergoes a two-electron reduction (in black) upon substrate oxidation, which is regenerated to its functional form by molecular oxygen leading to hydrogen peroxide production

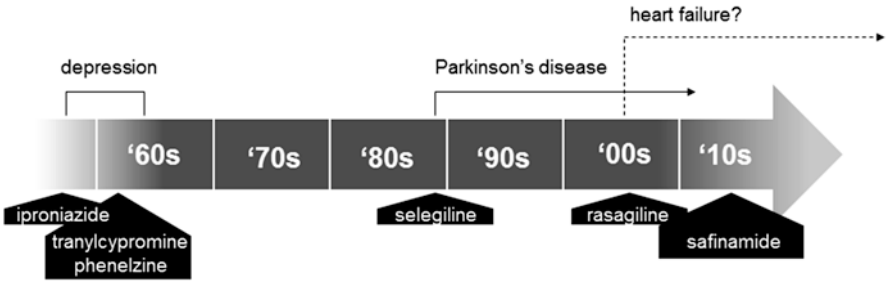


**Fig. 5.2** MAO inhibitors and their use in the clinical practice to treat neurological diseases

MAO also catalyzes the oxidation of secondary amines but has little or no activity in the oxidation of tertiary amine, with few exceptions such as the bioactivation of MPTP (*see* below). The field was somewhat dormant until the late 1950's when it was found that a mood elevating effect was observed in the treatment of tuberculosis patients with the drug isoniazide. Zeller and his group found that the target was MAO (Zeller and Barsky 1952) which led to the development and clinical use of iproniazide (the N-isopropyl modified form of isoniazide) as an antidepressant, followed by other MAO inhibitors such as phenelzine (phenylethylhydrazine) and tranylcypromine (Fig. 5.2). These drugs were found to be irreversible inhibitors of MAO with a side effect of hypertensive crisis if the diet was not controlled to limit the intake of foods rich in tyramine (the well-known "cheese effect"). These side effects resulted in a diminished use of MAO inhibitors in the treatment of clinical depression and to the development of alternate drugs and targets.

Later studies demonstrated that the enzyme is localized to the outer mitochondrial membrane (Schnaitman et al. 1967). The presence of two distinct enzyme activities (MAO A and MAO B which exhibit different substrate specificities) was hypothesized on the basis of differential inhibition by the irreversible inhibitors clorgyline (MAO A) and deprenyl (Fowler et al. 1982) and remained a controversial topic as to whether they were separate enzymes or were due to differing membrane environments. Definitive evidence for the existence of two separate enzymes came from the detection and sequencing of separate genes encoding the two enzymes (Bach et al. 1988) providing unequivocal proof for the existence of the two membrane-bound enzymes.

Once the existence of two separate enzymes was established, these proteins were shown to be differentially expressed in organs and tissues (Fig. 5.3a). MAO A is uniquely expressed in human placental mitochondria and MAO B is uniquely expressed in human platelet mitochondria. Other tissues have varying amounts of MAO A and MAO B, also depending on the mammalian species investigated. A major discovery in the MAO field occurred in the 1980s when it was found that the bio-activation of the compound MPTP (an impurity in synthetic heroin) to form MPP+ by MAO B led to the development of symptoms resembling those of Parkinson's patients (Langston et al. 1984a) and that this bio-activation process could be stopped by the administration of the acetylenic MAO inhibitor pargyline (Langston et al. 1984b). These observations set in motion the quest for new MAO

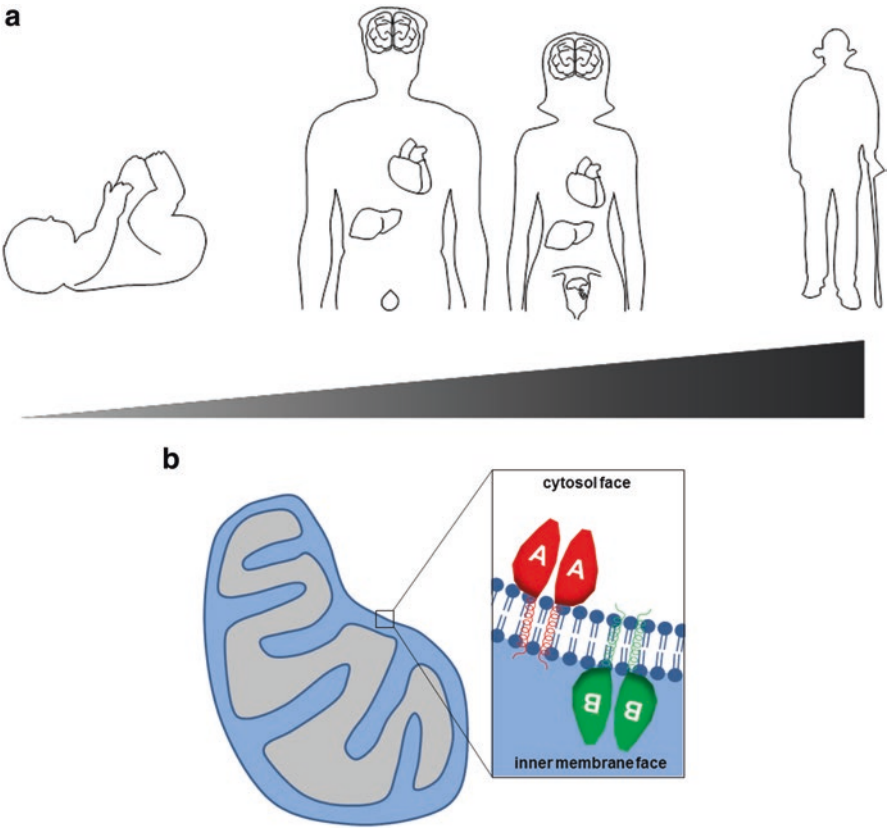


**Fig. 5.3** Expression of MAOs in humans. (**a**) Tissue and temporal expression. (**b**) Subcellular localization of rat liver MAOs and their interaction with the outer mitochondrial membrane

inhibitors as potential anti-Parkinson drugs that were specific for MAO B and, possibly, reversible to minimize the hypertensive side effects of earlier irreversible MAO inhibitors. To date, the MAO B specific inhibitors rasagiline and safinamide have been approved by the FDA for treatment of patients exhibiting early stages of Parkinson's disease (Fig. 5.2).

Recent studies have shown that MAO B expression in neuronal tissue increases 3–4 fold with age (Kumar et al. 2003) and that MAO A expression in cardiac cells increases ~6 fold on ageing (Maurel et al. 2003) (Fig. 5.3a). These observations suggest that ageing diseases could have a connection with increased MAO expression. As mentioned above, the side products of MAO catalysis are $H_2O_2$, $NH_4^+$ and aldehydes (Fig. 5.1). Hydrogen peroxide production is well established to be relevant in the generation of toxic reactive oxygen species (ROS) in mitochondria and could lead to an apoptotic response and cell death. Thus, the cell toxicity associated with increased MAO expression may be lowered by the action of MAO-specific inhibitors. MAO B expression and correlation with Alzheimer's disease is currently under investigation (Kim et al. 2016), whereas studies indicating an involvement of

MAO A with heart diseases prompted a new area of MAO research (*see* Sect. 10.6) (Fig. 5.2). Current technologies involving MAO gene deletions or replacement in experimental animal studies show promise in future studies to demonstrate the roles of MAO A and of MAO B in a range of disease states and therefore may be amenable to highly specific MAO inhibitors. As will be detailed in this chapter, the elucidations of the crystal structures of both enzymes has provided new insights into the difficult task of specific inhibitor design for each of these important membrane bound enzymes.

## 5.2 Molecular Properties and Subcellular Localization

The detailed descriptions of the molecular properties of MAO A MAO B came after procedures for isolation of the purified forms of each enzyme as outline in Sect. 10.3 and after delineation of their respective gene sequences (Bach et al. 1988). Both enzymes (independent of the species of origin) are flavoenzymes containing a single covalent FAD cofactor per monomer. In the case of MAO B, the covalent attachment is *via* a thioether linkage to Cys397 and the 8a–methylene of the isoalloxazine ring of the flavin (Kearney et al. 1971). In the case of MAO A, a similar thioether covalent linkage of the flavin ring to Cys406 is found (Nagy and Salach 1981). The flavin cofactor is essential for catalysis in either enzyme. Studies by Miller and Edmondson (1999) demonstrated that a series of flavin analogues could be covalently incorporated into either human enzyme expressed in a *RIB5* mutant of *Saccharomyces cerevisiae* and capable of reconstituting catalytic activities. Using a C406A mutant of human MAO A expressed in *Saccharomyces cerevisiae*, Nandigama and Edmondson (2000) demonstrated that flavin analogues converted to their FAD cofactors were capable of binding to the enzyme and reconstituting catalytic activity, thus demonstrating that covalent flavin binding is not essential in human MAO A. The flavin-deficient enzyme is incorporated in the mitochondrial membrane and is stable in that environment. Activity is rapidly lost, however, on detergent solubilization suggesting a stabilizing effect of the covalent flavin linkage on the structure of MAO A. Similar experiments were attempted for the C397A mutant of human MAO B without success.

Both human MAO A and MAO B are found to have a second post-translational modification in that their respective amino terminal residues are “blocked” by acetylation (Newton-Vinson et al. 2000; Li et al. 2002). No other post-translational modifications have been detected in either enzyme whether isolated from mammalian sources or by heterologous expression. Molecular “tags” such as His6 linkages or GFP probes can be incorporated into the amino terminus of either enzyme without altering catalytic activity or membrane localization.

For both MAO A and MAO B, the domain responsible for membrane binding is the C-terminal helix (*see* Sect. 10.4). Ito’s group (Mitoma and Ito 1992) first reported evidence for the involvement of this domain as responsible for mitochondrial membrane association by deletion of 28 residues from the C-terminus. Subsequent work by Shih’s group (Chen et al. 1996) demonstrated that replacement of the C-terminal

transmembrane helix domain of MAO B with that of MAO A would not support the formation of a functional chimeric form of MAO B and conversely, the C-terminal helix domain of MAO B could be substituted into MAO A producing a functional chimer. Shih's laboratory (Rebrin et al. 2001) using insect cell expression of truncated forms of MAO and unpublished work by Newton-Vinson and Edmondson has shown that a Δ37 truncated form of human MAO B expressed in *Pichia pastoris* still retained catalytic activity, but no longer was associated with outer mitochondrial membrane. A C-terminal truncated form of human MAO A has been expressed in *Saccharomyces cerevisiae* and is active after treatment with thiol reducing agents (Weyler 1994). This mutant is no longer associated with the mitochondria but still exhibited properties characteristic of a protein with hydrophobic character and affinity for membranes. The crystal structures of each enzyme (*see* below) provide definitive evidence for the C-terminal domains of either enzyme as the sites for association with the outer membrane of the mitochondrion.

The oligomeric state and topology of MAO A or of MAO B in the outer membrane of the mitochondrion has been addressed using a pargyline analogue modified with a nitroxide spin label (Upadhyay and Edmondson 2009). This inhibitor is covalently bound to the active site flavin as a flavocyanine adduct. Using pulsed EPR techniques, the distance between the nitroxide spin labels could be experimentally determined and this distance would then be used to decide whether the membrane bound enzyme is in a dimeric form. The data for MAO A and for MAO B show both enzymes to be bound in a dimeric form in the mitochondrial outer membrane of *Pichia pastoris*. Experiments using mitochondria from human placenta showed MAO A also to be dimeric. These data confirmed crystallographic data for the dimeric structure of human MAO B and the dimeric structure of rat MAO A (Ma et al. 2004). Human MAO A crystallizes as a monomer which is thought to occur *via* the dissociation of the detergent solubilized enzyme and the monomeric form then more readily crystallizes than the dimeric form, although both forms are found to exist in detergent solution using analytical ultracentrifuge techniques (De Colibus et al. 2005).

The topology of MAO A and MAO B in the outer mitochondrial membrane was initially addressed (Russell et al. 1979) using reactivity to antibodies without any definitive conclusions. In studies with the nitroxide pargyline analogue on MAO inhibition, it was found that MAO B could not be inhibited in rat liver mitochondria without disruption of the outer membrane and that MAO A is readily inhibited in intact mitochondria (Wang and Edmondson 2011). When similar experiments were attempted with intact mitochondria from *Pichia pastoris*, the opposite sensitivity is observed, with MAO B inhibited without disruption of the outer membrane and MAO A inhibition requiring mitochondrial disruption (Wang and Edmondson 2011). These experiments led to the conclusion that in rat liver mitochondria, MAO A is topologically situated on the cytosolic face of the outer membrane while MAO B is oriented to the inner membrane face (Fig. 5.3b). The finding that a different orientation is found in yeast suggests the membrane environment is responsible for this differential topology. Further work is required to determine whether this differential topology is present in mitochondria from other tissues and also the biological significance of the observed topology. A recent report has shown that magnetic beads containing a MAO A antibody can be used to selectively isolate mitochondria

from cell homogenate of cultured mammalian cells (Tang et al. 2012), which suggests a cytosolic orientation of MAO A in the mitochondria of these cultured cells. The significance of this question is how the vectorial orientation of MAO A and of MAO B might influence their respective sensitivities to inhibitors administered in the clinic.

## 5.3 Heterologous Expression of Recombinant MAOs

Initial studies of MAO A or of MAO B mainly utilized rat liver or brain mitochondrial preparations in which differentiation of their catalytic properties was achieved by selective inhibition by the irreversible acetylenic inhibitors clorgyline (MAO A) or deprenyl (MAO B). Alternatively, isozyme-specific substrates for MAO A (serotonin) or MAO B (benzylamine) can be used to selectively determine activities for the desired MAO activity. Initial applications of recombinant enzyme technology utilized COS cells to express and characterize chimeric constructs of human MAO A and B with the goal of selecting domains in each enzyme that would give rise to their selectivity for inhibitors and substrates (Gottowik et al. 1995; Chen et al. 1996). The development of purification procedures to obtain purified enzymes at reagent quantity levels used bovine liver mitochondria for MAO B (Salach 1979) and human placental mitochondria for MAO A (Weyler and Salach 1985). The advent of recombinant technology resulted in the high-level expression of human and rat MAO A in *Saccharomyces cerevisiae* (Weyler et al. 1990). Attempts to achieve high level expression of human MAO B in *Saccharomyces* resulted in only low levels of expressed enzyme (Urban et al. 1991). Both enzymes have been successfully expressed in baculovirus-infected insect cells (Rebrin et al. 2001) and that system has resulted in the commercial availability of membrane preparations of human MAO A and MAO B.

Further advances in the field progressed with the development of high level expression system for human MAO A (Li et al. 2002) and for human MAO B (Newton-Vinson et al. 2000) in the methylotrophic organism *Pichia pastoris*. This organism is a methylotropic yeast that grows to high cell density in aerobic conditions. Glycerol is used as a carbon source in oxidative fermentations resulting in the formation of high levels of mitochondria. These conditions provide the membrane "home" for the recombinant MAO A and MAO B isozymes. The genes for recombinant enzymes are incorporated into the genome of the organism by homologous recombination giving rise to stable transformants.

The *Pichia* system allows for expression and purification of rat MAO A (Wang and Edmondson 2010), rat MAO B (Upadhyay and Edmondson 2008) and of zebrafish MAO (Arslan and Edmondson 2010). In each case, high levels of expression were achieved with purification of reagent quantities of enzymes required for structural and mechanistic studies. The *Pichia* expression system has also proven to be successful for the expression of mutants of human MAO A and MAO B with useful applications in structural and functional studies by our and other laboratories (Hubálek et al. 2005; Li et al. 2006; Milczek et al. 2011).

## 5.4 Structures of Human MAOs

### *5.4.1 Human MAO B: A Bitopic Membrane-Spanning Dimer*

Membrane proteins are notoriously difficult to be crystallized and even those having a single bilayer-spanning segment do not elude this problem. MAOs are enzymes which have been known since the 1960s although their structural elucidation was achieved only during the '00s decade. They are eukaryotic proteins consisting of a 500-residue globular fold, featuring the typical two-domain topology that provides the framework for the FAD-dependent oxidation of neurotransmitter substrates, which is endowed with a C-terminal 30-residue hydrophobic α-helix that anchors the catalytic core to the outer mitochondrial membrane (Figs. 5.4, 5.5 and 5.6a). In mammals the two existing isozymes, MAO A and MAO B, share ~70% sequence identity and their amine oxidase domain is homologous to that of the water-soluble polyamine oxidases and flavin-dependent histone demethylases (Forneris et al. 2009). All these enzymes share few structural details and mechanistic aspects of the catalyzed reaction, which suggests that from a common evolutionary origin they acquired additional elements enabling them to act in different contexts. Bioinformatics prediction tools such as TOPCONS (Tsirigos et al. 2015) clearly indicate that MAOs gained a C-terminal membrane-binding region, corresponding to the hydrophobic residues 490-512 in human MAO B and 498-519 in human MAO A, with the last 8 residues in both proteins comprising positively-charged side chains that are likely to interact with the phospholipid heads. As described in the following paragraphs, structural studies confirmed this predictive analysis although a clear rationale of the mitochondrial surface localization of MAOs is still unknown. Many enzymes are adapted to work at the interface with the membrane environment to efficiently act on either hydrophilic or lipophilic substrates (Forneris and Mattevi 2008). In the case of MAOs, the membrane compartmentalization may be functional to match the synaptic vesicles containing the neurotransmitter substrates or, alternatively, the negatively-charged phospholipid heads may promote a localized enrichment of the protonated amine neurotransmitters. However, no experimental evidence is available to support any of these hypotheses.

The development of yeast heterologous expression systems proved very successful to obtain large quantities of recombinant membrane proteins (Emmerstorfer et al. 2014) and this holds also for MAOs that could be expressed in large amounts using *Pichia pastoris* (Newton-Vinson et al. 2000; Li et al. 2002). The first crystal structure of these enzymes was obtained for human MAO B in 2002 at 3.0 Å (Binda et al. 2002), which was followed many others in complex with different inhibitors at improved resolution up to 1.6 Å (Edmondson et al. 2009) (Fig. 5.4). A dimeric organization of this protein was clearly found in the crystal asymmetric unit, with more than 2000 $Å^2$ of the protein surface (corresponding to 15% of the total) at the interface with the other subunit (Fig. 5.4a). Each monomer consists of a large globular core from which a C-terminal α-helix protrudes in parallel to the dimer two-fold axis. Although the last 20 residues could not be modelled in the electron density map, the visible part of the α-helix is perfectly consistent with the 490-512 sequence

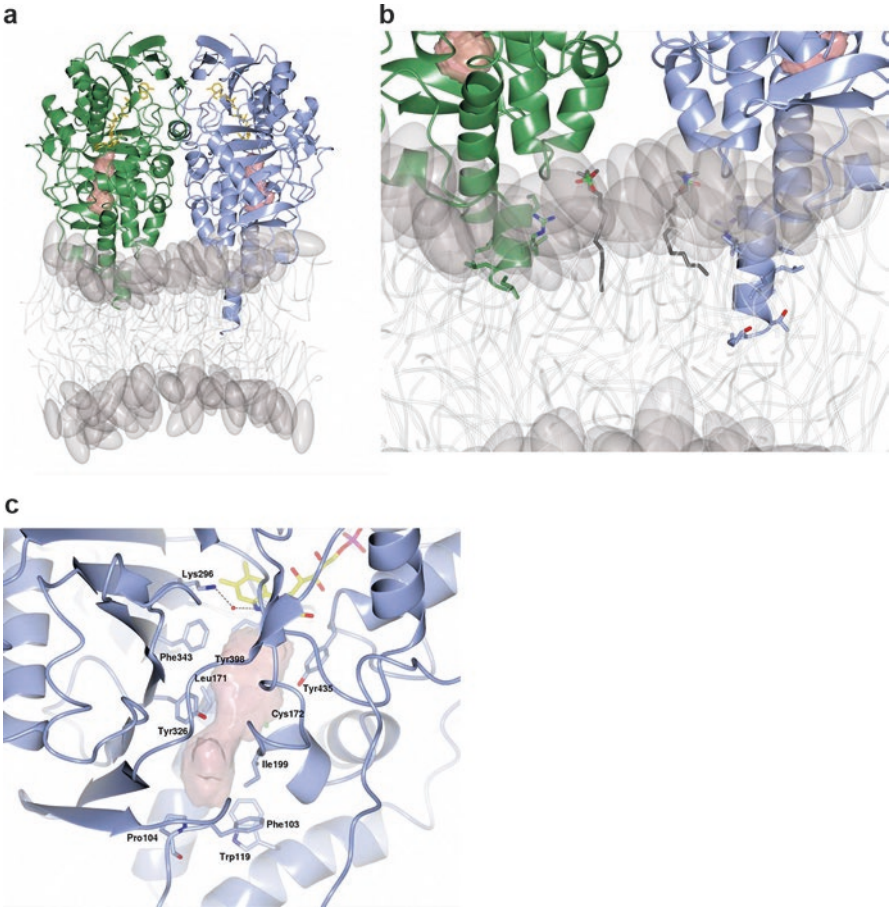


**Fig. 5.4** (**a**) Overall crystal structure of human MAO B (PDB code 2v5z; Binda et al. 2007) represented as a model of the protein dimer inserted in the phospholipid bilayer (in cartoon gray representation). The two monomers are colored in ice blue and lawn green, respectively, with each of them comprising the FAD cofactor (in yellow) and the active site cavity (pink surface). (**b**) Zoomed view of the C-terminal MAO B membrane-binding domain. In each of the two monomers the portion of the transmembrane helix visible in the electron density is highlighted by the residue side chains (residues 490–500 corresponding to sequence PGLLRLIGLTT in the monomer on the right). Carbon atoms are lawn green or ice blue depending on the monomer, nitrogens are blue, oxygens are red. Further structural studies on human MAO B (Bonivento et al. 2010; PDB code 2xcg) revealed a residual electron density which was attributed to detergent molecules lying longitudinal to the transmembrane helix (Zwittergent 3–12, represented as sticks with carbon atoms in dark gray, nitrogens in blue, oxygens in red, sulfurs in green). All structural figures in this chapter were produced by CCP4mg (McNicholas et al. 2011). (**c**) Zoomed view of the human MAO B active site (with respect to Fig. 5.4a the monomer has been rotated~90° around the axis of the C-terminal helix). Color code is as in Fig. 5.4b (FAD carbon atoms are in yellow). The active site cavity is represented as pink semi-transparent surface. The water molecule (red sphere) bridging Lys296 and the flavin N5 atom through H-bonds (dashed lines) is conserved in all human MAO B structures

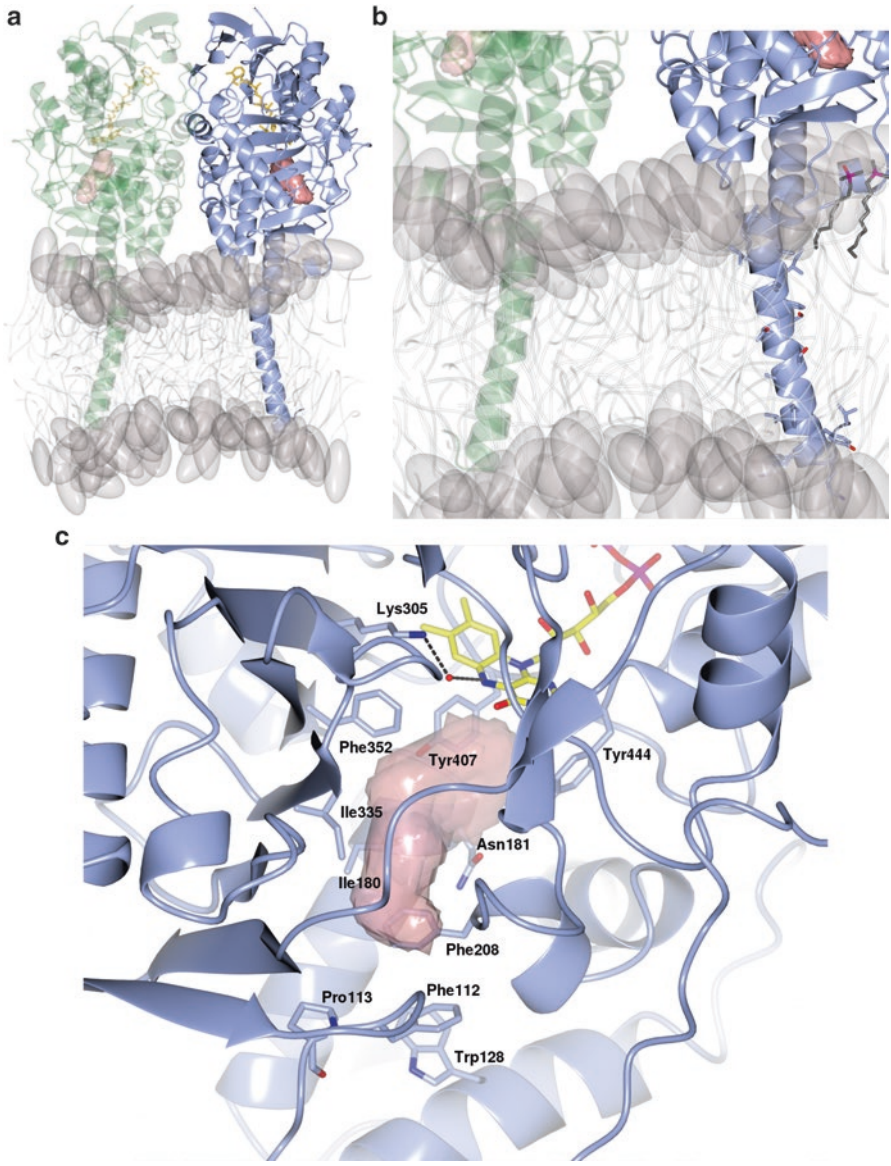


**Fig. 5.5** (**a**) Overall crystal structure of human MAO A (PDB code 2z5x; Son et al. 2008). As in a previously reported structure at lower resolution (De Colibus et al. 2005), human MAO A crystallizes as a monomer (ice blue ribbon structure, FAD in yellow). However, it has been demonstrated that, similarly to human MAO B, also the A isozyme is bound to the membrane in a dimeric form (see text). As the two enzymes share more than 70% of sequence identity and a very similar overall fold, a tentative model for the human MAO A dimer was generated based on the human MAO B structure. This was obtained by superposing the A monomer (ice blue) onto the corresponding mate subunit in the human MAO B (lawn green; represented as semi-transparent ribbon structure to indicate that it results from a modelling process). As a result of this procedure, no clashes

predicted to represent the membrane-spanning region. Within this, Arg494 is the only charged residue and, with its side chain pointing upwards, is properly positioned to be salt-bridged to the negatively-charged phospholipid heads (Fig. 5.4b). Moreover, an ordered detergent molecule was found to be bound to MAO B crystal structure with its hydrophobic chain lying along the C-terminal α-helix. Altogether, these observations suggest a reliable model for MAO B insertion into the mitochondrial membrane as that shown in Fig. 5.4a. The water-soluble globule comprises two domains, one that contains the covalently-bound FAD cofactor and the other designed for substrate binding. The latter is in direct contact with the membrane-spanning helix (Fig. 5.4b), whereas the interactions at the dimer interface are limited to the upper catalytic core of the protein. Thus, according to this model, the MAO B dimer sits on the bilayer with the base of the substrate-binding domain of each monomer independent from that of the other monomer.

The active site of human MAO B is formed by an elongated cavity (700 $Å^3$) that originates from the flavin isoalloxazine ring site and extends to the protein surface nearby the membrane bilayer (Fig. 5.4a,b). Most of the residues lining the cavity are hydrophobic, including Tyr398 and Tyr435 which stack parallel to each other in front of the flavin ring, generating an aromatic sandwich module that is also conserved in polyamine oxidases (Fig. 5.4c) (Forneris et al. 2009). At the bottom of this inner part of the cavity few water molecules were found in many human MAO B structures, creating a more hydrophilic environment that may favor the binding of the substrate amino group undergoing oxidation (Binda et al. 2003, 2007). Another feature of human MAO B active site which represents a hallmark of flavin-dependent amine oxidases is a lysine residue (Lys296) at the top of the flavin ring which is H-bonded to the cofactor N5 through a very well defined water molecule (Fig. 5.4c). It was demonstrated that this lysine residue is essential for the enzymatic activity of amine oxidases and it was postulated that the water molecule may mimic the position occupied by molecular oxygen during flavin reoxidation after the catalytic reaction (Henderson and Fitzpatrick 2010). On the other side of the cavity there is a surface loop (residues 99-110) that seals the active site from the exterior with the Phe103-Pro104 side chains creating a sort of cap together with Trp119 (Fig. 5.4c). The human MAO B cavity has a quite rigid scaffold and within the many human MAO B crystal structures in complex with various inhibitors the active site retains the same architecture. The only major conformational change occurs at Ile199 whose side chain position depends on the ligand present in the active site. Bulky

**Fig. 5.5** (continued) occurred at the interface of the reconstructed dimer, which suggests that this may represent a reliable model for the physiological oligomeric organization of human MAO A. (**b**) Zoomed view of the human MAO A membrane-binding domain consisting of the C-terminal helix (residues 498–527), which is almost fully visible in the electron density (until residue 524, corresponding to sequence VSGLLKIIGFSTSVTALGFVLYKYKLL; side chains highlighted as stick representation). Similarly to human MAO B, few ordered detergent molecules (decyldimethyl-phosphine oxide) could be modelled which interact with the transmembrane helix (represented as sticks with carbon atoms in dark gray, nitrogens in blue, oxygens in red, phosphors in magenta). (**c**) Zoomed view of the human MAO A active site. Color code and orientation is as in Fig. 5.4c. The H-bonds bridging Lys305 and the flavin N5 through a water molecule (red sphere) are represented as dashed lines

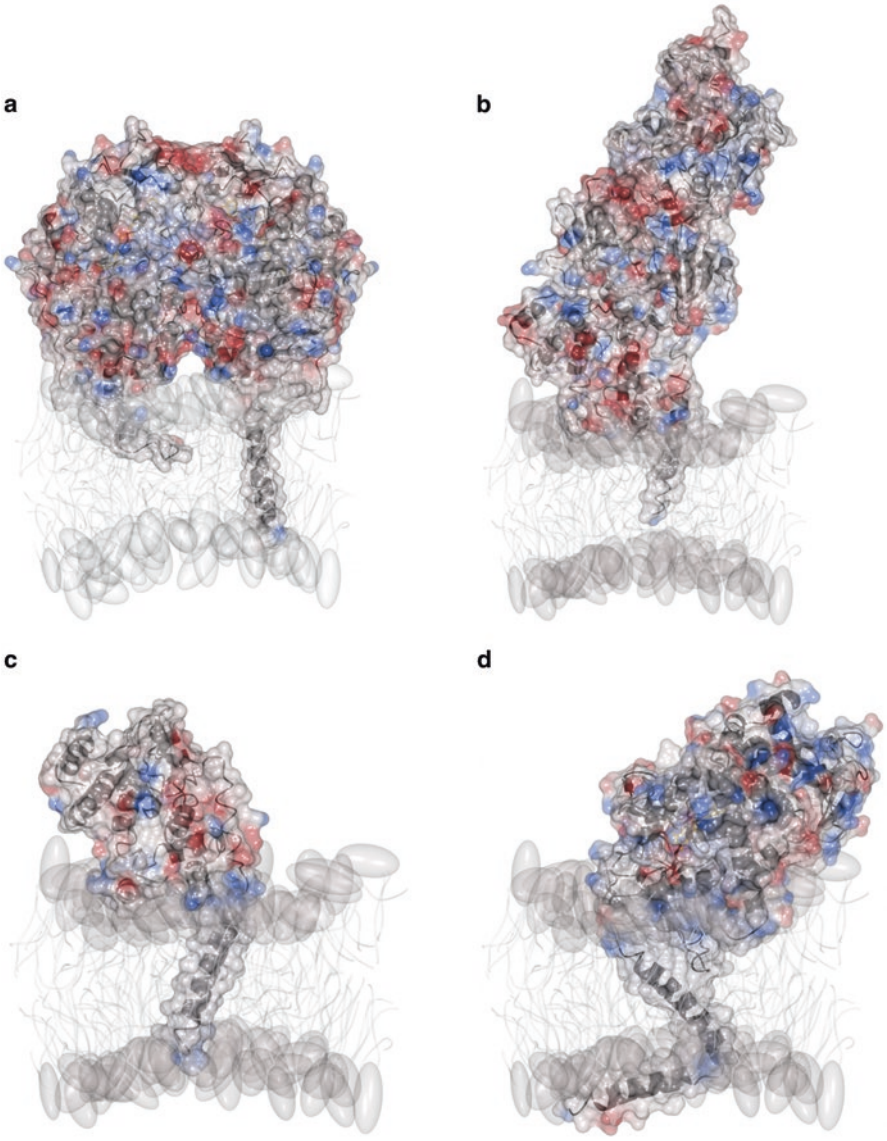


**Fig. 5.6** Structures of monotopic membrane proteins comparatively analyzed with human MAOs. Each molecule is represented as a black ribbon diagram with the semi-transparent surface electrostatic potential (negatively-charged and positively-charged patches are colored in red and blue, respectively. The phospholipid bilayer is as in Figs. 5.4 and 5.5. (**a**) Rat MAO A (PDB code 1o5w; Ma et al. 2004) features an overall dimeric fold highly similar to that of human MAO A and B. (**b**) Transglycosylase PBP1b from *E. coli* (PDB code 3vma; Sung et al. 2009). (**c**) Transglycosylase from *S. aureus* (PDB code 3vmt; Huang et al. 2012). (**d**) Lanosterol 14α-demethylase cytochrome P450 from *S. cerevisiae* (PDB code 4lxj; Monk et al. 2014)

molecules induce this residue to adopt an open conformation leaving the inner part of the cavity directly accessible from the surface loop (Fig. 5.4c). Instead, Ile199 exists in a closed position when smaller molecules occupy only the site in front of the flavin (Binda et al. 2003), therefore creating a dual-cavity active site.

### *5.4.2 Human MAO A: Details Make the Difference*

The structural characterization of human MAO B paved the way for studying the A isozyme, although this work turned out to be more difficult because of the lower biochemical stability of the detergent-solubilized recombinant protein. Human MAO A could be successfully extracted from the mitochondrial membrane particles and purified, but even using different detergents it eluted as a large molecular aggregate in size-exclusion chromatography which gave poorly diffracting crystals. In 2005 the structure of human MAO A in complex with clorgyline was reported at 3.0 Å (De Colibus et al. 2005) and few years later another group managed to improve the resolution up to 2.2 Å with the enzyme inhibited with harmine in a different crystallization condition (Son et al. 2008). In both cases the molecular arrangement in the crystals revealed a monomeric structure (Fig. 5.5a), although, as previously described, EPR studies using a spin-labelled covalent inhibitor demonstrated that, similarly to human MAO B, the A isozyme is also bound to the membrane in a dimeric form (Upadhyay et al. 2008a, b) (Fig. 5.3b). Most likely, the human MAO A dimer is less stable than that of human MAO B and the two monomers dissociate upon detergent-mediated extraction from the membrane.

The overall fold of human MAO A is very similar to that of MAO B and a model of its dimeric structure bound to the phospholipid bilayer was obtained by superposing the A monomer onto each of the MAO B dimer subunits (Fig. 5.5a). The human MAO A structure in complex with harmine (Son et al. 2008) could be solved with the C-terminal portion almost fully visible with residues 498-521 forming a long hydrophobic α-helix, perfectly in agreement with the prediction analysis. This α-helix includes Lys503 whose side chain adopts the same conformation as Arg494 in human MAO B, properly positioned to interact with the negatively-charged phospholipid heads (Fig. 5.5b). In addition, two ordered detergent molecules could be modeled in the electron density. Contrarily to what happens in MAO B they bind on the external side of the monomer with respect to the dimer interface (Fig. 5.5b), but in a conformation orienting their charged heads nearby the base of the protein and the hydrophobic chain alongside the membrane lipids. As a matter of fact, the human MAO A structure provided support to the membrane-bound model of these enzymes (Figs. 5.4 and 5.5).

Inspection of the human MAO A structure revealed a cavity of about 400 $Å^3$ in front of the FAD cofactor which represents the enzyme active site (Fig. 5.5a,c). This cavity space can host inhibitors such as harmine and clorgyline as showed by the available crystal structures (Son et al. 2008; De Colibus et al. 2005) and, though smaller, is supposed to be less rigid than that of human MAO B, as suggested by the

observation that some large inhibitors can inhibit human MAO A but not MAO B (Binda et al. 2010). This greater degree of plasticity may also account for the higher structural flexibility of the A isozyme and for its tendency to lose the dimeric state when extracted from the membrane. Nevertheless, in the conformation observed in the crystal structure the human MAO A active site cavity has a more compact shape which is determined by a quite limited number of structural details differing from human MAO B. Most of the residues are conserved including the lysine residue at the top of the flavin (Lys305), the aromatic sandwich in front of it (Tyr407 and Tyr444) and the surface loop at the entrance of the cavity (Fig. 5.5c). The differences are Asn181, Phe208 and Ile335 (Cys172, Ile199 and Tyr326 in MAO B, respectively). In particular, the last two mainly contribute to shape the active site and the larger side chain of Phe208 prevents the conformational change involving Ile199 of MAO B from giving the cavity a bipartite nature. As a matter of fact, the I199F mutation of human MAO B, as well as the double I199A-Y326A modification, generated an enzyme with ligand binding properties more similar to those of human MAO A (Hubálek et al. 2005; Milczek et al. 2011). These findings indicated that in human MAO A and B inhibitor and substrate specificities are finely regulated by subtle details of their respective active sites.

### *5.4.3 Comparison of Human Enzymes with Rat MAO A and Other Bitopic Membrane Proteins*

Human MAO A and B share almost 90% sequence identity with their respective rat homologs. The crystal structure of rat MAO A revealed an overall fold and an active site cavity highly similar to those of the human enzyme (Ma et al. 2004). The only difference is related to the oligomeric state which in rat MAO A is represented by a dimer that is structurally very similar to that of human MAO B (Fig. 5.6a). Nevertheless, as described above, the monomeric structure of human MAO A is likely to be a consequence of the detergent extraction from the membrane and the dimeric conformation of the rat enzyme supports even more this hypothesis. The residues that in human MAO A define the ligand specificity with respect to MAO B are also perfectly conserved in rat (Phe208 and Ile335), which is in agreement with the similar kinetics and inhibition properties across species. However, it was shown that even within the mitochondrial membrane environment the active site of human MAO A is more accessible than that of the rat enzyme (Upadhyay et al. 2008a, b), which should warn against any direct extrapolation of data derived from test experiments performed with rat animal models to humans.

Mammalian MAOs belong to the class of monotopic integral membrane proteins that consist of a water-soluble main body that is permanently bound to the phospholipid bilayer through a small domain. According to a structural classification (http://blanco.biomol.uci.edu/mpstruc), these membrane proteins were grouped on the basis of their functional properties that are mostly represented by enzymes such as

cyclooxygenases, hydrolases, glycosyltransferases, oxidases, etc. Many of them are associated to only one side of the membrane, mainly by an α-helix that is embedded with the phospholipids in a parallel orientation with respect to the plane of the bilayer. For example, this is the case of glycerol-3-phosphate dehydrogenase, a bacterial flavoenzyme at the crossroad of essential functions such as respiration, glycolysis and phospholipid biosynthesis, which has a dimeric structure with each monomer interacting with the membrane through an α-helix and part of a β-sheet (Yeh et al. 2008). Other monotopic membrane proteins, like MAOs, are instead anchored to the membrane through a domain that spans the entire bilayer through an N-terminal or C-terminal domain; for this reason they may be alternatively referred to as bitopic membrane proteins. Among these, the structure is available for two bacterial glycosyltranferases that are involved in cell wall biosynthesis (Sung et al. 2009; Huang et al. 2012). In both cases the extramembraneous domain is hooked into the phospholipid bilayer through an α-helix that originates from one side of the main body, with few hydrophobic residues at its base which stabilize the interaction with the membrane (Fig. 5.6b,c). Another type of bitopic membrane protein is represented by peptidases involved in cleavage of signal peptides and in protein ectodomain shedding. These proteins feature a large oligomeric organization with each monomer anchored to the membrane through an α-helix; nevertheless, the available structures of these proteins are limited to the extramembraneous catalytic domain (Nam et al. 2012; Arolas et al. 2012). A peculiar bitopic membrane-binding domain was found in a yeast cytochrome P450 enzyme playing a central role in sterol biosynthesis (Monk et al. 2014) (Fig. 5.6d). The crystal structure clearly showed that the catalytic domain of the protein is anchored to the membrane through a hydrophobic helix obliquely spanning the bilayer and followed by an amphipatic helix that is supposed to lie at the interface between the membrane and the lumen of the endoplasmic reticulum. This is considered the first structure of a full-length bitopic membrane protein, as in MAOs and glycosyltransferases the transmembrane helix terminates with few terminal residues that most likely lack a specific structured conformation and are simply embedded in the phospholipid head layer. Nevertheless, to our knowledge MAOs represent the only crystal structures so far available of human proteins with a transmembrane partially or fully visible in the electron density.

## 5.5 MAOs As Drug Targets for Neurological Diseases

### *5.5.1 Reversible and Irreversible Inhibitors*

Molecules targeting MAOs can be grouped in two classes: irreversible and reversible inhibitors, the first that inactivate the enzyme by a stable covalent linkage to the protein and the second that bind through weak interactions such as hydrogen bonds. From a molecular point of view, a thorough and in-depth analysis of the binding mechanism of a number of MAO B inhibitors could be carried out thanks to the high

crystal quality of this isozyme and has been already reviewed in detail (Edmondson et al. 2009). As described above, human MAO B active site is characterized by a well-defined hydrophobic cavity whose architecture is overall conserved among the structures in complex with chemically different inhibitors. Bulky reversible inhibitors endowed the cavity with a quite rigid structure with Ile199 in the open conformation and the surface loop 99-110 that seals the active site. The prototype of this case is safinamide that perfectly matches the cavity by orienting its hydrophilic moiety in front of the flavin and the aromatic body along the hydrophobic environment behind (Fig. 5.7a). This situation was found also with diphenyl-2-butene and farnesol (Edmondson et al. 2009) as well as with glitazone molecules (Binda et al. 2011a). Instead, reversible small inhibitors such as isatin (Fig. 5.7b) determine a dual-cavity conformation of human MAO B active site by binding to the space in front of the flavin and leaving the entrance cavity empty (or filled by water molecules), with the Ile199 gate in closed position that separates the two moieties. This plasticity of human MAO B active site cavity is also found with irreversible inhibitors. L-deprenyl and rasagiline (Edmondson et al. 2009; Fig. 5.7c), the two classic propargyl compounds that form a stable covalent linkage to the enzyme flavin cofactor (N5 atom), extend their aromatic moiety to induce Ile199 into the open conformation although they are not long enough to entirely fill the cavity such as in the case of safinamide. Instead, tranylcypromine forms a covalent bond with the C4A atom of the flavin and occupies only the space in close proximity with the isoalloxazine ring (Fig. 5.7d). A peculiar case of MAO B inhibition by tranylcypromine, which highlights even more strongly the "druggability" of the entire active site including the entrance cavity space, is related to the existence of imidazoline I2 binding sites on MAO enzymes. This hypothesis was based on the observation that there is a cooperative potentiation effect of MAO B inhibition by 2-(2-benzofuranyl)-2-imidazoline (2-BFI) when the enzyme is bound to tranylcypromine. The crystal structure provided a definitive demonstration showing both inhibitors bound to MAO B active site with 2-BFI occupying the entrance cavity and tranylcypromine covalently attached to the enzyme flavin (Fig. 5.7d) (Bonivento et al. 2010).

Knowledge of human MAO A inhibition mechanisms is more limited because this protein turned out to be much less tractable experimentally, which may be partly explained by a lower homogeneity of detergent preparations of the recombinant enzyme. Two crystal structures are available for human MAO A in complex with inhibitors. One of them is the structure of the enzyme inactivated by clorgyline, the classic MAO A-selective propargyl compound that forms a stable covalent bond with the flavin cofactor (De Colibus et al. 2005). The other is the structure with the harmine that, though reversibly, binds very tightly to MAO A active site (Son et al. 2008). In both cases the inhibitors interact with the enzyme active site by hydrophobic and van der Walls contacts and the active site architecture is conserved, except for Ile335 (corresponding to the gating residue Ile199 in human MAO B) which adopts different conformations. Nevertheless, it is known that human MAO A may be inhibited by bulky inhibitors which would hardly fit its small active site cavity (Binda et al. 2010; Esteban et al. 2014). Remarkably, some of these inhibitors cannot even bind to MAO B, which suggests that human MAO A cavity has a less rigid structure in agreement with the higher flexibility of this isozyme.

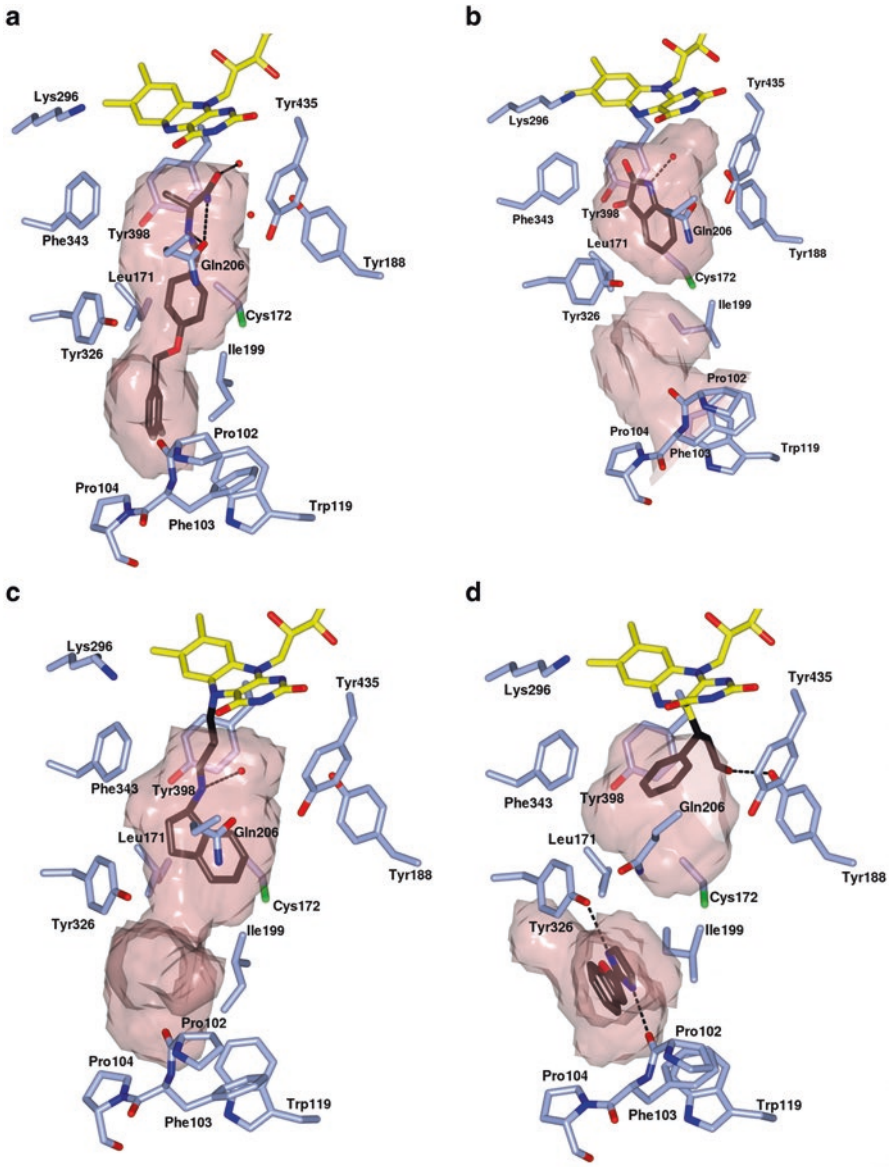


**Fig. 5.7** Structures of human MAO B active site in complex with inhibitors (carbon atoms in black). Residues are represented with carbons in ice blue; Gln206, Tyr188 and Pro102, which were not shown in Fig. 5.4c for the sake of clarity, are here added because they are involved in interactions with the inhibitor. Hydrogen bonds between the inhibitor and active site residues or water molecules are depicted as dashed lines. (**a**) Safinamide (PDB code 2v5z). (**b**) Isatin (PDB code 1oja). (**c**) Rasagiline (PDB code 1s2q). (**d**) Tranylcypromine (in the substrate cavity) and 2-BFI (in the entrance cavity) (PDB code 2xcg)

### 5.5.2 *Parkinson's Disease: Old and New Inhibitors*

As validated drug targets, MAOs have been the focus of many studies for the development of inhibitors to be used in the clinical practice of neurological pathologies (Al-Nuaimi et al. 2012) (Fig. 5.2). The established role of MAO B inhibition in the symptomatic treatment of Parkinson's disease is due to the specific activity of this enzyme within dopamine metabolism in the substantia nigra neurons that undergo degeneration (Dézsi and Vécsei 2017). However, it is known that many MAO inhibitors act also on other targets (Binda et al. 2011b) and a shared opinion exists that these molecules may have a general neuroprotective effect that results from cellular mechanisms other than MAO-dependent neurotransmitter degradation. Most likely this holds for Alzheimer's disease and other types of dementias (Hroudová et al. 2016), for which a multi-target approach is being under investigation as a promising new strategy to tackle the complexity of these pathological conditions (Ramsay et al. 2016; Orhan and Senol 2016).

In the specific case of Parkinson's disease, the first-line treatment is historically based on administration of L-dopa, the dopamine precursor that can cross the blood-brain-barrier. This medication is generally given in association with a MAO B selective inhibitor in order to prevent the enzymatic degradation of the re-introduced dopamine. The adverse side effects of MAO inhibition which were encountered with non-selective ligands used as antidepressants (Fig. 5.2) could be overcome by the development of propargyl-based compounds that specifically inactivate the B isozyme. Selegiline (L-deprenyl) was the first of these inhibitors to be clinically used and has been on the market since the late 1980s (Knoll 2000) (Fig. 5.2). In the first decade of this century the propargyl analog rasagiline was developed and approved, which features the same mechanism of action involving the irreversible inactivation of human MAO B by a covalent linkage to the enzyme cofactor (Mandel et al. 2005) (Figs. 5.2 and 5.7c). Contrarily to selegiline, rasagiline is not metabolized to amphetamine and is therefore devoid of the neurotoxic side effects of the other drug. In the same years, the idea emerged that MAO irreversible (though selective) inhibition should be avoided to favor a more controlled use of the drug and to prevent possible immunogenic side effects due to the covalent mark on the target protein. This led to the development of safinamide, a reversible MAO B-selective inhibitor that was recently FDA-approved as a new anti-Parkinson drug (Deeks 2015) (Figs. 5.2 and 5.7a). The pharmacological effects of safinamide are not limited to MAO B inhibition and derive from a multi-target action including sodium and calcium channel modulation. In general, the clinical practice confirmed that MAO B inhibitors are effective and safe medications that provide symptomatic benefit for Parkinson patients, both in association with L-dopa and as monotherapy (Robakis and Fahn 2015). In this regard, a hypothesis is emerging that L-dopa prolonged treatment might lead to its erroneous incorporation into proteins of the patient's brain as this molecule is the hydroxylated form of tyrosine, which *in vitro* was shown to induce cell toxicity (Chan et al. 2012). Although this is still a matter of debate, long treatments with L-dopa should be cautiously avoided while selective

MAO B inhibition can be safely adopted. In addition, besides the specific effect of increasing dopamine levels, reducing MAO activity is also beneficial to decrease the oxidative stress generated by the catalytic activity of the enzyme (Fig. 5.1). This exerts a neuroprotective action and is thought to be relevant also in non-neuronal tissues, as fully described in the next section.

## 5.6 A New Emerging Role of MAOs in Cardiomyopathies

Oxidative stress is thought to play a major role in both neurodegenerative and cardiovascular diseases that affect elderly populations, although the exact mechanisms underlying these processes are complex and not completely understood. As mentioned above, MAOs represent validated drug targets for neurodegenerative diseases due to their activity in the catabolism of neurotransmitters but also for their production of toxic ROS (Fig. 5.1). Both MAO A and MAO B are also expressed in non-neuronal tissues (Sivasubramaniam et al. 2003) and in rat heart the expression of MAO A is known to increase sixfold with ageing (Maurel et al. 2003) (Fig. 5.3a). In cardiomyocytes, ROS generates mitochondrial damage, impairs contractile function and triggers cell senescence (Kurokawa et al. 2014). As a matter of fact, serotonin and norepinephrine, which are physiological substrates of MAO A, regulate some cardiac functions and are involved in adverse tissue remodeling leading to heart failure (Kaludercic et al. 2010; Mialet-Perez et al. 2012). The specific mechanisms of MAO action in heart still need to be fully clarified and studies are ongoing to uncover the specific role of aldehyde and ROS that are both potentially toxic side-products of bioamine metabolism. It was demonstrated that in transgenic mice overexpressing MAO A enhanced levels of ROS and mitochondrial disfunction is linked to activation of p53 and downregulation of the mitochondrial regulator PGC1α (Villeneuve et al. 2013; Umbarkar et al. 2015). Altogether these data may open new avenues for therapeutic intervention to treat age-related cardiovascular diseases by using MAO inhibitors (Fig. 5.2).

**Acknowledgements** This work was supported by Fondazione Cariplo (grant n. 2014-0672 to C.B.).

## References

Al-Nuaimi SK, Mackenzie EM, Baker GB (2012) Monoamine oxidase inhibitors and neuroprotection: a review. Am J Ther 19:436–448

Arolas JL, Broder C, Jefferson T, Guevara T, Sterchi EE, Bode W, Stöcker W, Becker-Pauly C, Gomis-Rüth FX (2012) Structural basis for the sheddase function of human meprin β metalloproteinase at the plasma membrane. Proc Natl Acad Sci U S A 109:16131–16136

Arslan B, Edmondson DE (2010) Expression of zebrafish (*Danio rerio*) monoamine oxidase (MAO) in *Pichia pastoris*: purification and comparison with human MAO A and MAO B. Prot Expr Purif 70:290–297

Bach AW, Lan NC, Johnson DL, Abell CW, Bembenek ME, Kwan SW, Seeburg PH, Shih JC (1988) cDNA cloning of human liver monoamine oxidase A and B: molecular differences in enzymatic properties. Proc Natl Acad Sci U S A 85:4934–4938

Binda C, Newton-Vinson P, Hubalek F, Edmondson DE, Mattevi A (2002) Structure of human monoamine oxidase B, a drug target for the treatment of neurological disorders. Nat Struct Biol 9:22–26

Binda C, Li M, Hubalek F, Restelli N, Edmondson DE, Mattevi A (2003) Insights into the mode of inhibition of human mitochondrial monoamine oxidase B from high-resolution crystal structures. Proc Natl Acad Sci U S A 100:9750–9755

Binda C, Wang J, Pisani L, Caccia C, Carotti A, Salvati P, Edmondson DE, Mattevi A (2007) Structures of human monoamine oxidase B complexes with selective noncovalent inhibitors: safinamide and coumarin analogs. J Med Chem 50:5848–5852

Binda C, Valente S, Romanenghi M, Pilotto S, Cirilli R, Karytinos A, Ciossani G, Botrugno OA, Forneris F, Tardugno M, Edmondson DE, Minucci S, Mattevi A, Mai A (2010) Biochemical, structural, and biological evaluation of tranylcypromine derivatives as inhibitors of histone demethylases LSD1 and LSD2. J Am Chem Soc 132:6827–6833

Binda C, Aldeco M, Geldenhuys WJ, Tortorici M, Mattevi A, Edmondson DE (2011a) Molecular insights into human monoamine oxidase B inhibition by the glitazone anti-diabetes drugs. ACS Med Chem Lett 3:39–42

Binda C, Milczek EM, Bonivento D, Wang J, Mattevi A, Edmondson DE (2011b) Lights and shadows on monoamine oxidase inhibition in neuroprotective pharmacological therapies. Curr Top Med Chem 11:2788–2796

Bonivento D, Milczek EM, McDonald GR, Binda C, Holt A, Edmondson DE, Mattevi A (2010) Potentiation of ligand binding through cooperative effects in monoamine oxidase B. J Biol Chem 285:36849–36856

Chan SW, Dunlop RA, Rowe A, Double KL, Rodgers KJ (2012) L-DOPA is incorporated into brain proteins of patients treated for Parkinson's disease, inducing toxicity in human neuroblastoma cells in vitro. Exp Neurol 238:29–37

Chen K, HF W, Shih JC (1996) Influence of C-terminus on monoamine oxidase A and B catalytic activity. J Neurochem 66:797–803

De Colibus L, Li M, Binda C, Lustig A, Edmondson DE, Mattevi A (2005) Three-dimensional structure of human monoamine oxidase A (MAO A): relation to the structures of rat MAO A and human MAO B. Proc Natl Acad Sci U S A 102:12684–12689

Deeks ED (2015) Safinamide: first global approval. Drugs 75:705–711

Dézsi L, Vécsei L (2017) Monoamine oxidase B inhibitors in Parkinson's disease. CNS Neurol Disord Drug Targets 16:425–439

Edmondson DE, Binda C, Wang J, Upadhyay AK, Mattevi A (2009) Molecular and mechanistic properties of the membrane-bound mitochondrial monoamine oxidases. Biochemistry 48:4220–4230

Emmerstorfer A, Wriessnegger T, Hirz M, Pichler H (2014) Overexpression of membrane proteins from higher eukaryotes in yeasts. Appl Microbiol Biotechnol 98:7671–7698

Esteban G, Allan J, Samadi A, Mattevi A, Unzeta M, Marco-Contelles J, Binda C, Ramsay RR (2014) Kinetic and structural analysis of the irreversible inhibition of human monoamine oxidases by ASS234, a multi-target compound designed for use in Alzheimer's disease. Biochim Biophys Acta 1844:1104–1110

Forneris F, Mattevi A (2008) Enzymes without borders: mobilizing substrates, delivering products. Science 321:213–216

Forneris F, Battaglioli E, Mattevi A, Binda C (2009) New roles of flavoproteins in molecular cell biology: histone demethylase LSD1 and chromatin. FEBS J 276:4304–4312

Fowler CJ, Mantle TJ, Tipton KF (1982) The nature of inhibition of rat liver monoamine oxidase types A and B by the acetylenic inhibitors clorgyline, l-deprenyl, and pargyline. Biochem Pharmacol 17:3555–3561

Gottowik KJ, Malherbe P, Lang G, Da Prada M, Cesura AM (1995) Structure/function relationships of mitochondrial monoamine oxidase A and B chimeric forms. Eur J Biochem 230:934–942

Hare ML (1928) Tyramine oxidase: a new enzyme system in liver. Biochem J 22:968–979

Henderson Pozzi M, Fitzpatrick PF (2010) A lysine conserved in the monoamine oxidase family is involved in oxidation of the reduced flavin in mouse polyamine oxidase. Arch Biochem Biophys 498:83–88

Hroudová J, Singh N, Fišar Z, Ghosh KK (2016) Progress in drug development for Alzheimer's disease: an overview in relation to mitochondrial energy metabolism. Eur J Med Chem 121:774–784

Huang CY, Shih HW, Lin LY, Tien YW, Cheng TJ, Cheng WC, Wong CH, Ma C (2012) Crystal structure of Staphylococcus aureus transglycosylase in complex with a lipid II analog and elucidation of peptidoglycan synthesis mechanism. Proc Natl Acad Sci U S A 109:6496–6501

Hubálek F, Binda C, Khalil A, Li M, Mattevi A, Castagnoli N, Edmondson DE (2005) Demonstration of isoleucine 199 as a structural determinant for the selective inhibition of human monoamine oxidase B by specific reversible inhibitors. J Biol Chem 280:15761–11576

Kaludercic N, Takimoto E, Nagayama T, Feng N, Lai EW, Bedja D, Chen K, Gabrielson KL, Blakely RD, Shih JC, Pacak K, Kass DA, Di Lisa F, Paolocci N (2010) Monoamine oxidase A-mediated enhanced catabolism of norepinephrine contributes to adverse remodeling and pump failure in hearts with pressure overload. Circ Res 106:193–202

Kearney EB, Salach JI, Walker WH, Seng RL, Zeszotek E, Singer TP (1971) The covalently-bound flavin of hepatic monoamine oxidase. Isolation and sequence of a flavin peptide and evidence for binding at the 8-alpha position. Eur J Biochem 24:321–327

Kim D, Baik SH, Kang S, Cho SW, Bae J, Cha MY, Sailor MJ, Mook-Jung I, Ahn KH (2016) Close correlation of monoamine oxidase activity with progress of Alzheimer's disease in mice, observed by in vivo two-photon imaging. ACS Cent Sci 2:967–975

Knoll J (2000) (-)Deprenyl (Selegiline): past, present and future. Neurobiology (Bp) 8:179–199

Kumar MJ, Nicholls DG, Andersen JK (2003) Oxidative alpha-ketoglutarate dehydrogenase inhibition via subtle elevations in monoamine oxidase B levels results in loss of spare respiratory capacity – implications for Parkinson's disease. J Biol Chem 278:46432–46439

Kurokawa S, Niwano S, Niwano H, Murakami M, Ishikawa S, Masaki Y, Tamaki H, Toda T, Noda Y, Shimizu T, Izumi T, Ako J (2014) Cardiomyocyte-derived mitochondrial superoxide causes myocardial electrical remodeling by downregulating potassium channels and related molecules. Circ J 78:1950–1959

Langston JW, Irwin I, Langston EB, Forno LS (1984a) 1-Methyl-4-phenyl-1,2,3,6-tetrahydropyridinium ion (MPP+): identification of a metabolite of MPTP, a toxin selective for the *Substantia nigra*. Neurosci Lett 48:87–92

Langston JW, Irwin I, Langston EB, Forno LS (1984b) Pargyline prevents MPTP-induced parkinsonism in primates. Science 225:1480–1482

Li M, Hubálek F, Newton-Vinson P, Edmondson DE (2002) High-level expression of human liver monoamine oxidase A in Pichia pastoris: comparison with the enzyme expressed in Saccharomyes cerevisae. Prot Expr Purif 24:152–162

Li M, Binda C, Mattevi A, Edmondson DE (2006) Functional role of the "aromatic cage" in human monoamine oxidase B: structures and catalytic properties of Tyr435 mutant proteins. Biochemistry 45:4775–4784

Ma J, Yoshimura M, Yamashita E, Nakagawa A, Ito A, Tsukihara T (2004) Structure of rat monoamine oxidase A and its specific recognitions for substrates and inhibitors. J Mol Biol 338:103–114

Mandel S, Weinreb O, Amit T, Youdim MB (2005) Mechanism of neuroprotective action of the anti-Parkinson drug rasagiline and its derivatives. Brain Res Brain Res Rev 48:379–387

Maurel A, Hernandez C, Kunduzova O, Bompart G, Cambon C, Parini A, Frances B (2003) Age-dependent increase in hydrogen peroxide production by cardiac monoamine oxidase A in rats. Am J Phys Heart Circ Phys 284:H1460–H1467

McNicholas S, Potterton E, Wilson KS, Noble ME (2011) Presenting your structures: the CCP4mg molecular-graphics software. Acta Crystallogr D Biol Crystallogr 67(Pt 4):386–394

Mialet-Perez J, D'Angelo R, Villeneuve C, Ordener C, Negre-Salvayre A, Parini A, Vindis C (2012) Serotonin 5-HT2A receptor-mediated hypertrophy is negatively regulated by caveolin-3 in cardiomyoblasts and neonatal cardiomyocytes. J Mol Cell Cardiol 52:502–510

Milczek E, Binda C, Rovida S, Mattevi A, Edmondson DE (2011) The "gating" residues Ile199 and Tyr326 in human monoamine oxidase B function in substrate and inhibitor recognition. FEBS J 278:4860–4869

Miller JR, Edmondson DE (1999) Influence of flavin analogue structure on the catalytic activities and flavinylation reactions of recombinant human liver monoamine oxidases A and B. J Biol Chem 274:23515–23525

Mitoma J, Ito A (1992) Mitochondrial targeting signal of rat liver monoamine oxidase B is located at its carboxy terminus. J Biochem 111:20–24

Monk BC, Tomasiak TM, Keniya MV, Huschmann FU, Tyndall JD, O'Connell JD 3rd, Cannon RD, McDonald JG, Rodriguez A, Finer-Moore JS, Stroud RM (2014) Architecture of a single membrane spanning cytochrome P450 suggests constraints that orient the catalytic domain relative to a bilayer. Proc Natl Acad Sci U S A 111:3865–3870

Nagy J, Salach JI (1981) Identity of the active site flavin-peptide fragments from the human "A"-form and the bovine "B"-form of monoamine oxidase. Arch Biochem Biophys 208:388–394

Nam SE, Kim AC, Paetzel M (2012) Crystal structure of Bacillus subtilis signal peptide peptidase A. J Mol Biol 419:347–358

Nandigama RK, Edmondson DE (2000) Influence of FAD structure on its binding and activity with the C406A mutant of recombinant human liver monoamine oxidase A. J Biol Chem 275:20527–20532

Newton-Vinson P, Hubálek F, Edmondson DE (2000) High-level expression of human liver monoamine oxidase B in Pichia pastoris. Prot Expr Purif 20:334–345

Orhan IE, Senol FS (2016) Designing multi-targeted therapeutics for the treatment of Alzheimer's disease. Curr Top Med Chem 16:1889–1896

Ramsay RR, Majekova M, Medina M, Valoti M (2016) Key targets for multi-target ligands designed to combat neurodegeneration. Front Neurosci 10:375

Rebrin I, Geha RM, Chen K, Shih JC (2001) Effects of Carboxy-terminal truncations on the activity and solubility of human monoamine oxidase B. J Biol Chem 276:29499–29506

Robakis D, Fahn S (2015) Defining the role of the monoamine oxidase-B inhibitors for Parkinson's disease. CNS Drugs 29:433–441

Russell SM, Davey J, Mayer RJ (1979) The vectorial orientation of human monoamine oxidase in the mitochondrial outer membrane. Biochem J 181:7–14

Salach JI (1979) Monoamine oxidase from beef liver mitochondria: simplified isolation procedure, properties, and determination of its cysteinyl flavin content. Arch Biochem Biophys 192:128–137

Schnaitman C, Erwin VG, Greenawalt JW (1967) Submitochondrial localization of monoamine oxidase – an enzymatic marker for outer membrane of rat liver mitochondria. J Cell Biol 32:719–735

Sivasubramaniam SD, Finch CC, Rodriguez MJ, Mahy N, Billett EE (2003) A comparative study of the expression of monoamine oxidase-A and -B mRNA and protein in non-CNS human tissues. Cell Tissue Res 313:291–300

Son SY, Ma J, Kondou Y, Yoshimura M, Yamashita E, Tsukihara T (2008) Structure of human monoamine oxidase A at 2.2 Å resolution: the control of opening the entry for substrates/inhibitors. Proc Natl Acad Sci U S A 105:5739–5744

Sung MT, Lai YT, Huang CY, Chou LY, Shih HW, Cheng WC, Wong CH, Ma C (2009) Crystal structure of the membrane-bound bifunctional transglycosylase PBP1b from Escherichia coli. Proc Natl Acad Sci U S A 106:8824–8829

Tang B, Zhao L, Liang R, Zhang Y, Wang L (2012) Magnetic nanoparticles: an improved method for mitochondrial isolation. Mol Med Rep 5:1271–1276

Tsirigos KD, Peters C, Shu N, Käll L, Elofsson A (2015) Nucleic Acids Research 43 (Webserver issue), W401–W407

Umbarkar P, Singh S, Arkat S, Bodhankar SL, Lohidasan S, Sitasawad SL (2015) Monoamine oxidase-a is an important source of oxidative stress and promotes cardiac dysfunction, apoptosis, and fibrosis in diabetic cardiomyopathy. Free Radic Biol Med 87:263–273

Upadhyay AK, Edmondson DE (2008) Characterization of detergent purified recombinant rat liver monoamine oxidase B expressed in Pichia pastoris. Protein Expr Purif 59:349–356

Upadhyay AK, Edmondson DE (2009) Development of spin-labeled pargyline analogues as specific inhibitors of human monoamine oxidases A and B. Biochemistry 48:3928–3935

Upadhyay A, Borbat P, Wang J, Freed J, Edmondson DE (2008a) Determination of the oligomeric states of human and rat monoamine oxidases in the outer mitochondrial membrane and octyl β-D-glucopyranoside micelles using pulsed dipolar electron spin resonance spectroscopy. Biochemistry 47:1554–1566

Upadhyay AK, Wang J, Edmondson DE (2008b) Comparison of the structural properties of the active site cavities of human and rat monoamine oxidase A and B in their soluble and membrane-bound forms. Biochemistry 47:526–536

Urban P, Andersen JK, Hsu HPP, Pompon D (1991) Comparative membrane locations and activities of human monoamine oxidases expressed in yeast. FEBS Lett 286:142–146

Villeneuve C, Guilbeau-Frugier C, Sicard P, Lairez O, Ordener C, Duparc T, De Paulis D, Couderc B, Spreux-Varoquaux O, Tortosa F, Garnier A, Knauf C, Valet P, Borchi E, Nediani C, Gharib A, Ovize M, Delisle MB, Parini A, Mialet-Perez J (2013) p53-PGC-1α pathway mediates oxidative mitochondrial damage and cardiomyocyte necrosis induced by monoamine oxidase-A upregulation: role in chronic left ventricular dysfunction in mice. Antioxid Redox Signal 18:5–18

Wang J, Edmondson DE (2010) High-level expression and purification of rat monoamine oxidase A (MAO A) in *Pichia pastoris*: comparison with human MAO A. Prot Expr Purif 70:211–217

Wang J, Edmondson DE (2011) Topological probes of monoamine oxidases A and B in rat liver mitochondria: inhibition by TEMPO-substituted pargyline analogues and inactivation by proteolysis. Biochemistry 50:2499–2505

Weyler W (1994) Functional expression of C-terminally truncated human monoamine oxidase type A in *Saccharomyces cerevisiae*. J Neural Transm 41:3–15

Weyler W, Salach JI (1985) Purification and properties of mitochondrial monoamine oxidase type A from human placenta. J Biol Chem 260:13199–13207

Weyler W, Titlow CC, Salach JI (1990) Catalytically active monoamine oxidase Type A from human liver expressed in *Saccharomyces cerevisiae* contains covalent FAD. Biochem Biophys Res Commun 173:1205–1211

Yeh JI, Chinte U, Du S (2008) Structure of glycerol-3-phosphate dehydrogenase, an essential monotopic membrane enzyme involved in respiration and metabolism. Proc Natl Acad Sci U S A 105:3280–3285

Zeller EA, Barsky J (1952) In vivo inhibition of liver and brain monoamine oxidase by 1-Isonicotinyl-2-isopropyl hydrazine. Proc Soc Exp Biol Med 81:459–461

# Chapter 6
# Transient Receptor Potential (TRP) Channels

**Amrita Samanta, Taylor E. T. Hughes, and Vera Y. Moiseenkova-Bell**

**Abstract** Transient Receptor Potential (TRP) channels are evolutionarily conserved integral membrane proteins. The mammalian TRP superfamily of ion channels consists of 28 cation permeable channels that are grouped into six subfamilies based on sequence homology (Fig. 6.1). The canonical TRP (TRPC) subfamily is known for containing the founding member of mammalian TRP channels. The vanilloid TRP (TRPV) subfamily has been extensively studied due to the heat sensitivity of its founding member. The melastatin-related TRP (TRPM) subfamily includes some of the few known bi-functional ion channels, which contain functional enzymatic domains. The ankyrin TRP (TRPA) subfamily consists of a single chemo-nociceptor that has been proposed to be a target for analgesics. The mucolipin TRP (TRPML) subfamily channels are found primarily in intracellular compartments and were discovered based on their critical role in type IV mucolipidosis (ML-IV). The polycystic TRP (TRPP) subfamily is a diverse group of proteins implicated in autosomal dominant polycystic kidney disease (ADPKD). Overall, this superfamily of channels is involved in a vast array of physiological and pathophysiological processes making the study of these channels imperative to our understanding of subcellular biochemistry.

**Keywords** Transient receptor potential channels · TRPC · TRPV · TRPM · TRPA · TRPML · TRPP · Cryo-electron microscopy · Thermosensation · PKD1 · PKD2 · Polycystin

A. Samanta · V. Y. Moiseenkova-Bell (✉)
Department of Pharmacology, School of Medicine, Case Western Reserve University, Cleveland, OH, USA

Department of Physiology and Biophysics School of Medicine, Case Western Reserve University, Cleveland, OH, USA
e-mail: axs958@case.edu; vmb@pennmedicine.upenn.edu

T. E. T. Hughes
Department of Pharmacology, School of Medicine, Case Western Reserve University, Cleveland, OH, USA
e-mail: txh310@case.edu



J. R. Harris, E. J. Boekema (eds.), *Membrane Protein Complexes: Structure and Function*, Subcellular Biochemistry 87,
https://doi.org/10.1007/978-981-10-7757-9_6

## 6.1 Introduction

In order to survive, organisms have adapted to rapidly and accurately sense the environment around them. One group of biomolecules that play a key role in interpreting these environmental stimuli are a class of integral membrane protein called Transient Receptor Potential (TRP) channels. TRP channels are a class of cationic channels that act as signal transducer by altering membrane potential or intracellular calcium ($Ca^{2+}$) concentration. The TRP channel era began in 1969 when Cosens and Manning discovered a phenotype in drosophila that exhibited as blindness in the presence of constant bright light (Cosens and Manning 1969). This mutant strain was named *trp*, transient receptor potential, and cloning of the mutated *trp* gene identified the first member of the TRP superfamily (Cosens and Manning 1969). This superfamily constitutes a diverse group of polymodal ion channels that are mostly conserved from nematodes to humans. Based on sequence homology the mammalian TRP channel superfamily is classified into six subfamilies (Fig. 6.1): TRPC (Canonical), TRPV (Vanilloid), TRPM (Melastatin), TRPA (Ankyrin), TRPML (Mucolipin), and TRPP (Polycystic). The first four subfamilies are categorized as group 1 and the last two constitute group 2. In this chapter, each subfamily will be discussed in detail with emphasis on channels that have been extensively studied.

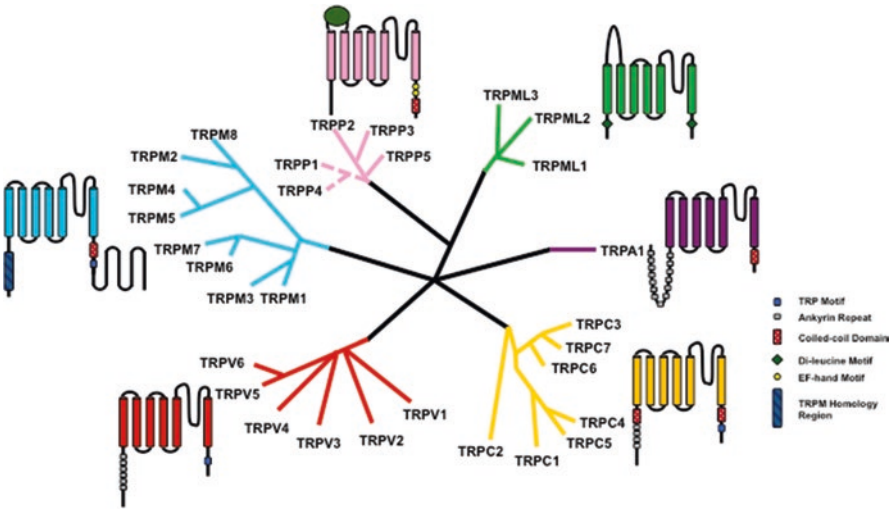


**Fig. 6.1** A schematic representation of the TRP superfamily of ion channels. Each branching group is representative of a subfamily of channels

## 6.2 TRPC Subfamily

The first subfamily of mammalian TRP channels studied is known as the TRPC subfamily or the canonical TRP channels. The founding member TRPC1 was cloned in 1995 and was discovered based on its sequence homology to the Drosophila *trp* gene (Wes et al. 1995). The seven members of this subfamily are commonly divided into four groups based on sequence homology (I) TRPC1; (II) TRPC2; (III) TRPC3, TRPC6, TRPC7; and (IV) TRPC4 and TRPC5 (Fig. 6.1). Here, TRPC2, TRPC3, TRPC6 and TRPC7 will be discussed together as explained in Sect. 6.2.3.

All seven members of this subfamily are structurally similar having six transmembrane helices, a putative hydrophobic pore forming loop, three to four ankyrin repeats, coiled-coil domains in the N- and C-terminus, a C-terminal proline rich region, a Calmodulin/$IP_3$ binding region and what is known as the TRP motif (Putney 2004; Vazquez et al. 2004). TRPC channels have been shown to form both heterotetramers and homotetramers within the TRP channel superfamily, with different members having certain preferences, for example, TRPC1 forms physiologically relevant functional channels with several TRPC channels including TRPC4, as well as, TRPV1, and TRPP2 (Ong et al. 2016; Dietrich et al. 2014).

The TRPC subfamily channels, like most other TRP channels, function as $Ca^{2+}$ permeable plasma membrane channels with varying $Ca^{2+}$ selectivity (Vazquez et al. 2004). The mechanism of regulation of these channels is contentious, with the two main hypotheses being store-operated channel activation and receptor-activated channel regulation (Vazquez et al. 2004). It appears, based on the current body of scientific research, that different members of this subfamily are activated based on one or both of these two methods depending on the expression system, expression level and the antibody used. Other research has also suggested mechanosensitive gating mechanisms (Dietrich et al. 2014). In spite of these experimental limitations, much is known about this subfamily of TRP channels.

### *6.2.1 TRPC1*

The founding member of this subfamily can also be considered the founding member of the mammalian TRP channel superfamily. TRPC1 was first cloned by the Montell group in 1995 because of its high sequence homology (~40%) to the Drosophila *trp* gene (Wes et al. 1995). This invertebrate *trp* gene was proposed to be a store-operated $Ca^{2+}$ channel and therefore mammalian homologues had potentially the same function. TRPC1 was originally found in fetal brain, liver and kidney tissues as well as adult heart, testes, ovaries and brain (Wes et al. 1995). Since then, it has been found to be broadly expressed in mammalian tissues (Dietrich et al. 2014). TRPC1 knockout mice have emerged as a highly successful tool for research of this channel *in vivo* (Dietrich et al. 2014). These models have implicated TRPC1 in skeletal muscle differentiation, organism growth and development,

immune regulation, tumor cell migration and Parkinson disease (Dietrich et al. 2014). In spite of being involved in these critical biological functions, TRPC1-/- mice have been reported to live a healthy and normal life (Dietrich et al. 2014).

TRPC1 monomers have been shown to create functional channels with not only other TRPC members, but also with TRP members outside its subfamily. For example, Tsiokas et al. showed that TRPC1/TRPP2 heterotetrameric channels form and operate in membrane bilayers (Dietrich et al. 2014; Tsiokas et al. 1999). TRPC1 has also been shown to interact with members of the TRPV subfamily (Dietrich et al. 2014). TRPC1 undergoes alternative splicing and there are currently five known splice variants with only three that have been shown to be translated to functional proteins (Dietrich et al. 2014). Different splice variants have been reported to affect channel functionality especially in heteromeric channels (Dietrich et al. 2014). Recently, there has also been a start codon found upstream of the currently used start codon for TRPC1. This has produced an extended form of TRPC1, which could be of interest for future studies of the protein (Dietrich et al. 2014).

As mentioned previously, TRPC1 was originally discovered as a potential store-operated $Ca^{2+}$ channel, but characterization of this channel did not show it to have the predicted traits of a store operated $Ca^{2+}$ channel or $I_{CRAC}$ activity (Ong et al. 2016). Still, TRPC1 has been shown to be involved in store-operated $Ca^{2+}$ entry (SOCE) through its interactions with Orai1 and STIM1 thus designating it as having $I_{SOC}$ activity (Ong et al. 2016). SOCE is a signaling cascade that is critical for an abundance of biological processes. When $Ca^{2+}$ is released from the endoplasmic reticulum the cytosolic $Ca^{2+}$ concentration increases which triggers activation of plasma membrane $Ca^{2+}$ channels ($I_{CRAC}$ or $I_{SOC}$). Evidence suggests that TRPC1 colocalizes with STIM1 and Orai1 in endoplasmic reticulum-plasma membrane (EM-PM) junctions wherein these two membranes exist in close proximity to one another (Ong et al. 2016). Orai1 has been shown to be necessary for TRPC1 activation, though different splice variants of TRPC1 seem to be modulated by Orai1 differently (Ong et al. 2016). Mechanosensitivity has also been discussed as a potential regulation method for this channel, but various expression systems have provided conflicting results to date (Dietrich et al. 2014).

### *6.2.2 TRPC4 & TRPC5*

TRPC4 and TRPC5 are often grouped with TRPC1 because they, like TRPC1, are inwardly rectifying and were originally hypothesized to be involved in SOCE (Vazquez et al. 2004). What distinguishes these two channels is their extended C-terminus that contains a PDZ binding domain. This domain has been shown to interact with NHERF, a scaffold protein that links plasma membrane proteins to the actin cytoskeleton (Voltz et al. 2001; Vazquez et al. 2004). Through this PDZ domain, TRPC4 has been shown to be activated downstream of $G_q$-coupled receptors and receptor tyrosine kinases (Clapham et al. 2005). The function of the PDZ domain in TRPC5 has not been as thoroughly explored. TRPC5 has generally been

found to behave as a receptor-operated calcium channel (Vazquez et al. 2004). Both TRPC4 and TRPC5 channel currents are potentiated by lanthanides in contrast to the inhibitory effects seen in store-operated channels and other TRPC channels (Vazquez et al. 2004).

### *6.2.3 TRPC2, TRPC3, TRPC6 & TRPC7*

TRPC2 is a pseudogene and therefore is not translated in humans, but it is expressed as a functional protein in other mammals. Here, it is grouped with TRPC3, TRPC6 and TRPC7 because these four members can all be directly activated by lipids, specifically diacylglycerol (DAG), a product of phosphatidylinositol 4,5-bisphosphate ($PI(4,5)P_2$) degradation (Svobodova and Groschner 2016). Though the other TRPC family members have been shown to be regulated by lipids, seen through their localization to lipid rafts (LRDs) and other lipid targeted cellular locations, for these four members lipid binding is necessary and sufficient for channel activation (Svobodova and Groschner 2016; Ong et al. 2016). A range of affinities for lipids has been reported for all TRPC subfamily channels, as well as a multitude of interaction mechanisms. Currently, both direct binding of lipids to cause activation, and indirect binding of lipids using adaptor proteins are possible for activation and/or localization for TRPC2, TRPC3, TRPC6 and TRPC7, since an exact lipid binding pocket has yet to be elucidated (Svobodova and Groschner 2016).

## 6.3 TRPV Subfamily

Transient receptor potential vanilloid (TRPV) channels were named based on the activation of the founding member of this group by capsaicin, a vanilloid-like molecule. This original TRPV channel was initially known as VR1 (Caterina et al. 1997). In this 1997 study, it was shown that VR1, expressed in sensory neurons, is activated by capsaicin, the active ingredient in chilies, by temperature higher than 42 °C and by protons. Due to the structural similarity of VR1 with other known TRP channels it was later renamed TRPV1. Subsequently five additional members of this subfamily were cloned and named TRPV2, TRPV3, TRPV4, TRPV5 and TRPV6 (Fig. 6.1) (Kanzaki et al. 1999; Smith et al. 2002; Xu et al. 2002; Strotmann et al. 2000; Liedtke et al. 2000; Caterina et al. 1999). Initially all the members of TRPV subfamily were thought to be heat sensors like TRPV1, but extensive physiological studies and knockout mice later revealed that although TRPV2-6 have more than 50% sequence homology with TRPV1, they do not all respond to temperature stimuli. Moreover, TRPV1-4 channels have nonselective cation conducting pores while the pores of TRPV5 and TRPV6 are highly calcium selective. Recently, high resolution structures of TRPV1 (Gao et al. 2016; Cao et al. 2013; Liao et al. 2013) (Fig. 6.2a, b), TRPV2 (Huynh et al. 2014, 2016; Zubcevic et al. 2016) (Fig. 6.2c, d)

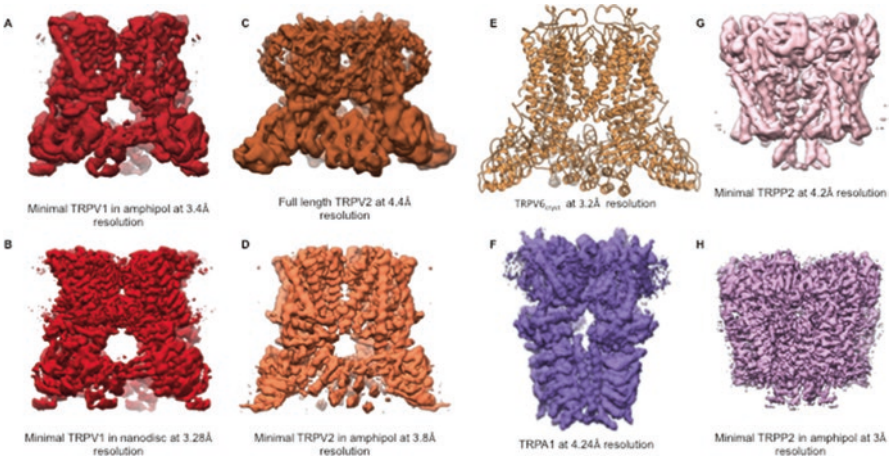


**Fig. 6.2** Select high resolution structures of TRP channels. (**a**) and (**b**) Cryo-EM density maps of TRPV1 (Liao et al. 2013; Gao et al. 2016). (**c**) and (**d**) Cryo-EM density maps of TRPV2 (Huynh et al. 2016; Zubcevic et al. 2016). (**e**) X-ray crystal structure of TRPV6 (Saotome et al. 2016). (**f**) Cryo-EM density map of TRPA1 (Paulsen et al. 2015). (**g**) and (**h**) Cryo-EM density maps of TRPP2 (Grieben et al. 2016; Shen et al. 2016)

and TRPV6 (Saotome et al. 2016) (Fig. 6.2e) have been resolved using cryo-electron microscopy (cryo-EM) and X-ray crystallography which has helped to elucidate the physiological characteristics of this subfamily as a whole as well as the finer details and differences of the individual members. These structures also provide the first glimpse into the architectural details of the TRP channel superfamily.

### *6.3.1 TRPV1*

TRPV1 is expressed in sensory neurons and is activated by capsaicin, protons, toxins and temperature in the noxious range (>42 °C), making it physiologically important for thermal and chemical nociception. To date, TRPV1 is the most well characterized and extensively studied mammalian TRP channel. These studies have provided a wealth of information about its physiological and biophysical properties as well as its role in disease and its potential as a therapeutic target.

Functional TRPV1 is a homotetramer, with each monomer consisting of six ankyrin repeats in the cytosolic N-terminal domain, a transmembrane domain containing six transmembrane helices (S1-S6) with a pore forming P-loop between S5 and S6 and a TRP domain in the cytosolic C-terminal domain. The crystal structure of the ankyrin repeat domain was solved in 2007 by Rachelle Gaudet's group (Lishko et al. 2007) and the first full length single particle cryo-EM structure of TRPV1 was resolved to 19 Å resolution (Moiseenkova-Bell et al. 2008).

The detailed architecture of a TRP channel was first elucidated in 2013 when the structure of a truncated, functional TRPV1 channel, called "minimal TRPV1", was resolved to 3.4 Å resolution (Liao et al. 2013) (Fig. 6.2a). This was also the first time that cryo-EM was used to reconstruct the 3D structure of a small membrane protein to near atomic resolution. Additionally, the structure of TRPV1 in the presence of the vanilloid agonist capsaicin and resiniferatoxin/Double-knot toxin (RTX/DkTx) were also resolved by the same group at that time to resolutions 4.2 Å and 3.8 Å respectively (Cao et al. 2013). This advancement in structural analysis of small proteins was possible due to the development of direct electron detectors, improved image processing algorithms that allowed correction of motion induced blurring, and the improvement of signal to noise ratio in cryo-EM data.

The near atomic resolution structure of minimal TRPV1 in the apo state displayed a fourfold symmetry along a central ion permeating pathway. The ion conducting pore is formed by transmembrane segments 5 and 6 (S5 and S6) and the pore forming P loop, which has an overall similarity to that of voltage gated $Na^+$ and $K^+$ channels. However, unlike the voltage gated ion channels where S1–S6 constitutes the voltage sensing domain and undergoes significant conformational rearrangement during channel gating, the S1-S4 of TRPV1 remains fairly static between closed, partially open and fully open state. Although the overall topology of the pore region is analogous to $Na_V$ channels, TRPV1 has a flexible selectivity filter due to the absence of hydrogen bonding within and between adjacent pore helices (Liao et al. 2013).

The flow of ions through the pore is controlled by a dual gating mechanism consisting of an upper gate located in the selectivity filter region and a lower gate formed by residue Ile679 (Fig. 6.3). Comparison of the apo state structure with the capsaicin bound and RTX/DkTx bound structures further illustrate the dual gate

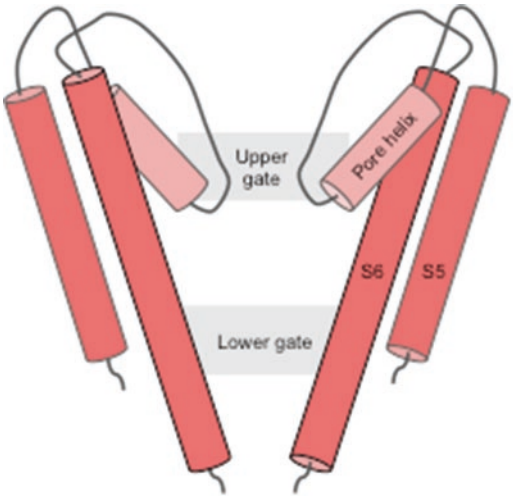


| TRP protein | Upper Gate | Lower Gate |
|---|---|---|
| TRPV1 | Gly643 and Met644 | Ile679 |
| TRPV2 | Gly604 and Met605 | Met643 |
| TRPV6 | Asp541 | Met577 |
| TRPA1 | Asp915 | Ile957 and Val961 |
| TRPP2 | Ile641, Gly642 and Asp643 | Leu677 and Asn681 |

**Fig. 6.3** A schematic representation of the the TRP channel pore showing the two regions of constriction (gates). The residues forming the two gates in various TRP proteins are listed in the Table on the right

architecture. In the apo state, the pore is constricted both at the selectivity filter region and at the lower gate (I679). In the capsaicin bound state, capsaicin does not affect the selectivity filter region, but the lower gate expands significantly. In the RTX/DkTx bound structure there is no apparent constriction in the ion-conducting path (Cao et al. 2013). Recently, the structure of TRPV1 reconstituted in nanodiscs was resolved at a higher resolution by the same group (Gao et al. 2016). The nanodisc-stabilized structures elucidated some of the important putative regions of lipid interaction with TRPV1 in a membrane bilayer system. The fully open RTX/DkTx bound state showed formation of a lipid, channel and toxin tripartite complex, suggesting how toxin binding stabilizes the open state. Aromatic side chain residues, tryptophan and phenylalnine, from finger 1 and finger 2 of the double-knot toxin forms hydrophobic interaction with the aliphatic tail of a phospholipid whose polar head group interacts with channel residues Arg534, present in the extracellular loop connecting S3 and S4, and Ser629, present in the pore loop domain, respectively. Additionally, the study also suggests the vanilloid-binding pocket, between S3, S4, S4-S5 linker and the TRP domain, to be a plausible phosphatidylinositide-binding region in the apo channel (Gao et al. 2016).

### *6.3.2 TRPV2*

The second member of the TRPV subfamily, TRPV2, was cloned because of its homology to TRPV1 (Kanzaki et al. 1999; Caterina et al. 1999). Like TRPV1, TRPV2 was described as a heat sensor, specifically as a noxious heat sensor (>52 °C) in heterologous expression systems. However, later studies and knockout mice models suggested otherwise since TRPV2 knockout mice displayed normal thermo sensation and had prenatal lethality (Park et al. 2011).

TRPV2 is ubiquitously expressed in various tissues types including both neuronal and non-neuronal tissues. This channel has been implicated in various physiological processes, such as nerve growth, and a variety of disease states, including cancer. The Moiseenkova-Bell lab has recently shown that TRPV2 has a punctate distribution in DRG neurons and other neuronal cell lines and it co-localizes with Rab7, a late endosomal marker in these cell lines (Cohen et al. 2015). Although TRPV1 and TRPV2 have 50% sequence homology and the overall structures at low resolution looks very similar, the near atomic resolution structures show some differences.

The structure of full length TRPV2 was first resolved at ~13 Å resolution in 2014 and was later resolved to ~5 Å in 2016 (Fig. 6.2c) (Huynh et al. 2014, 2016). This was the first time a full length TRP channel was resolved to near atomic resolution. Another group published ~4 Å resolution structure of a truncated TRPV2 construct (Fig. 6.2d) recently (Zubcevic et al. 2016). The pore region of TRPV2, like that of TRPV1, demonstrated two regions of constriction (Fig. 6.3), one in the selectivity filter region and another at the distal part S6 helix. However, the pore of full length apo TRPV2 was shown to be much wider than the pore of apo TRPV1, suggesting

apo TRPV2 may be able to accommodate partially hydrated cations and other large organic ions. Interestingly, the lower gate of apo TRPV2 is wider than that of RTX/DkTx bound TRPV1. The truncated structure of TRPV2 in the apo state, however, had a pore similar to that of apo TRPV1, with both the gates closed. This difference in the structures of TRPV2 can be attributed to either the truncation of the pore turret region or to the differences in channel properties between different mammalian orthologous (mouse vs rabbit).

### *6.3.3 TRPV3 & TRPV4*

TRPV3 and TRPV4 were also cloned and hypothesized to be heat sensors due to their homology to TRPV1. TRPV3 was found to be responsible for detecting innocuous warm temperature ranging from 31 to 39 °C. It is expressed in various tissues and organs, but the most pronounced expression of TRPV3 is in the epithelial cells of skin, the oral cavity and the gastrointestinal tract. TRPV3 knockout mice had strong deficit in response to innocuous heat sensitivity (Moqrich et al. 2005). However, a later study demonstrated that this deficit in thermo sensation was dependent on the background strain used for developing the knockout mice (Huang et al. 2011). Recently, TRPV3 has gained importance as a channel essential in maintaining skin health.

The role of TRPV4 in thermo sensation is also controversial with studies done in heterologous expression systems, native tissues and knockout mice giving conflicting results (Garcia-Elias et al. 2014; Guler et al. 2002; Huang et al. 2011). TRPV4 has a wide and varied expression pattern in the body (Everaerts et al. 2010). It has been shown to respond to osmotic changes in cellular environment and mechanical stress (Liedtke and Friedman 2003; Strotmann et al. 2000; Wu et al. 2007; Gao et al. 2003; Kohler et al. 2006). Therefore, it has an established role in osmoregulation and mechanotransduction in the body.

### *6.3.4 TRPV5 & TRPV6*

TRPV5 and TRPV6 are unique from other TRP channels in that they are highly calcium selective. Therefore, they have a significant contribution in calcium homeostasis in the body. TRPV5 and TRPV6 have high sequence homology (~75%) at the amino acid level and can form both homotetrameric and heterotetrameric functional units (Hoenderop et al. 2003). TRPV5 is exclusively expressed in the kidney, while TRPV6 has a wide tissue distribution, including in intestinal, pancreatic and placental tissues. Both TRPV5 and TRPV6 are present in the apical membrane of the epithelial cells and act as the entryway for $Ca^{2+}$ during absorption and reabsorption. They are constitutively active channels when present in the plasma membrane, but are inactivated in the presence of high $Ca^{2+}$, preventing $Ca^{2+}$ poisoning of the cells.

Recently the crystal structure of TRPV6 was resolved with some modifications ($TRPV6_{cryst}$) at 3.2 Å (Saotome et al. 2016) (Fig. 6.2e). Overall the structure is very similar to that of TRPV1 and TRPV2 (Cao et al. 2013; Huynh et al. 2016). The ion conducting pathway has two gates, one in the selectivity filter region formed by Asp541, which is critical for calcium selectivity, and the other at the lower end of the pore formed by Met577, similar to that of full length TRPV2 structure (Huynh et al. 2016). It was proposed that the selectivity filter of TRPV6 is more static in contrast to other TRPV channels. The flexibility of the selectivity filter was thought to be required for pore dilation as seen in ligand bound TRPV1 channel structures(Cao et al. 2013). A highly electro-negative outer region of the pore likely assists in the recruitment of $Ca^{2+}$ ions to the pore. It was further proposed that calcium permeation of TRPV6 occurs via a "knock-off" mechanism similar to that of $Ca_v$ channels and the rate-limiting step in this process is knocking off the $Ca^{2+}$ ion from D541 site (Saotome et al. 2016).

## 6.4 TRPM Subfamily

The melastatin-related TRP (TRPM) subfamily contains similar structural regions compared to the other TRP subfamilies, including the presence of six membrane spanning regions, cytoplasmic C- and N-terminal domains and a C-terminal TRP motif (Kraft and Harteneck 2005). TRPM channels also contain a C-terminal tetrameric coiled-coil domain, the structure of which was solved by the Minor Jr. group in 2008 using X-ray crystallography (Fujiwara and Minor 2008). Interestingly, each member of this subfamily contains an N-terminal 'TRPM homology region' that is involved in channel assembly and trafficking that is not seen in other TRP channels (Kraft and Harteneck 2005). Another defining characteristic of this subfamily is the lack of N-terminal ankyrin repeats that is commonly seen in other subfamilies (Kraft and Harteneck 2005). The large C-terminal sections of TRPM channels are highly varied between subfamily members with TRPM2, TRPM6 and TRPM7 containing active enzymatic domains in this region.

Originally, most members of this subfamily were cloned from cancerous tissues and were therefore implicated in tumorigenesis, proliferation and differentiation (Kraft and Harteneck 2005). After nearly two decades of research, members of this subfamily have also been found to be involved in temperature sensation, magnesium ($Mg^{2+}$) homeostasis and taste (Fujiwara and Minor 2008; Hashimoto and Kambe 2015). The TRPM subfamily has been shown to have vastly differing modes of activation, cation selectivities and tissue distributions (Hofmann et al. 2003). Here, the TRPM subfamily is presented in four groups based on structural similarity (I) TRPM1 & TRPM3 (II) TRPM4 & TRPM5 (III) TRPM2, TRPM6 & TRPM7 and (IV) TRPM8 (Fig. 6.1).

### 6.4.1 TRPM1 & TRPM3

The first member of the TRPM subfamily, TRPM1, originally named melastatin, is a $Ca^{2+}$ permeable ion channel that was first cloned from benign melanomas (Duncan et al. 1998). This protein was found to be an indicator of melanoma aggressiveness since it was found to be expressed at higher levels in non-metastatic melanomas (Duncan et al. 1998). Due to this correlation, TRPM1 was found to be a tumor suppressor and a potential prognostic marker for metastatic melanomas (Brozyna et al. 2016). In non-cancerous human tissues, TRPM1 is found only in the brain, melanocytes, macrophages and heart, all at very low levels (Fonfria et al. 2006).

TRPM3 is a $Ca^{2+}$ permeable, non-selective cation channel that can function as a homotetramer or in complex with TRPM1 (Held et al. 2015). Molecular activators of TRPM3 include sphingolipids, pregnenolone sulfate (PS), and nifedipine (Held et al. 2015). Other stimuli of TRPM3 include cell swelling and heat (40 °C) (Held et al. 2015). Although TRPM3 was originally thought to be involved in glucose induced insulin release in the β-cells of the pancreas, TRPM3 knockout mice showed normal glucose metabolism (Held et al. 2015). Other studies have shown that physiologically TRPM3 plays an important role in heat sensation in the somatosensory system (Held et al. 2015). Mutations in TRPM3 have been found in hereditary eye diseases such as cataracts and some high-tension glaucomas (Held et al. 2015).

### 6.4.2 TRPM4 & TPRM5

Both TRPM4 and TRPM5 are distinct from the other members of the TRPM subfamily, and the TRP family of channels in general, because they are impermeable to $Ca^{2+}$ (Zholos et al. 2011). Rather, they are only permeable to monovalent cations including sodium ($Na^{+}$) and potassium ($K^{+}$) (Zholos et al. 2011). Because of this, TRPM4 and TRPM5 are considered to be $Ca^{2+}$ activated, non-specific cation (CAN) channels (Kraft and Harteneck 2005). Voltage modulation of both of these channels has been reported and the sensitivity to $Ca^{2+}$ gating of these channels can be altered by changes in temperature, calmodulin binding, $PIP_2$ binding and channel phosphorylation (Zholos et al. 2011).

TRPM4 is highly expressed throughout the body with high levels present in the intestine and prostate (Fonfria et al. 2006). TRPM5, on the other hand, is expressed in discrete tissues with high expression in the intestines and taste buds (Fonfria et al. 2006; Zholos et al. 2011). In the taste buds, TRPM5 has been shown to be a transducer of bitter, sweet and umami taste sensation (Liman 2007). This was confirmed using mice models lacking functional TRPM5. These mice exhibited a drastic reduction in response to those tastes, while sour and salty taste sensations were unaffected (Liman 2007). Bitter, sweet and umami taste sensations are regulated by G-protein coupled receptor signal cascades and TRPM5 is thought to be a downstream target of these pathways (Liman 2007). The role of TRPM5 in the intestines is thought to be related to post-ingestion chemosensation (Liman 2007).

### 6.4.3 TRPM2, TRPM6 & TRPM7

TRPM2, TRPM6 and TRPM7 are unique because they are bifunctional proteins. In addition to being cation permeable channels, these TRPM members also contain functional enzymatic domains in their C-terminal segments (Kraft and Harteneck 2005). The catalytic domain of TRPM2 has sequence homology to Nudix hydrolases. TRPM2 has been shown to be activated by ADP-ribose and reactive oxygen species (ROS), which implicates this channel in cellular redox sensation (Kraft and Harteneck 2005). TRPM2 is permeable to $Ca^{2+}$, $Mg^{2+}$, and monovalent cations (Kraft and Harteneck 2005). In human tissues, TRPM2 was found to be widely expressed with the highest levels in the brain, macrophages and bone marrow (Fonfria et al. 2006).

TRPM6 and TRPM7 are highly sequence homologous and hence both have the ability to permeate $Mg^{2+}$, $Zn^{2+}$ and $Ca^{2+}$, though they are most often studied for their role in the whole organism and cellular $Mg^{2+}$ homeostasis (Komiya and Runnels 2015). The enzymatic domains of these two channels are classified as atypical alpha protein kinases (Kraft and Harteneck 2005). These two TRPM members have been shown to form functional heterotetrameric channels (Li et al. 2006). A lack of either TRPM6 or TRPM7 was found to be embryonically lethal and several magnesium-related diseases have been linked to mutations in these channels. For example, autosomal-recessive hypomagnesemia with secondary hypocalcemia (HSH) is correlated to mutations in the *TRPM6* gene (Nilius et al. 2007).

In spite of these similarities, the tissue distributions of TRPM6 and TRPM7 are widely divergent. TRPM6 is found at highest levels in the intestines where it has been shown to be involved in dietary $Mg^{2+}$ uptake (Hashimoto and Kambe 2015; Fonfria et al. 2006). It is also found at relatively high levels in the brain, pituitary, and the distal convoluted tubule (DCT) of the kidney (Fonfria et al. 2006). TRPM7, on the other hand, is ubiquitously expressed in the human body (Fonfria et al. 2006).

### 6.4.4 TRPM8

One of the most thoroughly explored members of this subfamily is TRPM8, which is best known for its cold sensing ability. In addition to thermosensation, TRPM8 has also been shown to be involved in pain sensation, thermoregulation, bladder function and cancer (Liu et al. 2016). TRPM8 is a non-selective, $Ca^{2+}$ permeable, outwardly rectifying cation channel (McKemy 2007; Liu et al. 2016). Of the TRPM subfamily, TRPM8 is the most selective for $Ca^{2+}$ with a selectivity ratio ($P_{Ca}/P_{Na}$) of 3.3 (Zholos et al. 2011). This channel was originally cloned from a prostate cDNA library screen (Tsavaler et al. 2001). It was found to be involved in prostate cancer, specifically there was found to be an androgen dependent overexpression of TRPM8 in androgen receptor positive prostate cancers (Liu et al. 2016). TRPM8 is involved in a variety of other cancers including adenocarcinoma, melanomas, as

well as lung and breast cancers (Liu et al. 2016). In 2002, two independent research groups identified TRPM8 as a cold (<28 °C) and menthol activated ion channel (McKemy et al. 2002; Peier et al. 2002). Other chemical agonists for TRPM8 include cooling agents such as eucalyptol and icilin (Liu et al. 2016). The temperature threshold of TRPM8 can be modulated by changes in membrane potential, arachidonic acid, lysophospholipids and $PIP_2$ (Liu et al. 2016). There is also evidence that G-proteins are involved in regulation of TRPM8, specifically, Gαq is involved in the inflammation mediated inhibition of TRPM8 (Liu et al. 2016).

## 6.5 TRPA Subfamily

Transient receptor potential ankyrin 1 (TRPA1) is the solitary member of the mammalian TRPA subfamily (Fig. 6.1). It was discovered as an ankyrin-like transmembrane protein, with similarities to existing TRP channels (Jaquemar et al. 1999). Like other TRP channels, TRPA1 also has a cytosolic N-terminal domain, a transmembrane domain containing six transmembrane helices with a transmembrane loop between S5 and S6 and a cytosolic C-terminal domain. It is a unique channel within the superfamily in that it lacks the TRP motif and it contains 14–17 ankyrin repeats in the N-terminal domain. This abundance of ankyrin repeats is why it is known as the ankyrin subfamily. TRPA1 was proposed to be a putative noxious cold sensor, but it is now best described as chemo-nociceptor, making it an ideal target for analgesics (Story et al. 2003). The TRPA1 channel is expressed in both peptidergic and non-peptidergic neurons like Aδ and C-fiber and in some myelinated Aβ-fibers (Zygmunt and Hogestatt 2014). It is also expressed in TRPV1 expressing neurons and in non-neuronal cells such as epithelial cells, melanocytes, mast cells, fibroblasts, and enterochromaffin cells (Zygmunt and Hogestatt 2014).

TRPA1 is a polymodal channel in a true sense. It is a homotetrameric, non-selective cation channel, activated by a long list of exogenous and endogenous compounds. The most well-known activators of TRPA1 are various cysteine and lysine reactive electrophilic molecules like allyl isothiocyanate (AITC), the active ingredient in mustard oil and wasabi, cinnamaldehyde which is an extract from cinnamon, allicin from garlic extract and acrolein from fume exhaust (Bautista et al. 2006; Bandell et al. 2004; Nilius et al. 2012). Additionally, TRPA1 is also activated by non-electrophilic molecules like menthol and cannabinoids (Jordt et al. 2004; Karashima et al. 2007). It is also modulated by various endogenous ligands like bradykinin, $H_2O_2$, and nitrated lipids like nitro oleic acid (Bandell et al. 2004; Takahashi et al. 2011; Takahashi and Mori 2011). Mutational studies along with other biochemical, electrophysiological and biophysical methods have established that the reactive ligands interact with TRPA1 via a cluster of cysteine and lysine residues present in the N-terminus of the channel (Hinman et al. 2006; Macpherson et al. 2007), but the molecular mechanism of TRPA1 channel modulation by non-reactive ligands is still largely unknown.

The first glimpse into the structure of TRPA1 was provided by a ~16 Å resolution EM structure resolved by the Moiseenkova-Bell lab in 2011 (Cvetkov et al. 2011). Although this structure provided insight regarding the boundaries of the transmembrane domain and cytoplasmic domain, it gave no information about the molecular architecture of TRPA1. In 2015, a near atomic resolution structure of TRPA1 at ~4 Å was resolved using cryo-EM (Fig. 6.2f) (Paulsen et al. 2015). Although full length protein was used for cryo-EM, 3D reconstruction was only successful for ~ 50% of the channel. Overall, the transmembrane domain structure resembles those of TRPV1 and V2 structures, containing six transmembrane helices and a reentrant pore loop, with some differences in the pore region. The ion path is gated by two restriction points, the upper gate is formed by Asp915 (Gly643 and Met644 in TRPV1) and the lower gate is made up of two hydrophobic residues Ile957 and Val961 (Ile679 in TRPV1) (Fig. 6.3). The outer region of the pore has two short pore helices similar to those seen in $Na_v$ channels. In the cytoplasmic region, the C-terminus forms a coiled coil central stalk-like domain, which is flanked by the ankyrin repeats of the N-terminus. Human TRPA1 is thought to have at least 16 ankyrin repeats, out of which only five were resolved in this ~4 Å structure, with the other 11 ankyrin repeats remaining unresolved (Fig. 6.2f) (Paulsen et al. 2015). 3D reconstructions of TRPA1 both in the presence of agonist and antagonists were performed, but no differences between the open and closed structures were identified. Therefore, these structures have served to elucidate the general molecular structure of TRPA1, but a full length TRPA1 structure and the molecular mechanisms of channel activation have remained elusive.

## 6.6 TRPML Subfamily

The mucolipin transient receptor potential (TRPML) subfamily consists of three $Ca^{2+}$ permeable cation channels known as TRPML1 (MCOLN1), TRPML2 (MCOLN2) and TRPML3 (MCOLN3) (Fig. 6.1). Physically, these channels are the smallest in the TRP superfamily with each channel measuring <600 amino acids in length (Noben-Trauth 2011; Flores and García-Añoveros 2011; Colletti and Kiselyov 2011). Though they have the typical TRP six transmembrane segments with cytosolic N- and C-termini, this subfamily has not been reported to contain any ankyrin repeats or a complete TRP motif (Noben-Trauth 2011; Flores and García-Añoveros 2011; Colletti and Kiselyov 2011). Additionally, these channels unlike others in the family are mostly localized to intracellular compartments instead of the plasma membrane (Venkatachalam et al. 2015). The localization of these channels is controlled by two di-leucine motifs, one in the N-terminus and the other in the C-terminus (Wang et al. 2014). Their function in intracellular compartments is not completely understood, but they are implicated in a variety of vesicular trafficking events (Venkatachalam et al. 2015). Another distinguishing feature of this subfamily is the presence of a large highly N-glycosylated luminal loop between the first and second transmembrane segments (Wang et al. 2014). Homomeric and heteromeric complexes for all three channels have been reported (Cuajungco et al. 2016).

### 6.6.1 TRPML1

The first member of the TRPML subfamily was discovered because of its role in the autosomal-recessive lysosomal storage disease (LSD) known as type IV mucolipidosis (ML-IV) (Bassi et al. 2000). Patients with ML-IV have a mutation in the TRPML1 gene which manifests on a cellular level as an accumulation of late endosomes and lysosomes (LELs) and a build up of lysosomal storage materials (Wang et al. 2014). These patients show cognitive impairment and compromised motor skills beginning in years 1–2 of life and this disorder has been shown to have a degenerative component (Venkatachalam et al. 2015). Research regarding TRPML1 tends to focus on understanding this disease in order to produce treatments for these patients.

TRPML1 is an inwardly rectifying $Ca^{2+}$ permeable cation channel that is localized to LELs (Wang et al. 2014). This channel is ubiquitously expressed and has been shown to be involved in membrane trafficking, signal transduction, and LEL ion homeostasis (Wang et al. 2014). Currently there are no known splice variants of human TRPML1 (Wang et al. 2014). There is a predicted phosphatidylinositol 3,4-bisphosphate ($PI(3,5)P_2$) binding site in the N-terminus of this protein and, like TRPML2 and TRPML3, the presence of $PI(3,5)P_2$ activates the channel (Wang et al. 2014). For TRPML1, it has also been reported that phosphatidylinositol 4,5-bisphosphate ($PI(4,5)P_2$) can inhibit activation (Venkatachalam et al. 2015). This is interesting because $PI(3,5)P_2$ is found in higher abundance in intracellular vesicles and $PI(4,5)P_2$ is present mostly on the plasma membrane (Venkatachalam et al. 2015; Wang et al. 2014). This could potentially mean that even though TRPML1 can be found on the plasma membrane, it may not be active due to the presence of $PI(4,5)P_2$ (Wang et al. 2014; Venkatachalam et al. 2015). TRPML1 is permeable to a wide range of divalent and monovalent cations including $Ca^{2+}$, $Fe^{2+}$, $Na^+$ and $K^+$. While TRPML1 is not permeable to protons, it is pH sensitive (Wang et al. 2014).

### 6.6.2 TRPML2 & TRPML3

TRPML2 is the least studied of this subfamily because it has not been implicated in any disease or phenotype (Cuajungco et al. 2016). Trafficking of TRPML2 is mediated via the ADP-ribosylation factor (ARF)-6 associated pathway (Venkatachalam et al. 2015). This channel is found primarily in lymphoid and myeloid tissues and due to this distribution, recent studies have focused on the role of TRPML2 in the immune system (Cuajungco et al. 2016). TRPML2 co-localizes with several immune-associated proteins such as MHC-I, TLRs and Fc-εRI and is thought to be involved in trafficking these proteins (Cuajungco et al. 2016). Unlike many other TRP channels TRPML2 is not regulated by changes in $Ca^{2+}$ levels or linoleic acid, but it is, as mentioned previously, activated by the presence of $PI(3,5)P_2$ and is pH sensitive (Cuajungco et al. 2016; Wang et al. 2014).

While TRPML3, like TRPML2, does not have any known role in human diseases, this channel is of interest because of its involvement in varitint-waddler (*Va*) mouse phenotypes (Cuajungco et al. 2016). In short, the gain of function mutation A419P in TRPML3 causes a $Ca^{2+}$ overload in melanocytes which results in a hearing loss, vestibular disfunction and abnormal pigmentation in mice (Cuajungco et al. 2016). Additionally, a correlation has been shown between down-regulated TRPML3 and viral and bacterial infections such as cytomegalovirus infection, hemophilus infection and chlamydial infection (Grimm et al. 2014).

TRPML3 is localized to early endosomes, recycling endosomes, and LELs (Grimm et al. 2014). The tissue distribution of TRPML3 is broad with higher expression levels in the organs of the endocrine system as well as the kidney, intestines and lungs (Grimm et al. 2014). High sodium levels and low pH have been shown to inactivate this channel (Grimm et al. 2014). The pH sensitivity of this channel is controlled by regions in the luminal loop between first and second transmembrane region (Grimm et al. 2014). Several splice variants of human TRPML3 have been reported (Grimm et al. 2014). TRPML3 knockout mice have been shown to live healthy normal lives, though the model is limited due to the differences in tissue expression of TRPML3 in mice and humans (Grimm et al. 2014).

## 6.7 TRPP Subfamily

The transient receptor potential polycystin subfamily of TRP channels consists of integral membrane proteins, mutations in which attribute to the pathological condition called autosomal dominant polycystic kidney disease (ADPKD). The founding members of this group, TRPP2 (PKD2) and TRPP1 (PKD1) were identified by positional cloning of disease causing genes of ADPKD (Mochizuki et al. 1996; Consortium 1994; Hughes et al. 1995).

ADPKD is one of the most common, monogenic, progressive disorders affecting 1 in 400–1000 humans. It is characterized by formation of fluid filled cysts and enlargement of the kidneys gradually leading to renal failure. ADPKD is also associated with formation of cysts in extra-renal tissues like the liver, kidney stone formation, as well as hypertension and cardiovascular abnormalities. Mutation of the PKD1 gene accounts for 85% of the disease and the PKD2 gene mutation account for all other cases. These two mutations have indistinguishable pathologies.

The TRPP subfamily of TRP channel is present throughout the animal kingdom and yeast, making it likely the most ancient member of the TRP family (Venkatachalam and Montell 2007). TRPP2 is structurally homologous to other TRP channels in having six transmembrane helices and intracellular amino and carboxyl termini. However, TRPP1 has a large extracellular N-terminus, 11 transmembrane helices and a relatively small cytoplasmic C-terminus. It does not have much semblance to the prototypical TRP channel structure and is also not a functional ion channel. Therefore, it was renamed as Polycystin1 (PC1), an integral membrane glycoprotein. Polycystin1 together with TRPP2 form a receptor-channel signaling

complex, which plays important physiological roles from maintaining left-right symmetry to tubular morphogenesis. After the discovery of the two founding members, two other TRPP proteins, TRPP3 and TRPP5 (Fig. 6.1) and four other Polycystin1-like proteins, PKD1L1, PKD1L2, PKD1L3 and PKDREJ (TRPP4) were identified.

### *6.7.1 Polycystin Family*

Polycystin1 (PC1), one of the founding members of the TRPP subfamily, is a 462 kDa integral membrane protein whose domain architecture suggests that it is involved in receptor signaling and cell adhesion. Polycystin1 has a wide tissue distribution and is highly expressed in the tubular epithelial cells of the kidney, pancreas, liver and brain. Perinatal lethality of knockout mice due to large cystic kidneys suggests that Polycystin1 plays an important developmental role in the kidney (Lu et al. 1997). In the fetal kidney, Polycistin1 is present in both the apical and basolateral side of the tubular epithelial cells. However, in the adult kidney it is localized to the basolateral side at the interface between cell contact and extracellular matrix (Wilson 2001). Polycystin1 forms multiprotein complexes with various cell adhesion proteins thereby participating in cell adhesion. It also forms a signaling complex with TRPP2 where Polcystin1 may act as a receptor for the TRPP2 ion channel. Although, Polycystin1 was initially named as TRPP1, due to its lack of significant structural and functional characteristics of a TRP channel, its nomenclature has been changed to Polycystin1.

To-date, no structure of Polycystin1 is available, but from sequence analysis it is predicted to have a large extracellular N-terminus with various motifs for protein-protein and protein-ligand interaction, a transmembrane domain containing 11 transmembrane helices and a relatively small C-terminus. The extracellular domain contains two cysteine flanked, leucine rich domains that have been shown to interact with various extracellular matrix proteins like collagen type 1, laminin and fibronectin (Malhas et al. 2002). It also has a putative C-type lectin domain similar to those found in selectin and might play role in protein carbohydrate interaction and $Ca^{2+}$ sensitivity. The most interesting feature of the large extracellular domain of Polycystin1 is the presence of 16 immunoglobulin (IG) like PKD domains (Fig. 6.4). The 10th PKD domain is highly conserved between humans and Fugu fish suggesting a role in ligand binding. The most distal part of the extracellular domain contains a stretch of 1000 amino acid residues that is homologous to the sea urchin for egg jelly (REJ). The REJ domain is required for proteolytic cleavage of the extracellular domain of Polycistin1 in a G-protein coupled receptor proteolytic site (Qian et al. 2002). The transmembrane domain of Polycystin1 has 11 transmembrane helices (S1–S11) out of which S6–S11 share high sequence homology to the transmembrane domain of TRPP2 protein and contains an equivalent loop domain between S6 and S7. The short C-terminus of Polycystin1 has multiple potential phosphorylation sites and is involved in protein-protein interaction. It has a putative coiled coil

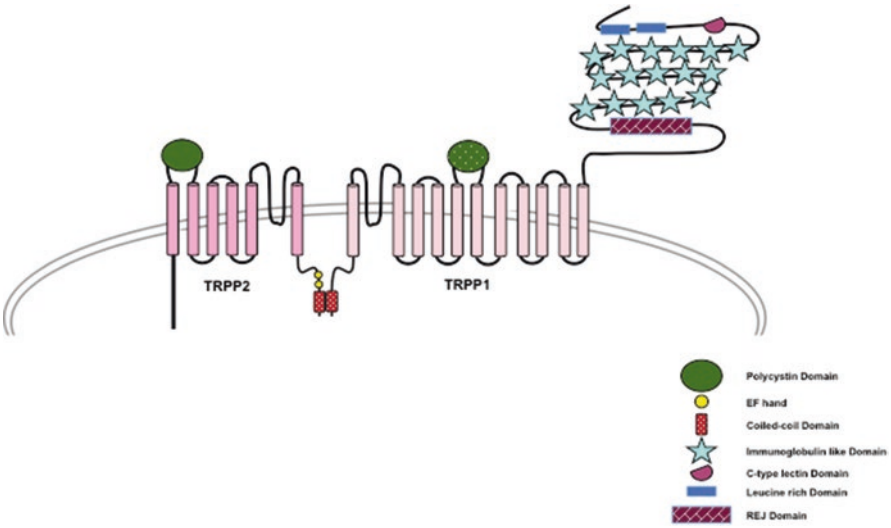


**Fig. 6.4** A schematic representation of TRPP1 and TRPP2 interacting with each other through their C-terminal region and forming the receptor-channel complex

domain that interacts with TRPP2, forming the receptor-channel complex (Fig. 6.4). The C-terminus can be cleaved and translocated to the nucleus in a process resembling Notch-mediated signaling via regulated intramembrane proteolysis (Chauvet et al. 2004).

Four other proteins that are related to Polycystin1 were identified by homology cloning and are now part of the Polycystin family. The members of Polycystin family have high sequence homology in their transmembrane segment but lower sequence similarity in the C-terminus and N-terminus. However, the family can be further categorized into two subsets based on their structural and physiological characteristics. PC1 and PKD1L1, both have a coiled coil domain in their C-terminus, but lack a functional ion channel-forming motif. On the contrary, PKD1L2, PKD1L3 and PKDREJ contain an ion transport motif but lack the coiled coil domain in the C-terminus.

### *6.7.2 TRPP2, TRPP3 and TRPP5*

TRPP2, a founding member of the TRPP subfamily, is the quintessential TRPP protein with an overall structural homology to other TRP ion channels. It has a ubiquitous expression pattern in the body although its precise subcellular localization and intracellular trafficking is debated, but there is general agreement about its presence in the primary cilia. TRPP2 is a tetrameric, nonselective monovalent and divalent cation permeable channel implicated in a wide array of cellular functions including fertilization, proliferation, mechanosensation and polarity (Giamarchi et al. 2006).

Each monomer of TRPP2 is a ~110 kDa protein containing a cytosolic N-terminal domain, a transmembrane domain made of six transmembrane helices (S1–S6) with a pore forming loop between S5 and S6 and a cytosolic C-terminus. The N-termini of TRPP channels are devoid of ankyrin repeats, but the C-terminal region contains a coiled coil domain, which is likely involved in protein-protein interaction, and an EF-hand motif. A unique feature of TRPP channels is the presence of a large extracellular loop between S1 and S2 consisting of 245 amino acid residues in TRPP2, 224 residues in TRPP3 and 225 amino acid residues in TRPP5 proteins.

Recently the structure of a "minimal" TRPP2 (hPKD2:198–703) construct reconstituted in nanodiscs and "truncated PC2 construct" in detergent were resolved to 3 Å and 4.2 Å resolution respectively, using cryo-EM (Fig. 6.2g, h) (Shen et al. 2016; Grieben et al. 2016). This structure gives a detailed understanding of the architecture of TRPP transmembrane domain. Overall the topology of this region is similar to other known Group1 TRP protein structures (TRPV1, TRPV2 and TRPA1) with S1 – S4 forming the voltage sensing domain (VSD) and S5 and S6 along with the reentrant pore loop forming the ion-conducting pathway. The pore of the TRPP2 channel also has two points of restriction, one residing in the selectivity filter region (Ile641, Gly642 and Asp643) and the second one located at the distal end of the pore (Leu677 and Asn681) near the inner leaflet of the bilayer (Fig. 6.3). The archetypical extracellular loop between S1 and S2 of TRPP proteins is named as the "polycystin" domain by the authors and acquires a novel three-layered fold; with the top layer comprising three α helices, the second layer made up of a five-stranded antiparallel β-sheet and the third layer consisting of two fingers (finger 1 and finger 2). This polcystin domain contributes to channel assembly via interaction with adjacent polycystin domain of other subunits and might also be instrumental in allosterically modulating the channel due its strategic location above the VSD.

TRPP3 was the first homologue of TRPP2 to be identified (Veldhuisen et al. 1999) followed by TRPP5. TRPP3 and TRPP5 have high levels of sequence homology to the transmembrane segment of TRPP2, 78% and 71% respectively. However, the amino and the carboxyl termini have a very low degree of sequence homology. The major difference between TRPP2 and TRPP3 is in their amino termini where TRPP3 lacks a 100 amino acid segment. TRPP3 is expressed in a wide variety of tissues including neurons, testis, kidney and non-myocyte cardiac tissue. The precise physiological function of TRPP3 and TRPP5 is still elusive.

## 6.8 Conclusions

TRP channels are polymodal channels in a true sense, in that most of the superfamily members can be activated by a multitude of stimuli. They were known to be vital for sensory physiology, but recent studies have established that TRP channels are crucial players in various other physiological and pathological conditions like cancer, renal physiology, cardiac health and neuronal development. Therefore, most TRP channels are important therapeutic targets. Though there is much known about

these channels, much controversy exists in this field regarding their physiological functions. This may be a result of the majority of the TRP channels originally being identified through sequence homology rather than function derived identification. Recent advancement in the field of cryo-EM has enabled near atomic resolution structures of some of the TRP channels, giving a glimpse into their molecular architecture. The structural information will help in establishing some of the functional characteristics of these channels and will also be beneficial for drug development. Resolving more structures will be important for the better understanding this family of ion channels.

## References

Bandell M, Story GM, Hwang SW, Viswanath V, Eid SR, Petrus MJ, Earley TJ, Patapoutian A (2004) Noxious cold ion channel TRPA1 is activated by pungent compounds and bradykinin. Neuron 41(6):849–857

Bassi MT, Manzoni M, Monti E, Pizzo MT, Ballabio A, Borsani G (2000) Cloning of the gene encoding a novel integral membrane protein, mucolipidin-and identification of the two major founder mutations causing mucolipidosis type IV. Am J Hum Genet 67(5):1110–1120. https://doi.org/10.1016/s0002-9297(07)62941-3

Bautista DM, Jordt SE, Nikai T, Tsuruda PR, Read AJ, Poblete J, Yamoah EN, Basbaum AI, Julius D (2006) TRPA1 mediates the inflammatory actions of environmental irritants and proalgesic agents. Cell 124(6):1269–1282. https://doi.org/10.1016/j.cell.2006.02.023

Brozyna AA, Guo H, Yang SE, Cornelius L, Linette G, Murphy M, Sheehan C, Ross J, Slominski A, Andrew Carlson J (2016) TRPM1 (melastatin) expression is an independent predictor of overall survival in clinical AJCC stage I and II melanoma patients. J Cutan Pathol. https://doi.org/10.1111/cup.12872

Cao E, Liao M, Cheng Y, Julius D (2013) TRPV1 structures in distinct conformations reveal activation mechanisms. Nature 504(7478):113–118. https://doi.org/10.1038/nature12823

Caterina MJ, Schumacher MA, Tominaga M, Rosen TA, Levine JD, Julius D (1997) The capsaicin receptor: a heat-activated ion channel in the pain pathway. Nature 389(6653):816–824. https://doi.org/10.1038/39807

Caterina MJ, Rosen TA, Tominaga M, Brake AJ, Julius D (1999) A capsaicin-receptor homologue with a high threshold for noxious heat. Nature 398(6726):436–441. https://doi.org/10.1038/18906

Chauvet V, Tian X, Husson H, Grimm DH, Wang T, Hiesberger T, Igarashi P, Bennett AM, Ibraghimov-Beskrovnaya O, Somlo S, Caplan MJ (2004) Mechanical stimuli induce cleavage and nuclear translocation of the polycystin-1 C terminus. J Clin Invest 114(10):1433–1443. https://doi.org/10.1172/jci21753

Clapham DE, Julius D, Montell C, Schultz G (2005) International union of pharmacology. XLIX. Nomenclature and structure-function relationships of transient receptor potential channels. Pharmacol Rev 57(4):427–450. https://doi.org/10.1124/pr.57.4.6

Cohen MR, Johnson WM, Pilat JM, Kiselar J, DeFrancesco-Lisowitz A, Zigmond RE, Moiseenkova-Bell VY (2015) Nerve growth factor regulates transient receptor potential vanilloid 2 via extracellular signal-regulated kinase signaling to enhance neurite outgrowth in developing neurons. Mol Cell Biol 35(24):4238–4252. https://doi.org/10.1128/MCB.00549-15

Colletti GA, Kiselyov K (2011) TRPML1. In: Islam MS (ed) Transient receptor potential channels. Springer Netherlands, Dordrecht, pp 209–219. https://doi.org/10.1007/978-94-007-0265-3_11

Consortium TEPKD (1994) The polycystic kidney disease 1 gene encodes a 14 kb transcript and lies within a duplicated region on chromosome 16. The European Polycystic Kidney Disease Consortium. Cell 77(6):881–894

Cosens DJ, Manning A (1969) Abnormal electroretinogram from a Drosophila mutant. Nature 224(5216):285–287

Cuajungco MP, Silva J, Habibi A, Valadez JA (2016) The mucolipin-2 (TRPML2) ion channel: a tissue-specific protein crucial to normal cell function. Pflugers Arch – Eur J Physiol 468(2):177–192. https://doi.org/10.1007/s00424-015-1732-2

Cvetkov TL, Huynh KW, Cohen MR, Moiseenkova-Bell VY (2011) Molecular architecture and subunit organization of TRPA1 ion channel revealed by electron microscopy. J Biol Chem 286(44):38168–38176. https://doi.org/10.1074/jbc.M111.288993

Dietrich A, Fahlbusch M, Gudermann T (2014) Classical transient receptor potential 1 (TRPC1): channel or channel regulator? Cell 3(4):939–962. https://doi.org/10.3390/cells3040939

Duncan LM, Deeds J, Hunter J, Shao J, Holmgren LM, Woolf EA, Tepper RI, Shyjan AW (1998) Down-regulation of the novel gene melastatin correlates with potential for melanoma metastasis. Cancer Res 58(7):1515–1520

Everaerts W, Nilius B, Owsianik G (2010) The vanilloid transient receptor potential channel TRPV4: from structure to disease. Prog Biophys Mol Biol 103(1):2–17. https://doi.org/10.1016/j.pbiomolbio.2009.10.002

Flores EN, García-Añoveros J (2011) TRPML2 and the evolution of mucolipins. In: Islam MS (ed) Transient receptor potential channels. Springer Netherlands, Dordrecht, pp 221–228. https://doi.org/10.1007/978-94-007-0265-3_12

Fonfria E, Murdock PR, Cusdin FS, Benham CD, Kelsell RE, McNulty S (2006) Tissue distribution profiles of the human TRPM cation channel family. J Recept Signal Transduct Res 26(3):159–178. https://doi.org/10.1080/10799890600637506

Fujiwara Y, Minor DL Jr (2008) X-ray crystal structure of a TRPM assembly domain reveals an antiparallel four-stranded coiled-coil. J Mol Biol 383(4):854–870. https://doi.org/10.1016/j.jmb.2008.08.059

Gao X, Wu L, O'Neil RG (2003) Temperature-modulated diversity of TRPV4 channel gating: activation by physical stresses and phorbol ester derivatives through protein kinase C-dependent and -independent pathways. J Biol Chem 278(29):27129–27137. https://doi.org/10.1074/jbc.M302517200

Gao Y, Cao E, Julius D, Cheng Y (2016) TRPV1 structures in nanodiscs reveal mechanisms of ligand and lipid action. Nature 534(7607):347–351. https://doi.org/10.1038/nature17964

Garcia-Elias A, Mrkonjic S, Jung C, Pardo-Pastor C, Vicente R, Valverde MA (2014) The TRPV4 channel. Handb Exp Pharmacol 222:293–319. https://doi.org/10.1007/978-3-642-54215-2_12

Giamarchi A, Padilla F, Coste B, Raoux M, Crest M, Honore E, Delmas P (2006) The versatile nature of the calcium-permeable cation channel TRPP2. EMBO Rep 7(8):787–793. https://doi.org/10.1038/sj.embor.7400745

Grieben M, Pike ACW, Shintre CA, Venturi E, El-Ajouz S, Tessitore A, Shrestha L, Mukhopadhyay S, Mahajan P, Chalk R, Burgess-Brown NA, Sitsapesan R, Huiskonen JT, Carpenter EP (2016) Structure of the polycystic kidney disease TRP channel Polycystin-2 (PC2). Nat Struct Mol Biol Adv Online Publ https://doi.org/10.1038/nsmb.3343; http://www.nature.com/nsmb/journal/vaop/ncurrent/abs/nsmb.3343.html-supplementaryinformation

Grimm C, Barthmes M, Wahl-Schott C (2014) Trpml3. Handb Exp Pharmacol 222:659–674. https://doi.org/10.1007/978-3-642-54215-2_26

Guler AD, Lee H, Iida T, Shimizu I, Tominaga M, Caterina M (2002) Heat-evoked activation of the ion channel, TRPV4. J Neurosci 22 (15):6408–6414. doi:20026679

Hashimoto A, Kambe T (2015) Mg, Zn and Cu transport proteins: a brief overview from physiological and molecular perspectives. J Nutr Sci Vitaminol 61(Suppl):S116–S118. https://doi.org/10.3177/jnsv.61.S116

Held K, Voets T, Vriens J (2015) TRPM3 in temperature sensing and beyond. Temperature 2(2):201–213. https://doi.org/10.4161/23328940.2014.988524

Hinman A, Chuang H-H, Bautista DM, Julius D (2006) TRP channel activation by reversible covalent modification. Proc Natl Acad Sci U S A 103(51):19564–19568. https://doi.org/10.1073/pnas.0609598103

Hoenderop JG, Voets T, Hoefs S, Weidema F, Prenen J, Nilius B, Bindels RJ (2003) Homo- and heterotetrameric architecture of the epithelial Ca2+ channels TRPV5 and TRPV6. EMBO J 22(4):776–785. https://doi.org/10.1093/emboj/cdg080

Hofmann T, Chubanov V, Gudermann T, Montell C (2003) TRPM5 Is a voltage-modulated and Ca2+-activated monovalent selective cation channel. Curr Biol 13(13):1153–1158. https://doi.org/10.1016/s0960-9822(03)00431-7

Huang SM, Li X, Yu Y, Wang J, Caterina MJ (2011) TRPV3 and TRPV4 ion channels are not major contributors to mouse heat sensation. Mol Pain 7:37. https://doi.org/10.1186/1744-8069-7-37

Hughes J, Ward CJ, Peral B, Aspinwall R, Clark K, San Millan JL, Gamble V, Harris PC (1995) The polycystic kidney disease 1 (PKD1) gene encodes a novel protein with multiple cell recognition domains. Nat Genet 10(2):151–160. https://doi.org/10.1038/ng0695-151

Huynh KW, Cohen MR, Chakrapani S, Holdaway HA, Stewart PL, Moiseenkova-Bell VY (2014) Structural insight into the assembly of TRPV channels. Structure 22(2):260–268. https://doi.org/10.1016/j.str.2013.11.008

Huynh KW, Cohen MR, Jiang J, Samanta A, Lodowski DT, Zhou ZH, Moiseenkova-Bell VY (2016) Structure of the full-length TRPV2 channel by cryo-EM. Nat Commun 7:11130. https://doi.org/10.1038/ncomms11130. http://www.nature.com/articles/ncomms11130-supplementary-information

Jaquemar D, Schenker T, Trueb B (1999) An ankyrin-like protein with transmembrane domains is specifically lost after oncogenic transformation of human fibroblasts. J Biol Chem 274(11):7325–7333

Jordt SE, Bautista DM, Chuang HH, McKemy DD, Zygmunt PM, Hogestatt ED, Meng ID, Julius D (2004) Mustard oils and cannabinoids excite sensory nerve fibres through the TRP channel ANKTM1. Nature 427(6971):260–265. https://doi.org/10.1038/nature02282

Kanzaki M, Zhang YQ, Mashima H, Li L, Shibata H, Kojima I (1999) Translocation of a calcium-permeable cation channel induced by insulin-like growth factor-I. Nat Cell Biol 1(3):165–170. https://doi.org/10.1038/11086

Karashima Y, Damann N, Prenen J, Talavera K, Segal A, Voets T, Nilius B (2007) Bimodal action of menthol on the transient receptor potential channel TRPA1. J Neurosci Off J Soc Neurosci 27(37):9874–9884. https://doi.org/10.1523/jneurosci.2221-07.2007

Kohler R, Heyken WT, Heinau P, Schubert R, Si H, Kacik M, Busch C, Grgic I, Maier T, Hoyer J (2006) Evidence for a functional role of endothelial transient receptor potential V4 in shear stress-induced vasodilatation. Arterioscler Thromb Vasc Biol 26(7):1495–1502. https://doi.org/10.1161/01.ATV.0000225698.36212.6a

Komiya Y, Runnels LW (2015) TRPM channels and magnesium in early embryonic development. Int J Dev Biol 59(7–9):281–288. https://doi.org/10.1387/ijdb.150196lr

Kraft R, Harteneck C (2005) The mammalian melastatin-related transient receptor potential cation channels: an overview. Pflugers Arch – Eur J Physiol 451(1):204–211. https://doi.org/10.1007/s00424-005-1428-0

Li M, Jiang J, Yue L (2006) Functional characterization of homo- and heteromeric channel kinases TRPM6 and TRPM7. J Gen Physiol 127(5):525–537. https://doi.org/10.1085/jgp.200609502

Liao M, Cao E, Julius D, Cheng Y (2013) Structure of the TRPV1 ion channel determined by electron cryo-microscopy. Nature 504(7478):107–112. https://doi.org/10.1038/nature12822

Liedtke W, Friedman JM (2003) Abnormal osmotic regulation in trpv4-/- mice. Proc Natl Acad Sci U S A 100(23):13698–13703. https://doi.org/10.1073/pnas.1735416100

Liedtke W, Choe Y, Martí-Renom MA, Bell AM, Denis CS, Šali A, Hudspeth AJ, Friedman JM, Heller S (2000) Vanilloid receptor–related osmotically activated channel (VR-OAC), a candidate vertebrate osmoreceptor. Cell 103(3):525–535. https://doi.org/10.1016/S0092-8674(00)00143-4

Liman ER (2007) TRPM5 and taste transduction. Handb Exp Pharmacol 179:287–298. https://doi.org/10.1007/978-3-540-34891-7_17

Lishko PV, Procko E, Jin X, Phelps CB, Gaudet R (2007) The ankyrin repeats of TRPV1 bind multiple ligands and modulate channel sensitivity. Neuron 54(6):905–918. https://doi.org/10.1016/j.neuron.2007.05.027

Liu Z, Wu H, Wei Z, Wang X, Shen P, Wang S, Wang A, Chen W, Lu Y (2016) TRPM8: a potential target for cancer treatment. J Cancer Res Clin Oncol 142(9):1871–1881. https://doi.org/10.1007/s00432-015-2112-1

Lu W, Peissel B, Babakhanlou H, Pavlova A, Geng L, Fan X, Larson C, Brent G, Zhou J (1997) Perinatal lethality with kidney and pancreas defects in mice with a targetted Pkd1 mutation. Nat Genet 17(2):179–181. https://doi.org/10.1038/ng1097-179

Macpherson LJ, Dubin AE, Evans MJ, Marr F, Schultz PG, Cravatt BF, Patapoutian A (2007) Noxious compounds activate TRPA1 ion channels through covalent modification of cysteines. Nature 445(7127):541–545. http://www.nature.com/nature/journal/v445/n7127/suppinfo/nature05544_S1.html

Malhas AN, Abuknesha RA, Price RG (2002) Interaction of the leucine-rich repeats of polycystin-1 with extracellular matrix proteins: possible role in cell proliferation. J Am Soc Nephrol 13(1):19–26

McKemy D (2007) TRPM8: the cold and menthol receptor. In: TRP ion channel function in sensory transduction and cellular signaling cascades. CRC Press/Taylor & Francis, Boca Raton

McKemy DD, Neuhausser WM, Julius D (2002) Identification of a cold receptor reveals a general role for TRP channels in thermosensation. Nature 416(6876):52–58. http://www.nature.com/nature/journal/v416/n6876/suppinfo/nature719_S1.html

Mochizuki T, Wu G, Hayashi T, Xenophontos SL, Veldhuisen B, Saris JJ, Reynolds DM, Cai Y, Gabow PA, Pierides A, Kimberling WJ, Breuning MH, Deltas CC, Peters DJ, Somlo S (1996) PKD2, a gene for polycystic kidney disease that encodes an integral membrane protein. Science 272(5266):1339–1342

Moiseenkova-Bell VY, Stanciu LA, Serysheva II, Tobe BJ, Wensel TG (2008) Structure of TRPV1 channel revealed by electron cryomicroscopy. Proc Natl Acad Sci U S A 105(21):7451–7455. https://doi.org/10.1073/pnas.0711835105

Moqrich A, Hwang SW, Earley TJ, Petrus MJ, Murray AN, Spencer KS, Andahazy M, Story GM, Patapoutian A (2005) Impaired thermosensation in mice lacking TRPV3, a heat and camphor sensor in the skin. Science (New York, NY) 307(5714):1468–1472. https://doi.org/10.1126/science.1108609

Nilius B, Owsianik G, Voets T, Peters JA (2007) Transient receptor potential cation channels in disease. Physiol Rev 87(1):165–217. https://doi.org/10.1152/physrev.00021.2006

Nilius B, Appendino G, Owsianik G (2012) The transient receptor potential channel TRPA1: from gene to pathophysiology. Pflugers Arch – Eur J Physiol 464(5):425–458. https://doi.org/10.1007/s00424-012-1158-z

Noben-Trauth K (2011) The TRPML3 channel: from gene to function. In: Islam MS (ed) Transient receptor potential channels. Springer Netherlands, Dordrecht, pp 229–237. https://doi.org/10.1007/978-94-007-0265-3_13

Ong HL, de Souza LB, Ambudkar IS (2016) Role of TRPC channels in store-operated calcium entry. Adv Exp Med Biol 898:87–109. https://doi.org/10.1007/978-3-319-26974-0_5

Park U, Vastani N, Guan Y, Raja SN, Koltzenburg M, Caterina MJ (2011) TRP vanilloid 2 knockout mice are susceptible to perinatal lethality but display normal thermal and mechanical nociception. J Neurosci 31(32):11425–11436. https://doi.org/10.1523/jneurosci.1384-09.2011

Paulsen CE, Armache JP, Gao Y, Cheng Y, Julius D (2015) Structure of the TRPA1 ion channel suggests regulatory mechanisms. Nature 520(7548):511–517. https://doi.org/10.1038/nature14367

Peier AM, Moqrich A, Hergarden AC, Reeve AJ, Andersson DA, Story GM, Earley TJ, Dragoni I, McIntyre P, Bevan S, Patapoutian A (2002) A TRP channel that senses cold stimuli and menthol. Cell 108(5):705–715

Putney JW Jr (2004) The enigmatic TRPCs: multifunctional cation channels. Trends Cell Biol 14(6):282–286. https://doi.org/10.1016/j.tcb.2004.04.002

Qian F, Boletta A, Bhunia AK, Xu H, Liu L, Ahrabi AK, Watnick TJ, Zhou F, Germino GG (2002) Cleavage of polycystin-1 requires the receptor for egg jelly domain and is disrupted by human autosomal-dominant polycystic kidney disease 1-associated mutations. Proc Natl Acad Sci U S A 99(26):16981–16986. https://doi.org/10.1073/pnas.252484899

Saotome K, Singh AK, Yelshanskaya MV, Sobolevsky AI (2016) Crystal structure of the epithelial calcium channel TRPV6. Nature 534(7608):506–511. https://doi.org/10.1038/nature17975

Shen PS, Yang X, DeCaen PG, Liu X, Bulkley D, Clapham DE, Cao E (2016) The structure of the polycystic kidney disease channel PKD2 in lipid nanodiscs. Cell 167(3):763–773.e711. https://doi.org/10.1016/j.cell.2016.09.048

Smith GD, Gunthorpe MJ, Kelsell RE, Hayes PD, Reilly P, Facer P, Wright JE, Jerman JC, Walhin JP, Ooi L, Egerton J, Charles KJ, Smart D, Randall AD, Anand P, Davis JB (2002) TRPV3 is a temperature-sensitive vanilloid receptor-like protein. Nature 418(6894):186–190. https://doi.org/10.1038/nature00894

Story GM, Peier AM, Reeve AJ, Eid SR, Mosbacher J, Hricik TR, Earley TJ, Hergarden AC, Andersson DA, Hwang SW, McIntyre P, Jegla T, Bevan S, Patapoutian A (2003) ANKTM1, a TRP-like channel expressed in nociceptive neurons, is activated by cold temperatures. Cell 112(6):819–829

Strotmann R, Harteneck C, Nunnenmacher K, Schultz G, Plant TD (2000) OTRPC4, a nonselective cation channel that confers sensitivity to extracellular osmolarity. Nat Cell Biol 2(10):695–702. https://doi.org/10.1038/35036318

Svobodova B, Groschner K (2016) Reprint of "Mechanisms of lipid regulation and lipid gating in TRPC channels". Cell Calcium 60(2):133–141. https://doi.org/10.1016/j.ceca.2016.06.010

Takahashi N, Mori Y (2011) TRP channels as sensors and signal integrators of redox status changes. Front Pharmacol 2:58. https://doi.org/10.3389/fphar.2011.00058

Takahashi N, Kuwaki T, Kiyonaka S, Numata T, Kozai D, Mizuno Y, Yamamoto S, Naito S, Knevels E, Carmeliet P, Oga T, Kaneko S, Suga S, Nokami T, Yoshida J-I, Mori Y (2011) TRPA1 underlies a sensing mechanism for O2. Nat Chem Biol 7(10):701–711. doi:http://www.nature.com/nchembio/journal/v7/n10/abs/nchembio.640.html – supplementary-information

Tsavaler L, Shapero MH, Morkowski S, Laus R (2001) Trp-p8, a novel prostate-specific gene, is up-regulated in prostate cancer and other malignancies and shares high homology with transient receptor potential calcium channel proteins. Cancer Res 61(9):3760–3769

Tsiokas L, Arnould T, Zhu C, Kim E, Walz G, Sukhatme VP (1999) Specific association of the gene product of PKD2 with the TRPC1 channel. Proc Natl Acad Sci U S A 96(7):3934–3939

Vazquez G, Wedel BJ, Aziz O, Trebak M, Putney JW Jr (2004) The mammalian TRPC cation channels. Biochim Biophys Acta 1742(1–3):21–36. https://doi.org/10.1016/j.bbamcr.2004.08.015

Veldhuisen B, Spruit L, Dauwerse HG, Breuning MH, Peters DJ (1999) Genes homologous to the autosomal dominant polycystic kidney disease genes (PKD1 and PKD2). Eur J Hum Genet 7(8):860–872. https://doi.org/10.1038/sj.ejhg.5200383

Venkatachalam K, Montell C (2007) TRP channels. Annu Rev Biochem 76:387–417. https://doi.org/10.1146/annurev.biochem.75.103004.142819

Venkatachalam K, Wong CO, Zhu MX (2015) The role of TRPMLs in endolysosomal trafficking and function. Cell Calcium 58(1):48–56. https://doi.org/10.1016/j.ceca.2014.10.008

Voltz JW, Weinman EJ, Shenolikar S (2001) Expanding the role of NHERF, a PDZ-domain containing protein adapter, to growth regulation. Oncogene 20(44):6309–6314. https://doi.org/10.1038/sj.onc.1204774

Wang W, Zhang X, Gao Q, Xu H (2014) TRPML1: an ion channel in the lysosome. Handb Exp Pharmacol 222:631–645. https://doi.org/10.1007/978-3-642-54215-2_24

Wes PD, Chevesich J, Jeromin A, Rosenberg C, Stetten G, Montell C (1995) TRPC1, a human homolog of a drosophila store-operated channel. Proc Natl Acad Sci U S A 92(21):9652–9656

Wilson PD (2001) Polycystin: new aspects of structure, function, and regulation. J Am Soc Nephrol 12(4):834–845

Wu L, Gao X, Brown RC, Heller S, O'Neil RG (2007) Dual role of the TRPV4 channel as a sensor of flow and osmolality in renal epithelial cells. Am J Physiol Ren Physiol 293(5):F1699–F1713. https://doi.org/10.1152/ajprenal.00462.2006

Xu H, Ramsey IS, Kotecha SA, Moran MM, Chong JA, Lawson D, Ge P, Lilly J, Silos-Santiago I, Xie Y, DiStefano PS, Curtis R, Clapham DE (2002) TRPV3 is a calcium-permeable temperature-sensitive cation channel. Nature 418(6894):181–186. https://doi.org/10.1038/nature00882

Zholos A, Johnson C, Burdyga T, Melanaphy D (2011) TRPM channels in the vasculature. Adv Exp Med Biol 704:707–729. https://doi.org/10.1007/978-94-007-0265-3_37

Zubcevic L, Herzik MA Jr, Chung BC, Liu Z, Lander GC, Lee SY (2016) Cryo-electron microscopy structure of the TRPV2 ion channel. Nat Struct Mol Biol 23(2):180–186. https://doi.org/10.1038/nsmb.3159

Zygmunt PM, Hogestatt ED (2014) TRPA1. Handb Exp Pharmacol 222:583–630. https://doi.org/10.1007/978-3-642-54215-2_23

# Chapter 7
# Mitochondrial Respiratory Chain Complexes


**Joana S. Sousa, Edoardo D'Imprima, and Janet Vonck**

**Abstract** Mitochondria are the power stations of the eukaryotic cell, using the energy released by the oxidation of glucose and other sugars to produce ATP. Electrons are transferred from NADH, produced in the citric acid cycle in the mitochondrial matrix, to oxygen by a series of large protein complexes in the inner mitochondrial membrane, which create a transmembrane electrochemical gradient by pumping protons across the membrane. The flow of protons back into the matrix via a proton channel in the ATP synthase leads to conformational changes in the nucleotide binding pockets and the formation of ATP. The three proton pumping complexes of the electron transfer chain are NADH-ubiquinone oxidoreductase or complex I, ubiquinone-cytochrome *c* oxidoreductase or complex III, and cytochrome *c* oxidase or complex IV. Succinate dehydrogenase or complex II does not pump protons, but contributes reduced ubiquinone. The structures of complex II, III and IV were determined by x-ray crystallography several decades ago, but complex I and ATP synthase have only recently started to reveal their secrets by advances in x-ray crystallography and cryo-electron microscopy. The complexes I, III and IV occur to a certain extent as supercomplexes in the membrane, the so-called respirasomes. Several hypotheses exist about their function. Recent cryo-electron microscopy structures show the architecture of the respirasome with near-atomic detail. ATP synthase occurs as dimers in the inner mitochondrial membrane, which by their curvature are responsible for the folding of the membrane into cristae and thus for the huge increase in available surface that makes mitochondria the efficient energy plants of the eukaryotic cell.

**Keywords** ATP synthase · ATP synthesis · Complex I · Complex II · Complex III · Complex IV · Cryo-electron microscopy · Mitochondria · Respirasome · Respiratory chain · X-ray crystallography

J. S. Sousa · E. D'Imprima · J. Vonck (✉)
Department of Structural Biology, Max Planck Institute of Biophysics, Frankfurt am Main, Germany
e-mail: janet.vonck@biophys.mpg.de



J. R. Harris, E. J. Boekema (eds.), *Membrane Protein Complexes: Structure and Function*, Subcellular Biochemistry 87,
https://doi.org/10.1007/978-981-10-7757-9_7

## Abbreviations

| | |
|---|---|
| cryo-EM | cryo-electron microscopy |
| IMM | inner mitochondrial membrane |
| IMS | intermembrane space |
| pmf | proton motive force |
| RET | reverse electron transfer |
| ROS | reactive oxygen species |
| TMH | transmembrane helices |

## 7.1 Introduction

Mitochondria are the power plants of the eukaryotic cell. They produce most of the huge amounts of ATP needed for the functioning of the cell. An athlete can turn over his or her body weight in ATP in a day. A series of large membrane protein complexes in the inner mitochondrial membrane (IMM) is responsible for this remarkable system. The chemical energy in the products of the citric acid cycle is converted into an electrochemical gradient over the IMM by a series of proton pumps. The protons flow back into the mitochondrial matrix via proton channels in the $F_1F_o$ ATP synthase complex and drive a mechanical rotation of the rotor, causing conformational changes in the nucleotide binding pockets of the $F_1$ subcomplex, thus converting ADP and phosphate to ATP. The respiratory chain complexes are among the largest membrane protein complexes in the cell. They transfer electrons from NADH and succinate to molecular oxygen via a number of redox cofactors including flavins, iron-sulfur clusters, hemes and ions. The proton pumps are NADH:ubiquinone oxidoreductase or complex I, which oxidizes NADH, transfers two electrons to ubiquinone and translocates four protons across the membrane, ubiquinol:cytochrome *c* oxidoreductase (complex III), which transfers electrons from ubiquinone to the peripheral electron carrier cytochrome *c* while translocating 4 protons, and cytochrome *c* oxidase (complex IV), which transfers electrons from cytochrome *c* to molecular oxygen and translocates two protons. In total 10 protons per NADH molecule are translocated across the IMM. Succinate dehydrogenase (complex II), which is part of both the citric acid cycle and the electron transfer chain, contributes additional electrons to ubiquinone that originate from succinate (Fig. 7.1). The mitochondrial respiratory chain derives from endosymbiont α-proteobacteria and all core subunits are highly conserved. However, most mitochondrial complexes have gained large numbers of accessory subunits (Fig. 7.1) with functions that are only now beginning to be understood. In recent years much progress has been made in understanding the structure and function of these complexes, driven by structural information from x-ray crystallography and cryo-electron microscopy (cryo-EM). In addition insight has been gained in their organization in the IMM: complex I, III

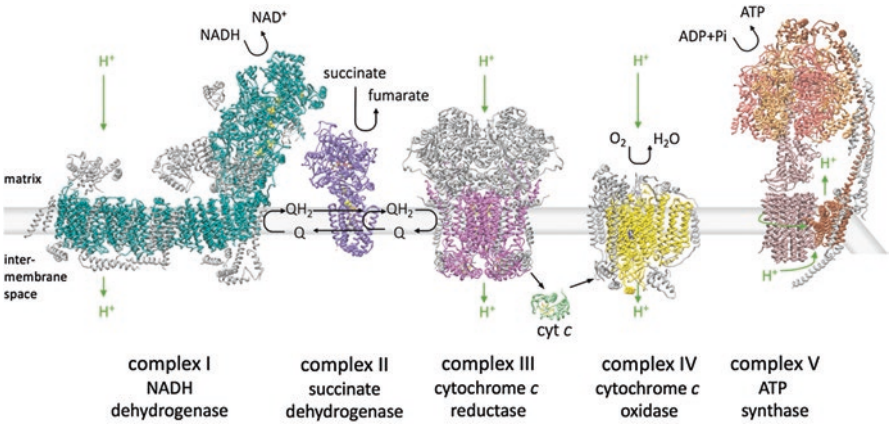


**Fig. 7.1** The mitochondrial respiratory chain in the IMM uses the energy in NADH and succinate produced in the citric acid cycle to produce ATP, the energy currency of the cell. Core subunits (colors) also present in bacteria are highly conserved, while the mitochondrial complexes have acquired accessory subunits (grey), often with still unknown functions. Accessory subunits of the ATP synthase bend the membrane and are responsible for the formation of cristae, lined with dimer rows of ATP synthase. Electrons enter the chain from NADH via complex I and from succinate via complex II. Complex I, III and IV pump protons across the IMM, which flow back into the matrix via the ATP synthase, driving the rotor to produce ATP. Proton flow is indicated by green arrows

and IV are found to occur to a large extent as supercomplexes, and the mitochondrial ATP synthase occurs in dimer rows, which are thought to be responsible for the shape of the inner membrane cristae. All these aspects are subject of this chapter.

## 7.2 Complex I

Complex I (NADH:ubiquinone oxidoreductase) plays a central role in cellular metabolism. By oxidizing NADH to $NAD^+$ in the mitochondrial matrix, it supplies reducing equivalents to support the tricarboxylic acid cycle (Krebs cycle) and the β-oxidation of fatty acids. Complex I represents the entry point of the electrons in the respiratory chain. In each catalytic cycle two electrons from NADH are used to reduce ubiquinone to ubiquinol, coupled with the vectorial transport of four protons across the IMM. The proton gradient generated contributes ~40% of the proton motive force (pmf) that is used for ATP synthesis and for the import and export of protein and metabolites to and from mitochondria. Complex I is also one of the main sources of reactive oxygen species (ROS) production, which has a huge impact on mitochondria and oxidative stress and may be one of the causes of ageing. Because of its central role in energy production, complex I defects have a noteworthy effect in tissues with a high metabolic rate like brain and heart, especially in early childhood.

### 7.2.1 Background and Nomenclature

Complex I is one of the largest membrane protein assemblies known and is the largest component of the respiratory chain. It belongs to the protein family of $H^+$- or $Na^+$-translocating NADH dehydrogenases (NDH), and more precisely it is a type I NADH dehydrogenase (NDH-I) (Kerscher et al. 2008). The other members of this protein family include type II NAD(P)H dehydrogenase (NDH-II), a non-proton pumping enzyme (Melo et al. 2004), and the sodium pumping NADH-quinone reductase ($Na^+$-NQR) (Barquera 2014). An analysis of 970 bacterial genomes showed the presence of complex I in the majority of Gram-negative bacteria and mostly in the phylum of Actinobacteria in Gram-positive bacteria (Friedrich and Scheide 2000; Spero et al. 2015).

With one exception (Spero et al. 2015), complex I was not found in 88 archaeal genomes investigated. In eukaryotes, complex I occurs in mitochondria of aerobic (Gabaldon et al. 2005) and anaerobic species (van Hellemond et al. 2003). It is absent in the fungal lineages of *Schizosaccharomyces* and Saccharomycetales, and the cryptomycotan fungus *Rozella* (Gabaldon et al. 2005; Marcet-Houben et al. 2009; James et al. 2013). In fermenting yeasts like *Saccharomyces cerevisiae* that do not contain complex I (Ohnishi et al. 1966), the NADH oxidoreductase activity is performed by the so-called alternative NADH dehydrogenases, a class of flavoenzymes that catalyze the same reaction as complex I but do not couple it to ion translocation over the membrane (Kerscher 2000).

With the only exception of the parasitic plant *Viscum scurruloideum*, which seems to lack complex I (Skippington et al. 2015), in the plant kingdom all mitochondria contain NDH-I (Gabaldon et al. 2005).

Complex I is an L-shaped enzyme composed of two elongated domains also referred to as "arms". The hydrophobic or membrane arm is inserted into the cytoplasmic membrane of bacteria or the IMM and the hydrophilic, peripheral or matrix arm protrudes into the bacterial cytoplasm or the mitochondrial matrix (Clason et al. 2010) (Fig. 7.2). An assembly of 14 core subunits, seven in the membrane arm and seven in the peripheral arm, represent the minimal model of complex I that is sufficient to catalyze the energy transduction and only these subunits are present in most bacteria. Crystal structures of the core subunits were determined first for the bacterial enzymes from *Thermus thermophilus* and *Escherichia coli* (Sazanov and Hinchliffe 2006; Efremov and Sazanov 2011; Baradaran et al. 2013). In eukaryotes the seven core subunits of the membrane arm are encoded by the mitochondrial genome and those of the hydrophilic arm by the nuclear genome.

In addition to the core subunits, mitochondrial complex I contains a large number of accessory subunits (up to ~50% of the total mass of the complex), the phylogenetic analysis of which sheds light on the evolution of complex I (Gabaldon et al. 2005). The best studied eukaryotic systems are complex I from bovine heart (Carroll et al. 2003), the obligate aerobic yeast *Yarrowia lipolytica* (Kerscher et al. 2004) and the fungus *Neurospora crassa* (Videira 1998) (Fig. 7.2). Structural data is avail-

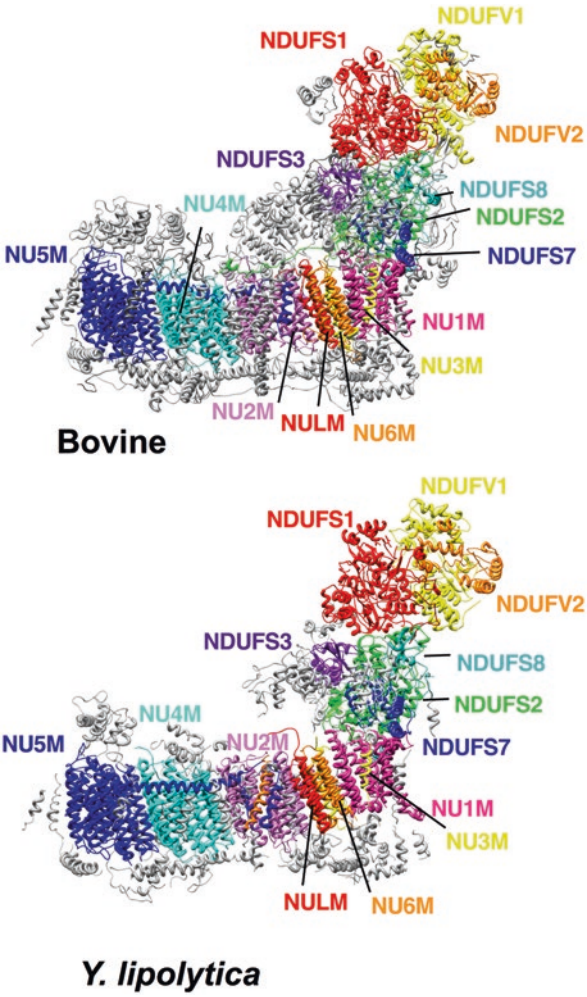


**Fig. 7.2** Structure of the mitochondrial complex I core subunits. The homologous bovine (pdb 5lc5) and *Y. lipolytica* (pdb 4wz7) core subunits and labels are colored the same. All accessory subunits are depicted in grey. The human nomenclature was applied

able for mammalian complex I from recent cryo-EM maps (Vinothkumar et al. 2014; Zhu et al. 2016; Fiedorczuk et al. 2016) and for *Y. lipolytica* from crystal structures (Hunte et al. 2010; Zickermann et al. 2015) and a cryo-EM map (D'Imprima et al. 2016).

The well-studied mammalian mitochondrial enzyme from bovine heart, of about 1 MDa molecular weight and with high homology to the human complex I, contains 44 different subunits and, as the SDAP subunit is present in two copies (Vinothkumar et al. 2014), 45 in total.

Since there is no uniform nomenclature, even for the central subunits, Table 7.1 shows the subunits for all commonly studied species. Unless differently indicated, the human nomenclature will be used.

**Table 7.1** Subunits of complex I in different species

| *Homo sapiens* | *Bos taurus* | *Y. lipolytica* | *T. thermophilus* | *P. denitrificans* | *E. coli* | comment | module |
|---|---|---|---|---|---|---|---|
| NDUFS1 | 75-kDa | NUAM | Nqo3 | Nqo3 | NuoG | 2 [4Fe4S] 1 [2Fe2S] | N |
| NDUFV1 | 51-kDa | NUBM | Nqo1 | Nqo1 | NuoF | FMN; NADH; [4Fe4S] | N |
| NDUFS2 | 49-kDa | NUCM | Nqo4 | Nqo4 | NuoD | Q-binding | Q |
| NDUFS3 | 30-kDa | NUGM | Nqo5 | Nqo5 | NuoC | | Q |
| NDUFV2 | 29-kDa | NUHM | Nqo2 | Nqo2 | NuoE | [2Fe2S] | N |
| NDUFS8 | TYKY | NUIM | Nqo9 | Nqo9 | NuoI | 2 [4Fe4S] | Q |
| NDUFS7 | PSST | NUKM | Nqo6 | Nqo6 | NuoB | Q-binding; [4Fe4S] | Q |
| NU1M | ND1 | NU1M | Nqo8 | Nqo8 | NuoH | mtDNA[a] | $P_P$ |
| NU2M | ND2 | NU2M | Nqo14 | Nqo14 | NuoN | mtDNA | $P_P$ |
| NU3M | ND3 | NU3M | Nqo7 | Nqo7 | NuoA | mtDNA | $P_P$ |
| NU4M | ND4 | NU4M | Nqo13 | Nqo13 | NuoM | mtDNA | $P_D$ |
| NU5M | ND5 | NU5M | Nqo12 | Nqo12 | NuoL | mtDNA | $P_D$ |
| NU6M | ND6 | NU6M | Nqo10 | Nqo10 | NuoJ | mtDNA | $P_P$ |
| NULM | ND4L | NULM | Nqo11 | Nqo11 | NuoK | mtDNA | $P_P$ |
| NDUFA2 | B8 | NI8M | | | | thioredoxin fold | N |
| NDUFS4 | AQDQ/ 18-kDa | NUYM | | pdNUYM | | | N |
| NDUFS6 | 13-kDa | NUMM | | pdNUMM | | $Zn^{2+}$ | N/Q |
| NDUFA12 | B17.2 | N7BM | | pdN7BM | | | N/Q |
| NDUFA7 | B14.5a | NUZM | | | | | Q |
| NDUFA5 | B13 | NUFM | | | | | Q |
| NDUFA9 | 39-kDa | NUEM | | | | NADPH | Q |
| NDUFA6 | B14 | NB4M | | | | LYR motif | Q |
| NDUFAB1 | SDAP | ACPM1 ACPM2 | | | | PP[b] PP[b] | Q $P_D$ |
| NDUFA1 | MWFE | NIMM | | | | 1 TMH[c] | $P_P$ |
| NDUFA3 | B9 | NI9M | | | | 1 TMH | $P_P$ |
| NDUFA8 | PGIV | NUPM | | | | Mia-$Cx_9C$ | $P_P$ |
| NDUFA11 | B14.7 | NUJM | | | | 4 TMH | $P_P$ |
| NDUFA13 | B16.6 | NB6M | | | | 1 TMH / GRIM-19 | $P_P$ |
| NDUFS5 | PFFD/ 15-kDa | NIPM | | | | Mia-$Cx_9C$ | $P_P$ |
| NDUFB3 | B12 | NB2M | | | | 1 TMH | $P_D$ |
| NDUFB4 | B15 | NB5M | | | | 1 TMH | $P_D$ |
| NDUFB7 | B18 | NB8M | | | | Mia-$Cx_9C$ | $P_D$ |
| NDUFB8 | ASHI | NIAM | | | | 1 TMH | $P_D$ |
| NDUFB9 | B22 | NI2M | | | | LYR motif | $P_D$ |
| NDUFB10 | PDSW | NIDM | | | | $Cx_yC$ | $P_D$ |
| NDUFB11 | ESSS | NESM | | | | 1 TMH | $P_D$ |
| NDUFV3 | 9-kDa | | | | | | N |
| NDUFC1 | KFYI | | | | | 1 TMH | $P_P$ |
| NDUFC2 | B14.5b | | | | | 1 TMH | $P_P$ |
| NDUFA10 | 42-kDa | | | | | | $P_P$ |
| NDUFB1 | MNLL | | | | | 1 TMH | $P_D$ |
| NDUFB2 | AGGG | | | | | 1 TMH | $P_D$ |
| NDUFB5 | SDGH | | | | | 1 TMH | $P_D$ |
| NDUFB6 | B17 | | | | | 1 TMH | $P_D$ |
| | | NUXM | | | | 2 TMH | $P_P$ |
| | | NEBM | | | | 1 TMH | $P_P$ |
| | | NUNM | | | | 1 TMH | $P_D$ |
| | | NUUM | | | | 1 TMH | $P_D$ |
| | | ST1 | | | | MST[d] | Q |
| | | | NQO15 | | | Frataxin family | N |
| | | | NQ016 | | | DUF3197 family | Q |

Table adapted from Wirth et al. (2016)

The core subunits in the hydrophilic and the membrane arm are shown in blue and red, respectively. The assignment of modules is according to Hunte et al. 2010. Q, quinone reduction module; N, NADH oxidation module; $P_P$ and $P_D$, proximal and distal proton pumping module, respectively

[a]Mitochondrial DNA; [b]Phosphopantetheine; [c]Transmembrane helix; [d]3-mercaptopyruvate:sulfur transferase

### 7.2.2 *Mechanism of Complex I*

The first step of the reaction catalyzed by complex I is NADH oxidation by a non-covalently bound flavin-mononucleotide (FMN) at the top of the hydrophilic arm, in the NUDFV1 subunit. The fast electron transfer between $C^{4N}$ of NADH and $N^5$ of FMN is mediated by a favorable geometry of the nicotinamide ring of NADH, which upon binding forms a stacking interaction with the isoalloxazine ring of FMN (Berrisford and Sazanov 2009). Next electrons are transferred along a chain of seven iron-sulfur (FeS) clusters (Fig. 7.3), spanning a distance of ~90 Å, to ubiquinone in the binding pocket formed by NU1M, NDUFS2 and NDUFS7 at the base of the hydrophilic arm. In the membrane arm, four antiporter-like structural motifs have been identified that are likely to transport one proton each per catalytic cycle. The redox and proton pumping mechanism are not only spatially separated, but they also occur in a remarkably different time-scale: the former ~100 μs and the latter about three orders of magnitude slower (Verkhovskaya et al. 2008; Sharma et al. 2015). The mechanism of coupling between electron transfer and proton translocation is still the least understood aspect of complex I. Currently the two main proposed models are: partially direct redox-driven coupling (Dutton et al. 1998; Ohnishi et al. 2010) and indirect or conformationally

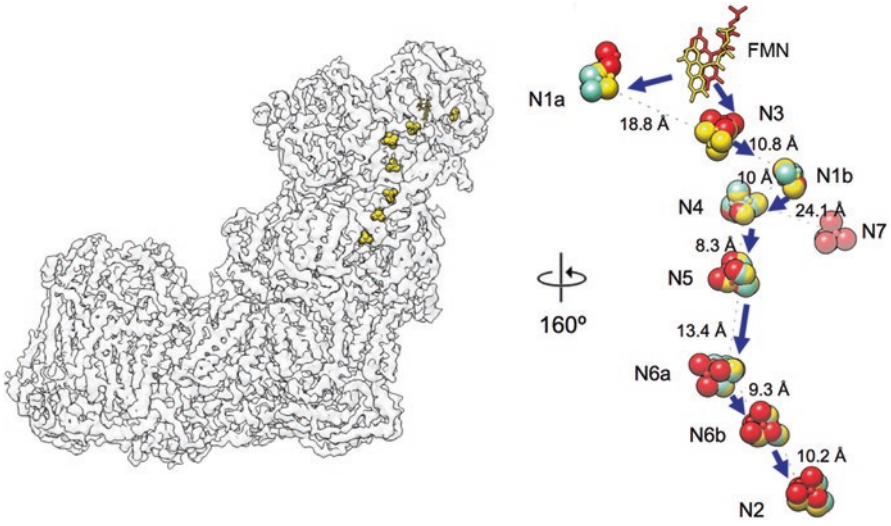


**Fig. 7.3** FeS clusters in mammalian, yeast and prokaryote complex I. On the left the coordinates of the ligands of bovine complex I (pdb 5lc5) are docked into the corresponding cryo-EM map (EMD-4032). On the right the coordinates of the FeS clusters of *Y. lipolytica* (pdb 4wz7) (blue) and *T. thermophilus* (pdb 4hea) (pink) were overlapped with the bovine structure (gold). The nomenclature from Baradaran et al. 2013 was used to assign the FeS clusters. Distances were calculated edge-to-edge from the coordinates of pdb 5lc5 except for the distance between clusters N4-N7 for which coordinates from pdb 4hea were used. The blue arrows show the electron flow from the FMN to the cluster N2

driven coupling (Yagi and Matsuno-Yagi 2003; Brandt 2006; Zickermann et al. 2015; Friedrich 2001). The reaction of mitochondrial complex I is fully reversible, and at the expense of the pmf the enzyme can also transfer electrons from ubiquinol upstream for $NAD^+$ reduction (the so called reverse electron transfer (RET)). This reaction *in vitro* is accompanied by increased production of superoxide, which is rapidly converted to $H_2O_2$ (Ambrosio et al. 1993; Turrens 2003).

### *7.2.3 The Dehydrogenase Domain*

The hydrophilic arm consists of the dehydrogenase domain (N module), which harbors the cofactors and the subunits involved in the oxidation of NADH and transfer of electrons to quinone, and the quinone-binding domain (Q module).

The N module comprises the core subunits NDUFS1, NDUFV1 and NDUFV2.

Eukaryotes harbor 8 and some bacteria 9 FeS clusters (Fig. 7.3). Binuclear clusters ([2Fe-2S]) contribute to broad absorbance peaks at 420, 470 and 560 nm, tetranuclear clusters ([4Fe-4S]) at 420 nm and FMN at 450 nm (Rasmussen et al. 2001; Euro et al. 2008; Hinchliffe and Sazanov 2005). Extensive studies over the years, particularly from Ohnishi's and Hirst's group using bovine complex I as the main model, allowed to establish the presence of EPR signals from two binuclear (N1a and N1b) and six tetranuclear FeS clusters (Ohnishi 1998; Roessler et al. 2010), making it one of the most complex FeS assemblies known. It has been shown that absorbance in these regions of the spectra decreases upon reduction of complex I (Rasmussen et al. 2001), but it is not possible to de-convolute spectra of individual redox centers, with the exception of the contribution from the high-potential cluster N2 and FMN (~240 mV and 350 mV respectively (Ohnishi 1998)). Due to these limitations a consensus on the assignment of EPR signals to FeS has been reached so far only for the clusters N1a in NDUFV2 and N1b in NDUFS1 (Gnandt et al. 2016; Ohnishi and Nakamaru-Ogiso 2008; Yakovlev et al. 2007). The clusters N3 and N2 are unambiguously assigned to subunits NDUFV1 and NDUFS7, respectively. The position of those clusters is particularly important, since cluster N3 is involved in accepting the electrons from the FMN and cluster N2 interfaces with the quinone (Fig. 7.3). The role of the cluster N1a is still highly debated; it resides at the opposite side of the FMN, separated from the main chain of clusters that connects the NADH oxidation site with the quinone reduction site. It seems to be important for the structure around the flavin site and an interesting hypothesis (Gnandt et al. 2016) proposes that it may serve as a "temporary deposit" of one electron when the most distal cluster N2 is reduced. This might be due to the fact that FeS clusters are one electron carriers and NADH and $FMNH_2$ are two electron donors.

In addition to the eight conserved FeS clusters, in *T. thermophilus* and *E. coli* and some other bacteria there is an additional FeS binding motif in subunit Nqo3 (NuoG), coordinating the tetranuclear cluster N7 (Fig. 7.3) as confirmed by the X-ray structure of the hydrophilic arm of *T. thermophilus* complex I (Sazanov and

Hinchliffe 2006). Since it is too far away from the main FeS chain to be involved in efficient electron tunneling (Page et al. 1999) and not conserved it is unlikely to have an important role in the electron-transfer chain reaction.

### *7.2.4 The Quinone Binding Module and the A/D Transition*

The interface between the membrane and hydrophilic arm is composed of structural elements of the NUM1, NUM3, NDUFS2, NDUFS7 and NDUFS8 subunits.

Different quinones with variable isoprenoid tails lengths are used as electron acceptors in different species. The mitochondrial enzyme uses ubiquinone, whereas the prokaryotic enzyme uses either menaquinone or ubiquinone. This cofactor is currently considered the key point at which the redox potential is coupled with the proton pumping in the membrane arm. Despite the recent high-resolution structural data from yeast (Zickermann et al. 2015), bovine (Zhu et al. 2016) and ovine (Fiedorczuk et al. 2016) complex I, the conformational changes that take place at the level of the Q module are difficult to interpret and the mechanism of coupling is still elusive. For example, the loops β1-β2 in the core subunit NDUFS2, which are thought to be critical for ubiquinone binding, can be in different conformations (Baradaran et al. 2013; Fiedorczuk et al. 2016; Zickermann et al. 2015; Zhu et al. 2016).

A very interesting characteristic of mitochondrial complex I is the fact that it can adopt two different states, the so called active (A) and de-active or dormant (D) state. The existence of two distinct catalytic forms of the enzyme was shown *in vitro* (Kotlyar and Vinogradov 1990; Roberts and Hirst 2012), in cultured cells and in mouse and rat tissue under ischemic conditions (Galkin et al. 2009; Chouchani et al. 2013). The A and D forms, first characterized for the mammalian enzyme (Kotlyar and Vinogradov 1990), are also evident in other vertebrates and certain yeasts, but have not been detected so far in prokaryotes (*Rhodobacter capsulatus*, *Paracoccus denitrificans*, or *E. coli*) (Maklashina et al. 2003; Grivennikova et al. 2003). Respiratory complex I in A and D state displays structural rearrangements in the Q module and remarkably different catalytic activity. During steady state aerobic respiration, the A form is predominant. It catalyzes the fast physiological NADH:ubiquinone oxidoreductase reaction with a linear rate over time and it is insensitive to cysteine-modifying reagents such as nitrosothiols, peroxynitrite or ROS. Conversely the D state is characterized by a lower activity and an initial lag phase, which was reported already in 1964 (Minakami et al. 1964). The lag phase can be prolonged in the presence of divalent cations or alkaline pH (Babot et al. 2014). If oxygen is absent the A-form spontaneously converts to the D-form, which can be re-activated in the case of re-oxygenation (given substrate ubiquinone availability). In recent years several groups reported strong evidence that the sensitivity of complex I to redox modifications is different for the A and D forms (Galkin and Moncada 2007; Gorenkova et al. 2013; Babot et al. 2014; Drose et al. 2014). Particularly in the D form the access of the ubiquinone head group to the terminal

FeS cluster N2 is somehow restricted due to conformational changes of the subunits that build the ubiquinone binding site, lowering the activity of the complex, in a similar way as rotenone (a potent inhibitor of complex I) when complex I is in the physiological A state, in the end preventing the formation of superoxide. The most intriguing hypothesis to explain the physiological role of the A/D transition in the view of recent biochemical data (reviewed in Drose et al. 2016) and the most detailed structural studies (Baradaran et al. 2013; Zickermann et al. 2015; Zhu et al. 2016; Fiedorczuk et al. 2016) proposes that the temporary and reversible deactivation of respiratory complex I *in situ* may prevent an "oxidative burst" mediated by ROS in the early stage of reperfusion when the oxygen level increases dramatically and the metabolic intermediates are not yet balanced (Chouchani et al. 2013). This would happen because upon re-oxygenation complex I initiates a strong sudden redox activity with high production rates of hydrogen peroxide, which may be prevented by locking the complex in a low activity state: the D state.

These discoveries highlight the importance of the A/D transition during oxidative stress and its potential biomedical relevance in translational medicine. In the light of these new findings the respiratory complex I becomes an attractive drug target for a chemical compound that can selectively affect the A/D state of the enzyme in order to treat ischemia-reperfusion (I/R) injury caused by an excess of production of ROS in myocardial infarction and stroke (Chouchani et al. 2014).

### *7.2.5 The Membrane Arm*

The membrane arm contains the proton pumping module, which is constituted by the seven core subunits NU1M, NU2M, NU3M, NU6M, NULM, NU4M and NU5M. Within this module four antiporter-like motifs have been identified that are thought to transport one proton each per catalytic cycle. The subunits NU2M, NU5M and NU4M each represent one proton transfer unit (Efremov and Sazanov 2011) and a fourth unit is built by subunits NU1M, NULM and NU6M (Baradaran et al. 2013) (Fig. 7.2).

Each antiporter-like subunit contains ten transmembrane helices (TMH) organized in two symmetry-related sets of five, each constituting a half-channel. The antiporter-like subunits are encoded by mitochondrial DNA and are conserved from bacteria to mammals. Although the proton extrusion pathways seem to be conserved between bacterial and mitochondrial complex I, there are some differences in the proton uptake routes (Zickermann et al. 2015; Baradaran et al. 2013; Efremov and Sazanov 2011). Experimental evidence that these antiporter-like subunits are functional is not abundant, but it has been shown that deletion of the gene for NDUFB7 results in the loss of the entire $P_D$ module, but generates complex I that still pumps two protons per cycle, i.e. at 50% stoichiometry (Drose et al. 2011). Furthermore, it is still unclear how the pumping cycle operates: if the pumping units work in sync or whether proton translocation is a two-step process that mirrors the two-step reduction of ubiquinone.

The hydrophobic arm contains a long horizontal -helix that runs along the concave side of the membrane arm on the matrix side (Fig. 7.2). This helix belongs to the core subunit NU5M and bridges the $P_D$ and $P_P$ modules. It has a variable length in different species, from ~60 Å in *Y. lipolytica* to ~110 Å in *E. coli*; the C-terminus of subunit NU5M is anchored to the NU2M subunit by two TMH in *Y. lipolytica* complex I, but only one TMH in the bacterial and bovine complex I (Zickermann et al. 2015; Efremov et al. 2010; Vinothkumar et al. 2014) (Fig. 7.2). The function of this -helix (HL-helix) is highly debated; first it was proposed to be a proton coupling element acting as a "piston" to transmit energy for proton pumping (Efremov et al. 2010), but several studies on the bacterial system do not support this hypothesis (Belevich et al. 2011; Steimle et al. 2015). Another hypothesis proposes that the HL helix with its anchoring is required for "clamping" the two proton pumping modules, providing structural stability (Wirth et al. 2016; Zhu et al. 2016).

Another characteristic of the membrane arm is the presence of charged and polar residues in the middle of the membrane, spanning from the quinone-binding site near the peripheral arm to the last membrane core subunit NU5M. These residues are mostly found in the discontinuous TMH and are surrounded by several water molecules (Baradaran et al. 2013; Zickermann et al. 2015). They seem to form a hydrophilic central region inside the membrane arm that is likely to play an important role in the proton pumping mechanism.

### *7.2.6 Accessory Subunits of Complex I*

Apart from the conserved 14 core subunits, mitochondrial complex I contains a large number of accessory or supernumerary subunits. They form a "cage" around the core subunits, in many species doubling the molecular weight of the complex (Fig. 7.4). The number of subunits which compose complex I ranges from 14 in proteobacteria (Weidner et al. 1993) to 45 in mammals (Carroll et al. 2006) and 49 in plants (Peters et al. 2013). In addition, a number of assembly factors have also been characterized (Merz and Westermann 2009; Carilla-Latorre et al. 2010; Bych et al. 2008; Lightowlers and Chrzanowska-Lightowlers 2013; Andrews et al. 2013). However, it should be noted that the distinction between assembly factors and accessory subunits is only based on whether the protein is retained in the mature complex I or not, independent of a role in the assembly process. Moreover, many accessory subunits/assembly factors may not survive purification of the complex, depending on the protocol used and the species under investigation. The ambiguity in the terminology used to address the accessory subunits reflects the fact that up to date very little is known about their function.

Most of the current knowledge about accessory subunits has been recently reviewed (Elurbe and Huynen 2016). All 31 accessory subunits in the mammalian complex were traced and localized (Zhu et al. 2016; Fiedorczuk et al. 2016), but the

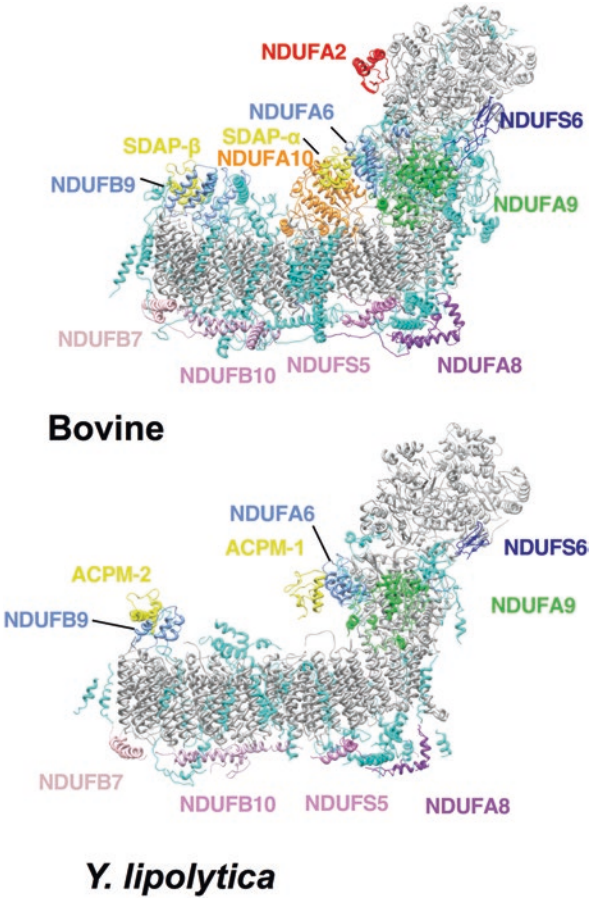


**Fig. 7.4** Structure of the mitochondrial complex I accessory subunits. The homologous accessory subunits of bovine (pdb 5lc5) and *Y. lipolytica* (pdb 4wz7) complex I which were assigned so far are colored the same. NDUFA2, mutations of which seem to be linked to Parkinson disease, is colored in red (Morais et al. 2014). NDUFA10 (which is not present in *Y. lipolytica*) is highlighted in orange. NDUFAB1 (yellow) is present in two copies in bovine and *Y. lipolytica*. They are named SDAP-α and SDAP-β and ACPM-1 and ACPM-2, respectively. NDUFA8, NDUFS5, NDUFB7 and NDUFB10, members of the twin Cys-$X_9$-Cys family (Longen et al. 2009), are located at the intermembrane space (IMS) side of complex I and are shown in different shades of pink. All other accessory subunits are depicted in cyan and the core subunits in grey

assignment of the *Y. lipolytica* subunits is still incomplete (Zickermann et al. 2015; D'Imprima et al. 2016) (Fig. 7.4). During evolution complex I accessory subunits co-evolved in many different ways, either maintaining, modifying or losing their original function. The only accessory subunits that appear to be unique for metazoa are NDUFA10, NDUFB6, NDUFV3, NDUFC1 and NDUFB1.

Accessory subunits for which some biochemical information is available include NDUFAB1, which has retained its original function. It is homologous to the acyl-carrier proteins from bacteria, chloroplast and mitochondria that are involved in fatty acid synthesis (Chan and Vogel 2010). In *Y. lipolytica* and bovine systems they are known as ACPM and SDAP, respectively. In mitochondria they often come in isoforms and they are implicated in the synthesis of the lipoic acid cofactor of α-ketoacid dehydrogenases (Hiltunen et al. 2010). Despite the fact that they have been reported to carry a covalently attached pantetheine-4′-phosphate group (Runswick et al. 1991) and the recent cryo-EM map of bovine complex I displays densities consistent with such a ligand, no activity has been reported (Zhu et al. 2016). Moreover, NDUFAB1 is the only subunit of complex I that is also present in fermenting yeasts lacking complex I like *S. cerevisiae*. Interestingly, in *Y. lipolytica* NDUFAB1 is present as two isoforms, ACPM1 and ACPM2, that exhibit different properties although they have a very similar sequence (Dobrynin et al. 2010). The phosphopantetheine binding serine in ACPM1 is required for *Y. lipolytica* viability, whereas the one in ACPM2 is only required for complex I activity (Dobrynin et al. 2010). In the bovine system NDUFAB1 is present as two identical copies of the SDAP protein (Fig. 7.4).

In both high-resolution structures of eukaryotic complex I, the NDUFAB1 accessory subunits are docked to the complex by two members of the LYR (leucine/tyrosine/arginine) motif protein family: NDUFA6 and NDUFB9. The mitochondrial LYR proteins are shown to be involved in the FeS protein biogenesis (Angerer 2015), raising the possibility that LYR family proteins may be involved in transferring the FeS clusters from the iron-sulfur cluster assembly enzyme IscU to recipient proteins (Maio et al. 2014).

The subunit NDUFA10 is homologous to deoxyribonucleoside kinases. It is regarded as specific for metazoa and was found only in some branches of higher eukaryotes, including mammals (Brandt 2006). It seems to be loosely bound to complex I and resides on the matrix side of the NU2M core subunit (Vinothkumar et al. 2014). Zhu et al. (2016) reported that in the structure the active site appears accessible and the key nucleoside kinase residues seem to be present, although no activity has been reported. NDUFA2 has a thioredoxin fold and in mammals and plants it has two cysteines that in the oxidized form of the protein may form a disulfide bond (Brockmann et al. 2004). It is not known whether this disulfide bond has a specific function and this is not conserved in fungi and some lower eukaryotes e.g. *C. elegans* (Brockmann et al. 2004). Since this protein was found to be phosphorylated by PINK1, a connection with Parkinson disease has been postulated (Morais et al. 2014).

An accessory subunit that seems to have been recruited at the early stages of eukaryotic evolution (Gabaldon et al. 2005) is NDUFA9. It is attached to the core subunits NDUFS7 and NDUFS3 in the hydrophilic arm. This protein belongs to the protein family of NAD-dependent short chain dehydrogenases/reductases (Fearnley and Walker 1992) and displays a NAD(P)-binding Rossmann fold with a parallel seven-stranded β-sheet. It was found to bind NADPH (Abdrakhmanova et al. 2006) and a density assigned as NADPH was observed in the recent cryo-EM

structures (Zhu et al. 2016; Fiedorczuk et al. 2016). Fiedorczuk et al. hypothesize that it may function as a redox sensor.

NDUFS6 resides in the hydrophilic arm at the interface between the NADH domain and the rest of the complex and it has been thoroughly characterized in *Y. lipolytica* (Kmita et al. 2015). Its C-terminal domain harbors a zinc-binding site formed by three cysteines and a histidine (Vinothkumar et al. 2014). This motif in the *Y. lipolytica* ortholog NUMM has been shown to bind a Zn atom and deletion of the whole gene or residues coordinating the Zn atom causes stalling of the final stage of complex I assembly (Kmita et al. 2015). The position of the Zn atom has also been confirmed in the mammalian enzyme (Zhu et al. 2016; Fiedorczuk et al. 2016).

Accessory subunits NDUFS5, NDUFB7, NDUFA8 and NDUFB10 are members of the twin Cys-$X_9$-Cys family (Longen et al. 2009) and they are located at the intermembrane face of complex I (Zhu et al. 2016) (Fig. 7.4). The former three proteins display CHCH domains (pairs of helices linked by two disulfide bonds) (Szklarczyk et al. 2011) and are substrate for the Mia40 oxidative-folding pathway (Banci et al. 2009).

Although the main and more frequent complex I deficiencies are related to malfunctions of core subunits, so far already 17 accessory subunits have been linked to complex I related diseases (Rodenburg 2016). It has been proposed that they may work as a protective case against ROS (Requejo et al. 2010), "insulating" the redox cofactors and thereby preventing electron transfer to molecular oxygen (Hirst 2011). However, this hypothesis does not agree with the data of $O_2$ reduction which are similar in eukaryotes and bacteria (Esterhazy et al. 2008) and it does not explain how the prokaryotic enzyme survives without all those accessory subunits.

### 7.2.7 *Complex I Link to Sulfur Metabolism in* Y. lipolytica

Knowledge about the function and catalytic activity of the accessory subunits of complex I is still lacking in most cases. Recently a function was proposed for an accessory subunit of *Y. lipolytica* complex I: ST1 (D'Imprima et al. 2016). The consistent presence of an extra ~34 kDa subunit in *Y. lipolytica* complex I preparations was reported in 2005 and this protein was identified as a member of the sulfur transferase protein family (E.C. 2.8.1) (Abdrakhmanova et al. 2005). Sulfur transferases are present in organisms of all phyla and transfer sulfur-containing groups, reviewed thoroughly in Bordo and Bork 2002. Although the members of this protein family differ largely at the sequence level, their tertiary structure seems to be highly conserved and resembles that of bovine rhodanese, the most studied and best characterized sulfur transferase (Ploegman et al. 1978). Depending on their substrate the sulfur transferase family can be divided in two subclasses; these are thiosulfate:sulfur transferases (TST; E.C. 2.8.1.1) and 3-mercaptopyruvate:sulfur transferases (MST; E.C. 2.8.1.2). Usually the CRXGX[R/T] sequence in the active loop of TSTs enzymes is used as a marker to distinguish them from MSTs, which contain CG[S/T] GVT (Bordo and Bork 2002). Since the amino acid sequence of *Y. lipolytica* ST1

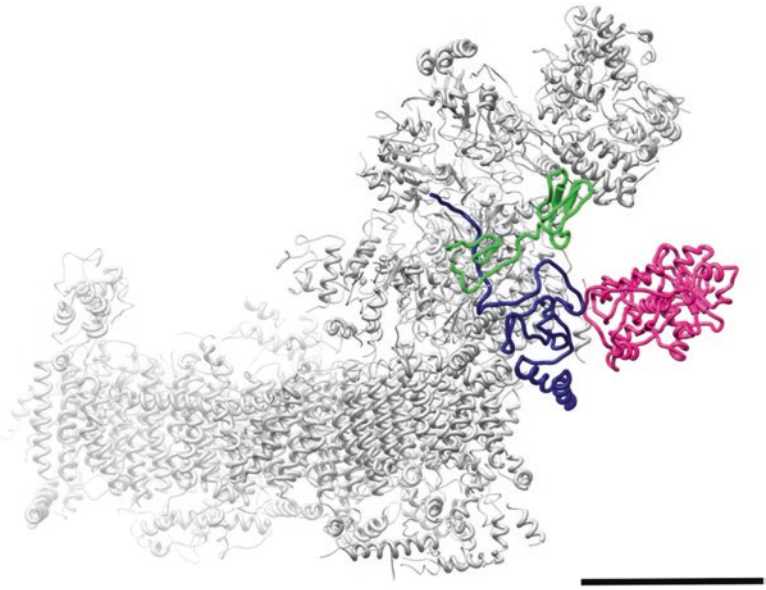

**Fig. 7.5** The accessory subunit ST1 in complex I from *Y. lipolytica*. The x-ray structure (pdb 4wz7) is displayed as grey ribbon and the homology model of ST1 (D'Imprima et al. 2016) in pink. The accessory subunits B8 and 13-kDa from bovine (pdb 5lc5) (homologues of N7BM and NUMM in *Y. lipolytica*) which form the interface are shown in green and blue, respectively. Scale bar: 50 Å

contains the sequence CGSGVT, the accessory subunit ST1 can be classified as an MST enzyme.

A cryo-EM map shows that ST1 is located on the side of the hydrophilic arm in the vicinity of the core subunit NDUFS2 (D'Imprima et al. 2016). Based on a comparison with the fully annotated structure of bovine complex I (Zhu et al. 2016), it can be concluded that the interface of ST1 with complex I is provided by the accessory subunits NDUFS6 and NDUFA12 (Fig. 7.5). This is in agreement with biochemical data showing that *Y. lipolytica* complex I mutants lacking the accessory subunits NUMM and N7BM (orthologues of NDUFS6 and NDUFS6, respectively) completely lack ST1 (Kmita et al. 2015). MST activity was measured in both purified *Y. lipolytica* complex I and for the ST1 protein heterologously expressed in *E. coli* (D'Imprima et al. 2016). No MST activity was detected in complex I preparations after being supplied by NADH or NADPH; moreover, no $H_2S$ formation was found in the presence of 3-MP and DTT in a ST1 deletion strain (Abdrakhmanova et al. 2005). These results prove that the observed sulfur transferase activity of the *Y. lipolytica* complex I preparation can be assigned to the accessory subunit ST1.

$H_2S$ is a potent and effective gasotransmitter that can have beneficial physiological implications or highly toxic effects, depending on the tissue and on the concentration in which it is released (see Wang 2012 for an exhaustive review).

A rapid catabolism that prevents the $H_2S$ cellular concentration to reach toxic levels might be achieved by directly linking ST1 $H_2S$ formation to a pathway for $H_2S$ consumption. An ideal candidate could be sulfide quinone reductase (SQR), a flavoprotein that supplies electrons into the respiratory chain via ubiquinone, which represents the main route of $H_2S$ detoxification in mitochondria (Yong and Searcy 2001). D'Imprima et al. propose that a not yet identified SQR in the mitochondrial membrane of *Y. lipolytica* may interact with ST1 bound to complex I, which thus provides a structural scaffold that connects the ubiquinone reduction with the biogenesis of $H_2S$ and its nearly instantaneous detoxification. It is tempting to speculate that *Y. lipolytica* uses this enzymatic pathway to provide electrons from $H_2S$ rather than NADH during stressful situations or in a very polluted environment, where this non-fermentative yeast was first discovered.

## 7.3 Complex II

Complex II or succinate dehydrogenase, also named succinate-coenzyme Q reductase or mitochondrial succinate:ubiquinone oxidoreductase (mitochondrial SQR) (EC 1.3.5.1) is the only respiratory chain complex that does not pump protons across the IMM. It is part of the citric acid cycle, where it catalyzes the oxidation of succinate to fumarate, coupled to the reduction of ubiquinone to ubiquinol. Ubiquinol is a substrate for complex III and thus complex II provides a second direct link between the citric acid cycle and the respiratory chain, apart from NADH that enters the respiratory chain at the level of complex I. Complex II is homologous to quinol:fumarate reductase (QFR), which performs the reverse reaction and is found in anaerobic cells respiring with fumarate as terminal electron acceptor (Hägerhäll 1997). Unlike the other respiratory chain complexes, which have additional subunits in eukaryotes, complex II has the same composition in mitochondria and prokaryotes. It consists of two hydrophilic proteins, a flavoprotein (Fp) containing an FAD cofactor and an iron-sulfur protein (Ip) with three FeS clusters, and a membrane anchoring domain, in mitochondria consisting of the two transmembrane proteins, CybL and CybS, with one heme. The membrane domain is less conserved than the catalytic subunits and can consist of one or two proteins with one, two or no heme groups (Hägerhäll 1997).

Crystal structures were first determined from prokaryotic QFR (Iverson et al. 1999; Lancaster et al. 1999) and complex II (Yankovskaya et al. 2003). The structure of the 124-kDa porcine mitochondrial complex II was determined in 2005 (pdb 1zoy) (Sun et al. 2005), followed by the very similar avine complex (Huang et al. 2006). The 68-kDa Fp protein has a Rossmann fold and contains the FAD cofactor, the electron acceptor for succinate, in an extended conformation (Fig. 7.6). As was already known for many years (Kearney 1960; Walker and Singer 1970) the FAD is covalently bound to a histidine side chain. The 29-kDa Ip protein contains three iron-sulfur clusters, a [2Fe-2S], [4Fe-4S] and [3Fe-4S], and forms the core of the complex, connecting with Fp on one side and with the membrane anchor on the other side. The two membrane-anchor proteins, CybL (15 kDa) and CybS (11 kDa),

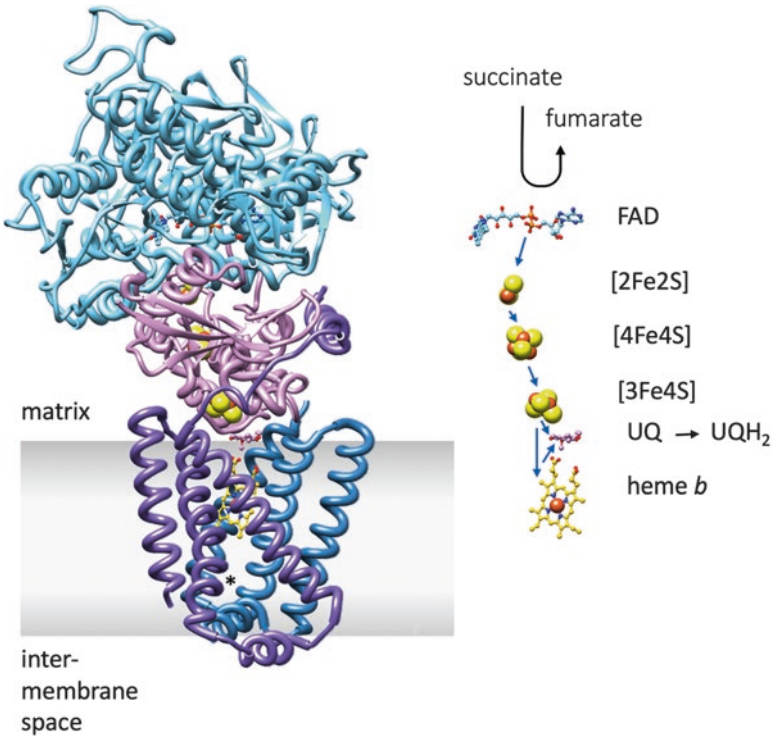


**Fig. 7.6** Structure of complex II (porcine heart, pdb 1zoy) (Sun et al. 2005). The FAD binding protein (Fp) is shown in light blue; iron-sulfur protein (Ip) in pink; the transmembrane proteins CybL and CybS in purple and dark blue, respectively. The putative membrane region is shaded in gray. The Qd site is indicated by an asterisk. On the right side, the prosthetic groups constituting the electron transfer pathway are shown together with ubiquinone. The electron transfer flow to the Qp site is indicated by blue arrows

each have three TMH and a heme *b* is coordinated between them. The heme iron is coordinated by the imidazole of two histidines, one from each subunit. The succinate and ubiquinone binding sites in the structure were probed with inhibitors. A 3.5-Å crystal structure (1zp0) (Sun et al. 2005) shows 3-nitropropionate (NPA), a succinate analog and a strong inhibitor for the succinate-oxidation enzymatic activity of complex II, in the expected position near the FMN group of FAD. TTFA (2-thenoyltrifluoroacetone) is an inhibitor for the ubiquinone reduction of complex II by occupying its ubiquinone-binding sites. Two TTFA molecules were found in the crystal structure, one in the proximity of the [3Fe-4S] cluster on the matrix side (Qp) and one at the distal side of the transmembrane anchor near the IMS (Qd) (Fig. 7.6). These sites confirm biochemical evidence for two ubiquinone-binding sites in mitochondrial complex II (Hägerhäll 1997). Comparison with the prokaryotic structures and sequence analysis confirm the position of the matrix binding site, with contributing residues from both transmembrane subunits and the Ip (Sun

et al. 2005). While the Fp and Ip subunits are highly conserved from prokaryotes to mitochondria, the membrane anchor is more divergent with sequence identities <20%, implying a different function of this region, and the distal ubiquinone-binding site appears to be specific for mitochondria (Sun et al. 2005).

## 7.4 Complex III

Complex III, also known as cytochrome $bc_1$, is the second enzyme in the mitochondrial respiratory chain, to which the distinct substrate-dependent branches of the chain converge. This complex couples the electron transfer from $QH_2$ to cytochrome *c* with the translocation of protons across the IMM (Trumpower and Gennis 1994).

### *7.4.1 Structure of Complex III*

Close to 50 crystal structures of the eukaryotic $bc_1$ complex have been produced in the last 20 years. The first complete structure was obtained in 1998 for the bovine complex (Iwata et al. 1998). The structures include native and inhibitor bound states of the enzyme from beef, chicken and yeast and were invaluable for progress in the field. Complex III is a symmetrical dimer, with three core subunits that are highly conserved from bacteria to mammals (Yang and Trumpower 1986). Additionally, up to eight supernumerary subunits can be present in the mitochondrial complex, for a total of 11 subunits per monomer in the mammalian enzyme (Schägger et al. 1986) (Fig. 7.7). The conserved, catalytically active subunits are cytochrome *b* (cyt *b*), with two *b*-type hemes ($b_L$ and $b_H$), cytochrome $c_1$ (cyt $c_1$), with one *c*-type heme ($c_1$), and the Rieske iron-sulfur protein (ISP) that encloses a high-potential [2Fe-2S] cluster (Yang and Trumpower 1986). Cyt *b* is the only mitochondrial-encoded subunit from complex III and it harbors two distinct quinone-binding sites located on opposite sides of the membrane (Xia et al. 1997). The $Q_o$ site, located on the positive side, serves quinol oxidation, while at the $Q_i$ site quinone (or semiquinone, $SQ^{\bullet-}$) is reduced. This integral membrane protein forms the center of the complex, to which both cyt $c_1$ and ISP anchor through a single TMH (Xia et al. 1997). The soluble domains of the cyt $c_1$ and ISP subunits accommodate the respective cofactors and are located in the IMS (Xia et al. 1997). Cytochrome *c* interacts with the $bc_1$ complex through the soluble domain of cyt $c_1$ (Lange and Hunte 2002).

The supernumerary subunits do not participate in electron transfer and proton pumping and are most likely required for assembly, stability, modulation and regulation of the complex. These subunits are Core 1, Core 2, ISP presequence and subunits 6 to 10 (Iwata et al. 1998). Core 1 and Core 2 are the two largest subunits of the complex and were initially proposed to occupy a central position in the structure (Silman et al. 1967), though later studies proved their peripheral structural and

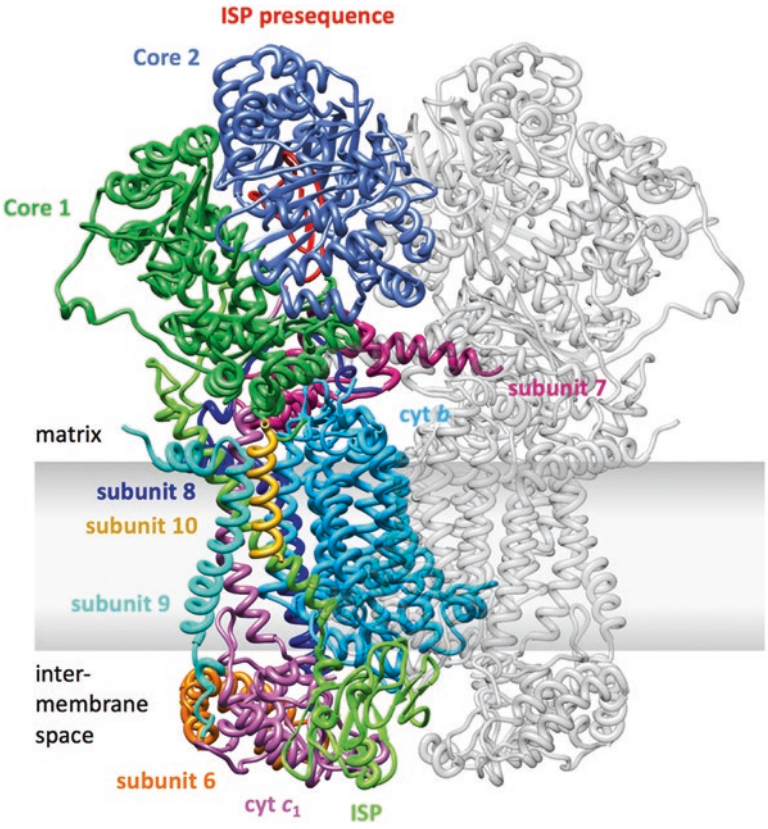


**Fig. 7.7** Structure of complex III (bovine heart, pdb 1bgy) (Iwata et al. 1998). Subunits are color-coded in one monomer, the second monomer is presented in grey. The putative membrane region is shaded in gray

functional role. These subunits are located in the mitochondrial matrix and are homologous to the matrix processing peptidase (MPP). Accordingly, the Core proteins have been suggested to be responsible for the cleavage of the ISP signal peptide. This hypothesis is supported by the presence of the ISP presequence in the mature complex from vertebrates as a stoichiometric subunit, within the cavity formed by Core 1 and Core 2 (Iwata et al. 1998), and also by measurements of proteolytic activity for the bovine proteins (Deng et al. 1998; Deng et al. 2001). However, a clear demonstration of this processing protease activity for maturation of the complex has not been achieved (Berry et al. 2013). Subunit 6 interacts with cyt $c_1$ and has been suggested to conserve the environment of the heme and aid cytochrome *c* binding (Nakai et al. 1993; Yang and Trumpower 1994). In the matrix, subunit 7 is at the interface with the membrane and contacts the Core 2 subunit of the opposite monomer (Xia et al. 1997; Iwata et al. 1998). The remaining supernu-

merary subunits 8, 9 and 10 have a single TMH each and surround the conserved membrane domain (Xia et al. 1997; Iwata et al. 1998).

Complex III is an obligate dimer and although rapid electron equilibration between the $b_L$ hemes (Castellani et al. 2010; Lanciano et al. 2011) and conformational communication between $Q_o$ and $Q_i$ sites have been proven (Covian and Trumpower 2006), it is still controversial whether the monomers function cooperatively or independently (Khalfaoui-Hassani et al. 2012; Hong et al. 2012). One notable feature of the cytochrome $bc_1$ dimer is the topology of the ISP. Each ISP subunit spans the two monomers, with its TMH associated with one monomer while the soluble domain with the [2Fe-2S] cluster transfers electrons from quinol to cytochrome *c* in the other monomer. Complex III biogenesis has been extensively studied in yeast, allowing a comprehensive description of this multistep process (Zara et al. 2009; Conte et al. 2015). Recent studies have shown that the dimerization occurs early in the assembly pathway and irrespective of expression of the ISP (Conte et al. 2015). The first intermediate forms by association of subunits 7 and 8 to cyt *b*. Subcomplexes containing cyt $c_1$, Core 1 and Core 2 are then added to the early core, followed by subunits 6 and 9 for generation of the late core subcomplex, which exists as an immature dimer. Lastly, the late core is activated by incorporation of ISP and subunit 10 (Zara et al. 2009; Conte et al. 2015). Several nuclear-encoded enzymes aid the formation and assembly of complex III, with some of these integrating the intermediate structures.

### *7.4.2 Mechanism of Complex III*

The reaction catalyzed by cytochrome $bc_1$ proceeds according to the modified Q-cycle mechanism, based on Peter Mitchell's original proposal (Mitchell 1972, 1976) (Fig. 7.8). Upon binding of quinol at the $Q_o$ site, one electron is transferred to the oxidized [2Fe-2S] cluster of the ISP that subsequently reduces heme $c_1$ (high potential chain). The reduced cyt $c_1$ finally transfers the electron to the soluble carrier cytochrome *c*. The unstable $SQ^{\bullet-}$ radical generated at the $Q_o$ site donates the second electron to the low potential chain, consisting of hemes $b_L$ and $b_H$ from cyt *b*. At the $Q_i$ site, a quinone molecule is reduced to $SQ^{\bullet-}$ by the high potential heme $b_H$. To complete the Q-cycle, a second quinol is oxidized at the $Q_o$ site for reduction of a second cytochrome *c* molecule and reduction of the stabilized $SQ^{\bullet-}$ to quinol at the $Q_i$ site. The topological separation of the $Q_o$ and $Q_i$ sites allows the vectorial transport of protons across the membrane, with the uptake of two $H^+$ at the negative side for quinol production and the release of four $H^+$ at the positive side (two per quinol molecule that is oxidized). The mechanism used for the electron bifurcation observed at the $Q_o$ site is however still unknown.

The unique features of the ISP are also key for the catalytic mechanism of complex III. The soluble domain of the ISP has been shown to occupy different positions in the several crystal structures of the complex, where the distances between the [2Fe-2S] cluster and the $Q_o$ site or heme $c_1$ are incompatible with efficient elec-

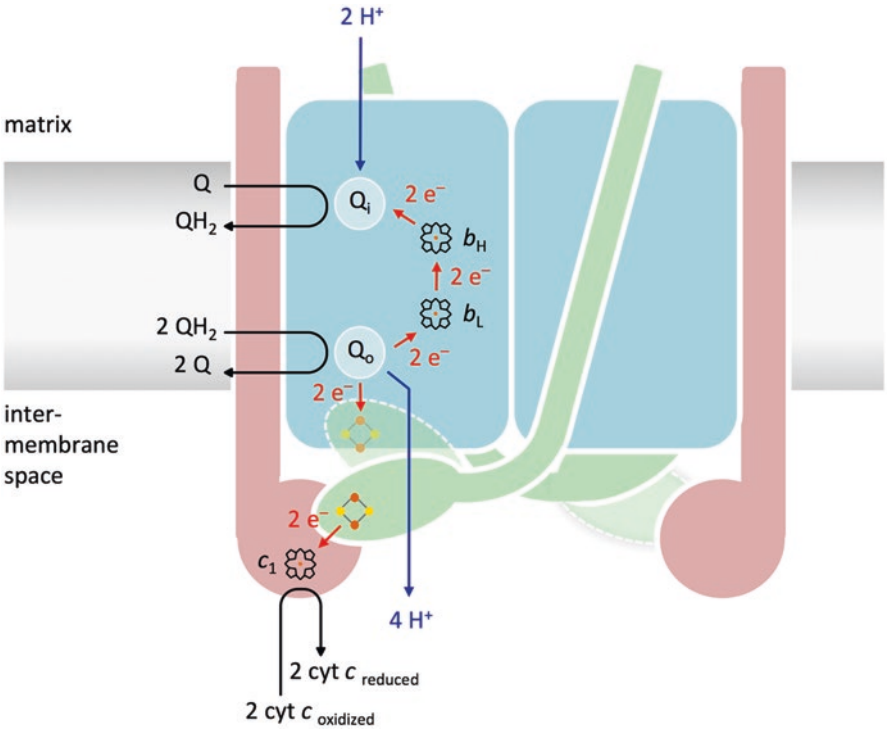


**Fig. 7.8** Cytochrome $bc_1$ Q-cycle mechanism. Cytochrome *b*, cytochrome $c_1$ and ISP are depicted in blue, pink and green, respectively. The soluble domain of the ISP is represented in two different conformations, corresponding to the *b* and *c* positions. Blue arrows indicate the uptake and release of protons, while red arrows illustrate transfer of electrons. Q, quinone. $QH_2$, quinol. The membrane is depicted in gray

tron transfer (Page et al. 1999). The observed differences result from the distinct conformations adopted by this domain; it has been shown that for the electron transfer between the $Q_o$ site and heme $c_1$ to take place, the soluble domain of the ISP must undergo significant conformational changes (Darrouzet et al. 2000). The movement between the *b* position (close to the $Q_o$ site) and the *c* position (close to cyt $c_1$) allows the complex to optimize the distances between the cofactors for a productive electron transfer (Iwata et al. 1998).

As stated earlier, complex III is an obligate dimer. However, studies of a heterodimeric cytochrome $bc_1$ from *Paracoccus denitrificans* with an inactivating mutation in one of the $Q_o$ sites revealed the same activity levels as the wild-type enzyme (Castellani et al. 2010). These results imply that under normal steady-state conditions only one $Q_o$ site is active at a given time, confirming that the complex operates according to the half-of-the-sites reactivity model. This model postulates also that the activation switch between monomers should be random. The half-of-the-sites mechanism should reduce the leakage of electrons to oxygen and, therefore, the formation of ROS. Additionally, it was shown that an asymmetric binding to the

$Q_i$ sites allows both $Q_o$ sites to be active simultaneously. This explains the increased activity observed in presence of low concentrations of antimycin A, an inhibitor of the $Q_i$ site (Castellani et al. 2010).

Complex III contributes significantly to the production of ROS in the cell (McLennan and Degli Esposti 2000). In contrast to complex I that generates superoxide exclusively in the matrix, complex III releases ROS in the IMS and possibly in the matrix as well (St-Pierre et al. 2002; Muller et al. 2004). In addition to the damaging effects of mitochondrial ROS, evidence for a regulatory role of ROS produced by the $bc_1$ complex has been reported. In particular, it has been proposed that complex III-derived ROS contribute to the cellular adaptive response to hypoxia and related cardioprotective ischemic preconditioning (Chandel 2010), adipocyte differentiation (Tormos et al. 2011) and apoptosis (Soberanes et al. 2009). Treatments with myxothiazol or stigmatellin, $Q_o$ site inhibitors, reduce or abolish ROS production, while inhibition by antimycin A, at the $Q_i$ site, produces a drastic increase in these species (Bleier and Drose 2013). These observations prove that production of ROS by complex III occurs primarily at the $Q_o$ site. The rate of ROS generation is also closely linked to the membrane potential (Rottenberg et al. 2009) and the redox state of the Q-pool (Drose and Brandt 2008). Two putative mechanisms can explain the generation of ROS by the $SQ^{\bullet-}$ radicals at the $Q_o$ site: a *semiforward* electron transfer or a *semireverse* electron transfer (Bleier and Drose 2013; Lanciano et al. 2013). In the *semiforward* model, the leakage of electrons is thought to accrue from an increased accumulation or stabilization of the $SQ^{\bullet-}$ at the $Q_o$ site, compared to the normal turnover in the native enzyme. This reaction may become significant at inhibition by antimycin A, for a highly reduced Q-pool, high membrane potential or specific mutations of the $Q_o$ site. Concurrently, the *semireverse* model advances that the production of ROS results from a reverse electron transfer from the reduced heme $b_L$ to $SQ^{\bullet-}$ and subsequently oxygen. Results supporting either mechanism have been reported (Sarewicz et al. 2010; Quinlan et al. 2011).

Mutations of complex III are not among the most frequent causes of mitochondrial diseases, but they are still linked to a large number of pathologies. Most mitochondrial disorders associated with complex III dysfunction result from mutations of the cytochrome *b* subunit or of the assembly factor BCS1L (Meunier et al. 2013), which is required for translocation and incorporation of the ISP on cytochrome $bc_1$.

## 7.5 Complex IV

Cytochrome *c* oxidase (complex IV) is the terminal oxidase in the mitochondrial respiratory chain and reduces $O_2$ to $H_2O$ while pumping protons across the IMM. This member of the heme-copper oxidases family is probably the best understood enzyme from the three mitochondrial proton pumping respiratory complexes, made possible by the 2.8 Å x-ray structures of the bovine and bacterial enzyme published in 1995 and 1996 (Tsukihara et al. 1995; Iwata et al. 1995; Tsukihara et al. 1996) that stimulated experimental studies with a wide range of techniques.

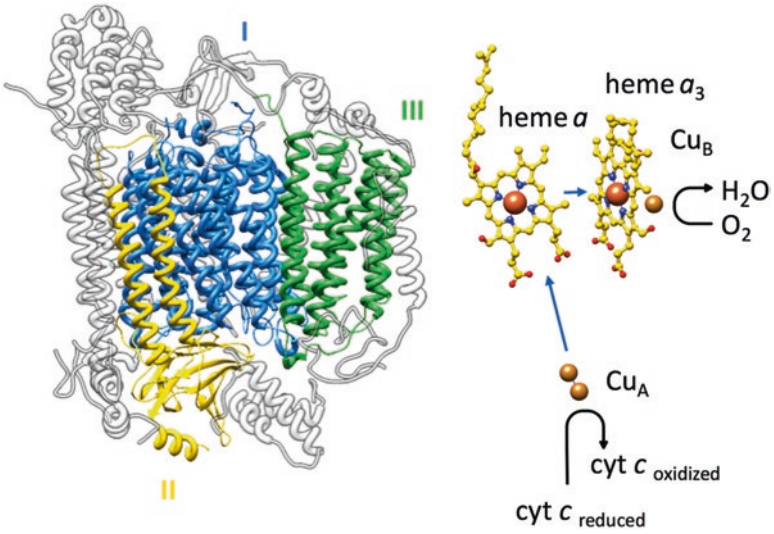


**Fig. 7.9** Structure of complex IV (bovine heart, pdb 1occ) (Tsukihara et al. 1996). Core subunits are color-coded and accessory subunits are shown in grey. Right: redox metal centers that participate in the electron transfer from cytochrome *c* to dioxygen. The electron transfer flow is indicated by blue arrows

### *7.5.1 Core Subunits of Complex IV*

Complex IV is composed of 14 different subunits in mammals and birds, from which only the three mitochondrial-encoded subunits I, II and III are present in the simpler bacterial enzyme (Fig. 7.9). Subunit I is a membrane embedded subunit, with 12 TMH and three of the four cofactors, heme *a*, heme $a_3$ and $Cu_B$. The fourth catalytic site, $Cu_A$, is located in subunit II, which is anchored by two TMH and has a soluble domain in the IMS, to which cytochrome *c* binds. Subunit III with seven TMH stabilizes the other two core proteins and acts as an initial proton acceptor in one of the transfer pathways (Varanasi and Hosler 2012; Alnajjar et al. 2014).

### *7.5.2 The Catalytic Cycle of Complex IV*

As stated earlier, cytochrome *c* oxidase contains four redox-active metal centers: $Cu_A$, heme *a* ($Fe_a$) and a binuclear center composed of heme $a_3$ ($Fe_{a3}$) and $Cu_B$ (Fig. 7.9). In each catalytic cycle, four reduced cytochrome *c* molecules donate sequentially one electron to $Cu_A$, which is transferred through $Fe_a$ to the active site. Concurrently to each electron transfer to the $Fe_{a3}/Cu_B$ binuclear center, the uptake of two protons occurs; in total eight protons are taken from the matrix, from which half

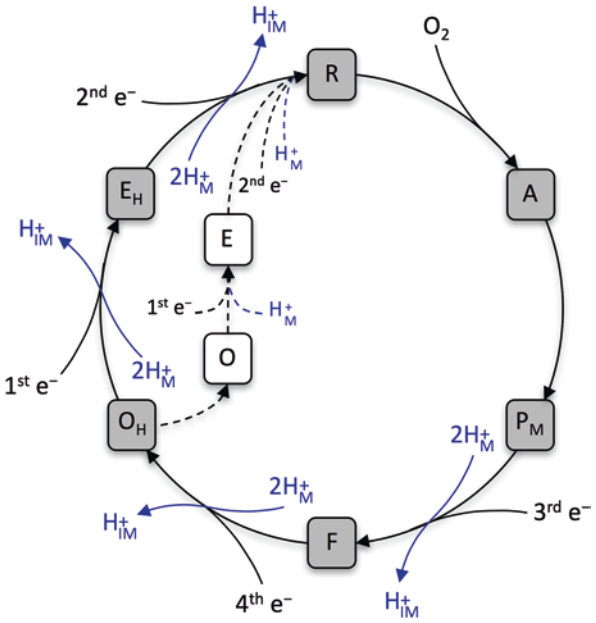


**Fig. 7.10** Catalytic cycle of cytochrome *c* oxidase. Dashed arrows indicate the transitions between reductive phase intermediates not coupled to proton pumping. Blue arrows represent the uptake and release of protons on the matrix and IMS side, respectively

are used for water formation in the binuclear center and the other four are pumped across the membrane into the IMS (Wikström 1977).

Numerous reaction intermediates with specific redox and protonation states of $Fe_{a3}$ and $Cu_B$ have been identified, which contributed to the formulation of a detailed model of the catalytic cycle (Konstantinov 2012; Popovic 2013; Sharma and Wikström 2016; Yoshikawa and Shimada 2015). This can be divided in two phases: the reductive phase and the oxidative phase (Fig. 7.10). In the reductive phase, oxidized complex IV (*$O_H$ state*) receives sequentially two electrons from two molecules of cytochrome *c*; the first electron, together with a proton from the matrix, produces the one-electron reduced intermediate (*$E_H$-state*), while the second electron and proton produce the reduced state (*R-state*). During the reductive phase a hydroxide ion in the binuclear center remaining from the previous cycle is protonated and released as water. The *R-state* has two electrons in the binuclear center (mixed-valence state) and in anaerobic conditions two more electrons, bound to heme *a* and $Cu_A$ (fully-reduced state).

In the oxidative reaction phase, four electrons are transferred to $O_2$ for its reduction to $H_2O$. This phase starts with $O_2$ binding to cytochrome *c* oxidase in the *R-state*. The reduced binuclear site rapidly reacts with $O_2$ for formation of the oxygen adduct intermediate (*A-state*). The simultaneous transfer of four electrons to the molecule of $O_2$ converts the *A-state* to the peroxy intermediate (*$P_M$-state*). Three of these electrons are donated by the binuclear center (two from $Fe_{a3}$ and one from $Cu_B$), while an amino acid residue in the vicinity of the active site provides the fourth electron. This residue is thought to be Tyr244, which is covalently bound to one of the histidine ligands of $Cu_B$. The conversion of the *$P_M$-state* to the ferryl-oxo

intermediate (*F-state*) requires the entry of a third electron into the enzyme, provided by the third cytochrome *c* molecule, and the uptake of a proton from the matrix. In the *F-state* a water molecule is formed. Delivery of the fourth electron by cytochrome *c* and a proton from the matrix produces the fully-oxidized high-energy state of the enzyme ($O_H$*-state*). The formation of the $O_H$*-state* marks the transition to the reductive phase of a new cycle.

It is important to note that the structure of cytochrome *c* oxidase and, in particular, the nonsequential four electron reduction of the bound $O_2$ molecule are crucial for the negligible production of ROS by this complex (Muramoto et al. 2010).

### *7.5.3 Proton Pumping by Complex IV*

The following transitions in the catalytic cycle are accompanied by pumping of one proton across the membrane: $P_M \rightarrow F$, $F \rightarrow O_H$, $O_H \rightarrow E_H$ and $E_H \rightarrow R$. The fully-oxidized low-energy state (*O-state*), which may form in the absence of an electron donor by relaxation of the $O_H$*-state*, and the subsequent one-electron reduced state (*E-state*) are not capable of proton pumping upon reduction and most likely are not natural states during the turnover of complex IV (Belevich et al. 2006).

It has been proposed that the transfer of the protons in the interior of complex IV for water formation and proton pumping occurs through a hydrogen bond network or by mobile water molecules in the hydronium state. Three proton transfer pathways have been described for the mitochondrial enzyme: D-, K- and H-channel (Wikström et al. 2015). Several studies have identified the D-channel as the pathway for the four protons that are pumped into the IMS during the catalytic cycle and also for the uptake of one or two of the chemical protons used at the binuclear center for water formation (Konstantinov et al. 1997; Brzezinski and Adelroth 1998). The D-channel includes ten water molecules and ends approximately in the middle of the membrane at a glutamic acid residue. The K-channel extends from a glutamic acid residue near the conserved lysine on the matrix side of subunit II to the conserved tyrosine close to the binuclear center. Only a few water molecules have been shown to be present in the channel, which is lined by numerous hydrophobic residues of subunit I. This pathway is responsible for the uptake of one or two chemical protons during the reductive phase (Konstantinov et al. 1997; Brzezinski and Adelroth 1998). High-resolution structures of the enzyme from bovine heart mitochondria revealed a third pathway called H-channel, which crosses the membrane all the way from the matrix to the IMS (Tsukihara et al. 1995). This channel consists of water-filled cavities and is lined by several polar residues and passes far from the catalytic site of complex IV. The enzyme from bovine heart with several mutations in the H-channel presented normal turnover activity, but no proton translocation (Tsukihara et al. 2003; Shimokata et al. 2007). In bacteria, with few exceptions the residues that compose the H-channel are conserved. However, site-directed mutations of this channel in the bacterial complex showed no effects in either turnover activity or proton pumping (Lee et al. 2000; Salje et al. 2005). In an attempt to

reconcile this results, the H-channel has been suggested not to be involved in proton pumping, but instead to work as a dielectric channel for minimization of the thermodynamic cost of moving electrons from the membrane surface into the nonpolar membrane domain where heme *a* is located (Rich and Marechal 2013).

### *7.5.4 Accessory Subunits of Complex IV*

The accessory subunits of cytochrome *c* oxidase strongly depress the activity of the core subunits and have a fundamental role in the regulation of the complex. Subunit IV is the largest of the supernumerary subunits (Fig. 7.11) and binds ATP, being responsible for the allosteric ATP-inhibition of complex IV at high cytosolic ATP/ADP-ratios (Arnold and Kadenbach 1997). This inhibition is dependent on the phosphorylation of subunit I and its disruption leads to an increase of the membrane potential and ROS production in mitochondria, associated with apoptosis and degenerative diseases. Subunit Va and Vb are both located exclusively in the matrix. The former was shown to abolish the allosteric ATP-inhibition upon binding to the thyroid hormone T2 (3,5-diiofothyronine) in the enzyme from bovine heart (Arnold et al. 1998b). Subunit Vb contains a Zn site with a classic zinc finger motif and it has been suggested to play a role in the assembly of the complex (Galati et al. 2009). This subunit also interacts with the regulatory subunit of the cAMP-dependent protein kinase A for a cAMP-dependent inhibition of complex IV (Yang et al. 1998). Subunit VIa has one TMH and a small soluble domain in the IMS and has been implicated in stimulation of thermogenesis for maintenance of the body temperature


**Fig. 7.11** Structure of bovine complex IV accessory subunits (pdb 1occ) (Tsukihara et al. 1996). Accessory subunits are color-coded and core subunits are shown in grey

in response to different stimuli in muscle and other tissues (Anthony et al. 1993; Lee and Kadenbach 2001). The only subunit located exclusively in the IMS is subunit VIb, which has been proposed to participate in cytochrome *c* binding and that, together with subunit VIa, stabilizes the dimeric state in which the protein was crystallized. Both subunits VIIa and VIIb have a single TMH and small extramembrane domains in the matrix and IMS, respectively. The first one was shown to form protein-protein contacts with complex III in the respirasome (Sousa et al. 2016; Gu et al. 2016; Letts et al. 2016), while the latter has been proposed to be essential for complex IV assembly and activity (Indrieri et al. 2012). Also subunit VIIc is involved in the formation of the respirasome by interaction with complex I (Sousa et al. 2016; Gu et al. 2016; Letts et al. 2016). No specific function has been proposed for subunits VIc and VIII, each with one TMH.

The most recently identified subunit of complex IV was initially thought to belong to complex I and named NDUFA4 (Carroll et al. 2003; Carroll et al. 2006). This subunit is encoded in the nucleus and is loosely attached to the rest of the enzyme, and its assignment was controversial (Hirst et al. 2003). However, NDUFA4 was shown to interact with subunits of complex IV and to be an essential subunit for its biogenesis (Balsa et al. 2012; Pitceathly et al. 2013). Recently a new cytochrome *c* subunit was identified in *Saccharomyces cerevisiae* named Cox26; however, this subunit is not conserved in higher eukaryotes (Levchenko et al. 2016).

Cytochrome *c* oxidase occurs in different isoforms. Subunits VIa, VIIa and VIII were first shown to have distinct isoforms in heart and liver mitochondria. The isoforms VIa-H, VIIa-H, VIII-H and VIa-L, VIIa-L, VIII-L are predominant in skeletal muscle cells and all other tissues, respectively (Schlerf et al. 1988). Isoforms of subunits VIa and VIIa were also shown to have specific expression patterns during development (Ewart et al. 1991; Bonne et al. 1993; Parsons et al. 1996). A third isoform of subunit VIII (VIII-3) was identified, for which the level of specificity is still not known (Huttemann et al. 2003b). Subunit IV has a lung-specific isoform (IV-2) (Huttemann et al. 2001) and subunit VIb (and possibly VIIb) a testes-specific isoform (VIb-2; VIIb-2) (Huttemann et al. 2003a). The expression of these tissue-specific and developmental-specific isoforms introduces an extra level of regulation of complex IV activity.

### *7.5.5 Complex IV Deficiencies*

Numerous pathologies have been reported after a perturbation of complex IV assembly or function (Rak et al. 2016). Few of these reports are associated to mutations of nuclear-encoded subunits of complex IV, as is the case for other respiratory complexes. Mutations of the mitochondrial-encoded subunits I, II and III are linked to a large number of different phenotypes and have been often observed, but even more frequently complex IV deficiencies have their origin in mutations of specific assembly factors. The diversity of phenotypes has been accredited to the degree of heteroplasmy in the case of subunits I, II and III and to the existence of several of the nuclear-encoded subunits in distinct isoforms.

## 7.6 Supramolecular Organization of the Respiratory Chain Complexes

The organization of the respiratory complexes in the mitochondrial membrane has been extensively debated for decades. Originally, it was proposed that the components of the respiratory chain were packed in the membrane, forming high order structures that allowed efficient electron transfer (Chance and Williams 1955). This solid-state model was however quickly discredited and gave place to the fluid or random collision model. The new paradigm was that each complex exists as a single entity that freely diffuses in the membrane and electron transfer occurs during random collisions (Hackenbrock et al. 1986). The existence of stable supercomplexes of complexes III and IV in some prokaryotes was considered specific for these species (Iwasaki et al. 1995). Only at the beginning of the twenty-first century, through solubilization with mild detergents like digitonin and analysis by blue-native polyacrylamide gel electrophoresis, supercomplexes were shown to be present in eukaryotes (Schägger and Pfeiffer 2000). Negative stain electron microscopy (EM) studies showed that these supercomplexes had a defined structure, including $I_1III_2$ complexes from plants (Dudkina et al. 2005a), $I_1III_2$ and $I_1III_2IV_1$ from bovine heart (Schäfer et al. 2006), and $III_2IV_2$ and $III_2IV_1$ complexes from *S. cerevisiae* (which lacks complex I) (Heinemeyer et al. 2007). These results introduced the currently established plasticity model, according to which the respiratory complexes exist free in the membrane but also as large supramolecular structures (Acin-Pérez et al. 2008). Since their first isolation, numerous stoichiometric supercomplexes formed by complexes I, III and IV have been identified, while the association of complex II in such structures was hypothesized in only a few cases (Acin-Pérez et al. 2008; Schönfeld et al. 2010). Studies with bovine heart mitochondria suggest that all complex I is associated in supercomplexes, while approximately 30% of complex III and more than 85% of complex IV exists as free enzymes (Schägger and Pfeiffer 2001).

### *7.6.1 The Respirasome*

Special interest has been devoted to the study of the respirasome ($I_1III_2IV_1$), which contains all the enzymes required for the electron transfer from NADH to molecular oxygen and is conserved in all higher eukaryotes. It is the most abundant supercomplex in bovine heart mitochondria (Schägger and Pfeiffer 2000, 2001; Schäfer et al. 2006) and has higher activity than the species lacking complex IV (Schäfer et al. 2006). Its three-dimensional structure has been studied by EM and after initial structures from 33–18 Å where the relative orientation of the complexes could be seen (Schäfer et al. 2007; Althoff et al. 2011; Dudkina et al. 2011) structures with sub-nanometer resolution were recently produced for several mammalian species (Gu et al. 2016; Letts et al. 2016; Sousa et al. 2016). The overall arrangement of the complexes is conserved in all respirasome structures; the complex III dimer lies on

the inner side of the complex I membrane arc, while complex IV is located at the distal end of the membrane arm of complex I and adjacent to complex III (Fig. 7.12). The three complexes are associated by several direct protein-protein interactions that mostly involve accessory subunits. The contacts between complex I and complex III are the most extensive within the respirasome, with subunits B22 (NDUFB9) and B14.7 (NDUFA11) of complex I interacting with Core 1 and subunit 8 of complex III, respectively. Additionally, Core 1, and also subunit 10, of complex III associate with subunit VIIa of complex IV. Only one core subunit among the three complexes is involved in the stabilization of the supercomplex; this subunit is ND5 (NU5M) from complex I, which binds subunit VIIc of complex IV. Lipid-mediated interactions are equally important for supercomplex stability. In particular, cardiolipin, which exists almost exclusively in the IMM, has been shown to be required for formation of supercomplexes (Mileykovskaya and Dowhan 2014).

The assembly process of the supercomplexes, and more significantly of the respirasome, is still unknown. Two conflicting models have been proposed based on studies performed in higher eukaryotes. According to the first model, the respirasome is formed by association of the mature individual complexes (Acin-Pérez et al. 2008; Guerrero-Castillo et al. 2016). Conversely, evidence for the formation of the respirasome by a progressive integration of single subunits or intermediate assemblies has been also reported (Moreno-Lastres et al. 2012). In the latter case, it was suggested that in addition to the direct assembly in supercomplexes, biogenesis of complexes III and IV might occur independently, while mature complex I is exclusively assembled in the respirasome. At this moment, only one protein has been unquestionably identified as a supercomplex assembly factor; SCAFI is required for the association of complex IV into supercomplexes but does not affect the assembly or stability of the individual complex (Lapuente-Brun et al. 2013; Cogliati et al. 2016).

### *7.6.2 Functions of the Respirasome*

Advantages of the organization of the respiratory chain in supercomplexes have been hotly debated, with the possibilities ranging from structural to kinetic and other functional roles. From a structural perspective, supercomplexes have been proposed to be required for proper expression of complex I, by contributing to its assembly or stabilization. This hypothesis gained force with the identification of several combined deficiencies in patients with mitochondrial disorders, where impaired expression of complex III induces the secondary loss of complex I (Bruno et al. 2003; Lamantea et al. 2002). Similar effects were observed in mammalian cells with complex IV deficiencies (D'Aurelio et al. 2006; Vempati et al. 2009; Diaz et al. 2006). Recent reports suggested that the degradation of complex I in the absence of complexes III or IV might be due to the accumulation of reduced quinone and consequent ROS production through RET (Guarás et al. 2016).

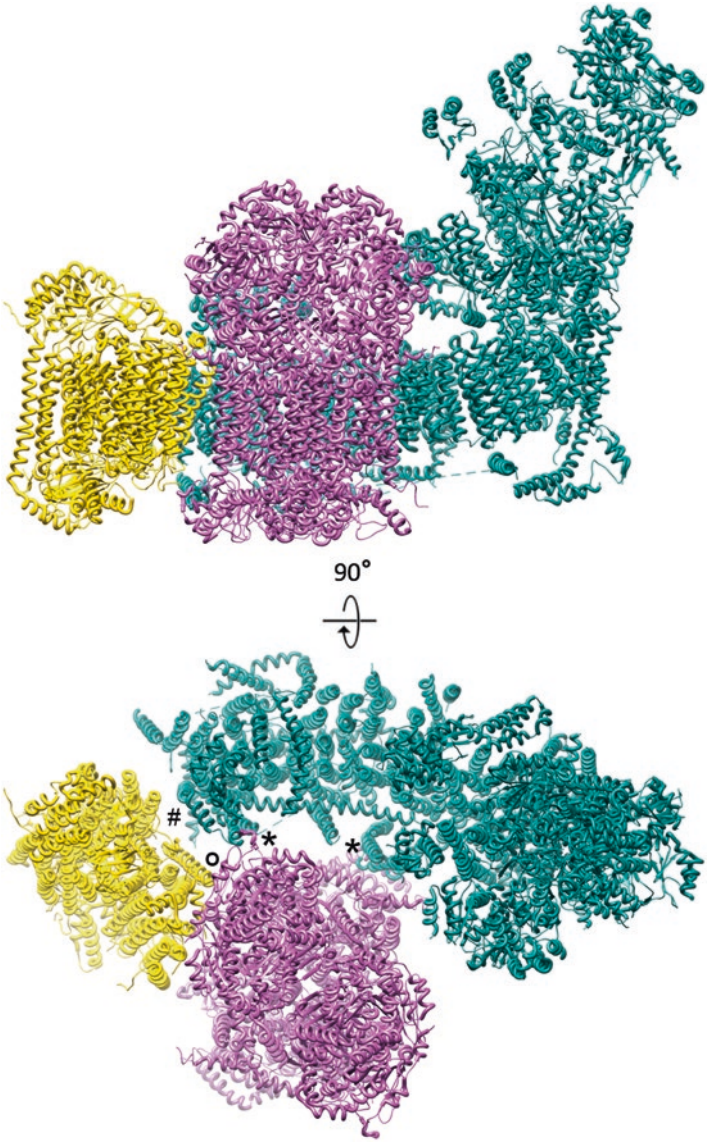


**Fig. 7.12** Structure of respirasome (bovine heart, pdb 5luf) (Sousa et al. 2016). View perpendicular to the membrane (top) and from the matrix (bottom). Complex I is shown in dark cyan, complex III in pink and complex IV in yellow. *: contacts between subunits of complex I and III; **#**: I and IV; **O**: III and IV as described in the text

However, several studies showed also that inhibition of complex III or IV activity is insufficient to prompt complete degradation of complex I (Acin-Pérez et al. 2004; Guarás et al. 2016), suggesting that physical interaction with other respiratory complexes is most likely important for maintaining complex I levels.

Another possible function of the respiratory supercomplexes relates to ROS production. By enhancing the ratio of free to superassembled complex I, the production of ROS was also increased (Maranzana et al. 2013), showing that the supramolecular organization of the respiratory chain reduces the leakage of electrons from complex I. Similar observations were reported upon destabilization of supercomplexes from *Saccharomyces cerevisiae* that contain only complexes III and IV, which imply that also ROS production by complex III might be reduced (Chen et al. 2012; Vukotic et al. 2012).

Finally, one of the most discussed advantages of supercomplexes has been the possibility of enhanced catalysis and efficiency of the electron transfer due to substrate channeling (Fig. 7.13). Substrate channeling is the direct transfer of an intermediate between the active sites of two enzymes that catalyze consecutive reactions. In the case of the respirasome, channeling of both quinone and cytochrome *c* were hypothesized. Contradictory results regarding channeling of cytochrome *c* between complex III and complex IV hinder a conclusion in this case. However, channeling of quinone from complex I to complex III within the respirasome has found support in numerous reports. Studies by flux control analysis found that both enzymes are rate-limiting for NADH oxidation, suggesting a relevant functional association (Bianchi et al. 2004; Lapuente-Brun et al. 2013). In case of channeling, a partition of the quinone pool would also be observed, with dedicated populations for succinate and NADH-dependent respiration. This compartmentalization explains for example why a reduction of complex III levels can impair succinate-dependent electron transfer, while NADH oxidation is maintained, due to the association of all the available complex III to complex I (Lapuente-Brun et al. 2013). Further arguments in favor of quinone channeling have been provided by the architecture of the respirasome. Early structures of this supercomplex revealed that the quinone-binding sites of complex I and the central monomer of complex III are aligned and within a short diffusion distance (Althoff et al. 2011). Recently, a functional asymmetry of the complex III dimer was observed in one structure of the bovine superassembly, where the central monomer preferentially catalyzes cytochrome *c* reduction (Sousa et al. 2016). The non-involvement of the outer monomer in the transfer of electrons from ubiquinol to the soluble carrier could be explained by the larger distance between the quinone-binding sites, which is incompatible with substrate channeling. Despite all the evidence supporting a kinetic advantage associated with respirasome formation, no consensus has been reached until now.

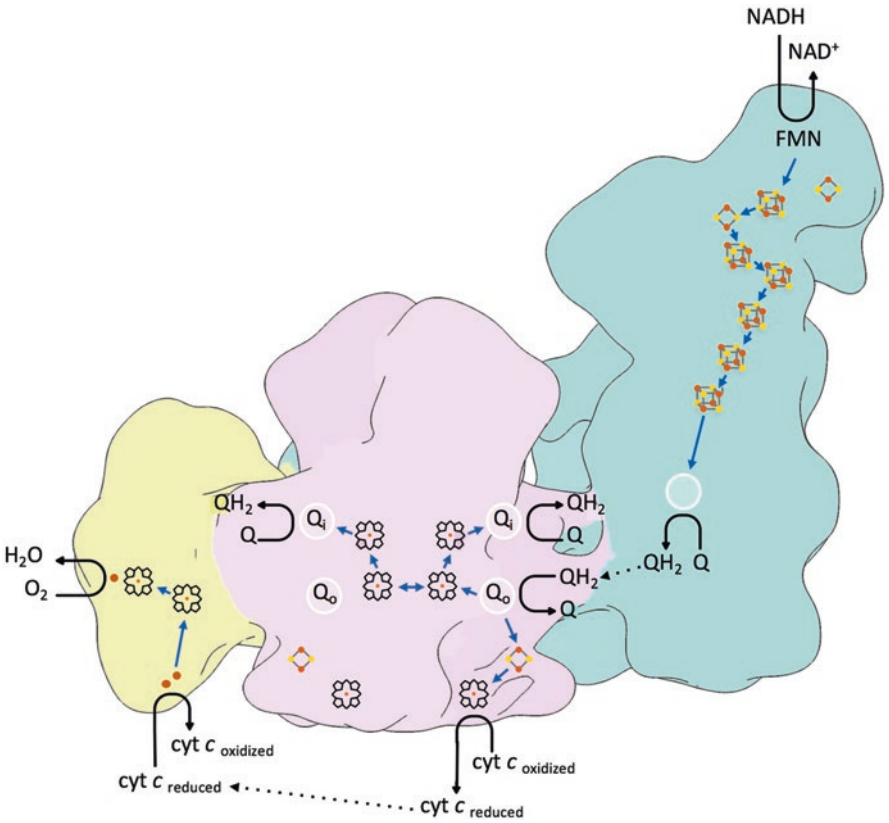


**Fig. 7.13** Electron and substrate transfer in the respirasome according to the channeling model. Rapid electron equilibration between $b_L$ hemes allows quinone reduction in either monomer of complex III. Quinone oxidation occurs preferentially at the central monomer of complex III. Complex I, III and IV are depicted in blue, pink and yellow, respectively. Quinone-binding sites are represented by circles. Blue arrows indicate transfer of electrons and dotted arrows diffusion of substrates. Reactions are indicated by black arrows

### *7.6.3 Plasticity of the Supramolecular Organization in the IMM*

The ratio between free complexes and supercomplexes in the IMM is highly regulated, varying among cell types and in response to physiological stimuli. Disorganization of the cristae during apoptotic remodeling of the mitochondrial architecture leads to impaired assembly of supercomplexes, while the narrowing of cristae observed during starvation conditions favors supercomplex formation (Cogliati et al. 2013). Also the lipid composition of the IMM is critical in the

supercomplex dynamics; whereas cardiolipin is required for the formation of supercomplexes, depletion of other lipids such as phosphatidylethanolamine stabilizes these structures (Bottinger et al. 2012). The dynamics of supercomplexes is further regulated by the transmembrane electrochemical potential, with the formation of superassemblies being favored at lower values (Quarato et al. 2011). Additionally, the acidification of the mitochondrial matrix, as induced during hypoxia, can promote the dissociation of respirasomes (Ramirez-Aguilar et al. 2011). Post-translational modifications have been also conjectured to influence supercomplex formation, however no correlation has yet been established.

The plasticity of the respiratory chain organization might be imperative for metabolic regulation. For instance, glucose feeds more electrons into the respiratory chain through NADH and therefore through complex I and the respirasome, whereas fatty acid oxidation largely contributes electrons through an FAD-linked pathway that is favored by free complexes (Lenaz and Genova 2016). A change in the equilibrium between free complexes and supercomplexes might be used for adaptation to substrate availability, ensuring their efficient oxidation. The plasticity observed might also modulate the production of ROS and therefore cellular activity, since these are known to act as signaling molecules (Whelan and Zuckerbraun 2013).

## 7.7 ATP Synthase

The proton gradient created by the respiratory chain drives a membrane-embedded rotor, the $F_o$ part of the $F_1F_o$ ATP synthase, and ATP is generated by conformational changes in the three nucleotide-binding pockets of the $F_1$ head by the binding change mechanism (Boyer 1993; Abrahams et al. 1994; Boyer 1997). The ATP synthase is a combination of two molecular machines and can act as an ion-gradient driven ATP synthase or as an ion pump powered by ATP hydrolysis. The binding change mechanism was first proposed by Paul Boyer (reviewed in (Boyer 1997)) and later confirmed by x-ray structures of the bovine $F_1$ in John Walker's laboratory (Abrahams et al. 1994). Rotation of the γ subunit was shown directly (Noji et al. 1997) by fixing a $\alpha_3\beta_3\gamma$ complex to a glass surface through the β subunit with a fluorescent actin filament attached to γ. After adding ATP, the rotation could be observed under a microscope. Also the direction of rotation for hydrolysis (counterclockwise as viewed from the membrane domain) was unambiguously determined by this experiment. ATP synthase consists of eight or nine different subunits in bacteria which are conserved across most species including mitochondria and chloroplasts, while mitochondrial ATP synthase has acquired more subunits (Table 7.2).

**Table 7.2** Subunits of ATP synthase in different species

| *E. coli* | Chloroplasts | Mammals | Yeasts | *Polytomella* | Location and function |
|---|---|---|---|---|---|
| α3 | α3 | α3 | α3 | α3 | $F_1$ head |
| β3 | β3 | β3 | β3 | β3 | $F_1$ head/catalytic subunit |
| γ | γ | γ | γ | γ | Central stalk/rotor |
| ε | ε | δ | δ | δ | Central stalk/rotor |
| | | ε | ε | ε | Central stalk/rotor |
| δ | δ | OSCP | OSCP | OSCP | Peripheral stalk |
| – | – | *d* | *d* | – | Peripheral stalk |
| – | – | F6 | *h* | – | Peripheral stalk |
| *b* | *b* | *b* | 4 | – | $F_o$/peripheral stalk |
| *b* | *b*’ | A6L | 8 | – | $F_o$/peripheral stalk[a] |
| *a* | *a* | *a* | 6 | *a* | $F_o$/stator/proton channel |
| *c*12 | *c*14 | *c*8 | 9/*c*10 | *c*10 | $F_o$/rotor/proton channel |
| – | – | f | f | – | $F_o$/stator/dimerization |
| – | – | – | *i* | – | $F_o$/stator |
| – | – | *e* | *e* | – | $F_o$/dimerization |
| – | – | *g* | *g* | – | $F_o$/dimerization |
| – | – | – | *k* | – | $F_o$/dimerization |
| – | – | IF1 | IF1 | – | ATPase inhibitor |
| – | – | – | – | ASA1–9 | Peripheral stalk[b] |

[a]The relation between the *b* subunit and 8/A6L was established by Hahn et al. (2016)
[b]*Polytomella* and *Chlamydomonas* have an elaborate peripheral stalk consisting of 9 different subunits without known relatives (van Lis et al. 2003; van Lis et al. 2007)

## *7.7.1 Composition and Subunits*

### 7.7.1.1 $F_1$ Head

The soluble or $F_1$ part is the catalytic head, consisting of an alternating arrangement of three α and three β subunits, arranged around the γ subunit, which is part of the rotor (Fig. 7.14). The α and β subunits are homologous and have the same fold, but only the β subunit is catalytic. The α subunits permanently contain a nucleotide without a known function, while the nucleotide-binding pockets of the β subunits are in turn in an open, loose and tight state upon rotation of the asymmetric γ subunit, which forms a long α helix coiled coil. Numerous crystal structures of $F_1$ in the ground state or ADP-inhibited state (reviewed in (Walker 2013)) show that two of the three nucleotide-binding sites in the β subunit have a similar conformation and contain either ADP and AMP-PNP (a non-hydrolysable ATP analogue), two ADP, or two AMP-PNP. The third site has a very different conformation and is almost always empty. The three sites interconvert upon rotation of the γ subunit.

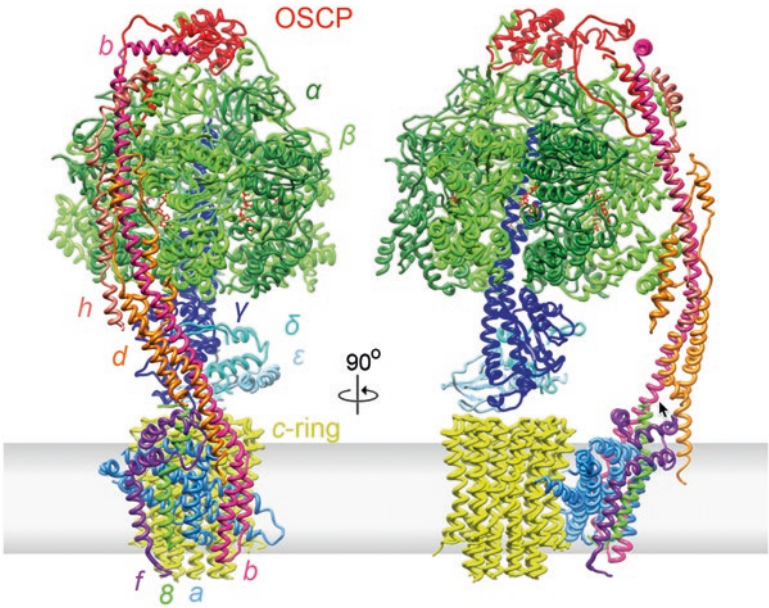


**Fig. 7.14** Subunit composition of mitochondrial ATP synthase from *Yarrowia lipolytica* (Hahn et al. 2016). View from the dimer interface (left) and from the side (right)

### 7.7.1.2 The Rotor

The rotor shaft is a coiled coil formed by the long N-terminal and C-terminal helices of the γ subunit. The central part of γ is attached to a membrane-embedded ring of *c*-subunits, together with the δ subunit (ε in bacteria) and in mitochondria another small protein, confusingly called ε (Fig. 7.14). The *c*-subunits are helix hairpins with a conserved negatively charged amino acid (in most species a glutamate, but an aspartate in *E. coli*) in the middle of the outer helix. This residue is expected to be protonated, so neutral, when in contact with the lipid environment of the membrane, but deprotonated and charged in the hydrophilic contact site with the stator. The number of subunits in the rotor ring was long an issue of debate, until structural data (Stock et al. 1999; Seelert et al. 2000; Stahlberg et al. 2001) showed that the number varies between species. By now, in bacterial ATP synthases rings have been found with 9 to 15 subunits (Stahlberg et al. 2001; Pogoryelov et al. 2005; Meier et al. 2006; Fritz et al. 2008; Pogoryelov et al. 2009; Matthies et al. 2009; Morales-Rios et al. 2015; Preiss et al. 2015), chloroplasts have 14 (Seelert et al. 2000; Seelert et al. 2009), while mammalian mitochondrial ATP synthase has 8 subunits (Watt et al. 2010) and those in yeasts (Stock et al. 1999; Hahn et al. 2016) and green algae (Allegretti et al. 2015) have 10. A rotor ring of *n* *c*-subunits yields 3 ATP per *n* translocated ions, so the stoichiometry has bioenergetic implications. The primary structure of the *c*-subunit determines the stoichiometry, and a region at the top of the

inner helix appears to be the major contributor. A conserved sequence GxGxGxG enables a close packing of the helices in the $c_{11}$-ring of *Ilyobacter tartaricus* (Vonck et al. 2002), the first ring for which the x-ray structure was solved (Meier et al. 2005). The glycines are exchanged to alanine or serine in some species (Liu et al. 2011), for example to AxAxAxA in the alkaliphilic soil bacterium *Bacillus pseudofirmus* OF4, resulting in a reduced curvature and thus a larger ring with 13 subunits (Preiss et al. 2010). Mutations in this motif can alter the stoichiometry (Pogoryelov et al. 2012; Preiss et al. 2013), and mutants of *B. pseudofirmus* OF4 with a smaller $c_{12}$-ring grew slower than the wt $c_{13,}$ showing a direct connection between the ion-to-ATP ratio and cell physiology (Preiss et al. 2013).

#### 7.7.1.3 Rotation Mechanism and the *a* Subunit

Before the structure of the *c*-ring was known, rotation of the ring was already hypothesized to occur by a "Brownian ratchet" mechanism, where the ring carries out random Brownian motions and only neutral (protonated) glutamates can enter the lipid phase, thus imposing directionality on the rotation of the ring (Junge et al. 1997; Vik and Antonio 1994). In this model, two half-channels allow access to the protonation site from either side of the membrane and the direction of rotation (and thus ATP synthesis or hydrolysis) depends on the electrochemical gradient. The first structures of the rotor ring (Meier et al. 2005; Murata et al. 2005) supported this model, and evidence for the postulated half-channels accessible from the two sides of the membrane also emerged (Angevine and Fillingame 2003; Fillingame and Steed 2014). However, the structure of the stator, the *a* subunit, remained elusive. The *a* subunit was predicted to have 5–7 TMH, with a consensus tending to 5 (Vik and Dao 1992; Cain and Simoni 1986), but the helix boundaries were uncertain and differed considerably between models. The highest sequence similarity is found at the C-terminus, which contains a completely conserved and essential arginine residue as well as several other conserved polar residues. Several residues in this region could be exchanged (Cain and Simoni 1988; Hatch et al. 1995) or crosslinked to the *c*-subunits (Jiang and Fillingame 1998; Moore and Fillingame 2008), leading to a model where the C-terminus contains two TMH facing the *c*-ring as part of a four-helix bundle (Schwem and Fillingame 2006). Attempts to purify the *a* subunit were often unsuccessful, although a preparation in a chloroform-methanol-water mixture gave promising results for NMR measurements (Dmitriev et al. 2004) and a two-dimensional crystal of a bacterial $F_o$ subcomplex appeared to show the four-helix bundle (Hakulinen et al. 2012). Attempts to crystallize the whole ATP synthase always yielded a structure lacking the stator (Stock et al. 1999; Pagadala et al. 2011; Giraud et al. 2012; Hahn et al. 2016). The introduction of direct electron detectors finally led to cryo-EM maps of intact ATP synthase complexes with sufficient resolution to solve the *a* subunit enigma. The first structure was the unusually stable mitochondrial dimer from the chlorophyll-less green alga *Polytomella* (Allegretti et al. 2015), soon followed by a monomeric bovine complex (Zhou et al. 2015) and the dimer of the yeast *Y. lipolytica* (Hahn et al. 2016). Apart from these

mitochondrial complexes, also a cryo-EM map of a vacuolar ATPase (Zhao et al. 2015) and its membrane domain (Mazhab-Jafari et al. 2016) were determined, as well as the first x-ray structure of an almost complete ATP synthase, from *Paracoccus denitrificans* (Morales-Rios et al. 2015). The ATP synthase structures all showed the same architecture of the *a* subunit: the predicted four-helix bundle with the two C-terminal helices facing the *c*-ring, but unexpectedly, the bundle is almost horizontal in the membrane. The distantly related V-ATPase also displays two helices facing the rotor at the same angle, showing the ancient and essential nature of this feature. All structures are at intermediate resolution where side chains are not yet visible, so the interpretation is not unambiguous. However, the known interaction of the C-terminal part of the *a* subunit with the *c*-ring places this region in the helix hairpin next to the ring and the availability of thousands of sequences and the observed high structural homology between available structures place restraints on possible models (Fig. 7.15). For example, although the two C-terminal helices are the most conserved parts of the structure, the loop between them has a variable length. The presence of two conserved, interchangeable pairs (His-Glu and Arg-Gln) (Cain and Simoni 1988; Hatch et al. 1995) with a member on each helix fixes the relative orientation (Allegretti et al. 2015). A model for the bovine *a* subunit was built using constraints from analysis of evolutionary covariance in the sequences (Zhou et al. 2015). From the bovine and yeast structures (Zhou et al. 2015; Hahn et al. 2016) almost the entire *a* subunit was assigned, and the models are very similar. The structure consists of six helices: a vertical TMH with the N-terminus in the IMS, an amphipathic helix on the matrix surface, and two helix hairpins forming a bundle at a high angle in the membrane (Fig. 7.16). These features are conserved in bacterial, mitochondrial and chloroplast *a* subunit sequences (Fig. 7.15) and can also be recognized in partially unassigned features of the *Polytomella* cryo-EM map (EMD-2852) (Allegretti et al. 2015) and the bacterial x-ray structure (pdb 5dn6) (Morales-Rios et al. 2015), as well as in the structure of monomeric ATP synthase from the yeast *Pichia angusta* (Vinothkumar et al. 2016).

The two C-terminal helices (5 and 6) are highly conserved in all $F_1F_o$ ATP synthases and are characterized by a series of charged or polar residues in a hydrophobic environment. The helices form a hairpin at an angle of ~20° to the membrane plane, with a loop near the IMS surface and the termini on the matrix side. The length of the loop is not conserved (Fig. 7.15), but the region is highly hydrophobic, in agreement with its location in the membrane interior, and includes one or several proline residues in most species, which probably contribute to breaking of the helices and/or forming a bend. The proton entrance on the IMS side is near the helix5-6 loop. The helix closest to the IMS, in most structures interpreted as helix 5, curves around the *c*-ring (Fig. 7.16). Conserved hydrophilic residues in this region on helix 5 and 6 line an aqueous cavity on the matrix side, where the protons will be released from the *c*-ring after almost a complete rotation of the ring. The conserved arginine of subunit *a* is located between the two proton channels and its charged side chain would prevent passage of a protonated, uncharged glutamate on the *c*-ring and thus ensure unidirectional rotation of the rotor. The resulting direction (counterclockwise as seen from the matrix for ATP synthesis) fits the observation (Noji et al. 1997).

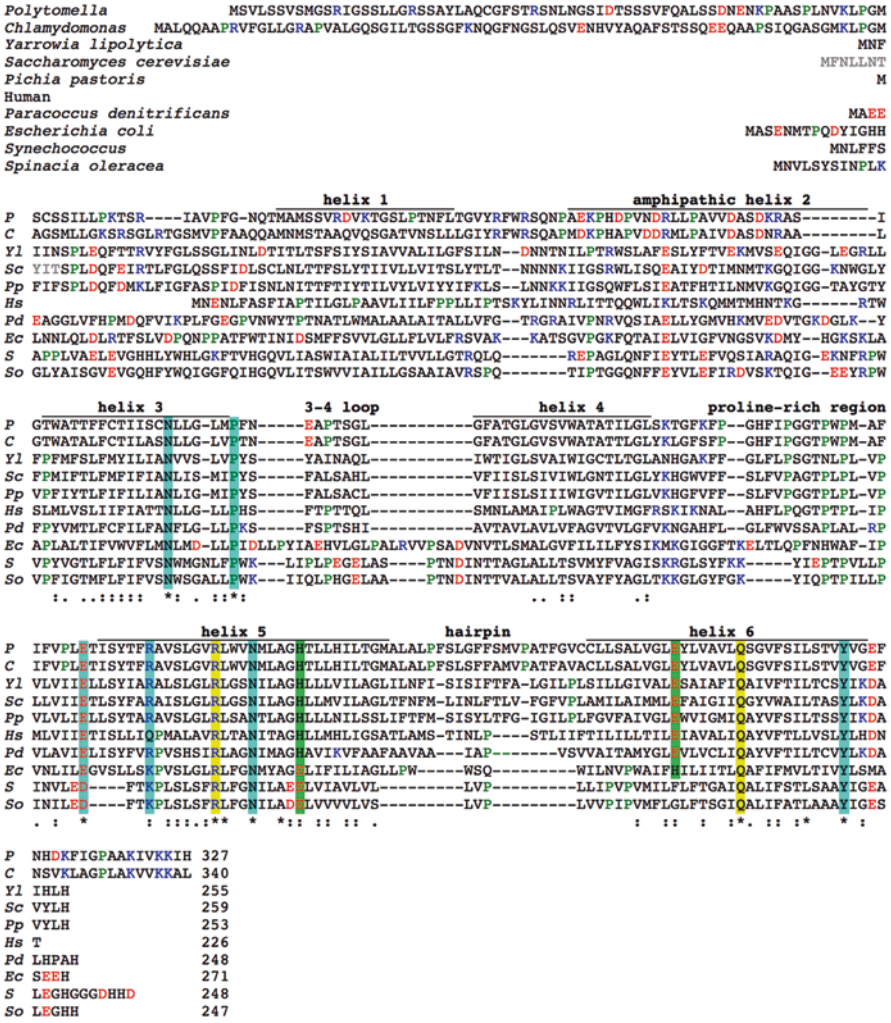


**Fig. 7.15** Sequence alignment of the *a* subunit. Shown are mitochondrial ATP synthase (*Polytomella* and *Chlamydomonas*; the yeasts *Y. lipolytica*, *S. cerevisiae* and *P. pastoris*; human); the bacteria *P. denitrificans* (an α-proteobacterium related to the ancestor of mitochondria), *E. coli* and *Synechococcus* (a cyanobacterium related to the ancestor of chloroplasts), and chloroplast ATP synthase from spinach. Positively charged residues are shown in blue, negative ones in red font, prolines in green. Highly conserved residues are highlighted in cyan, and two pairs of interchangeable residues in yellow (including the essential arginine) and green. The approximate helix boundaries and other conserved features are indicated above the alignment. The cleaved N-terminal presequence in *S. cerevisiae* is shown in grey font

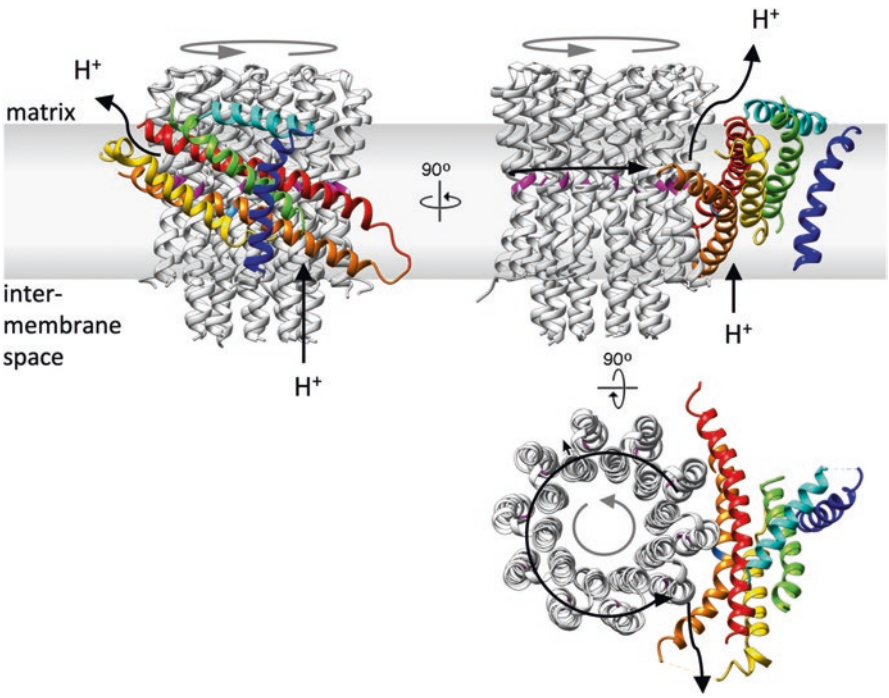


**Fig. 7.16** The *a* subunit and *c*-ring form the proton translocation channel in ATP synthase. Shown is the model from the yeast *Y. lipolytica* (Hahn et al. 2016). Grey, $c_{10}$-ring; color, *a* subunit. Blue, helix 1; cyan, amphipathic helix 2; green and yellow, helix 3 and 4 forming a horizontal helix hairpin; orange and red, helix 5 and 6 forming the second helix hairpin, which is adjacent to the *c*-ring. The conserved arginine on helix 5 is shown in cyan and the glutamates on the *c*-ring in magenta. Black arrows indicate proton flow and grey arrows ring rotation during ATP synthesis. Left, view from the dimer interface; right, view along the *a/c* interface; bottom, view from the matrix

#### 7.7.1.4 The Peripheral Stalk

The central stalk (the γ subunit), confirmed as the rotor in the $F_1$ x-ray structure (Abrahams et al. 1994) was visible in early EM images (Gogol et al. 1987) connecting $F_1$ and $F_o$. However, the complete architecture of the complex and especially the membrane-bound $F_o$ part and its connection to $F_1$ was still not clear. Biochemical evidence implicated unassigned subunits in a second stalk as part of a stator to counteract rotation of the head (Collinson et al. 1996; Ogilvie et al. 1997), which was confirmed by cryo-EM (Wilkens and Capaldi 1998). Such a feature was also seen in bacterial V-type ATPase (Boekema et al. 1997), which later turned out to have two peripheral stalks (Boekema et al. 1999; Bernal and Stock 2004; Vonck et al. 2009; Lau and Rubinstein 2010, 2012). In bacteria, the peripheral stalk is made up of the δ subunit, the equivalent of OSCP in mitochondria, on top of the head, and two *b* subunits, either two copies of the same protein or one each of homologous *b* and *b*'

proteins. The *b* subunits are predicted to be mainly α-helical with an N-terminal transmembrane domain, and the two subunits are thought to form a dimer. The N-terminal TMH of *b* from *E. coli* was solved by NMR (Dmitriev et al. 1999).

While the bacterial structure is conserved in chloroplast ATP synthase, the mitochondrial complex has a more elaborate peripheral stalk, consisting in the mammalian enzyme of the soluble OSCP, *b*, *d* and $F_6$ subunits and membrane subunits A6L and *f*. The yeast protein has a similar composition (Table 7.2). Crystal structures of subcomplexes of the soluble part of the bovine ATP synthase (Kane Dickson et al. 2006; Rees et al. 2009) showed that the mitochondrial peripheral stalk is mainly α-helical. Cryo-EM structures of the complete bovine (Rubinstein et al. 2003; Baker et al. 2012) and yeast (Lau et al. 2008) ATP synthase indicated a distinct curvature of the stalk, different from the crystal structure, apparently caused by its anchoring in the membrane domain (Baker et al. 2012). The stator seems to have an essential role not only in keeping the $F_1$ head stationary during rotation of the rotor but also in positioning the *a* subunit correctly relative to the *c*-ring. The cryo-EM structure of the dimer from the yeast *Yarrowia lipolytica* showed the architecture of the complete stator (Fig. 7.12). Behind the horizontal helix bundle of the *a* subunit run six TMH, which were interpreted as belonging to subunit *i*, *f, 8, a,* and the first and second TMH of *b* (Hahn et al. 2016). Subunit *8* appears to be the equivalent of the second bacterial *b* subunit, although the matrix C-terminal part of subunit *8* is truncated to different extents in the mitochondrial enzyme (Hahn et al. 2016). The *f* subunit and the first TMH of *b* are specific for mitochondria and do not occur in bacteria. The *f* subunit has an extension in the IMS and seems to make the main dimer contact (Hahn et al. 2016).

### *7.7.2 ATP Synthase Dimerization and Crista Morphology*

Submitochondrial particles of 70–80 Å diameter were recognized in early electron microscopic images in regular patterns on the cristae and correctly shown to be facing the matrix (Parsons 1963; Stoeckenius 1963). These features were initially named “elementary particles” and assumed to contain the complete respiratory chain (Fernández-Morán 1962), but later shown to be the $F_1$ ATPase (Kagawa and Racker 1966). First indications for a higher-order structure of the ATP synthase came from rapid-freeze deep-etch techniques on the cristae of *Paramecium* (Allen et al. 1989), where double rows of $F_1$ in a helical array around the tubular cristae were found. The occurrence of double rather than single rows suggested that the building blocks are dimers of ATP synthase. Dimers of ATP synthases were later found on Blue-Native-PA gels after solubilization of mitochondrial membranes with mild detergents, in all phyla: yeasts (Arnold et al. 1998a), fungi (Krause et al.

2004b), mammals (Schägger and Pfeiffer 2000; Krause et al. 2005; Cortes-Hernandez et al. 2007; Dencher et al. 2007), and higher plants (Eubel et al. 2003; Krause et al. 2004a). The corresponding bands were eluted from the gels and examined by EM, providing direct evidence for ATP synthase dimers in many species (Minauro-Sanmiguel et al. 2005; Dudkina et al. 2005b; Dudkina et al. 2006; Thomas et al. 2008; Cano-Estrada et al. 2010). The dimers were associated via their membrane domains, which included angles of 40–90°, strongly suggesting that the dimers were responsible for bending the IMM and dictating cristae morphology (Dudkina et al. 2005b; Minauro-Sanmiguel et al. 2005; Dudkina et al. 2006). Direct evidence for this came from cryo-electron tomography of submitochondrial particles of several species (Strauss et al. 2008; Dudkina et al. 2010; Davies et al. 2011; Davies et al. 2012), where dimer rows of ATP synthase were seen on all highly curved crista edges.

### *7.7.3 Dimer-Specific Subunits of ATP Synthase*

The small membrane-associated proteins *e, g* and *k* were identified as dimer-specific subunits in yeast (Arnold et al. 1998a). These mitochondrial subunits are not necessary for ATPase or ATP synthase activity, but deletion of the genes for *e* or *g* resulted in mitochondria that lacked ATP synthase dimers and had abnormal morphology with the inner membranes forming onion-like multilayered structures (Paumard et al. 2002; Giraud et al. 2002). The location of the *e* and *g* subunits in the ATP synthase complex was determined by comparing low resolution EM maps of yeast core ATP synthase and bovine ATP synthase with *e* and *g* attached (Lau et al. 2008; Baker et al. 2012) and is at the periphery of the $F_o$ domain.

The cryo-EM maps of mammalian (Zhou et al. 2015) and yeast (Hahn et al. 2016) ATP synthase both show a similar feature in this region: a funnel-shaped density in the membrane with a helix-like protrusion in the IMS. Subunit *e* is predicted to have an N-terminal TMH containing an essential GxxxG motif, suggesting a role in helix-helix interaction (Arselin et al. 2003), and a hydrophilic C-terminus located in the IMS, that would account for the observed helix protrusion (Fig. 7.17). Subunit *g* has an N-terminal matrix domain and a predicted C-terminal TMH also containing a conserved GxxxG motif. GxxxG motifs are often found to be important for mediating the interaction of TMH (Senes et al. 2004). Subunits *e* and *g* may thus form a tight heterodimer in the membrane. The helices in such a tight dimer would not be resolved at a resolution lower than ~6 Å, and may be forming the funnel-shaped density in the cryo-EM maps. The density is located near the *b* subunit, in support of the observation that the *g*-subunit can be crosslinked to the N-terminus of *b* in the matrix and that deleting the first TMH of *b* results in the loss of *g* and dissociation of the dimer (Soubannier et al. 2002).

The cryo-EM map of the *Yarrowia* ATP synthase dimer (Hahn et al. 2016) surprisingly showed that the *e* and *g* subunits are located at the outside of the $F_o$ dimer, not as expected in the center where they would mediate dimer formation (Vonck and Schäfer 2009). Interestingly, the bovine ATP synthase monomer including *e* and *g*

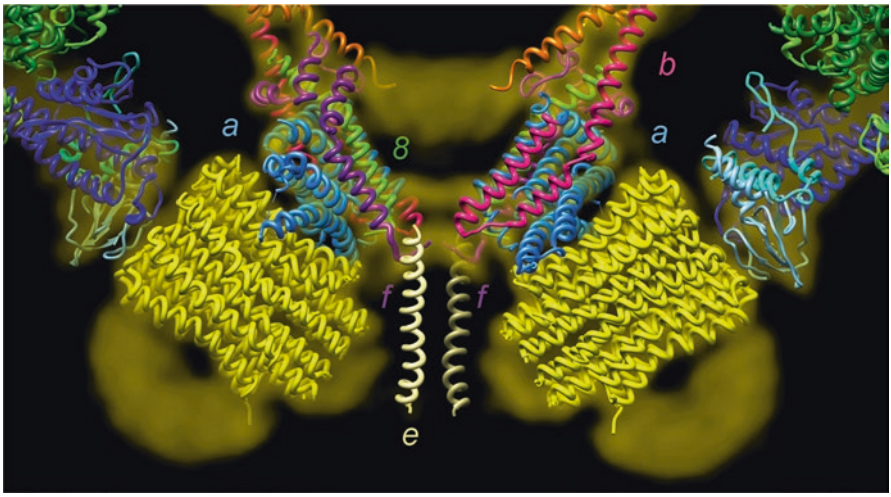


**Fig. 7.17** The dimer interface of the *Y. lipolytica* ATP synthase model with a slab of the cryo-EM map superimposed (Hahn et al. 2016). The dimer contact is on the IMS side only. The khaki helix extending in the IMS is probably the C-terminus of subunit *e.* Detergent is visible on the matrix side of the dimer interface and around the *c*-rings

has a bent detergent belt, suggesting that the role of the *eg* heterodimer is in bending the membrane (Baker et al. 2012). A monomer of the *Yarrowia* enzyme, lacking these subunits, has a straight detergent belt (Hahn et al. 2016) (Fig. 7.18), confirming this role. The sequence of both the *e* and *g* subunit contains several conserved charged or polar residues around the GxxxG motif in the putative TMH, which might be involved in specific interactions with the membrane components. The bending of the membrane probably orients the monomers in such a way that the dimerization subunits can establish dimer contacts (Fig. 7.17).

### *7.7.4 Assembly of ATP Synthase*

Although bacterial ATP synthases have been expressed cell-free (Matthies et al. 2011) or heterologously (Zhang et al. 2014) and were fully assembled and active, mitochondrial ATP synthase assembly is highly regulated and depends on specific chaperones. The assembly of $\alpha_3\beta_3$ requires Atp11p and Atp12p, which bind specifically to β and α, respectively and prevent aggregate formation (Ludlam et al. 2009). Although most subunits are encoded in the nucleus, in most species the $F_o$ subunits *a, c* and subunit 8 are mitochondrially encoded. In yeast, at least three proteins are required for $F_o$ assembly, Atp10p, Atp23p and Atp25p. The first two are involved in incorporation of the *a* subunit into the complex (Tzagoloff et al. 2004; Osman et al. 2007; Zeng et al. 2007). Atp23p cleaves the N-terminal presequence (10 residues in *S. cerevisiae*, Fig. 7.15); however, there is an Atp23p homolog in human

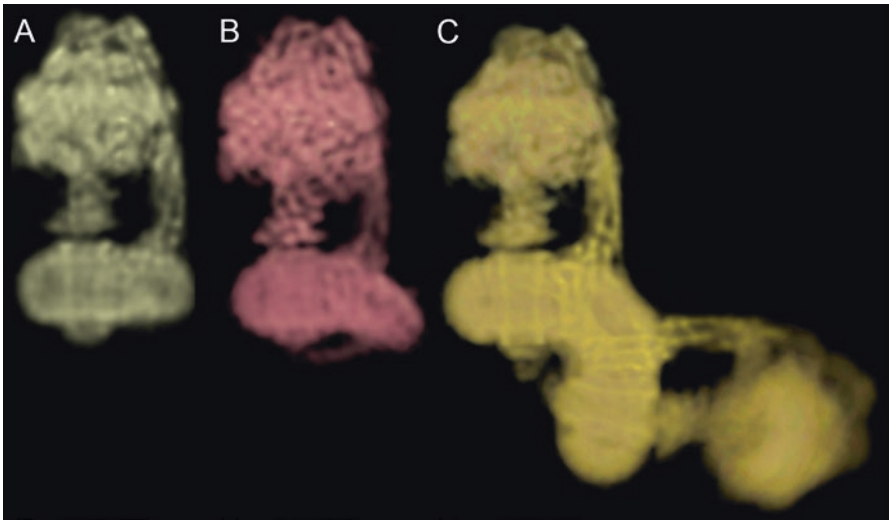


**Fig. 7.18** Subunit *e* and *g* bend the IMM. (**a**): Monomeric ATP synthase of *Y. lipolytica*, where subunit *e* and *g* were lost during purification The detergent belt forms a straight ring around $F_o$ (Hahn et al. 2016). (**b**): Monomeric bovine ATP synthase (EMD-3165) (Zhou et al. 2015). Subunits *e* and *g* were retained during purification. The detergent belt is bent. (**c**): Dimeric ATP synthase of *Y. lipolytica* has a bent detergent belt. Subunits *e* and *g* were retained during purification in the mild detergent digitonin (Hahn et al. 2016)

mitochondria, where the *a* subunit does not have an extension (Osman et al. 2007; Zeng et al. 2007); the additional function of Atp23p is unknown. Atp25p is thought to be required for the assembly of the rotor ring (Zeng et al. 2008). Assembly of ATP synthase appears to be modular, with one subcomplex consisting of $F_1$ with the *c*-ring and another the mitochondrial encoded *a* subunit and subunit 8, transiently interacting with Atp10p, together with at least some peripheral stalk subunits (Rak et al. 2011). Recently a complex was identified, consisting of the IMM subunits Ina17 and Ina22, that plays a role in peripheral stalk assembly (Lytovchenko et al. 2014), and thus the coupling of the two motors and completion of the complex.

### *7.7.5 Evolution of Rotary ATPases*

ATP synthase is an ancient machine that was already present in the last universal common ancestor (LUCA) (Weiss et al. 2016). The bacterial and archaeal versions share the basic architecture, and homology of the catalytic head and of the ion-translocating subunits is still easily recognizable. Both the bacterial and archaeal ATP synthase are still functional in eukaryotes. The bacterial version is found in both energy producing organelles, the chloroplast and mitochondrion, while the archaeal enzyme yielded the vacuolar (V-type) ATPase, an ATP-driven proton pump involved in vacuolar pH homeostasis. Whereas the chloroplast enzyme is similar to

the bacterial ancestor, the V-type ATPase and the mitochondrial enzyme have gained new subunits, most with a regulatory function, but in the case of the mitochondrial enzyme also a structural role in affecting membrane morphology. While the functional units of the ATP synthase, namely the $\alpha_3\beta_3$ head, the γ subunit, the *c*-ring and the *a* subunit have remained remarkably similar, the differences between bacterial and mitochondrial ATP synthase involve the peripheral stalk, in a way that does not affect the ATP synthase function of the complex. Whereas in the bacterial enzyme the peripheral stalk consists of only the δ subunit and two copies of *b*, the mammalian and fungal lineage have added several other subunits to the soluble part of the stalk as well as the membrane domain. While the advantage of the more robust soluble part is not yet clear, it is interesting to note that the accessory membrane subunits, *f*, *e,* and *g,* are involved in membrane bending and dimer formation, leading to the folding of the IMM into cristae. The resulting huge gain in IMM surface area is responsible for the large respiratory capacity of the mitochondria and thus an adequate ATP supply to meet the high energy demands of eukaryotic cells. So gain of a new role by ATP synthase appears to have had a huge impact on eukaryotic evolution. Many questions remain about ATP synthase dimerization however. In green algae such as *Chlamydomonas* and *Polytomella* the whole peripheral stalk has been replaced by unrelated proteins, forming a very stable dimer (Allegretti et al. 2015) with a different dimer angle than that in mammals and fungi. So far the structure of the 9 ASA (ATP synthase associated) subunits and a possible relation to the mammalian dimerization subunits is not known.

## 7.8 Concluding Remarks

The mitochondrial respiratory chain has a central role in energy metabolism and decades of work have been devoted to elucidating its structure and function. Crystallization of these large membrane protein complexes has been a major challenge and the elucidation of many structures by x-ray crystallography since the 1980s have brought huge breakthroughs. The recent revolution in cryo-EM has greatly advanced our knowledge of the mitochondrial respiratory chain for all still incompletely understood complexes, from complex I (Vinothkumar et al. 2014; Zhu et al. 2016; Fiedorczuk et al. 2016; D'Imprima et al. 2016) to the respirasome (Letts et al. 2016; Gu et al. 2016; Sousa et al. 2016) to ATP synthase (Allegretti et al. 2015; Zhou et al. 2015; Hahn et al. 2016). However, many questions remain regarding not only the detailed structure, but especially the mechanism of the complexes. The mode of action of complex I and coupling of ubiquinone reduction to proton translocation, the function of the respirasome, and the atomic structure of $F_o$ and the proton path through the *a* subunit are still not understood. It is to be expected that further progress in cryo-EM instrumentation and image processing techniques will lead to better structures of the mitochondrial respiratory chain complexes in different conformational states and a full understanding of the function of this amazing machinery.

## References


Abdrakhmanova A, Dobrynin K, Zwicker K, Kerscher S, Brandt U (2005) Functional sulfurtransferase is associated with mitochondrial complex I from *Yarrowia lipolytica*, but is not required for assembly of its iron–sulfur clusters. FEBS Lett 579(30):6781–6785. https://doi.org/10.1016/j.febslet.2005.11.008

Abdrakhmanova A, Zwicker K, Kerscher S, Zickermann V, Brandt U (2006) Tight binding of NADPH to the 39-kDa subunit of complex I is not required for catalytic activity but stabilizes the multiprotein complex. Biochim Biophys Acta 1757:1676–1682. https://doi.org/10.1016/j.bbabio.2006.09.003

Abrahams JP, Leslie AG, Lutter R, Walker JE (1994) Structure at 2.8 Å resolution of $F_1$ ATPase from bovine heart mitochondria. Nature 370:621–628

Acin-Pérez R, Bayona-Bafaluy MP, Fernández-Silva P, Moreno-Loshuertos R, Pérez-Martos A, Bruno C, Moraes CT, Enríquez JA (2004) Respiratory complex III is required to maintain complex I in mammalian mitochondria. Mol Cell 13:805–815

Acin-Pérez R, Fernández-Silva P, Peleato ML, Pérez-Martos A, Enriquez JA (2008) Respiratory active mitochondrial supercomplexes. Mol Cell 32:529–539

Allegretti M, Klusch N, Mills DJ, Vonck J, Davies KM, Kühlbrandt W (2015) Horizontal membrane-intrinsic α-helices in the stator *a*-subunit of an F-type ATP synthase. Nature 521:237–240

Allen RD, Schroeder CC, Fok AK (1989) An investigation of mitochondrial inner membranes by rapid-freeze deep-etch techniques. J Cell Biol 108(6):2233–2240

Alnajjar KS, Hosler J, Prochaska L (2014) Role of the N-terminus of subunit III in proton uptake in cytochrome *c* oxidase of *Rhodobacter sphaeroides*. Biochemistry 53(3):496–504. https://doi.org/10.1021/bi401535q

Althoff T, Mills DJ, Popot J-L, Kühlbrandt W (2011) Assembly of electron transport chain components in bovine mitochondrial supercomplex $I_1III_2IV_1$. EMBO J 30:4662–4664

Ambrosio G, Zweier JL, Duilio C, Kuppusamy P, Santoro G, Elia PP, Tritto I, Cirillo P, Condorelli M, Chiariello M et al (1993) Evidence that mitochondrial respiration is a source of potentially toxic oxygen free radicals in intact rabbit hearts subjected to ischemia and reflow. J Biol Chem 268(25):18532–18541

Andrews B, Carroll J, Ding S, Fearnley IM, Walker JE (2013) Assembly factors for the membrane arm of human complex I. Proc Natl Acad Sci U S A 110(47):18934–18939. https://doi.org/10.1073/pnas.1319247110

Angerer H (2015) Eukaryotic LYR proteins interact with mitochondrial protein complexes. Biology (Basel) 4(1):133–150. https://doi.org/10.3390/biology4010133

Angevine CA, Fillingame RH (2003) Aqueous access channels in subunit *a* of rotary ATP synthase. J Biol Chem 278:6066–6074. https://doi.org/10.1074/jbc.M210199200

Anthony G, Reimann A, Kadenbach B (1993) Tissue-specific regulation of bovine heart cytochrome *c* oxidase activity by ADP via interaction with subunit VIa. Proc Natl Acad Sci U S A 90(5):1652–1656. https://doi.org/10.1073/pnas.90.5.1652

Arnold S, Kadenbach B (1997) Cell respiration is controlled by ATP, an allosteric inhibitor of cytochrome-c oxidase. Eur J Biochem 249:350–354

Arnold I, Pfeiffer K, Neupert W, Stuart RA, Schägger H (1998a) Yeast mitochondrial $F_1F_0$-ATP synthase exists as a dimer: identification of three dimer-specific subunits. EMBO J 17(24):7170–7178

Arnold S, Goglia F, Kadenbach B (1998b) 3,5-diiodothyronine binds to subunit Va of cytochrome-c oxidase and abolishes the allosteric inhibition of respiration by ATP. Eur J Biochem 252(2):325–330. https://doi.org/10.1046/j.1432-1327.1998.2520325.x

Arselin G, Giraud M-F, Dautant A, Vaillier J, Brethes D, Coulary-Salin B, Schaeffer J, Velours J (2003) The GxxxG motif of the transmembrane domain of subunit e is involved in the dimerization/oligomerization of the yeast ATP synthase complex in the mitochondrial membrane. Eur J Biochem 270:1875–1884

Babot M, Birch A, Labarbuta P, Galkin A (2014) Characterisation of the active/de-active transition of mitochondrial complex I. Biochim Biophys Acta 1837(7):1083–1092. https://doi.org/10.1016/j.bbabio.2014.02.018

Baker LA, Watt IN, Runswick MJ, Walker JE, Rubinstein JL (2012) Arrangement of subunits in intact mammalian mitochondrial ATP synthase determined by cryo-EM. Proc Natl Acad Sci U S A 00:1–2

Balsa E, Marco R, Perales-Clemente E, Szklarczyk R, Calvo E, Landázuri MO, Enríquez JA (2012) NDUFA4 is a subunit of complex IV of the mammalian electron transport chain. Cell Metab 16(3):378–386. https://doi.org/10.1016/j.cmet.2012.07.015

Banci L, Bertini I, Cefaro C, Ciofi-Baffoni S, Gallo A, Martinelli M, Sideris DP, Katrakili N, Tokatlidis K (2009) MIA40 is an oxidoreductase that catalyzes oxidative protein folding in mitochondria. Nat Struct Mol Biol 16(2):198–206. https://doi.org/10.1038/nsmb.1553

Baradaran R, Berrisford JM, Minhas GS, Sazanov LA (2013) Crystal structure of the entire respiratory complex I. Nature 494(7438):443–448. https://doi.org/10.1038/nature11871

Barquera B (2014) The sodium pumping NADH:quinone oxidoreductase ($Na^+$-NQR), a unique redox-driven ion pump. J Bioenerg Biomembr 46(4):289–298. https://doi.org/10.1007/s10863-014-9565-9

Belevich I, Verkhovsky MI, Wikström M (2006) Proton-coupled electron transfer drives the proton pump of cytochrome c oxidase. Nature 440(7085):829–832. https://doi.org/10.1038/nature04619

Belevich G, Knuuti J, Verkhovsky MI, Wikström M, Verkhovskaya M (2011) Probing the mechanistic role of the long α-helix in subunit L of respiratory complex I from Escherichia coli by site-directed mutagenesis. Mol Microbiol 82(5):1086–1095. https://doi.org/10.1111/j.1365-2958.2011.07883.x

Bernal RA, Stock D (2004) Three-dimensional structure of the intact *Thermus thermophilus* $H^+$-ATPase/synthase by electron microscopy. Structure 12:1789–1798

Berrisford JM, Sazanov LA (2009) Structural basis for the mechanism of respiratory complex I. J Biol Chem 284(43):29773–29783. https://doi.org/10.1074/jbc.M109.032144

Berry EA, De Bari H, Huang L-S (2013) Unanswered questions about the structure of cytochrome bc1 complexes. Biochim Biophys Acta Bioenerg 1827(11):1258–1277

Bianchi C, Genova ML, Parenti Castelli G, Lenaz G (2004) The mitochondrial respiratory chain is partially organized in a supercomplex assembly: kinetic evidence using flux control analysis. J Biol Chem 279(35):36562–36569

Bleier L, Drose S (2013) Superoxide generation by complex III: from mechanistic rationales to functional consequences. BBA-Bioenergetics 1827(11–12):1320–1331. https://doi.org/10.1016/j.bbabio.2012.12.002

Boekema EJ, Ubbink-Kok T, Lolkema JS, Brisson A, Konings WN (1997) Visualization of a peripheral stalk in V-type ATPase: evidence for the stator structure essential to rotational catalysis. Proc Natl Acad Sci U S A 94:14291–14293

Boekema EJ, van Breemen JFL, Brisson A, Ubbink-Kok T, Konings WN, Lolkema JS (1999) Connecting stalks in V-type ATPase. Nature 401:37–38

Bonne G, Seibel P, Possekel S, Marsac C, Kadenbach B (1993) Expression of human cytochrome-c-oxidase subunits during fetal development. Eur J Biochem 217(3):1099–1107. https://doi.org/10.1111/j.1432-1033.1993.tb18342.x

Bordo D, Bork P (2002) The rhodanese/Cdc25 phosphatase superfamily. Sequence-structure-function relations. EMBO Rep 3(8):741–746. https://doi.org/10.1093/embo-reports/kvf150

Bottinger L, Horvath SE, Kleinschroth T, Hunte C, Daum G, Pfanner N, Becker T (2012) Phosphatidylethanolamine and cardiolipin differentially affect the stability of mitochondrial respiratory chain supercomplexes. J Mol Biol 423(5):677–686. https://doi.org/10.1016/j.jmb.2012.09.001

Boyer PD (1993) The binding change mechanism for ATP synthase – some probabilities and possibilities. Biochim Biophys Acta 1140:215–250

Boyer PD (1997) The ATP synthase: a splendid molecular machine. Annu Rev Biochem 66:717–749

Brandt U (2006) Energy converting NADH:quinone oxidoreductase (complex I). Annu Rev Biochem 75:69–92. https://doi.org/10.1146/annurev.biochem.75.103004.142539

Brockmann C, Diehl A, Rehbein K, Strauss H, Schmieder P, Korn B, Kühne R, Oschkinat H (2004) The oxidized subunit B8 from human complex I adopts a thioredoxin fold. Structure 12(9):1645–1654. https://doi.org/10.1016/j.str.2004.06.021

Bruno C, Santorelli FM, Assereto S, Tonoli E, Tessa A, Traverso M, Scapolan S, Bado M, Tedeschi S, Minetti C (2003) Progressive exercise intolerance associated with a new muscle-restricted nonsense mutation (G142X) in the mitochondrial cytochrome b gene. Muscle Nerve 28(4):508–511. https://doi.org/10.1002/mus.10429

Brzezinski P, Adelroth P (1998) Pathways of proton transfer in cytochrome c oxidase. J Bioenerg Biomembr 30(1):99–107. https://doi.org/10.1023/A:1020567729941

Bych K, Kerscher S, Netz DJ, Pierik AJ, Zwicker K, Huynen MA, Lill R, Brandt U, Balk J (2008) The iron-sulphur protein Ind1 is required for effective complex I assembly. EMBO J 27(12):1736–1746. https://doi.org/10.1038/emboj.2008.98

Cain BD, Simoni RD (1986) Impaired proton conductivity resulting from mutations in the *a* subunit of $F_1F_o$ ATPase in *Escherichia coli*. J Biol Chem 261:10043–10050

Cain BD, Simoni RD (1988) Interaction between Glu-219 and His-245 within the *a* subunit of $F_1F_o$ ATPase in *Escherichia coli*. J Biol Chem 263:6602–6612

Cano-Estrada A, Vázquez-Acevedo M, Villavicencio-Queijeiro A, Figueroa-Martínez F, Miranda-Astudillo H, Cordeiro Y, Mignaco JA, Foguel D, Cardol P, Lapaille M, Remacle C, Wilkens S, González-Halphen D (2010) Subunit–subunit interactions and overall topology of the dimeric mitochondrial ATP synthase of Polytomella sp. Biochim Biophys Acta 1797(8):1439–1448. https://doi.org/10.1016/j.bbabio.2010.02.024

Carilla-Latorre S, Gallardo ME, Annesley SJ, Calvo-Garrido J, Grana O, Accari SL, Smith PK, Valencia A, Garesse R, Fisher PR, Escalante R (2010) MidA is a putative methyltransferase that is required for mitochondrial complex I function. J Cell Sci 123(Pt 10):1674–1683. https://doi.org/10.1242/jcs.066076

Carroll J, Fearnley IM, Shannon RJ, Hirst J, Walker JE (2003) Analysis of the subunit composition of complex I from bovine heart mitochondria. Mol Cell Proteomics 2(2):117–126. https://doi.org/10.1074/mcp.M300014-MCP200

Carroll J, Fearnley IM, Skehel JM, Shannon RJ, Hirst J, Walker JE (2006) Bovine complex I is a complex of 45 different subunits. J Biol Chem 281:32724–32727

Castellani M, Covian R, Kleinschroth T, Anderka O, Ludwig B, Trumpower BL (2010) Direct demonstration of half-of-the-sites reactivity in the dimeric cytochrome bc1 complex: enzyme with one inactive monomer is fully active but unable to activate the second ubiquinol oxidation site in response to ligand binding at the ubiquinone reduction site. J Biol Chem 285(1):502–510. https://doi.org/10.1074/jbc.M109.072959

Chan DI, Vogel HJ (2010) Current understanding of fatty acid biosynthesis and the acyl carrier protein. Biochem J 430(1):1–19. https://doi.org/10.1042/BJ20100462

Chance B, Williams GR (1955) A method for the localization of sites for oxidative phosphorylation. Nature 176:250–254

Chandel NS (2010) Mitochondrial regulation of oxygen sensing. Adv Exp Med Biol 661:339–354. https://doi.org/10.1007/978-1-60761-500-2_22

Chen YC, Taylor EB, Dephoure N, Heo JM, Tonhato A, Papandreou I, Nath N, Denko NC, Gygi SP, Rutter J (2012) Identification of a protein mediating respiratory supercomplex stability. Cell Metab 15(3):348–360. https://doi.org/10.1016/j.cmet.2012.02.006

Chouchani ET, Methner C, Nadtochiy SM, Logan A, Pell VR, Ding S, James AM, Cocheme HM, Reinhold J, Lilley KS, Partridge L, Fearnley IM, Robinson AJ, Hartley RC, Smith RA, Krieg T, Brookes PS, Murphy MP (2013) Cardioprotection by S-nitrosation of a cysteine switch on mitochondrial complex I. Nat Med 19(6):753–759. https://doi.org/10.1038/nm.3212

Chouchani ET, Pell VR, Gaude E, Aksentijevic D, Sundier SY, Robb EL, Logan A, Nadtochiy SM, Ord EN, Smith AC, Eyassu F, Shirley R, CH H, Dare AJ, James AM, Rogatti S, Hartley RC, Eaton S, Costa AS, Brookes PS, Davidson SM, Duchen MR, Saeb-Parsy K, Shattock MJ,

Robinson AJ, Work LM, Frezza C, Krieg T, Murphy MP (2014) Ischaemic accumulation of succinate controls reperfusion injury through mitochondrial ROS. Nature 515(7527):431–435. https://doi.org/10.1038/nature13909

Clason T, Ruiz T, Schägger H, Peng G, Zickermann V, Brandt U, Michel H, Radermacher M (2010) The structure of eukaryotic and prokaryotic complex I. J Struct Biol 169(1):81–88

Cogliati S, Frezza C, Soriano ME, Varanita T, Quintana-Cabrera R, Corrado M, Cipolat S, Costa V, Casarin A, Gomes LC, Perales-Clemente E, Salviati L, Fernandez-Silva P, Enriquez JA, Scorrano L (2013) Mitochondrial cristae shape determines respiratory chain supercomplexes assembly and respiratory efficiency. Cell 155(1):160–171. https://doi.org/10.1016/j.cell.2013.08.032

Cogliati S, Calvo E, Loureiro M, Guaras AM, Nieto-Arellano R, Garcia-Poyatos C, Ezkurdia I, Mercader N, Vázquez J, Enriquez JA (2016) Mechanism of super-assembly of respiratory complexes III and IV. Nature 539(7630):579–582

Collinson IR, Skehel JM, Fearnley IM, Runswick MJ, Walker JE (1996) The $F_1F_o$-ATPase complex from bovine heart mitochondria: the molar ratio of the subunits in the stalk region linking the $F_1$ and $F_o$ domains. Biochemistry 34:12640–12646

Conte A, Papa B, Ferramosca A, Zara V (2015) The dimerization of the yeast cytochrome bc(1) complex is an early event and is independent of Rip1. Biochim Biophys Acta 1853(5):987–995. https://doi.org/10.1016/j.bbamcr.2015.02.006

Cortes-Hernandez P, Vázquez-Memije ME, Garcia JJ (2007) *ATP6* homoplasmic mutations inhibit and destabilize the human $F_1F_0$-ATP synthase without preventing enzyme assembly and oligomerization. J Biol Chem 282:1051–1058

Covian R, Trumpower BL (2006) Regulatory interactions between ubiquinol oxidation and ubiquinone reduction sites in the dimeric cytochrome bc(1) complex. J Biol Chem 281(41):30925–30932. https://doi.org/10.1074/jbc.M604694200

D'Aurelio M, Gajewski CD, Lenaz G, Manfredi G (2006) Respiratory chain supercomplexes set the threshold for respiration defects in human mtDNA mutant cybrids. Hum Mol Genet 15(13):2157–2169. https://doi.org/10.1093/hmg/ddl141

D'Imprima E, Mills DJ, Parey K, Brandt U, Kühlbrandt W, Zickermann V, Vonck J (2016) Cryo-EM structure of respiratory complex I reveals a link to mitochondrial sulfur metabolism. Biochim Biophys Acta 1857:1935–1942

Darrouzet E, Valkova-Valchanova M, Moser CC, Dutton PL, Daldal F (2000) Uncovering the [2Fe2S] domain movement in cytochrome bc1 and its implications for energy conversion. Proc Natl Acad Sci U S A 97(9):4567–4572

Davies KM, Strauss M, Daum B, Kief JH, Osiewacz HD, Rycovska A, Zickermann V, Kühlbrandt W (2011) Macromolecular organization of ATP synthase and complex I in whole mitochondria. Proc Natl Acad Sci U S A 108:14121–14126

Davies KM, Anselmi C, Wittig I, Faraldo-Gómez JD, Kühlbrandt W (2012) Structure of the yeast $F_1F_o$-ATP synthase dimer and its role in shaping the mitochondrial cristae. Proc Natl Acad Sci U S A 109(34):13602–13607

Dencher NA, Frenzel M, Reifschneider NH, Sugawa M, Krause F (2007) Proteome alterations in rat mitochondria caused by aging. Ann N Y Acad Sci 1100:291–298

Deng K, Zhang L, Kachurin AM, Yu L, Xia D, Kim H, Deisenhofer J, Yu C-A (1998) Activation of a matrix processing peptidase from the crystalline cytochrome bc complex of bovine heart mitochondria. J Biol Chem 273(33):20752–20757

Deng K, Shenoy SK, Tso S-C, Yu L, Yu C-A (2001) Reconstitution of mitochondrial processing peptidase from the core proteins (subunits I and II) of bovine heart mitochondrial cytochrome bc complex. J Biol Chem 276(9):6499–6505

Diaz F, Fukui H, Garcia S, Moraes CT (2006) Cytochrome *c* oxidase is required for the assembly/stability of respiratory complex I in mouse fibroblasts. Mol Cell Biol 26:4872–4881

Dmitriev O, Jones PC, Jiang W, Fillingame RH (1999) Structure of the membrane domain of subunit *b* of the *Escherichia coli* $F_0F_1$ ATP synthase. J Biol Chem 274(22):15598–15604

Dmitriev OY, Altendorf K, Fillingame RH (2004) Subunit a of the E. coli ATP synthase: reconstitution and high resolution NMR with protein purified in a mixed polarity solvent. FEBS Lett 556:35–38

Dobrynin K, Abdrakhmanova A, Richers S, Hunte C, Kerscher S, Brandt U (2010) Characterization of two different acyl carrier proteins in complex I from *Yarrowia lipolytica*. Biochim Biophys Acta 1797(2):152–159. https://doi.org/10.1016/j.bbabio.2009.09.007

Drose S, Brandt U (2008) The mechanism of mitochondrial superoxide production by the cytochrome bc complex. J Biol Chem 283(31):21649–21654. https://doi.org/10.1074/jbc.M803236200

Drose S, Krack S, Sokolova L, Zwicker K, Barth HD, Morgner N, Heide H, Steger M, Nubel E, Zickermann V, Kerscher S, Brutschy B, Radermacher M, Brandt U (2011) Functional dissection of the proton pumping modules of mitochondrial complex I. PLoS Biol 9(8):e1001128. https://doi.org/10.1371/journal.pbio.1001128

Drose S, Brandt U, Wittig I (2014) Mitochondrial respiratory chain complexes as sources and targets of thiol-based redox-regulation. Biochim Biophys Acta 1844(8):1344–1354. https://doi.org/10.1016/j.bbapap.2014.02.006

Drose S, Stepanova A, Galkin A (2016) Ischemic A/D transition of mitochondrial complex I and its role in ROS generation. Biochim Biophys Acta 1857(7):946–957. https://doi.org/10.1016/j.bbabio.2015.12.013

Dudkina NV, Eubel H, Keegstra W, Boekema EJ, Braun HP (2005a) Structure of a mitochondrial supercomplex formed by respiratory-chain complexes I and III. Proc Natl Acad Sci U S A 102:3225–3229

Dudkina NV, Heinemeyer J, Keegstra W, Boekema EJ, Braun HP (2005b) Structure of dimeric ATP synthase from mitochondria: an angular association of monomers induces the strong curvature of the inner membrane. FEBS Lett 579(25):5769–5772

Dudkina NV, Sunderhaus S, Braun HP, Boekema EJ (2006) Characterization of dimeric ATP synthase and cristae membrane ultrastructure from *Saccharomyces* and *Polytomella* mitochondria. FEBS Lett 580(14):3427–3432

Dudkina NV, Oostergetel GT, Lewejohann D, Braun H-P, Boekema EJ (2010) Row-like organization of ATP synthase in intact mitochondria determined by cryo-electron tomography. Biochim Biophys Acta 1797(2):272–277

Dudkina NV, Kudryashev M, Stahlberg H, Boekema EJ (2011) Interaction of complexes I, III, and IV within the bovine respirasome by single particle cryoelectron tomography. Proc Natl Acad Sci U S A 108(37):15196–15200

Dutton PL, Moser CC, Sled VD, Daldal F, Ohnishi T (1998) A reductant-induced oxidation mechanism for complex I. Biochim Biophys Acta 1364(2):245–257

Efremov RG, Sazanov LA (2011) Structure of the membrane domain of respiratory complex I. Nature 476(7361):414–420. https://doi.org/10.1038/nature10330

Efremov RG, Baradaran R, Sazanov LA (2010) The architecture of respiratory complex I. Nature 465:441–447

Elurbe DM, Huynen MA (2016) The origin of the supernumerary subunits and assembly factors of complex I: a treasure trove of pathway evolution. Biochim Biophys Acta 1857(7):971–979. https://doi.org/10.1016/j.bbabio.2016.03.027

Esterhazy D, King MS, Yakovlev G, Hirst J (2008) Production of reactive oxygen species by complex I (NADH:ubiquinone oxidoreductase) from *Escherichia coli* and comparison to the enzyme from mitochondria. Biochemistry 47(12):3964–3971. https://doi.org/10.1021/bi702243b

Eubel H, Jänsch L, Braun HP (2003) New insights into the respiratory chain of plant mitochondria. Supercomplexes and a unique composition of complex II. Plant Physiol 133:274–286

Euro L, Bloch DA, Wikström M, Verkhovsky MI, Verkhovskaya M (2008) Electrostatic interactions between FeS clusters in NADH:ubiquinone oxidoreductase (complex I) from Escherichia coli. Biochemistry 47(10):3185–3193. https://doi.org/10.1021/bi702063t

Ewart GD, Zhang YZ, Capaldi RA (1991) Switching of bovine cytochrome-c-oxidase subunit VIa isoforms in skeletal-muscle during development. FEBS Lett 292(1–2):79–84. https://doi.org/10.1016/0014-5793(91)80839-U

Fearnley IM, Walker JE (1992) Conservation of sequences of subunits of mitochondrial complex I and their relationships with other proteins. Biochim Biophys Acta 1140(2):105–134

Fernández-Morán H (1962) Low-temperature electron microscopy and X-ray diffraction studies of lipoprotein components in lamellar systems. Circulation 26:1039–1065

Fiedorczuk K, Letts JA, Degliesposti G, Kaszuba K, Skehel M, Sazanov LA (2016) Atomic structure of the entire mammalian mitochondrial complex I. Nature 538:406–410. https://doi.org/10.1038/nature19794

Fillingame RH, Steed PR (2014) Half channels mediating $H^+$ transport and the mechanism of gating in the $F_o$ sector of *Escherichia coli* $F_1F_o$ ATP synthase. Biochim Biophys Acta 1837:1063–1068

Friedrich T (2001) Complex I: a chimaera of a redox and conformation-driven proton pump? J Bioenerg Biomembr 33(3):169–177

Friedrich T, Scheide D (2000) The respiratory complex I of bacteria, archaea and eukarya and its module common with membrane-bound multisubunit hydrogenases. FEBS Lett 479(1–2):1–5

Fritz M, Klyszejko AL, Morgner N, Vonck J, Brutschy B, Muller DJ, Meier T, Müller V (2008) An intermediate step in the evolution of ATPases – a hybrid $F_o$-$V_o$ rotor in a bacterial $Na^+$ $F_1F_o$ ATP synthase. FEBS J 275(9):1999–2007

Gabaldon T, Rainey D, Huynen MA (2005) Tracing the evolution of a large protein complex in the eukaryotes, NADH:ubiquinone oxidoreductase (Complex I). J Mol Biol 348(4):857–870. https://doi.org/10.1016/j.jmb.2005.02.067

Galati D, Srinivasan S, Raza H, Prabu SK, Hardy M, Chandran K, Lopez M, Kalyanaraman B, Avadhani NG (2009) Role of nuclear-encoded subunit Vb in the assembly and stability of cytochrome c oxidase complex: implications in mitochondrial dysfunction and ROS production. Biochem J 420:439–449. https://doi.org/10.1042/Bj20090214

Galkin A, Moncada S (2007) S-nitrosation of mitochondrial complex I depends on its structural conformation. J Biol Chem 282(52):37448–37453. https://doi.org/10.1074/jbc.M707543200

Galkin A, Abramov AY, Frakich N, Duchen MR, Moncada S (2009) Lack of oxygen deactivates mitochondrial complex I: implications for ischemic injury? J Biol Chem 284(52):36055–36061. https://doi.org/10.1074/jbc.M109.054346

Giraud M-F, Paumard P, Soubannier V, Vaillier J, Arselin G, Salin B, Schaeffer J, Brethes D, di Rago J-P, Velours J (2002) Is there a relationship between the supramolecular organization of the mitochondrial ATP synthase and the formation of cristae? Biochim Biophys Acta 1555:174–180

Giraud M-F, Paumard P, Sanchez C, Brèthes D, Velours J, Dautant A (2012) Rotor architecture in the yeast and bovine $F_1$-c-ring complexes of F-ATP synthase. J Struct Biol 177(2):490–497. https://doi.org/10.1016/j.jsb.2011.10.015

Gnandt E, Dorner K, Strampraad MF, de Vries S, Friedrich T (2016) The multitude of iron-sulfur clusters in respiratory complex I. Biochim Biophys Acta 1857(8):1068–1072

Gogol EP, Lücken U, Capaldi RA (1987) The stalk connecting the $F_1$ and $F_0$ domains of ATP synthase visualized by electron microscopy of unstained specimens. FEBS Lett 219:274–278

Gorenkova N, Robinson E, Grieve DJ, Galkin A (2013) Conformational change of mitochondrial complex I increases ROS sensitivity during ischemia. Antioxid Redox Signal 19(13):1459–1468. https://doi.org/10.1089/ars.2012.4698

Grivennikova VG, Serebryanaya DV, Isakova EP, Belozerskaya TA, Vinogradov AD (2003) The transition between active and de-activated forms of NADH:ubiquinone oxidoreductase (Complex I) in the mitochondrial membrane of *Neurospora crassa*. Biochem J 369(Pt 3):619–626. https://doi.org/10.1042/BJ20021165

Gu J, Wu M, Guo R, Yan K, Lei J, Gao N, Yang M (2016) The architecture of the mammalian respirasome. Nature 537:639–643. https://doi.org/10.1038/nature19359

Guarás A, Perales-Clemente E, Calvo E, Acín-Pérez R, Loureiro-Lopez M, Pujol C, Martínez-Carrascoso I, Nunez E, García-Marqués F, Rodríguez-Hernández MA, Cortés A, Diaz F,

Pérez-Martos A, Moraes CT, Fernández-Silva P, Trifunovic A, Navas P, Vazquez J, Enríquez JA (2016) The CoQH /CoQ ratio serves as a sensor of respiratory chain efficiency. Cell Rep 15(1):197–209. https://doi.org/10.1016/j.celrep.2016.03.009

Guerrero-Castillo S, Baertling F, Kownatzki D, Wessels HJ, Arnold S, Brandt U, Nijtmans L (2016) The assembly pathway of mitochondrial respiratory chain complex I. Cell Metab. https://doi.org/10.1016/j.cmet.2016.09.002. (in press)

Hackenbrock CR, Chazotte B, Gupte SS (1986) The random collision model and a critical assessment of diffusion and collision in mitochondrial electron transport. J Bioenerg Biomembr 18:331–368

Hägerhäll C (1997) Succinate: quinone oxidoreductases. Variations on a conserved theme. Biochim Biophys Acta 1320:107–141

Hahn A, Parey K, Bublitz M, Mills DJ, Zickermann V, Vonck J, Kühlbrandt W, Meier T (2016) Structure of a complete ATP synthase dimer reveals the molecular basis of inner mitochondrial membrane morphology. Mol Cell 63:445–456. https://doi.org/10.1016/j.molcel.2016.05.037

Hakulinen JK, Klyszejko AL, Hoffmann J, Eckhardt-Strelau L, Brutschy B, Vonck J, Meier T (2012) A structural study on the architecture of the bacterial ATP synthase $F_o$ motor. Proc Natl Acad Sci U S A 109:E2050–E2056

Hatch LP, Cox GB, Howitt SM (1995) The essential arginine residue at position 210 in the *a* subunit of the *Escherichia coli* ATP synthase can be transferred to position 252 with partial retention of activity. J Biol Chem 270(49):29407–29412

Heinemeyer J, Braun HP, Boekema EJ, Kouril R (2007) A structural model of the cytochrome c reductase/oxidase supercomplex from yeast mitochondria. J Biol Chem 282(16):12240–12248

Hiltunen JK, Autio KJ, Schonauer MS, Kursu VA, Dieckmann CL, Kastaniotis AJ (2010) Mitochondrial fatty acid synthesis and respiration. Biochim Biophys Acta 1797(6–7):1195–1202. https://doi.org/10.1016/j.bbabio.2010.03.006

Hinchliffe P, Sazanov LA (2005) Organization of iron-sulfur clusters in respiratory complex I. Science 309:771–774

Hirst J (2011) Why does mitochondrial complex I have so many subunits? Biochem J 437(2):e1–e3. https://doi.org/10.1042/BJ20110918

Hirst J, Carroll J, Fearnley IM, Shannon RJ, Walker JE (2003) The nuclear encoded subunits of complex I from bovine heart mitochondria. Biochimica et Biophysica Acta-Bioenergetics 1604(3):135–150. https://doi.org/10.1016/S0005-2728(03)00059-8

Hong S, Victoria D, Crofts AR (2012) Inter-monomer electron transfer is too slow to compete with monomeric turnover in bc 1 complex. Biochimica et Biophysica Acta (BBA)-Bioenergetics 1817(7):1053–1062

Huang LS, Sun G, Cobessi D, Wang AC, Shen JT, Tung EY, Anderson VE, Berry EA (2006) 3-nitropropionic acid is a suicide inhibitor of mitochondrial respiration that, upon oxidation by complex II, forms a covalent adduct with a catalytic base arginine in the active site of the enzyme. J Biol Chem 281(9):5965–5972. https://doi.org/10.1074/jbc.M511270200

Hunte C, Zickermann V, Brandt U (2010) Functional modules and structural basis of conformational coupling in mitochondrial complex I. Science 329:448–451. https://doi.org/10.1126/science.1191046

Huttemann M, Kadenbach B, Grossman LI (2001) Mammalian subunit IV isoforms of cytochrome c oxidase. Gene 267(1):111–123. https://doi.org/10.1016/S0378-1119(01)00385-7

Huttemann M, Jaradat S, Grossman LI (2003a) Cytochrome c oxidase of mammals contains a testes-specific isoform of subunit VIb – the counterpart to testes-specific cytochrome c? Mol Reprod Dev 66(1):8–16. https://doi.org/10.1002/mrd.10327

Huttemann M, Schmidt TR, Grossman LI (2003b) A third isoform of cytochrome c oxidase subunit VIII is present in mammals. Gene 312:95–102. https://doi.org/10.1016/S0378-1119(03)00604-8

Indrieri A, van Randen VA, Tiranti V, Morleo M, Iaconis D, Tammaro R, D'Amato I, Conte I, Maystadt I, Demuth S, Zvulunov A, Kutsche K, Zeviani M, Franco B (2012) Mutations in COX7B cause microphthalmia with linear skin lesions, an unconventional mitochondrial disease. Am J Hum Genet 91(5):942–949. https://doi.org/10.1016/j.ajhg.2012.09.016

Iverson TM, Luna-Chavez C, Cecchini G, Rees DC (1999) Structure of the *Escherichia coli* fumarate reductase respiratory complex. Science 284:1961–1966

Iwasaki T, Matsuura K, Oshima T (1995) Resolution of the aerobic respiratory system of the thermoacidophilic archaeon, *Sulfolobus* sp. strain 7. I. The archaeal terminal oxidase supercomplex is a functional fusion of respiratory complexes III and IV with no *c*-type cytochromes. J Biol Chem 270(52):30881–30892

Iwata S, Ostermeier C, Ludwig B, Michel H (1995) Structure at 2.8 Å resolution of cytochrome c oxidase from Paracoccus denitrificans. Nature 376(6542):660–669. https://doi.org/10.1038/376660a0

Iwata S, Lee JW, Okada K, Lee JK, Iwata M, Rasmussen B, Link TA, Ramaswamy S, Jap BK (1998) Complete structure of the 11-subunit mitochondrial cytochrome $bc_1$ complex. Science 281:64–71

James TY, Pelin A, Bonen L, Ahrendt S, Sain D, Corradi N, Stajich JE (2013) Shared signatures of parasitism and phylogenomics unite Cryptomycota and microsporidia. Curr Biol 23(16):1548–1553. https://doi.org/10.1016/j.cub.2013.06.057

Jiang W, Fillingame RH (1998) Interacting helical faces of subunits *a* and *c* in the $F_1F_0$ ATP synthase of *Escherichia coli* defined by disulfide cross-linking. Proc Natl Acad Sci U S A 95:6607–6612

Junge W, Lill H, Engelbrecht S (1997) ATP synthase: an electrochemical transducer with rotatory mechanics. Trends Biochem Sci 22:420–423

Kagawa Y, Racker E (1966) Partial resolution of the enzymes catalyzing oxidative phosphorylation. X. Correlation of morphology and function in submitochondrial particles. J Biol Chem 341(10):2475–2482

Kane Dickson V, Silvester JA, Fearnley IM, Leslie AGW, Walker JE (2006) On the structure of the stator of the mitochondrial ATP synthase. EMBO J 25(12):2911–2918

Kearney EB (1960) Studies on succinic dehydrogenase. XII. Flavin component of the mammalian enzyme. J Biol Chem 235:865–877

Kerscher SJ (2000) Diversity and origin of alternative NADH:ubiquinone oxidoreductases. Biochim Biophys Acta 1459(2–3):274–283

Kerscher S, Grgic L, Garofano A, Brandt U (2004) Application of the yeast *Yarrowia lipolytica* as a model to analyse human pathogenic mutations in mitochondrial complex I (NADH:ubiquinone oxidoreductase). Biochim Biophys Acta 1659:197–205. https://doi.org/10.1016/j.bbabio.2004.07.006

Kerscher S, Drose S, Zickermann V, Brandt U (2008) The three families of respiratory NADH dehydrogenases. Results Probl Cell Differ 45:185–222. https://doi.org/10.1007/400_2007_028

Khalfaoui-Hassani B, Lanciano P, Lee DW, Darrouzet E, Daldal F (2012) Recent advances in cytochrome bc(1): inter monomer electronic communication? FEBS Lett 586:617–621. https://doi.org/10.1016/j.febslet.2011.08.032

Kmita K, Wirth C, Warnau J, Guerrero-Castillo S, Hunte C, Hummer G, Kaila VRI, Zwicker K, Brandt U, Zickermann V (2015) Accessory NUMM (NDUFS6) subunit harbors a Zn-binding site and is essential for biogenesis of mitochondrial complex I. Proc Natl Acad Sci U S A 112(18):5685–5690. https://doi.org/10.1073/pnas.1424353112

Konstantinov AA (2012) Cytochrome c oxidase: intermediates of the catalytic cycle and their energy-coupled interconversion. FEBS Lett 586(5):630–639. https://doi.org/10.1016/j.febslet.2011.08.037

Konstantinov AA, Siletsky S, Mitchell D, Kaulen A, Gennis RB (1997) The roles of the two proton input channels in cytochrome c oxidase from Rhodobacter sphaeroides probed by the effects of site-directed mutations on time-resolved electrogenic intraprotein proton transfer. Proc Natl Acad Sci U S A 94(17):9085–9090. https://doi.org/10.1073/pnas.94.17.9085

Kotlyar AB, Vinogradov AD (1990) Slow active/inactive transition of the mitochondrial NADH-ubiquinone reductase. Biochim Biophys Acta 1019(2):151–158

Krause F, Reifschneider NH, Vocke D, Seelert H, Rexroth S, Dencher NA (2004a) "Respirasome"-like supercomplexes in green leaf mitochondria of spinach. J Biol Chem 279(46):48369–48375

Krause F, Scheckhuber CQ, Werner A, Rexroth S, Reifschneider NH, Dencher NA, Osiewacz HD (2004b) Supramolecular organization of cytochrome *c* oxidase- and alternative oxidase-

dependent respiratory chains in the filamentous fungus *Podospora anserina*. J Biol Chem 279(25):26453–26461
Krause F, Reifschneider NH, Goto S, Dencher NA (2005) Active oligomeric ATP synthases in mammalian mitochondria. Biochem Biophys Res Commun 329:583–590
Lamantea E, Carrara F, Mariotti C, Morandi L, Tiranti V, Zeviani M (2002) A novel nonsense mutation (Q352X) in the mitochondrial cytochrome b gene associated with a combined deficiency of complexes I and III. Neuromuscul Disord 12(1):49–52
Lancaster CR, Kröger A, Auer M, Michel H (1999) Structure of fumarate reductase from Wolinella succinogenes at 2.2 Å resolution. Nature 402:377–385
Lanciano P, Lee D-W, Yang H, Darrouzet E, Daldal F (2011) Intermonomer electron transfer between the low-potential b hemes of cytochrome bc. Biochemistry 50(10):1651–1663. https://doi.org/10.1021/bi101736v
Lanciano P, Khalfaoui-Hassani B, Selamoglu N, Ghelli A, Rugolo M, Daldal F (2013) Molecular mechanisms of superoxide production by complex III: a bacterial versus human mitochondrial comparative case study. BBA-Bioenergetics 1827(11–12):1332–1339. https://doi.org/10.1016/j.bbabio.2013.03.009
Lange C, Hunte C (2002) Crystal structure of the yeast cytochrome $bc_1$ complex with its bound substrate cytochrome *c*. Proc Natl Acad Sci U S A 99(5):2800–2805
Lapuente-Brun E, Moreno-Loshuertos R, Acín-Pérez R, Latorre-Pellicer A, Colás C, Balsa E, Perales-Clemente E, Quirós PM, Calvo E, Rodríguez-Hernández MA, Navas P, Cruz R, Carracedo A, López-Otin C, Pérez-Martos A, Fernández-Silva P, Fernandez-Vizarra E, Enríquez JA (2013) Supercomplex assembly determines electron flux in the mitochondrial electron transport chain. Science 340(6140):1567–1570. https://doi.org/10.1126/science.1230381
Lau WCY, Rubinstein JL (2010) Structure of intact *Thermus thermophilus* V-ATPase by cryo-EM reveals organization of the membrane-bound $V_O$ motor. Proc Natl Acad Sci U S A 107(4):1367–1372. https://doi.org/10.1073/pnas.0911085107
Lau WCY, Rubinstein JL (2012) Subnanometre-resolution structure of the intact *Thermus thermophilus* $H^+$-driven ATP synthase. Nature 481(7380):214–218. https://doi.org/10.1038/nature10699
Lau WCY, Baker LA, Rubinstein JL (2008) Cryo-EM structure of the yeast ATP synthase. J Mol Biol 382(5):1256–1264
Lee I, Kadenbach B (2001) Palmitate decreases proton pumping of liver-type cytochrome c oxidase. Eur J Biochem 268(24):6329–6334. https://doi.org/10.1046/j.0014-2956.2001.02602.x
Lee HM, Das TK, Rousseau DL, Mills D, Ferguson-Miller S, Gennis RB (2000) Mutations in the putative H-channel in the cytochrome c oxidase from Rhodobacter sphaeroides show that this channel is not important for proton conduction but reveal modulation of the properties of heme a. Biochemistry 39(11):2989–2996. https://doi.org/10.1021/bi9924821
Lenaz G, Genova ML (2016) Respiratory cytochrome supercomplexes. In: Cytochrome complexes: evolution, structures, energy transduction, and signaling. Springer, Dordrecht, pp 585–628
Letts JA, Fiedorczuk K, Sazanov LA (2016) The architecture of respiratory supercomplexes. Nature 537:644–648. https://doi.org/10.1038/nature19774
Levchenko M, Wuttke J-M, Römpler K, Schmidt B, Neifer K, Juris L, Wissel M, Rehling P, Deckers M (2016) Cox26 is a novel stoichiometric subunit of the yeast cytochrome c oxidase. Biochim Biophys Acta Mol Cell Res 1863(7):1624–1632
Lightowlers RN, Chrzanowska-Lightowlers ZM (2013) Human pentatricopeptide proteins: only a few and what do they do? RNA Biol 10(9):1433–1438. https://doi.org/10.4161/rna.24770
Liu J, Fackelmayer OJ, Hicks DB, Preiss L, Meier T, Sobie EA, Krulwich TA (2011) Mutations in a helix-1 motif of the ATP synthase c-subunit of *Bacillus pseudofirmus* OF4 cause functional deficits and changes in the c-ring stability and mobility on sodium dodecyl sulfate–polyacrylamide gel. Biochemistry 50(24):54897–55506
Longen S, Bien M, Bihlmaier K, Kloeppel C, Kauff F, Hammermeister M, Westermann B, Herrmann JM, Riemer J (2009) Systematic analysis of the twin Cx C protein family. J Mol Biol 393(2):356–368. https://doi.org/10.1016/j.jmb.2009.08.041

Ludlam A, Brunzelle J, Pribyl T, Xu X, Gatti DL, Ackerman SH (2009) Chaperones of $F_1$-ATPase. J Biol Chem 284:17138–17146

Lytovchenko O, Naumenko N, Oeljeklaus S, Schmidt B, von der Malsburg K, Deckers M, Warscheid B, van der Laan M, Rehling P (2014) The INA complex facilitates assembly of the peripheral stalk of the mitochondrial $F_1F_o$-ATP synthase. EMBO J 33(15):1624–1638

Maio N, Singh A, Uhrigshardt H, Saxena N, Tong WH, Rouault TA (2014) Cochaperone binding to LYR motifs confers specificity of iron sulfur cluster delivery. Cell Metab 19(3):445–457. https://doi.org/10.1016/j.cmet.2014.01.015

Maklashina E, Kotlyar AB, Cecchini G (2003) Active/de-active transition of respiratory complex I in bacteria, fungi, and animals. Biochim Biophys Acta 1606(1–3):95–103

Maranzana E, Barbero G, Falasca AI, Lenaz G, Genova ML (2013) Mitochondrial respiratory supercomplex association limits production of reactive oxygen species from complex I. Antioxid Redox Sign 19(13):1469–1480. https://doi.org/10.1089/ars.2012.4845

Marcet-Houben M, Marceddu G, Gabaldon T (2009) Phylogenomics of the oxidative phosphorylation in fungi reveals extensive gene duplication followed by functional divergence. BMC Evol Biol 9:295. https://doi.org/10.1186/1471-2148-9-295

Matthies D, Preiß L, Klyszejko AL, Muller DJ, Cook GM, Vonck J, Meier T (2009) The $c_{13}$ ring from a thermoalkaliphilic ATP synthase reveals an extended diameter due to a special structural region. J Mol Biol 388:611–618

Matthies D, Haberstock S, Joos F, Dötsch V, Vonck J, Bernhard F, Meier T (2011) Cell-free expression and assembly of ATP synthase. J Mol Biol 413(3):593–603

Mazhab-Jafari MT, Rohou A, Schmidt C, Bueler SA, Benlekbir S, Robinson CV, Rubinstein JL (2016) Atomic model for the membrane-embedded $V_o$ motor of a eukaryotic V-ATPase. Nature 539:118–122. https://doi.org/10.1038/nature19828

McLennan HR, Degli Esposti M (2000) The contribution of mitochondrial respiratory complexes to the production of reactive oxygen species. J Bioenerg Biomembr 32(2):153–162. https://doi.org/10.1023/A:1005507913372

Meier T, Polzer P, Diederichs K, Welte W, Dimroth P (2005) Structure of the rotor ring of F-type $Na^+$-ATPase from *Ilyobacter tartaricus*. Science 308:659–662

Meier T, Ferguson SA, Cook GM, Dimroth P, Vonck J (2006) Structural investigations of the membrane-embedded rotor ring of the F-ATPase from *Clostridium paradoxum*. J Bacteriol 188(22):7759–7764

Melo AM, Bandeiras TM, Teixeira M (2004) New insights into type II NAD(P)H:quinone oxidoreductases. Microbiol Mol Biol Rev 68(4):603–616. https://doi.org/10.1128/MMBR.68.4.603-616.2004

Merz S, Westermann B (2009) Genome-wide deletion mutant analysis reveals genes required for respiratory growth, mitochondrial genome maintenance and mitochondrial protein synthesis in Saccharomyces cerevisiae. Genome Biol 10(9):R95. https://doi.org/10.1186/gb-2009-10-9-r95

Meunier B, Fisher N, Ransac S, Mazat JP, Brasseur G (2013) Respiratory complex III dysfunction in humans and the use of yeast as a model organism to study mitochondrial myopathy and associated diseases. Biochim Biophys Acta 1827(11–12):1346–1361. https://doi.org/10.1016/j.bbabio.2012.11.015

Mileykovskaya E, Dowhan W (2014) Cardiolipin-dependent formation of mitochondrial respiratory supercomplexes. Chem Phys Lipids 179:42–48. https://doi.org/10.1016/j.chemphyslip.2013.10.012

Minakami S, Schindler FJ, Estabrook RW (1964) Hydrogen transfer between reduced diphosphopyridine nucleotide dehydrogenase and the respiratory chain. I. Effect of sulfhydryl inhibitors and phospholipase. J Biol Chem 239:2042–2048

Minauro-Sanmiguel F, Wilkens S, Garcia JJ (2005) Structure of dimeric mitochondrial ATP synthase: novel $F_0$ bridging features and the structural basis of mitochondrial cristae biogenesis. Proc Natl Acad Sci U S A 102(35):12356–12358

Mitchell P (1972) Chemiosmotic coupling in energy transduction – logical development of biochemical knowledge. J Bioenerg 3(1-2):5–24. https://doi.org/10.1007/Bf01515993

Mitchell P (1976) Possible molecular mechanisms of protonmotive function of cytochrome systems. J Theor Biol 62(2):327–367. https://doi.org/10.1016/0022-5193(76)90124-7

Moore KJ, Fillingame RH (2008) Structural interactions between transmembrane helices 4 and 5 of subunit a and the subunit c ring of *Escherichia coli* ATP synthase. J Biol Chem 283:31726–31735

Morais VA, Haddad D, Craessaerts K, De Bock P-J, Swerts J, Vilain S, Aerts L, Overbergh L, Grünewald A, Seibler P, Klein C, Gevaert K, Verstreken P, De Strooper B (2014) PINK1 loss-of-function mutations affect mitochondrial complex I activity via NdufA10 ubiquinone uncoupling. Science 344:203–207. https://doi.org/10.1126/science.1249161

Morales-Rios E, Montgomery MG, Leslie AGW, Walker JE (2015) Structure of ATP synthase from *Paracoccus denitrificans* determined by X-ray crystallography at 4.0 Å resolution. Proc Natl Acad Sci U S A. https://doi.org/10.1073/pnas.1517542112

Moreno-Lastres D, Fontanesi F, García-Consuegra I, Martín MA, Arenas J, Barrientos A, Ugalde C (2012) Mitochondrial complex I plays an essential role in human respirasome assembly. Cell Metab 15:324–335. https://doi.org/10.1016/j.cmet.2012.01.015

Muller FL, Liu YH, Van Remmen H (2004) Complex III releases superoxide to both sides of the inner mitochondrial membrane. J Biol Chem 279(47):49064–49073. https://doi.org/10.1074/jbc.M407715200

Muramoto K, Ohta K, Shinzawa-Itoh K, Kanda K, Taniguchi M, Nabekura H, Yamashita E, Tsukihara T, Yoshikawa S (2010) Bovine cytochrome c oxidase structures enable O reduction with minimization of reactive oxygens and provide a proton-pumping gate. Proc Natl Acad Sci U S A 107(17):7740–7745. https://doi.org/10.1073/pnas.0910410107

Murata T, Yamato I, Kakinuma Y, Leslie AGW, Walker JE (2005) Structure of the rotor of the V-type $Na^+$-ATPase from *Enterococcus hirae*. Science 308:654–658

Nakai M, Endo T, Hase T, Tanaka Y, Trumpower BL, Ishiwatari H, Asada A, Bogaki M, Matsubara H (1993) Acidic regions of cytochrome c are essential for ubiquinol-cytochrome c reductase activity in yeast cells lacking the acidic QCR6 protein. J Biochem 114(6):919–925

Noji H, Yasuda R, Yoshida M, Kinosita K (1997) Direct observation of the rotation of $F_1$-ATPase. Nature 386:299–302

Ogilvie I, Aggeler R, Capaldi RA (1997) Cross-linking of the δ subunit to one of the three α subunits has no effect on functioning, as expected if δ is a part of the stator that links the $F_1$ and $F_0$ parts of the *Escherichia coli* ATP synthase. J Biol Chem 272:16652–16656

Ohnishi T (1998) Iron-sulfur clusters/semiquinones in complex I. Biochim Biophys Acta 1364(2):186–206

Ohnishi T, Nakamaru-Ogiso E (2008) Were there any "misassignments" among iron-sulfur clusters N4, N5 and N6b in NADH-quinone oxidoreductase (complex I)? Biochim Biophys Acta 1777(7–8):703–710. https://doi.org/10.1016/j.bbabio.2008.04.032

Ohnishi T, Kawaguchi K, Hagihara B (1966) Preparation and some properties of yeast mitochondria. J Biol Chem 241(8):1797–1806

Ohnishi ST, Salerno JC, Ohnishi T (2010) Possible roles of two quinone molecules in direct and indirect proton pumps of bovine heart NADH-quinone oxidoreductase (complex I). Biochim Biophys Acta 1797(12):1891–1893. https://doi.org/10.1016/j.bbabio.2010.06.010

Osman C, Wilmes C, Tatsuta T, Langer T (2007) Prohibitins interact genetically with Atp23, a novel processing peptidase and chaperone for the $F_1F_o$-ATP synthase. Mol Biol Cell 18:627–635

Pagadala V, Vistain L, Symersky J, Mueller DM (2011) Characterization of the mitochondrial ATP synthase from yeast *Saccharomyces cerevisae*. J Bioenerg Biomembr 43:333–347

Page CC, Moser CC, Chen X, Dutton PL (1999) Natural engineering principles of electron tunnelling in biological oxidation-reduction. Nature 402(6757):47–52. https://doi.org/10.1038/46972

Parsons DF (1963) Negative staining of thinly spread cells and associated virus. J Cell Biol 16:620–626

Parsons WJ, Williams RS, Shelton JM, Luo YA, Kessler DJ, Richardson JA (1996) Developmental regulation of cytochrome oxidase subunit VIa isoforms in cardiac and skeletal muscle. Am J Physiol-Heart C 270(2):H567–H574

Paumard P, Vaillier J, Coulary B, Schaeffer J, Soubannier V, Mueller DM, Brethes D, di Rago J-P, Velours J (2002) The ATP synthase is involved in generating mitochondrial cristae morphology. EMBO J 21(3):221–230

Peters K, Belt K, Braun HP (2013) 3D gel map of *Arabidopsis* complex I. Front Plant Sci 4:153. https://doi.org/10.3389/fpls.2013.00153

Pitceathly RDS, Rahman S, Wedatilake Y, Polke JM, Cirak S, Foley AR, Sailer A, Hurles ME, Stalker J, Hargreaves I, Woodward CE, Sweeney MG, Muntoni F, Houlden H, UK10K Consortium, Taanman J-W, Hanna MG (2013) NDUFA4 mutations underlie dysfunction of a cytochrome c oxidase subunit linked to human neurological disease. Cell Rep 3(6):1795–1805. https://doi.org/10.1016/j.celrep.2013.05.005

Ploegman JH, Drent G, Kalk KH, Hol WG (1978) Structure of bovine liver rhodanese. I. Structure determination at 2.5 Å resolution and a comparison of the conformation and sequence of its two domains. J Mol Biol 123(4):557–594

Pogoryelov D, Yu J, Meier T, Vonck J, Dimroth P, Müller DJ (2005) The $c_{15}$ ring of the *Spirulina platensis* F-ATP synthase: $F_1/F_0$ symmetry mismatch is not obligatory. EMBO Rep 6(11):1045–1052

Pogoryelov D, Yildiz Ö, Faraldo-Gómez JD, Meier T (2009) High-resolution structure of the rotor ring of a proton-dependent ATP synthase. Nat Struct Mol Biol 16(10):1068–1073. https://doi.org/10.1038/nsmb.1678

Pogoryelov D, Klyszejko AL, Krasnoselska G, Heller E-M, Leone V, Langer JD, Vonck J, Müller DJ, Faraldo-Gómez JD, Meier T (2012) Engineering rotor ring stoichiometries in ATP synthases. Proc Natl Acad Sci U S A 109:E1599–E1608

Popovic DM (2013) Current advances in research of cytochrome c oxidase. Amino Acids 45(5):1073–1087. https://doi.org/10.1007/s00726-013-1585-y

Preiss L, Yildiz Ö, Hicks DB, Krulwich TA, Meier T (2010) A new type of proton coordination in an $F_1F_o$-ATP synthase rotor ring. PLoS Biol 8(8):443

Preiss L, Klyszejko AL, Hicks DB, Liu J, Fackelmayer OJ, Yildiz Ö, Krulwich TA, Meier T (2013) The c-ring stoichiometry of ATP synthase is adapted to cell physiological requirements of alkaliphilic *Bacillus pseudofirmus* OF4. Proc Natl Acad Sci U S A 110:7874

Preiss L, Langer JD, Yildiz Ö, Eckhardt-Strelau L, Guillemont JEG, Koul A, Meier T (2015) Structure of the mycobacterial ATP synthase $F_0$ rotor ring in complex with the anti-TB drug bedaquiline. Sci Adv 1(4):e1500106. https://doi.org/10.1126/sciadv.1500106

Quarato G, Piccoli C, Scrima R, Capitanio N (2011) Variation of flux control coefficient of cytochrome c oxidase and of the other respiratory chain complexes at different values of protonmotive force occurs by a threshold mechanism. BBA-Bioenergetics 1807(9):1114–1124. https://doi.org/10.1016/j.bbabio.2011.04.001

Quinlan CL, Gerencser AA, Treberg JR, Brand MD (2011) The mechanism of superoxide production by the antimycin-inhibited mitochondrial Q-cycle. J Biol Chem 286(36):31361–31372. https://doi.org/10.1074/jbc.M111.267898

Rak M, Gokova S, Tzagoloff A (2011) Modular assembly of yeast mitochondrial ATP synthase. EMBO J 30:920–930. https://doi.org/10.1038/emboj.2010.364

Rak M, Benit P, Chretien D, Bouchereau J, Schiff M, El-Khoury R, Tzagoloff A, Rustin P (2016) Mitochondrial cytochrome c oxidase deficiency. Clin Sci 130(6):393–407. https://doi.org/10.1042/Cs20150707

Ramirez-Aguilar SJ, Keuthe M, Rocha M, Fedyaev VV, Kramp K, Gupta KJ, Rasmusson AG, Schulze WX, van Dongen JT (2011) The composition of plant mitochondrial supercomplexes changes with oxygen availability. J Biol Chem 286(50):43045–43053. https://doi.org/10.1074/jbc.M111.252544

Rasmussen T, Scheide D, Brors B, Kintscher L, Weiss H, Friedrich T (2001) Identification of two tetranuclear FeS clusters on the ferredoxin-type subunit of NADH:ubiquinone oxidoreductase (complex I). Biochemistry 40(20):6124–6131

Rees DM, Leslie AGW, Walker JE (2009) The structure of the membrane extrinsic region of bovine ATP synthase. Proc Natl Acad Sci U S A 106(51):21597–21601

Requejo R, Hurd TR, Costa NJ, Murphy MP (2010) Cysteine residues exposed on protein surfaces are the dominant intramitochondrial thiol and may protect against oxidative damage. FEBS J 277(6):1465–1480. https://doi.org/10.1111/j.1742-4658.2010.07576.x

Rich PR, Marechal A (2013) Functions of the hydrophilic channels in protonmotive cytochrome c oxidase. J R Soc Interface 10(86). https://doi.org/10.1098/rsif.2013.0183

Roberts PG, Hirst J (2012) The deactive form of respiratory complex I from mammalian mitochondria is a $Na^+/H^+$ antiporter. J Biol Chem 287(41):34743–34751. https://doi.org/10.1074/jbc.M112.384560

Rodenburg RJ (2016) Mitochondrial complex I-linked disease. Biochim Biophys Acta 1857(7):938–945. https://doi.org/10.1016/j.bbabio.2016.02.012

Roessler MM, King MS, Robinson AJ, Armstrong FA, Harmer J, Hirst J (2010) Direct assignment of EPR spectra to structurally defined iron-sulfur clusters in complex I by double electron-electron resonance. Proc Natl Acad Sci U S A 107(5):1930–1935. https://doi.org/10.1073/pnas.0908050107

Rottenberg H, Covian R, Trumpower BL (2009) Membrane potential greatly enhances superoxide generation by the cytochrome bc complex reconstituted into phospholipid vesicles. J Biol Chem 284(29):19203–19210. https://doi.org/10.1074/jbc.M109.017376

Rubinstein JL, Walker JE, Henderson R (2003) Structure of the mitochondrial ATP synthase by electron cryomicroscopy. EMBO J 22(23):6182–6192

Runswick MJ, Fearnley IM, Skehel JM, Walker JE (1991) Presence of an acyl carrier protein in NADH:ubiquinone oxidoreductase from bovine heart mitochondria. FEBS Lett 286(1–2):121–124

Salje J, Ludwig B, Richter OMH (2005) Is a third proton-conducting pathway operative in bacterial cytochrome c oxidase? Biochem Soc Trans 33:829–831

Sarewicz M, Borek A, Cieluch E, Swierczek M, Osyczka A (2010) Discrimination between two possible reaction sequences that create potential risk of generation of deleterious radicals by cytochrome $bc_1$: implications for the mechanism of superoxide production. BBA-Bioenergetics 1797(11):1820–1827. https://doi.org/10.1016/j.bbabio.2010.07.005

Sazanov LA, Hinchliffe P (2006) Structure of the hydrophilic domain of respiratory complex I from *Thermus thermophilus*. Science 311:1430–1436

Schäfer E, Seelert H, Reifschneider NH, Krause F, Dencher NA, Vonck J (2006) Architecture of active mammalian respiratory chain supercomplexes. J Biol Chem 281:15370–15375

Schäfer E, Dencher NA, Vonck J, Parcej DN (2007) Three-dimensional structure of the respiratory chain supercomplex $I_1III_2IV_1$ from bovine heart mitochondria. Biochemistry 44(46):12579–12585

Schägger H, Pfeiffer K (2000) Supercomplexes in the respiratory chain of yeast and mammalian mitochondria. EMBO J 19(8):1777–1783

Schägger H, Pfeiffer K (2001) The ratio of oxidative phosphorylation complexes I–V in bovine heart mitochondria and the composition of respiratory chain supercomplexes. J Biol Chem 276:37861–37867

Schägger H, Link TA, Engel WD, Von Jagow G (1986) Isolation of the eleven protein subunits of the bc complex from beef heart. Methods Enzymol 126:224–237

Schlerf A, Droste M, Winter M, Kadenbach B (1988) Characterization of 2 different genes (CDNA) for cytochrome c oxidase subunit Vla from heart and liver of the rat. EMBO J 7(8):2387–2391

Schönfeld P, Więckowski MR, Lebiedzińska M, Wojtczak L (2010) Mitochondrial fatty acid oxidation and oxidative stress: lack of reverse electron transfer-associated production of reactive oxygen species. Biochimica et Biophysica Acta (BBA)-Bioenergetics 1797(6):929–938

Schwem BE, Fillingame RH (2006) Cross-linking between helices within subunit *a* of *Escherichia coli* ATP synthase defines the transmembrane packing of a four-helix bundle. J Biol Chem 281:37861–37867

Seelert H, Poetsch A, Dencher NA, Engel A, Stahlberg H, Müller DJ (2000) Proton-powered turbine of a plant motor. Nature 405:418–419

Seelert H, Dani DN, Dante S, Hauß T, Krause F, Schäfer E, Frenzel M, Poetsch A, Rexroth S, Schwaßmann HJ, Suhai T, Vonck J, Dencher NA (2009) From protons to OXPHOS supercomplexes and Alzheimer's disease: structure–dynamics–function relationships of energy-transducing membranes. Biochim Biophys Acta – Bioenergetics 1787:657–671

Senes A, Engel DE, DeGrado WF (2004) Folding of helical membrane proteins: the role of polar, GxxxG-like and proline motifs. Curr Opin Struct Biol 14:465–479

Sharma V, Wikström M (2016) The role of the K-channel and the active-site tyrosine in the catalytic mechanism of cytochrome c oxidase. BBA-Bioenergetics 1857(8):1111–1115. https://doi.org/10.1016/j.bbabio.2016.02.008

Sharma V, Belevich G, Gamiz-Hernandez AP, Róg T, Vattulainen I, Verkhovskaya ML, Wikström M, Hummer G, Kaila VRI (2015) Redox-induced activation of the proton pump in the respiratory complex I. Proc Natl Acad Sci U S A 112(37):11571–11576. https://doi.org/10.1073/pnas.1503761112

Shimokata K, Katayama Y, Murayama H, Suematsu M, Tsukihara T, Muramoto K, Aoyama H, Yoshikawa S, Shimada H (2007) The proton pumping pathway of bovine heart cytochrome c oxidase. Proc Natl Acad Sci U S A 104(10):4200–4205. https://doi.org/10.1073/pnas.0611627104

Silman HI, Rieske JS, Lipton SH, Baum H (1967) A new protein component of complex 3 of mitochondrial electron transfer chain. J Biol Chem 242(21):4867–4875

Skippington E, Barkman TJ, Rice DW, Palmer JD (2015) Miniaturized mitogenome of the parasitic plant *Viscum scurruloideum* is extremely divergent and dynamic and has lost all nad genes. Proc Natl Acad Sci U S A 112(27):E3515–E3524. https://doi.org/10.1073/pnas.1504491112

Soberanes S, Urich D, Baker CM, Burgess Z, Chiarella SE, Bell EL, Ghio AJ, De Vizcaya-Ruiz A, Liu J, Ridge KM, Kamp DW, Chandel NS, Schumacker PT, Mutlu GM, Budinger GRS (2009) Mitochondrial ccomplex III-generated oxidants activate ASK1 and JNK to induce alveolar epithelial cell death following exposure to particulate matter air pollution. J Biol Chem 284(4):2176–2186. https://doi.org/10.1074/jbc.M808844200

Soubannier V, Vaillier J, Paumard P, Coulary B, Schaeffer J, Velours J (2002) In the absence of the first membrane-spanning segment of subunit 4(b), the yeast ATP synthase is functional but does not dimerize or oligomerize. J Biol Chem 277:10739–10745

Sousa JS, Mills DJ, Vonck J, Kühlbrandt W (2016) Functional asymmetry and electron flow in the bovine respirasome. eLife 5:e21290. https://doi.org/10.7554/eLife.21290

Spero MA, Aylward FO, Currie CR, Donohue TJ (2015) Phylogenomic analysis and predicted physiological role of the proton-translocating NADH:quinone oxidoreductase (complex I) across bacteria. mBio 6(2):e00389–e00315. https://doi.org/10.1128/mBio.00389-15

Stahlberg H, Müller DJ, Suda K, Fotiadis D, Engel A, Meier T, Matthey U, Dimroth P (2001) Bacterial $Na^+$-ATP synthase has an undecameric rotor. EMBO Rep 2(3):229–233

Steimle S, Schnick C, Burger EM, Nuber F, Kramer D, Dawitz H, Brander S, Matlosz B, Schafer J, Maurer K, Glessner U, Friedrich T (2015) Cysteine scanning reveals minor local rearrangements of the horizontal helix of respiratory complex I. Mol Microbiol 98(1):151–161. https://doi.org/10.1111/mmi.13112

Stock D, Leslie AG, Walker JE (1999) Molecular architecture of the rotary motor in ATP synthase. Science 286:1700–1705

Stoeckenius W (1963) Some observations of negatively stained mitochondria. J Cell Biol 17:443–454

St-Pierre J, Buckingham JA, Roebuck SJ, Brand MD (2002) Topology of superoxide production from different sites in the mitochondrial electron transport chain. J Biol Chem 277(47):44784–44790

Strauss M, Hofhaus G, Schröder RR, Kühlbrandt W (2008) Dimer ribbons of ATP synthase shape the inner mitochondrial membrane. EMBO J 27:1154–1160

Sun F, Huo X, Zhai Y, Wang A, Xu J, Su D, Bartlam M, Rao Z (2005) Crystal structure of mitochondrial respiratory membrane protein complex II. Cell 121(7):1043–1057. https://doi.org/10.1016/j.cell.2005.05.025

Szklarczyk R, Wanschers BF, Nabuurs SB, Nouws J, Nijtmans LG, Huynen MA (2011) NDUFB7 and NDUFA8 are located at the intermembrane surface of complex I. FEBS Lett 585(5):737–743. https://doi.org/10.1016/j.febslet.2011.01.046

Thomas D, Bron P, Weimann T, Dautant A, Giraud M-F, Paumard P, Salin B, Cavalier A, Velours J, Brèthes D (2008) Supramolecular organization of the yeast $F_iF_o$-ATP synthase. Biol Cell 100(10):591–601

Tormos KV, Anso E, Hamanaka RB, Eisenhart J, Joseph J, Kalyanaraman B, Chandel NS (2011) Mitochondrial complex III ROS regulate adipocyte differentiation. Cell Metab 14(4):537–544. https://doi.org/10.1016/j.cmet.2011.08.007

Trumpower BL, Gennis RB (1994) Energy transduction by cytochrome complexes in mitochondrial and bacterial respiration – the enzymology of coupling electron-transfer reactions to transmembrane proton translocation. Ann Rev Biochem 63:675–716. https://doi.org/10.1146/annurev.biochem.63.1.675

Tsukihara T, Aoyama H, Yamashita E, Tomizaki T, Yamaguchi H, Shinzawa-Itoh K, Nakashima R, Yaono R, Yoshikawa S (1995) Structures of metal sites of oxidized bovine heart cytochrome c oxidase at 2.8 Å. Science 269(5227):1069–1074. https://doi.org/10.1126/science.7652554

Tsukihara T, Aoyama H, Yamashita E, Tomizaki T, Yamaguchi H, Shinzawa-Itoh K, Nakashima R, Yaono R, Yoshikawa S (1996) The whole structure of the 13-subunit oxidized cytochrome c oxidase at 2.8 Å. Science 272:1136–1144

Tsukihara T, Shimokata K, Katayama Y, Shimada H, Muramoto K, Aoyama H, Mochizuki M, Shinzawa-Itoh K, Yamashita E, Yao M, Ishimura Y, Yoshikawa S (2003) The low-spin heme of cytochrome c oxidase as the driving element of the proton-pumping process. Proc Natl Acad Sci U S A 100:15304–15309

Turrens JF (2003) Mitochondrial formation of reactive oxygen species. J Physiol 552(Pt 2):335–344. https://doi.org/10.1113/jphysiol.2003.049478

Tzagoloff A, Barrientos A, Neupert W (2004) Atp10p assists assembly of Atp6p into the $F_0$ unit of the yeast mitochondrial ATPase. J Biol Chem 279:19775–19780

van Hellemond JJ, van der Klei A, van Weelden SW, Tielens AG (2003) Biochemical and evolutionary aspects of anaerobically functioning mitochondria. Philos Trans R Soc Lond Ser B Biol Sci 358(1429):205–213. https://doi.org/10.1098/rstb.2002.1182

van Lis R, Atteia A, Mendoza-Hernandez G, Gonzalez-Halphen D (2003) Identification of novel mitochondrial protein components of *Chlamydomonas reinhardtii*. A proteomic approach. Plant Physiol 132:318–330

van Lis R, Mendoza-Hernández G, Groth G, Atteia A (2007) New insights into the unique structure of the $F_0F_1$-ATP synthase from the chlamydomonad algae *Polytomella* sp. and *Chlamydomonas reinhardtii*. Plant Physiol 144:1190–1199

Varanasi L, Hosler JP (2012) Subunit III-depleted cytochrome c oxidase provides insight into the process of proton uptake by proteins. Biochim Biophys Acta 1817(4):545–551. https://doi.org/10.1016/j.bbabio.2011.10.001

Vempati UD, Han XL, Moraes CT (2009) Lack of cytochrome c in mouse fibroblasts disrupts assembly/stability of respiratory complexes I and IV. J Biol Chem 284(7):4383–4391. https://doi.org/10.1074/jbc.M805972200

Verkhovskaya ML, Belevich N, Euro L, Wikström M, Verkhovsky MI (2008) Real-time electron transfer in respiratory complex I. Proc Natl Acad Sci U S A 105(10):3763–3767. https://doi.org/10.1073/pnas.0711249105

Videira A (1998) Complex I from the fungus *Neurospora crassa*. Biochim Biophys Acta 1364(2):89–100

Vik SB, Antonio BJ (1994) Mechanism of proton translocation by $F_iF_0$ ATP synthases suggested by double mutants of the *a* subunit. J Biol Chem 269:30364–30369

Vik SB, Dao NN (1992) Prediction of transmembrane topology of $F_0$ proteins from *Escherichia coli* $F_iF_0$ ATP synthase using variational and hydrophobic membrane analyses. Biochim Biophys Acta 1140:199–207

Vinothkumar KR, Zhu J, Hirst J (2014) Architecture of mammalian respiratory complex I. Nature 515(7525):80–84. https://doi.org/10.1038/nature13686

Vinothkumar KR, Montgomery MG, Liu S, Walker JE (2016) Structure of the mitochondrial ATP synthase from *Pichia angusta* determined by electron cryo-microscopy. Proc Natl Acad Sci U S A 113:12709–12714. https://doi.org/10.1073/pnas.1615902113

Vonck J, Schäfer E (2009) Supramolecular organization of protein complexes in the mitochondrial inner membrane. Biochim Biophys Acta 1793(1):117–124

Vonck J, Krug von Nidda T, Meier T, Matthey U, Mills DJ, Kühlbrandt W, Dimroth P (2002) Molecular architecture of the undecameric rotor of a bacterial $Na^+$-ATP synthase. J Mol Biol 321(2):307–316

Vonck J, Pisa KY, Morgner N, Brutschy B, Müller V (2009) Three-dimensional structure of $A_1A_0$ ATP synthase from the hyperthermophilic archaeon *Pyrococcus furiosus* by electron microscopy. J Biol Chem 284(15):10110–10119

Vukotic M, Oeljeklaus S, Wiese S, Vögtle FN, Meisinger C, Meyer HE, Zieseniss A, Katschinski DM, Jans DC, Jakobs S, Warscheid B (2012) Rcf1 mediates cytochrome oxidase assembly and respirasome formation, revealing heterogeneity of the enzyme complex. Cell Metab 15(3):336–347

Walker JE (2013) The ATP synthase: the understood, the uncertain and the unknown. Biochem Soc Trans 41:1–16. https://doi.org/10.1042/BST20110773

Walker WH, Singer TP (1970) Identification of the covalently bound flavin of succinate dehydrogenase as 8α-(histidyl) flavin adenine dinucleotide. J Biol Chem 245:4224–4225

Wang R (2012) Physiological implications of hydrogen sulfide: a whiff exploration that blossomed. Physiol Rev 92(2):791–896. https://doi.org/10.1152/physrev.00017.2011

Watt IN, Montgomery MG, Runswick MJ, Leslie AGW, Walker JE (2010) Bioenergetic cost of making an adenosine triphosphate molecule in animal mitochondria. Proc Natl Acad Sci U S A 107:16823–16827

Weidner U, Geier S, Ptock A, Friedrich T, Leif H, Weiss H (1993) The gene locus of the proton-translocating NADH: ubiquinone oxidoreductase in *Escherichia coli*. Organization of the 14 genes and relationship between the derived proteins and subunits of mitochondrial complex I. J Mol Biol 233(1):109–122. https://doi.org/10.1006/jmbi.1993.1488

Weiss MC, Sousa FL, Mrnjavac N, Neukirchen S, Roettger M, Nelson-Sathi S, Martin WF (2016) The physiology and habitat of the last universal common ancestor. Nat Microbiol 1:16116. https://doi.org/10.1038/NMICROBIOL.2016.116

Whelan SP, Zuckerbraun BS (2013) Mitochondrial signaling: forwards, backwards, and in between. Oxid Med Cell Longev. https://doi.org/10.1155/2013/351613

Wikström MK (1977) Proton pump coupled to cytochrome c oxidase in mitochondria. Nature 266(5599):271–273

Wikström M, Sharma V, Kaila VRI, Hosler JP, Hummer G (2015) New perspectives on proton pumping in cellular respiration. Chem Rev 115(5):2196–2221. https://doi.org/10.1021/cr500448t

Wilkens S, Capaldi RA (1998) ATP synthase's second stalk comes into focus. Nature 393:29

Wirth C, Brandt U, Hunte C, Zickermann V (2016) Structure and function of mitochondrial complex I. Biochim Biophys Acta 1857(7):902–914. https://doi.org/10.1016/j.bbabio.2016.02.013

Xia D, Yu C-A, Kim H, Xia J, Kachurin AM, Zhang L, Yu L, Deisenhofer J (1997) Crystal structure of the cytochrome bc complex from bovine heart mitochondria. Science 281:64–71

Yagi T, Matsuno-Yagi A (2003) The proton-translocating NADH-quinone oxidoreductase in the respiratory chain: the secret unlocked. Biochemistry 42(8):2266–2274. https://doi.org/10.1021/bi027158b

Yakovlev G, Reda T, Hirst J (2007) Reevaluating the relationship between EPR spectra and enzyme structure for the iron sulfur clusters in NADH:quinone oxidoreductase. Proc Natl Acad Sci U S A 104(31):12720–12725. https://doi.org/10.1073/pnas.0705593104

Yang XH, Trumpower BL (1986) Purification of a three-subunit ubiquinol-cytochrome c oxidoreductase complex from Paracoccus denitrificans. J Biol Chem 261(26):12282–12289

Yang M, Trumpower BL (1994) Deletion of QCR6, the gene encoding subunit six of the mitochondrial cytochrome bc complex, blocks maturation of cytochrome c, and causes temperature-sensitive petite growth in Saccharomyces Cerevisiae. J Biol Chem 269(2):1270–1275

Yang W-L, Iacono L, Tang W-M, Chin K-V (1998) Novel function of the regulatory subunit of protein kinase A: regulation of cytochrome c oxidase activity and cytochrome c release. Biochemistry 37(40):14175–14180. https://doi.org/10.1021/bi981402a

Yankovskaya V, Horsefield R, Törnroth S, Luna-Chavez C, Miyoshi H, Léger C, Byrne B, Cecchini G, Iwata S (2003) Architecture of succinate dehydrogenase and reactive oxygen species generation. Science 299:700–704

Yong R, Searcy DG (2001) Sulfide oxidation coupled to ATP synthesis in chicken liver mitochondria. Comp Biochem Physiol B Biochem Mol Biol 129(1):129–137

Yoshikawa S, Shimada A (2015) Reaction mechanism of cytochrome c oxidase. Chem Rev 115(4):1936–1989. https://doi.org/10.1021/cr500266a

Zara V, Conte L, Trumpower BL (2009) Evidence that the assembly of the yeast cytochrome bc complex involves the formation of a large core structure in the inner mitochondrial membrane. FEBS J 276(7):1900–1914. https://doi.org/10.1111/j.1742-4658.2009.06916.x

Zeng X, Neupert W, Tzagoloff A (2007) The metallopeptidase encoded by ATP23 has a dual function in processing and assembly of subunit 6 of mitochondrial ATPase. Mol Biol Cell 18:617–623

Zeng X, Barros MH, Shulman T, Tzagoloff A (2008) ATP25, a new nuclear gene of Saccharomyces cerevisiae required for expression and assembly of the Atp9p subunit of mitochondrial ATPase. Mol Biol Cell 19:1366–1377

Zhang C, Allegretti M, Vonck J, Langer JD, Marcia M, Peng G, Michel H (2014) Production of a fully assembled and active form of *Aquifex aeolicus* $F_IF_O$ ATP synthase in *Escherichia coli*. BBA – Gen Subj 1840(1):34–40. https://doi.org/10.1016/j.bbagen.2013.08.023

Zhao J, Benlekbir S, Rubinstein JL (2015) Electron cryomicroscopy observation of rotational states in a eukaryotic V-ATPase. Nature 521:241–245

Zhou A, Rohou A, Schep DG, Bason JV, Montgomery MG, Walker JE, Grigorieff N, Rubinstein JL (2015) Structure and conformational states of the bovine mitochondrial ATP synthase by cryo-EM. eLife 3:e10180. https://doi.org/10.7554/eLife.10180

Zhu J, Vinothkumar KR, Hirst J (2016) Structure of mammalian respiratory complex I. Nature 536(7616):354–358. https://doi.org/10.1038/nature19095

Zickermann V, Wirth C, Nasiri H, Siegmund K, Schwalbe H, Hunte C, Brandt U (2015) Mechanistic insight from the crystal structure of mitochondrial complex I. Science 347:44–49. https://doi.org/10.1126/science.1259859

# Chapter 8
# The SarcoEndoplasmic Reticulum Calcium ATPase


**Joseph O. Primeau, Gareth P. Armanious, M'Lynn E. Fisher, and Howard S. Young**

**Abstract** The calcium pump (a.k.a. $Ca^{2+}$-ATPase or SERCA) is a membrane transport protein ubiquitously found in the endoplasmic reticulum (ER) of all eukaryotic cells. As a calcium transporter, SERCA maintains the low cytosolic calcium level that enables a vast array of signaling pathways and physiological processes (e.g. synaptic transmission, muscle contraction, fertilization). In muscle cells, SERCA promotes relaxation by pumping calcium ions from the cytosol into the lumen of the sarcoplasmic reticulum (SR), the main storage compartment for intracellular calcium. X-ray crystallographic studies have provided an extensive understanding of the intermediate states that SERCA populates as it progresses through the calcium transport cycle. Historically, SERCA is also known to be regulated by small transmembrane peptides, phospholamban (PLN) and sarcolipin (SLN). PLN is expressed in cardiac muscle, whereas SLN predominates in skeletal and atrial muscle. These two regulatory subunits play critical roles in cardiac contractility. While our understanding of these regulatory mechanisms are still developing, SERCA and PLN are one of the best understood examples of peptide-transporter regulatory interactions. Nonetheless, SERCA appeared to have only two regulatory subunits, while the related sodium pump (a.k.a. $Na^+$, $K^+$-ATPase) has at least nine small transmembrane peptides that provide tissue specific regulation. The last few years have seen a renaissance in our understanding of SERCA regulatory subunits. First, structures of the SERCA-SLN and SERCA-PLN complexes revealed molecular details of their interactions. Second, an array of micropeptides concealed within long non-coding RNAs have been identified as new SERCA regulators. This chapter will describe our current understanding of SERCA structure, function, and regulation.

**Keywords** Sarcoplasmic reticulum · Calcium ATPase · Phospholamban · Sarcolipin

J. O. Primeau · G. P. Armanious · M. E. Fisher · H. S. Young (✉)
Department of Biochemistry, University of Alberta, Edmonton, Alberta, Canada
e-mail: jprimeau@ualberta.ca; garmanio@ualberta.ca; mlynn1@ualberta.ca; hyoung@ualberta.ca



J. R. Harris, E. J. Boekema (eds.), *Membrane Protein Complexes: Structure and Function*, Subcellular Biochemistry 87,
https://doi.org/10.1007/978-981-10-7757-9_8

## Abbreviations

| | |
|---|---|
| Å | Angstrom |
| ADP | Adenosine Diphosphate |
| AKAP | A Kinase Anchoring Protein |
| Akt | Protein Kinase B |
| $AlF_4$ | Aluminum Tetrafluoride |
| ALN | Another-Regulin |
| AMP | Adenosine Monophosphate |
| AMPPCP | Phosphomethylphosphonic Acid Adenylate Ester |
| ATP | Adenosine triphosphate |
| CAMKII | Calcium/Calmodulin Dependent Protein Kinase II |
| CPA | Cyclopiazonic acid |
| dSCLa | *Drosophila* Sarcolamban Isoform A |
| dSCLb | *Drosophila* Sarcolamban Isoform B |
| DWORF | Dwarf Open Reading Frame |
| ELN | Endoregulin |
| ER | Endoplasmic Reticulum |
| GDP | Guanosine Diphosphate |
| GTP | Guanosine Triphosphate |
| HAX1 | HS-1 Associated Protein |
| hDWORF | Human Dwarf Open Reading Frame |
| hMLN | Human Myoregulin |
| hPLN | Human Phospholamban |
| Hsp20 | Small Heat Shock Protein 20 |
| hSLN | Human Sarcolipin |
| I-1 | Inhibitor-1 |
| $K_{Ca}$ | Apparent Calcium Affinity |
| mALN | Mouse Another-Regulin |

## 8.1 Introduction

A hallmark of eukaryotic cells is the presence of intracellular membrane systems, which create subcellular compartments and functionally specialized aqueous environments that are distinct from the cytosol. These intricate intracellular membrane systems include the endoplasmic reticulum (ER), nucleus, Golgi apparatus, endosomes and lysosomes, and mitochondria, amongst others. These organelles perform distinct, essential physiological functions within the cell, and in many instances these functions require signal transduction pathways involving calcium as a second messenger (Berridge et al. 2003). For the signaling pathways to work, spatial and temporal calcium levels are tightly controlled and highly regulated. The cytosolic calcium concentration is necessarily maintained at low resting levels (<100 nM),

while the concentration of calcium within organelles can be much higher (~mM). The signaling pathways then rely on a rapid rise in cytosolic calcium to initiate a signal, and a rapid decrease in cytosolic calcium to terminate the signal (Carafoli and Krebs 2016). Organelles such as the ER and mitochondria contain specialized calcium handling systems for the release and recovery of intracellular calcium stores.

A signature example of organellar calcium storage and intracellular signaling is the sarcoplasmic reticulum (SR), a specialized form of ER found in muscle cells. In addition to carrying out functions normally associated with the ER, the SR is the primary storage site for the calcium used to trigger muscle contraction (Doroudgar and Glembotski 2013). On the one hand, the SR must provide an environment for proper enzymatic function of proteins involved in protein folding, lipid synthesis, and the control of cell fate via apoptosis and cell growth. On the other hand, calcium stored in the SR is mobilized by calcium release channels for the activation of the contractile machinery within the cytosol (systole). Following muscle contraction, most of the cytosolic calcium is then recovered into the SR to initiate muscle relaxation (diastole). The release and recovery of calcium into the SR lumen ensures that the cell can begin the contraction-relaxation cycle anew. Importantly, the luminal storage of calcium is essential for a diverse array of functions, as well as the contractile role of the SR (Bers 2008).

This brings us to the star of this particular chapter in the *Subcellular Biochemistry* series – the **S**arco/**E**ndoplasmic **R**eticulum **C**alcium **A**TPase, also know as **SERCA**, the calcium pump, or $Ca^{2+}$-ATPase. The removal of cytosolic calcium into the lumen of the SR is primarily achieved by SERCA, a member of the P-type ATPase superfamily of primary active transporters. Generally speaking, P-type ATPases are a large family of evolutionarily related membrane proteins that span bacteria, archaea and eukaryotes (Palmgren and Nissen 2011). The integral membrane "pumps" perform active transport of a diverse array of ions and lipids across biological membranes. The best characterized members of this family include SERCA ($Ca^{2+}$-ATPase) and the sodium pump ($Na^+/K^+$-ATPase). The sodium pump is found in all eukaryotic cells where it maintains the cellular membrane potential by transporting sodium and potassium across the plasma membrane and against their concentration gradients. SERCA is also found in all eukaryotic cells where it maintains the low cytosolic calcium concentration by transporting calcium ions across the ER and SR membranes. In the case of SERCA, the hydrolysis of ATP is coupled to the translocation of two calcium ions across the SR membrane and against their concentration gradient. SERCA counter-transports two-to-three protons out of the SR, though a proton gradient is not maintained across the SR membrane. Indeed, the generalized reaction scheme for P-type ATPases involves the exchange (active transport) of two different metal ions across a membrane at the expense of ATP (Post-Albers scheme; Fig. 8.1). Proposed almost 50 years ago, the Post-Albers scheme is a simplistic but relevant description of calcium transport by SERCA and the high (E1) and low (E2) affinity states that SERCA populates during the reaction cycle and vectorial ion transport.

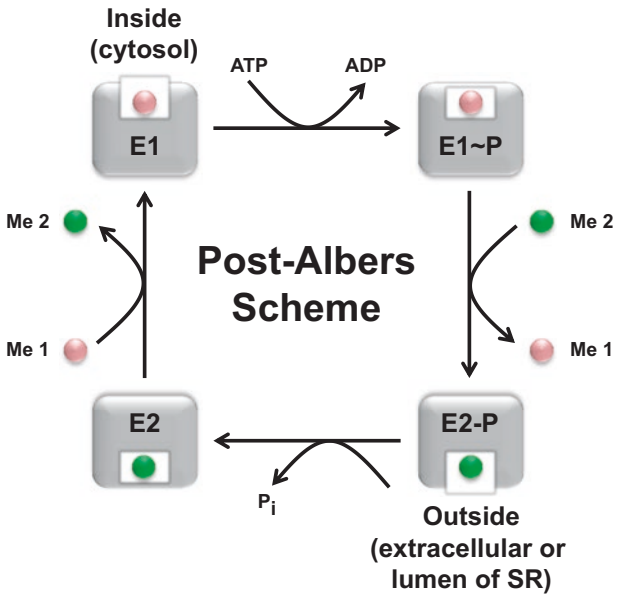


**Generalized reaction scheme for P-type ATPases**

$$n\text{Me1(out)} + m\text{Me2(in)} + \text{ATP} \longrightarrow n\text{Me1(in)} + m\text{Me2(out)} + \text{ADP} + \text{P}_\text{i}$$

**Fig. 8.1 Generalized Post-Albers scheme for P-type ATPases**. Metal ions (Me1) from one side of the membrane (e.g. cytosol) are transported to the opposite side of the membrane (e.g. lumen of the SR), while different metal ions (Me2) are transported in the opposite direction (e.g. lumen to the cytosol). The type and number of metal ions, or lipids, that are transported in each direction vary between different P-type ATPases (*n* and *m* are integers). A central generalization of this scheme is that P-type ATPases switch between two major conformations, an E1 state with ion binding sites facing one side of the membrane and an E2 state with ion binding sites facing the other side of the membrane. E1 has high affinity and E2 has low affinity for the primary metal ion (Me1)

## 8.2 SERCA Isoform Diversity and Tissue Distribution

Our detailed understanding of the structure and function of P-type ATPases is attributable to SERCA1a, the isoform present in and easily isolated from rabbit fast twitch skeletal muscle. It is presumed that the structure and function of SERCA1a is generally reflective of the entire family of P-type ATPases (Moller et al. 2010). Calcium pumps appear to be present in all living organisms from prokaryotes to mammals, though our understanding of prokaryotic calcium pumps remains rudimentary. Of the eukaryotic calcium pumps, three multigene families and nine members are currently known. There are three genes that encode SERCA pumps (SERCA1-3 or ATP2A1-3), four that encode plasma membrane calcium pumps (PMCA1-4 or ATP2B1-4), and two that encode secretory pathway calcium pumps (SPCA1-2 or ATPC2A1-2). These genes give rise to more than 40 different splice

variants, which results in an impressive diversification of form, function, regulation, and physiological role (Brini et al. 2012).

In vertebrates, SERCA paralogues are encoded by a family of three genes – SERCA1, SERCA2, and SERCA3 – located on three different chromosomes. This family is highly conserved, with SERCA1 and SERCA2 being ~84% identical and SERCA3 being ~75% identical to either of the other paralogues. The isoform diversity of SERCA is amplified by alternative splicing of transcripts, which occur mainly in the C-terminus of the protein. These splicing variations give rise to thirteen currently known isoforms (SERCA1a-b, SERCA2a-d, and SERCA3a-f) (Wuytack et al. 2002; Dally et al. 2010). These SERCA isoforms exhibit both tissue and developmental specificity, reflecting their diversified functionality. The SERCA1 gene encodes two spliced variants primarily expressed in adult (SERCA1a; 994 residues) and fetal-neonatal (SERCA1b; 1001 residues) fast-twitch skeletal muscle. The SERCA1a and SERCA1b isoforms are functionally equivalent and differ by only seven additional residues at the C-terminus. While there is no specific structure or function associated with the extended C-terminus of SERCA1b, it is highly charged and may play a role in skeletal muscle development (Kosa et al. 2015). It is also interesting to consider that the C-terminus of the related sodium pump inserts into the membrane domain and modulates sodium affinity (Toustrup-Jensen et al. 2009). Thus, the short extension found in SERCA1b may modulate function during the developmental switch from fetal to adult skeletal muscle.

The SERCA2 gene is best known for encoding both the ubiquitous and cardiac-specific isoforms of SERCA (Vangheluwe et al. 2005). In all, four isoforms (SERCA2a-d) are generated by alternative splicing of the SERCA2 gene transcript. SERCA2b is a ubiquitous isoform expressed in all cell types, whereas SERCA2a is restricted to cardiac muscle, slow-twitch skeletal muscle and smooth muscle cells. In humans, SERCA2a encodes for a 997 amino acid protein and SERCA2b for a 1042 amino acid protein. These two isoforms differ by an unusual addition of 45 amino acids at the C-terminus, which gives SERCA2b an 11th transmembrane helix and places the C-terminus on the opposite side of the membrane in the lumen of the SR. The luminal tail and 11th transmembrane helix of SERCA2b imbue the highest calcium affinity amongst the SERCA isoforms (Gorski et al. 2012; Vandecaetsbeek et al. 2009). A relatively new SERCA2c isoform has been shown to encode a functional form of SERCA2 expressed in cardiac muscle (Gelebart et al. 2003). This isoform is partially encoded by a short intronic sequence that results in a novel, truncated C-terminus. It is tempting to speculate that in line with the logic of the 2b tail having a regulatory capacity, this truncated version allows for regulatory control via the multiple recently identified single pass regulatory subunits (PLN, SLN, DWORF, ALN, etc.). Along with SERCA2a and SERCA2b, ventricular muscle appears to contain three SERCA isoforms. Finally, a novel SERCA2 variant (SERC2d) has been identified in skeletal muscle, though the significance and functionality of this isoform remains unknown (Chemaly et al. 2013).

The third SERCA gene, SERCA3, encodes the most splice variants with six known isoforms (SERCA3a-f). SERCA3 isoforms are expressed in non-muscle tissues including hematopoietic cells, platelets, epithelial cells, endothelial cells, and fibroblasts; however, it has also been found in cardiomyocytes (Dally et al. 2010). All SERCA3 isoforms have been found to be functional, though they appear

to differently modulate cytosolic calcium and ER calcium load. Compared to the high prevalence of the muscle and ubiquitous SERCA isoforms (SERCA1 & SERCA2), SERCA3 is a more divergent, specialized isoform with the functional characteristics of a fast, low-affinity calcium pump. That said, most cells likely contain multiple isoforms and splice variants as a means of diversifying intracellular calcium signaling on both global cellular and localized subcellular scales.

## 8.3 SERCA Structure, Function, and Physiology

### *8.3.1 Function and Physiology*

SERCA isoforms are highly conserved and predicted to share the same general fold, transmembrane topology and tertiary structure. Indeed, the highly conserved nature of SERCAs underlies the sensitivity of all isoforms to sub-nanomolar inhibition by the plant-derived sesquiterpene thapsigargin (Fig. 8.2) (Sagara et al. 1992). In contrast, other P-type ATPases such as the sodium pump are relatively insensitive to thapsigargin. The sequence differences between SERCA1, SERCA2, SERCA3, and their splice variants are thought to involve relatively minor alterations in structure, which impart small variations in the calcium affinity and turnover rate of the different isoforms. For instance, the SERCA3 isoforms are faster, lower-affinity calcium pumps, while the SERCA2b isoform is a slower, higher-affinity calcium pump. Similarly, the small structural differences inherent in the many SERCA isoforms accounts for cell-specific functional and development differences at the level of ER and SR calcium handling. The one exception to this is the novel splice variation and sequence difference that occurs in the ubiquitous SERCA2b isoform. An extra, 11th transmembrane helix in SERCA2b imparts a higher calcium affinity and creates a luminal C-terminus that may sense and respond to the environment in the ER (Vandecaetsbeek et al. 2009).

Comparing fast-twitch skeletal and cardiac muscle provides insight into the tissue specificity of SERCA isoforms that diversifies cellular calcium signaling and enables vital physiological processes. Fast-twitch skeletal muscle contracts quickly and strongly in response to a “voluntary” impulse, and it is the primary source of sudden, powerful bursts of movement (e.g. boxing). In contrast, cardiac muscle contracts more slowly, with variable force, and in a continuous “involuntary” and rhythmic fashion (heartbeat). As stated above, the primary SERCA isoform in fast twitch skeletal muscle is SERCA1a and the isoform in cardiac muscle is SERCA2a. Studies exploring the differences between SERCA1a and SERCA2a have demonstrated that SERCA1a has a comparable calcium affinity to SERCA2a and a maximal activity that is approximately double that of SERCA2a (SERCA1a is a faster pump) (Reddy et al. 1996). In addition, the density of SERCA1a is higher in skeletal muscle SR than SERCA2a is in cardiac muscle SR. Of course, there are many other contributing protein and metabolic factors that delineate fast-twitch skeletal and

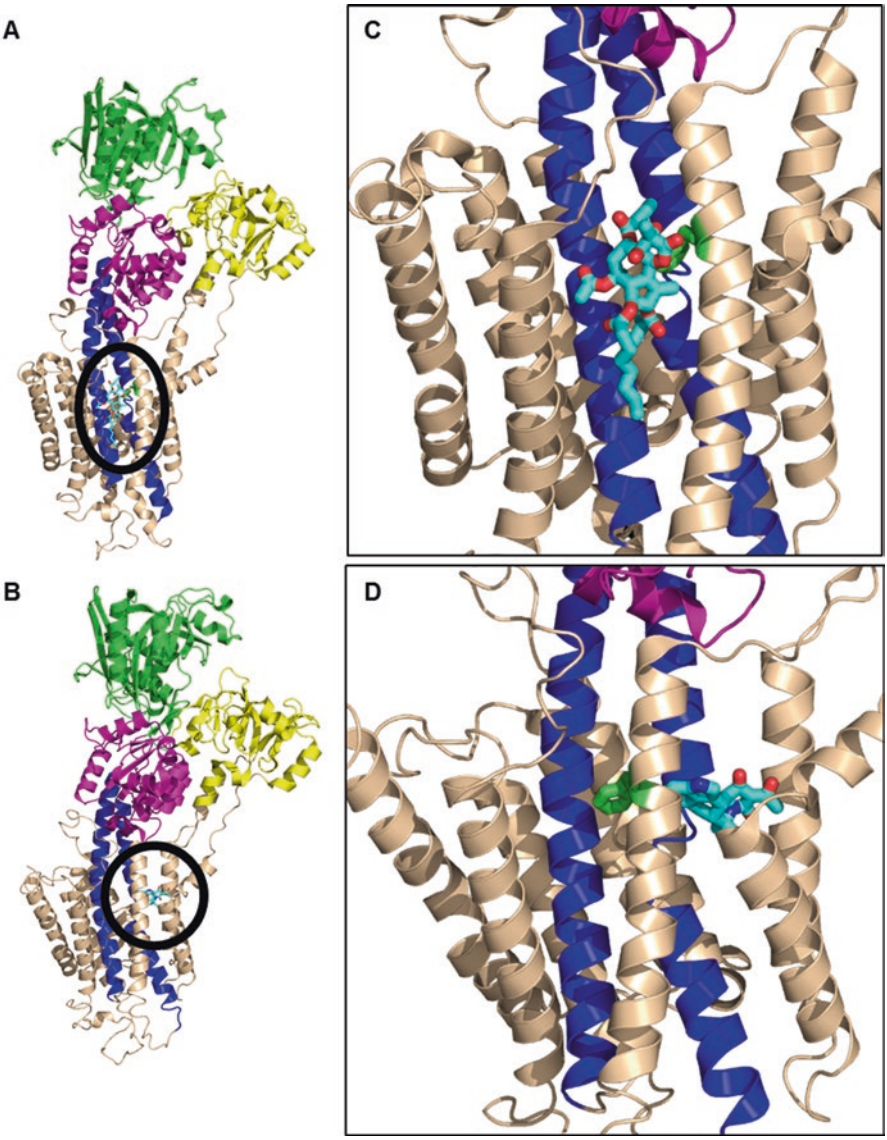


**Fig. 8.2 Structures of SERCA bound to thapsigargin (TG) and cyclopiazonic acid (CPA).** Overall structures of the E2•TG (**a**) and E2P•CPA (**b**) states of SERCA in a cartoon representation (PDB accession codes 3AR4 and 3FPB, respectively). The A (yellow), P (magenta), and N (green) domains are indicated, and M4 and M5 are shown in blue. (**c**) TG (stick format) binds alongside M3 of SERCA and $Phe^{256}$ (green stick format) is a key determinant of high affinity binding of the inhibitor. (**d**) CPA (stick format) binds in the calcium access channel of SERCA, surrounded by M1, M2, and M3. For further details on inhibitor binding, refer to the original publications (Toyoshima and Nomura 2002, *Nature* 418:605–11; Moncoq et al. 2007, J Biol Chem 282:9748–57; Laursen et al. 2009, J Biol Chem 284:13513–8)

cardiac muscle. However, these tissue-specific differences in SERCA function and distribution allow skeletal muscle fibers to achieve a faster rate of calcium uptake, larger calcium load and more forceful contractile function. It is also important to remember that skeletal and cardiac muscle cells contain multiple SERCA isoforms, which likely contribute to additional diversification of function depending on the compliment and abundance of isoforms present in a particular cell type. For instance, cardiomyocytes appear to contain at least four isoforms – SERCA2a, SERCA2b, SERCA2c and SERCA3b (Lipskaia et al. 2014).

### *8.3.2 Function and Structure*

The sodium pump was the first P-type ATPase identified in 1957 (Skou 1957), and this seminal observation earned Jens Christian Skou the 1997 Nobel Prize in Chemistry. Since this discovery, the P-type ATPases have emerged as a superfamily of membrane-embedded pumps that span all kingdoms of life and transport monovalent and divalent cations, heavy metals, and lipids. For the majority of these pumps, the mechanism of transport and physiological role remain unknown. Nonetheless, the SERCA calcium pump – specifically SERCA1a from rabbit skeletal muscle – has become a paradigm for the P-type ATPase family thanks to another major breakthrough in the field. In the year 2000, Chikashi Toyoshima and colleagues reported the first crystal structure of SERCA with bound calcium ions (Toyoshima et al. 2000). For those working in the field, it was a stunning revelation of the architectural complexity and molecular structure of a P-type ATPase. Since then, more than 60 structures of SERCA have been deposited in the Protein Data Bank, effectively mapping out the entire calcium transport reaction cycle (Fig. 8.3).

The myriad structures of SERCA have provided insight into the mechanism by which these P-type pumps use ATP to move ions across the membrane. The vast majority of these structures have come from the Toyoshima and Nissen laboratories, though our laboratory has also contributed novel insights into the structure of SERCA (Laursen et al. 2009; Moncoq et al. 2007) (Fig. 8.2). SERCA is a 110 kDa protein consisting of ten transmembrane helices that coordinate two calcium ions for transport into the SR lumen and two-to-three protons for counter-transport into the cytoplasm. While the SR membrane sequesters the transported calcium against a concentration gradient, the SR membrane does not maintain a proton gradient. The side-by-side calcium binding sites are formed by four of the ten transmembrane helices (M4, M5, M6 & M8), and two of these transmembrane helices (M4 & M6) are partially unwound in the middle of the membrane. The helix unwinding allows for the placement of the two calcium binding sites at the same height in the membrane and coordination of the two ions by both side chain and backbone carbonyl interactions. The first calcium ion (site I) is coordinated by side chain interactions with $Asn^{768}$ and $Glu^{771}$ from M5, $Thr^{799}$ and $Asp^{800}$ from M6, and $Glu^{908}$ from M8. Binding of the first calcium ion, and transition to the E1 state, is thought to induce a conformational change in M4 to allow binding of the second calcium ion (site II).

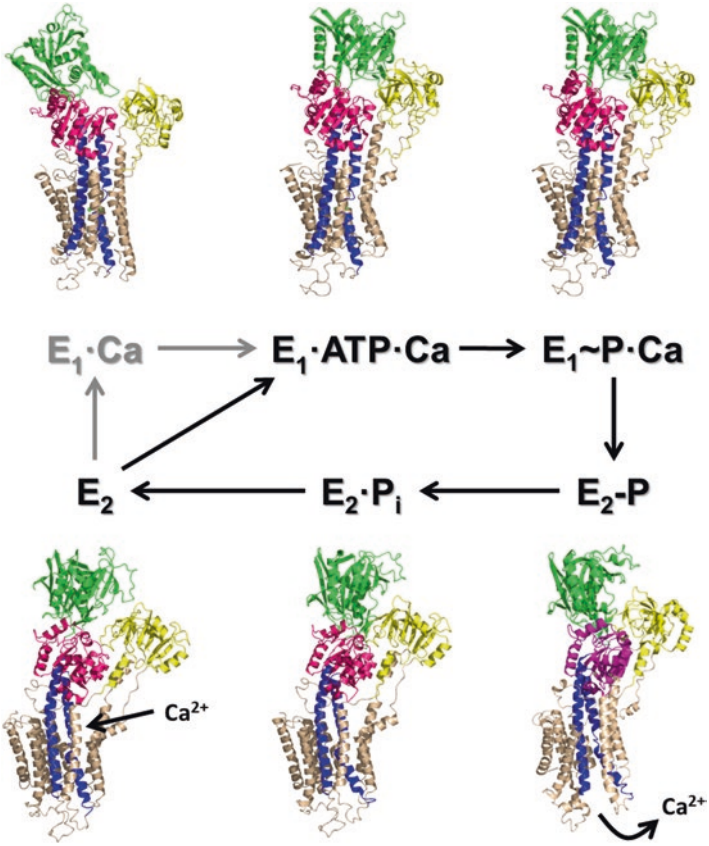


**Fig. 8.3 Structural intermediates in the SERCA calcium transport cycle.** SERCA structures representing key intermediates in the calcium transport cycle. **E2** – Ground state of the enzyme with 2-3 bound protons from the luminal side of the SR membrane. **E1•Ca** – Release of 2-3 protons and binding of 2 calcium ions from the cytosolic side of the membrane. **E1•ATP•Ca** – ATP and calcium bound state in which the enzyme is poised to initiate transport. **E1~P•Ca** – Phosphorylation from ATP with the formation of an occluded calcium-bound state. **E2-P** – The conversion of an E1 to an E2 state following release of ADP and calcium to the SR lumen. **E2•$P_i$** – The formation of an occluded proton-bound state, followed by dephosphorylation and return to the E2 ground state. Under normal physiological conditions, SERCA likely transitions directly from E2 to E1•ATP•Ca. The structures are shown as a tan cartoon representation, with the A-domain in yellow, N-domain in green, P-domain in magenta, and helices M4 and M5 in blue

The second calcium ion binds along the path of M4 in the gap created by helix unwinding. This allows both side chain ($Glu^{309}$ from M4; $Asn^{796}$ and $Asp^{800}$ from M6) and backbone carbonyl oxygens ($Val^{304}$, $Ala^{305}$ and $Ile^{307}$ from M4) to contribute to ion coordination.

Of the four transmembrane helices that coordinate calcium ions, two are very long (M4 & M5; ~60Å) and extend into the cytoplasmic domain of the protein. Technically speaking, M4 is not a continuous helix because it is unwound in the

center of the membrane; however, it is part of a structural core that links the transmembrane and cytoplasmic domains of SERCA (Moller et al. 2010). SERCA possesses three cytoplasmic domains that sit atop the transmembrane domain "impaled" on M4 and M5 – the nucleotide-binding (N), phosphorylation (P), and actuator (A) domains. The heart of the protein is the P domain, which contains the conserved aspartate residue ($Asp^{351}$) that is the target of phosphoryl-transfer from ATP. The γ-phosphate of ATP is covalently passed with the retention of energy to this catalytic aspartate residue. The N domain, with its high affinity binding site for ATP, emerges from the P domain. The N domain undergoes significant movement as the bound ATP must travel over 25 Å to reach its target catalytic $Asp^{351}$ in the P domain to facilitate phosphoryl-transfer. In the primary structure, M4 is followed by the first half of the P domain, the N domain, the second half of the P domain, and then M5. The N domain sits atop the protein furthest from the membrane and it is connected to the P domain by a narrow hinge region ($Thr^{358}$-Asn-$Gln^{360}$ and the signature $Asp^{601}$-Pro-Pro-$Arg^{604}$ motif). The N domain contains conserved residues required for nucleotide recognition, such as $Phe^{487}$ and $Lys^{515}$, and the hinge region allows a large range of domain motion for catalytic activation once nucleotide is bound. The two halves of the P domain come together to form a Rossman fold, where the N-terminal portion packs against M4 and the C-terminal portion packs against M5. $Asp^{351}$ lies atop the central β-strand that joins the two halves of the P domain. This intriguing split topology of M4-M5 and the P domain is capped by the N domain, thereby linking calcium binding in the membrane, nucleotide binding in the N domain, and catalytic activation of $Asp^{351}$ in the P domain. Finally, the A domain is the most N-terminal domain and it sits atop transmembrane segments M1, M2, and M3. This domain consists of a "jelly roll" β-rich region between M2 and M3 and an N-terminal α-helical region that precedes M1 and packs against the β-rich region. As a result, the A domain is connected to M1, M2, and M3 by flexible linkers that allow large-range motions that accompany ATP utilization and ion movement. The A domain contains a signature sequence of the P-type ATPases, $Thr^{181}$-Gly-Glu-$Ser^{184}$ (TGES), which is essential for dephosphorylation of $Asp^{351}$ in the later stages of the transport cycle. From a historical perspective, it is interesting to recall that several residues on the A domain were the targets of early proteolysis experiments that defined the E1 and E2 conformational states. The large movements of the A domain and the associated linkers in the absence and presence of calcium alternately exposed and buried residues such as $Arg^{198}$ (MacLennan et al. 1985).

With this domain architecture, SERCA uses the energy of ATP to move ions through the membrane. In the process, it passes through several major reaction intermediates typically denoted $E_1$, $E_1P$, $E_2P$, and $E_2$ (Fig. 8.3), where E1 refers to a high affinity state and E2 a low affinity state for calcium binding (de Meis and Vianna 1979). The progression through the cycle involves rigid-body movements of the cytoplasmic domains and complex deformations of the transmembrane helices. The structures of the intermediates are hugely different from one another, and it is fascinating to see how they combine to animate the ion transport cycle. The P domain, containing the conserved $Asp^{351}$, is locked against M4 and M5 of the membrane domain. A main feature of the calcium transport cycle is that the P domain

adopts a distinct orientation in each of the reaction intermediates, moving in a concerted way with M4 and M5. In addition, the N and A domains adopt remarkably distinct orientations in each reaction intermediate, due to their flexible connections to the rest of the protein. In contrast to the rigid-body movements of the cytoplasmic domains, the membrane domain undergoes plastic deformations of helices M1-M6. The rearrangements in the transmembrane domain cause the calcium-binding sites to alternately access the cytosolic and luminal sides of the membrane. Upon phosphoryl-transfer from ATP to $Asp^{351}$, the A domain undergoes a large rotation that allows the conserved TGES motif to displace ADP now occupying the ATP binding site in the N domain. Because the A domain is directly linked to M2 and M3, it serves to transduce movement in the cytoplasmic domain to conformational changes in the transmembrane domain (calcium ion occlusion). The A domain ultimately makes contact with both the P and N domains, such that the TGES motif can initiate the dephosphorylation event and continue the cycle. This association causes significant movement in M2 to M5, thereby exposing the calcium binding sites to the SR lumen and allowing calcium release. The direct connections between the ion binding sites in the membrane and the cytoplasmic domains provide a plausible mechanism for calcium transport, $H^+$ counter-transport, and phosphorylation and dephosphorylation of $Asp^{351}$. For a more detailed description of the structure and function of SERCA, there are a number of excellent reviews available (*see* Moller et al. 2010; Toyoshima 2008, 2009).

With the many structures of SERCA available in the Protein Data Bank, one might assume that we understand everything there is to know about the calcium transport cycle. Sadly, or perhaps interestingly, this is not true. First, the structures provide snapshots of the stable intermediates SERCA adopts as it progresses through the reaction cycle, and it gives us an impressive vision of the mechanics of calcium transport. However, the molecular and energetic constraints that drive each step in the reaction cycle from ATP hydrolysis to calcium transport against a concentration gradient remain challenging to delineate. As an example, consider the transition from the E1•$Ca_2$•ATP state to the E1~P•$Ca_2$•ADP state following transfer of the γ-phosphate to $Asp^{351}$ with nearly complete conservation of energy. The structures of these two intermediates are known and represented by E1•$Ca_2$•AMPPCP and E1~$AlF_4$•$Ca_2$•ADP complexes, respectively (Sorensen et al. 2004). These structures are identical, yet they possess distinct biochemical characteristics – in particular, only the E1~$AlF_4$•$Ca_2$•ADP complex adopts a stable occluded state, a pre-requisite for progression to the next intermediate in the transport cycle. Second, while such details may be of particular interest in the P-type ATPase field, the large number of structures available for SERCA does not mean that we have mapped the entire structural landscape of SERCA intermediates (there continue to be surprises in the field!). As an example, recent structures of SERCA in complex with the regulatory subunits phospholamban (PLN) and sarcolipin (SLN) revealed an unanticipated conformation of SERCA (Winther et al. 2013; Toyoshima et al. 2013; Akin et al. 2013). In the complexes, SERCA adopts a previously undescribed E1-like state with formed calcium binding sites that are open to the cytosol. In the two crystal structures of the SERCA-SLN complex, magnesium ions sit adjacent to the two

calcium binding sites (sites I & II). In one of the structures (Winther et al. 2013), two magnesium ions were found (adjacent to $Asp^{800}$ and $Glu^{309}$), and in the other structure (Toyoshima et al. 2013), one magnesium ion was found (adjacent to $Ala^{305}$). At physiological concentrations, magnesium is expected to interact with the calcium binding sites and modulate the transport cycle (Henderson et al. 1994; Peinelt and Apell 2002), though the reaction cycle cannot progress without both calcium and ATP binding. In this E1-like state, the E2-to-E1 transition has begun and the calcium sites are formed, though the magnesium ions must be displaced for calcium to bind. It is interesting to note that the SERCA-PLN complex is remarkably similar but does not appear to have a bound magnesium (Akin et al. 2013).

## 8.4 SERCA Regulator Complexes, Coming of Age

Historically, PLN and SLN were the only known regulators of SERCA (Kirchberber et al. 1975; Wawrzynow et al. 1992; Odermatt et al. 1998). PLN is a 52 amino acid integral membrane protein found in cardiac and smooth muscle (Simmerman et al. 1986a), and SLN is a homologous 31 amino acid integral membrane protein found in skeletal and atrial muscle (Odermatt et al. 1998). The canonical model for SERCA regulation by PLN and SLN involved a reversible one-to-one association that lowers the apparent calcium affinity of SERCA (Stokes 1997a), and this has classically been termed SERCA inhibition. The inhibition is maximal at low physiological calcium concentrations (~0.1 μM cytosolic calcium) and reversed at higher calcium concentrations (>1 μM) (Fig. 8.4). However, this simplistic picture of SERCA regulation has recently evolved to include new regulatory peptides and novel functions for PLN and SLN. Most of these regulatory processes are restricted to the SR of skeletal and cardiac muscle; however, a ubiquitous regulatory mechanism in the ER is encoded in the SERCA2b isoform and new non-muscle regulators of SERCA have been discovered.

### *8.4.1 Phospholamban*

PLN is a 52 amino acid, monotopic integral membrane protein that is best known for its regulatory role in the heart. PLN is found predominantly in ventricular cardiac muscle, and to a lesser extent in slow-twitch skeletal muscle, smooth muscle, and atrial muscle. PLN contains 3 domains (Fig. 8.4) – a transmembrane helix responsible for most of its inhibitory properties (residues ~31–52), a short, unstructured linker region (residues ~21–30), and a soluble cytoplasmic helix that is thought to be more dynamic (residues ~1–20). PLN was discovered as the major target of phosphorylation in isolated SR membranes, and it was named accordingly (phospholamban was derived from *phosphate* and the Greek word '*to receive*') (Kirchberber et al. 1975; Katz 1998). This reflects the observation that protein

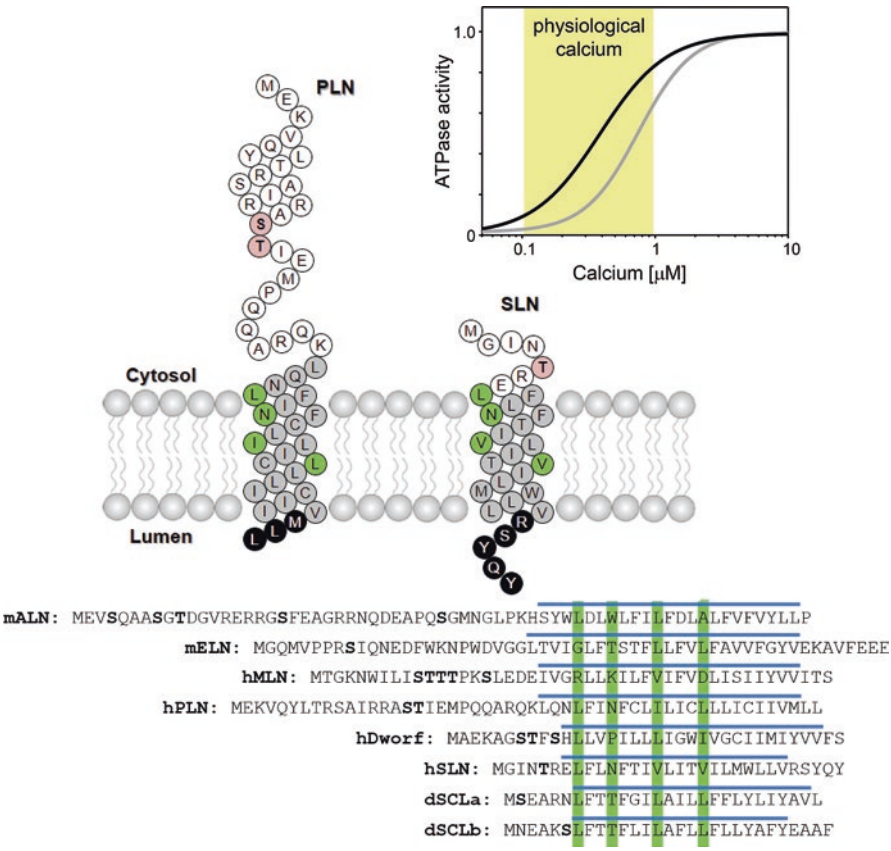


**Fig. 8.4** Primary structures and topology diagrams of SERCA regulatory subunits. Human phospholamban (PLN) and sarcolipin (SLN) are shown as topology diagrams with the cytosolic (white), transmembrane (grey) and luminal (black) domains indicated. Residues in PLN and SLN transmembrane domains that are essential for function are colored green. Inset is a typical curve for calcium-dependent SERCA ATPase activity in the absence (black line) and presence (grey line) of PLN. Also shown is a sequence alignment of mouse another-regulin (mALN), mouse endoregulin (mELN), human myoregulin (hMLN), human PLN (hPLN), human DWORF (hDWORF), human SLN (hSLN), and drosophila sarcolamban a and b isoforms (dSCLa & dSCLb). Our alignment is based on the essential residues in PLN and SLN and maximum superposition of the transmembrane domains (blue bars). It is interesting that the SERCA activator DWORF has a proline instead of the essential asparagine found in PLN ($Asn^{34}$) and SLN ($Asn^{11}$)

kinase A (PKA) regulates cardiac contractility by phosphorylating $Ser^{16}$ in the N-terminal domain of PLN. In cardiac and smooth muscle, PLN is a reversible, calcium-dependent inhibitor of SERCA, which modulates cardiac contractility in response to physiological cues (Kirchberger et al. 1975; Simmerman et al. 1986b; MacLennan and Kranias 2003; Luo et al. 1994). SERCA inhibition by PLN is a dynamic process that depends on the cytosolic calcium concentration, the phosphorylation state of PLN, and the oligomeric state of PLN (Simmerman et al.

1986b). First, PLN physically interacts with and inhibits SERCA at sub-micromolar calcium concentrations, and this is reversed by micromolar calcium concentrations (Asahi et al. 2000). Maximal SERCA inhibition occurs within the physiological window of cytosolic calcium (0.1–1.0 μM). Second, the inhibition is relieved by phosphorylation of PLN in a mechanism that is linked to β-adrenergic stimulation and PKA (Tada et al. 1976a, 1983). Third, PLN forms a homopentamer which is in dynamic equilibrium with the inhibitory monomer (Cornea et al. 1997). The pentamer has been described as an inactive storage form of PLN, though it is required for physiological function (Chu et al. 1998) and it also interacts with SERCA (Glaves et al. 2011; Stokes et al. 2006). The synergistic effect of these various regulatory mechanisms is a modulation of SR calcium stores and cardiac contractility that can be finely tuned in response to activity, stress, or disease.

A primary mechanism for modulating SR calcium stores is through catecholamines, which act through the β-adrenergic pathway to activate PKA and phosphorylate several cardiac proteins (Fig. 8.5). The goal of this pathway is to modulate cardiac output by targeting the contractile apparatus and calcium-handling proteins. Phosphorylation of PLN by PKA has a major impact on cardiac contractility via a mechanism that reverses the inhibitory properties of PLN and increases the apparent calcium affinity of SERCA (Tada et al. 1976b). Monomeric PLN inhibits SERCA and phosphorylation of PLN is believed to cause dissociation from SERCA and oligomerization of PLN into storage pentamers (Stokes 1997b; Kimura et al. 1997a; Cornea et al. 1997). PLN has two adjacent phosphorylation sites – it is phosphorylated at $Ser^{16}$ by PKA (Tada et al. 1974) and at $Thr^{17}$ by $Ca^{2+}$/calmodulin-dependent protein kinase II (Tada et al. 1983) and Akt (Catalucci et al. 2009). Separately, or in combination, phosphorylation at these sites is important for proper cardiac function (Bartel et al. 2000). It is not well defined as to whether these sites are phosphorylated independently and have separate effects on the inhibition of SERCA or are phosphorylated concurrently and have a synergistic effect on inhibition. There is some consensus that the main mode of regulation is through PKA and $Ser^{16}$, while $Thr^{17}$ provides a means for tuning or terminating the response depending on physiological or pathophysiological conditions (Mattiazzi and Kranias 2014). Nonetheless, the intricacies of PLN inhibition of SERCA are of great clinical relevance in terms of cardiac health, where disruptions to the calcium cycle in the heart lead to contractile dysfunction, cardiac hypertrophy, and dilated cardiomyopathy (Haghighi et al. 2003; Landstrom et al. 2011; Schmitt et al. 2003, 2009; DeWitt et al. 2006; Haghighi et al. 2006).

Functionally, PLN inhibition is measured as an effect on the apparent calcium affinity of SERCA, with the main target being the SERCA2a isoform. However, PLN also inhibits SERCA1a and SERCA2b, but not SERCA3 (Toyofuko et al. 1994). SERCA inhibition is primarily encoded by the transmembrane domain of PLN (~80% of inhibition; Trieber et al. 2009), while the linker region mitigates the inhibitory interaction, and the N-terminal helix allows for reversibility of inhibition via phosphorylation (and ~20% of the inhibitory activity). The transmembrane domain of PLN contains the structural determinants for SERCA inhibition (e.g.

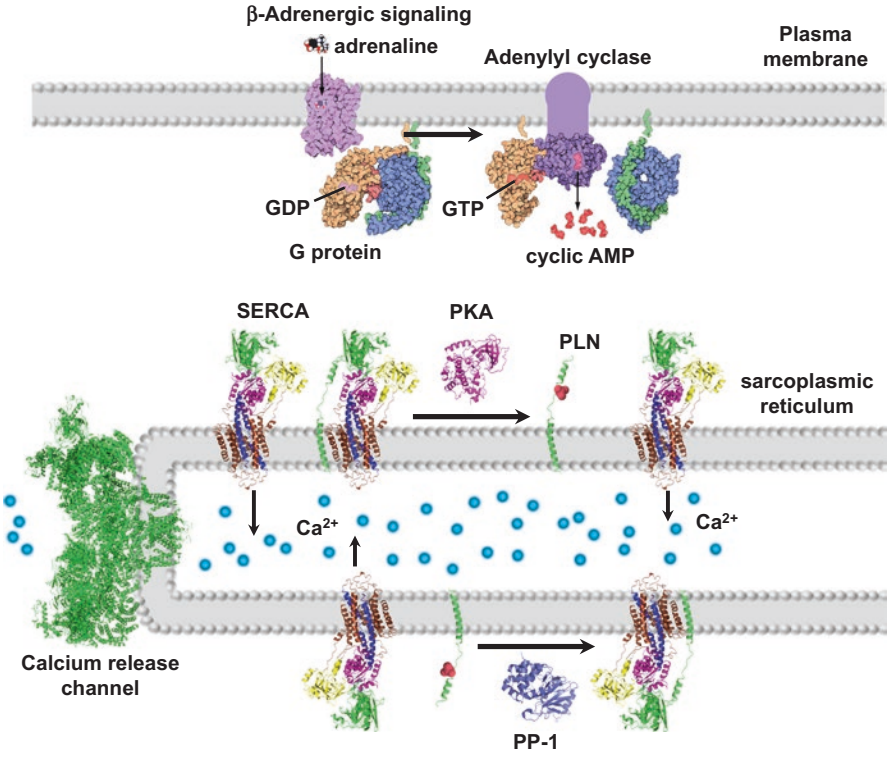


**Fig. 8.5 Schematic representation of SERCA-dependent calcium homeostasis in cardiac muscle.** The β-adrenergic signaling pathway is activated by catecholamines, which in turn increases cyclic AMP levels via activation of a G-protein and adenylyl cyclase. The cyclic AMP binds to the regulatory subunit of protein kinase A (PKA), which activates the catalytic subunit. The catalytic subunit of PKA phosphorylates phospholamban (PLN) and relieves SERCA inhibition. A protein phosphatase (PP-1) can dephosphorylate PLN and restore SERCA inhibition. The calcium release channel is responsible for the large increase in cytosolic calcium that triggers muscle contraction, and SERCA recovers the calcium into the lumen of the sarcoplasmic reticulum (SR) and triggers muscle relaxation. A comparatively large pool of SERCA and PLN molecules allow for dynamic modulation of cardiac muscle relaxation and SR calcium load for subsequent contractions. This is one of the mechanisms that facilitates dynamic contractility of the heart during rest, stress and exercise. The adrenergic signaling illustrations are courtesy of David S. Goodsell and the RCSB PDB, Molecules of the Month (http://pdb101.rcsb.org/motm/58)

Leu$^{31}$ & Asn$^{34}$) and structural determinants that are responsible for homopentamer formation (Leu-Ile zipper motif; e.g. Leu$^{37}$ & Ile$^{40}$) (Kimura et al. 1997b; Autry and Jones 1997). The monomeric form of PLN is sufficient for SERCA inhibition, though the recent crystal structures demonstrate that the interaction site could also accommodate an oligomeric form of PLN (Akin et al. 2013). By default, the PLN pentamer has been described as an inactive storage form, though there has been no direct demonstration of the functional capacity of oligomeric forms of PLN. It is clear that the pentameric form of PLN is required for cardiac contractility (Chu

et al. 1998). In addition, there is evidence that the PLN pentamer interacts with SERCA at an accessory site (M3) distinct from the inhibitory site (M2, M6 & M9) (Glaves et al. 2011; Stokes et al. 2006), and there is evidence that the PLN pentamer may form a cation selective channel (Kovacs et al. 1988; Smeazzetto et al. 2011, 2013).

The linker region of PLN (residues ~21–30) modulates the interaction of PLN's transmembrane domain with SERCA through charge repulsion. Residues such as $Arg^{25}$ and $Lys^{27}$ of PLN are proximal to residues such as $Arg^{324}$ and $Lys^{328}$ of SERCA. These adjacent charges are thought to "tune" the interaction of the transmembrane domain to achieve modest SERCA inhibition over a precise, physiological range of calcium concentrations. Furthermore, this linker region must transmit the reversal of inhibition from the N-terminal domain ($Ser^{16}$ & $Thr^{17}$) to the transmembrane domain (residues ~31–52). As stated above, PLN is phosphorylated at $Ser^{16}$ via the β-adrenergic pathway as a direct result of sympathetic nervous system activation. PKA targets $Ser^{16}$ through the consensus recognition motif of $Arg^{13}$-Arg-Ala-$Ser^{16}$ (Simmerman et al. 1986a). Once phosphorylated, $Ser^{16}$ may form salt bridges with $Arg^{13}$ and/or $Arg^{14}$, thereby distorting the N-terminal helix of PLN and relieving SERCA inhibition (Sugita et al. 2006). Phosphorylation alters the conformational dynamics of PLN's cytoplasmic domain and the interaction with SERCA (Gustavsson et al. 2013; Karim et al. 2006). PKA can target and phosphorylate PLN monomers bound to SERCA. In this context, PKA recognition of PLN is the first step in the reversal of SERCA inhibition and phosphorylation of $Ser^{16}$ serves to maintain the non-inhibitory state. PKA can also target PLN monomers in the context of the PLN pentamer (Ceholski et al. 2012a; Wittmann et al. 2015) and shift the dynamic monomer-pentamer equilibrium toward the PLN pentamer (Cornea et al. 1997). The PKA recognition motif is absolutely required for this to occur, though there are additional, unique structural determinants that allow PKA to recognize SERCA-bound PLN ($Arg^{9}$ & $Ser^{10}$) and the PLN pentamer ($Arg^{9}$) (Ceholski et al. 2012a). There is ongoing debate whether phosphorylation causes the PLN monomer to dissociate from SERCA following phosphorylation, though we consider PLN to be a subunit of SERCA. Instead, conformational changes in the N-terminal domain of PLN are transmitted to the transmembrane domain, which allows calcium translocation to occur without PLN dissociation from SERCA. We acknowledge that it may be advantageous, under physiological conditions such as exercise or stress, to fully dissociate the SERCA-PLN complex for maximal SERCA turnover.

The residues of PLN that directly associate with the catalytic subunit of PKA span from approximately $Lys^{3}$ to $Ile^{18}$. In addition to the canonical recognition motif, PKA has a preference for upstream positively-charged residues and downstream hydrophobic residues. $Arg^{9}$ and $Ile^{18}$ of PLN fit these criteria, though not much attention has yet been focused on $Ile^{18}$. Extensive mutagenesis of $Arg^{9}$ in PLN revealed that PKA has a strong preference for this residue, particularly in the pentameric state. In the peptide binding groove of PKA, $Arg^{9}$ of PLN packs against $Glu^{203}$ and $Asp^{241}$ of PKA, and this has a strong influence on substrate recognition. PKA recognizes substrates by conformational selection (Masterson et al. 2010), and the

most efficient substrates are peptides in solution because of their conformational dynamics (e.g. Kemp et al. 1975). Indeed, PKA-mediated phosphorylation is most efficient for a peptide corresponding to the cytoplasmic domain of PLN. By comparison, phosphorylation is less efficient for monomeric, full-length PLN, and far less efficient for the PLN pentamer or the SERCA-PLN complex. $Arg^{9}$, as well as $Ser^{10}$, and $Ile^{18}$, assist in the recognition of PLN when its conformational dynamics are more constrained (i.e. PLN pentamer or SERCA-PLN complex). $Arg^{9}$ is so important for PLN function and β-adrenergic signaling that human mutations at this locus ($Arg^{9}$-to-Cys & $Arg^{9}$-to-Leu) give rise to lethal, hereditary dilated cardiomyopathy. These mutations abrogate PLN function and create a kinetic trap for PKA, sequestering it from phosphorylating other cellular targets (Schmitt et al. 2003; Ceholski et al. 2012a, b).

Perhaps equally important to phosphorylation of PLN by PKA is the dephosphorylation by Protein Phosphatase-1 (PP-1), which reactivates PLN for SERCA inhibition (MacDougall et al. 1991; Steenaart et al. 1992). However, very little is known about the sequence determinants of PLN that govern its dephosphorylation. In addition, it remains uncertain as to which isoform of PP-1 dephosphorylates PLN in the myocardium. PP-1β is the major isoform that co-localizes with the SERCA-PLN complex in cardiomyocytes, though PP-1α and PP-1γ can also dephosphorylate PLN. PP-2 has also been reported to dephosphorylate PLN (MacDougall et al. 1991). Regardless of which isoform is responsible for dephosphorylation of PLN in human myocardium, it is well-known that PP-1 activity has significant control over SERCA-PLN function and cardiac contractility. As another layer of complexity, these proteins form a regulatory complex at the level of the SR that includes SERCA, PLN, A kinase anchoring protein (AKAP18δ & γ), PKA (catalytic & regulatory subunits), PP-1, inhibitor-1 (I-1), small heat shock protein 20 (Hsp20), the HS-1 associated protein X-1 (HAX1), small ubiquitin-related modifier (SUMO-1), and phosphodiesterase (PDE4D, 3A). Furthermore, these interactions may involve oligomeric assemblies of both SERCA (Blackwell et al. 2016) and PLN (Glaves et al. 2011; Wittmann et al. 2015; Haghighi et al. 2014). Finally, one must keep in mind that the copy number of SERCA and PLN molecules far exceeds the calcium release channel. Thus, compared to calcium release, calcium recovery involves a large "pool" of SERCA pumps that can be differentially and dynamically activated or supressed depending on cardiac output.

### *8.4.2 Sarcolipin*

Historically, the SERCA regulator PLN received much attention because of its role in cardiac muscle and the potential link to human heart disease (this link was later confirmed; Schmitt et al. 2003; Haghighi et al. 2003). Comparatively, SLN received less attention because it was assumed to mirror PLN function in skeletal muscle and the potential human health implications were not obvious. However, with the recent identification of novel functions for SLN, attention has refocused on this important SERCA regulator. SLN is a 31 residue, mostly α-helical, integral membrane protein

(Fig. 8.4) that is the principle regulator of SERCA in skeletal and atrial muscle. SLN is structurally and functionally homologous to PLN and it is postulated to regulate SERCA in a similar manner (Odermatt et al. 1998). SLN contains a short, variable cytoplasmic domain (residues ~1–7), a transmembrane α-helix (residues ~8–26), and a short, highly-conserved luminal tail (residues 27–31). Like PLN, SLN alters the apparent calcium affinity of SERCA by binding in a groove formed by transmembrane helices M2, M6, and M9 (Fig. 8.6). Crystal structures of a SERCA-SLN complex reveal SLN binding to an E1-like state of SERCA (Winther et al. 2013; Toyoshima et al. 2013). However, despite the homology to PLN, there are substantial differences in the way that SLN regulates SERCA. Most of the inhibitory properties of SLN are encoded in its unique and highly conserved C-terminal tail ($Arg^{27}$-Ser-Tyr-Gln-$Tyr^{31}$ (Gorski et al. 2013)). Indeed, this C-terminal RSYQY sequence can be transferred to the C-terminus of a generic transmembrane helix, turning it into a SERCA inhibitor with SLN-like properties. In the SERCA-SLN crystal structures, the RSYQY sequence is helical and not in direct contact with SERCA, suggesting that it serves to position SLN in the inhibitory groove of SERCA for optimal inhibition. For instance, the arginine and tyrosine residues

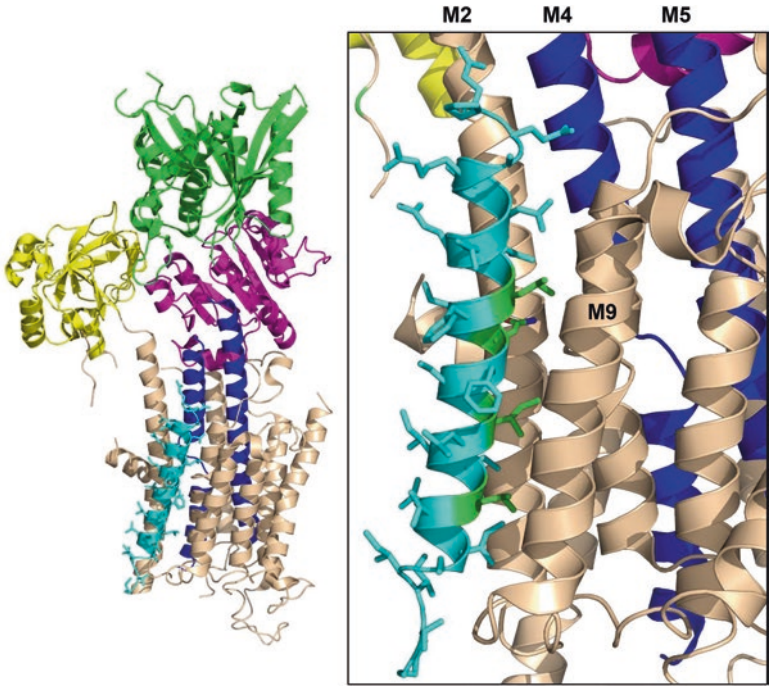


**Fig. 8.6 Structure of a SERCA-PLN complex where SERCA adopts an E1-like conformation.** The structure (PDB accession code 4y3u) is shown as a tan cartoon representation with the A-domain (yellow), N-domain (green), P-domain (magenta), and helices M4 and M5 (blue) indicated. PLN (cyan) lies in a groove between M2 and M6, and is shown with side chains. The four essential residues of PLN, $Leu^{31}$, $Asn^{34}$, $Ile^{38}$, and $Leu^{42}$ (green) line the interface with SERCA

could sit at the hydrocarbon core-water interface of the lipid bilayer, thereby positioning the transmembrane helix relative to SERCA. However, the RSYQY luminal tail is a distinct, essential and transferrable domain that contributes directly to SERCA inhibition (Gorski et al. 2013). Thus, it seems likely that the SERCA-SLN inhibitory complex involves contacts between the RSYQY luminal tail of SLN and the luminal loops and calcium-exit channel of SERCA.

In addition to altering the apparent calcium affinity of SERCA ($K_{Ca}$), one of the signatures of SLN inhibition is a decrease in the maximal activity of SERCA ($V_{max}$) (Gorski et al. 2013; Sahoo et al. 2013). The opposite trend has been observed for PLN, which increases the maximal activity of SERCA at saturating calcium concentrations (Reddy et al. 2003; Ceholski et al. 2012b; Trieber et al. 2005, 2009). These trends have been consistently observed using a highly purified membrane reconstitution system (co-reconstituted proteoliposomes), though other reports in the literature suggest that SLN could either decrease (Hughes et al. 2007; Tupling et al. 2002; Babu et al. 2006) or increase (Odermatt et al. 1998) the $V_{max}$ of SERCA. Nonetheless, it is clear that SLN is a distinct regulatory subunit of the SERCA calcium pump, and this has culminated in the observation that SLN may also possess a unique physiological role in the regulation and maintenance of body temperature, a process termed thermogenesis. It has been reported that SLN promotes futile cycling of SERCA and increases the net balance of ATP consumption to calcium transport. The excess ATP hydrolysis contributes to heat production. Considering that skeletal muscle makes up ~40% of body mass, SERCA and SLN may be major contributors to non-shivering, muscle-based thermogenesis (Bal et al. 2012). In addition, the abundance of skeletal muscle, and the role of SLN, make it a potential contributor to metabolic demand and human disorders such as obesity, diabetes, and metabolic syndrome.

Finally, it seems obvious that there must be an elaborate regulatory axis that targets SERCA-SLN, similar to that described above for SERCA-PLN. This is particular true for atrial muscle, where SLN and PLN are both present in a potential ternary, super-inhibitory complex with SERCA (MacLennan et al. 2003). However, relatively little is known about SLN regulation. The N-terminus of SLN has a conserved threonine residue ($Thr^5$) that appears to be a target for phosphorylation. Two kinases have been reported to target SLN, calcium-calmodulin dependent protein kinase II (CaMKII) (Bhupathy et al. 2009) and serine/threonine kinase 16 (Gramolini et al. 2006). It is also clear that $Thr^5$ is important for normal SLN function and that phospho-mimetic mutations destroy function (Bhupathy et al. 2009), though the physiological mechanisms and consequences remain unknown. The cytoplasmic domain of SLN is the likely site for binding scaffolding proteins (AKAPs) and regulatory complex formation (kinases, phosphatases, etc.). However, this concept is obfuscated by the fact that the cytoplasmic domain of SLN is the most variable region and unique in humans. This sequence is MGINTRE in humans and MERSTQE in mice and many other mammals, and this contrasts sharply with the highly conserved cytoplasmic domain of SLN. Perhaps this variability reflects the relative role of SLN in different organisms and the requirement for thermogenesis, as well as skeletal and atrial muscle calcium homeostasis and contractility.

### *8.4.3 New Regulatory Peptides*

Of the P-type ATPases, the sodium pump ($Na^+$,$K^+$-ATPase) is the most extensively regulated by small auxiliary subunits. There are at least seven regulatory subunits in mammals that act as tissue-specific regulators of the sodium pump. When combined with the isoform diversity of the α and β subunits (recall that the sodium pump is an αβ heterodimer), there is an incredible level of combinatorial expression of the three subunits for tissue-specific ion homeostasis and regulation (4 α isoforms, 3 β isoforms and 7 regulatory subunits). These regulatory subunits belong to the FXYD family of small integral membrane proteins (Garty and Karlish 2006), which include well defined sequence elements including a signature FXYD motif. By comparison, the complexity of SERCA isoforms and regulatory subunits appeared to be much more limited (3 α isoforms and 2 regulatory subunits). However, the landscape of SERCA regulation has changed dramatically over the last few years with the discovery of several new subunits (Fig. 8.4).

#### 8.4.3.1 Sarcolamban

The first discovery began with the identification of small open reading frames (smORFs) in *Drosophila* that were annotated as a long noncoding RNA. They were found to encode two small integral membrane proteins (Magny et al. 2013) with some homology to PLN and SLN (thus, the name sarcolamban derived from sarcolipin & phospholamban). The two peptides were 28 and 29 amino acids in length (SCL, isoforms A & B) and they were found to regulate calcium homeostasis and contractility in the *Drosophila* heart. These peptides are conserved in species ranging from insects to humans, suggesting an early evolutionary origin for the regulation of calcium homeostasis in cardiac muscle. Like SLN, SCL has a short N-terminal, cytoplasmic domain (residues ~1–7) followed by a predicted transmembrane helix of ~20 amino acids (residues ~7–26). A few residues at the C-terminus may be non-helical, though they are distinct from the conserved RSYQY luminal domain of SLN. Both SCL isoforms contain a serine residue in their N-terminal domain, $Ser^2$ in isoform A and $Ser^6$ in isoform B, which raises the possibility of regulation by phosphorylation.

#### 8.4.3.2 Myoregulin

The convergence of techniques such as bioinformatics, transcriptomics, and proteomics eventually led to the identification of hundreds of putative coding smORFs in vertebrate long noncoding RNAs. Since these smORFs encode theoretical peptides of less than ~100 amino acids, they have been described as micropeptides within the microproteome. However, these peptides have been overlooked because of the large number of potential smORFs and the difficulty in determining if they

are truly expressed and functional. Anderson and colleagues analyzed a long non-coding RNA from skeletal muscle, which concealed a 46 amino acid transmembrane peptide that is expressed in skeletal muscle (Anderson et al. 2015). Termed myoregulin (MLN), the peptide resembles PLN and SLN in primary and secondary structural characteristics, and it alters the apparent calcium affinity of SERCA in a manner similar to PLN and SLN. Similar to PLN, MLN has a long N-terminal, cytoplasmic domain (residues ~1–20) followed by a predicted transmembrane helix of ~23 amino acids (residues ~21–43), and a few residues at the C-terminus that may be non-helical. To examine if MLN is functional in skeletal muscle, MLN knockout mice were generated. The mice exhibited enhanced skeletal muscle performance and increased SR calcium content, suggesting that MLN plays an important physiological role in these processes.

Despite these advances, we know very little about MLN function and regulation. MLN shares several identical residues to the transmembrane domain of PLN and SLN (Fig. 8.4) and likely occupies the same inhibitory cleft of SERCA formed by transmembrane segments M2, M6 and M9 (Fig. 8.6). This is not an unreasonable assumption, as SERCA exhibits low selectivity and interacts with a wide range of hydrophobic peptides in this binding groove (Afara et al. 2008; Afara et al. 2006; Gorski et al. 2013). Alanine mutagenesis of key residues shared by MLN, PLN and SLN ($Leu^{29}$, $Phe^{30}$, $Leu^{33}$) were reported to ablate MLN inhibition in myoblasts, suggesting that the role of hydrophobic residues in SERCA inhibition is very similar. However, there is no data on the propensity of MLN to form oligomers as has been seen for PLN and SLN. In addition, we lack information on MLN regulation, which is likely to play a role in the modulation of SERCA-dependent calcium homeostasis in skeletal muscle contractility. Given the more extensive expression pattern of MLN in skeletal muscle relative to SLN (at least in mice), MLN may be the main regulator of SERCA-dependent skeletal muscle performance. Furthermore, if MLN is more prevalent than SLN, how does this impact our understanding of SERCA and SLN in non-shivering thermogenesis? What are the relative expression levels of these two regulators, and do they interact with each other or form a ternary complex with SERCA? Nonetheless, the discovery of MLN has opened a remarkable new window into skeletal muscle contractility and athletic performance.

#### 8.4.3.3 DWORF

With the discovery of sarcolamban and MLN, it seemed likely that additional long non-coding RNAs could encode small proteins. A bioinformatics approach based on this reasoning uncovered a smORF within a muscle-specific transcript, which was called dwarf open reading frame (*DWORF*) (Nelson et al. 2016). *DWORF* turned out to encode a 35 amino acid transmembrane peptide and regulator of SERCA, which is expressed in the heart and slow-twitch skeletal muscle (i.e. soleus and diaphragm). DWORF was found to co-localize with SERCA in SR membranes, where it interacts with SERCA and displaces endogenous inhibitors such as PLN. In mice, overexpression of DWORF in cardiomyocytes increased SR calcium content

and peak calcium transients, suggesting that SERCA is more active in the presence of DWORF. In the absence of DWORF, slow-twitch muscle exhibited reduced SERCA activity, though delayed relaxation kinetics were only observed under maximal force load. These characteristics are consistent with a SERCA activator that counter-balances PLN in ventricular muscle, a remarkable new concept in the regulation of cardiac contractility. DWORF is the only small peptide known to increase SERCA activity, and this is in stark contrast to the super-inhibitory combinatorial effect that occurs when SERCA is exposed to both PLN and SLN (MacLennan et al. 2003). Thus, PLN and DWORF may represent a novel "yin and yang" of calcium transport regulation in cardiac muscle. If this is correct, there must be an elaborate regulatory system for the rheostatic balance of the PLN-inhibited and DWORF-dysinhibited states of SERCA. Similar to SLN, DWORF has a short N-terminal cytoplasmic domain (residues ~1–10) followed by a predicted transmembrane helix of ~22 amino acids (residues ~11–32), and a few residues at the C-terminus that may be non-helical. While DWORF regulation remains completely unknown, there are three potential sites for phosphorylation in the cytoplasmic domain ($Ser^6$, $Thr^7$ & $Ser^8$), which may be targets of the AGC kinase group (GPS 2.0 (Xue et al. 2008)).

DWORF is an endogenous peptide activator of SERCA; however, all other known SERCA regulators are inhibitors, meaning that they lower the apparent calcium affinity of SERCA. The one exception is SERCA2b, where the luminal tail increases the affinity of this isoform for calcium. This luminal tail is a C-terminal splice variant and extension of SERCA2a that adds an 11th transmembrane helix and places the C-terminus of the SERCA2b in the SR lumen. The SERCA2b tail (M11) does not appear to interact with the canonical inhibitory site (M2, M6 & M9), but instead interacts with M7 and M10 of SERCA (Vandecaetsbeek et al. 2009). This latter site is equivalent to the interaction of the β-subunit transmembrane helix with the sodium pump. Importantly, the SERCA 2b tail is a genuine activator of SERCA in that it increases the affinity of the pump for calcium. In contrast, DWORF appears to bind to the inhibitory groove of SERCA, but it does not directly activate calcium transport. Instead it displaces PLN (or SLN, MLN) and thereby frees SERCA from PLN-mediated inhibition (Nelson et al. 2016). There are human mutations in PLN that display this same behavior (e.g. $Arg^9$-to-Cys). This particular mutant is a loss-of-function form of PLN that preferentially interacts with SERCA and prevents binding of wild-type PLN (under heterozygous conditions) (Ceholski et al. 2012b). Thus, it is possible to interact with the inhibitory groove without inhibiting SERCA, though it may not be possible to truly activate SERCA (increase its calcium affinity) from this site.

#### 8.4.3.4 And Another, and Another …

Perhaps because PLN and SLN were already known, knowledge of their sequences aided the discovery of other muscle-specific micropeptides (e.g. MLN, DWORF). However, multiple SERCA isoforms are present in all cell and tissue types, and they play a role in a vast array of signaling pathways and physiological processes. On the

one hand, it is not unreasonable to assume that SERCA regulatory peptides exist in other tissue and cell types, with a similar complexity as has been found in muscle. On the other hand, some of this complexity is already fulfilled by the SERCA2b isoform, which is the ubiquitous ER calcium pump with a unique luminal tail that may provide a point for regulation. This dilemma was recently resolved with the identification of two new transmembrane peptides – endoregulin (ELN) and another-regulin (ALN) – that regulate SERCA in non-muscle cell types (Anderson et al. 2016). ELN is a 56 amino acid peptide and ALN is a 65 amino acid peptide, which makes them larger members of the family of SERCA regulators (Fig. 8.4). Both have topologies similar to PLN and MLN, with C-terminal transmembrane helices that reside in ER membranes and physically interact with and inhibit SERCA. ALN has a long N-terminal cytoplasmic domain (residues ~1–41) followed by a predicted transmembrane helix of ~23 amino acids (residues ~42–64), and a C-terminal proline residue ($Pro^{65}$). ELN has a shorter N-terminal cytoplasmic domain (residues ~1–24) followed by a predicted transmembrane helix of ~23 amino acids (residues ~25–47), and a charged C-terminus with one lysine and five glutamate residues (residues ~48–56).

Comparing the expression patterns of the different SERCA isoforms and micropeptides, there is a striking level of overlap for some combinations (Anderson et al. 2016). The SERCA1a isoform and MLN appear to be co-expressed in skeletal muscles and absent in most other tissues. Similarly, the ubiquitous expression pattern of the SERCA2b isoform is mirrored by ALN, and the endothelial and epithelial expression pattern of SERCA3 isoforms is mirrored by ELN. By comparison, the expression patterns of SERCA2a, PLN, and SLN are much more restricted to heart muscle (PLN in ventricular and atrial muscle; SLN in atrial muscle). If this is correct, the best known SERCA regulators PLN and SLN may be the most restricted in tissue distribution and perhaps function, while the newly identified family of regulators may provide the bulk of SERCA regulation in all other tissues. Of course, it will be important to delineate these expression profiles in humans compared to mice.

## 8.5 Future Directions

There are a large number of structures available for SERCA in the Protein Data Bank (63 at present), and our current understanding of SERCA, PLN, and SLN structure and function is quite detailed. Indeed, one might consider the field mature and further advances incremental (at least, that is what the peer reviewers keep telling us). However, this is contrasted sharply by the discovery of novel SERCA structural intermediates (Winther et al. 2013; Toyoshima et al. 2013; Akin et al. 2013) and the dramatic expansion of SERCA regulatory subunits in both muscle and non-muscle tissues (Nelson et al. 2016; Anderson et al. 2015, 2016; Magny et al. 2013). As it turns out, we know very little about the regulatory networks that control SERCA-dependent calcium homeostasis, and they appear to be quite elaborate. For instance, if PLN is a reversible inhibitor that dissociates from SERCA, why do we

need DWORF to displace PLN and activate SERCA? How is this process regulated by the signaling pathways that modulate cardiac output?

That said, we look forward to (at least) three major areas of discovery in the coming years. The first is the regulatory networks that control calcium homeostasis in muscle and nonmuscle cells. Considering that there are multiple SERCA isoforms in most cell types, and now multiple SERCA regulatory subunits in some tissues, there must be an elaborate regulatory network and spatio-temporal control mechanism for fine-tuning calcium handling. After all, in muscle alone, calcium is a known regulator of many physiological processes including contraction, energy metabolism, cell death and survival, organelle function, amongst others. It is important to understand these regulatory networks because aberrant calcium homeostasis is a salient feature of human heart failure. The second area of discovery is the regulation of other P-type ATPases by small accessory subunits. Some are already known such as the SERCA regulatory subunits described above and the sodium pump FXYD proteins. Other examples might include regulatory domains encoded in the linear sequences such as SERCA2b and the plasma membrane calcium pumps. We postulate that small integral-membrane regulatory subunits may be a more common feature of the P-type ATPase superfamily than currently appreciated. Consider that humans encode fourteen type IV P-type ATPases (P4-ATPases) that act as phospholipid flippases and maintain lipid asymmetry in a variety of membranes. In turn, lipid asymmetry plays a role in endocytosis and exocytosis, cell motility, apoptosis, lipid and energy homeostasis, amongst many other vital physiological processes. Are the other P-type ATPases, such as these P4-ATPases and the heavy metal P1-ATPases, also regulated by a cadre of accessory subunits? Finally, the third major area of discovery is the identification of hundreds of potential coding smORFs in vertebrate long noncoding RNAs. As stated above, these smORFs encode theoretical peptides of less than ~100 amino acids. How extensive is the microproteome and what are the hitherto unknown physiological targets? We postulate that there is an extensive microproteome that regulates transporters, channels, and signaling pathways in a tissue-specific and spatio-temporal manner. However, our current understanding of this microproteome (Magny et al. 2013; Anderson et al. 2015; Anderson et al. 2016; Nelson et al. 2016) may be akin to the early discoveries of microRNAs (Lee et al. 1993; Wightman et al. 1993).

## References

Afara MR, Trieber CA, Glaves JP, Young HS (2006) Rational design of peptide inhibitors of the sarcoplasmic reticulum calcium pump. Biochemistry 45(28):8617–8627. https://doi.org/10.1021/bi0523761

Afara MR, Trieber CA, Ceholski DK, Young HS (2008) Peptide inhibitors use two related mechanisms to alter the apparent calcium affinity of the sarcoplasmic reticulum calcium pump. Biochemistry 47(36):9522–9530. https://doi.org/10.1021/bi800880q

Akin BL, Hurley TD, Chen Z, Jones LR (2013) The structural basis for phospholamban inhibition of the calcium pump in sarcoplasmic reticulum. J Biol Chem. https://doi.org/10.1074/jbc.M113.501585

Anderson DM, Anderson KM, Chang CL, Makarewich CA, Nelson BR, McAnally JR, Kasaragod P, Shelton JM, Liou J, Bassel-Duby R, Olson EN (2015) A micropeptide encoded by a putative long noncoding RNA regulates muscle performance. Cell. https://doi.org/10.1016/j.cell.2015.01.009

Anderson DM, Makarewich CA, Anderson KM, Shelton JM, Bezprozvannaya S, Bassel-Duby R, Olson EN (2016) Widespread control of calcium signaling by a family of SERCA-inhibiting micropeptides. Sci Signal 9(457):ra119. https://doi.org/10.1126/scisignal.aaj1460

Asahi M, McKenna E, Kurzydlowski K, Tada M, MacLennan D (2000) Physical interactions between phospholamban and sarco(endo)plasmic reticulum $Ca^{2+}$-ATPases are dissociated by elevated $Ca^{2+}$, but not by phospholamban phosphorylation, vanadate, or thapsigargin, and are enhanced by ATP. J Biol Chem 275:15034–15038

Autry J, Jones L (1997) Functional co-expression of the canine cardiac $Ca^{2+}$ pump and phospholamban in Spodoptera frugiperda (Sf21) cells reveals new insights on ATPase regulation. J Biol Chem 272:15872–15880

Babu GJ, Bhupathy P, Petrashevskaya NN, Wang H, Raman S, Wheeler D, Jagatheesan G, Wieczorek D, Schwartz A, Janssen PM, Ziolo MT, Periasamy M (2006) Targeted overexpression of sarcolipin in the mouse heart decreases sarcoplasmic reticulum calcium transport and cardiac contractility. J Biol Chem 281(7):3972–3979. doi:M508998200 [pii] 10.1074/jbc.M508998200

Bal NC, Maurya SK, Sopariwala DH, Sahoo SK, Gupta SC, Shaikh SA, Pant M, Rowland LA, Goonasekera SA, Molkentin JD, Periasamy M (2012) Sarcolipin is a newly identified regulator of muscle-based thermogenesis in mammals. Nat Med 18(10):1575–1579. https://doi.org/10.1038/nm.2897

Bartel S, Vetter D, Schlegel WP, Wallukat G, Krause EG, Karczewski P (2000) Phosphorylation of phospholamban at threonine-17 in the absence and presence of beta-adrenergic stimulation in neonatal rat cardiomyocytes. J Mol Cell Cardiol 32(12):2173–2185. doi:10.1006/jmcc.2000.1243 [doi] S0022-2828(00)91243-4 [pii]

Berridge MJ, Bootman MD, Roderick HL (2003) Calcium signalling: dynamics, homeostasis and remodelling. Nat Rev Mol Cell Biol 4(7):517–529. https://doi.org/10.1038/nrm1155

Bers DM (2008) Calcium cycling and signaling in cardiac myocytes. Annu Rev Physiol 70:23–49. https://doi.org/10.1146/annurev.physiol.70.113006.100455

Bhupathy P, Babu GJ, Ito M, Periasamy M (2009) Threonine-5 at the N-terminus can modulate sarcolipin function in cardiac myocytes. J Mol Cell Cardiol 47 (5):723-729. doi:S0022-2828(09)00307-1 [pii] 10.1016/j.yjmcc.2009.07.014

Blackwell DJ, Zak TJ, Robia SL (2016) Cardiac calcium ATPase dimerization measured by cross-linking and fluorescence energy transfer. Biophys J 111(6):1192–1202. https://doi.org/10.1016/j.bpj.2016.08.005

Brini M, Cali T, Ottolini D, Carafoli E (2012) Calcium pumps: why so many? Compr Physiol 2(2):1045–1060. https://doi.org/10.1002/cphy.c110034

Carafoli E, Krebs J (2016) Why calcium? How calcium became the best communicator. J Biol Chem 291(40):20849–20857. https://doi.org/10.1074/jbc.R116.735894

Catalucci D, Latronico MV, Ceci M, Rusconi F, Young HS, Gallo P, Santonastasi M, Bellacosa A, Brown JH, Condorelli G (2009) Akt increases sarcoplasmic reticulum Ca2+ cycling by direct phosphorylation of phospholamban at Thr17. J Biol Chem 284(41):28180–28187. https://doi.org/10.1074/jbc.M109.036566

Ceholski DK, Trieber CA, Holmes CF, Young HS (2012a) Lethal, hereditary mutants of phospholamban elude phosphorylation by protein kinase A. J Biol Chem 287(32):26596–26605. https://doi.org/10.1074/jbc.M112.382713

Ceholski DK, Trieber CA, Young HS (2012b) Hydrophobic imbalance in the cytoplasmic domain of phospholamban is a determinant for lethal dilated cardiomyopathy. J Biol Chem 287(20):16521–16529. https://doi.org/10.1074/jbc.M112.360859

Chemaly E, Bobe R, Adnot S, Hajjar R, Lipskaia L (2013) Sarco (Endo) plasmic reticulum calcium atpases (SERCA) isoforms in the normal and diseased cardiac, vascular and skeletal muscle. J Cardiovasc Dis Diagn 1(3):112

Chu G, Li L, Sato Y, Harrer JM, Kadambi VJ, Hoit BD, Bers DM, Kranias EG (1998) Pentameric assembly of phospholamban facilitates inhibition of cardiac function in vivo. J Biol Chem 273(50):33674–33680

Cornea RL, Jones LR, Autry JM, Thomas DD (1997) Mutation and phosphorylation change the oligomeric structure of phospholamban in lipid bilayers. Biochemistry 36:2960–2967

Dally S, Corvazier E, Bredoux R, Bobe R, Enouf J (2010) Multiple and diverse coexpression, location, and regulation of additional SERCA2 and SERCA3 isoforms in nonfailing and failing human heart. J Mol Cell Cardiol 48(4):633–644. https://doi.org/10.1016/j.yjmcc.2009.11.012

de Meis L, Vianna AL (1979) Energy interconversion by the Ca2+-dependent ATPase of the sarcoplasmic reticulum. Annu Rev Biochem 48:275–292. https://doi.org/10.1146/annurev.bi.48.070179.001423

DeWitt MM, MacLeod HM, Soliven B, McNally EM (2006) Phospholamban R14 deletion results in late-onset, mild, hereditary dilated cardiomyopathy. J Am Coll Cardiol 48(7):1396–1398. doi:S0735-1097(06)01837-7 [pii] 10.1016/j.jacc.2006.07.016 [doi]

Doroudgar S, Glembotski CC (2013) New concepts of endoplasmic reticulum function in the heart: programmed to conserve. J Mol Cell Cardiol 55:85–91. https://doi.org/10.1016/j.yjmcc.2012.10.006

Garty H, Karlish SJ (2006) Role of FXYD proteins in ion transport. Annu Rev Physiol 68:431–459. https://doi.org/10.1146/annurev.physiol.68.040104.131852

Gelebart P, Martin V, Enouf J, Papp B (2003) Identification of a new SERCA2 splice variant regulated during monocytic differentiation. Biochem Biophys Res Commun 303(2):676–684

Glaves JP, Trieber CA, Ceholski DK, Stokes DL, Young HS (2011) Phosphorylation and mutation of phospholamban alter physical interactions with the sarcoplasmic reticulum calcium pump. J Mol Biol 405(3):707–723. https://doi.org/10.1016/j.jmb.2010.11.014

Gorski PA, Trieber CA, Lariviere E, Schuermans M, Wuytack F, Young HS, Vangheluwe P (2012) Transmembrane helix 11 is a genuine regulator of the endoplasmic reticulum Ca2+ pump and acts as a functional parallel of beta-subunit on alpha-Na+,K+-ATPase. J Biol Chem 287(24):19876–19885. https://doi.org/10.1074/jbc.M111.335620

Gorski PA, Glaves JP, Vangheluwe P, Young HS (2013) Sarco(endo)plasmic reticulum calcium ATPase (SERCA) inhibition by sarcolipin is encoded in its luminal tail. J Biol Chem 288(12):8456–8467. https://doi.org/10.1074/jbc.M112.446161

Gramolini AO, Trivieri MG, Oudit GY, Kislinger T, Li W, Patel MM, Emili A, Kranias EG, Backx PH, Maclennan DH (2006) Cardiac-specific overexpression of sarcolipin in phospholamban null mice impairs myocyte function that is restored by phosphorylation. Proc Natl Acad Sci U S A 103(7):2446–2451. doi:0510883103 [pii] 10.1073/pnas.0510883103 [doi]

Gustavsson M, Verardi R, Mullen DG, Mote KR, Traaseth NJ, Gopinath T, Veglia G (2013) Allosteric regulation of SERCA by phosphorylation-mediated conformational shift of phospholamban. Proc Natl Acad Sci U S A 110(43):17338–17343. https://doi.org/10.1073/pnas.1303006110

Haghighi K, Kolokathis F, Pater L, Lynch RA, Asahi M, Gramolini AO, Fan GC, Tsiapras D, Hahn HS, Adamopoulos S, Liggett SB, Dorn GW, 2nd, MacLennan DH, Kremastinos DT, Kranias EG (2003) Human phospholamban null results in lethal dilated cardiomyopathy revealing a critical difference between mouse and human. J Clin Invest 111 (6):869-876. https://doi.org/10.1172/JCI17892 [doi]

Haghighi K, Kolokathis F, Gramolini AO, Waggoner JR, Pater L, Lynch RA, Fan GC, Tsiapras D, Parekh RR, Dorn GW 2nd, MacLennan DH, Kremastinos DT, Kranias EG (2006) A mutation in the human phospholamban gene, deleting arginine 14, results in lethal, hereditary cardiomyopathy. Proc Natl Acad Sci U S A 103(5):1388–1393. doi:0510519103 [pii] 10.1073/pnas.0510519103 [doi]

Haghighi K, Bidwell P, Kranias EG (2014) Phospholamban interactome in cardiac contractility and survival: a new vision of an old friend. J Mol Cell Cardiol 77C:160–167. https://doi.org/10.1016/j.yjmcc.2014.10.005

Henderson IM, Starling AP, Wictome M, East JM, Lee AG (1994) Binding of Ca2+ to the (Ca(2+)-Mg2+)-ATPase of sarcoplasmic reticulum: kinetic studies. Biochem J 297(Pt 3):625–636

Hughes E, Clayton JC, Kitmitto A, Esmann M, Middleton DA (2007) Solid-state NMR and functional measurements indicate that the conserved tyrosine residues of sarcolipin are involved directly in the inhibition of SERCA1. J Biol Chem 282(36):26603–26613. https://doi.org/10.1074/jbc.M611668200

Karim CB, Zhang Z, Howard EC, Torgersen KD, Thomas DD (2006) Phosphorylation-dependent conformational switch in spin-labeled phospholamban bound to SERCA. J Mol Biol 358(4):1032–1040. doi:S0022-2836(06)00250-6 [pii] 10.1016/j.jmb.2006.02.051 [doi]

Katz AM (1998) Discovery of phospholamban. A personal history. Ann N Y Acad Sci 853:9–19

Kemp BE, Bylund DB, Huang TS, Krebs EG (1975) Substrate specificity of the cyclic AMP-dependent protein kinase. Proc Natl Acad Sci U S A 72(9):3448–3452

Kimura Y, Kurzydlowski K, Tada M, MacLennan DH (1997a) Phospholamban inhibitory function is activated by depolymerization. J Biol Chem 272(24):15061–15064

Kimura Y, Kurzydlowski K, Tada M, MacLennan DH (1997b) Phospholamban inhibitory function is enhanced by depolymerization. J Biol Chem 272:15061–15064

Kirchberber MA, Tada M, Katz AM (1975) Phospholamban: a regulatory protein of the cardiac sarcoplasmic reticulum. Recent Adv Stud Cardiac Struct Metab 5:103–115

Kirchberger M, Tada M, Katz A (1975) Phospholamban: a regulatory protein of the cardiac sarcoplasmic reticulum. Recent Adv Stud Cardiac Struct Metab 5:103–115

Kosa M, Brinyiczki K, van Damme P, Goemans N, Hancsak K, Mendler L, Zador E (2015) The neonatal sarcoplasmic reticulum $Ca^{2+}$-ATPase gives a clue to development and pathology in human muscles. J Muscle Res Cell Motil 36(2):195–203. https://doi.org/10.1007/s10974-014-9403-z

Kovacs RJ, Nelson MT, Simmerman HK, Jones LR (1988) Phospholamban forms $Ca^{2+}$-selective channels in lipid bilayers. J Biol Chem 263(34):18364–18368

Landstrom AP, Adekola BA, Bos JM, Ommen SR, Ackerman MJ (2011) PLN-encoded phospholamban mutation in a large cohort of hypertrophic cardiomyopathy cases: summary of the literature and implications for genetic testing. Am Heart J 161(1):165–171. doi:S0002-8703(10)00675-7 [pii] 10.1016/j.ahj.2010.08.001

Laursen M, Bublitz M, Moncoq K, Olesen C, Moeller JV, Young HS, Nissen P, Morth JP (2009) Cyclopiazonic acid is complexed to a divalent metal ion when bound to the sarcoplasmic reticulum Ca2+-ATPase. J Biol Chem 284:13513–13518. doi:C900031200 [pii]10.1074/jbc.C900031200 [doi]

Lee RC, Feinbaum RL, Ambros V (1993) The C. elegans heterochronic gene lin-4 encodes small RNAs with antisense complementarity to lin-14. Cell 75(5):843–854

Lipskaia L, Keuylian Z, Blirando K, Mougenot N, Jacquet A, Rouxel C, Sghairi H, Elaib Z, Blaise R, Adnot S, Hajjar RJ, Chemaly ER, Limon I, Bobe R (2014) Expression of sarco (endo) plasmic reticulum calcium ATPase (SERCA) system in normal mouse cardiovascular tissues, heart failure and atherosclerosis. Biochim Biophys Acta 1843(11):2705–2718. https://doi.org/10.1016/j.bbamcr.2014.08.002

Luo W, Grupp IL, Harrer J, Ponniah S, Grupp G, Duffy JJ, Doetschman T, Kranias EG (1994) Targeted ablation of the phospholamban gene is associated with markedly enhanced myocardial contractility and loss of beta-agonist stimulation. Circulation Res 75:401–409

MacDougall LK, Jones LR, Cohen P (1991) Identification of the major protein phosphatases in mammalian cardiac muscle which dephosphorylate phospholamban. Eur J Biochem 196(3):725–734

MacLennan D, Kranias E (2003) Phospholamban: a crucial regulator of cardiac contractility. Nat Rev Mol Cell Biol 4:566–577

MacLennan DH, Brandl CJ, Korczak B, Green NM (1985) Amino-acid sequence of a $Ca^{2+}$ + $Mg^{2+}$-dependent ATPase from rabbit muscle sarcoplasmic reticulum, deduced from its complementary DNA sequence. Nature 316:696–700

MacLennan DH, Asahi M, Tupling AR (2003) The regulation of SERCA-type pumps by phospholamban and sarcolipin. Ann NY Acad Sci 986:472–480

Magny EG, Pueyo JI, Pearl FM, Cespedes MA, Niven JE, Bishop SA, Couso JP (2013) Conserved regulation of cardiac calcium uptake by peptides encoded in small open reading frames. Science 341(6150):1116–1120. https://doi.org/10.1126/science.1238802

Masterson LR, Cheng C, Yu T, Tonelli M, Kornev A, Taylor SS, Veglia G (2010) Dynamics connect substrate recognition to catalysis in protein kinase A. Nat Chem Biol 6(11):821–828. doi:nchembio.452 [pii]10.1038/nchembio.452

Mattiazzi A, Kranias EG (2014) The role of CaMKII regulation of phospholamban activity in heart disease. Front Pharmacol 5:5. https://doi.org/10.3389/fphar.2014.00005

Moller JV, Olesen C, Winther AM, Nissen P (2010) The sarcoplasmic Ca2+-ATPase: design of a perfect chemi-osmotic pump. Q Rev Biophys 43(4):501–566. doi:S003358351000017X [pii] 10.1017/S003358351000017X

Moncoq K, Trieber C, Young H (2007) The molecular basis for cyclopiazonic acid inhibition of the sarcoplasmic reticulum calcium pump. J Biol Chem 282:9748–9757

Nelson BR, Makarewich CA, Anderson DM, Olson EN (2016) A peptide encoded by a transcript annotated as long noncoding RNA enhances SERCA activity in muscle. Science 351:271–275

Odermatt A, Becker S, Khanna VK, Kurzydlowski K, Leisner E, Pette D, MacLennan DH (1998) Sarcolipin regulates the activity of SERCA1, the fast-twitch skeletal muscle sarcoplasmic reticulum Ca -ATPase. J Biol Chem 273(20):12360–12369

Palmgren MG, Nissen P (2011) P-type ATPases. Annu Rev Biophys 40:243–266. https://doi.org/10.1146/annurev.biophys.093008.131331

Peinelt C, Apell HJ (2002) Kinetics of the Ca(2+), H(+), and Mg(2+) interaction with the ion-binding sites of the SR Ca-ATPase. Biophys J 82(1 Pt 1):170–181. https://doi.org/10.1016/S0006-3495(02)75384-8

Reddy LG, Jones LR, Pace RC, Stokes DL (1996) Purified, reconstituted cardiac $Ca^{2+}$-ATPase is regulated by phospholamban but not by direct phosphorylation with $Ca^{2+}$/calmodulin-dependent protein kinase. J Biol Chem 271:14964–14970

Reddy L, Cornea R, Winters D, McKenna E, Thomas D (2003) Defining the molecular components of calcium transport regulation in a reconstituted membrane system. Biochemistry 42:4585–4592

Sagara Y, Fernandez-Belda F, de Meis L, Inesi G (1992) Characterization of the inhibition of intracellular Ca transport ATPases by thapsigargin. J Biol Chem 267(18):12606–12613

Sahoo SK, Shaikh SA, Sopariwala DH, Bal NC, Periasamy M (2013) Sarcolipin protein interaction with sarco(endo)plasmic reticulum Ca2+ ATPase (SERCA) is distinct from phospholamban protein, and only sarcolipin can promote uncoupling of the SERCA pump. J Biol Chem 288(10):6881–6889. https://doi.org/10.1074/jbc.M112.436915

Schmitt JP, Kamisago M, Asahi M, Li GH, Ahmad F, Mende U, Kranias EG, MacLennan DH, Seidman JG, Seidman CE (2003) Dilated cardiomyopathy and heart failure caused by a mutation in phospholamban. Science 299(5611):1410–1413. doi:10.1126/science.1081578 [doi] 299/5611/1410 [pii]

Schmitt JP, Ahmad F, Lorenz K, Hein L, Schulz S, Asahi M, Maclennan DH, Seidman CE, Seidman JG, Lohse MJ (2009) Alterations of phospholamban function can exhibit cardiotoxic effects independent of excessive sarcoplasmic reticulum Ca2+-ATPase inhibition. Circulation 119(3):436–444. doi:CIRCULATIONAHA.108.783506 [pii] 10.1161/CIRCULATIONAHA.108.783506

Simmerman HK, Collins JH, Theibert JL, Wegener AD, Jones LR (1986a) Sequence analysis of phospholamban. Identification of phosphorylation sites and two major structural domains. J Biol Chem 261(28):13333–13341

Simmerman HKB, Collins JH, Theibert JL, Wegener AD, Jones LR (1986b) Sequence analysis of phospholamban: identification of phosphorylation sites and two major structural domains. J Biol Chem 261:13333–13341

Skou J (1957) The influence of some cations on an adenosine triphosphatase from peripheral nerves. Biochim Biophys Acta 23:394–401

Smeazzetto S, Schroder I, Thiel G, Moncelli MR (2011) Phospholamban generates cation selective ion channels. Phys Chem Chem Phys. https://doi.org/10.1039/c1cp20460b

Smeazzetto S, Saponaro A, Young HS, Moncelli MR, Thiel G (2013) Structure-function relation of phospholamban: modulation of channel activity as a potential regulator of SERCA activity. PLoS One 8(1):e52744. https://doi.org/10.1371/journal.pone.0052744

Sorensen T, Moller J, Nissen P (2004) Phosphoryl transfer and calcium ion occlusion in the calcium pump. Science 304:1672–1675

Steenaart NA, Ganim JR, Di Salvo J, Kranias EG (1992) The phospholamban phosphatase associated with cardiac sarcoplasmic reticulum is a type 1 enzyme. Arch Biochem Biophys 293(1):17–24

Stokes D (1997a) Keeping calcium in its place: $Ca^{2+}$-ATPase and phospholamban. Curr Opin Struct Biol 7:550–556

Stokes DL (1997b) Keeping calcium in its place: Ca(2+)-ATPase and phospholamban. Curr Opin Struct Biol 7(4):550–556. doi:S0959-440X(97)80121-2 [pii]

Stokes DL, Pomfret AJ, Rice WJ, Glaves JP, Young HS (2006) Interactions between $Ca^{2+}$-ATPase and the pentameric form of phospholamban in two-dimensional co-crystals. Biophys J 90(11):4213–4223. https://doi.org/10.1529/biophysj.105.079640

Sugita Y, Miyashita N, Yoda T, Ikeguchi M, Toyoshima C (2006) Structural changes in the cytoplasmic domain of phospholamban by phosphorylation at Ser16: a molecular dynamics study. Biochemistry 45(39):11752–11761. https://doi.org/10.1021/bi061071z

Tada M, Kirchberger MA, Repke DI, Katz AM (1974) The stimulation of calcium transport in cardiac sarcoplasmic reticulum by adenosine 3':5'-monophosphate-dependent protein kinase. J Biol Chem 249(19):6174–6180

Tada M, Kirchberger M, Katz A (1976a) Regulation of calcium transport in cardiac sarcoplasmic reticulum by cyclic AMP-dependent protein kinase. Recent Adv Stud Cardiac Struct Metab 9:225–239

Tada M, Kirchberger MA, Katz AM (1976b) Regulation of calcium transport in cardiac sarcoplasmic reticulum by cyclic AMP-dependent protein kinase. Recent Adv Stud Cardiac Struct Metab 9:225–239

Tada M, Inui M, Yamada M, Kadoma M, Kuzuya T, Abe H, Kakiuchi S (1983) Effects of phospholamban phosphorylation catalyzed by adenosine 3′:5′-monophosphate- and calmodulin-dependent protein kinases on calcium transport ATPase of cardiac sarcoplasmic reticulum. J Mol Cell Cardiol 15(5):335–346

Toustrup-Jensen MS, Holm R, Einholm AP, Schack VR, Morth JP, Nissen P, Andersen JP, Vilsen B (2009) The C terminus of Na+,K+-ATPase controls Na+ affinity on both sides of the membrane through Arg935. J Biol Chem 284(28):18715–18725. https://doi.org/10.1074/jbc.M109.015099

Toyofuko T, Kurzydlowski K, Tada M, MacLennan DH (1994) Amino acids Glu2 to Ile18 in the cytoplasmic domain of phospholamban are essential for functional association with the Ca-ATPase of sarcoplasmic reticulum. J Biol Chem 269:3088–3094

Toyoshima C (2008) Structural aspects of ion pumping by Ca2+-ATPase of sarcoplasmic reticulum. Arch Biochem Biophys 476(1):3–11. https://doi.org/10.1016/j.abb.2008.04.017

Toyoshima C (2009) How Ca2+-ATPase pumps ions across the sarcoplasmic reticulum membrane. Biochim Biophys Acta 1793(6):941–946. https://doi.org/10.1016/j.bbamcr.2008.10.008

Toyoshima C, Nakasako M, Nomura H, Ogawa H (2000) Crystal structure of the calcium pump of sarcoplasmic reticulum at 2.6 A resolution. Nature 405:647–655

Toyoshima C, Iwasawa S, Ogawa H, Hirata A, Tsueda J, Inesi G (2013) Crystal structures of the calcium pump and sarcolipin in the Mg2+-bound E1 state. Nature (London) 495(7440):260–264. https://doi.org/10.1038/nature11899

Trieber CA, Douglas JL, Afara M, Young HS (2005) The effects of mutation on the regulatory properties of phospholamban in co-reconstituted membranes. Biochemistry 44(9):3289–3297. https://doi.org/10.1021/bi047878d

Trieber CA, Afara M, Young HS (2009) Effects of phospholamban transmembrane mutants on the calcium affinity, maximal activity, and cooperativity of the sarcoplasmic reticulum calcium pump. Biochemistry 48(39):9287–9296. https://doi.org/10.1021/bi900852m

Tupling AR, Asahi M, MacLennan DH (2002) Sarcolipin overexpression in rat slow twitch muscle inhibits sarcoplasmic reticulum Ca2+ uptake and impairs contractile function. J Biol Chem 277(47):44740–44746. https://doi.org/10.1074/jbc.M206171200

Vandecaetsbeek I, Trekels M, De Maeyer M, Ceulemans H, Lescrinier E, Raeymaekers L, Wuytack F, Vangheluwe P (2009) Structural basis for the high Ca2+ affinity of the ubiquitous SERCA2b $Ca^{2+}$ pump. Proc Natl Acad Sci U S A 106(44):18533–18538. https://doi.org/10.1073/pnas.0906797106

Vangheluwe P, Raeymaekers L, Dode L, Wuytack F (2005) Modulating sarco(endo)plasmic reticulum Ca2+ ATPase 2 (SERCA2) activity: cell biological implications. Cell Calcium 38(3-4):291–302. https://doi.org/10.1016/j.ceca.2005.06.033

Wawrzynow A, Theibert JL, Murphy C, Jona I, Martonosi A, Collins JH (1992) Sarcolipin, the "proteolipid" of skeletal muscle sarcoplasmic reticulum, is a unique, amphipathic, 31-residue peptide. Arch Biochem Biophys 298(2):620–623

Wightman B, Ha I, Ruvkun G (1993) Posttranscriptional regulation of the heterochronic gene lin-14 by lin-4 mediates temporal pattern formation in C. elegans. Cell 75(5):855–862

Winther AM, Bublitz M, Karlsen JL, Moller JV, Hansen JB, Nissen P, Buch-Pedersen MJ (2013) The sarcolipin-bound calcium pump stabilizes calcium sites exposed to the cytoplasm. Nature (London) 495(7440):265–269. https://doi.org/10.1038/nature11900

Wittmann T, Lohse MJ, Schmitt JP (2015) Phospholamban pentamers attenuate PKA-dependent phosphorylation of monomers. J Mol Cell Cardiol 80:90–97. https://doi.org/10.1016/j.yjmcc.2014.12.020

Wuytack F, Raeymaekers L, Missiaen L (2002) Molecular physiology of the SERCA and SPCA pumps. Cell Calcium 32(5-6):279–305

Xue Y, Ren J, Gao X, Jin C, Wen L, Yao X (2008) GPS 2.0, a tool to predict kinase-specific phosphorylation sites in hierarchy. Mol Cell Proteomics 7(9):1598–1608. https://doi.org/10.1074/mcp.M700574-MCP200

# Chapter 9
# Organization of Plant Photosystem II and Photosystem I Supercomplexes


**Roman Kouřil, Lukáš Nosek, Dmitry Semchonok, Egbert J. Boekema, and Petr Ilík**

**Abstract** In nature, plants are continuously exposed to varying environmental conditions. They have developed a wide range of adaptive mechanisms, which ensure their survival and maintenance of stable photosynthetic performance. Photosynthesis is delicately regulated at the level of the thylakoid membrane of chloroplasts and the regulatory mechanisms include a reversible formation of a large variety of specific protein-protein complexes, supercomplexes or even larger assemblies known as megacomplexes. Revealing their structures is crucial for better understanding of their function and relevance in photosynthesis. Here we focus our attention on the isolation and a structural characterization of various large protein supercomplexes and megacomplexes, which involve Photosystem II and Photosystem I, the key constituents of photosynthetic apparatus. The photosystems are often attached to other protein complexes in thylakoid membranes such as light harvesting complexes, cytochrome $b_6f$ complex, and NAD(P)H dehydrogenase. Structural models of individual supercomplexes and megacomplexes provide essential details of their architecture, which allow us to discuss their function as well as physiological significance.

**Keywords** Photosystem I · Photosystem II · Clear native gel electrophoresis · Electron microscopy · Supercomplex · Megacomplex

R. Kouřil (✉) · L. Nosek · P. Ilík
Department of Biophysics, Faculty of Science, Centre of the Region Haná for Biotechnological and Agricultural Research, Palacký University, Olomouc, Czech Republic
e-mail: roman.kouril@upol.cz; lukas.nosek@upol.cz; petr.ilik@upol.cz

D. Semchonok · E. J. Boekema
Electron Microscopy Group, Groningen Biomolecular Sciences and Biotechnology Institute, University of Groningen, Groningen, The Netherlands
e-mail: d.o.semchonok@rug.nl; e.j.boekema@rug.nl



J. R. Harris, E. J. Boekema (eds.), *Membrane Protein Complexes: Structure and Function*, Subcellular Biochemistry 87,
https://doi.org/10.1007/978-981-10-7757-9_9

## 9.1 Introduction to Molecular Organization of Photosynthetic Apparatus

The apparatus responsible for primary photosynthetic reactions is embedded in the thylakoid membrane (Fig. 9.1). The membrane forms a flexible, three-dimensional network, in which regular stacks of thylakoids (grana) are interconnected by unstacked (stroma) thylakoids. Thylakoids enclose a single aqueous space – the thylakoid lumen, whereas the chloroplast space outside the thylakoids is called the stroma. Major components of the photosynthetic apparatus in thylakoids are integral membrane protein complexes Photosystem II (PSII) and Photosystem I (PSI), which form, together with other protein complexes, the core of the photosynthetic apparatus. PSI and PSII together with the light harvesting complex (LHC) and cytochrome $b_6f$ (Cyt$b_6f$) complex mediate linear electron transport across the thylakoid membrane leading to the reduction of $NADP^+$ to NADPH. Except of these four major complexes, there are also other protein components in the thylakoid membrane, such as the PROTON GRADIENT REGULATION 5 (PGR5) complex, PGR5-LIKE1 (PGRL1) complex and NAD(P)H dehydrogenase (NDH) complex, which mediate cyclic electron transport (Kramer et al. 2004; Munekage et al. 2004; Shikanai 2016). Both linear and cyclic electron transport pathway are coupled to the translocation of protons across the thylakoid membrane, which leads to the generation of a transmembrane ΔpH gradient utilized by ATP synthase to produce ATP (Albertsson 2001; Nelson and Yocum 2006).

In thylakoid membranes of plants, PSII and PSI are spatially separated. PSII complexes are preferentially embedded in the grana regions, although a minor fraction of the PSII complexes is present also in the stroma membranes in the form of monomers, where they participate in the PSII repair cycle (see e.g. Baena-Gonzalez and Aro 2002; Järvi et al. 2015). On the other hand, PSI complexes are confined exclusively to the stroma thylakoids and grana margins. The presence of PSI

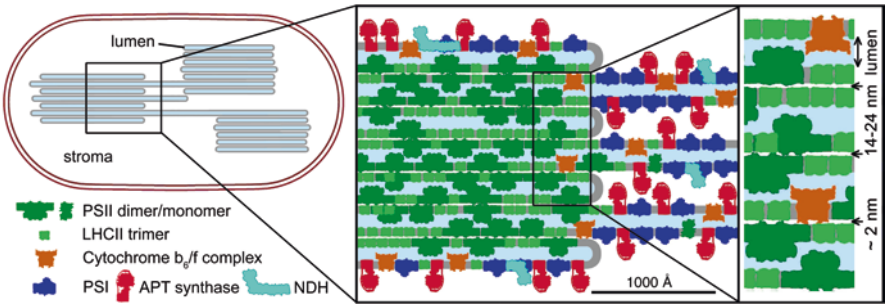


**Fig. 9.1** Model of the thylakoid membrane organization within the chloroplast. The model shows a chloroplast with three stacks of grana membranes, connected by stroma membranes. A cross-section of the granum shows a specific distribution of major components of photosynthetic apparatus such as Photosystem II, Photosystem I, cytochrome $b_6f$ complex, NDH dehydrogenase and ATP-synthase (Modified from Dekker and Boekema 2005)

extrinsic subunits, which face the stroma, precludes the entry of the PSI complexes into the grana stacks and similar limitation applies also to ATP synthase and NDH dehydrogenase. In the case of the Cyt$b_6f$ complex there is no such structural limitation and this complex is considered to be evenly distributed in the thylakoid membrane (Fig. 9.1) (Albertsson 2001; Dekker and Boekema 2005).

Organization of both PSII and PSI complexes shares a common motif, as both these complexes consist of two functional moieties – a core complex and a peripheral antenna system. The core complex contains the reaction center with all the cofactors necessary for photochemical reactions, whereas the peripheral antenna system optimizes and regulates the light harvesting capacity of the photosystems. The core complexes are highly conserved among prokaryotic and eukaryotic photosynthetic organisms, but the organization and composition of the light harvesting antenna system (LHCs) show a great variability.

The core complex of PSII is present as a homodimer. In land plants, this dimer is specifically associated with a variable number of monomeric and trimeric Lhcb antenna proteins (LHCII), forming together various types of large PSII-LHCII supercomplexes. The ability of PSII to control and regulate the antenna size and thus also the amount of absorbed light energy is extremely important for plants experiencing varying natural light conditions. The PSI core complex is present in the form of a monomer in the thylakoid membrane (Boekema et al. 2001; Kouřil et al. 2005a). However, isolated plant PSI complexes have been also found in larger oligomeric forms such as dimers, trimers and tetramers, which resemble trimeric and tetrameric forms of cyanobacterial PSI (Boekema et al. 1987; Semchonok et al. 2016). The native origin of plant PSI oligomers has not been clearly confirmed yet, therefore they are still considered to be artificial (Boekema et al. 2001, Kouřil et al. 2005a). The light harvesting capacity of the plant PSI core complex is increased by four attached Lhca proteins (LHCI), which form a crescent-shaped belt associated with the core complex (Boekema et al. 2001). In contrast to PSII complexes, where the LHCII antenna size is very variable, the LHCI antenna size and the stoichiometry of Lhca proteins of the plant PSI-LHCI supercomplex remains very stable even under different light conditions (Ballottari et al. 2007) (*see* the Sects. 9.3 and 9.4 below for details about structural organization of PSII and PSI).

In the last few decades, extensive biochemical evidence has been provided of the ability of photosynthetic proteins to form different supercomplexes, in analogy with respiratory proteins in mitochondria (*see* Dudkina et al. 2010a, b). For example, the PSI-LHCI supercomplex is known to form larger assemblies with other protein complexes, such as LHCII trimers, the Cyt$b_6f$ complex and NDH dehydrogenase. On the other hand, PSII-LHCII supercomplexes are known to form larger megacomplexes only via association with each other. A direct proof of the existence of the PSI-containing supercomplexes and the PSII megacomplexes can be obtained by clarification of their structures. However, structural characterization of large protein assemblies is often a very challenging task, because they are formed only transiently in the membrane and they are very fragile, which makes their purification in native form difficult. Here we describe our current experimental approach for the isolation and structural characterization of large photosynthetic supercomplexes or

even megacomplexes. We use optimized clear native polyacrylamide gel electrophoresis (CN-PAGE) for their separation and single particle electron microscopy for their structural characterization. The current knowledge about their structure, function and physiological significance is summarized in the following text.

## 9.2 Separation of Native Photosynthetic Supercomplexes for Their Structural Analysis

The first step to structural analysis of photosynthetic supercomplexes using electron microscopy (EM) is their isolation in sufficient quantity and homogeneity by a procedure that preserves their native form. Nowadays, two separation techniques are used most frequently – sucrose gradient ultracentrifugation and native polyacrylamide gel electrophoresis. Ultracentrifugation on a sucrose gradient allows an efficient separation of different types of photosynthetic protein complexes, as has been shown in several structural studies (e.g. Caffarri et al. 2009; Albanese et al. 2016; Wei et al. 2016). However, this technique is very time-consuming, as a single run may take about 10–20 h, and requires expensive equipment. In addition, prior to the preparation of the specimen for electron microscopy, a dialysis step is often indispensable to lower the sucrose concentration, which can severely reduce contrast of individual particles in electron micrographs. The main advantage of this method is the possibility to separate a large amount of sample in one separation run. Native electrophoresis also allows very efficient separation of native photosynthetic supercomplexes and megacomplexes of high molecular weight. Recent studies clearly show that separated protein complexes can be easily extracted from a gel and analyzed by EM (e.g. Knispel et al. 2012; Kouřil et al. 2014, 2016; Nosek et al. 2017). Although the electrophoretic technique enables separation of rather small sample volumes compared to the ultracentrifugation, the yield of isolated protein complexes is still sufficient for the EM technique. Moreover, a short separation time (about 2–3 h) and inexpensive equipment make the technique very attractive.

Undoubtedly, the above-mentioned techniques are gradually replacing other separation techniques such as gel filtration or affinity chromatography (e.g. van Roon et al. 2000; Drop et al. 2011). While the gel filtration suffers from a lower resolution and undesirable dilution of separated protein complexes, the affinity chromatography requires construction of a tag (e.g. the His6-tag) with no adverse effect on functional and structural properties of the tagged protein. Nevertheless, there is a continuous effort to search for mild separation techniques, which would further shorten the separation time and would allow the separation of fragile protein assemblies. Recently, free-flow electrophoresis was shown to be a promising technique (Yadav et al. 2017).

### 9.2.1 Native Polyacrylamide Gel Electrophoresis

Considering both scientific and practical aspects of the purification of photosynthetic supercomplexes, including time necessary for one separation and equipment expenses, native electrophoresis appears to be the best compromise. There are two variants of native electrophoresis, known as blue native electrophoresis (BN-PAGE) and clear native electrophoresis (CN-PAGE). Both native electrophoretic techniques differ in the agent used to provide the solubilized complexes the negative charge necessary for their movement in the electric field. While BN-PAGE uses an anionic dye Coomassie Brilliant blue (CBB), CN-PAGE applies a mild anionic detergent sodium deoxycholate.

The separation of protein complexes using BN-PAGE provides very good resolution, as the negatively charged CBB dye is directly adsorbed on the protein complexes. However, there are some indications that CBB disturbs the weakest protein-protein interactions. Moreover, the estimation of enzymatic activity of separated protein complexes and detection of fluorescently labeled proteins can be also hampered due to the presence of CBB (Wittig and Schägger 2005). To avoid this undesirable effect, a high-resolution CN-PAGE has been developed (Wittig et al. 2007), where CBB was replaced by the mild anionic detergent sodium deoxycholate, which is able to provide the negative charge without the disturbance of weak protein-protein interactions.

### 9.2.2 Solubilization of Photosynthetic Supercomplexes

Prior to the electrophoretic separation, the protein complexes have to be efficiently extracted from the lipid biological membranes. For this purpose, it is necessary to use mild detergents that are able to disrupt lipid-lipid and lipid-protein interactions on one hand and preserve protein-protein interactions on the other hand. Nowadays, a broad spectrum of different detergents can be used for this purpose (*see* Crepin et al. 2016), however, a screening of their solubilization properties indicates that non-ionic surfactants, like the dodecyl-maltosides (DDM) (the α- and β- anomers) and digitonin, are the most suitable for the solubilization of protein complexes from the thylakoid membranes. While there is a negligible difference in the α-DDM and β-DDM chemical structure, there is a considerable difference in their physical properties, which is evidenced by the stronger solubilizing power of β-DDM compared to α-DDM (see e.g. Pagliano et al. 2012; Barera et al. 2012).

It is important to keep in mind that both the lipid composition and lipid/protein ratio in the thylakoid membrane are species dependent and can also strongly vary under different environmental conditions. The same holds for the stability and abundance of a given type of photosynthetic protein complex. Therefore, to achieve an optimal solubilization of thylakoid membranes in each particular case, not only the type of the detergent has to be selected, but also its concentration has to be carefully

determined. The response of a sample to a detergent can be screened using so-called detergent concentration line, when a defined amount of sample is treated with a gradually increasing amount of the selected detergent. Using this approach it is possible to find the optimal solubilization conditions, which provide a maximal yield of a desired protein complex.

An example of this optimization procedure is shown for a solubilization of thylakoid membranes from *Arabidopsis thaliana* with a focus on large PSI-containing supercomplexes. In our optimization approach, we have decided to test both α- and β-DDM as solubilization agents (Figs. 9.2 and 9.3, respectively). Figure 9.2a shows that in the molecular weight range above 1 MDa (approx. The upper half of the gel), a milder solubilization using α-DDM was efficient for the isolation of larger forms of PSII supercomplexes or even PSII megacomplexes, which was further confirmed by the measurement of PSII fluorescence at room temperature (Fig. 9.2b). Fluorescence measurement enables unambiguous distinction between PSII and PSI containing complexes, as the fluorescence quantum yield of PSI is very low at room temperature, whereas the yield of PSII is high. Although the amount of separated PSII supercomplexes and megacomplexes significantly increased with increasing concentration of the detergent, the amount of PSI-containing high molecular weight bands (PSI hmw) increased only negligibly. A less mild solubilization of the thylakoid membrane using β-DDM led to a complete disappearance of the PSII megacomplex band and a substantial disruption of the largest PSII supercomplex into smaller forms. The yield of PSI-containing supercomplexes was still rather low (Fig. 9.3).

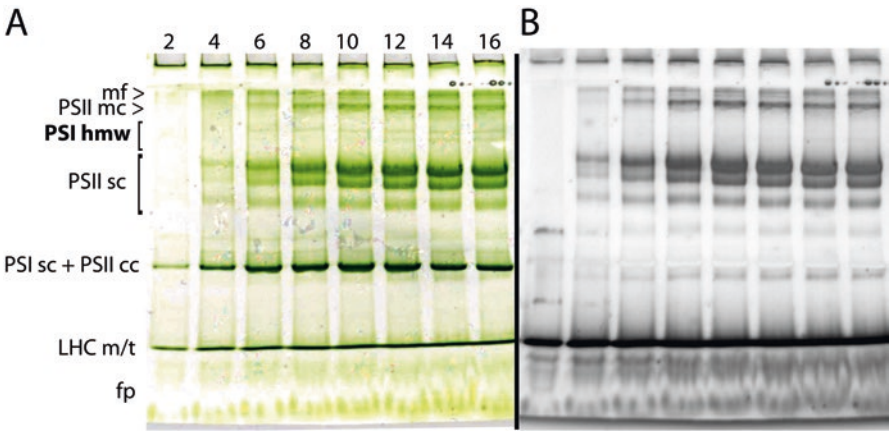


**Fig. 9.2** Electrophoretic separation of *Arabidopsis thaliana* thylakoid membranes solubilized by increasing amount of α-DDM. (**a**) colour image of the gel, (**b**) room temperature fluorescence of supercomplexes from the same gel. 2–16: DDM/chl ratio, *mf* membrane fragments, *PSII mc* megacomplexes of PSII, *PSI hmw* high molecular weight PSI-containing bands, *PSII sc* supercomplexes of PSII, *PSI sc* supercomplex of PSI, *PSII cc* core complex of PSII, *LHCm/t* LHC monomers and trimers, *fp* free pigments. For a better resolution of hmw protein complexes, a polyacrylamide gel with 4–8% gradient was used

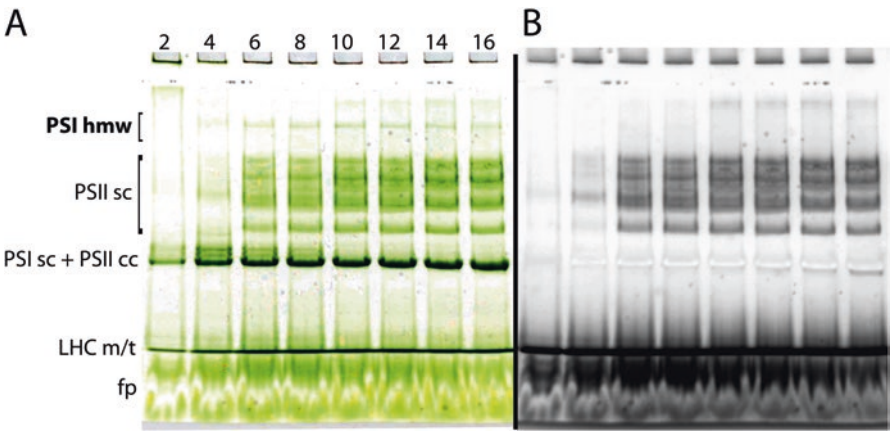


**Fig. 9.3** Electrophoretic separation of *Arabidopsis thaliana* thylakoid membranes solubilized by increasing amount of β-DDM. (**a**) colour image of the gel, (**b**) room temperature fluorescence of supercomplexes from the same gel. 2–16: DDM/chl ratio, *PSI hmw* high molecular weight PSI-containing bands, *PSII sc* supercomplexes of PSII, *PSI sc* supercomplex of PSI, *PSII cc* core complex of PSII, *LHCm/t* LHC monomers and trimers, *fp* free pigments. For a better resolution of hmw protein complexes, a polyacrylamide gel with 4–8% gradient was used

As the yield of high molecular weight (hmw) PSI-containing complexes from *Arabidopsis thaliana* was very small, we decided to test another plant species. Figures 9.4 and 9.5 show repeated electrophoretic separations of photosynthetic complexes from thylakoid membranes isolated from barley leaves (*Hordeum vulgare*) after solubilization with α- and β-DDM. Inspection of obtained results indicates that in the barley sample solubilized with β-DDM, two dense PSI hmw bands were detected. After evaluating the effect of detergent concentration on the band densities (Fig. 9.5, values 2–16), the DDM/chl ratio 8 was selected as optimal. At this ratio, we obtained the highest densities of both the PSI hmw bands. After a brief screening of the two bands by electron microscopy, we found the PSI-NDH supercomplex in the lower one. The upper band was found to contain oligomers of PSI complexes. In conclusion, despite the fact that the PSI-NDH supercomplex was initially discovered in *Arabidopsis thaliana* (Peng et al. 2008), we found that barley was a more suitable plant material for the isolation and structural characterization of this supercomplex (Kouřil et al. 2014). This demonstrates the importance of optimization of isolation and separation conditions preceding the structural analysis.

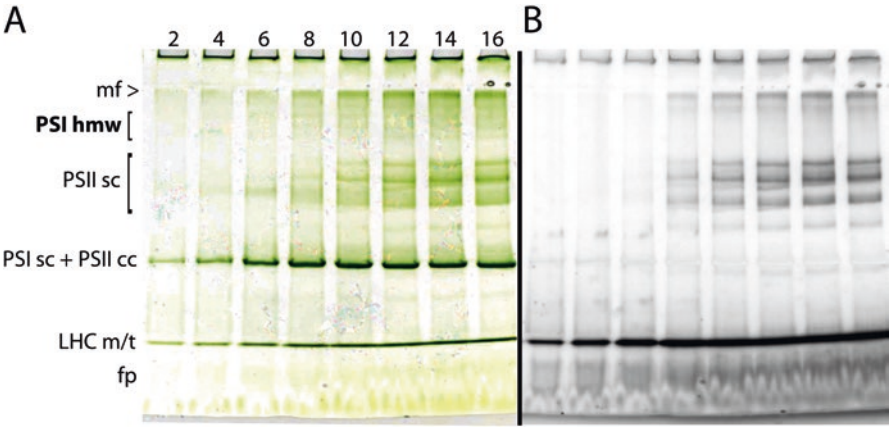


**Fig. 9.4** Electrophoretic separation of barley (*Hordeum vulgare*) thylakoid membranes solubilized by increasing amount of α-DDM. (**a**) colour image of the gel, (**b**) room temperature fluorescence of supercomplexes from the same gel. 2–16: DDM/chl ratio, mf: membrane fragments, *PSI hmw* high molecular weight PSI-containing bands, *PSII sc* supercomplexes of PSII, *PSI sc* supercomplex of PSI, *PSII cc* core complex of PSII, *LHCm/t* LHC monomers and trimers, *fp* free pigments. For a better resolution of hmw protein complexes, a polyacrylamide gel with 4–8% gradient was used

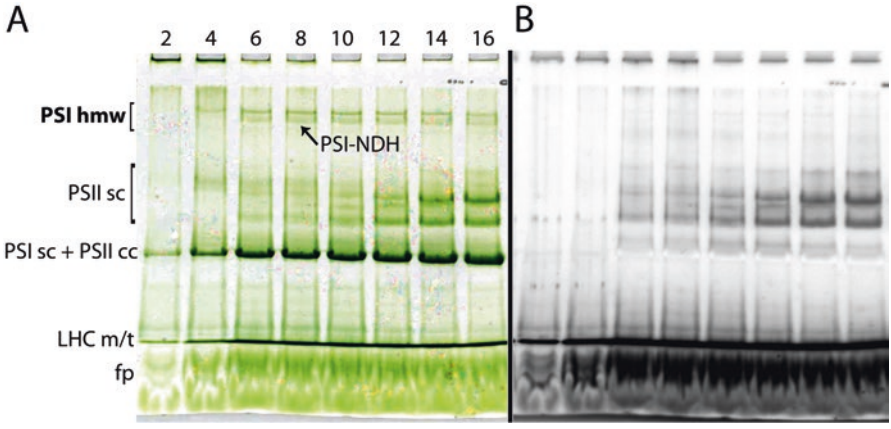


**Fig. 9.5** Electrophoretic separation of barley (*Hordeum vulgare*) thylakoid membranes solubilized by increasing amount of β-DDM. (**a**) colour image of the gel, (**b**) room temperature fluorescence of supercomplexes from the same gel. 2–16: DDM/chl ratio, *PSI hmw* high molecular weight PSI-containing bands, *PSI-NDH* PSI-NDH supercomplex, *PSII sc* supercomplexes of PSII, *PSI sc* supercomplex of PSI, *PSII cc* core complex of PSII, *LHCm/t* LHC monomers and trimers, *fp* free pigments. For a better resolution of hmw protein complexes, a polyacrylamide gel with 4–8% gradient was used

### *9.2.3 Preparation of Specimens for Structural Analysis*

Once the separation of desired protein complexes using CN-PAGE is optimized, the proteins have to be extracted from the gel prior to specimen preparation for single particle electron microscopy (Boekema et al. 2009). There are several methods available.

A procedure allowing a direct transfer of separated complexes from a native gel to the carbon coated grid was developed by Knispel and colleagues (2012). They placed the grid directly on the gel band with proteins of interest and relied on a spontaneous adsorption of protein complexes on the grid surface. This method is indeed very simple, however, its efficiency can be hampered by physical properties of separated complexes (i.e. size and shape), as we observed e.g. for large PSII supercomplexes.

Another option is the extraction of protein complexes into a buffer solution prior to specimen preparation. Generally, there are two methods: electro elution and spontaneous elution. Using the electro elution, the complexes are electrically forced from the gel and retained on a hydrophobic membrane, where they get concentrated. This method is fast, effective and quantitative, but requires specific and costly equipment. In addition, for our purpose it appears unsuitable, because the predominantly hydrophobic photosynthetic complexes can irreversibly aggregate on the hydrophobic membrane, which is highly undesirable for structural studies. On the other hand, spontaneous elution represents a convenient method with no special demands. It is based on simple free elution of complexes from the excised gel band into an elution buffer during a couple of hours. When spontaneous elution is performed, the excised gel band with complexes of interest is cut into small pieces and fully immersed into a small amount of elution buffer. We found this method to be very effective, as evidenced by several structural studies (i.e. Nosek et al. 2017; Kouřil et al. 2014, 2016). Once the complexes are extracted from the gel into solution, the electron microscopy specimen is prepared by a pipetting of the eluate on the glow-discharged carbon coated grid.

## 9.3 Structural Characterization of Plant Photosystem II Supercomplexes

The plant PSII is a large and highly variable multi-subunit protein supercomplex. The variability originates in the capability of the PSII core dimer to associate with a variable amount of LHCII proteins. This, together with a low stability of isolated PSII-LHCII supercomplexes, makes the structural analysis of this supercomplex via X-ray crystallography very difficult, because this technique requires a highly purified and concentrated sample. So far, X-ray crystallography was employed to obtain high resolution structures of some PSII components, including two extrinsic subunits of the plant PSII core complex, PsbP (Ifuku et al. 2004) and PsbQ (Calderone

et al. 2003; Balsera et al. 2005), and two types of antenna proteins, LHCII trimer (Liu et al. 2004; Standfuss et al. 2005) and Lhcb4 (Pan et al. 2011). On the other hand, single particle electron microscopy, which is less demanding with respect to sample homogeneity and quantity, turned out to be an indispensable technique in the structural research of the plant PSII-LHCII supercomplexes (*see* Kouřil et al. 2012; Pagliano et al. 2013; Caffarri et al. 2014 for recent reviews).

### *9.3.1 Composition and Organization of Photosystem II Supercomplex in Land Plants*

PSII core complex functions as a homo-dimer ($C_2$) (Hankamer et al. 1997). Each monomer contains a reaction center (RC), which is formed by two large intrinsic subunits PsbA and PsbD (also called D1 and D2 protein, respectively), PsbE and PsbF subunits (the cytochrome b559 complex), and PsbI. These subunits bind most of the redox cofactors and pigments that are necessary for the photochemical reactions and initiation of the electron transport across the thylakoid membrane. The absorption cross-section of the RC is further increased by its association with inner antenna proteins PsbB and PsbC (also called CP47 and CP43, respectively). RC is also associated with about a dozen low-molecular weight pigment-free subunits, which are important for the stabilization of the entire $C_2$ and for its association with additional peripheral light harvesting proteins. Finally, there are three extrinsic subunits, PsbO, PsbP and PsbQ, which associate to the PSII core complex from the lumenal site and constitute the oxygen evolving complex with the $Mn_4CaO_5$ cluster that is responsible for water oxidation (*see* e.g. Pagliano et al. 2013; Caffarri et al. 2014 for more details).

The light harvesting capacity of the $C_2$ is significantly enhanced by the peripheral LHCII complex, which is composed of six pigment-binding proteins, Lhcb1-6. In addition to supplying the RC with excitation energy, these proteins also play an important structural role in the photo-protection of PSII against photo-oxidative damage by excessive light. Lhcb1-3 proteins are the most abundant and they form several types of trimers. As the ratio between Lhcb1, Lhcb2, and Lhcb3 proteins is about 8:3:1 (Jansson 1994), this implies that they can form either homotrimers (composed of either Lhcb1 or Lhcb2) or heterotrimers (composed of Lhcb1, Lhcb2 and Lhcb3). Lhcb4-6 proteins (also called CP29, CP26, and CP24, respectively) represent a minor fraction of LHCII. They are present as monomers and mediate the specific association of LHCII trimers to the PSII core complex and thus are important for the formation of the PSII-LHCII supercomplex. According to the character of the binding to $C_2$, the LHCII trimers were designated as "S" and "M" (Strongly and Moderately bound LHCII trimers, respectively) (Dekker and Boekema 2005; Kouřil et al. 2012), occasionally $C_2$ can associate also with "L" trimers (Loosely bound) (Boekema et al. 1999a, b). However, biochemical data indicate that in the thylakoid membrane, up to eight LHCII trimers can be present per $C_2$ (Peter and Thornber 1991; Broess et al. 2008; van Oort et al. 2010), which implies that there is probably a pool of "extra" LHCII, which has unknown location with respect to the $C_2$.

Our knowledge of the architecture of the PSII-LHCII supercomplexes has been significantly improved over the last 20 years (*see* Dekker and Boekema 2005; Kouřil et al. 2012; Pagliano et al. 2013). Single particle EM revealed 2D projection maps of different types of PSII-LHCII supercomplexes (Boekema et al. 1995, 1998, 1999a, b) and a gradual improvement of their resolution allowed a precise localization of individual subunits (Yakushevska et al. 2003; Caffarri et al. 2009). Figure 9.6 shows three forms of the PSII-LHCII supercomplex, which can be separated by CN-PAGE after a mild solubilization of thylakoid membranes using α-DDM (Fig. 9.2). The largest and the most abundant form of the supercomplex consists of PSII core complex with two copies of the S trimers and two copies of the M trimers, the so-called $C_2S_2M_2$ supercomplex (Fig. 9.2, the top PSII sc band). The binding of the S trimer is mediated by Lhcb5 and Lhcb4, while the M trimer binds with the help of the Lhcb6 protein (Fig. 9.6c, f). The smaller forms of the PSII-LHCII supercomplex, which are less abundant (*see* Fig. 9.2), lack either one or both M trimers (Fig. 9.6a, b, d, e). Experiments with barley *viridis zb63* mutant, which is character-

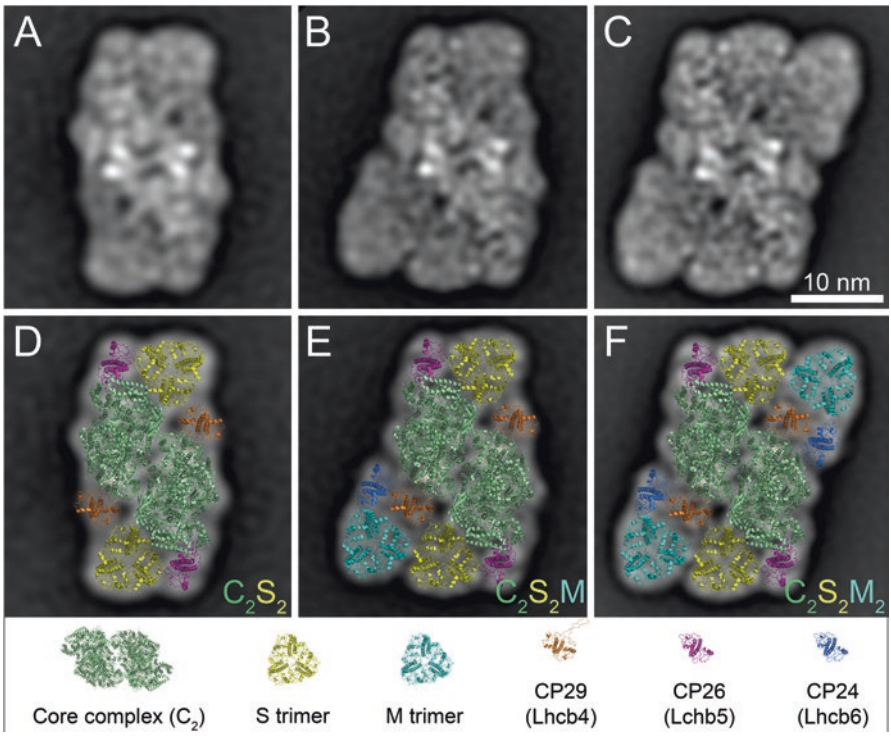


**Fig. 9.6** Projection maps of different forms of PSII supercomplexes from *Arabidopsis thaliana* revealed by single particle electron microscopy and image analysis. (**a**) Projection map of PSII $C_2S_2$ supercomplex, (**b**) $C_2S_2M$ supercomplex and (**c**) $C_2S_2M_2$ supercomplex. (**d**–**f**) Structural models of the PSII supercomplexes obtained by fitting the high resolution structures of the plant PSII supercomplex (Caffarri et al. 2009; Wei et al. 2016)

ized by a reduced LHCII to a minimal size due to the lack of PSI, indicate that the $C_2S_2$ supercomplex (Fig. 9.6a, d) represents the smallest physiologically relevant form of the supercomplex (Morosinotto et al. 2006).

Interestingly, the peripheral PSII antenna system can not only vary in its size, but it exhibits also small structural flexibility (Fig. 9.7). The flexibility within the peripheral antenna and, in particular, the flexibility of the M-trimer, Lhcb4, and Lhcb6 proteins, leads to several distinct conformations of the PSII supercomplex. Image analysis of a large data set (about 400,000 particles) shows that in the most abundant form of PSII supercomplex (approx. 60%), there is a gap between the Lhcb4, the S trimer and the core complex (Fig. 9.7a, d). A shift of the M trimer together with the Lhcb4/Lhcb6 region induces a small displacement of the S trimer and Lhcb5 (Fig. 9.7b, e), which leads to a tighter packing of the antenna in about 25% of analyzed projections. In the remaining 15% of analyzed data, the rotational shift of both the M trimers with the Lhcb4/Lhcb6 proteins induces additional lateral movement of the two halves of the dimeric core complex (Fig. 9.7c, f). The origin of the antenna flexibility still remains unknown. Single particle EM analysis of samples from dark-adapted plants and plants with light-induced NPQ excluded a

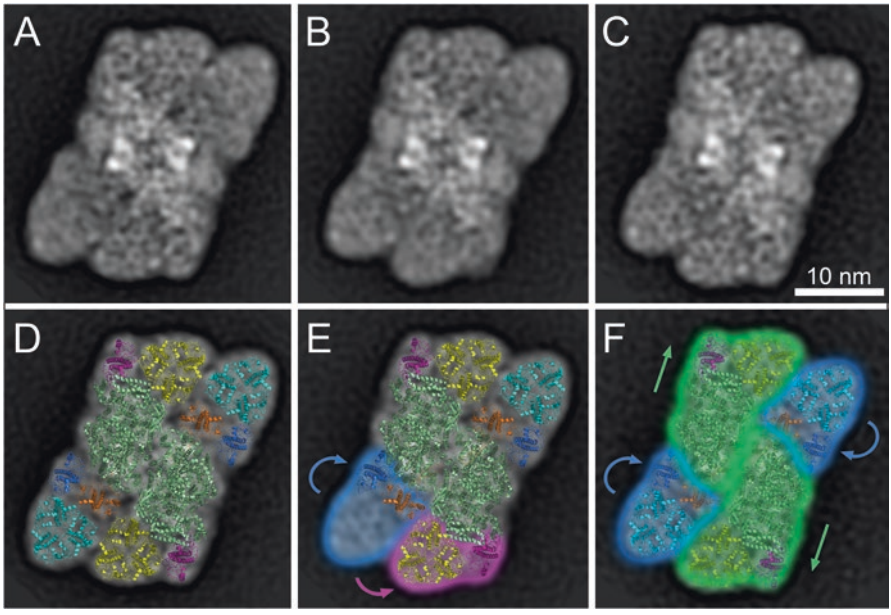


**Fig. 9.7** Structural flexibility of the PSII $C_2S_2M_2$ supercomplexes from *Arabidopsis thaliana* revealed by single particle electron microscopy and image analysis. Projection maps of a standard PSII $C_2S_2M_2$ supercomplex (**a**) and the $C_2S_2M_2$ supercomplexes with slightly different organization of LHCII antenna proteins and PSII core complex (**b**, **c**). (**d**–**f**) Structural models of the PSII supercomplexes obtained by fitting the high resolution structures of the plant PSII supercomplex (Caffarri et al. 2009, Wei et al. 2016). (**e**, **f**) The flexible parts of the PSII supercomplex and their movements with respect to the standard $C_2S_2M_2$ supercomplex are highlighted (See Fig. 9.6 for color coding)

direct relation between the particular antenna conformation and a light treatment (data not shown). Similarly, no direct connection with the presence of PsbS or zeaxanthin was observed (data not shown).

Recently, a breakthrough in the structural characterization of the PSII supercomplex was achieved, when the 3D structure of the $C_2S_2$ supercomplex was obtained using cryo electron microscopy at 3.2 Å resolution (Wei et al. 2016). This study significantly improved the resolution of the previous 3D structures (Nield et al. 2000; Nield and Barber 2006) and improved our knowledge about the organization of the whole supercomplex. A precise localization of individual Lhcb proteins shed more light on a possible energy transfer pathways between antenna and core complex. Nevertheless, solving the 3D structure of the complete $C_2S_2M_2$ supercomplex remains a challenging task for future research, especially due to the fragility of the supercomplex and the antenna flexibility.

### *9.3.2 Organization of Photosystem II Supercomplex in Pinaceae*

The $C_2S_2M_2$ supercomplex was first found in representatives of flowering plants (angiosperms), the phylogenetically youngest land plants (e.g. spinach, pea, *Arabidopsis*) (Boekema et al. 1999a; Caffarri et al. 2009; Pagliano et al. 2014). Until recently, it had been assumed that the overall architecture of the $C_2S_2M_2$ supercomplex is conserved throughout the evolution of land plants, as the structure of this supercomplex in liverworts (Harrer 2003), the evolutionary oldest land plants, is similar to $C_2S_2M_2$ in angiosperms. Surprisingly, our recent study on PSII-LHCII supercomplexes in Norway spruce (*Picea abies*) revealed that the architecture and the subunit composition of PSII-LHCII supercomplex are not uniform in all land plants (Kouřil et al. 2016). Genome and transcriptome analysis of Norway spruce showed a lack of functional *Lhcb6* and *Lhcb3* genes, which notably changes the structural organization of the $C_2S_2M_2$ supercomplex (Fig. 9.8) (Kouřil et al. 2016). Due to the absence of Lhcb3 (a constituent of the M trimer, Dainese and Bassi 1991) and Lhcb6, the M trimer associates to the PSII complex in a different manner, which has never been observed in land plants before. Interestingly, the same orientation of the M and S trimers has been recently described in an evolutionarily older organism, the green alga *Chlamydomonas reinhardtii*, which also lacks the Lhcb6 protein (Fig. 9.8c, f) (Tokutsu et al. 2012; Drop et al. 2014).

The Lhcb6 and Lhcb3 proteins are known to be crucial for the management of absorbed light in land plants. The interaction between these proteins is important for the stable attachment of the M trimers to PSII complex (Kovacs et al. 2006; Caffarri et al. 2009; Kouřil et al. 2013). Therefore, these proteins can control the PSII antenna size during both plant adaptation and acclimation to different light conditions (Bailey et al. 2001; Ballottari et al. 2007; Betterle et al. 2009; Kouřil et al. 2013), optimize macro-organization of PSII supercomplexes and control connectiv-

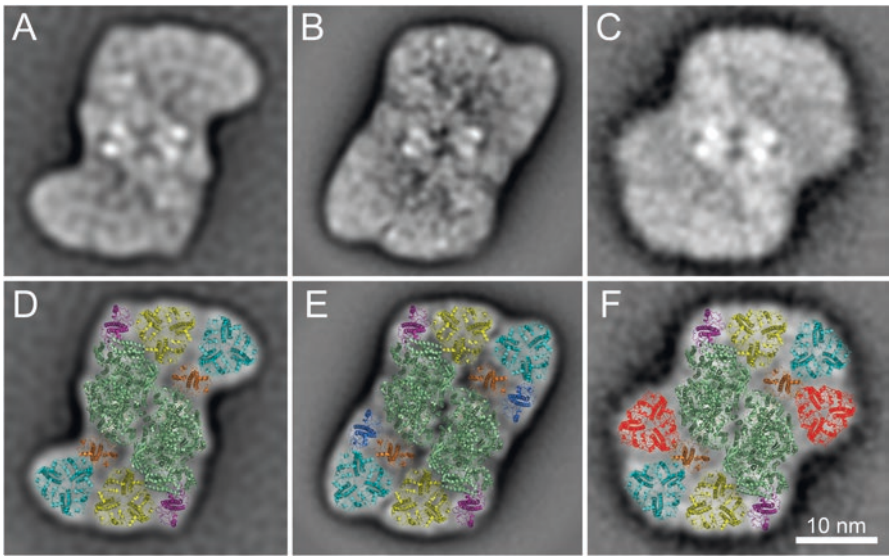


**Fig. 9.8** Projection maps of PSII supercomplexes from different plant species revealed by single particle electron microscopy and image analysis. Projection maps of (**a**) PSII supercomplex ($C_2S_2M_2$) from Norway spruce (*Picea abies*), (**b**) PSII supercomplex ($C_2S_2M_2$) from *Arabidopsis thaliana*, (**c**) PSII supercomplex ($C_2S_2M_2N_2$) from green alga *Chlamydomonas reinhardtii* (Adapted from Drop et al. 2014). (**d**–**f**) Structural models of different forms of the PSII supercomplexes obtained by fitting the high resolution structures of the plant PSII supercomplex (Caffarri et al. 2009; Wei et al. 2016) (See Fig. 9.6 for color coding)

ity between PSII cores (Kovacs et al. 2006; Caffarri et al. 2009). These factors are crucial to accomplish a maximum efficiency of PSII photochemistry and play a key role in effective photo-protective dissipation of absorbed light energy (so-called non-photochemical quenching, NPQ) (Kovacs et al. 2006). Namely Lhcb6 is known to play an important role in NPQ of land plants, as it provides an interaction site for PsbS (Kovacs et al. 2006), a protein that is essential for the induction of NPQ (Li et al. 2000). The current model of NPQ suggests that upon exposure to excessive light, a part of the PSII-LHCII supercomplex containing Lhcb6, Lhcb4 and the M trimer dissociates, which leads to the PsbS-dependent NPQ (Betterle et al. 2009; Johnson et al. 2011).

A thorough genome and transcriptome analysis revealed that the absence of the Lhcb3 and Lhcb6 proteins is not limited to *Picea abies*. We have shown that these proteins are also absent in the gymnosperm genera *Picea* and *Pinus* (family Pinaceae) and *Gnetum* (Gnetales) (Kouřil et al. 2016). This is quite surprising, as the appearance of both Lhcb3 and Lhcb6 had been assumed to be crucial for the transition of photosynthetic organisms from aquatic habitat to land (Koziol et al. 2007; Alboresi et al. 2008; de Bianchi et al. 2008; Büchel 2015). A possible physiological benefit of the loss of these proteins in Pinaceae and Gnetales families remains to be clarified.

### 9.3.3 Association of Photosystem II Supercomplexes into Megacomplexes

The ability of the plant PSII-LHCII supercomplexes to associate with other proteins of the photosynthetic apparatus and to form even larger assemblies is rather limited. To our knowledge, there is only indirect biochemical evidence of the interactions of PSII-LHCII supercomplexes with PsbS protein (Gerotto et al. 2015; Correa-Galvis et al. 2016) or PSI complex (Yokono et al. 2015; Chen et al. 2016), which is still awaits a structural elucidation.

However, there is structural evidence of specific associations between two copies of PSII-LHCII supercomplexes into PSII megacomplexes (Boekema et al. 1999a, b; Yakushevska et al. 2001b; Caffarri et al. 2009; Jarvi et al. 2011; Albanese et al. 2016; Nosek et al. 2017). The PSII-LHCII supercomplexes associated in parallel can further associate into larger semi-crystalline arrays, which can be occasionally observed in grana membranes and which are believed to be important for the optimization and regulation of photosynthetic processes (Boekema et al. 1999a, b, 2000; Yakushevska et al. 2001a, b; Kirchhoff et al. 2007; Daum et al. 2010; Kouřil et al. 2012, 2013; Kirchhoff 2013; Tietz et al. 2015).

Recently, optimization of isolation of PSII megacomplexes using CN-PAGE (Fig. 9.2) allowed us to perform their thorough analysis. Single particle EM revealed a large variability in their formation (Nosek et al. 2017). A majority of analyzed PSII megacomplexes (about 80%) were formed by various parallel associations of two PSII-LHCII supercomplexes (Fig. 9.9a–e), which has been observed in previous studies. Structural models of their interactions indicate that the megacomplexes are formed by interactions between core complexes, M trimers and monomeric antenna proteins Lhcb5 and Lhcb6. Interestingly, the interaction between the core complex and Lhcb6 protein is already strong enough to form a stable megacomplex (Fig. 9.9d). Moreover, the involvement of additional LHCII trimers in the binding interactions gave rise to a unique type of the parallel PSII megacomplex (Fig. 9.9e). The additional LHCII trimers seem to be crucial for the formation of this type of the megacomplex (Fig. 9.9e), as no analogous PSII megacomplexes without these trimers were observed. Furthermore, single particle image analysis revealed novel variable associations between two non-parallel PSII-LHCII supercomplexes (Fig. 9.9f–l). Their structural models indicate that core complexes, S and M trimers, monomeric antenna proteins Lhcb5 and Lhcb6, and additional LHCII trimers are involved, to a different extent, in the mutual interactions between the two supercomplexes.

As the PSII megacomplexes were observed in several plant species (Boekema et al. 1999a, b; Yakushevska et al. 2001b; Caffarri et al. 2009; Jarvi et al. 2011; Nosek et al. 2017), their formation can be considered as a general property of the plant PSII-LHCII supercomplex. A successful identification of PSII megacomplexes in isolated grana membranes (Kirchhoff et al. 2008; Kouřil et al. 2011; Nosek et al. 2017) strongly supports their natural origin and physiological significance. A reversible formation of PSII megacomplexes can effectively modulate and control

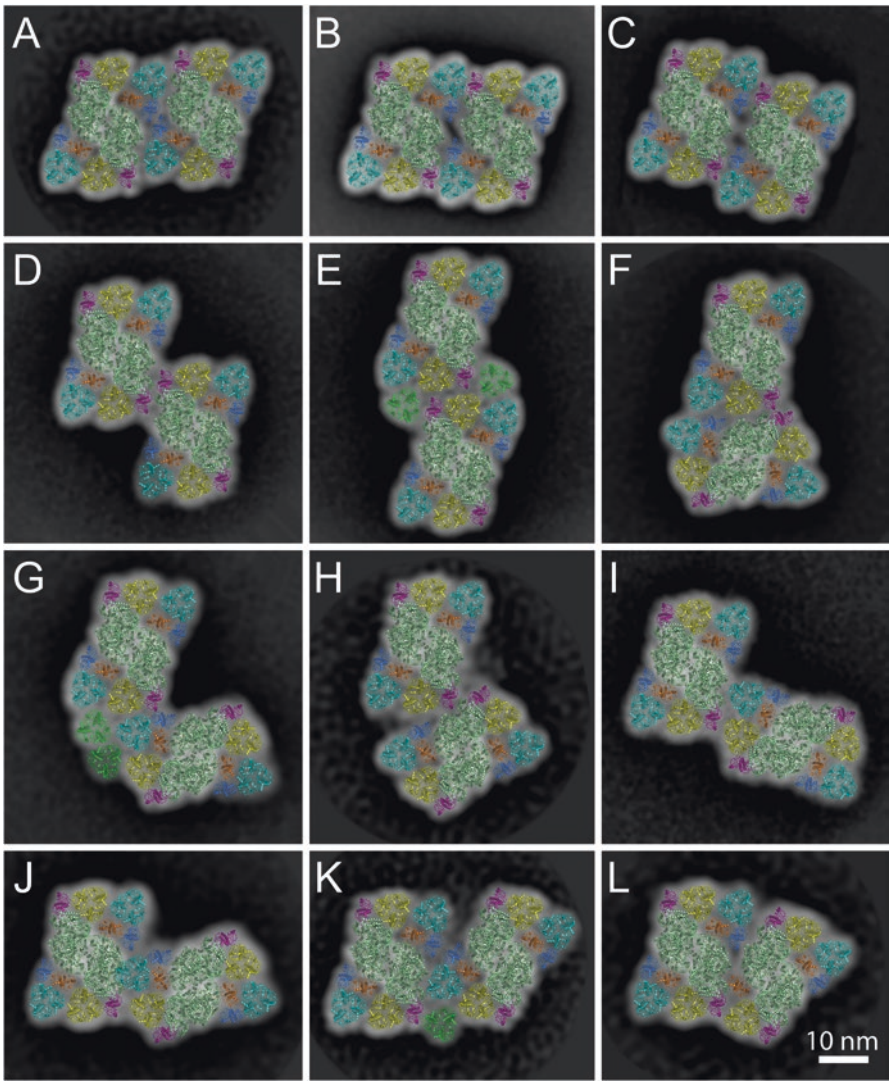


**Fig. 9.9** Projection maps of *Arabidopsis thaliana* PSII megacomplexes revealed by single particle electron microscopy and image analysis. (**a**–**l**) Structural models of different forms of the PSII megacomplexes obtained by fitting the high resolution structures of the plant PSII supercomplex (Caffarri et al. 2009, Wei et al. 2016) (See Fig. 9.6 for color coding. The additional LHCII trimers are depicted in green)

the overall antenna size and effectively regulate a photochemical usage of absorbed light energy by plants in a changing environment (Ballottari et al. 2007; Kouřil et al. 2013; Albanese et al. 2016).

## 9.4 Structural Characterization of Plant Photosystem I Supercomplexes

PSI is a pigment-binding supercomplex, which works as a light-driven plastocyanin:ferredoxin oxidoreductase. The PSI core complex coordinates the components responsible for a light-driven electron transfer and specifically associates with a membrane-embedded light harvesting complex, LHCI, which extends its light-harvesting capacity. Initial structural research of a plant PSI-LHCI supercomplex largely profited from a high structural homology of the plant core complex with the cyanobacterial counterpart, as the latter was successfully studied using X-ray crystallography at atomic resolution (Krauss et al. 1996; Schubert et al. 1997; Jordan et al. 2001). The first structural details of the organization of the entire plant PSI-LHCI supercomplex were provided by single particle EM, which revealed an asymmetric binding of the LHCI proteins to one side of the core complex (Boekema et al. 2001). Due to an extensive effort of the research group of Nathan Nelson, the first high-resolution structure of the PSI-LHCI supercomplex was solved by X-ray crystallography at 4.4 Å (Ben-Shem et al. 2003) and a gradually improved up to 2.8 Å (Amunts et al. 2007, 2010; Mazor et al. 2015; Qin et al. 2015). As we show below, a combination of X-ray data and single particle EM maps is very advantageous for solving the structures of even larger assemblies between the PSI-LHCI supercomplex and additional proteins of the plant photosynthetic apparatus like the NDH complex, LHCII or Cyt$b_6f$ complex.

### *9.4.1 Composition and Organization of Photosystem I Supercomplex in Land Plants*

X-ray structures of the plant PSI-LHCI supercomplex show that a stable form of the PSI core complex consists of 12 subunits PsaA – PsaL (Ben-Shem et al. 2003; Amunts et al. 2007, 2010; Mazor et al. 2015; Qin et al. 2015). There are only a few core subunits (PsaG, H, N-P, R), which are specific to green plants. Both PsaG and PsaH are stably bound to the core and were found to play important roles in the stabilization of the core complex (Varotto et al. 2002; Jensen et al. 2002), and in the docking of phosphorylated LHCII during state transitions, respectively (Lunde et al. 2000, Kouřil et al. 2005b, see also Sect. 9.4.3). PsaN-PsaP and PsaR subunits were found to occasionally associate with the PSI core complex. As both PsaN and PsaR subunits were identified in the crystal structure of the core complex only under specific crystallization conditions, they are not considered as its stable parts and their exact functions remain unclear (Amunts et al. 2010). PsaO and PsaP are subunits which have not been identified in any crystal structure of plant PSI-LHCI supercomplex yet (see also Nelson and Yocum 2006, Busch and Hippler 2011 for reviews).

The light harvesting complex of PSI consists of four peripheral light harvesting proteins Lhca1-4. They are evenly expressed and form two heterodimers, which create together a crescent-shaped belt at the PsaF/J site of the core complex (Boekema et al. 2001; Ben-Shem et al. 2003). One dimer is composed of Lhca1 and Lhca4 proteins and interacts with PSI core complex via PsaG and PsaB subunits (Lhca1) and via the PsaF subunit (Lhca4). The other dimer is formed by Lhca2 and Lhca3 proteins. Lhca2 associates with PSI core complex via PsaA and PsaJ and Lhca3 interacts via PsaA and PsaK (Jansson et al. 1996; Ben-Shem et al. 2003). The individual Lhca proteins in the PSI-LHCI supercomplex are not mutually interchangeable, which was demonstrated on mutants lacking individual Lhca subunits (Wientjes et al. 2009). In addition, there are two light harvesting proteins, Lhca5 and Lhca6, which are expressed at a very low level and bind, in contrast to other Lhca1-4 proteins, to PSI in a sub-stoichiometric amount (Klimmek et al. 2006). The exact role of Lhca5 and Lhca6 was unclear, until the mutants lacking these subunits were constructed. Analysis of these mutants indicated direct involvement of Lhca5 and Lhca6 in the formation and stabilization of the PSI-NDH supercomplex (Peng et al. 2008, 2009; Kouřil et al. 2014) (see the Sect. 9.4.2).

### *9.4.2 Structure of Photosystem I and NAD(P)H Dehydrogenase Supercomplex*

The chloroplast NDH complex, which is similar to bacterial respiratory complex I, mediates one type of cyclic electron transport around PSI (Burrows et al. 1998; Kofer et al. 1998; Shikanai et al. 1998). This pathway is highly important for plants especially under stress conditions, as it helps to protect the photosynthetic apparatus against oxidative stress by preventing over-reduction of the chloroplast stroma (see Yamori and Shikanai 2016 for recent review). Biochemical analysis of the NDH complex revealed its association with PSI in the thylakoid membrane (Aro et al. 2005; Peng et al. 2008), and one NDH complex was proposed to associate with up to two copies of PSI (Peng and Shikanai 2011). The formation of the PSI-NDH supercomplex was found to be a prerequisite for the efficient operation of the NDH cyclic electron pathway (Peng et al. 2009). Surprisingly, two minor light harvesting proteins, Lhca5 and Lhca6, whose roles in relation to PSI had been enigmatic, were found to be directly involved in the formation of the PSI-NDH supercomplex (Peng et al. 2009). Thus, revealing the structure of the giant PSI-NDH supercomplex was keenly awaited.

Single particle EM analysis provided the first structural evidence of the presence of the $PSI_2$-NDH supercomplex in barley plants and its role in electron transport was proposed (Kouřil et al. 2014). In agreement with the former biochemical data, the supercomplex was formed by two copies of PSI, which were attached to one NDH complex. In addition, a smaller sub-complex, formed by one PSI associated to one NDH, was also found (Kouřil et al. 2014). A pseudo-atomic model of the

$PSI_2$-NDH supercomplex, constructed by a fitting the EM projection map with the X-ray structures of PSI and the bacterial respiratory complex (Amunts et al. 2010; Baradaran et al. 2013), indicates that the PSI complexes interact with the NDH complex through sites on LHCI (Fig. 9.10h). Our recent structural analysis revealed the same two types of the PSI-NDH supercomplexes in *Arabidopsis thaliana* (Fig. 9.10a, b). In addition, in Arabidopsis we have found even larger assemblies of the PSI-NDH supercomplex, where up to four PSI were associated to one copy of the NDH complex (Fig. 9.10c–f). However, due to a lower resolution, we were not able to unambiguously determine how the extra PSI complexes associate to the $PSI_2$-NDH supercomplex. Interestingly, we observed a unique association of two PSI to two NDH complexes (Fig. 9.10g), which indicate that these complexes might be able to form large PSI-NDH clusters in the thylakoid membrane.

### *9.4.3 Structure of Photosystem I and Light Harvesting Complex II Supercomplex*

Optimal photosynthetic performance is achieved when the light absorption by both PSII and PSI is balanced. As the absorption properties of the two photosystems are different and the spectral composition and intensity of the sunlight can considerably vary during the day, plants have developed a mechanism of a rapid adjustment of the relative absorption cross-sections of both photosystems called state transitions (Bonaventura and Myers 1969; Bennett 1977). The adjustment involves a reversible migration of phosphorylated LHCII between PSII and PSI, which compensates for the absorption imbalance (Allen 1992; Wollman 2001; Minagawa 2011). Under a

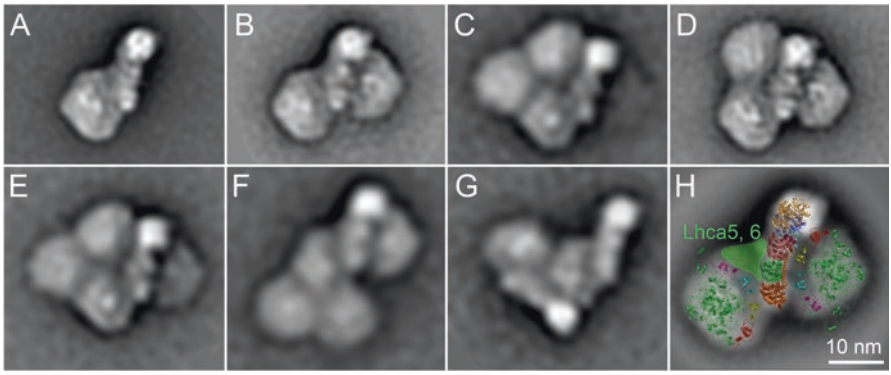


**Fig. 9.10** Projection maps of different *Arabidopsis thaliana* PSI-NDH supercomplexes revealed by single particle electron microscopy and image analysis. (**a**) Projection map of the $PSI_1$-NDH supercomplex, (**b**) projection map of the $PSI_2$-NDH supercomplex, (**c**, **d**) projection maps of two different $PSI_3$-NDH supercomplexes, (**e**, **f**) projection maps of two different $PSI_4$-NDH supercomplexes, (**g**) projection map of dimeric $PSI_1$-NDH supercomplexes, (**h**) structural model of the $PSI_2$-NDH supercomplexes according to Kouřil et al. (2014)

preferential excitation of PSII, the activated Stn7 kinase (Bellafiore et al. 2005) phosphorylates LHCII, which subsequently moves from PSII and associates with PSI (state 2). Conversely, under a preferential excitation of PSI, the Stn7 kinase is inactivated and the LHCII phosphatase (Pribil et al. 2010; Shapiguzov et al. 2010) dephosphorylates LHCII, inducing its return back to PSII (state 1).

Although there is ample functional evidence for the occurrence of state transitions, the structure of the PSI-LHCII supercomplex remained uncharacterized for a long time, especially due to difficult purification of the supercomplex with yield too low for structural analysis. The first structural details about the architecture of the PSI-LHCII supercomplex were revealed by single particle EM of a crude, non-purified protein extract, obtained via mild solubilization of Arabidopsis thylakoid membranes using digitonin (Kouřil et al. 2005b). We have found that the PSI-LHCII supercomplex forms a pear-shaped particle, where the LHCII associates with PSI at the PsaA site between the PsaK and PsaH subunits (Fig. 9.11a, e). Recent structural analysis of free-flow electrophoretic fractions revealed even larger forms of the PSI-LHCII supercomplexes (Yadav et al. 2017). The largest assembly represented a dimer of the PSI-LHCII particles (Fig. 9.11b). A pseudo-atomic model indicates that the two PSI-LHCI complexes interact with each other from the PsaH side and the LHCII trimers also considerably contribute to the dimer formation (Fig. 9.11f). In addition, PSI-LHCII supercomplexes containing two LHCII trimers were also identified (Fig. 9.11c, d). The second LHCII binds at the peripheral antenna LHCI

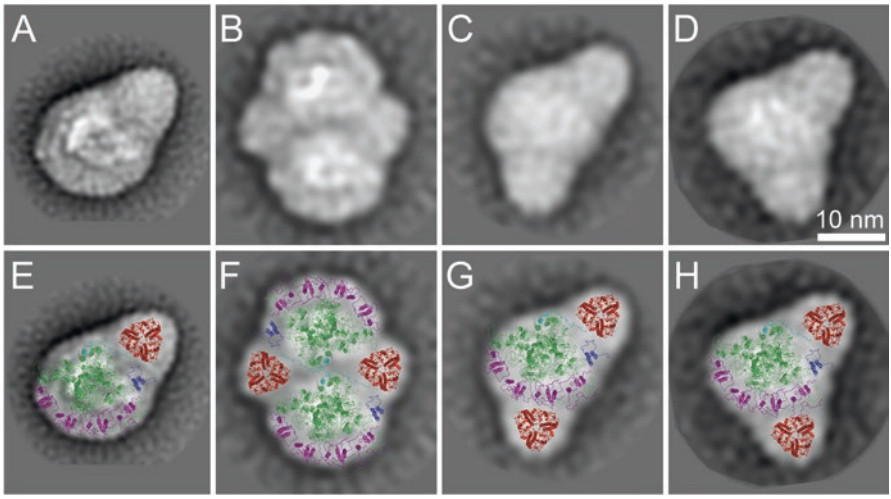


**Fig. 9.11** Projection maps of different *Arabidopsis thaliana* PSI-LHCII supercomplexes revealed by single particle electron microscopy and image analysis. (**a**) PSI-LHCII supercomplex, (**b**) dimer of the PSI-LHCII supercomplex, (**c**, **d**) PSI-LHCII supercomplexes with additional LHCII trimer attached. (E-H) Structural models of the PSI-LHCII supercomplexes obtained by fitting the high resolution structures of the plant PSI complex (Mazor et al. 2015) (PSI core complex in green, PsaH in cyan, PsaK in blue, LHCI in magenta) and LHCII trimer (red) (Standfuss et al. 2005). LHCII trimer binds to the PSI core complex at the PsaH/PsaK side (**e**, **f**), additional LHCII trimer associates with the PSI complex at the LHCI site (**g**, **h**) (Adapted from Yadav et al. 2017)

of PSI (Fig. 9.11g, h). Our structural data clearly show that different types of the PSI-LHCII supercomplexes can be formed during state transitions and more than one LHCII trimer can associate with PSI. The novel associations indicate that our current view of the state transitions is rather limited and deserves further attention.

One of the still unanswered questions related to state transitions is where do the migrating LHCII trimers come from? Do the phosphorylated LHCII trimers represent the M trimers from $C_2S_2M_2$ supercomplexes or rather trimers from the free pool of LHCII? Based on a higher ratio of the $C_2S_2M/C_2S_2M_2$ particles in state 2 it has been proposed that the M trimer is involved in the association with PSI (Kouřil et al. 2005b; Dietzel et al. 2011). However, further experiments questioned the proposed scenario, as a lower amount of the $C_2S_2M_2$ supercomplexes in state 2 could be explained just by a higher sensitivity of the supercomplexes to a detergent treatment upon phosphorylation and the L trimers or LHCII from the free pool were proposed to play a key role in state transitions (Galka et al. 2012; Wientjes et al. 2013).

### 9.4.4 *Structure of Photosystem I and Cytochrome $b_6f$ Supercomplex*

PSI has the ability to form supercomplexes with Cyt$b_6f$ complex. Several years ago, a supercomplex composed of PSI and Cyt$b_6f$ complex was biochemically described in the green alga *Chlamydomonas reinhardtii* (Iwai et al. 2010). This PSI-Cyt$b_6f$ supercomplex was proposed to contain three additional minor components – LHCII, FNR and PGRL1 – and was considered to play a role in cyclic electron flow. The first structural evidence of this supercomplex was obtained from a study of *Arabidopsis thaliana* membrane protein complexes, quickly purified with free-flow electrophoresis (Yadav et al. 2017). Electron microscopy analysis indicated that the Cyt$b_6f$ complex binds to PSI either as a monomer or as a dimer. The interaction between PSI and Cyt$b_6f$ is very loose and can be easily disrupted by detergents during purification, which could probably be explained by the fact that the rectangular-shaped Cyt$b_6f$ dimer binds to PSI at its short side (Fig. 9.12a).

A low-resolution 3D model was calculated from filtered projection maps, obtained by single particle EM (Fig. 9.12d). The high-resolution structures of PSI (Mazor et al. 2015) and the Cyt$b_6f$ complex (Stroebel et al. 2003; Kurisu et al. 2003) have been characterized before and could be modeled into the electron microscopy density map (Yadav et al. 2017). The shape of the Cyt$b_6f$ complex is highly asymmetrical with respect to the membrane (Stroebel et al. 2003, Kurisu et al. 2003), because unlike PSI, it protrudes strongly on the lumenal side of the membrane. This was very helpful to establish the binding position of Cyt$b_6f$ complex (Fig. 9.12d). Modelling shows that the Cyt$b_6f$ complex binds on the side of the PsaB subunit, next to the PsaG subunit of PSI core and the Lhca1 subunit of the peripheral antenna (Fig. 9.12e). The small protein plastocyanin functions as an electron transporter between the cytochrome f subunit of Cyt$b_6f$ complex and PSI. Minimizing this distance (black circles, Fig. 9.12e) could be the reason why the Cyt$b_6f$ complex binds to PSI with its short side rather than with its long side.

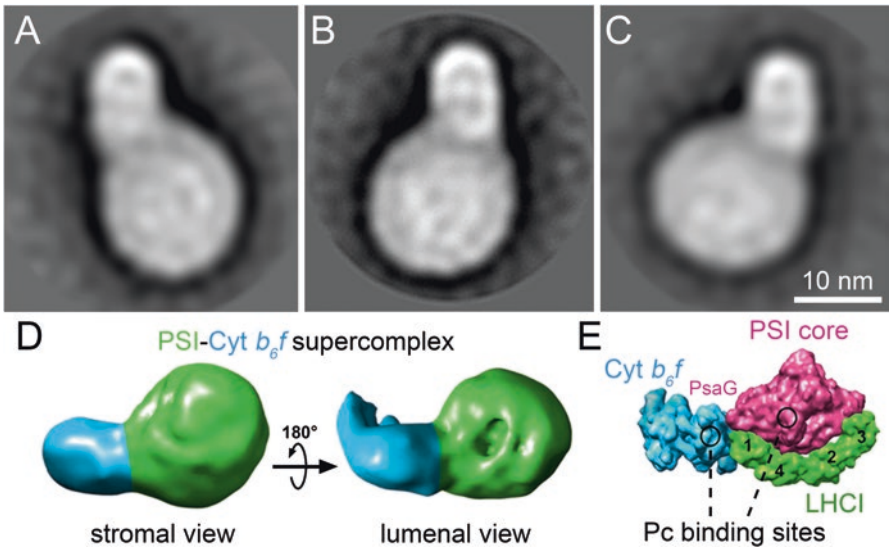


**Fig. 9.12** Projection maps of *Arabidopsis thaliana* PSI-Cyt$b_6f$ supercomplexes revealed by single particle electron microscopy and image analysis. (**a**–**c**) Different views of the supercomplexes consisting of PSI complex and a dimer of the Cyt$b_6f$ complex. (**d**) Reconstructed 3D model of the PSI-Cyt$b_6f$ supercomplex visualized from the stromal and lumenal sides, PSI complex in green, Cyt$b_6f$ complex in light blue. (**e**) Model of the PSI-Cyt$b_6f$ supercomplex with the PSI core (purple), LHCI (green, positions of the Lhca1-4 proteins is indicated by numbers), and Cyt$b_6f$ complex (light blue) (Adapted from Yadav et al. 2017)

Over the last years it became obvious that PSI is undoubtedly a key protein in the regulation of electron flow. As PSI is involved in linear electron flow and two types of cyclic electron flow, it is important for modulation of the ATP:NADPH production and for the prevention of photo-oxidative damage under stress conditions (Burrows et al. 1998; Shikanai et al. 1998; Munekage et al. 2004). PSI uses light energy to mediate electron transfer from plastocyanin to ferredoxin, which then transports electrons from PSI to FNR in linear electron flow or to either Cyt$b_6f$ complex or NDH in cyclic electron flow. This electron transport via plastocyanin and ferredoxin is diffusion-limited. Therefore, the regulation of the distances between electron carriers via the formation of supercomplexes of PSI with NDH or Cyt$b_6f$ complex can control kinetics of the cyclic electron flows. We hypothesize that fine tuning of distances between PSI, NDH and Cyt$b_6f$ complex in supercomplexes and/or small membrane domains can control activity of the two types of cyclic electron flow. However, how this works in detail is not clear yet. So far, the analysis of the structures of the supercomplexes has not revealed the localization of small but essential components of the two types of cyclic electron flow, such as PGRL1, PGRL5 and FNR. Also LHCII was not found to be a component of the plant PSI-Cyt$b_6f$ supercomplex, although PSI-LHCII supercomplexes are present in fair amounts in plant thylakoid membranes.

## 9.5 Future Perspectives

Currently, we have a very good knowledge of the architecture of all main components of the photosynthetic apparatus in thylakoid membranes at near atomic resolution. Single particle EM revealed the ability of the components to associate into large assemblies, which were shown to have physiological relevance. In our opinion, future structural studies on photosynthetic complexes should be more focused on the organization of photosynthetic complexes in the thylakoid membrane. Recent cryo electron tomography studies indicate that it is possible to resolve PSII core complexes directly in the membrane (Daum et al. 2010; Kouřil et al. 2011). This is largely due to a presence of extrinsic subunits of oxygen evolving complex, which enhance the contrast of the PSII particles with respect to the surrounding membrane. Recent instrumentation development in the field of cryo EM, leading to a significant improvement of a contrast in electron micrographs (see e.g. Fernandez-Leiro and Scheres 2016 for a recent review), is promising with respect to the possibility to visualize also other photosynthetic complexes with large hydrophilic domains (e.g. Cyt$b_6f$ complex and NDH complex). A visual monitoring of photosynthetic complexes and their distribution in the thylakoid membrane under different environmental conditions would open up a whole new chapter in photosynthesis research.

**Acknowledgements** This work was supported by the grant project LO1204 (Sustainable development of research in the Centre of the Region Haná) from the National Program of Sustainability I from the Ministry of Education, Youth and Sports, Czech Republic. Dr. Roman Kouřil was supported by a Marie Curie Career Integration Grant call FP7-PEOPLE-2012-CIG (322139). We acknowledge funding by the European Union's Horizon 2020 research and innovation programme under grant agreement no. 675006.

## References

Albanese P, Nield J, Alejandro J et al (2016) Isolation of novel PSII-LHCII megacomplexes from pea plants characterized by a combination of proteomics and electron microscopy. Photosynth Res 130(1–3):19–31

Albertsson PÅ (2001) A quantitative model of the domain structure of the photosynthetic membrane. Trends Plant Sci 6(8):349–354

Alboresi A, Caffarri S, Nogue F et al (2008) In silico and biochemical analysis of *Physcomitrella patens* photosynthetic antenna: identification of subunits which evolved upon land adaptation. PLoS One 3:e2033

Allen JF (1992) Protein phosphorylation in regulation of photosynthesis. Biochim Biophys Acta 1098:275–335

Amunts A, Drory O, Nelson N (2007) The structure of a plant photosystem I supercomplex at 3.4 Å resolution. Nature 447:58–63

Amunts A, Toporik H, Borovikova A et al (2010) Structure determination and improved model of plant photosystem I. J Biol Chem 285:3478–3486

Aro EM, Suorsa M, Rokka A et al (2005) Dynamics of photosystem II: a proteomic approach to thylakoid protein complexes. J Exp Bot 56:347–356

Baena-Gonzalez E, Aro EM (2002) Biogenesis, assembly and turnover of photosystem II units. Phil Trans R Soc Lond B 357:1451–1460

Bailey S, Walters RG, Jansson S et al (2001) Acclimation of Arabidopsis thaliana to the light environment: the existence of separate low light and high light responses. Planta 213:794–801

Ballottari M, Dall'Osto L, Morosinotto T et al (2007) Contrasting behavior of higher plant photosystem I and II antenna systems during acclimation. J Biol Chem 282:8947–8958

Balsera M, Arellano JB, Revuelta JL et al (2005) The 1.49 Å resolution crystal structure of PsbQ from photosystem II of *Spinacia oleracea* reveals a PPII structure in the N-terminal region. J Mol Biol 350:1051–1060

Baradaran R, Berrisford JM, Minhas GS et al (2013) Crystal structure of the entire respiratory complex I. Nature 494:443–448

Barera S, Pagliano C, Pape T et al (2012) Characterization of PSII-LHCII supercomplexes isolated from pea thylakoid membrane by one-step treatment with alpha- and beta-dodecyl-D-maltoside. Philos Trans R Soc Lond Ser B Biol Sci 367(1608):3389–3399

Bellafiore S, Barneche F, Peltier G et al (2005) State transitions and light adaptation require chloroplast thylakoid protein kinase STN7. Nature 433:892–895

Bennett J (1977) Phosphorylation of chloroplast membrane polypeptides. Nature 269:344–346

Ben-Shem A, Frolow F, Nelson N (2003) Crystal structure of plant photosystem I. Nature 426:630–635

Betterle N, Ballottari M, Zorzan S et al (2009) Light-induced dissociation of an antenna hetero-oligomer is needed for non-photochemical quenching induction. J Biol Chem 284(22):15255–15266

Boekema EJ, Dekker JP, van Heel MG et al (1987) Evidence for a trimeric organization of the photosystem I complex from the thermophililc cyanobacterium *Synechococcus* sp. FEBS Lett 217(2):283–286

Boekema EJ, Hankamer B, Bald D et al (1995) Supramolecular structure of the photosystem-II complex from green plants and cyanobacteria. Proc Natl Acad Sci U S A 92(1):175–179

Boekema EJ, van Roon H, Dekker JP (1998) Specific association of photosystem II and light-harvesting complex II in partially solubilized photosystem II membranes. FEBS Lett 424:95–99

Boekema EJ, van Roon H, Calkoen F et al (1999a) Multiple types of association of photosystem II and its light-harvesting antenna in partially solubilized photosystem II membranes. Biochemistry 38:2233–2239

Boekema EJ, van Roon H, van Breemen JFL et al (1999b) Supramolecular organization of photosystem II and its light-harvesting antenna in partially solubilized photosystem II membranes. Eur J Biochem 266:444–452

Boekema EJ, van Breemen JFL, van Roon H et al (2000) Arrangement of photosystem II supercomplexes in crystalline macrodomains within the thylakoid membrane of green plant chloroplasts. J Mol Biol 301:1123–1133

Boekema EJ, Jensen PE, Schlodder E et al (2001) Green plant photosystem I binds light-harvesting complex I on one side of the complex. Biochemistry 40:1029–1036

Boekema EJ, Folea M, Kouřil R (2009) Single particle electron microscopy. Photosynth Res 102:189–196

Bonaventura C, Myers J (1969) Fluorescence and oxygen evolution from *Chlorella pyrenoidosa*. Biochim Biophys Acta 189:366–383

Broess K, Trinkunas G, van Hoek A et al (2008) Determination of the excitation migration time in photosystem II – consequences for the membrane organization and charge separation parameters. Biochim Biophys Acta 1777:404–409

Büchel C (2015) Evolution and function of light harvesting proteins. J Plant Physiol 172:62–75

Burrows PA, Sazanov LA, Svab Z et al (1998) Identification of a functional respiratory complex in chloroplasts through analysis of tobacco mutants containing disrupted plastid ndh genes. EMBO J 17:868–876

Busch A, Hippler M (2011) The structure and function of eukaryotic photosystem I. Biochim Biophys Acta 1807:864–877

Caffarri S, Kouřil R, Kereïche S et al (2009) Functional architecture of higher plant photosystem II supercomplexes. EMBO J 28:3052–3063
Caffarri S, Tibiletti T, Jennings RC (2014) A comparison between plant photosystem I and photosystem II architecture and functioning. Curr Protein Pept Sci 15(4):296–331
Calderone V, Trabucco M, Vujicić A et al (2003) Crystal structure of the PsbQ protein of photosystem II from higher plants. EMBO Rep 4(9):900–905
Chen F, Dong G, Wu L et al (2016) A nucleus-encoded chloroplast protein YL1 is involved in chloroplast development and efficient biogenesis of chloroplast ATP synthase in rice. Sci Rep 6:32295
Correa-Galvis V, Poschmann G, Melzer M et al (2016) PsbS interactions involved in the activation of energy dissipation in *Arabidopsis*. Nat Plants 2:15225
Crepin A, Santabarbara S, Caffarri S (2016) Biochemical and spectroscopic characterization of highly stable photosystem II supercomplexes from Arabidopsis. J Biol Chem 291(36):19157–19171
Dainese P, Bassi R (1991) Subunit stoichiometry of the chloroplast photosystem-II antenna system and aggregation state of the component chlorophyll-a/b binding-proteins. J Biol Chem 266:8136–8142
Daum B, Nicastro D, Austin J et al (2010) Arrangement of photosystem II and ATP synthase in chloroplast membranes of spinach and pea. Plant Cell 22:1299–1312
de Bianchi S, Dall'Osto L, Tognon G et al (2008) Minor antenna proteins CP24 and CP26 affect the interactions between photosystem II subunits and the electron transport rate in grana membranes of Arabidopsis. Plant Cell 20:1012–1028
Dekker JP, Boekema EJ (2005) Supermolecular organization of the thylakoid membrane proteins in green plants. Biochim Biophys Acta 1706:12–39
Dietzel L, Bräutigam K, Steiner S et al (2011) Photosystem II supercomplex remodeling serves as an entry mechanism for state transitions in *Arabidopsis*. Plant Cell 23(8):2964–2977
Drop B, Webber-Birungi M, Fusetti F et al (2011) Photosystem I of Chlamydomonas reinhardtii contains nine light-harvesting complexes (Lhca) located on one side of the core. J Biol Chem 286(52):44878–44887
Drop B, Webber-Birungi M, Yadav SKN et al (2014) Light-harvesting complex II (LHCII) and its supramolecular organization in *Chlamydomonas reinhardtii*. Biochim Biophys Acta 1837:63–72
Dudkina NV, Oostergetel GT, Braun HP et al (2010a) Row-like organization of ATP synthase in intact mitochondria determined by cryo-electron tomography. Biochim Biophys Acta 1797:272–277
Dudkina NV, Kouřil R, Bultema JB et al (2010b) Imaging of organelles by electron microscopy reveals protein-protein interactions in mitochondria and chloroplasts. FEBS Lett 584:2510–2515
Fernandez-Leiro R, Scheres SH (2016) Unravelling biological macromolecules with cryo-electron microscopy. Nature 537:339–346
Galka P, Santabarbara S, Thi THK et al (2012) Functional analyses of the plant photosystem I-light-harvesting complex II supercomplex reveal that light-harvesting complex II loosely bound to photosystem II is a very efficient antenna for photosystem I in state II. Plant Cell 24:2963–2978
Gerotto C, Franchin C, Arrigoni G et al (2015) In vivo identification of photosystem II light harvesting complexes interacting with photosystem II subunit S. Plant Physiol 168:1747–1761
Hankamer B, Barber J, Boekema EJ (1997) Structure and membrane organization of photosystem II in green plants. Annu Rev Plant Physiol Plant Mol Biol 48:641–671
Harrer R (2003) Associations between light-harvesting complexes and photosystem II from *Marchantia polymorpha* L. determined by two- and three-dimensional electron microscopy. Photosynth Res 75:249–258
Ifuku K, Nakatsu T, Kato H et al (2004) Crystal structure of the PsbP protein of photosystem II from *Nicotiana tabacum*. EMBO Rep 5(4):362–367
Iwai M, Takizawa K, Tokutsu R et al (2010) Isolation of the elusive supercomplex that drives cyclic electron flow in photosynthesis. Nature 464(7292):1210–1203

Jansson S (1994) The light–harvesting chlorophyll a/b binding-proteins. Biochim Biophys Acta 1184:1–19

Jansson S, Andersen B, Scheller HV (1996) Nearest-neighbor analysis of higher-plant photosystem I holocomplex. Plant Physiol 112:409–420

Jarvi S, Suorsa M, Paakkarinen V et al (2011) Optimized native gel systems for separation of thylakoid protein complexes: novel super- and mega-complexes. Biochem J 439:207–214

Järvi S, Suorse M, Aro EM (2015) Photosystem II repair in plant chloroplasts – regulation, assisting proteins and shared components with photosystem II biogenesis. Biochim Biophys Acta 1847:900–909

Jensen PE, Rosgaard L, Knoetzel J et al (2002) Photosystem I activity is increased in the absence of the PSI-G subunit. J Biol Chem 277(4):2798–2803

Johnson MP, Goral TK, Duffy CD et al (2011) Photoprotective energy dissipation involves the reorganization of photosystem II light-harvesting complexes in the grana membranes of spinach chloroplasts. Plant Cell 23(4):1468–1479

Jordan P, Fromme P, Witt HT et al (2001) Three-dimensional structure of photosystem I at 2.5 Å resolution. Nature 411:909–917

Kirchhoff H (2013) Architectural switches in plant thylakoid membranes. Photosynth Res 116:481–487

Kirchhoff H, Haase W, Wegner S et al (2007) Low-light-induced formation of semicrystalline photosystem II arrays in higher plant chloroplasts. Biochemistry 46:11169–11176

Kirchhoff H, Lenhert S, Büchel C et al (2008) Probing the organization of photosystem II in photosynthetic membranes by atomic force microscopy. Biochemistry 47:431–440

Klimmek F, Sjodin A, Noutsos C et al (2006) Abundantly and rarely expressed Lhc protein genes exhibit distinct regulation patterns in plants. Plant Physiol 140:793–804

Knispel RW, Kofler C, Boicu M et al (2012) Blotting protein complexes from native gels to electron microscopy grids. Nat Methods 9:182–184

Kofer W, Koop HU, Wanne G et al (1998) Mutagenesis of the genes encoding subunits A, C, H, I, J and K of the plastid NAD(P)H-plastoquinone-oxidoreductase in tobacco by polyethylene glycol-mediated plastome transformation. Mol Gen Genet 258:166–173

Kouřil R, van Oosterwijk N, Yakushevska AE et al (2005a) Photosystem I: a search for green plant trimers. Photochem Photobiol Sci 4:1091–1094

Kouřil R, Zygadlo A, Arteni AA et al (2005b) Structural characterization of a complex of photosystem I and light-harvesting complex II of *Arabidopsis thaliana*. Biochemistry 44:10935–10940

Kouřil R, Oostergetel GT, Boekema EJ (2011) Fine structure of granal thylakoid membrane organization using cryo electron tomography. Biochim Biophys Acta 1807:368–374

Kouřil R, Dekker JP, Boekema EJ (2012) Supramolecular organization of photosystem II in green plants. Biochim Biophys Acta 1817:2–12

Kouřil R, Wientjes E, Bultema JB et al (2013) High-light vs. low-light: effect of light acclimation on photosystem II composition and organization in *Arabidopsis thaliana*. Biochim Biophys Acta 1827:411–419

Kouřil R, Strouhal O, Nosek L et al (2014) Structural characterization of a plant photosystem I and NAD(P)H dehydrogenase supercomplex. Plant J 77:568–576

Kouřil R, Nosek L, Bartoš J et al (2016) Evolutionary loss of light-harvesting proteins Lhcb6 and Lhcb3 in major land plant groups – break-up of current dogma. New Phytol 210:808–814

Kovacs L, Damkjær J, Kereïche S (2006) Lack of the light-harvesting complex CP24 affects the structure and function of the grana membranes of higher plant chloroplasts. Plant Cell 18:3106–3120

Koziol AG, Borza T, Ishida KI et al (2007) Tracing the evolution of the light-harvesting antennae in chlorophyll a/b-containing organisms. Plant Physiol 143:1802–1816

Kramer DM, Avenson TJ, Edwards GE (2004) Dynamics flexibility in the light reactions of photosynthesis governed by both electron and proton transfer reactions. Trends Plant Sci 9:349–357

Krauss N, Schubert WD, Klukas O et al (1996) Photosystem I at 4 Å resolution represents the first structural model of a joint photosynthetic reaction centre and core antenna system. Nat Struct Biol 3(11):965–973

Kurisu G, Zhang H, Smith JL et al (2003) Structure of the cytochrome b6f complex of oxygenic photosynthesis: tuning the cavity. Science 302:1009–1014
Li XP, BjörkmanO Shich C et al (2000) A pigment-binding protein essential for regulation of photosynthetic light harvesting. Nature 403:391–395
Liu Z, Yan H, Wang K et al (2004) Crystal structure of spinach light-harvesting complex at 2.72 Å resolution. Nature 428:287–292
Lunde C, Jensen PE, Haldrup A et al (2000) The PSI-H subunit of photosystem I is essential for state transitions in plant photosynthesis. Nature 408:613–615
Mazor Y, Borovikova A, Nelson N (2015) The structure of plant photosystem I super-complex at 2.8 Å resolution. Elife 4:e07433
Minagawa J (2011) State transitions – the molecular remodeling of photosynthetic supercomplexes that controls energy flow in the chloroplast. Biochim Biophys Acta 1807:897–905
Morosinotto T, Bassi R, Frigerio S et al (2006) Biochemical and structural analyses of a higher plant photosystem II supercomplex of a photosystem I-less mutant of barely. Consequences of a chronic over-reduction of the plastoquinone pool. FEBS J 273:4616–4630
Munekage Y, Hashimoto M, Miyake C et al (2004) Cyclic electron flow around photosystem I is essential for photosynthesis. Nature 429:579–582
Nelson N, Yocum CF (2006) Structure and function of photosystems I and II. Ann Rev Plant Biol 57:521–565
Nield J, Barber J (2006) Refinement of the structural model for the photosystem II supercomplex of higher plants. Biochim Biophys Acta 1757:353–361
Nield J, Orlova EV, Morris EP et al (2000) 3D map of the plant photosystem II supercomplex obtained by cryoelectron microscopy and single particle analysis. Nat Struct Biol 7(1):44–47
Nosek L, Semchonok D, Boekema EJ et al (2017) Structural variability of plant photosystem II megacomplexes in thylakoid membranes. Plant J 89:104–111
Pagliano C, Barera S, Chimirri F et al (2012) Comparison of the alpha and beta isomeric forms of the detergent n-dodecyl-D-maltoside for solubilizing photosynthetic complexes from pea thylakoid membranes. Biochim Biophys Acta 1817:1506–1515
Pagliano C, Saracco G, Barber J (2013) Structural, functional and auxiliary proteins of photosystem II. Photosynth Res 116:167–188
Pagliano C, Nield J, Marsano F et al (2014) Proteomic characterization and three-dimensional electron microscopy study of PSII-LHCII supercomplexes from higher plants. Biochim Biophys Acta 1837:1454–1462
Pan X, Li M, Wan T et al (2011) Structural insights into energy regulation of light-harvesting complex CP29 from spinach. Nat Struct Mol Biol 18:309–315
Peng LW, Shikanai T (2011) Supercomplex formation with photosystem I is required for the stabilization of the chloroplast NADH dehydrogenase-like complex in Arabidopsis. Plant Physiol 155:1629–1639
Peng LW, Shimizu H, Shikanai T (2008) The chloroplast NAD(P)H dehydrogenase complex interacts with photosystem I in Arabidopsis. J Biol Chem 283:34873–34879
Peng LW, Fukao Y, Fujiwara M et al (2009) Efficient operation of NAD(P)H dehydrogenase requires supercomplex formation with photosystem I via minor LHCI in Arabidopsis. Plant Cell 21:3623–3640
Peter GF, Thornber JP (1991) Biochemical-composition and organization of higher-plant photosystem-II light-harvesting pigment-proteins. J Biol Chem 266:16745–16754
Pribil M, Pesaresi P, Hertle A et al (2010) Role of plastid protein phosphatase TAP38 in LHCII dephosphorylation and thylakoid electron flow. PLoS Biol 8:e1000288
Qin X, Suga M, Kuang T et al (2015) Structural basis for energy transfer pathways in the plant PSI-LHCI supercomplex. Science 348(6238):989–995
Schubert WD, Klukas O, Krauss N et al (1997) Photosystem I of *Synechococcus elongatus* at 4 Å resolution: comprehensive structure analysis. J Mol Biol 272(5):741–769
Semchonok DA, Li M, Bruce BD et al (2016) Cyro-EM structure of a tetrameric cyanobacterial photosystem I complex reveals novel subunit interactions. Biochim Biophys Acta 1857:1619–1626

Shapiguzov A, Ingelsson B, Samol I et al (2010) The PPH1 phosphatase is specifically involved in LHCII dephosphorylation and state transitions in Arabidopsis. Proc Natl Acad Sci U S A 107:4782–4787

Shikanai T (2016) Chloroplast NDH: a different enzyme with a structure similar to that of respiratory NADH dehydrogenase. Biochim Biophys Acta 1857:1015–1022

Shikanai T, Endo T, Hashimoto T et al (1998) Directed disruption of the tobacco ndhB gene impairs cyclic electron flow around photosystem I. Proc Natl Acad Sci U S A 95:9705–9709

Standfuss R, van Scheltinga ACT, Lamborghini M et al (2005) Mechanisms of photoprotection and nonphotochemical quenching in pea light harvesting complex at 2.5 Å resolution. EMBO J 24:919–928

Stroebel D, Choquet Y, Popot JL et al (2003) An atypical haem in the cytochrome $b_6f$ complex. Nature 426:413–418

Tietz S, Puthiyaveetil S, Enlow HM et al (2015) Functional implications of photosystem II crystal formation in photosynthetic membranes. J Biol Chem 290:14091–14106

Tokutsu R, Kato N, Bui KH et al (2012) Revisiting the supramolecular organization of photosystem II in *Chlamydomonas reinhardtii*. J Biol Chem 287:31574–31581

van Oort B, Alberts M, de Bianchi S et al (2010) Effect of antenna-depletion in photosystem II on excitation energy transfer in *Arabidopsis thaliana*. Biophys J 98:922–931

van Roon H, van Breemen JFL, de Werd FL et al (2000) Solubilization of green plant thylakoid membranes with *n*-dodecyl-α,D-maltoside. Implications for the structural organization of the photosystem II, photosystem I, ATP synthase and cytochrome $b_6f$ complexes. Photosynth Res 64:155–166

Varotto C, Pesaresi P, Jahns P et al (2002) Single and double knockouts of the genes for photosystem I subunits G, K, and H of Arabidopsis. Effects on photosystem I composition, photosynthetic electron flow, and state transitions. Plant Physiol 129:616–624

Wei X, Su X, Cao P et al (2016) Structure of spinach photosystem II-LHCII supercomplex at 3.2 Å resolution. Nature 534(7605):69–74

Wientjes E, Oostergetel GT, Jansson S et al (2009) The role of Lhca complexes in the supramolecular organization of higher plant photosystem I. J Biol Chem 284:7803–7810

Wientjes E, Drop B, Kouřil R et al (2013) During state 1 to state 2 transition in *Arabidopsis thaliana*, the photosystem II supercomplex gets phosphorylated but does not disassemble. J Biol Chem 288:32821–32826

Wittig I, Schägger H (2005) Advantages and limitations of clear-native PAGE. Proteomics 5:4338–4346

Wittig I, Karas M, Schägger H (2007) High resolution clear native electrophoresis for in-gel functional assays and fluorescence studies of membrane protein complexes. Mol Cell Proteomics 6:1215–1225

Wollman FA (2001) State transitions reveal the dynamics and flexibility of the photosynthetic apparatus. EMBO J 20:3623–3630

Yadav KNS, Semchonok DA, Nosek L et al (2017) Supercomplexes of plant photosystem I with cytochrome b6f, light-harvesting complex II and NDH. Biochim Biophys Acta 1858:12–20

Yakushevska AE, Jensen PE, Keegstra W et al (2001a) Supermolecular organization of photosystem II and its associated light-harvesting antenna in *Arabidopsis thaliana*. Eur J Biochem 268:6020–6021

Yakushevska AE, Ruban AV, Jensen PE et al (2001b) Supermolecular organization of photosystem II and its associated light-harvesting antenna in the wild- type and npq4 mutant of *Arabidopsis thaliana*. In: PS2001 proceedings: 12th international congress on photosynthesis. CSIRO Publishing, Melbourne, p S5

Yakushevska AE, Keegstra W, Boekema EJ et al (2003) The structure of photosystem II in Arabidopsis: localization of the CP26 and CP29 antenna complexes. Biochemistry 42:806–813

Yamori W, Shikanai T (2016) Physiological functions of cyclic electron transport around photosystem I in sustaining photosynthesis and plant growth. Annu Rev Plant Biol 67:81–106

Yokono M, Takabayashi A, Akimoto S et al (2015) A megacomplex composed of both photosystem reaction centres in higher plants. Nat Commun 6:6675

# Chapter 10
# The Cytochrome $b_6f$ Complex: Biophysical Aspects of Its Functioning in Chloroplasts


**Alexander N. Tikhonov**

**Abstract** This chapter presents an overview of structural properties of the cytochrome (Cyt) $b_6f$ complex and its functioning in chloroplasts. The Cyt $b_6f$ complex stands at the crossroad of photosynthetic electron transport pathways, providing connectivity between Photosystem (PSI) and Photosysten II (PSII) and pumping protons across the membrane into the thylakoid lumen. After a brief review of the chloroplast electron transport chain, the consideration is focused on the structural organization of the Cyt $b_6f$ complex and its interaction with plastoquinol ($PQH_2$, reduced form of plastoquinone), a mediator of electron transfer from PSII to the Cyt $b_6f$ complex. The processes of $PQH_2$ oxidation by the Cyt $b_6f$ complex have been considered within the framework of the Mitchell's Q-cycle. The overall rate of the intersystem electron transport is determined by $PQH_2$ turnover at the quinone-binding site $Q_o$ of the Cyt $b_6f$ complex. The rate of $PQH_2$ oxidation is controlled by the intrathylakoid $pH_{in}$, which value determines the protonation/deprotonation events in the $Q_o$-center. Two other regulatory mechanisms associated with the Cyt $b_6f$ complex are briefly overviewed: (*i*) redistribution of electron fluxes between alternative (linear and cyclic) pathways, and (*ii*) "state transitions" related to redistribution of solar energy between PSI and PSII.

**Keywords** Photosynthesis · Chloroplasts · Electron transport control · Cytochrome $b_6f$ complex · Plastoquinone

A. N. Tikhonov (✉)
Faculty of Physics, Moscow State University, Moscow, Russia
e-mail: an_tikhonov@mail.ru



J. R. Harris, E. J. Boekema (eds.), *Membrane Protein Complexes: Structure and Function*, Subcellular Biochemistry 87,
https://doi.org/10.1007/978-981-10-7757-9_10

## Abbreviations

| | |
|---|---|
| CBC | Calvin-Benson cycle |
| CEF1 | cyclic electron flow around photosystem I |
| ETC | electron transport chain |
| Fd | ferredoxin |
| FNR | ferredoxin-NADP-oxidoreductase |
| ISP | iron-sulfur protein |
| LEF | linear electron flow |
| LHCI | light-harvesting complex I |
| LHCII | light-harvesting complex II |
| NDH | NDH(P)H dehydrogenase complex |
| NPQ | non-photochemical quenching |
| $P_{680}$ | special chlorophyll pair in PSII |
| $P_{700}$ | special chlorophyll pair in PSI |
| Pc | plastocyanin |
| PCET | proton-coupled electron transfer |
| PQ and $PQH_2$ | plastoquinone and plastoquinol, respectively |
| PSA | photosynthetic apparatus |
| PSI and PSII | photosystem I and photosystem II respectively |
| Q, SQ and $QH_2$ | general notations for three accessible redox states of quinone species – quinone (Q), semiquinone (SQ) and quinol ($QH_2$) |
| $TMQH_2$ | trimethylbenzoquinol |
| UQ and $UQH_2$ | ubiquinone and ubiquinol, respectively |
| WOC | water-oxidizing complex |

## 10.1 Introduction

Photosynthesis is one of the most important processes in nature. Photosynthetic organisms of oxygenic type (cyanobacteria, algae, higher plants), using the solar energy, assimilate carbon dioxide and produce molecular oxygen. The energy of light quanta absorbed by the pigment-protein complexes of photosystem I (PSI) and photosystem II (PSII) is converted into the energy of separated charges in photoreaction centers (Blankenship 2002; Cardona et al. 2012; Müh et al. 2012; Ruban 2012; Mamedov et al. 2015). The light-driven actuation of photoreaction centers initiates electron transfer along the photosynthetic electron transport chain (ETC). Two electrons extracted from the water molecule split by the water-oxidizing complex (WOC) of PSII, are passed to the terminal electron acceptor of PSI, $NADP^+$. PSI complex delivers electrons to $NADP^+$ through ferredoxin (Fd) and ferredoxin-NADP-oxidoreductase (FNR): PSI → Fd → FNR → $NADP^+$. The cytochrome (Cyt) $b_6f$ complex is another multisubunit complex, which plays a crucial role in photosynthetic electron transport, because it stands at the crossroad of electron transport

pathways between PSII and PSI. These photosystems are interconnected via the membrane-bound Cyt $b_6f$ complex and mobile electron carriers, plastoquinone (PQ), plastocyanin (Pc): $H_2O \rightarrow$ PSII $\rightarrow$ PQ $\rightarrow b_6f \rightarrow$ Pc $\rightarrow$ PSI. Electron transfer from $H_2O$ to $NADP^+$ is accompanied by alkalization of stroma (the volume between the chloroplast envelope and thylakoids) and acidification of the *intra*-thylakoid lumen (the internal volume of thylakoids). The light-induced uptake of protons from the bulk of stroma and the proton release in the lumen lead to generation of the *trans*-thylakoid difference in electrochemical potentials of hydrogen ions, $\Delta\tilde{m}_{H^+}$ (often termed as the proton-motive force), which serves as the driving force for operation of the ATP synthase complex $CF_0$ - $CF_1(ADP + P_i \rightarrow ATP + H_2O)$ (Mitchell 1966; Blankenship 2002; Junge and Nelson 2015). The macroergic products of the light-induced stages of photosynthesis, ATP and NADPH, are used mainly in biosynthetic reactions of the Calvin-Benson cycle (CBC) (Edwards and Walker 1983; Blankenship 2002).

In this Chapter, the structural and functional properties of the Cyt $b_6f$ complex are considered in the context of its interaction with $PQH_2$ (the double-reduced form of PQ) and feedback regulation of electron transport in chloroplasts. The reaction of $PQH_2$ oxidation by the Cyt $b_6f$ complex represents the "bottle-neck" link in the ETC between PSII and PSI, which virtually determines the overall rate of the intersystem electron transport in chloroplasts. The redox state of the PQ pool plays the pivoting role in regulation of photosynthetic processes, because it serves the role of a peculiar "sensor" (for review, see Pesaresi et al. 2010) that triggers the short-term and long-term mechanisms of photosynthetic apparatus (PSA) response to varying environmental conditions (Kramer et al. 2004; Cruz et al. 2007; Eberhard et al. 2008; Demmig-Adams et al. 2012; Horton 2012; Rochaix 2014; Puthiyaveetil et al. 2016). The flexibility of PSA functioning in chloroplasts is achieved by cooperation of several feedback mechanisms of electron transport control. These regulatory mechanisms include different events: (*i*) pH-dependent control of $PQH_2$ oxidation by the Cyt $b_6f$ complex, (*ii*) optimization of the light quanta partitioning between PSI and PSII ("state transitions") triggered by the Cyt $b_6f$ complex, and (*iii*) redistribution of electron fluxes through alternative pathways of electron transport. All these mechanisms are associated with the functioning of the Cyt $b_6f$ complex.

## 10.2 Photosynthetic Electron Transport Chain

The multisubunit electron-transport complexes are embedded into lamellar membranes of thylakoids, closed vesicles situated under the chloroplast envelope. Figure 10.1 depicts a scheme of basic electron transport pathways in chloroplasts. The peculiarities of functioning photoreaction centers of PSI, PSII, and the Cyt $b_6f$ complex are briefly considered below.

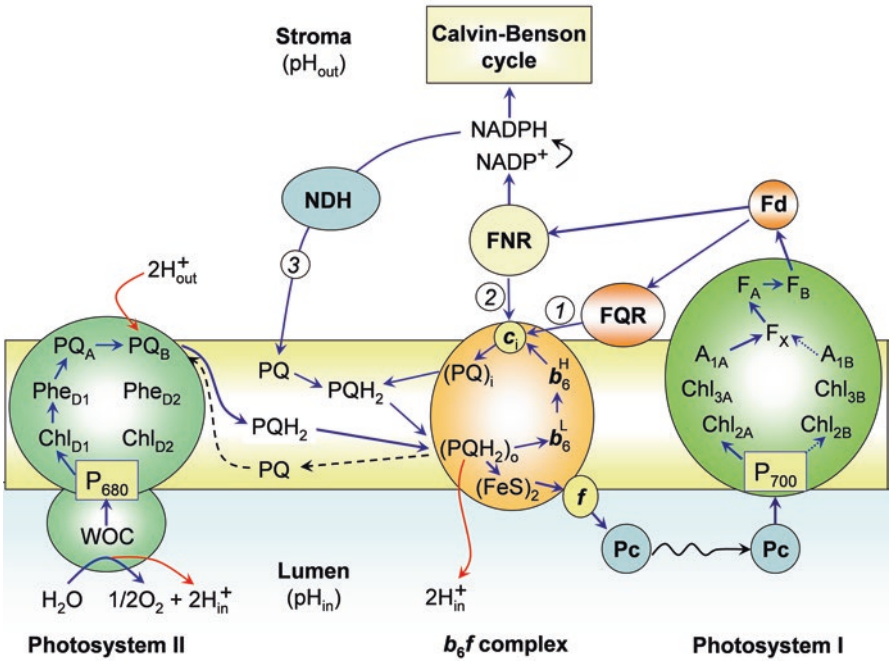


**Fig. 10.1** A scheme of electron transport pathways in chloroplasts and the arrangement of protein complexes (Photosystem I, Photosystem II, Cyt $b_6f$, FNR, and NDH) in the thylakoid membrane. Two electrons extracted from the water molecule in Photosystem II are transferred to plastoquinone (PQ), reducing PQ to plastoquinol ($PQH_2$). Electrons from $PQH_2$ are transferred via the Cyt $b_6f$ complex to reduce plastocyanin (Pc). Photosystem I oxidizes Pc on the lumenal side of the thylakoid membrane and reduces ferredoxin (Fd) on the stromal side of the membrane. Reduced Fd molecules donate electrons to $NADP^+$. Reduced and protonated NADPH molecules are consumed in the Calvin-Benson cycle. Electron transport processes are accompanied by accumulation of hydrogen ions in the thylakoid lumen (Modified from Figure 1 in Tikhonov 2014)

### *10.2.1 Photosystems I and II*

*Photosystem I* The multisubunit pigment-protein PSI complex catalyzes electron transfer from Pc (or Cyt $c_6$ in cyanobacteria) on the lumenal side of thylakoids to Fd (or flavodoxin) located in stroma (Brettel 1997; Jordan et al. 2001; Fromme et al. 2001; Nelson and Yocum 2006; Shelaev et al. 2010; Mamedov et al. 2015). Reduced ferredoxin ($Fd^-$) passes an electron to FNR, which provides the two-electron reduction of $NADP^+$ to NADPH. The core domain of the PSI complex contains a special pair of chlorophyll (Chl) *a* molecules ($Chl_{1A}$ and $Chl_{1B}$) located at the interface of subunits PsaA and PsaB, which form the primary electron donor termed $P_{700}$. The light-induced excitation of $P_{700}$ induces charge separation in PSI: excited center $P^*_{700}$ donates an electron to the primary electron acceptor ($Chl_{2A}$ or $Chl_{2B}$). On the acceptor side of PSI, electron carriers are arranged as two quasi-symmetrical cofactor branches, which consist of two Chl *a* molecules ($Chl_{2A}$ and $Chl_{3A}$ in A-branch;

$Chl_{2B}$ and $Chl_{3B}$ in B-branch) and one phylloquinone molecule ($A_{1A}$ or $A_{1B}$, respectively). The two branches converge at the acceptor $F_X$ (one of three $[FeS]_4$ clusters of PSI, $F_X$, $F_A$, and $F_B$). There are experimental evidences in favor of preferential role of A-branch in electron transfer on the acceptor side of PSI (for references, see Mamedov et al. 2015). From reduced $F_X$ the electron is transferred to Fd via the redox centers $F_A$ and $F_B$ ($F_X \rightarrow F_A \rightarrow F_B \rightarrow Fd$). Reduced Fd molecules deliver electrons to $NADP^+$ via FNR (Fig. 10.1).

Oxidized center $P_{700}^+$ accepts an electron from reduced Pc ($Pc^-$), which, in turn, accepts an electron from the Cyt $b_6f$ complex. Pc serves the role of the electron transfer shuttle, which, moving within the lumen, connects electronically the Cyt $b_6f$ complex and PSI. Lateral diffusion of $Pc^-$ inside the lumen, and further donation of an electron from $Pc^-$ to $P_{700}^+$, do not limit electron transport between PSII and PSI. Oxidation of $Pc^-$ by $P_{700}^+$ occurs more rapidly ($t_{1/2} < 200$ μs, at ambient temperatures) than electron transfer from PSII to Pc via the PQ pool and Cyt $b_6f$ complex ($t_{1/2} \geq 4 - 20$ ms) (Stiehl and Witt 1969; Witt 1979; Haehnel 1984).

*Photosystem II* PSII contains the primary electron donor $P_{680}$ and the water-oxidizing complex (WOC). Two electrons extracted from $H_2O$ in WOC ($H_2O \rightarrow 1/2O_2 + 2H^+ + 2e^-$) are used to reduce PQ to $PQH_2$. Transfer of electrons from $H_2O$ to PQ molecules proceeds as the result of consecutive one-electron reactions induced by light quanta absorbed by the light-harvesting antenna of PSII. A special pair of Chl *a* molecules embedded into the core of the PSII complex form the primary electron donor in PSII termed $P_{680}$ (for review, see Cardona et al. 2012, Müh et al. 2012). There are two branches of electron cofactors on the acceptor side of PSII, A-branch and B-branch. Excited redox center $P_{680}^*$ donates an electron to the primary electron acceptor of A-branch, Chl *a* molecule termed $Chl_{D1}$, which, in its turn, passes the electron to the secondary acceptor pheophytin (Phe): $P_{680}^* \rightarrow Chl_{D1} \rightarrow Phe_{D1}$. Reduced Phe donates the electron to the primary plastoquinone $PQ_A$ tightly bound to PSII ($Phe^- PQ_A PQ_B \rightarrow Phe\, PQ_A^- PQ_B$). $PQ_A^-$ reduces the secondary plastoquinone $PQ_B$ bound to PSII ($PQ_A^- PQ_B \rightarrow PQ_A PQ_B^-$). The second electron donated by $P_{680}^*$ to $PQ_A$ provides the double-electron reduction of $PQ_B$ ($PQ_A^- PQ_B^- \rightarrow PQ_A PQ_B^=$), which is followed by protonation of $PQ_B^=$ due to the uptake of two protons from stroma ($PQ_B^= + 2H_{out}^+ \rightarrow PQ_B H_2$). Reduced secondary plastoquinone, $PQ_B H_2$, dissociates from PSII in exchange for a new oxidized PQ molecule. Diffusing in the membrane, the hydrophobic $PQH_2$ molecule reaches the Cyt $b_6f$ complex. After binding of $PQH_2$ to the $Q_o$-center of this complex, the $PQH_2$ molecule oxidizes, donating two electrons to appropriate electron acceptors of the Cyt $b_6f$ complex and releasing two protons, which finally migrate into the bulk phase of the thylakoid lumen. On the donor side of PSII, decomposition of water molecules in the WOC is accompanied by the release of protons into the lumen. The overall balance of electron and proton transport processes in PSII is the following: (*i*) two electrons extracted from one $H_2O$ molecule are used to reduce PQ to $PQH_2$, and (*ii*) two protons are taken up from stroma and two protons apper in the lumen per one $PQH_2$ molecule formed ($H_2O + PQ + 2H_{out}^+ \rightarrow 1/2O_2 + PQH_2 + 2H_{in}^+$).

### 10.2.2 *The Role of Cytochrome* $b_6f$ *Complex in the Pathway Between Photosystems I and II*

The Cyt $b_6f$ complex (plastoquinol:plastocyanin oxidoreductase) is organized as the hetero-oligomeric protein complex, which mediates electron transfer between PSII and PSI by oxidizing $PQH_2$ and reducing Pc. Three-dimentional structures of this complex were initially obtained at a resolution of 3.0–3.1 Å from the thermophilic filamentous cyanobacterium *Mastigocladus laminosus* (PDB entry 1VF5; Kurisu et al. 2003), and the green alga *Chlamydomonas reinhardtii* (PDB entry 1Q90; Stroebel et al. 2003), in the presence of the quinone analogue inhibitor, tri-decyl-stigmatellin (TDS). The crystal structures of the Cyt $b_6f$ complexes from *M. laminosus* and *C. reinhardtii* are similar. The Cyt $b_6f$ complex is organized as the functional dimer of multisubunit monomers (Fig. 10.2). Dimeric organization of the Cyt $b_6f$ complex is similar, in general, to that of the Cyt $bc_1$ complex of the Cyt *bc* family (Xia et al. 1997, 2013; Iwata et al. 1998; Berry et al. 2000; Crofts 2004a; Cramer et al. 2006, 2011). Each multisubunit monomer of the functional dimer of the Cyt $b_6f$ complex consists of eight polypeptide subunits with 13 *trans*-membrane helixes, including four "large" (16–31 kDa) polypeptide subunits (petA, B, C, and D): the iron-sulfur protein (ISP) Rieske, the Cyt $b_6$ and Cyt *f* proteins, and subunit IV (Fig. 10.3). "Small" (3.3–4.1 kDa) hydrophobic subunits (petG, L, M, and N), each of them containing one *trans*-membrane helix, are arranged at the outside periphery of the monomer ensembly of petA, B, C, and D subunits.

The catalytic functions of the Cyt $b_6f$ complex are provided by four redox centers bound to the "large" subunits: the Rieske iron-sulfur cluster [$Fe_2S_2$], two hemes of the Cyt $b_6$ (the low-potential heme $b_6^L$ and the high-potential heme $b_6^H$), and heme *f* of the Cyt *f*. These cofactors are involved in the electron transfer reactions within the Cyt $b_6f$ complex. Furthermore, there are three unusual prosthetic groups: (1) Chl *a*, (2) $\beta$ -carotene, and (3) a unique heme $c_i$ (Stroebel et al. 2003), which is often

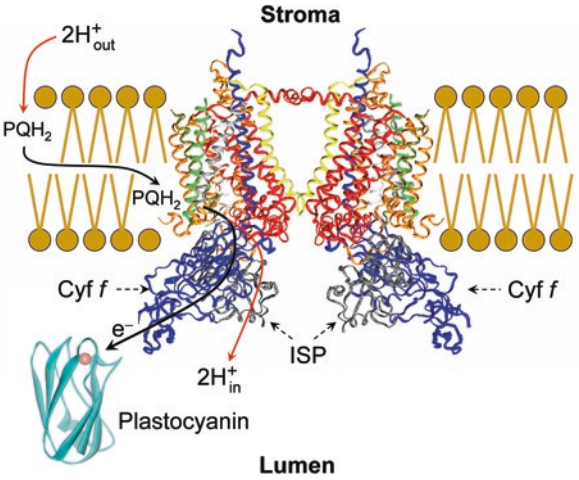


**Fig. 10.2** The side view of the dimeric Cyt $b_6f$ complex from *Chlamydomonas reinhardtii* (PDB entry 1Q90, Stroebel et al. 2003). Figure was produced using Accelerys DV visualizer software package (http://www.accelrys.com) (Modified from Figure 2 in Tikhonov 2014)

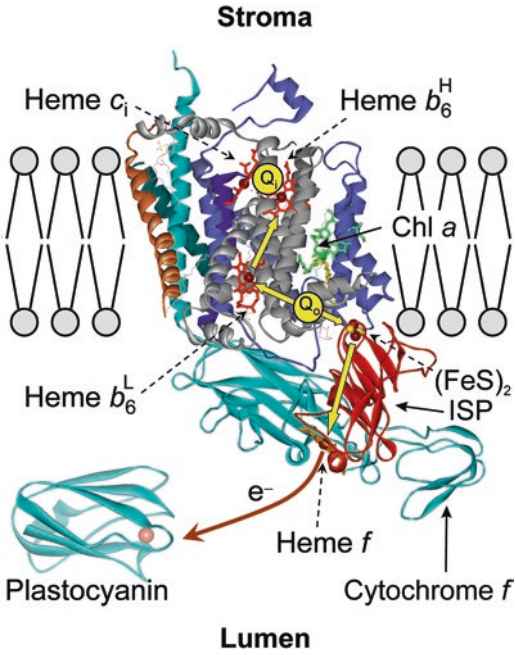


**Fig. 10.3** Overview of structure and function of the Cyt $b_6f$ complex from *Chlamydomonas reinhardtii* (PDB entry 1Q90, Stroebel et al. 2003). The view is perpendicular to the membrane plane. Colour code of main polypeptides: cyan, Cyt *f*; grey, Cyt $b_6$; purple, the iron-sulfur protein; blue, subunit IV. Cofactors: red, hemes $b_6^L$, $b_6^H$, and $c_i$, as indicated; orange, heme *f*; Fe atoms are shown as dark red spheres; green, Chl *a*. For true colours of subunits and cofactors see the online version of this Chapter. Plastoquinone binding site $Q_o$ is positioned between heme $b_6^L$ and the $[Fe_2S_2]$ cluster of the iron-sulfur protein. Plastoquinone binding site $Q_i$ is placed between hemes $b_6^H$ and $c_i$ (Modified from Figure 3 in Tikhonov 2014. Figure was produced using Accelrys DV visualizer software package (http://www.accelrys.com))

termed as heme $c_n$ because of its location on the "negative" side of the membrane (Kurisu et al. 2003). Heme $c_i(c_n)$ is bound covalently to the Cyt $b_6f$ complex in close proximity to the high-potential heme $b_6^H$. The Cyt $b_6$ and Cyt *f* subunits are functionally analogous to the Cyt $b_6$ and Cyt $c_1$ proteins in the mitochondrial and bacterial Cyt $bc_1$ complexes (Xia et al. 1997, 2013; Iwata et al. 1998; Berry et al. 2000; Crofts 2004a). The Cyt $b_6f$ complex contains the binding centers for $PQH_2$ and PQ molecules. Crystallization of the Cyt $b_6f$ complexes with quinone analogue inhibitors, TDS and NQNO (2*n*–nonyl-4-hydroxy-quinoline-*N*-oxide) revealed two sites for quinone binding: the $Q_o$-center (quinol oxidase) and the $Q_i$-center (quinone reductase) (Yamashita et al. 2007). The quinone exchange cavity of the site $Q_o$ is positioned near the $[Fe_2S_2]$ cluster of the ISP. Site $Q_i$ is located on the stromal side of the complex, at the interface between heme $c_i$ and the large inter-protein quinone exchange cavity.

Oxidation of $PQH_2$ occurs at the catalytic center $Q_o$, which is situated in the cavity at the interface between the Cyt $b_6$ subunit and the ISP. This center is oriented

towards the lumenal side of the thylakoid membrane. The oxidation of $PQH_2$ in the $Q_o$ -site is accompanied by dissociation of two protons, which finally appear in the aqueous bulk phase of the thylakoid lumen. According to the Q-cycle mechanism first suggested by Peter Mitchell (1976), the two-electron oxidation of $PQH_2$ in the $Q_o$ -center is a bifurcated reaction (Berry et al. 2000; Crofts 2004a, b; Osyczka et al. 2004, 2005; Mulkidjanian 2005; Cramer et al. 2006, 2011; Crofts et al. 2013; Xia et al. 2013). One electron is directed from $PQH_2$ to a high-potential chain, the other electron travels along a low-potential chain (Fig. 10.3). The first electron comes to Pc through the high-potential redox chain, which consists of the ISP and Cyt $f$ ($PQH_2 \rightarrow ISP \rightarrow Cyt\,f \rightarrow Pc$). The second electron is directed to reduce PQ at the $Q_i$ -site on the stromal side, traveling through the low- and high-potential hemes $b_6^L$ and $b_6^H : \left(PQH^{\circ}\right)_o \rightarrow b_6^L \rightarrow b_6^H \rightarrow \left(PQ\right)_i$. Here, $(PQH^{\bullet})_o$ denotes the semiquinone form of plastoquinone formed upon the bifurcated oxidation of $PQH_2$ at the $Q_o$-site, $(PQ)_i$ denotes the PQ molecule bound to the quinone-binding site $Q_i$ located in the stromal part of the Cyt $b_6f$ complex.

In the $Q_i$-center, after two successive steps of PQ reduction to $PQ^{=}$, two protons are taken up from stroma ($PQ + 2e^- + 2H^+_{out} \rightarrow PQH_2$). The protonated (electrically neutral) $PQH_2$ molecule dissociates from the $Q_i$-site and now it can bind to the vacant $Q_o$-site to be oxidized on the lumenal side of the Cyt $b_6f$ complex. Due to the round trip of one electron in the Q-cycle, the proton pumping activity of the Cyt $b_6f$ complex increases by a factor of 2. Taking into account the overall balance of PQ turnover in the Q-cycle, we see that two hydrogen ions are pumped into the lumen per one electron ($H^+/e^- = 2$) transferred from $PQH_2$ to $P^+_{700}$ via the high-potential chain ($ISP \rightarrow Cyt\ f \rightarrow Pc \rightarrow P^+_{700}$). Note that the unique heme $c_i$ may be an adaptation of photosynthetic organisms for cyclic route of electron flow around PSI. Electrons from the acceptor side of PSI may return to the $Q_i$-center of the Cyt $b_6f$ complex via Fd, FNR, and/or an atypical heme $c_i$ (Kurisu et al. 2003; Stroebel et al. 2003; Munekage et al. 2004; Joliot and Joliot 2005; Shikanai 2007).

### *10.2.3 The Cytochrome* $b_6f$ *Complex and Alternative Pathways of Electron Transport*

The Cyt $b_6f$ complex is the participant of cyclic electron transport around PSI. On the acceptor side of PSI, apart from the mainstream pathway of electron flow to the CBC (the so-called "linear" electron flow, LEF), the electron flux may be diverted to cyclic routes around PSI. Cyclic electron flow around PSI (CEF1) is important for fine-tuning of the energy and redox balance in chloroplasts. There is general consensus that CEF1 helps to sustain the ratio ATP/NADPH = 3/2 required for optimal functioning of the CBC (for review, see Bendall and Manasse 1995; Allen 2003; Cruz et al. 2007; Johnson 2011; Strand et al. 2016). The light-induced transfer of four electrons from two $H_2O$ molecules to two $NADP^+$ molecules driven by the tandem operation of PSII and PSI ($2H_2O + 2NADP^+ \rightarrow O_2 + 2NADPH$) is

accompanied by pumping of 12 protons into the thylakoid lumen. This number of protons is insufficient for synthesis of three ATP molecules required to provide the ratio ATP/NADPH = 3/2. Actually, in chloroplasts the stoichiometric ratio $n = H^+/ATP$ for the ATP synthase reaction ($ADP + P_i + nH_{in} \rightarrow ATP + nH_{out}$) is higher than $n = 4$ (Seelert et al. 2000; Junge and Nelson 2015; Turina et al. 2016). Therefore, 12 protons translocated inside the thylakoid per two NADPH molecules formed is insufficient to maintain the required ratio ATP/NADPH = 3/2. Additional pumping of protons coupled to operation of CEF1 could contribute to generation of $\Delta\tilde{m}_{H^+}$, providing synthesis of "extra" ATP molecules. Thus, the synergism of two pathways, LEF and CEF1, helps to maintain the ratio ATP/NADPH = 3/2 required for $CO_2$ fixation in the CBC. Even a relatively small contribution of CEF1 to generation of ΔpH may be enough to supplement ATP formation, providing thus the well-balanced ATP/NADPH ratio. CEF1 is also important for effective responses of PSA to fluctuations of light intensity, thereby avoiding the risk of photodamage to chloroplasts (Suorsa et al. 2012; Kono and Terashima 2014; Kono et al. 2014; Yamori and Shikanai 2016).

Most of CEF1 pathways involve the Cyt $b_6f$ complex (Fig. 10.1). Recent genetic and biochemical studies clarified the physiological role of CEF1 and helped to elucidate the participation of different chloroplast proteins in CEF1 (for review, see Shikanai 2007).There are several routes of electron flow on the acceptor side of PSI, when electrons from PSI may be delivered to different channels (for recent review, see Strand et al. 2016). Electrons from PSI can be recycled to PQ from either reduced Fd ($Fd^-$) or NADPH ("short" and "long" rounds, respectively). There are two "short' pathways of CEF1 related to electron transfer from $Fd^-$ to PQ molecule bound to the $Q_i$-center mediated by the ferredoxin-plastoquinone-reductase (FQR) and FNR, without the participation of NADPH (pathways *1* and *2* depicted in Fig. 10.1). The "long" pathway of CEF1 involves the formation of NADPH and return of electrons through the chloroplast NAD(P)H-dehydrogenase (NDH): PSI → Fd → FNR → NADPH → NDH → PQ (Fig. 10.1, pathway *3*).

One of the "short" routes of CEF1 implies the participation of the elusive FQR complex: PSI → Fd → FQR → PQ → $b_6f$ (Bendall and Manasse 1995). It has been demonstrated that the products of two genes, *PGR5* (proton gradient regulation) and *PGRL1* (*PGR5*–like protein 1), may be involved into Fd-dependent CEF1 in eukaryotes (Munekage et al. 2002, 2004, 2008; Shikanai 2007; DalCorso et al. 2008; Suorsa et al. 2012; Hertle et al. 2013). Plants deficient in one of these proteins show disturbed CEF1, suggesting that *PGR5* and *PGRL1* may be considered as the components of FQR. The exact role of these proteins in CEF1 was unclear until it was demonstrated that *PGRL1* accepted electrons from $Fd^-$ in a *PGR5*-dependent manner and reduced PQ (Hertle et al. 2013). These observations serve as compelling evidence that *PGRL1* operates as the elusive FQR protein. It is interesting to note that *PGRL1* is the redox regulated protein, its activity requires a Fe-containing cofactor and six redox-active cysteine residues. *PGR5* is used for electron transfer from $Fd^-$ to *PGRL1*. Both proteins, *PGR5* and *PGRL1*, are necessary for PSA protection against photodamage induced by rapid fluctuations of ambient light (Munekage et al. 2008; Suorsa et al. 2012).

Another "short" route of Fd-dependent CEF1 implies the return of electrons from PSI to PQ through the FNR complex. The formation of a supercomplex FNR - $b_6f$ (Zhang et al. 2001; Benz et al. 2010) may facilitate the direct electron transfer to the $Q_i$-site of the Cyt $b_6f$ complex (Fig. 10.1, pathway 2). However, the nature of the immediate electron donor to PQ molecule at the $Q_i$-site is under debate (Shikanai 2007; DalCorso et al. 2008; Iwai et al. 2010; Johnson 2011). There are reasons to believe that an atypical heme $c_i$ positioned on the stromal side of the Cyt $b_6f$ complex may serve as the immediate electron donor to PQ (Kurisu et al. 2003; Stroebel et al. 2003; Alric et al. 2005; Cramer et al. 2006, 2011; Hasan et al. 2013a). The PQ molecule bound to the $Q_i$-center may be reduced to $PQH_2$ by electrons coming from different chains. One electron comes from the high-potential heme $b_6^H$, whereas the second electron will arrive from PSI (Fig. 10.1, pathways *1* and *2*). The reduced $PQH_2$ molecule dissociates from the $Q_i$-site and then can return to the $Q_o$-center, participating in the next cycle of $PQH_2$ turnover.

In the "long" (NADPH-dependent) route of CEF1, the NDH complex returns electrons from NADPH (and/or NADH) to the intersystem ETC (Fig. 10.1, pathway 3). Genetic and biochemical data give unequivocal evidence for participation of the chloroplast NDH in the "long" route of CEF1 (Burrows et al. 1998; Endo et al. 1998; Shikanai et al. 1998; Joët et al. 2001; Shikanai 2016). There are indications that the NDH and PSI complexes can form a supercomplex (NDH-PSI) in higher plants (Peng et al. 2008, 2009) and cyanobacteria (Kubota et al. 2009). The location of NDH in the stromal lamellae close to PSI as well as an elevated content of NDH in the bundle sheath cells of $C_4$ plants with high levels of CEF1 (Kubicki et al. 1996) support the notion of NDH participation in CEF1.

### *10.2.4 Lateral Heterogeneity of Thylakoid Membranes*

The participation of the Cyt $b_6f$ complex in CEF1 depends on its location in the thylakoid membrane. The arrangement of membrane-embedded electron transport complexes and mobile electron carriers with respect to stromal and granal thylakoids is shown schematically in Fig. 10.4. It is well-known fact that PSI, PSII, and ATP synthase ($CF_0$ - $CF_1$) complexes are distributed nonuniformly over the membranes of granal and stromal thylakoids (Albertsson 2001; Staehelin 2003; Dekker and Boekema 2005). Stacked thylakoids of grana are enriched with PSII; most PSI and $CF_0$ - $CF_1$ complexes are localized in the unstacked domains of stroma-exposed thylakoids, grana margins, and grana end membranes. The Cyt $b_6f$ complexes are spread almost uniformly along the thylakoid membranes (Anderson 1982). About 55% of the Cyt $b_6f$ complexes are localized in appressed membranes of grana, and about 45% of complexes are distributed over the stromal lamellae, in the margins and grana end membranes. Although significant amounts of PSI, PSII, and Cyt $b_6f$ complexes are laterally segregated in the thylakoid membrane, most of them are in close contact. The content of different electron-transport complexes and their ratio (PSII/$b_6f$/PSI) are variable, being sensitive to the plant growth conditions (for

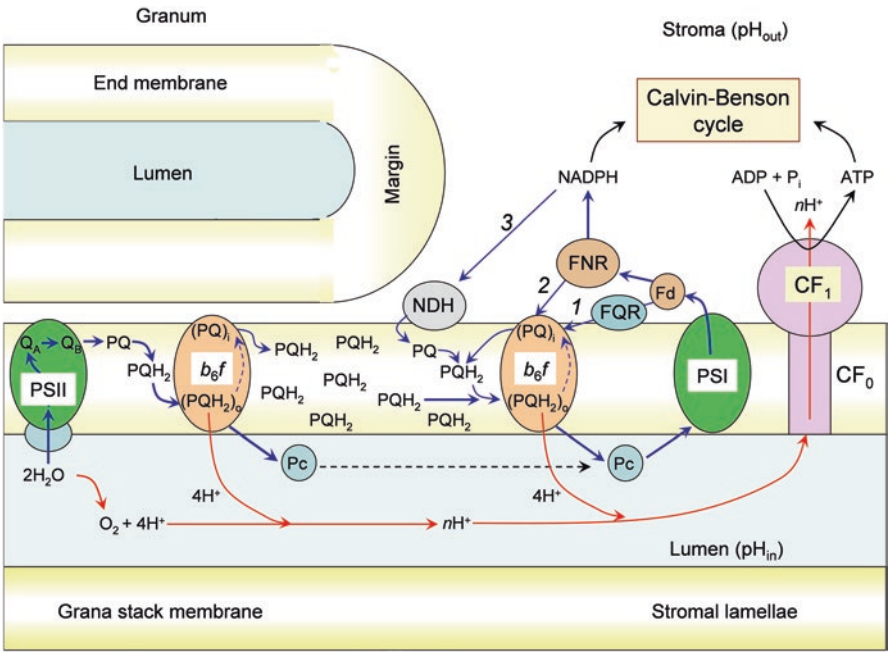


**Fig. 10.4** A scheme of the possible arrangement of the electron transport and ATP synthase complexes in the stromal and granal domains of the thylakoid membrane (Modified from Figure 4 in Tikhonov 2014)

review, see Anderson et al. 1988; Lichtenthaler and Babani 2004; Eberhard et al. 2008; Schöttler et al. 2015; Puthiyaveetil et al. 2016). The amounts of PQ and Pc are higher than that of PSI or PSII. The relative capacity of the PQ pool, related to PSII, was estimated as PQ/PSII ~ 10 times (Stiehl and Witt 1969; Witt 1979; Haehnel 1984).

It is important to note that there are two population of the Cyt $b_6f$ complex, that differ from each other with respect to their location in the stromal and granal domains of thylakoid membranes. Under the normal physiological conditions, grana-exposed thylakoids are assembled in the form of grana consisting of tightly packed thylakoid disks. Because of steric restrictions, direct contacts of granal Cyt $b_6f$ complexes with the FNR complexes will be excluded. This circumstance suggests that only the stroma-exposed fraction of Cyt $b_6f$ complexes may participate in the CEF1 reactions (Joliot and Joliot 2005, 2006). Although significant amounts of PSI and PSII complexes are laterally segregated, most of them are in close contact with the Cyt $b_6f$ complexes (Albertsson 2001). The proximal location of the Cyt $b_6f$ complexes to PSII in granal domains of thylakoid membranes should facilitate electron transfer between PSII and the Cyt $b_6f$ complexes due to a short distance for $PQH_2$ diffusion in the lipid phase of the membrane (Kirchhoff 2013, 2014). This circumstance may shed a light on the nature of the rate-limiting step in the intersystem chain of electron transport, considered below.

### 10.2.5 The Rate-Limiting Step in the Intersystem Chain of Electron Transport

The rate of PQ turnover is determined by several events: PQ reduction to $PQH_2$ $\left(PQ_B + 2e^- + 2H^+_{out} \rightarrow PQ_BH_2\right)$, dissociation of $PQH_2$ from PSII, its diffusion towards the Cyt $b_6f$ complex, and oxidation of $PQH_2$ at the $Q_o$-site. The peculiarities of chloroplast architecture raise the question as to whether or not the lateral and transverse diffusion of $PQH_2$ molecules within the thylakoid membrane would restrict the intersystem electron transfer. Which stage of $PQH_2$ oxidation determines the rate of $PQH_2$ turnover, either the lateral diffusion of $PQH_2$ in the membrane between spatially separated electron transport complexes or $PQH_2$ oxidation after its binding to the Cyt $b_6f$ complex? There are indications that the lateral diffusion of $PQH_2$ may restrain electron transfer from PSII to PSI under certain conditions (Lavergne and Joliot 1991; Kirchhoff 2008, 2014). Diffusion of $PQH_2$ within the membrane may be retarded due to obstructed diffusion of $PQH_2$ through the lipid domains, over-crowded with densely packed protein complexes. In the meantime, as noted above, the distribution of Cyt $b_6f$ complexes among PSII complexes located in granal thylakoids minimizes the average distance traversed by PQ molecules, providing rapid turnover of the PQ shuttle between the Cyt $b_6f$ and PSII complexes.

In earlier work (Stiehl and Witt 1969), these authors scrutinized in detail the PQ turnover in spinach chloroplasts by optical methods. Redox transients of $PQH_2$ were measured by monitoring absorption changes in the UV region. It was demonstrated that $PQH_2$ delivered electrons to $P^+_{700}$ (via intermediates) with the half-time $t_{1/2} \approx 15 - 17.5$ ms. Similar times were obtained by Haehnel for Cyt $f$ and $P^+_{700}$ reduction (Haehnel 1973, 1976a, b). Electron transfer from the Cyt $b_6f$ complex to $P^+_{700}$ occured much more rapidly than $PQH_2$ oxidation: $t_{1/2} \approx 35 - 350$ μs for electron transfer from Cyt $f$ to Pc, and $t_{1/2} \approx 20 - 200$ μs for electron transfer from Pc to $P^+_{700}$ (Haehnel 1984; Hope 2000). These results unequivocally demonstrated that $PQH_2$ interaction with the Cyt $b_6f$ complex to be the rate-limiting event in the chain of electron transport processes between PSII and PSI.

There is strong evidence that within a wide range of experimental conditions (pH, ionic strength, and temperature) $PQH_2$ formation and its diffusion in the membrane do not limit the intersystem electron transport. The light-induced reduction of PQ in PSII $\left(PQ_B + 2e^- + 2H^+_{out} \rightarrow PQ_BH_2\right)$, dissociation of $PQ_BH_2$ from PSII ($PQ_BH_2 \rightarrow PQH_2$) and $PQH_2$ diffusion to the Cyt $b_6f$ complex occur more rapidly than $PQH_2$ interaction with the Cyt $b_6f$ complex (Haehnel 1976a; Tikhonov et al. 1984). This statement can be illustrated by the experimental data presented in Fig. 10.5. In chloroplasts pre-illuminated with the far-red light ($\lambda_{max}$ = 707 nm) exciting predominantly PSI, the PQ pool and most of $P_{700}$ centers become oxidized because of negligible injection of electrons from PSII to the intersystem ETC. In response to a short flash of white light exciting both photosystems, electrons donated by PSII are used to reduce oxidized centers $P^+_{700}$ (Fig. 10.5a). In the particular case of $Mg^{2+}$-depleted chloroplasts, the reduction of $P^+_{700}$ proceeds after a well-resolved

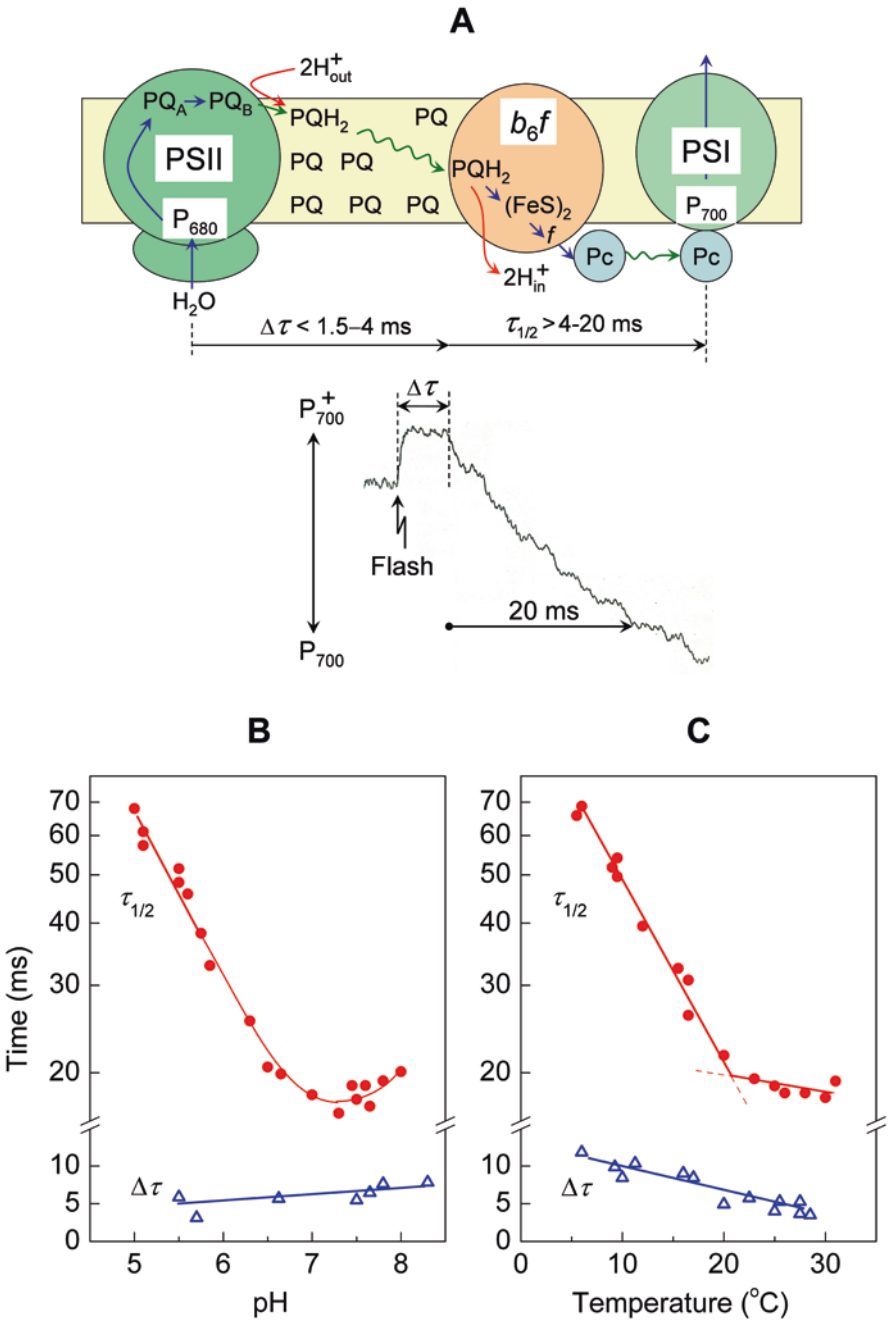


**Fig. 10.5** Panel **A** shows the kinetics of $P_{700}$ redox transients induced by a short pulse ($t_{1/2}$ = 7 μs) of white light given on the background of a continuous far-red light ($\lambda_{max}$ = 707 nm). Panels **B** and **C** illustrate the influence of pH and temperature on kinetic parameters $\Delta t$ and $\tau_{1/2}$ for $P_{700}$ transients (see panel **A** for definition) (Modified figures adopted from Tikhonov (2014, panel A) and Tikhonov et al. (1984, panels **B** and **C**))

lag-phase, the duration of which ($\Delta\tau$) involves the time of $PQH_2$ formation and diffusion across and along the thylakoid membrane towards the Cyt $b_6f$ complex. The half-time of $P_{700}^+$ reduction, which is determined mainly by electron transfer from $PQH_2$ bound to the Cyt $b_6f$ complex, is markedly higher than the lag-phase $\Delta\tau$ (Fig. 10.5a). This observation demonstrates that $PQH_2$ oxidation at the $Q_o$-site of the Cyt $b_6f$ complex represents the "bottle-neck" in the ETC between PSII and PSI, which controls the overall rate of the intersystem electron transport. Actually, the interaction of $Pc^-$ with $P_{700}^+$ usually occurs much more rapidly ($t_{1/2} \leq 200$ μs, at ambient temperatures) than electron transfer from $PQH_2$ to Pc via the Cyt $b_6f$ complex (Stiehl and Witt 1969; Witt 1979; Haehnel 1984). The duration of the lag-phase $\Delta\tau$ is sensitive to $Mg^{2+}$-induced structural changes in chloroplasts. At physiological concentrations of $MgCl_2$ (2–4 mM), $\Delta\tau$ is significantly shorter than in $Mg^{2+}$-depleted chloroplasts, although the addition of $MgCl_2$ had no marked effect on $\tau_{1/2}$ (Tikhonov et al. 1984). Since the lag-phase $\Delta\tau$ is always shorter ($\Delta\tau \leq 4$ ms) than the half-time of $P_{700}^+$ reduction ($t_{1/2} \approx 18 - 20$ ms), one can conclude that the formation of $PQH_2$ and its diffusion to the Cyt $b_6f$ complex occur more rapidly than $PQH_2$ oxidation at the $Q_o$-site.

A significant difference between kinetic parameters $\Delta\tau$ and $\tau_{1/2}$ was observed over a wide range of pH (Fig. 10.5b) and temperature (Fig. 10.5c). These observations provide clear evidence that the overall rate of the intersystem electron transfer is determined mainly by $PQH_2$ oxidation at the $Q_o$-site, a rate that decelerates with the lumen acidification and a decrease in temperature. Short times of $PQH_2$ diffusion from PSII to the Cyt $b_6f$ complex may be accounted for, at least partly, by the close neighbourhood of these complexes in the granal domains of the thylakoid membrane. Note that the temperature dependence of $P_{700}^+$ reduction in isolated bean chloroplasts reveals the characteristic "break" at ≈20°C. Below this temperature (≤20°C), kinetic parameter $\tau_{1/2}$ (the half-time of $P_{700}^+$ reduction) strongly depends on the temperature; at higher temperatures (≥20°C), $\tau_{1/2}$ is almost independent of temperature. As it was demonstrated in earlier works (Tikhonov et al. 1980, 1983), this peculiarity of the temperature dependence of $\tau_{1/2}$ (as well as the rate of ATP synthesis) strongly correlates with thermo-induced structural changes detected in the lipid phase of the thylakoid membrane with the lipid-soluble spin-probes (nitroxide radicals). One can speculate, therefore, that thermoinduced changes in the lipid phase of the thylakoid membrane can affect the rate of PQ turnover. For instance, "solidification" of the lipid bilayer with lowering the temperature may reduce the rate of the $PQH_2$ - $b_6f$ complex formation, and/or would cause the slowing down of $PQH_2$ oxidation due to decelerated release of protons into the lumen, which is considered as the prerequisite for $PQH_2$ oxidation by the Cyt $b_6f$ complex.

The notion that a relatively high mobility of $PQH_2$ in the thylakoid membrane finds support from computer simulation of PQ diffusion, suggests that $PQH_2$ could travel farther than 290 nm in 10 ms (Tremmel et al. 2003). This estimate is in agreement with experimental data, demonstrating that electron transfer between PSII to PSI is not limited by $PQH_2$ migration along the thylakoid membrane. High rates of $PQH_2$ diffusion in the thylakoid membrane suggest that the rate of PQ turnover in

chloroplasts is determined predominantly by the events associated with the $PQH_2$ penetration to the $Q_o$-cavity and its oxidation within the Cyt $b_6f$ complex (for review, see Tikhonov 2013, 2014).

Summing up the above reasonings, one can conclude that the light-induced reduction of PQ to $PQH_2$ in PSII occurs much more rapidly than $PQH_2$ oxidation by the Cyt $b_6f$ complex. It is noteworthy, however, that experimental data for partial reactions of electron transfer within the Cyt $b_6f$ complex are often scattered, depending on the system investigated and its metabolic state. For instance, the post-illumination reduction of Cyt *f* in different species of intact leaves was characterized by half-times ranging from 20 to 28 ms for a wide range of light intensities (up to 2800 of photons μmol $m^{-2}s^{-1}$, Kramer et al. 1999). Alternatively, several authors reported a more rapid turnover of the Cyt $b_6f$ complex in leaves (Harbinson and Hedley 1989; Laisk et al. 2005). Relatively short apparent times of Cyt *f* and Cyt *b* reduction ($t_{1/2} \approx 3 - 6$ ms) are typical of intact *C. reinhardtii* cells (Soriano et al. 1996; Ponamarev and Cramer 1998) and the cyanobacterium *Synechococcus* sp. PCC 7002 (Yan and Cramer 2003). Dispersion of kinetic data might be explained by several reasons, e.g., due to differences between the species and variable stoichiometry between PSII, Cyt $b_6f$, and PSI complexes (Schöttler et al. 2015; Puthiyaveetil et al. 2016). Variability of electron capacities of redox partners on the donor and acceptor sides of the Cyt $b_6f$ complex may also influence the kinetic behaviour of the system, exaggerating or underestimating the contributions of rapid and slow phases of electron transport processes (for recent discussion of this point, see Tikhonov 2016). Nevertheless, the rate of $PQH_2$ oxidation in the Cyt $b_6f$ complex comprises the rate-limiting step in the chain of electron transport between PSII and PSI.

Let us now consider another aspect of $PQH_2$ interaction with the Cyt $b_6f$ complex related to variability of the rates of $PQH_2$ oxidation and $P_{700}^+$ reduction. Speaking of kinetic peculiarities of $PQH_2$ interaction with the Cyt $b_6f$ complex, one has to take into account connectivity between spatially separated electron transport complexes via the mobile electron carriers, PQ and Pc (this scenario is depicted symbolically in Fig. 10.6a). Spatially separated PSII and Cyt $b_6f$ complexes can interact with each other due to rapid diffusion of $PQH_2$ and PQ molecules within the thylakoid membrane and fast diffusion of Pc molecules in the lumen. An apparent rate of electron transfer from $PQH_2$ to PSI is sensitive to the redox status of the ETC. With the rise of $PQH_2$ concentration, the probability of formation of the substrate-enzyme complex $PQH_2$ - $b_6f$ increases, thereby accelerating the overall rate of electron flow from PSII to $P_{700}^+$. This point can be illustrated by the data presented in Fig. 10.6b, which shows that the initial rate of $P_{700}^+$ reduction ($R_{P_{700}}$) in response to light pulses of various duration increases with the rise of a number of electrons per $P_{700}$ ($N_e$) injected from PSII into the intersystem ETC (Tikhonov et al. 1980). Saturation of kinetic parameter $R_{P_{700}}$ at sufficiently high numbers of electrons injected ($N_e > 2$) implies that the proton-coupled electron transfer (PCET) events, taking place within the Cyt $b_6f$ complex after $PQH_2$ binding to the $Q_o$-center, determine the rate of $PQH_2$ turnover. A similar result was reported by Haehnel (1973) who observed acceleration of $P_{700}^+$ reduction with an increase in the number of consecutive light flashes illuminating spinach chloroplasts. Analysis of experimental data on the redox

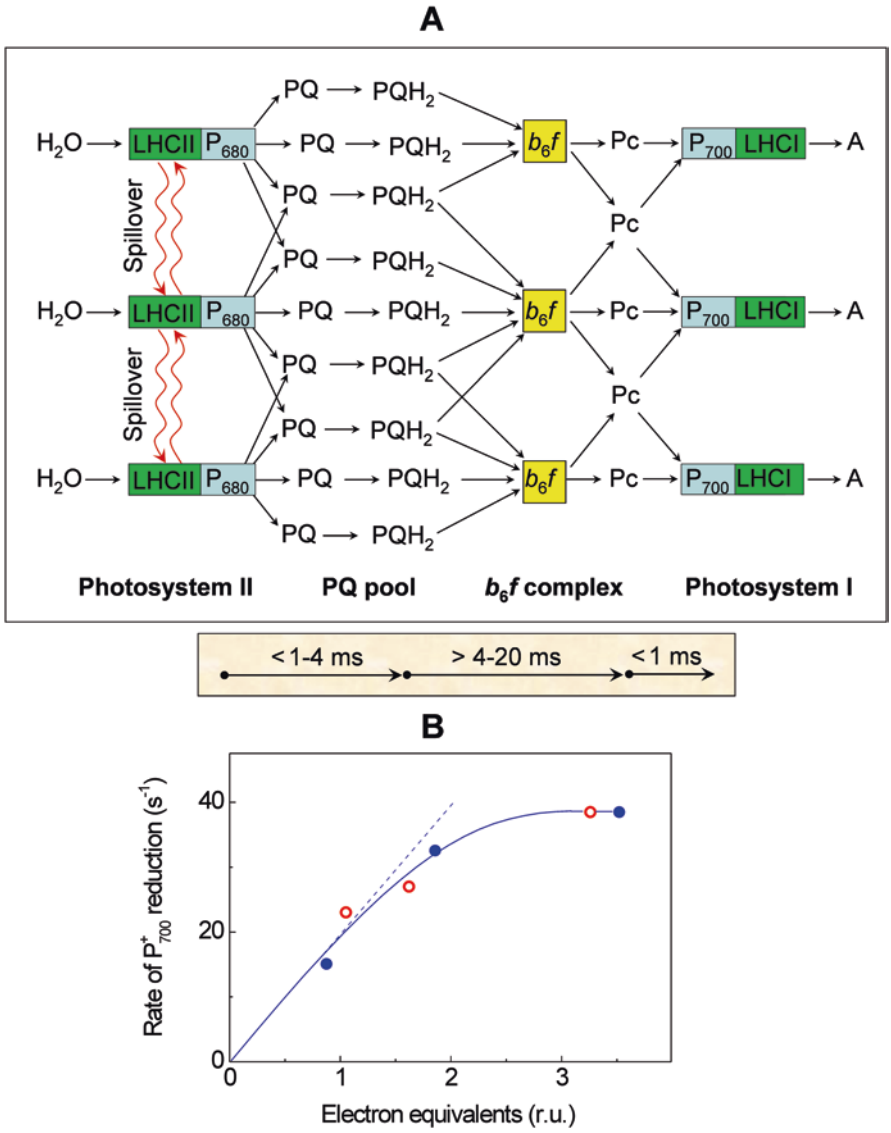


**Fig. 10.6** Panel **A** illustrates the connectivity between different electron transport complexes by means of mobile electron carriers, plastoquinone (PQ) and plastocyanin (Pc); ripple-type arrows (termed "spillover") symbolize the excitonic mechanism of interaction between the light harvesting complexes of PSII (LHCII), after (Tikhonov and Vershubskii 2017). Panel **B** shows the dependence of the initial rate of post-illumination reduction of $P_{700}^{+}$ in bean chloroplasts *versus* an average number of electrons (per $P_{700}$) injected into the intersystem electron transport chain in response to light pulses of different duration. Kinetic data used in plot **B** were compiled from Figs. 7 and 8 presented in (Tikhonov et al. 1980). Open and closed circles correspond to measurements at 20 °C and 29 °C, respectively

transients of $P_{700}$ within the framework of a mathematical model also suggests that even significant attenuation of PSII activity (for instance, due to generation of NPQ) may not cause drastic reduction of electron flow through PSI during the action of a sufficiently strong continuous actinic light (Tikhonov and Vershubskii 2017). This result can be explained by "electronic" and/or "excitonic" connectivity between different PSII units (Siggel et al. 1972; Tikhonov and Ruuge 1979; Haehnel 1982; Stirbet 2013). At sufficiently strong actinic light, the overall flux of electrons between PSII and PSI would maintain at a high level even upon the attenuation of PSII activity, provided the rate-limiting step of electron transfer is beyond the stage of $PQH_2$ formation (Tikhonov and Vershubskii 2017). This is because the $PQH_2$ pool serves as the redox buffer, which can accumulate electron equivalents capable of reducing $P_{700}^+$ via the Cyt $b_6f$ complex and Pc.

## 10.3 Plastoquinol Interaction with the Cytochrome $b_6f$ Complex

### *10.3.1 Q-Cycle*

Oxidation of $PQH_2$ occurs after its penetration into the quinone-exchange cavity and binding to the $Q_o$-center positioned on the lumenal side of the Cyt $b_6f$ complex. One can say that two reagents, $PQH_2$ and oxidized ISP ($ISP_{ox}$), form the "enzyme-substrate" complex (ES-complex). According to the earlier models of quinol oxidation, electron transfer from the quinol molecule to the $ISP_{ox}$ proceeds only after the quinol deprotonation reaction ($QH_2 \rightarrow QH^- + H^+$).[1] The "proton-gated affinity change" (Link 1997) and the "proton-gated charge transfer" (Brandt 1996; Brandt and Okun 1997) mechanisms imply that it is the anion form of the quinol ($QH^-$) that binds to the $Q_o$-center and then donates electron donor to oxidized redox center of the Rieske protein ($ISP_{ox}$). Crofts and collaborators suggested that the formation of the ES-complex does not need the dissociation of a proton from $QH_2$, but involves the dissociated form of the $ISP_{ox}$ (Crofts 2004a, b; Crofts et al. 2013). The ES-complex $QH_2$ - $ISP_{ox}$ is stabilized by the hydrogen bond between the -OH group of the quinol molecule and the imidazolate ring of deprotonated $ISP_{ox}$ (Fig. 10.7). The redox center of the ISP contains the $[Fe_2S_2]$ cluster, one of the Fe atoms of which is ligated by two His residues (His136 and His155 in *C. reinhardtii*). In the oxidized state, this cluster is diamagnetic (spin $S = 0$) due to the antiferromagnetic coupling between two $Fe^{3+}$ ions. In the reduced state, the $[Fe_2S_2]$ cluster becomes paramagnetic (spin $S = 1/2$) and, therefore, it can be detected by the electron paramagnetic resonance method at cryogenic temperatures (Zhang et al. 1996; Soriano et al. 2002).

[1] Here and below, the general terms $QH_2$ and Q are used to denote the quinol and quinone species, regardless of their origin (plastoquinone, PQ, or ubiquinone, UQ). SQ designates the redox states of semiquinone species, either plastosemiquinone (in the $b_6f$ complex) or ubisemiquinone (in the $bc_1$ complex), regardless of their protonation state.

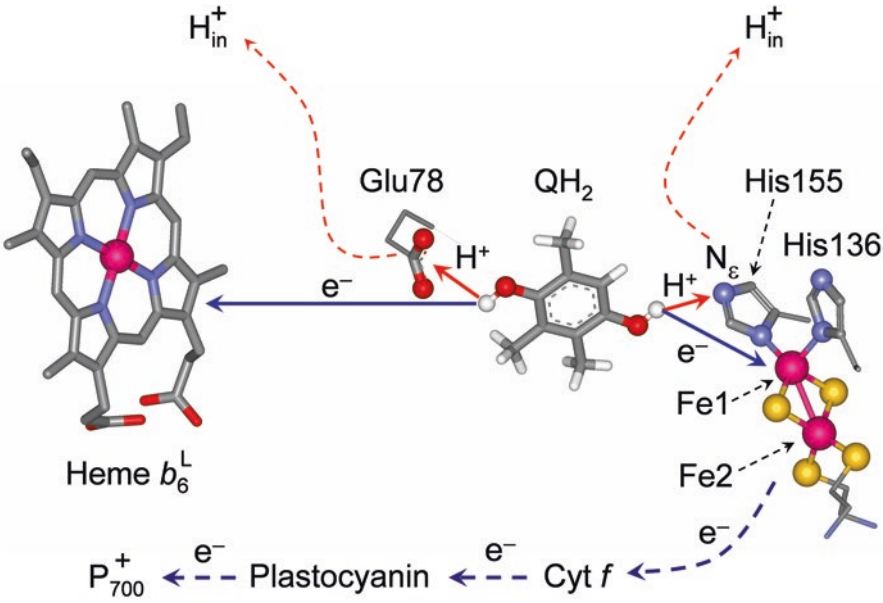


**Fig. 10.7** Schematic representation of electron and proton transfer reactions upon the two-electron oxidation of quinol at the $Q_o$-site of the Cyt $b_6f$ complex from *Chlamydomonas reinhardtii* (PDB entry 1Q90, Stroebel et al. 2003). Figure was produced using Accelerys DV visualizer software package (http://www.accelrys.com)

The bifurcated reaction of $PQH_2$ oxidation proceeds as two *concerted* reactions of *proton-coupled* electron transfer (PCET): (*i*) $PQH_2 \rightarrow SQ + e^- + H^+$, and (*ii*) $SQ \rightarrow PQ + e^- + H^+$, where SQ denotes the semiquinone form of PQ or ubiquinone (UQ) (Berry et al. 2000; Cramer et al. 2006, 2011; Hasan et al. 2013a; Crofts 2004a, b; Crofts et al. 2013; Snyder et al. 2000; Cape et al. 2007). The term "proton-coupled" means that reactions (*i*) and (*ii*) are tightly coupled to proton transfer from $PQH_2$ and SQ to appropriate proton-accepting groups, respectively. The term "concerted" implies that both reactions (*i*) and (*ii*) occur simultaneously (or almost simultaneously) (Osyczka et al. 2004, 2005; Zhu et al. 2007).

*Plastoquinol Oxidation Reactions* The pictorial scheme of events associated with the bifurcated (two-electron) oxidation of $PQH_2$ within the framework of the Mitchellian Q-cycle is shown in Fig. 10.8. The turnover of $PQH_2$ molecules in the $Q_o$-center starts with the first reaction of electron transfer. Oxidized iron-sulfur cluster of the ISP ( $ISP_{ox}$ ) serves as the primary electron acceptor in the high-potential redox chain reduced by $PQH_2$:

$$PQH_2 + ISP_{ox} \rightarrow PQH^{\bullet} + ISP^{\bar{\bullet}}_{red}H^+. \qquad (10.1)$$

This reaction is the PCET process, in which the electron and proton transfer proceed as tightly coupled events. Structural data suggest that the $N_\varepsilon$ atom of the histidine residue, which ligates the $[Fe_2S_2]$ cluster of the ISP extrinsic domain of the Cyt $b_6f$

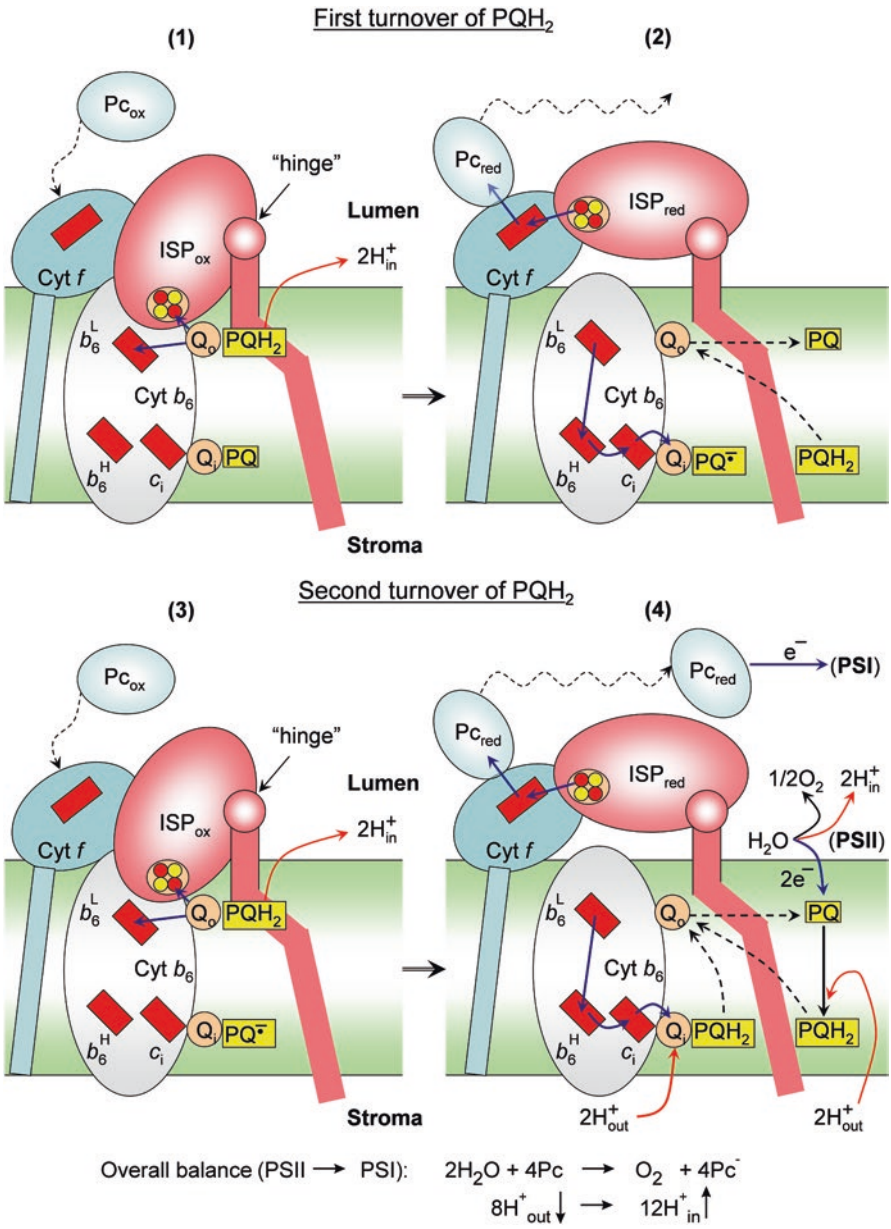


**Fig. 10.8** A sketch illustrating plastoquinone turnover in the Cyt $b_6f$ complex within the framework of the Q-cycle model

complex (His155 in *C. reinhardtii* or His129 in *M. laminosus*), is the prime candidate for the role of the recipient accepting the proton from $PQH_2$ (Fig. 10.7). This residue of the ISP is within hydrogen-bonding distance from the –OH group of the quinol. The formation of the hydrogen bond between this group and the $N_\varepsilon$ atom of the neighboring histidine is considered as an essential prerequisite for the first reaction (10.1) of quinol oxidation (Hsueh et al. 2010; Lhee et al. 2010). The notion about the formation of such a hydrogen bond finds strong support from spectroscopic (EPR, NMR, and ATR-FTIR) studies of the $bc_1$ complex (Samoilova et al. 2002; Zu et al. 2003; Iwaki et al. 2005; Lin et al. 2006; Hsueh et al. 2010; Lhee et al. 2010), which is akin to the $b_6f$ complex.

The plastosemiquinone molecule formed as the result of the first PCET reaction (10.1) will be in the neutral form ($PQH^\bullet$). In the second PCET reaction (10.2), $PQH^\bullet$ donates an electron to the low-potential heme $b_6^L$ of the low-potential branch of the Cyt $b_6f$ complex:

$$PQH^\bullet + \text{Cyt } b_6^L\,(\text{ox}) \rightarrow PQ + \text{Cyt } b_6^L\,(\text{red}) + H^+. \tag{10.2}$$

In chloroplasts, the key role in the proton migration from $PQH^\bullet$ to the lumen belongs to the proton-accepting carboxyl group of glutamate (Glu78). Glu 78 is part of a highly conserved PEWY sequence of subunit IV, which participates in the formation of the quinone-binding pocket of the $Q_o$-center. The proton-accepting group of Glu78 is positioned between the $PQH_2$ molecule and heme $b_6^L$ (Fig. 10.7). This group may serve as the primary recipient of the proton from $PQH^\bullet$ (Zito et al. 1998). It has been suggested, on the basis of structural and mutagenesis data for the Cyt $bc_1$ complex, that Glu in the PEWY-span accepts a proton from the neutral semiquinone, and delivers it by rotation of the carboxylic side chain to the proton exit channel, leaving the anionic form of SQ in the $Q_o$-site (Victoria et al. 2013). Mutagenesis of Glu78 is known to impair turnover of the Cyt $b_6f$ complex in *C. reinhardtii* (Zito et al. 1998; Finazzi 2002). A similar effect of the impediment to $UQH_2$ oxidation has been described for the Cyt $bc_1$ complex (Victoria et al. 2013).The proton from the carboxyl group of Glu78 migrates to the lumen through one of putative proton-conducting pathways (Hasan et al. 2013c; Tikhonov 2014).

The reduced $ISP_{red}$ passes an electron to heme *f* located in the peripheral domain of the Cyt *f* protein. The ISP occupies a cleft between the large and small domains of Cyt *f* (Fig. 10.3). A key step of electron transfer from the $[Fe_2S_2]$ cluster of the ISP to the Cyt *f* heme involves the large-scale conformational changes within the Cyt $b_6f$ complex. A distance between the redox cluster $[Fe_2S_2]$ docked nearby the $Q_o$-center and heme *f* is too long (≈ 26 Å) in order to provide physiologically rapid direct transfer of electrons from the $ISP_{red}$ to Cyt *f* by the mechanism of quantum mechanical tunneling (Page et al. 1999). However, a high mobility of the extrinsic domain of the ISP containing the redox cluster $[Fe_2S_2]$ should facilitate electron transfer between the $ISP_{red}$ and oxidized Cyt *f*. It is likely that after the reduction of ISP its extrinsic domain moves from the proximal position in the vicinity of the $Q_o$-site towards the distal position close to the heme *f*, thereby providing electron

transfer from the $ISP_{red}$ to Cyt *f*. This case is cartooned as the transition from the state (1) to state (2) shown in Fig. 10.8.

There are several lines of evidence for a high mobility of the extrinsic domain of the ISP containing the redox center $[Fe_2S_2]$ within the whole ensemble of the Cyt $b_6f$ complex (Breyton 2000; Heimann et al. 2000; Soriano et al. 2002; Roberts et al. 2002; Yan and Cramer 2003; de Vitry et al. 2004). One of the convincing arguments in favor of the cluster $[Fe_2S_2]$ mobility, which paves the way for electronic communication between the ISP and Cyt *f*, may be considered from the results of the X-ray data on the Cyt $b_6f$ complex from *M. laminosus* (Hasan et al. 2013b). This conclusion stems from extensive crystallographic disorder of the ISP extrinsic domain indicating its conformational flexibility. The ISP disorder has been observed in the Cyt $b_6f$ complex supplemented with anionic lipids. This indicated that the electric charges on the lipid headgroups may influence motion of the ISP extrinsic domain within the Cyt $b_6f$ complex. Structural data first obtained for a variety of Cyt $bc_1$ complexes of different origin present the apt evidence for the long-range movements of the flexible domain of the ISP containing the Rieske $[Fe_2S_2]$ cluster (for review, see Darrouzet et al. 2001; Xia et al. 2013). Two different positions of the $[Fe_2S_2]$ cluster relative to heme $c_1$ have been found in the X-ray crystallographic structures in the presence or absence of various inhibitors, suggesting the large-scale movement of the extrinsic domain of the ISP containing the $[Fe_2S_2]$ cluster (Iwata et al. 1998; Kim et al. 1998; Zhang et al. 1998; Esser et al. 2006).

The long-range "tethered" diffusion of the $[Fe_2S_2]$ cluster towards heme *f* enables electron transfer from $ISP_{red}$ to Cyt *f* and further to plastocyanin. After oxidation and deprotonation of the $ISP_{red}$ $\left(ISP_{red}^{\bullet}H^{+} + f \rightarrow ISP_{ox} + f^{-} + H_{in}^{+}\right)$, its mobile extrinsic domain returns from the distant (Fig. 10.8, panel 2) to the proximal position near the $Q_o$-site (Fig. 10.8, panel 3). Note that the movements of the ISP extrinsic domain between the proximal ($Q_o$-site) and distal positions (heme *f* in the Cyt $b_6f$ complex or heme $c_1$ in the Cyt $bc_1$ complex) are more rapid than the overall process of quinol oxidation. A mutagenesis study of the ISP in *C. reinhardtii* (de Vitry et al. 2004) indicated that the protein-linking domain of the chloroplast ISP was much more flexible than its counterpart in mitochondria. This was explained by the greater flexibility of the polyglycine hinge in the Cyt $b_6f$ complex than of the polyalanine hinge in the Cyt $bc_1$ complex (Yan and Cramer 2003).

The destiny of the second electron donated by $PQH_2$ differs from that of the first electron. After the removal of the first electron and proton from $PQH_2$ in the $Q_o$-center (the first PCET reaction), the extrinsic domain of the ISP moves towards heme *f*. Displacement of the redox center $[Fe_2S_2]$ away from the $Q_o$-site precludes the thermodynamically favorable donation of the second electron from SQ to the high-potential branch, directing the SQ radical to reduce the low-potential heme $b_6^L$. After electron transfer from the plastosemiquinone $PQH^{\bullet}$ to the low-potential heme $b_6^L$ (reaction 2), the electron is transferred to the high-potential heme $b_6^H$ and further to heme $c_i$, towards the PQ binding site $Q_i$ on the stromal side of the Cyt $b_6f$ complex, reducing $(PQ)_i$ to its plastosemiquinone anion-radical species $\left(PQ^{\bullet-}\right)_i$

(Fig. 10.8, panel 2).[2] After the second turn of $PQH_2$ turnover, $PQH_2$ forms in the $Q_i$-center, $\left(PQ^{\bullet-}\right)_i + e^- + 2H^+_{out} \rightarrow \left(PQH_2\right)_i$, and then dissociates into the membrane (Fig. 10.8, panels 3 and 4).

Taking into account that two protons appear in the lumen per one $H_2O$ molecule oxidized in the WOC of PSII ($H^+/e^- = 1$) and four protons are pumped into the lumen per two electrons transferred to PSI through the Cyt $b_6f$ complex ($H^+/e^- = 2$), the overall stoichiomentry of proton and electron transport is $H^+/e^- = 3$. This means that three hydrogen ions will appear into the lumen per one electron transferred from PSII to PSI. Thus, the operation of the Q-cycle enhances the proton/electron stoichiometry, increasing the efficiency of proton pumping into the lumen, as was first predicted by Peter Mitchell who put forward his brilliant idea of the Q-cycle as early as 1976 (Mitchell 1976). It is note worthy to stress that two-thirds of the *trans*-thyalkoid pH difference (ΔpH) in oxygenic photosynthesis originates from the proton pumping by the Cyt $b_6f$ complex.

*Proton Exit Pathways* Oxidation of $PQH_2$ occurs as the proton-coupled reactions, in which two protons migrate into the aqueous bulk phase of the lumen. Each of two steps of the $PQH_2$ oxidation reaction is accompanied by deprotonation. Analysis of the crystal structure of the Cyt $b_6f$ complex from *C. reinhardtii* (PDB entry 1Q90) revealed two putative pathways for proton relase from the $PQH_2$ molecule oxidized at the $Q_o$-site (Fig. 10.9). The side residue of His ligating the $[Fe_2S_2]$ cluster of the ISP (His155 in *C. reinhardtii*, or His129 in *M. laminosus*) may serve the role of the immediate recipient of the first proton donated by $PQH_2$. Being bound to this His residue of the extrinsic domain of ISP, the proton extracted from $PQH_2$ starts traveling along the exit route to the aqueous bulk phase of the lumen. After oxidation of protonated $ISP_{red}$ by Cyt $f\left(ISP^{\bullet-}_{red}H^+ + f \rightarrow ISP_{ox} + f^- + H^+_{in}\right)$ its affinity for a proton decreases and the proton releases from the ISP, migrating to the lumen through the *intra*-protein proton-conducting channel containing water molecules. The structural and biochemical data indicate that the water molecules of the proton-conductive chain, in addition to the surrounding amino acid residues, play an important role in Cyt *f* functioning (Ponamarev and Cramer 1998; Sainz et al. 2000). Interruption of the internal water chain, which forms a path for proton migration, impairs the operation of the Cyt $b_6f$ complex: electron transport from the ISP to Cyt *f* decelerates, and the concerted reduction of Cyt $b_6$ and Cyt *f* is lost. An alternative point of view on the nature of the primary recipient of the proton donated by quinol has been suggested by Postila et al. (2013), who scrutinized the problem on the basis of atomic molecular dynamics simulations for the Cyt $bc_1$ complex. They suggested that water molecules positioned in suitable places of the $Q_o$-site nearby the $UQH_2$ molecule could act as the primary proton-receiving partners in the two-electron oxidation of $UQH_2$.

[2] It is likely that this species will appear in the form of the anion-radical $PQ^{\bullet-}$, because the p$K$ values of semiquinones are usually fall in the range below the stromal pH establishes under the normal physiological conditions ($pH_{out}$~7 − 8).

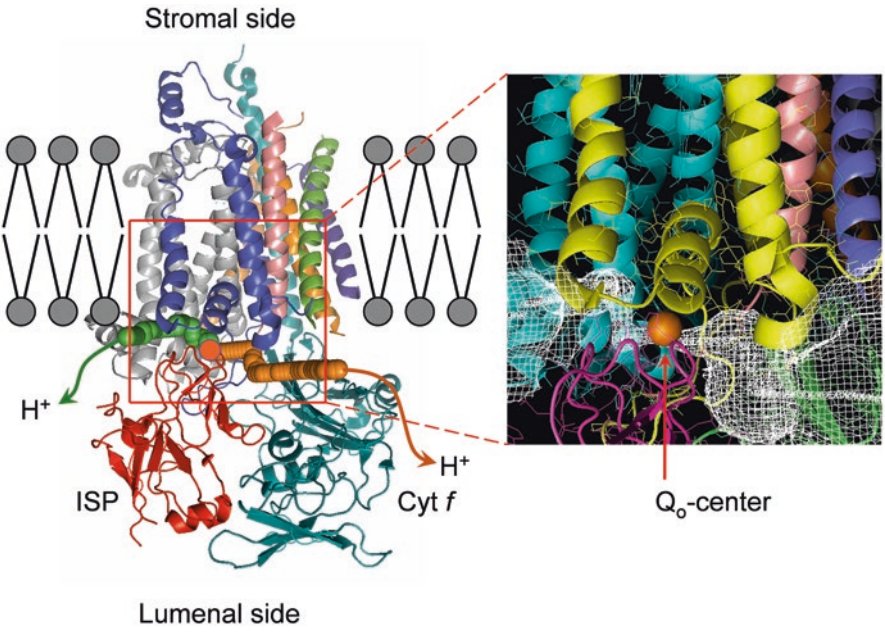


**Fig. 10.9** Side view of the monomeric fragment the Cyt $b_6f$ complex from *Chlamydomonas reinhardtii* (PDB entry 1Q90, Stroebel et al. 2003), which demonstrate putative exit pathways for protons dissociating from the $Q_o$-site to the thylakoid lumen. The traces of the proton-conducting pathways (shown by green and brown spheres) were found in collaboration with B.V.Trubitsin, using the program Caver for detection of possible channels for traveling mobile molecules inside protein structures (Chovancová et al. 2012). The program output was visualized using PyMOL Molecular Graphics System

Oxidation of semiquinone $PQH^{\bullet}$ formed after the first PCET reaction is also accompanied by the proton release into the lumen ($PQH^{\bullet} + b_6^{L}(ox) \rightarrow PQ + b_6^{L}(red) + H_{in}^{+}$). The proton released from $PQH^{\bullet}$ migrates to the lumen through the second putative proton-conducting channel (Tikhonov 2013, 2014). As noted above, it is likely that $PQH^{\bullet}$ donates a proton to the neighboring acidic group ($-COO^{-}$) of Glu78 positioned in subunit IV between the quinone binding center $Q_o$ and heme $b_6^{L}$ (Fig. 10.7). From Glu78 the proton migrates to the lumen. The crystal structure of the Cyt $b_6f$ complex from *M. laminosus* (Hasan et al. 2013c) suggests that the proton-accepting group of Glu3 located in subunit G may attract a proton from Glu78 and then release it to the aqueous bulk phase of the lumen.

*Proton Entry Pathways* At the PQ binding $Q_i$-center located on the "negative" (stromal) side of the Cyt $b_6f$ complex, reduced PQ molecules undergo protonation through the proton-conductive pathways oriented towards the aqueous bulk phase of stroma. Refined crystal structure (2.70 Å) of the Cyt $b_6f$ complex from *M. laminosus* (Hasan et al. 2013c) revealed a unique short pathway for proton transfer to the $Q_i$-site, which involves two residues of the Cyt $b_6$ protein ($H_{out}^{+}(aq) \rightarrow Asp20 \rightarrow arg\,207 \rightarrow Q_i$). The Asp20 side chain is located on the

surface of the Cyt $b_6f$ complex; therefore, it has direct access to the aqueous phase. Both steps of the proton transfer within the Cyt $b_6$ protein (Asp20 → Arg207 and Arg207 → $Q_i$) are mediated by hydrogen bonds. Arg207 has access to $(PQ)_i$ as well as heme $c_i$. Another putative way of proton transfer may be mediated by the surface residues Lys24. In addition to these proton transfer pathways, the acidic side chains of Glu29 and Asp35 (subunit IV) may be involved in proton transfer from stroma to the PQ molecule, reduced at the $Q_i$-center (Hasan et al. 2013c).

### *10.3.2 Kinetics of Plastoquinol Oxidation*

The elucidation of the mechanism of $PQH_2$ oxidation is a key to understanding the nature of the rate-limiting step in the intersystem ETC. Molecular machinery of quinol oxidation in the Cyt complexes of *bc* type have been scrutinized in a number of original works and related review articles (see Berry et al. 2000; Crofts 2004a, b; Crofts et al. 1999a, b, 2000, 2006, 2013; Mulkidjanian 2005; Xia et al. 2013). There are several events that have been considered to explain the nature of the rate-limiting step of quinol oxidation: (*i*) the formation of the quinol-ISP complex (Mulkidjanian 2005), (*ii*) deprotonation of the neutral quinol to the anionic form ($PQH_2 \rightarrow PQH^- + H^+_{in}$) and the formation of the "enzyme-substrate" complex ($PQH^-/ISP_{ox}$) followed by $PQH^-$ oxidation (Brandt and Okun 1997; Link 1997; Rich 2004), and (*iii*) constrained diffusion of the ISP mobile domain between the $PQH_2$ binding site $Q_o$ and Cyt *f* (or Cyt $c_1$) (Izrailev et al. 1999; Crofts et al. 1999a, b; Darrouzet et al. 2001). Structural, kinetic and thermodynamic aspects of $PQH_2$ oxidation at the $Q_o$-site are considered below.

Structural and kinetic data suggest that the round-trip movements of the mobile domain of the ISP between the $Q_o$-site and heme *f* could determine only partly the turnover rate of the Cyt $b_6f$ complex. A flexible "detail" of the ISP machinery (a "hinge") provides restricted tethered diffusion of the extrinsic domain containing the redox $[Fe_2S_2]$ cluster. However, the flip-flop motions of the $[Fe_2S_2]$ cluster between the proximal and distal positions are rapid as compared to the rate of $PQH_2$ oxidation; therefore, they should not limit the overall rate of PQ turnover. According to (Yan and Cramer 2003; de Vitry et al. 2004), electron transfer from the $ISP_{red}$ to heme *f* may occur more rapidly ($t_{1/2} \leq 2 - 4$ ms) than the overall rate of $PQH_2$ oxidation ($t_{1/2} \geq 4 - 20$ ms, Stiehl and Witt 1969; Haehnel 1984). This implies that the rate of $PQH_2$ oxidation should be determined predominantly by the processes associated with the formation of the substrate-enzyme complex $PQH_2/ISP_{ox}$ and intrinsic reactions related to $PQH_2$ oxidation within the Cyt $b_6f$ complex.

Analyzing experimental data on ubiquinol ($UQH_2$) oxidation in the $bc_1$ complex in the purple photosynthetic bacterium *Rhodobacter sphaeroides*, Crofts and collaborators concluded that the activated step of $UQH_2$ oxidation was in a reaction step after the formation of the $UQH_2/ISP_{ox}$ complex (Hong et al. 1999). The pH-dependence of the rate of $UQH_2$ oxidation reflected the p*K* of the oxidized ISP ($ISP_{ox}$) and requirement for the deprotonated form of $ISP_{ox}$ in formation of the

$UQH_2/ISP_{ox}$ complex. Conclusive argument in favor of the first electron transfer reaction as the rate-limiting step of quinol oxidation was based on experimental data in strains with mutations in the ISP that lowered its redox potential $E_m$. The overall rate of $UQH_2$ oxidation was determined by the driving force for the first electron transfer, $\Delta G_1^0 = -zF\left(E_{m(ISP)} - E_{m(QH_2/SQ)}\right)$, but was almost independent of the driving force for the second electron transfer, $\Delta G_2^0 = -zF\left(E_{m(b_L)} - E_{m(SQ/Q)}\right)$ (Crofts 2004b; Crofts et al. 2013). This strongly suggests that the stage of electron transfer from the quinol molecule to $ISP_{ox}$ is the rate-limiting step of bifurcated oxidation of quinol.

Electron transfer from quinol to the redox center of $ISP_{ox}$ is tightly coupled to the concerted proton transfer to an appropriate proton-accepting group. As noted above, the $N_\varepsilon$ atom of the histidine residue liganding to the Fe1 atom the $[Fe_2S_2]$ cluster is the prime candidate for the role of the primary recipient of the proton donated by $PQH_2$. Figure 10.10a illustrates the scenario of protonation/deprotonation events associated with the reduction/oxidation of the ISP. The affinity of the ISP for protons depends on its redox state (Zu et al. 2003; Iwaki et al. 2005; Lin et al. 2006; Hsueh et al. 2010; Lhee et al. 2010). The deprotonated state of $ISP_{ox}$ is likely an obligatory prerequisite for the first step of $PQH_2$ oxidation (Fig. 10.10a); therefore, the $pK_{ox}$ value of the $ISP_{ox}$ will determine the pH-dependence of the rate of this reaction. In photosynthetic systems of oxygenic type, the p$K$ value of functional proton-accepting groups of $ISP_{ox}$ is characterized by $pK_{ox} \approx 6 - 6.5$ (Finazzi 2002; Soriano et al. 2002). *Ex facte* the affinity of the ISP for a proton should increase with the acquisi-

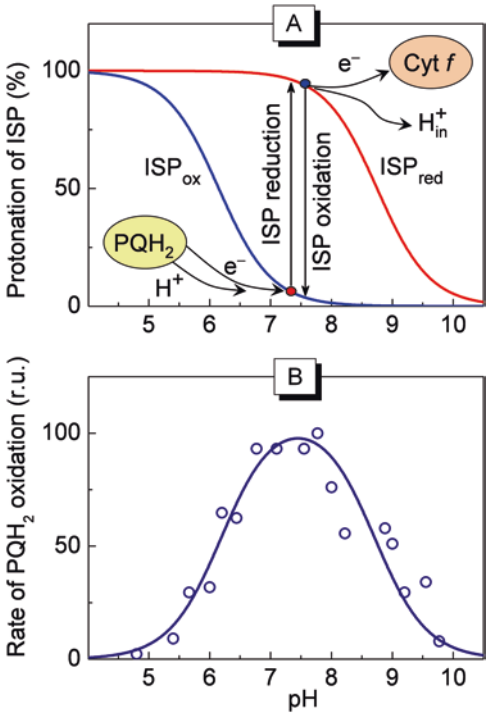


**Fig. 10.10** A diagram illustrating redox-dependent protonation/deprotonation of the ISP protein (**A**), and pH-dependence of $PQH_2$ oxidation by isolated cytochrome $b_6f$ complex (**B**). Open circles shown in panel **B** are taken from Fig. 4 in (Hope et al. 1994); solid line represents the result of simulation according to Eq. (10.3) for parameters $pK_{ox} = 6.2$ and $pK_{red} = 8.7$ (see text for explanations) (Modified from Figure 9 in Tikhonov 2014)

tion of the negative charge by the redox cluster [$Fe_2S_2$]. That is why $pK_{ox}$ increases to $pK_{red} \approx 8.3 - 8.9$ after the ISP reduction. This means that under the normal physiological conditions ($pH_{in} \le pH_{out} \le 8$) the $ISP_{red}$ will keep tightly the proton accepted from $PQH_2$. After oxidation of the reduced and protonated form of the ISP, its affinity to the proton decreases (Fig. 10.10a), and the proton will dissociate into the lumen via a proton-conducting channel ( $ISP_{red}^{\bullet}H^+ + Cyt\ f_{ox} \rightarrow ISP_{ox} + Cyt\ f_{red} + H_{in}^+$ ).

Let us consider the pH-dependence of the $PQH_2$ oxidation rate. At any given pH, the rate of $PQH_2$ oxidation will be controlled by two factors: (*i*) a probability of finding the oxidized $ISP_{ox}$ in deprotonated state, $p(ISP_{ox})$, the value of which is determined by $pK_{ox}$, and (*ii*) a probability of finding reduced ISP in protonated state, $p\left(ISP_{red}^{\bullet}H^+\right)$ , determined by the $pK_{red}$ value. Therefore, the overall rate of $PQH_2$ oxidation, $k_1$, will be proportional to the product $p\left(ISP_{ox}\right) \times p\left(ISP_{red}^{\bullet}H^+\right)$. Elementary calculations lead to the following term (Tikhonov 2014):

$$k_1 \propto 10^{pK_{red}-pH} \times \left(1+10^{pK_{red}-pH}\right)^{-1} \times \left(1+10^{pK_{ox}-pH}\right)^{-1}. \tag{10.3}$$

Equation (10.3) predicts the bell-shape pH-dependence of the rate constant $k_1$, which reflects the $pK_{ox}$ and $pK_{red}$ values of the ISP. Figure 10.10b shows that formula (10.3) adequately describes experimental pH-dependence of the rate of $PQH_2$ oxidation by the Cyt $b_6f$ complex if $pK_{ox} = 6.2$ and $pK_{red} = 8.7$ (Hope et al. 1994).

### *10.3.3 Energy Profiles of Electron Transport Reactions in the $Q_o$-Site*

The energy profile of bifurcated oxidation of $PQH_2$ can shed additional light on the nature of this reaction. Thermodynamic aspects of $PQH_2$ oxidation can be illustrated by the comparison of the redox potential profiles for electron carriers of the high-potential ($PQH_2 \rightarrow ISP \rightarrow f \rightarrow Pc \rightarrow P_{700}$) and the low-potential ( $PQH^{\bullet} \rightarrow b_6^L \rightarrow b_6^H \rightarrow c_i \rightarrow \left(PQ\right)_i$ ) redox chains shown in Fig. 10.11. The overall change in Gibbs free energy upon the two-electron oxidation of $PQH_2$ is negative. As the result of complete turnover of $PQH_2$ in the Q-cycle, one electron extracted from $PQH_2$ reaches one of $P_{700}^+$ centers, and this is the energy-favorable (down-hill) processes. However, the fact of the mater is that the first step of $PQH_2$ oxidation (electron transfer $PQH_2 \rightarrow ISP_{ox}$ with the formation of $PQH^{\bullet}$) is the energy-uphill process, although the overall reaction of two-electron oxidation of $PQH_2$ is thermodynamically favorable process (Fig. 10.11). By analogy with the Cyt $bc_1$ complex (for references, see Hong et al. 1999; Crofts et al. 2000; Crofts 2004a, b), it is safe to suggest that in the Cyt $b_6f$ complex this stage of electron transfer proceeds through the energy barrier, which decelerates the overall reaction of $PQH_2$ oxidation. Plastosemiquinone $PQH^{\bullet}$ formed in the result of the first electron transfer is a strong reductant capable of reducing the low-potential heme $b_6^L$. High reducing activity of $PQH^{\bullet}$ is a general property of semiquinone species, because most of the redox

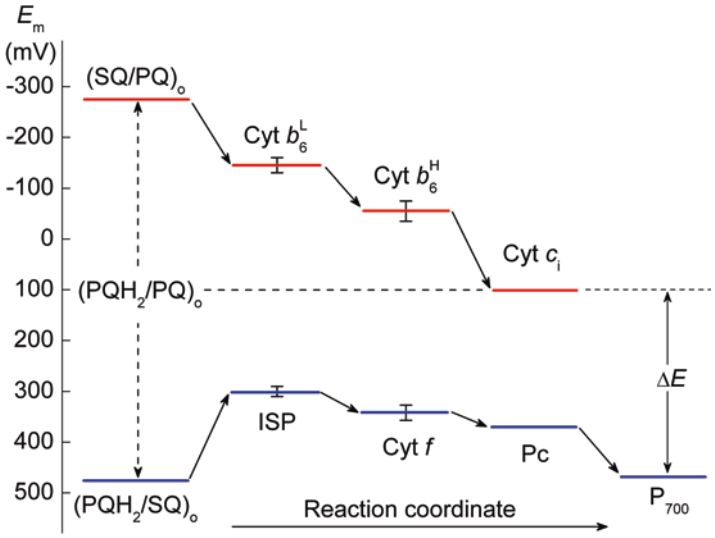


**Fig. 10.11** A diagram of the midpoint redox-potentials of electron carriers of the high-potential (ISP, Cyt *f*, Pc, and $P_{700}$) and low-potential (hemes $b_6^L$, $b_6^H$, and $c_i$) branches of electron transport in the Cyt $b_6f$ complex. The levels of the midpoint potentials shown here are the averaged values taken from the literature for *Chlamydomonas reinhardtii* (Alric et al. 2005; Hasan et al. 2013a; Nelson and Yocum 2006; Pierre et al. 1995; Zito et al. 1998)

couples SQ/Q are characterized by relatively low values of their redox potentials (Clark 1960). Further reactions of electron transfer along the low-potential and high-potantial chains proceed spontaneously with the loss of free energy.

Let us compare the midpoint potentials of one-electron redox couples $PQH_2$/SQ and SQ/PQ ($E_{m(PQH_2/SQ)}$ and $E_{m(SQ/PQ)}$) involved in electron transport along the high- and low-potential chains (Fig. 10.11). For the redox couple $PQH_2$/PQ, the mid-point potential $E_{m(PQH_2/PQ)}$ can be measured directly, since $PQH_2$ and PQ are relatively stable species. However, direct determination of $E_{m(PQH_2/SQ)}$ and $E_{m(SQ/PQ)}$ is problematic, because semiquinones are extremely reactive species. These potentials may be evaluated indirectly (Mitchell 1976; Chobot et al. 2008) using the relationship (10.4):

$$E_{m(PQH_2/PQ)} = \frac{1}{2}\left(E_{m(PQH_2/SQ)} + E_{m(SQ/PQ)}\right). \tag{10.4}$$

According to Gill and Tuteja (2010) and Bleier and Dröse (2013), semiquinone species transiently formed in the $Q_o$-centers of the Cyt $bc_1$ and Cyt $b_6f$ complexes are able to reduce molecular oxygen $O_2$ to superoxide radical, $O_2^{\bullet-}$. The standard redox potential relative to $10^5$ Pa of $O_2$ is $E_{0(O_2^{\bullet-}/O_2)} = -330$ mV; the redox potential relative to 1 M $O_2$ equals to −160 mV (Wood 1988). This implies a rather low value for $E_{m(SQ/Q)}$. Assuming that $E_{m(Q^{\bullet-}/Q)} \approx -280$ mV is sufficient to provide generation of superoxide radicals in mitochondria, Snyder et al. (2000) inferred that $E_{m(UQH_2/SQ)} \sim 460$ mV. This potential falls in the broad range of $E_{m(UQH_2/SQ)}$ values

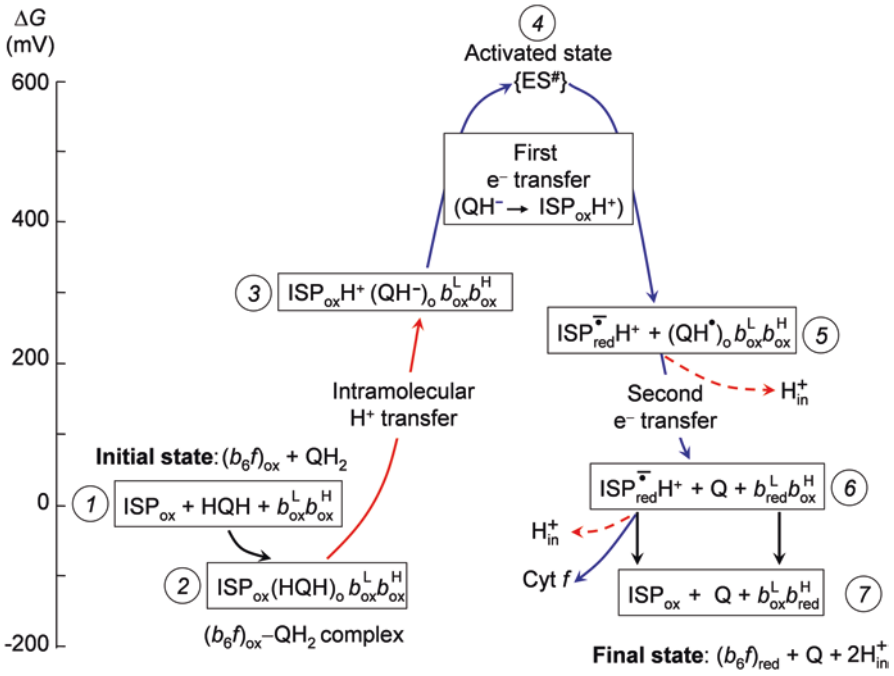


**Fig. 10.12** Plausible energy profile of bifurcated two-electron reaction of quinol oxidation at the $Q_o$-site (Modified Figure 11 from Tikhonov 2014)

(from 310 to 776 mV) obtained from kinetic data for the Cyt $bc_1$ complex in *Rhodobacter sphaeroides* (Hong et al. 1999; Cape et al. 2007). Similar estimates were obtained from the measurements of SQ generation at the $Q_o$-site in the Cyt $bc_1$ complex (Cape et al. 2007). These estimates are in agreement with experimental evidence that in the Cyt complexes of the *bc* family the rate of quinol oxidation is largely determined by the first electron transfer reaction (see Crofts 2004a, b). Thus, taking into account the estimated values of $E_{m(PQH_2/SQ)}$ and $E_{m(ISP)}$ (Fig. 10.11), we can conclude that electron transfer from $PQH_2$ to the $ISP_{ox}$ is the energy-uphill process that limits the overall rate of $PQH_2$ oxidation (see also Malnoë et al. 2011). The increase in free energy upon the first electron transfer ( $PQH_2 \xrightarrow{e^-} ISP_{ox}$ ) is compensated by the free energy decrease in the energy-favorable reactions $SQ \xrightarrow{e^-} b_6^L \xrightarrow{e^-} b_6^H$.

Figure 10.12 depicts the sequence of events associated with the reaction of $PQH_2$ oxidation according to the "proton-first-then-electron" (PT/ET) transfer mechanism favoured by Crofts et al. (2013). After the formation of the $PQH_2$ - $ISP_{ox}$ complex (the downhill transition *1* → *2*), the proton transfer from $PQH_2$ to the $ISP_{ox}$ occurs (the uphill transition *2* → *3*). This step is accompanied by the free energy rise $DG_{proton} = 2.303 \times RT \times \left(pK_{PQH_2} - pK_{ISP_{ox}}\right) > 0$ (the so-called "Brønsted barrier"). The transfer of a proton towards the ISP moiety promotes the electron transfer, resulting in the production of $ISP^{\bullet}_{red}H^+$ and $PQH^{\bullet}$ (the transition *3* → *4* → *5* over the activation barrier *4*). $ISP^{\bullet}_{red}H^+$ dissociates from the $Q_o$-center and moves towards

heme *f* (state 5). Then, after the second PCET reaction, oxidized quinone dissociates from the $Q_o$-center (the downhill transition *5* → *6*). Further electron transfer (the downhill transition *6* → *7*) will stabilize charge separation after the completion of the $PQH_2$ oxidation cycle at the $Q_o$-site.

Quantum chemical calculations for a model system consisting of $TMQH_2$ (trimethylbenzoquinol, the "bobtail" analog of $PQH_2$), the $[Fe_2S_2]$ cluster, and surrounding them amino acid residues of the Cyt $b_6f$ complex (Fig. 10.13a), support the notion that the PCET from $PQH_2$ to $ISP_{ox}$ is the "uphill" process, which hampers the overall rate of $PQH_2$ oxidation (Frolov and Tikhonov 2009). According to density functional theory (DFT) computations, the transfer of a hydrogen atom from the quinol molecule to the nearest nitrogen atom of His155 is the endoergonic process ($\Delta E \approx 10$ kcal/mol) with a rather high energy barrier (Fig. 10.13b). The rate constant for this process was calculated using the Moser–Dutton ruler for evaluation of the rate of electron tunneling between redox centers (Page et al. 1999) expanded by Crofts (2004b) for PCET reactions. The rate constant of $TMQH_2$ oxidation in the model system was evaluated as $k_{PCET}$~40 – 170 $s^{-1}$ (Frolov and Tikhonov 2009). These estimates correspond to the half-times of $PQH_2$ oxidation $t_{1/2} = \ln 2/k_{PCET}$~4 – 17 ms. These values are in a reasonably good agreement with experimental data for electron transfer from $PQH_2$ to $P_{700}^+$ (Sect. 10.2.5).

What type of the mechanism for electron transfer in the $Q_o$-centers, "sequential" or "concerted", is realized in the Cyt $b_6f$ and $bc_1$ complexes? This question still remains a challenge to molecular bioenergenics. "Sequential" mechanism ($PQH_2 \xrightarrow{-e^-} SQ \xrightarrow{-e^-} PQ$) implies that the first and the second electron transfer reactions occur separately, with a certain time-delay between the steps. In this case, SQ radicals appear transiently as the intermediate species (Cape et al. 2006). A genuine "concerted" mechanism implies that the long-lived SQ species will not form if the bifurcated oxidation of $PQH_2$ proceeds in a single step as a time-concerted transfer of two electrons (Osyczka et al. 2004, 2005). In the latter case, both steps are realized simultaneously (within picoseconds-microseconds), with no SQ intermediate available to participate in side reactions. The truly concerted mechanism could be realized when both the redox partners, the $[Fe_2S_2]$ cluster and heme $b_6^L$, are oxidized. Simultaneous reduction of ISP and Cyt $b_L$ with $t_{1/2}$~250 microsecond was observed during ubiquinol oxidation in the bovine Cyt $bc_1$ complex (Zhu et al. 2007). Concerted oxidation of $PQH_2$ precludes the accumulation of SQ, thereby avoiding the formation of harmful superoxide radicals ($SQ \rightarrow O_2$) (Cape et al. 2006).

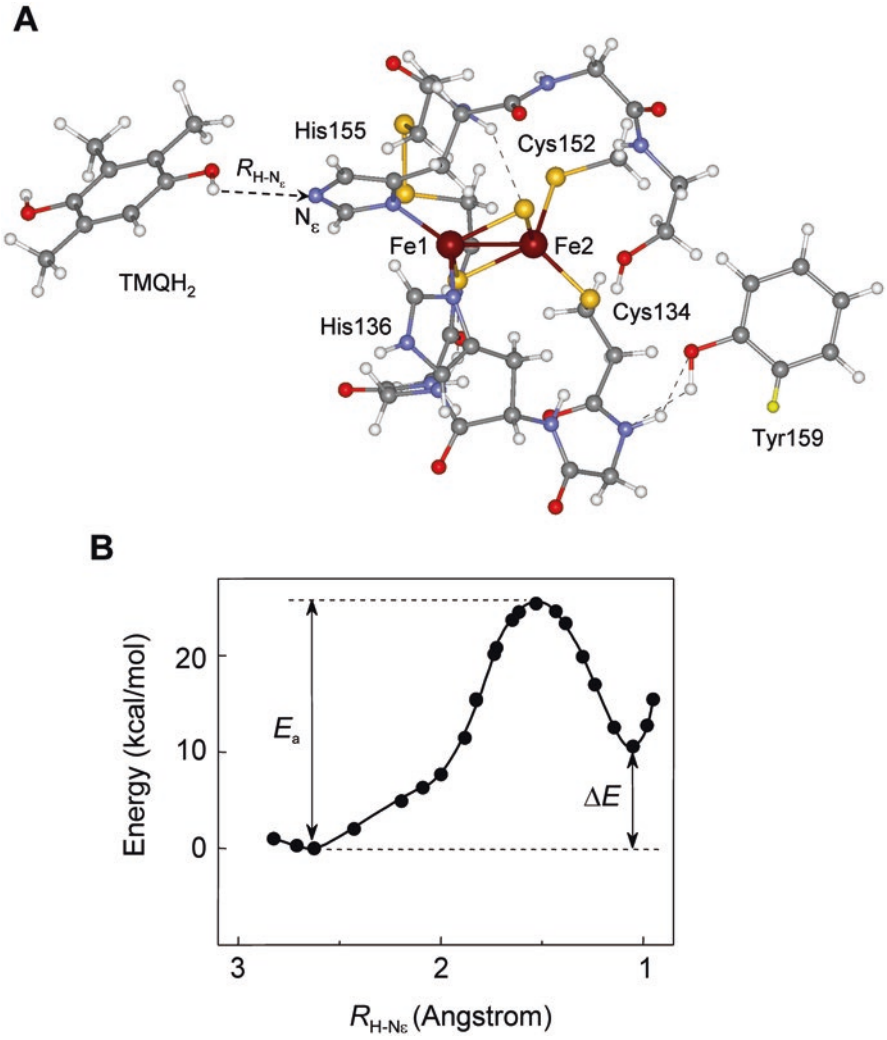


**Fig. 10.13** Panel **A –** Quantum chemical part of the model system, which includes trimethylbenzoquinol ($TMQH_2$, the analogue of $PQH_2$), the $[Fe_2S_2]$ cluster, and surrounding them amino acid residues of the Cyt $b_6f$ complex, Cys134-Thr135-His136-Leu137-Gly138-Cys139, Cys152, Cys154-His155-Gly156-Ser157, Tyr159 (Frolov and Tikhonov 2009). $TMQH_2$ was placed at the position of quinone inhibitor TDS in the crystal structure of the Cyt $b_6f$ complex from *Chlamydomonas reinhardtii* (PDB entry 1Q90, Stroebel et al. 2003)
Panel **B** – The plot of the model system energy *versus* the reaction coordinate $R_{H-N\varepsilon}$, which simulates changes in the potential energy of the model system upon the displacement of the H atom from $TMQH_2$ to the $N_\varepsilon$ atom of His155 (after Frolov and Tikhonov 2009)

## 10.4 Regulation of the Intersystem Electron Transport

### *10.4.1 pH-Dependent Control of the Intersystem Electron Transport*

Apart from the role of the molecular device for electron transport and proton pumping, the Cyt $b_6f$ complex participates in feedback regulation of electron transport. The light-induced acidification of the thylakoid lumen is the key factor of down-regulation of the intersystem electron transport (Rumberg and Siggel 1969; Tikhonov et al. 1981, 1984; Harbinson and Hedley 1989; Foyer et al. 2012; Järvi et al. 2013; Tikhonov 2013). Down-regulation of the intersystem electron transport is associated with two basic effects caused by the light-induced decrease in the intrathylakoid $pH_{in}$: (*i*) the retardation of $PQH_2$ oxidation, and (*ii*) the attenuation of PSII activity. The first mechanism of electron transport contol is realized in the stage of $PQH_2$ oxidation at the $Q_o$-site of the Cyt $b_6f$ complex (for review, see Tikhonov 2013, 2014, 2015). Acidification of the lumen impedes the oxidation of $PQH_2$ due to the back "pressure" from the protons accumulating inside the thylakoids on the functional proton-accepting groups, thereby decreasing the rate of $PQH_2$ oxidation (Figs. 10.5b and 10.10b). The influence of $pH_{in}$ on the rate of $PQH_2$ oxidation is likely to reflect the effect of $pH_{in}$ on the formation of hydrogen bonds between $PQH_2$ and the nearby proton-accepting groups in the $Q_o$-center (the $N_\varepsilon$ atom of His155/His129 and the carboxyl group of Glu78). Note that electron transfer from Cyt *f* to Pc is independent of $pH_{in}$ (Finazzi 2002). Acidification of the lumen also acts as a signal for enhancement of excess energy dissipation in the light-harvesting antenna of PSII, i.e., non-photochemical quenching (NPQ) of Chl *a* excitation (Eberhard et al. 2008; Horton 2012; Ruban 2012). Both mechanisms, the slowing down of PQ turnover and generation of NPQ, cause deceleration of electron flow from PSII to PSI at excess of irradiation, protecting PSA against solar stress (for review, see Li et al. 2009, Demmig-Adams et al. 2012, Horton 2012, Rochaix 2014, Jallet et al. 2016).

### *10.4.2 Redox-Dependent Regulation of Electron Transport and State Transitions*

Other regulatory mechanisms are associated with the light-induced activation of metabolic processes and redistribution of electrons fluxes between alternative electron transport pathways, which are controlled by the redox state of the chloroplast ETC. The light-induced activation of the CBC reactions is a striking example of pH- and redox-dependent regulation of metabolic processes in photosynthetic systems. The CBC is inactive in dark-adapted chloroplasts. The light-induced alkalization of stroma and redox-dependent activation of the CBC enzymes speed up the outflow of electrons from PSI to the CBC (Buchanan 1980; Edwards and Walker

1983; Andersson 2008; Michelet et al. 2013; Balsera et al. 2016). In addition to acceleration of LEF (PSII → PSI → CBC) due to activation of the CBC reactions, there are redox-dependent mechanisms of redistribution of electron fluxes between the LEF and CEF1 pathways. The partitioning of electron fluxes on the donor side of PSI is controlled by competition between the LEF and CEF1 pathways for reducing equivalents (Joliot and Joliot 2005; Breyton et al. 2006; Johnson 2011). Relatively slow consumption of NADPH in the CBC, which is peculiar to dark-adapted chloroplasts, would divert electrons from LEF to CEF1, thereby supporting generation of ΔpH and ATP synthesis (Kramer et al. 2004). In the meantime, with the light-induced activation of the CBC reactions, the contribution of CEF1 will decrease in favor of LEF.

The mechanism of electron transport control associated with the redistribution of light energy between the light-harvesting complexes of PSI and PSII is triggered by the "check-point device" operating at the level of the Cyt $b_6f$ complex. This regulatory mechanism relates to the so-called "state transitions" phenomenon. It is well established fact that the redox state of the PQ pool serves as a signal about the "traffic jam" on the pathway between PSII and PSI (see Bennett 1977; Allen 1992; Haldrup et al. 2001; Lemeille and Rochaix 2010; Rochaix 2014; Puthiyaveetil et al. 2016). The over-reduction of the PQ pool triggers a protein kinase that catalyses phosphorylation of the loosely bound light-harvesting complexes of PSII. This process is induced by $PQH_2$ binding to the $Q_o$-site of the Cyt $b_6f$ complex (Vener et al. 1997; Zito et al. 1999). In plants, there are three forms of LHCII trimers, which differ with respect to their association with PSII: "strong", "moderate", and "loose" binding to PSII (Galka et al. 2012; Puthiyaveetil et al. 2016). The loosely bound form of phosphorylated LHCII dissociates from the PSII-LHCII supercomplex and migrates to PSI, thereby increasing the light harvesting capacity of PSI (see cartoon in Fig. 10.14). Such a structural remodelling of PSA, termed "State 1 → State 2" transition, enhances PSI activity at expense of PSII, promoting the reoxidation of the $PQH_2$ pool. Redistribution of energy in favour of PSI is a reversible process: after a decrease in the concentration of $PQH_2$, LHCII becomes dephosphorylated due to chloroplast phosphatases. Dephosphorylation of LHCII allows its return to the grana domains enriched with PSII ("State 2 → State 1" transition), increasing the light absorption in PSII. Remodelling of PSA associated with state transitions provides short-term responses (in the minute range) of photosynthetic organisms to variations of light intensity. Thus, reversible transitions "State 1 ↔ State 2" provide the optimal balance of absorbed light energy between PSI and PSII upon fluctuations of the environment light (Tikkanen and Aro 2012, Tikkanen et al. 2012).

A molecular device, which receives the signal from the $PQH_2$ pool and triggers state transitions, is inherent to the Cyt $b_6f$ complex. Activation of the LHCII kinase is initiated by $PQH_2$ binding to the $Q_o$-site. A strong correlation between the $PQH_2$ occupancy at the $Q_o$-center and the LHCII kinase activity of chloroplasts has been found in (Vener et al. 1997, Zito et al. 1999). In *C. reinhardtii*, activation of the LHCII kinase is mediated through the protein kinase Stt7, which becomes phosphorylated in State 2 conditions. Protein kinase Stt7 acts in catalytic amounts (Stt7/LHCII ~ 1/200) (Lemeille et al. 2009). Stt7 has an ortholog STN7 in *Arabidopsis*

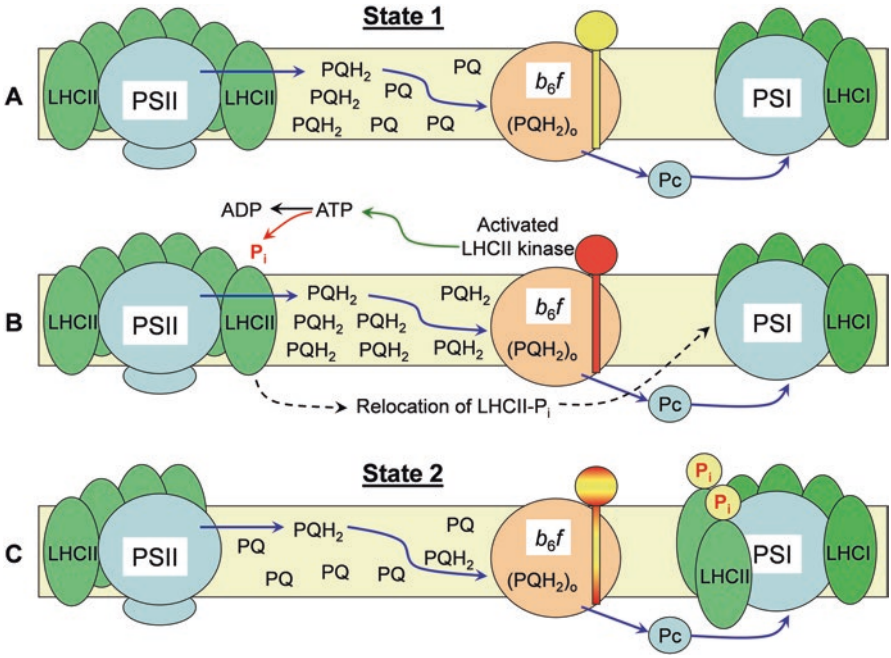


**Fig. 10.14** A schematis representation of state transitions triggered by the $PQH_2$ binding to the Cyt $b_6f$ complex (see explanations in text) (Modified Figure 15 from Tikhonov 2014)

and other land plants (Bellafiore et al. 2005). The knock out of STN7 inhibits phosphorylation of LHCII and state transitions. A putative mechanism of kinase activation due to $PQH_2$-induced conformational changes in the Cyt $b_6f$ complex has been suggested in (Hasan et al. 2013a). However, a complete chain of events leading to state transitions is still unclear. The Stt7/STN7 kinase is the redox-regulated enzyme, which contains the catalytic and regulatory domains (Bellafiore et al. 2005; Lemeille et al. 2009). The catalytic domain is facing the stroma, the regulatory domain is exposed to the thylakoid lumen. These domains are separated by a transmembrane helix with two Cys residues essential for the enzyme activity. The redox state of Cys residues may be regulated by Fd and thioredoxin through the membrane-bound thiol oxidoreductases (Lennartz et al. 2001; Motohashi and Hisabori 2006; Dietz and Pfannschmidt 2011). The over-reduced electron acceptors on the acceptor side of PSI will cause the reduction of Cys residues, thereby promoting dephosphorylation of the kinase and eventually inducing the "State 2 → State 1" transition, upon which PSI activity will lessen.

## 10.5 Concluding Remarks

Summing up a brief overview of structural and functional properties of the Cyt $b_6f$ complex, one can conclude that the overall rate of quinol oxidation is determined by $PQH_2$ turnover at the $Q_o$-site. The rates of PQ reduction to $PQH_2$ in PSII and its diffusion to the Cyt $b_6f$ complex do not limit the overall rate of electron transfer between PSII and PSI. The rate-limiting step in the intersystem electron transport is associated with $PQH_2$ oxidation at the $Q_o$-site in the Cyt $b_6f$ complex. It is the first step of the bifurcated reaction of $PQH_2$ oxidation (electron transfer from $PQH_2$ to $ISP_{ox}$) that restricts the rate of $PQH_2$ oxidation. The rate of this process is controlled by the intrathylakoid pH, values of which determine the protonation/deprotonation events in the $Q_o$-center of the Cyt $b_6f$ complex. The feedback control of $PQH_2$ oxidation is governed by the intrathylakoid $pH_{in}$. The acidification of the lumen causes deceleration of $PQH_2$ oxidation, thus impeding the intersystem electron transport. The Cyt $b_6f$ complex stands at the crossroad of alternative pathways of electron transport, providing flexibility and adaptability of the photosynthetic apparatus by means of two regulatory mechanisms: (*i*) redistribution of electron fluxes between alternative pathways (LEF and CEF1), and (*ii*) "state transitions" associated with the redistribution of solar energy between PSI and PSII.

**Acknowledgments** This work was supported in part by the Russian Foundation for Basic Research (RFBR Project 15-04-03790a).

## References

Albertsson PÅ (2001) A quantitative model of the domain structure of the photosynthetic membrane. Trends Plant Sci 6:349–354

Allen JF (1992) Protein phosphorylation in regulation of photosynthesis. Biochim Biophys Acta 1098:275–335

Allen JF (2003) Cyclic, pseudocyclic and noncyclic photophosphorylation: new links in the chain. Trends Plant Sci 8:15–19

Alric J, Pierre Y, Picot D et al (2005) Spectral and redox characterization of the heme $c_i$ of the cytochrome $b_6f$ complex. Proc Natl Acad Sci U S A 102:15860–15865

Anderson JM (1982) Distribution of the cytochromes of spinach chloroplasts between the appressed membranes of grana stacks and stroma-exposed thylakoid regions. FEBS Lett 138:62–66

Anderson JM, Chow WS, Goodchild DJ (1988) Thylakoid membrane organisation in sun/shade acclimation. Funct Plant Biol 15:11–26

Andersson I (2008) Catalysis and regulation in Rubisco. J Exp Bot 59:1555–1568

Balsera M, Schürmann P, Buchanan BB (2016) Redox regulation in chloroplasts. In: Kirchhoff H (ed) Chloroplasts. Current research and future trends. Caister Academic Press, Norfolk, pp 187–207

Bellafiore S, Barneche F, Peltier G et al (2005) State transitions and light adaptation require chloroplast thylakoid protein kinase STN7. Nature 433:892–895

Bendall DS, Manasse RS (1995) Cyclic photophosphorylation and electron transport. Biochim Biophys Acta 1229:23–38

Bennett J (1977) Phosphorylation of chloroplast membrane polypeptides. Nature 269:344–346

Benz JP, Lintala M, Soll J et al (2010) A new concept for ferredoxin-NADP(H) oxidoreductase binding to plant thylakoids. Trends Plant Sci 15:608–613
Berry EA, Guergova-Kuras M, Huang L et al (2000) Structure and function of cytochrome *bc* complexes. Annu Rev Biochem 69:1005–1075
Blankenship RE (2002) Molecular mechanisms of photosynthesis. Blackwell Science, Oxford
Bleier L, Dröse S (2013) Superoxide generation by complex III: from mechanistic rationales to functional consequences. Biochim Biophys Acta 1827:1320–1231
Brandt U (1996) Bifurcated ubihydroquinone oxidation in the cytochrome $bc_1$ complex by proton-gated charge transfer. FEBS Lett 387:1–6
Brandt U, Okun JG (1997) Role of deprotonation events in ubihydroquinone: cytochrome c oxidoreductase from bovine heart and yeast mitochondria. Biochemistry 36:11234–11240
Brettel K (1997) Electron transfer and arrangement of the redox cofactors in photosystem I. Biochim Biophys Acta 1318:322–373
Breyton C (2000) Conformational changes in the cytochrome $b_6f$ complex induced by inhibitor binding. J Biol Chem 275:13195–13201
Breyton C, Nandha B, Johnson G et al (2006) Redox modulation of cyclic electron flow around photosystem I in C3 plants. Biochemistry 45:13465–13475
Buchanan BB (1980) Role of light in the regulation of chloroplast enzymes. Annu Rev Plant Physiol 31:341–374
Burrows PA, Sazanov LA, Svab Z et al (1998) Identification of a functional respiratory complex in chloroplasts through analysis of tobacco mutants containing disrupted plastid *ndh* genes. EMBO J 17:868–876
Cape JL, Bowman MK, Kramer DM (2006) Understanding the cytochrome *bc* complexes by what they don't do. The Q-cycle at 30. Trends Plant Sci 11:46–55
Cape JL, Bowman MK, Kramer DM (2007) A semiquinone intermediate generated at the $Q_o$ site of the cytochrome $bc_1$ complex: importance for the Q-cycle and superoxide production. Proc Natl Acad Sci U S A 104:7887–7892
Cardona T, Sedoud A, Cox N et al (2012) Charge separation in Photosystem II: a comparative and evolutionary overview. Biochim Biophys Acta 1817:26–43
Chobot SE, Zhang H, Moser CC et al (2008) Breaking the Q-cycle: finding new ways to study $Q_o$ through thermodynamic manipulations. J Bioenerg Biomembr 40:501–507
Chovancová E, Pavelka A, Beneš P et al (2012) CAVER 3.0: a tool for the analysis of transport pathways in dynamic protein structures. PloS Comput Biol 8:e1002708
Clark WM (1960) Oxidation-reduction potentials of organic systems. Williams and Wilkins, Baltimore
Cramer WA, Zhang H, Yan J et al (2006) Transmembrane traffic in the cytochrome $b_6f$ complex. Annu Rev Biochem 75:769–790
Cramer WA, Hasan SS, Yamashita E (2011) The Q cycle of cytochrome *bc* complexes: A structure perspective. Biochim Biophys Acta 1807:788–802
Crofts AR (2004a) The cytochrome $bc_1$ complex: function in the context of structure. Annu Rev Physiol 66:689–733
Crofts AR (2004b) Proton-coupled electron transfer at the $Q_o$-site of the $bc_1$ complex controls the rate of ubihydroquinone oxidation. Biochim Biophys Acta 1655:77–92
Crofts AR, Guergova-Kuras M, Huang L-S et al (1999a) Mechanism of ubiquinol oxidation by the $bc_1$ complex: role of the iron sulfur protein and its mobility. Biochemistry 38:15791–15806
Crofts AR, Hong S, Zhang Z et al (1999b) Physicochemical aspects of the movement of the Rieske iron sulfur protein during quinol oxidation by the $bc_1$ complex from mitochondria and photosynthetic bacteria. Biochemistry 38:15827–15839
Crofts AR, Guergova-Kuras M, Kuras R et al (2000) Proton-coupled electron transfer at the $Q_o$-site: what type of mechanism can account for the high activation barrier? Biochim Biophys Acta 1459:456–466
Crofts AR, Lhee S, Crofts SB et al (2006) Proton pumping in the $bc_1$ complex: a new gating mechanism that prevents short circuits. Biochim Biophys Acta 1757:1019–1034

Crofts AR, Hong S, Wilson C et al (2013) The mechanism of ubihydroquinone oxidation at the $Q_o$-site of the cytochrome $bc_1$ complex. Biochim Biophys Acta 1827:1362–1377
Cruz JA, Avenson TJ, Kanazawa A et al (2007) Plasticity in light reactions of photosynthesis for energy production and photoprotection. J Exp Bot 56:395–406
DalCorso G, Pesaresi P, Masiero S et al (2008) A complex containing PGRL1 and PGR5 is involved in the switch between linear and cyclic electron flow in *Arabidopsis*. Cell 132:273–285
Darrouzet E, Moser CC, Dutton PL et al (2001) Large scale domain movement in cytochrome $bc_1$: a new device for electron transfer in proteins. Trends Biochem Sci 26:445–451
de Vitry C, Ouyang Y, Finazzi G et al (2004) The chloroplast Rieske iron-sulfur protein: at the crossroad of electron transport and signal transduction. J Biol Chem 279:44621–44627
Dekker JP, Boekema EJ (2005) Supermolecular organization of the thylakoid membrane proteins in green plants. Biochim Biophys Acta 1706:12–39
Demmig-Adams B, Cohu CM, Muller O et al (2012) Modulation of photosynthetic energy conversion efficiency in nature: from seconds to seasons. Photosynth Res 113:75–88
Dietz K-J, Pfannschmidt T (2011) Novel regulators in photosynthetic redox control of plant metabolism and gene expression. Plant Physiol 155:1477–1485
Eberhard S, Finazzi G, Wollman FA (2008) The dynamics of photosynthesis. Annu Rev Genet 42:463–515
Edwards GE, Walker DA (1983) $C_3$, $C_4$: mechanisms, and cellular and environmental regulation of photosynthesis. Blackwell, Oxford
Endo T, Shikanai T, Sato F et al (1998) NAD(P)H dehydrogenase-dependent, antimycin A-sensitive electron donation to plastoquinone in tobacco chloroplasts. Plant Cell Physiol 39:1226–1231
Esser L, Gong X, Yang S et al (2006) Surface-modulated motion switch: capture and release of iron-sulfur protein in the cytochrome $bc_1$ complex. Proc Natl Acad Sci U S A 103:13045–13050
Finazzi G (2002) Redox-coupled proton pumping activity in cytochrome $b_6f$, as evidenced by the pH dependence of electron transfer in whole cells of *Chlamydomonas reinhardtii*. Biochemistry 41:7475–7482
Foyer CH, Neukermans J, Queval G et al (2012) Photosynthetic control of electron transport and the regulation of gene expression. J Exp Bot 63:1637–1661
Frolov AE, Tikhonov AN (2009) The oxidation of plastoquinol by a cytochrome $b_6f$ complex: a density functional theory study. Russian J Phys Chem A 83:506–508
Fromme P, Jordan P, Krauss N (2001) Structure of photosystem I. Biochim Biophys Acta 1507:5–31
Galka P, Santabarbara S, Khuong TTH et al (2012) Functional analyses of the plant photosystem I-light-harvesting complex II supercomplex reveal that light-harvesting complex II loosely bound to Photosystem II is a very efficient antenna for Photosystem I in state II. Plant Cell 24:2963–2978
Gill SS, Tuteja N (2010) Reactive oxygen species and antioxidant machinery in abiotic stress tolerance in crop plants. Plant Physiol Biochem 48:909–930
Haehnel W (1973) Electron transport between plastoquinone and chlorophyll $a_I$. Biochim Biophys Acta 305:618–631
Haehnel W (1976a) The reduction kinetics of chlorophyll $a_1$ as an indicator for proton uptake between the light reactions in chloroplasts. Biochim Biophys Acta 440:506–521
Haehnel W (1976b) The ratio of the two light reactions and their coupling in chloroplasts. Biochim Biophys Acta 423:499–509
Haehnel W (1982) On the functional organization of electron transport from plastoquinone to photosystem I. Biochim Biophys Acta 682:245–247
Haehnel W (1984) Photosynthetic electron transport in higher plants. Annu Rev Plant Physiol 35:659–693
Haldrup A, Jensen PE, Lunde C, Scheller HV (2001) Balance of power: a view of the mechanism of photosynthetic state transitions. Trends Plant Sci 6:301–305
Harbinson J, Hedley CL (1989) The kinetics of P-700$^+$ reduction in leaves: a novel *in situ* probe of thylakoid functioning. Plant Cell and Environ 12:357–369

Hasan SS, Yamashita E, Cramer WA (2013a) Transmembrane signaling and assembly of the cytochrome $b_6f$-lipidic charge transfer complex. Biochim Biophys Acta 1827:1295–1308
Hasan SS, Stofleth JT, Yamashita E et al (2013b) Lipid-induced conformational changes within the cytochrome $b_6f$ complex in oxygenic photosynthesis. Biochemistry 52:2649–2654
Hasan SS, Yamashita E, Baniulis D et al (2013c) Quinone-dependent proton transfer pathways in the photosynthetic cytochrome $b_6f$ complex. Proc Natl Acad Sci 110:4297–4302
Heimann S, Ponamarev MV, Cramer WA (2000) Movement of the Rieske iron-sulfur protein in the p-side bulk aqueous phase: effect of lumenal viscosity on redox reactions of the cytochrome $b_6f$ complex. Biochemistry 39:2692–2699
Hertle AP, Blunder T, Wunder T et al (2013) PGRL1 is the elusive ferredoxin-plastoquinone reductase in photosynthetic cyclic electron flow. Mol Cell 49:511–523
Hong SJ, Ugulava N, Guergova-Kuras M et al (1999) The energy landscape for ubihydroquinone oxidation at the $Q_o$-site of the $bc_1$ complex in *Rhodobacter sphaeroides*. J Biol Chem 274:33931–33944
Hope AB (2000) Electron transfers amongst cytochrome *f*, plastocyanin and photosystem I: kinetics and mechanisms. Biochim Biophys Acta 1456:5–26
Hope AB, Valent P, Matthews DB (1994) Effects of pH on the kinetics of redox reactions in and around the cytochrome *bf* complex in an isolated system. Photosynth Res 42:111–120
Horton P (2012) Optimization of light harvesting and photoprotection: molecular mechanisms and physiological consequences. Phil Trans R Soc B 367:3455–3465
Hsueh K-L, Westler WM, Markley JL (2010) NMR investigations of the Rieske protein from *Thermus thermophilus* support a coupled proton and electron transfer mechanism. J Am Chem Soc 132:7908–7918
Iwai M, Takizawa K, Tokutsu R et al (2010) Isolation of the elusive supercomplex that drives cyclic electron flow in photosynthesis. Nature 464:1210–1213
Iwaki M, Yakovlev G, Hirst J et al (2005) Direct observation of redox-linked histidine protonation changes in the iron–sulfur protein of the cytochrome $bc_1$ complex by ATR-FTIR spectroscopy. Biochemistry 44:4230–4237
Iwata S, Lee JW, Okada K et al (1998) Complete structure of the 11-subunit bovine mitochondrial cytochrome $bc_1$ complex. Science 281:64–71
Izrailev S, Crofts AR, Berry EA et al (1999) Steered molecular dynamics simulation of the Rieske subunit motion in the cytochrome $bc_1$ complex. Biophys J 77:1753–1768
Jallet D, Cantrell M, Peers G (2016) New players for photoprotection and light acclimation. In: Kirchhoff H (ed) Chloroplasts. Current research and future trends. Caister Academic Press, Norfolk, pp 133–159
Järvi S, Gollan PJ, Aro E-M (2013) Understanding the roles of the thylakoid lumen in photosynthetic regulation. Front Plant Sci. https://doi.org/10.3389/fpls.2013.00434
Joët T, Cournac L, Horvath EM et al (2001) Increased sensitivity of photosynthesis to antimycin A induced by inactivation of the chloroplast *ndhB* gene. Evidence for a participation of the NADH-dehydrogenase complex to cyclic electron flow around photosystem I. Plant Physiol 125:1919–1929
Johnson GN (2011) Physiology of PSI cyclic electron transport in higher plants. Biochim Biophys Acta 1807:906–911
Joliot P, Joliot A (2005) Quantification of cyclic and linear flows in plants. Proc Natl Acad Sci U S A 102:4913–4918
Joliot P, Joliot A (2006) Cyclic electron flow in C3 plants. Biochim Biophys Acta 1757:362–368
Jordan P, Fromme P, Witt HT et al (2001) Three-dimensional structure of photosystem I at 2.5 Å resolution. Nature 411:909–917
Junge W, Nelson N (2015) ATP synthase. Annu Rev Biochem 83:631–657
Kim H, Xia D, Yu CA et al (1998) Inhibitor binding changes domain mobility in the iron–sulphur protein of the mitochondrial $bc_1$ complex from bovine heart. Proc Natl Acad Sci U S A 95:8026–8033

Kirchhoff H (2008) Significance of protein crowding, order and mobility for photosynthetic membrane functions. Biochem Soc Trans 36:967–970
Kirchhoff H (2013) Architectural switches in plant thylakoid membranes. Photosynth Res 116:481–487
Kirchhoff H (2014) Diffusion of molecules and macromolecules in thylakoid membranes. Biochim Biophys Acta 1837:495–502
Kono M, Terashima I (2014) Long-term and short-term responses of the photosynthetic electron transport to fluctuating light. J Photochem Photobiol B 137:89–99
Kono M, Noguchi K, Terashima I (2014) Roles of cyclic electron flow around PSI (CEF-PSI) and $O_2$-dependent alternative pathways in regulation of the photosynthetic electron flow in short-term fluctuating light in Arabidopsis thaliana. Plant Cell Physiol 55:990–1004
Kramer DM, Sacksteder CA, Cruz JA (1999) How acidic is the lumen? Photosynth Res 60:151–163
Kramer DM, Avenson TJ, Edwards GE (2004) Dynamic flexibility in the light reactions of photosynthesis governed by both electron and proton transfer reactions. Trends Plant Sci 9:349–357
Kubicki A, Funk E, Westhoff P et al (1996) Differential expression of plastome-encoded *ndh* genes in mesophyll and bundle-sheath chloroplasts of the $C_4$ plant *Sorghum bicolor* indicates that the complex I-homologous NAD(P)H-plastoquinone oxidoreductase is involved in cyclic electron transport. Planta 199:276–281
Kubota K, Sakurai I, Katayama K et al (2009) Purification and characterization of photosystem I complex from *Synechocystis sp*. PCC 6803 by expressing histidine-tagged subunits. Biochim Biophys Acta 1797:98–105
Kurisu G, Zhang H, Smith JL et al (2003) Structure of the cytochrome $b_6f$ complex of oxygenic photosynthesis: tuning the cavity. Science 302:1009–1014
Laisk A, Eichelmann H, Oja V et al (2005) Control of cytochrome $b_6f$ at low and high light intensity and cyclic electron transport in leaves. Biochim Biophys Acta 1708:79–90
Lavergne J, Joliot P (1991) Restricted diffusion in photosynthetic membranes. Trends Biochem Sci 16:129–134
Lemeille S, Rochaix J-D (2010) State transitions at the crossroad of thylakoid signaling pathways. Photosynth Res 106:33–46
Lemeille S, Willig A, Depège-Fargeix N et al (2009) Analysis of the chloroplasts protein kinase Stt7 during state transition. PLoS Biol 7 e1000045, 664–673
Lennartz K, Plucken H, Seidler A et al (2001) *HCF164* encodes a thioredoxin-like protein involved in the biogenesis of the cytochrome $b_6f$ complex in Arabidopsis. Plant Cell 13:2539–2551
Lhee S, Kolling DRJ, Nair SK et al (2010) Modifications of protein environment of the [2Fe-2S] cluster of the $bc_1$ complex: effects on biophysical properties of the Rieske iron-sulfur protein and on the kinetics of the complex. J Biol Chem 285:9233–9248
Li Z, Wakao S, Fischer BB et al (2009) Sensing and responding to excess light. Annu Rev Plant Biol 60:239–260
Lichtenthaler HK, Babani F (2004) Light adaptation and senescence of the photosynthetic apparatus. Changes in pigment composition, chlorophyll fluorescence parameters and photosynthetic activity. In: Papageorgiou GC, Govindjee (eds) Chlorophyll *a* fluorescence: a signature of photosynthesis, Advances in photosynthesis and respiration, vol 19. Springer, Dordrecht, pp 713–736
Lin I-J, Chen Y, Fee JA, Song J et al (2006) Rieske protein from *Thermus thermophilus*: $^{15}N$ NMR titration study demonstrates the role of iron-ligated histidines in the pH dependence of the reduction potential. J Am Chem Soc 128:10672–10673
Link TA (1997) The role of the "Rieske" iron sulfur protein in the hydroquinone oxidation ($Q_p$) site of the cytochrome $bc_1$ complex: the "proton-gated affinity change" mechanism. FEBS Lett 412:257–264
Malnoë A, Wollman F-A, de Vitry C et al (2011) Photosynthetic growth despite a broken Q-cycle. Nature Communications 2:301. https://doi.org/10.1038/ncomms1299/www.nature.com/naturecommunications

Mamedov M, Govindjee, Nadtochenko V et al (2015) Primary electron transfer processes in photosynthetic reaction centers from oxygenic organisms. Photosynth Res 125:51–63
Michelet L, Zaffagnini M, Morisse S et al (2013) Redox regulation of the Calvin–Benson cycle: something old, something new. Front Plant Sci 4:Article 470. https://doi.org/10.3389/fpls.2013.00470
Mitchell P (1966) Chemiosmotic coupling in oxidative and photosynthetic phosphorylation. Biol Rev 41:445–502
Mitchell P (1976) Possible molecular mechanisms of the protonmotive function of cytochrome systems. J Theor Biol 62:327–367
Motohashi K, Hisabori T (2006) HCF164 receives reducing equivalents from stromal thioredoxin across the thylakoid membrane and mediates reduction of target proteins in the thylakoid lumen. J Biol Chem 281:35039–35047
Müh F, Glöckner C, Hellmich J et al (2012) Light-induced quinone reduction in photosystem II. Biochim Biophys Acta 1817:44–65
Mulkidjanian AY (2005) Ubiquinol oxidation in the cytochrome $bc_1$ complex: reaction mechanism and prevention of short-circuiting. Biochim Biophys Acta 1709:5–34
Munekage Y, Hojo M, Meurer J et al (2002) *PGR5* is involved in cyclic electron flow around photosystem I and is essential for photoprotection in *Arabidopsis*. Cell 110:361–371
Munekage Y, Hashimoto M, Miyake C et al (2004) Cyclic electron flow around photosystem I is essential for photosynthesis. Nature 429:579–582
Munekage Y, Genty B, Peltier G (2008) Effect of PGR5 impairment on photosynthesis and growth in *Arabidopsis thaliana*. Plant Cell Physiol 49:1688–1698
Nelson N, Yocum CF (2006) Structure and function of photosystems I and II. Annu Rev Plant Biol 57:521–565
Osyczka A, Moser CC, Daldal F et al (2004) Reversible redox energy coupling in electron transfer chains. Science 427:607–612
Osyczka A, Moser CC, Dutton L (2005) Fixing the Q cycle. Trends Biochem Sci 30:176–182
Page CC, Moser CC, Chen X et al (1999) Natural engineering principles of electron tunnelling in biological oxidation-reduction. Nature 402:47–52
Peng LW, Shimizu H, Shikanai T (2008) The chloroplast NAD(P)H dehydrogenase complex interacts with Photosystem I in *Arabidopsis*. J Biol Chem 283:34873–34879
Peng LW, Fukao Y, Fujiwara M et al (2009) Efficient operation of NAD(P)H dehydrogenase requires supercomplex formation with Photosystem I via minor LHCI in *Arabidopsis*. Plant Cell 21:3623–3640
Pesaresi P, Hertle A, Pribil M et al (2010) Optimizing photosynthesis under fluctuating light. The role of the Arabidopsis STN7 kinase. Plant Signal Behav 5:21–25
Pierre Y, Breyton C, Kramer D, Popot J-L (1995) Purification and characterization of the cytochrome $b_6f$ complex from Chlamydomonas reinhardtii. J Biol Chem 270:29342–29349
Ponamarev MV, Cramer WA (1998) Perturbation of the internal water chain in cytochrome *f* of oxygenic photosynthesis: loss of concerted reduction of cytochromes *f* and *b*. Biochemistry 37:17199–17208
Postila PA, Kaszuba K, Sarewicz M et al (2013) Key role of water in proton transfer at the $Q_o$-site of the cytochrome $bc_1$ complex predicted by atomistic molecular dynamics simulations. Biochim Biophys Acta 1827:761–768
Puthiyaveetil S, Kirchhoff H, Hohner R (2016) Structural and functional dynamics of the thylakoid membrane system. In: Kirchhoff H (ed) Chloroplasts. Current research and future trends. Caister Academic Press, Norfolk, pp 59–87
Rich PR (2004) The quinone chemistry of *bc* complexes. Biochim Biophys Acta 1658:165–171
Roberts AG, Bowman MK, Kramer DM (2002) Certain metal ions are inhibitors of cytochrome $b_6f$ complex 'Rieske' iron-sulfur protein domain movements. Biochemistry 41:4070–4079
Rochaix J-D (2014) Regulation and dynamics of the light-harvesting system. Annu Rev Plant Biol 65:287–309

Ruban A (2012) The photosynthetic membrane: molecular mechanisms and biophysics of light harvesting. Wiley-Blackwell, Oxford
Rumberg B, Siggel U (1969) pH changes in the inner phase of the thylakoids during photosynthesis. Naturwissenschaften 56:130–132
Sainz G, Carrell CJ, Ponamarev MV et al (2000) Interruption of the internal water chain of cytochrome *f* impairs photosynthetic function. Biochemistry 39:9164–9173
Samoilova RI, Kolling D, Uzawa T et al (2002) The interaction of the Rieske iron sulfur protein with occupants of the $Q_o$-site of the $bc_1$ complex, probed by 1D and 2D electron spin echo envelope modulation. J Biol Chem 277:4605–4608
Schöttler MA, Tôth SZ, Boulouis A, Kahlau S (2015) Photosynthetic complex stoichiometry dynamics in higher plants: biogenesis, function, and turnover of ATP synthase and the cytochrome $b_6f$ complex. J Exp Bot 66:2373–2400
Seelert H, Poetsch A, Dencher NA et al (2000) Structural biology. Proton-powered turbine of a plant motor. Nature 405:418–419
Shelaev IV, Gostev FE, Mamedov MD et al (2010) Femtosecond primary charge separation in photosystem I. Biochim Biophys Acta 1797:1410–1420
Shikanai T (2007) Cyclic electron transport around photosystem I: Genetic approaches. Plant Biol 58:199–217
Shikanai T (2016) Chloroplast NDH: a different enzyme with a structure similar to that of respiratory NADH dehydrogenase. Biochim Biophys Acta 1857:1015–1022
Shikanai T, Endo T, Hashimoto et al (1998) Directed disruption of the tobacco *ndhB* gene impairs cyclic electron flow around photosystem I. Proc Natl Acad Sci U S A 95:9705–9709
Siggel U, Renger G, Stiehl HH et al (1972) Evidence for electronic and ionic interaction between electron transport chains in chloroplasts. Biochim Biophys Acta:328–335
Snyder CH, Gutierrez-Cirlos EB, Trumpower BL (2000) Evidence for a concerted mechanism of ubiquinol oxidation by the cytochrome $bc_1$ complex. J Biol Chem 275:13535–13541
Soriano GM, Ponamarev MV, Tae G-S et al (1996) Effect of the interdomain basic region of cytochrome *f* on its redox reactions *in vivo*. Biochemistry 35:14590–14598
Soriano GM, Guo L-W, de Vitry C et al (2002) Electron transfer from the Rieske iron-sulfur protein (ISP) to cytochrome *f in vitro.* Is a guided trajectory of the ISP necessary for competent docking? J Biol Chem 277:41865–41871
Staehelin LA (2003) Chloroplast structure: from chlorophyll granules to supra-molecular architecture of thylakoid membranes. Photosynth Res 76:185–196
Stiehl HH, Witt HT (1969) Quantitative treatment of the function of plastoquinone in photosynthesis. Z Naturforsch 24b:1588–1598
Stirbet A (2013) Excitonic connectivity between photosystem II units: what is it, and how to measure it. Photosynth Res 116:189–214
Strand DD, Fisher N, Kramer DM (2016) Distinct energetics and regulatory functions of the two major cyclic electron flow pathways in chloroplasts. In: Kirchhoff H (ed) Chloroplasts. Current research and future trends. Caister Academic Press, Norfolk, pp 89–100
Stroebel D, Choquet Y, Popot J-L et al (2003) An atypical heam in the cytochrome $b_6f$ complex. Nature 426:413–418
Suorsa M, Järvi S, Grieco M et al (2012) PROTON GRADIENT REGULATION5 is essential for proper acclimation of *Arabidopsis* photosystem I to naturally and artificially fluctuating light conditions. Plant Cell 24:2934–2948
Tikhonov AN (2013) pH-dependent regulation of electron transport and ATP synthesis in chloroplasts. Photosynth Res 116:511–534
Tikhonov AN (2014) The cytochrome $b_6f$ complex at the crossroad of photosynthetic electron transport pathways. Plant Physiol Biochem 81:163–183
Tikhonov AN (2015) Induction events and short-term regulation of electron transport in chloroplasts: an overview. Photosynth Res 125:65–94

Tikhonov AN (2016) Modeling electron and proton transport in chloroplasts. In: Kirchhoff H (ed) Chloroplasts. Current Research and Future Trends. Caister Academic Press, Norfolk, pp 101–134

Tikhonov AN, Ruuge EK (1979) Electron paramagnetic resonance study of electron transport in photosynthetic systems. VIII. The interplay between two photosystems and kinetics of P700 redox transients under various conditions of flash excitation. Molec Biol (Moscow) 13:1085–1097

Tikhonov AN, Vershubskii AV (2017) Connectivity between electron transport complexes and modulation of photosystem II activity in chloroplasts. Photosynth Res 133:103–114

Tikhonov AN, Khomutov GB, Ruuge EK (1980) Electron spin resonance study of electron transport in photosynthetic systems. IX. Temperature dependence of the kinetics of P700 redox transients in bean chloroplasts induced by flashes with different duration. Molec Biol (Moscow) 14:157–172

Tikhonov AN, Khomutov GB, Ruuge EK et al (1981) Electron transport control in chloroplasts. Effects of photosynthetic control monitored by the intrathylakoid pH. Biochim Biophys Acta 637:321–333

Tikhonov AN, Timoshin AA, Blumenfeld LA (1983) The kinetics of electron transport translocation of protons and photophosphorylation in chloroplasts and their relationship with the thermo-induced structural changes in the thylakoid membrane. Molec Biol (Moscow) 17:1236–1248

Tikhonov AN, Khomutov GB, Ruuge EK (1984) Electron transport control in chloroplasts. Effects of magnesium ions on the electron flow between two photosystems. Photobiochem Photobiophys 8:261–269

Tikkanen M, Aro E-M (2012) Thylakoid protein phosphorylation in dynamic regulation of photosystem II in higher plants. Biochim Biophys Acta 1817:232–238

Tikkanen M, Grieco M, Nurmi M et al (2012) Regulation of the photosynthetic apparatus under fluctuating growth light. Philos Trans R Soc Lond B 367:3486–3493

Tremmel IG, Kirchhoff H, Weis E et al (2003) Dependence of plastoquinol diffusion on the shape, size, and density of integral thylakoid proteins. Biochim Biophis Acta 1603:97–109

Turina P, Petersen J, Gräber P (2016) Thermodynamics of proton transport coupled ATP synthesis. Biochim Biophys Acta 1857:653–664

Vener AV, van Kan PJ, Rich PR et al (1997) Plastoquinol at the quinol oxidation site of reduced cytochrome *bf* mediates signal transduction between light and protein phosphorylation: Thylakoid protein kinase deactivation by a single-turnover flash. Proc Natl Acad Sci U S A 94:1585–1590

Victoria D, Burton R, Crofts AR (2013) Role of the –PEWY-glutamate in catalysis at the $Q_o$-site of the Cyt $bc_1$ complex. Biochim Biophys Acta 1827:365–386

Witt HT (1979) Energy conversion in the functional membrane of photosynthesis. Analysis by light pulse and electric pulse methods. The central role of the electric field. Biochim Biophys Acta 505:355–427

Wood PM (1988) The potential diagram for oxygen at pH 7. Biochem J 253:287–289

Xia D, C-A Y, Kim H et al (1997) Crystal structure of the cytochrome $bc_1$ complex from bovine heart mitochondria. Science 277:60–66

Xia D, Esser L, Tang W-K et al (2013) Structural analysis of cytochrome $bc_1$ complexes: Implications to the mechanism of function. Biochim Biophys Acta 1827:1278–1294

Yamashita E, Zhang H, Cramer WA (2007) Structure of the cytochrome $b_6f$ complex: Quinone analogue inhibitors as ligands of heme $c_n$. J Mol Biol 370:39–52

Yamori W, Shikanai T (2016) Physiological functions of cyclic electron transport around photosystem I in sustaining photosynthesis and plant growth. Annu Rev Plant Biol 67:81–106

Yan J, Cramer WA (2003) Functional insensitivity of the cytochrome $b_6f$ complex to structure changes in the hinge region of the Rieske iron–sulfur protein. J Biol Chem 278:20926–20933

Zhang H, Carrell CJ, Huang D et al (1996) Characterization and crystallization of the lumen side domain of the chloroplast Rieske iron-sulfur protein. J Biol Chem 271:31360–31366

Zhang Z, Huang L, Shulmeister VM et al (1998) Electron transfer by domain movement in cytochrome $bc_1$. Nature 392:677–684

Zhang H, Whitelegge JP, Cramer WA (2001) Ferredoxin: $NADP^+$ oxidoreductase is a subunit of the chloroplast cytochrome $b_6f$ complex. J Biol Chem 276:38159–38165

Zhu J, Egawa T, Yeh S-R et al (2007) Simultaneous reduction of iron-sulfur protein and cytochrome $b_L$ during ubiquinol oxidation in cytochrome $bc_1$ complex. Proc Natl Acad Sci U S A 104:4864–4869

Zito F, Finazzi G, Joliot P et al (1998) Glu78, from the conserved PEWY sequence of subunit IV, has a key function in the cytochrome $b_6f$ turnover. Biochemistry 37:10395–10403

Zito F, Finazzi G, Delosme R et al (1999) The $Q_o$ site of cytochrome $b_6f$ complexes controls the activation of the LHCII kinase. EMBO J 18:2961–2969

Zu Y, Manon M-J, Couture MM-J et al (2003) Reduction potentials of Rieske clusters: Importance of the coupling between oxidation state and histidine protonation state. Biochemistry 42:12400–12408

# Chapter 11
# Ryanodine Receptor Structure and Function in Health and Disease

**Gaetano Santulli, Daniel Lewis, Amedee des Georges, Andrew R. Marks, and Joachim Frank**

**Abstract** Ryanodine receptors (RyRs) are ubiquitous intracellular calcium ($Ca^{2+}$) release channels required for the function of many organs including heart and skeletal muscle, synaptic transmission in the brain, pancreatic beta cell function, and vascular tone. In disease, defective function of RyRs due either to stress (hyperadrenergic and/or oxidative overload) or genetic mutations can render the channels leaky to $Ca^{2+}$ and promote defective disease-causing signals as observed in heat failure, muscular dystrophy, diabetes mellitus, and neurodegerative disease. RyRs are massive structures comprising the largest known ion channel-bearing macromolecular complex and exceeding 3 million Daltons in molecular weight. RyRs mediate the rapid release of $Ca^{2+}$ from the endoplasmic/sarcoplasmic reticulum (ER/SR) to stimulate cellular functions through $Ca^{2+}$-dependent processes. Recent advances in single-particle cryogenic electron microscopy (cryo-EM) have enabled the determination of atomic-level structures for RyR for the first time. These structures have illuminated the mechanisms by which these critical ion channels function and interact with regulatory ligands. In the present chapter we discuss the structure, functional elements, gating and activation mechanisms of RyRs in normal and disease states.

**Keywords** Ryanodine receptor (RyR) · Calcium release channel · Cryo-EM · Endoplasmic reticulum · Sarcoplasmic reticulum

G. Santulli
The Wu Center for Molecular Cardiology, Department of Physiology and Cellular Biophysics, Columbia University Medical Center, New York, NY, USA

The Wilf Family Cardiovascular Research Institute and the Einstein-Mount Sinai Diabetes Research Center, Department of Medicine, Albert Einstein College of Medicine – Montefiore University Hospital, New York, NY, USA
e-mail: gsantulli001@gmail.com

D. Lewis
Department of Physiology and Cellular Biophysics, Columbia University, New York, NY, USA
e-mail: drl2107@cumc.columbia.edu



J. R. Harris, E. J. Boekema (eds.), *Membrane Protein Complexes: Structure and Function*, Subcellular Biochemistry 87,
https://doi.org/10.1007/978-981-10-7757-9_11

## 11.1 Ryanodine Receptors: Physiology and Function

Ryanodine receptors (RyRs) control calcium ($Ca^{2+}$) release from intracellular endoplasmic/sarcoplasmic reticulum (ER/SR) stores (Santulli et al. 2017b). RyRs are found ubiquitously in mammals, and three different variants (RyR1, RyR2, and RyR3) are known. RyR1 is the major form in skeletal muscle (Inui et al. 1987; Takeshima et al. 1989; Marks et al. 1989); RyR2 is the major form in cardiac muscle (Nakai et al. 1990; Otsu et al. 1990; Brillantes et al. 1992), and is also involved in cognitive function (Liu et al. 2012) and in insulin secretion from pancreatic beta cells (Santulli et al. 2015a); RyR3, originally identified in the brain (Nakashima et al. 1997; Hakamata et al. 1992), is widely expressed (Zhang et al. 2011; Lanner et al. 2010) but its function is less well understood.

In muscle cells RyRs are expressed early in development (Rosemblit et al. 1999; Brillantes et al. 1994b), and their expression is regulated by stress signals (Maki et al. 1996). They are required for excitation-contraction coupling, which translates an electrical signal into a mechanical output via the second messenger $Ca^{2+}$ (Santulli and Marks 2015). The closely related inositol 1,4,5-trisphosphate receptors (IP3Rs) are also found in most cell types and require the second messenger IP3 for activation (Harnick et al. 1995; Yuan et al. 2016; Santulli et al. 2017a). In skeletal muscle there is a mechanical interaction between RyR1 on the sarcoplasmic reticulum (SR) membrane and the dihydropyridine receptor ($Ca_v1.1$) on specialized invaginations of the sarcolemma, called transverse tubules, leading to rapid $Ca^{2+}$ release (Rios and

A. des Georges
Advanced Science Research Center at the Graduate Center of the City University of New York, New York, NY, USA

Department of Chemistry & Biochemistry, City College of New York, New York, NY, USA

Ph.D. Program in Biochemistry, The Graduate Center of the City University of New York, New York, NY, USA
e-mail: Amedee.desGeorges@asrc.cuny.edu

A. R. Marks
Department of Medicine, Columbia University, New York, NY, USA

Department of Physiology and Cellular Biophysics, Columbia University, New York, NY, USA
e-mail: arm42@cumc.columbia.edu

J. Frank (✉)
Department of Biochemistry and Molecular Biophysics, Columbia University, New York, NY, USA

Department of Biological Sciences, Columbia University, New York, NY, USA
e-mail: jf2192@cumc.columbia.edu

Brum 1987; Nelson et al. 2013; Santulli et al. 2017b). In cardiac muscle the depolarization of the plasma membrane activates $Ca^{2+}$ influx via the L-type $Ca^{2+}$ channel (LCC, $Ca_v1.2$), which in turn activates RyR2 via $Ca^{2+}$-induced $Ca^{2+}$ release (Fabiato and Fabiato 1975; Santulli et al. 2017b). At low cytosolic $Ca^{2+}$ (~100–200 nM), RyR channels are closed, with extremely low open probability ($P_o$). The $P_o$ increases at submicromolar levels of cytosolic $Ca^{2+}$, reaching a maximal $P_o$ at ~10 μM. Cytosolic $Ca^{2+}$ concentrations above ~10 μM lower the $P_o$ (Bezprozvanny et al. 1991). This behavior points to the presence of two $Ca^{2+}$ binding sites with different affinities, a moderate-affinity (μM $K_D$) $Ca^{2+}$ activation binding site (des Georges et al. 2016) and a lower-affinity (~100 μM $K_D$) $Ca^{2+}$-dependent inhibition site.

As $Ca^{2+}$ is involved in many cell signaling pathways of critical importance, mutations affecting the proper function and regulation of the $Ca^{2+}$-release channel RyR can have severe impact on cellular function. In particular, RyRs are crucial for muscle function, and mutations in the receptor can lead to a number of heart and skeletal muscle pathologies. For instance, mutations in RyR1 are implicated in malignant hyperthermia (MH) and central core disease (CCD) (Quane et al. 1993; Santulli et al. 2017b), while mutations in RyR2 can lead to cardiac arrhythmias (Vest et al. 2005; Xie et al. 2015; Lehnart et al. 2004; Marks et al. 2002; Xie et al. 2013). Understanding the structure of these channels and the mechanism by which they function may enable the design of therapeutics to stabilize damaged RyRs in order to restore normal function.

## 11.2 Early Attempts to Determine RyR Structure

The gigantic size and large variability of the RyR structure have hindered attempts to obtain highly ordered crystals amenable to X-ray crystallography. Only the structures of individual domains were solved to high resolution: a 559-residue fraction of the N-terminal domain (Lobo et al. 2009), representing 11% of the sequence of the entire channel, and the SPRY1 and tandem-repeat domains (Yuchi et al. 2015). However, the best crystals of the channel in its entirety, obtained in a collaboration between the Marks and Hendrickson labs, did not diffract beyond a resolution of 7 Å (Clarke and Hendrickson, personal communication).

For very large molecules such as RyR, several advantages of the single-particle cryogenic electron microscopy (cryo-EM) approach (Frank 2016) over X-ray crystallography come to bear (also see separate section below): first, high-resolution 3D information can be obtained from the 2D projection images of the molecule flash-frozen in solution, obviating the need for ordered crystals; and second, structural heterogeneity inherent to the function of the molecule may be studied as multiple conformers can be retrieved through the use of image classification.

These aspects prompted us early on, in collaboration with Sidney Fleischer at Vanderbilt University, to try using the single-particle electron microscopy technique on detergent-solubilized RyR, resulting in first image averages of the negatively stained channel in the top view (Saito et al. 1988). Soon after that, first three-dimensional reconstructions of the stained (Wagenknecht et al. 1989) and unstained, frozen-hydrated RyR1 (Radermacher et al. 1992, 1994; Wagenknecht and

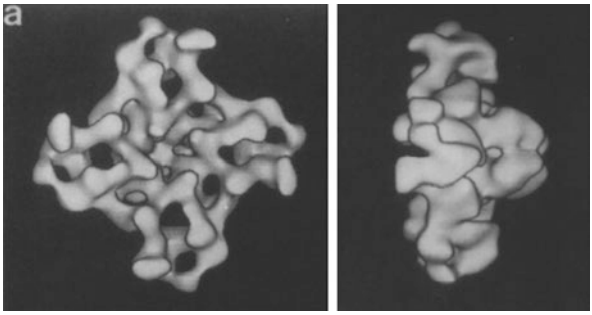


**Fig. 11.1 First cryo-EM reconstruction of the RyR1 $Ca^{2+}$-release channel (top and side view)**. The RyR1 channel was reconstructed from ~500 particles at 30 Å resolution (Reproduced with permission from Radermacher et al. 1994)

Radermacher 1995) (Fig. 11.1) and RyR2 (Sharma et al. 1998) channels were obtained. The resolution of these first reconstructions was quite limited, but they revealed the overall fourfold symmetric (C4) mushroom-shaped architecture, with the four copies of a large cytosolic domain forming an umbrella, and a small cylindric transmembrane domain containing the pore. Each monomer, or "wing" of the cytosolic umbrella domain, was seen to be perforated by large cavities.

Even as the performance of electron microscopes and the sophistication of image processing programs improved, the resolution of RyR density maps did not keep pace for several years, for an important technical reason: reconstructions were limited by the severe orientation bias as RyR molecules prefer to lie on the carbon-coated grid in their C4-symmetry view, face-up or face-down. In such a situation, the reconstruction is strongly distorted as the resolution is anisotropic, producing biased and misleading representations of the structure. Still, significant progress was achieved in identifying locations of critical effector binding sites on the molecule (see review by Hamilton and Serysheva 2009). The problem of strong view preference of the molecule was finally resolved by preparing the EM grids with the water layer freely suspended over holes, yielding first reconstructions of the closed RyR1 channel with isotropic resolution (Samsò et al. 2005). Details regarding the issues related to view preference of RyR have been reviewed in Baker et al. (2015).

However, until recently, there still existed a fundamental obstacle preventing resolutions better than 5 Å to be reached by single-particle cryo-EM for any structures except for those with very high symmetry, such as icosahedral viruses. The obstacle was presented by the suboptimal performance of recording media in the electron microscope. Density maps of RyR1 with best resolutions in the 10 Å range were interpreted with "helix hunter" programs (Jiang et al. 2007; Baker et al. 2007) that attempt to place helices and other secondary structure elements into the reconstructed density map, based on sequence information and low-resolution localizations of binding sites. On this basis, first tentative all-atomic structures were built for the RyR1 channel in its entirety or for the functionally most relevant, pore-forming region (Ludtke et al. 2005; Samsò et al. 2009). In order to map the low-resolution density map to the sequence of the molecule, Liu and co-workers developed a method of genetic GFP insertion and cryo-EM difference mapping, first applied to RyR2 (Liu et al. 2004). Even at these low resolutions, the masses of density due to insertion of GFP become visible in the difference map as a signal with high statistical significance. This strategy allowed the approximate positions of divergent regions of RyR to be determined.

In 2012 the first direct electron detectors came on the market, which have signal-to-noise ratios and modulation transfer functions superior to those of film and much superior to the only online recording medium then available, the CCD camera. The introduction of these new cameras into electron microscopy spurred an avalanche of molecular structures with resolutions ranging from 2 to 4 Å, allowing chain tracing, sequence-guided modeling and, in the 2–3 Å range, even *ab initio* modeling. In 2015, the first atomic structures of RyR1 in its closed state were published by three groups, all taking advantage of this new data collection technology (Efremov et al. 2015; Yan et al. 2015; Zalk et al. 2015). Meanwhile several additional structures in different states have been described for RyR1 (des Georges et al. 2016; Wei et al. 2016; Bai et al. 2016) and for RyR2 (Peng et al. 2016). The vast increase of knowledge presented by the cryo-EM studies in the past 2 years will be illuminated in the following sections of this review, and its implications will be discussed in the context of human disease. In particular, the newest structures offer a first glimpse on the dynamic mechanism of channel activation and gating (see Van Petegem 2016; Clarke and Hendrickson 2016).

## 11.3 A Primer on Single-Particle Cryo-EM

### *11.3.1 Method of Sample Preparation and Reconstruction*

Cryo-EM is a technique of imaging in which a frozen-hydrated sample is visualized in the transmission electron microscope (Dubochet et al. 1981, 1986). Contrast is produced by the difference in elastic scattering (*i.e.*, scattering without loss of energy) between protein (or nucleic acids when applicable) and the surrounding matrix of ice. A frozen-hydrated sample is obtained by quick freeze-plunging of the EM grid (a round 3 mm-diameter copper or gold grid), on which the liquid sample has been deposited, into liquid ethane that is kept at liquid nitrogen temperature. Blotting of excess liquid ensures that the thickness of the aqueous sample will be in the range of thicknesses (~100 nm) that can be penetrated by the 200-kV or 300-kV electron beam of commercial transmission electron microscopes. Both the high speed of freeze-plunging and the low heat capacity of the grid ensure rapid temperature change of the sample (estimated as $10^5$ degrees Celsius/s). Under these conditions water turns into vitreous (non-crystalline) ice, that is, ice possessing very similar density and amorphous structure as liquid water. The resulting embedment of the molecule in vitreous ice is essential for preserving its native structure. Preparation of samples with consistent ice thickness in the correct range is made possible by "vitrification robots,", which contain an environmental chamber for control of temperature and humidity and have provisions for automated blotting and rapid plunging of the grid.

The single-particle approach in cryo-EM (see Frank et al. 2002; Frank 2016; Nogales 2016) is distinct from approaches involving crystals (with two-dimensional

or helical symmetry) in that the molecules to be visualized are suspended freely in the aqueous buffer, without contacts with neighboring molecules. Thus, there are no constraints on the conformations they can assume, and, provided that the processes of purification and freezing themselves do not significantly alter their structure, the molecules are depicted in their native range of conformations and binding states.

The molecules are visualized as 2D projection images, which carry both amplitude and phase information in the Fourier domain and thus, unlike in X-ray crystallography, obviate the need for phasing. High-resolution 3D information can then be retrieved by alignment of these projections into a common 3D reference frame. The single-particle approach requires, however, that the molecules assume all possible views without major gaps in orientation distribution, as a precondition for artifact-free three-dimensional reconstruction. As pointed out above, many of the early structural studies of the RyR were adversely affected by strong preference of molecules for the top view, rendering the reconstructions difficult to interpret.

After the grid is plunged into the cryogen, it is transferred into the electron microscope, being kept under liquid nitrogen temperature at all times. In the imaging experiment, a beam with low electron dose (in our experiments 25–80$e^{-}/Å^{2}$) is employed to prevent radiation damage, but at such doses the images are very noisy. The need for collecting large numbers of images, often going in the hundreds of thousands, is due to four reasons: (1) the very low signal-to-noise ratio of the images, (2) beam-induced movement, charging of the specimen and other blurring effects, (3) the need to cover the entire angular range, and (4) the need to sample all major conformations co-existing in the specimen.

The recording of micrographs has been revolutionized recently with the introduction of direct electron detection cameras that possess high signal-to-noise ratio and a modulation transfer function extending to high spatial frequencies (i.e., small spacings in the image) (McMullan et al. 2009; McMullan et al. 2014). Micrographs are recorded as stacks of frames (“movies”), enabling correction of drift and electron beam-induced movement (Brilot et al. 2012; Li et al. 2013) and the weighting of frames according to accumulated electron dose (Grant and Grigorieff 2015). After this pre-processing step the images are sorted, or classified, using maximum-likelihood programs such as RELION (Scheres 2012). Reconstructions from the resulting classes display the whole range of structures co-existing in the sample.

## 11.4 Structures of the Channel Obtained by High-Resolution Cryo-EM

The above-mentioned advances in single-particle cryo-EM have spurred a revolution in structural biology, enabling the reconstruction of atomic-resolution maps for membrane proteins (Liao et al. 2013). This development has allowed the determination of high-resolution structures of RyRs, for the first time providing a mechanistic understanding of how the channel functions in healthy tissue and giving clues as to how it may be affected in disease states.

As mentioned above, the structure of RyR1 in a closed state, without $Ca^{2+}$ or other activating ligands, was determined in three recent studies at resolutions ranging from 3.8 Å to 6.1 Å and allowed the building of an atomic-level model of the RyR channel core (Yan et al. 2015) and poly-alanine-level models of the RyR cytoplasmic shell (Zalk et al. 2015; Yan et al. 2015; Efremov et al. 2015). These structures gave us a better understanding of the overall architecture of RYRs, homotetramer of four 5037-residue protomers with a combined mass of 2.2 mega-Daltons, and divided between pore, activation domain and cytoplasmic shell.

The structures confirmed that the pore domain belongs to the 6TM family of ion channels (Hille 2001) and contains a pseudo-voltage sensor domain (pVSD). RyR has unique features compared to other 6TM-family ion channels, which includes an insertion between S2 and S3 helices (S2S3 domain), a 90 Å long pore helix ending with a C-terminal domain containing a zinc finger and an acidic disordered loop between S1 and S2 (Yan et al. 2015; Fan et al. 2015). A polyproline segment in the S2S3 domain may be a binding site for SH3 domain-containing proteins (des Georges et al. 2016), which by their interaction with this extension of the pVSD may regulate channel function.

A notable feature of the activation domain is that it contains a domain in the shape of a thumb and forefingers (TaF), which clamps the zinc finger-containing C-terminal domain (CTD) (Fig. 11.2), thereby providing the allosteric coupling between the pore and the shell of the receptor. Presence of an EF-hand motif in the activation domain interacting with the pVSD hinted at a putative mechanism of activation by $Ca^{2+}$ (Wei et al. 2016). This putative mechanism later proved not to be correct (Guo et al. 2016; des Georges 2016), but this interaction between the EF-hand and the pVSD may have an important functional role, which remains to be determined.

The shell of RyR is principally composed of three α-solenoid repeats. The core solenoid (CSol), which is part of the activation domain, links the pore domain to the shell. The other α-solenoid repeats are the bridging (BSol), and N-terminal (NTD-C), that are joined by a fourth junctional solenoid (JSol) which provides a bridge between all the other ones (des Georges et al. 2016). These solenoids incorporate small folds of other domains, yielding numerous interdomain interfaces in the cytosolic shell. Other domains in the cytosolic shell include the SPRY domains (SPRY1-SPRY3) (Lau and Van Petegem 2014), EF-hands (EF1&2) (Xiong et al. 2006), RyR repeat pairs (RY1&2 and RY3&4) (Yuchi et al. 2015; Sharma et al. 2012), and the N-terminal domains (NTD-A and NTD-B) (Amador et al. 2009).

Three major interfaces provide inter-protomer contacts: SPRY2 with Bsol, NTD-A with NTD-B, and NTD-A with BSol (where the second domain is on the adjacent protomer). These interdomain and interprotomer contacts have been implicated in channel gating (Tung et al. 2010), linking the control of shell dynamics with pore opening. The picture emerging is of the RyR as a large complex network of interconnected helices (Fig. 11.2), which enables allosteric coupling of conformational changes over the span of the entire channel. Many proteins interact with the large cytoplasmic shell and take advantage of this allosteric coupling to allow a range of stimuli to exert control over the channel function (Lanner et al. 2010; Van Petegem 2015).

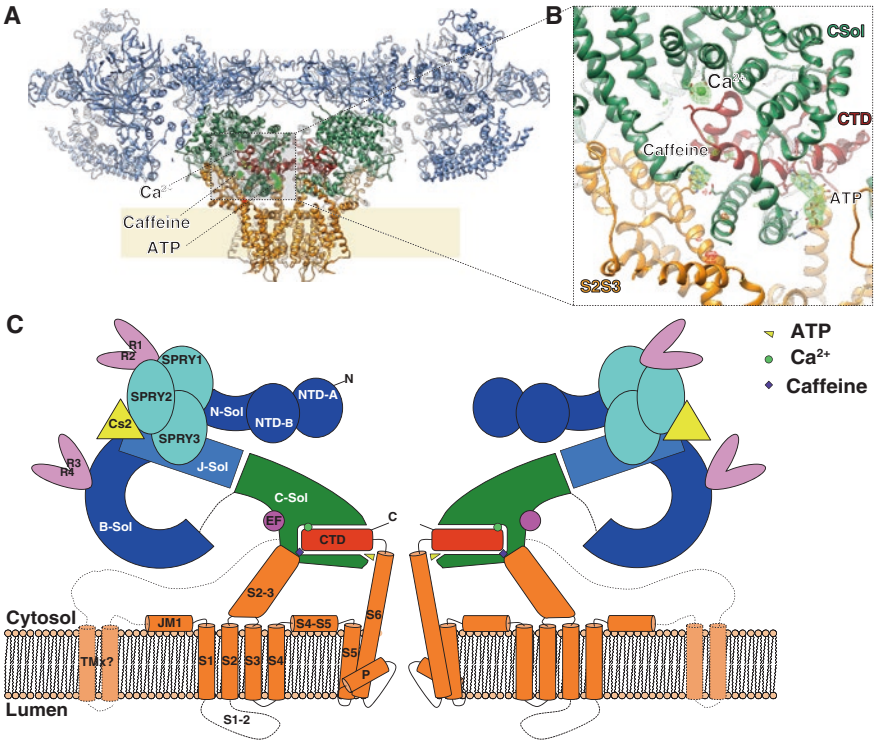


**Fig. 11.2 Architecture of the ryanodine receptor**. (**a**) Ribbon representation, with the shell (residues 1–3666; light blue), core solenoid (residues 3667–4253; green), pore domain (residues 4540–4956; orange), and CTD (residues 4957–5037; dark red). (**b**) Zoom onto the CTD area showing ligands and locally aligned difference density map calculated between the EGTA-only map and $Ca^{2+}$, ATP, and caffeine map (green/red mesh), contoured at 5s. (**c**) Schematic representation of RyR1. J-sol, junctional solenoid; B-sol, bridge solenoid; C-sol, core solenoid; N-sol, N-terminus solenoid. TMx, putative additional transmembrane helices (Reproduced with permission from Zalk et al. 2015)

Important keys for understanding this allosteric coupling between the shell and pore of the channel comes from a most recent study showing a series of structures, and their conformational variabilities, which change upon binding with different combinations of ligands (des Georges et al. 2016). These results have provided the important insight that there are in fact different modes of mechanical coupling, and that these modes are switched upon binding of activating ligands (Clarke and Hendrickson 2016).

## 11.5 RyR Activation: A Close Look

RyR contains multiple domains forming binding sites for functional ligands, including ions (primarily $Ca^{2+}$ and $Mg^{2+}$), proteins including calstabin, calmodulin, the voltage-gated $Ca^{2+}$ channel $Ca_v$ and small molecules such as adenine nucleotides, and caffeine (des Georges et al. 2016; Hwang et al. 2012; Choi et al. 2017; Santulli et al. 2017b). These ligands can bias the channel towards specific functional states and $P_o$. Most importantly, RyR gating is regulated by $Ca^{2+}$ with a characteristic bell-shaped curve (Bezprozvanny et al. 1991), suggesting that RyR must have two $Ca^{2+}$ binding sites of differing activities. ATP is also a well characterized physiological activating ligand likely to be constitutively bound in physiological conditions since cellular ATP concentration in skeletal muscles is very high (~5 mM; Kushmerick et al. 1992). $Ca^{2+}$ and ATP are known to have synergistic effect on RyR gating, with the highest $P_o$ when both are present. Although probably not physiological, addition of caffeine increases the $P_o$ to an even greater extent ($P_o = 0.91$; des Georges et al. 2016).

It is a striking observation that those three synergistic activating ligands bind at the CTD interdomain interface (des Georges et al. 2016; Fig. 11.2), which is itself directly linked to the pore helix via its Zinc-finger domain. This finding together with the observation that both $Ca^{2+}$ and ATP/caffeine produce the same or very similar changes in the position of the core solenoid with respect to the CTD (des Georges et al. 2016) can explain their synergistic effect. It also explains why caffeine potentiates RyR $Ca^{2+}$ binding. As caffeine and $Ca^{2+}$ binding produce a similar conformational change in the region of the CTD, caffeine acts as an allosteric agonist of $Ca^{2+}$, thereby shifting the sensitivity to $Ca^{2+}$ towards lower concentrations (Porta et al. 2011).

The ATP binding site is at the interface formed by the C-terminal portion of the TaF and the S6c-CTD junction (Fig. 11.2). The adenine moiety binds in the T intersection formed by the pore helix and the CTD, next to the Zinc finger motif, and may play a similar structural role, maintaining the geometry of the junction. This would explain why adenine nucleotides are competitive partial agonists of RyR1 while adenosine is an antagonist (Chan et al. 2000; Laver et al. 2001). Other nucleotide phosphates have been shown to not activate RyR.

The triphosphate tail of ATP binds to positively charged residues on the TaF domain of the core solenoid. ATP thereby acts as a bridge between the CTD and the TaF domain, triggering the conformational change between those two domains necessary for gating. As the number of phosphate groups is reduced, the interaction with the TaF positive charges is weakened or abolished and no longer bridges the TaF to the CTD. This observation explains the difference in affinity and channel $P_o$ between ATP, ADP and AMP, and may provide a mechanism contributing to muscle fatigue (Rullman et al. 2013; Bellinger et al. 2008a; Chan et al. 2000).

This change in the conformation of the core solenoid with respect to the CTD upon $Ca^{2+}$ and ATP/caffeine binding activates the channel and allows the lateral displacement of the whole protomer as a rigid unit, resulting in opening of the pore. The fact that ligand binding restricts the range of observed positions of the cytoplasmic shell (des Georges et al. 2016; Fig. 11.3) implies that this observed ligand-dependent conformational change of the core solenoid renders the whole protomer assembly more rigid. This change appears to allow pore opening, but the exact gating mechanism is still unknown. We can postulate two possible and non-exclusive mechanisms: (1) the more rigid assembly allows coupling of the thermal movement of the shell to bending of the S6 pore helix; (2) the conformational change releases a still unknown locking interaction, which allows the outward movement of the protomer and pore opening.

The key to the gating mechanism may potentially lie in the pseudo-voltage sensor (pVSD), a domain whose function in RyR is still not well understood. It has been shown that voltage potential on the SR membrane has an effect on RyR gating (Endo 2009), which would imply that the pVSD is playing a role in gating, despite the domain lacking most of the voltage-sensing charges on S4. The S2 helix and RyR-specific S2-S3 domain of the pVSD, together with the EF1/EF2 domain have also been implicated in $Ca^{2+}$-dependent inactivation of RyR (Gomez and Yamaguchi 2014; Gomez et al. 2016). It has been observed that the EF hand domain comes closer to the S2-S3 domain upon channel opening (des Georges et al. 2016; Wei et al. 2016). A tentative hypothesis could be that low affinity $Ca^{2+}$-binding on one of those domains triggers a repulsion, pushing those two domains apart and thereby preventing channel opening.

RyRs have a high degree of sequence and structure homology with another intracellular $Ca^{2+}$ release channel, the IP3R (Santulli et al. 2017a). IP3Rs are found in the ER and mediate the release of intracellular $Ca^{2+}$ in response to external stimuli. RyRs and IP3Rs have ~40% homology in the core regions, indicating a common origin for $Ca^{2+}$ release channels (Santulli et al. 2017a). However, the $IP_3R$ does not include much of the cytoplasmic shell and, most notably, lacks the large Bsol (Santulli et al. 2017a). Of particular interest, the extended pore helix, CTD and activation domain are conserved between these two channels, meaning that they have the same or very similar mechanisms of activation by $Ca^{2+}$ (Santulli et al. 2017a). In IP3R, the CTD is further extended and directly links to the NTD and the IP3 binding site (Fan et al. 2015). Conformational changes induced by IP3 can therefore be directly linked or relayed to $Ca^{2+}$ binding and gating (Fig. 11.4). In the case of RyR, gating is linked to mechanical coupling of the shell and pore, in IP3R, gating is probably coupled to IP3 binding by a very similar mechanism.

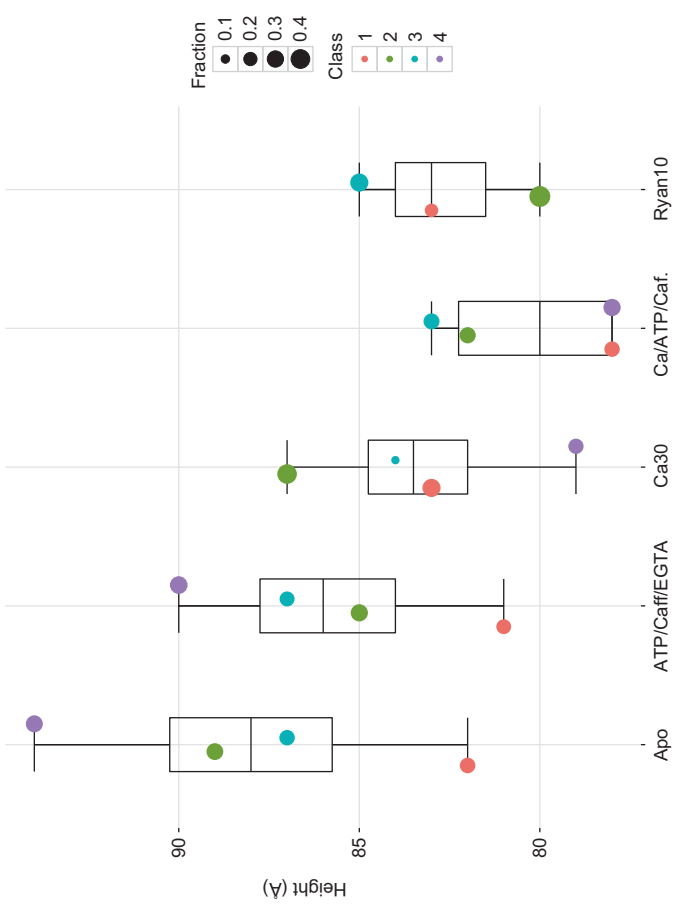


**Fig. 11.3 Ligand-dependent change in cytoplasmic shell motions amplitude**. Box and whisker plot of the height measurement of the RY1&2 domain with respect to the SR membrane plane for each class of each dataset. The fraction of particles of each class is represented by the size of the circular marker for each dataset; the class number is given by the color of the marker (Reproduced with permission from des Georges et al. 2016)

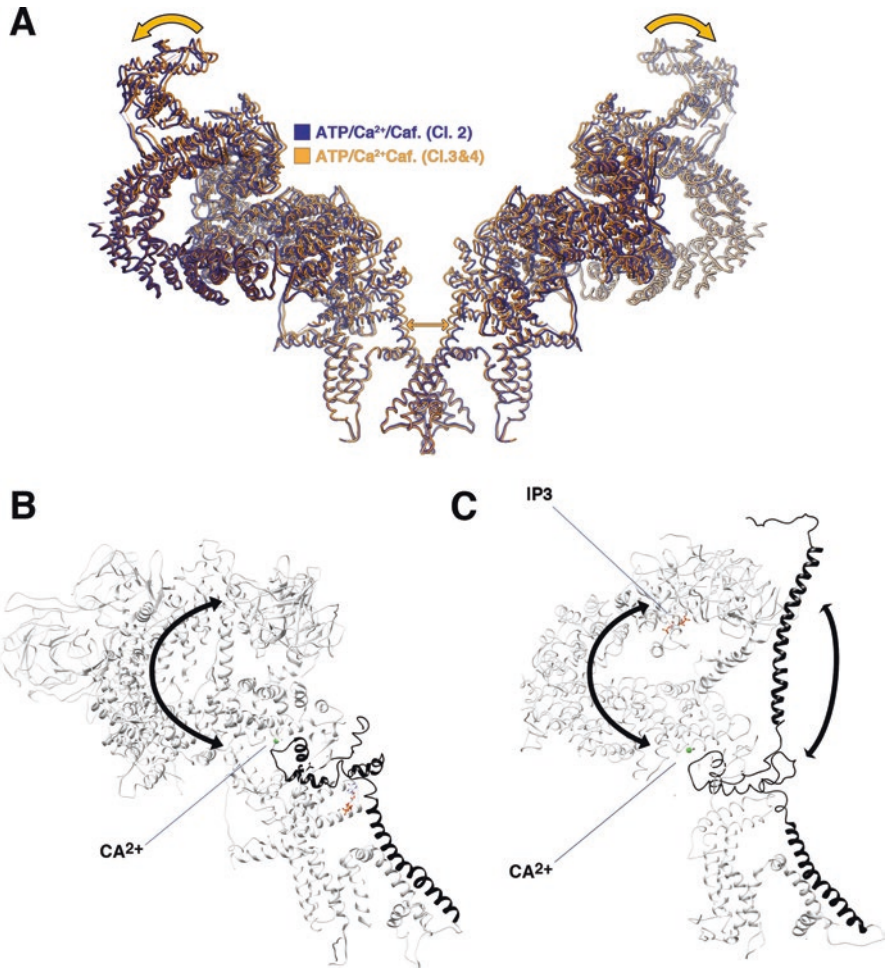


**Fig. 11.4 Similarities in allosteric coupling and gating in RyR and IP3R.** (**a**) RyR gating is linked to an outwards rigid body motion of opposing protomers resulting in opening of the pore (orange arrows). The ligand-bound closed and open classes are shown in yellow and blue. (**b, c**) Allosteric coupling between RyR (**b**) and IP3R (**c**) cytoplasmic shell and pore helix via the C-terminal domain. Pore helix and CTD are in black. The rest of the molecule is white. $Ca^{2+}$ (green dot) and IP3 (represented in sticks) are shown in their know binding site. Arrows show possible paths of allosteric coupling

## 11.6 Mapping of Channel Dynamics by Cryo-EM

RyR gating is triggered by $Ca^{2+}$-induced conformational changes in the core solenoid and CTD that couple cytoplasmic shell movement to pore opening (des Georges et al. 2016). The cytoplasmic shell dynamics therefore plays a direct role in channel

gating by $Ca^{2+}$, and must play an integral role in $Ca^{2+}$ release triggered by mechanical coupling with the dihydropyridine receptor. The channel dynamics is also tightly regulated by numerous factors that influence gating including calstabin and calmodulin. It is therefore important to study the complex dynamics of this very large ion channel in order to better understand its function and regulation. Cryo-EM is uniquely placed to do this, as the single-particle method allows the sorting of individual macromolecules based on their conformational state.

In order to appreciate the cryo-EM data analysis for a molecule exhibiting dynamic behavior in the sample, it is important to understand that maximum-likelihood classification by programs such as RELION (Scheres 2012) entails a user decision on how many discrete classes ($K$) the algorithm should distinguish. In the case of RyR1, for any choice of $K$, multiple classes with different conformations are found, distinguished by the position of the cytosolic wing domains (des Georges et al. 2016), suggesting that the structure of the isolated receptor is fluctuating as a result of Brownian motion. Binding of ligands ($Ca^{2+}$, caffeine/ATP, or $Ca^{2+}$ + caffeine/ATP) changes the range and distribution of cytosolic domain positions found and, as pointed out before, the preference for closed versus open channel. Since increasing $K$, the number of classes, leads to an ever-increasing number of reconstructions with ever-finer increments in conformational changes, it is safe to say that the discrete classes found are samples from an underlying continuum – reflecting variability of the large molecule that results from being exposed to thermal agitation in the surrounding solvent. (It should be pointed out in this context that the movies showing transitions between the open and closed channel in the work by des Georges et al. 2016 were obtained by morphing between two to four structures, without support by data in between).

The analysis using discrete classes described in des Georges et al. (2016) (classification voluntarily limited to K = 4 with fourfold symmetry imposed in order to reduce the complexity of the analysis), unveiled the conformational changes necessary for gating and the conformation of the open state of the channel. It also showed that the height of the cytoplasmic shell with respect to the membrane plane both lowers and reduces its range of attainable conformations with ligand binding (Fig. 11.3). Activating ligands therefore reinforce the mechanical coupling between the pore and the shell, which must be an integral part of the gating mechanism. Still, even with caffeine/ATP and $Ca^{2+}$ bound, the analysis shows that the cytoplasmic shell has an important level of intrinsic flexibility not well depicted by the small number of discrete classes used in the analysis.

The continuous character of the distribution of states is in fact borne out by the application of a new kind of analysis that allows continuous ordering of data due to conformational changes to be tracked (Dashti et al. 2014; Frank and Ourmazd 2016). When this method is applied to the data collected in the study of RyR1 bound with various combinations of ligands (des Georges et al. 2016), we indeed see that the channel in each sample assumes an entire continuum of states – albeit with different distributions – exhibiting a combination of wing motions, motions of the activation domain, and channel openings and closings (Dashti et al. 2017). This analysis prom-

ises to lead to more profound insights into the nature and dynamics of channel activation and gating than obtainable from single reconstructions in open and closed states (see Van Petegem 2016). It may also be a well-suited tool to study how the numerous regulatory factors shift the equilibrium of states and modulate gating.

## 11.7 Modulation of RyR Dynamics and Gating

A number of factors affect RyR function in the cell, and a better understanding of their effect on RyR dynamics may be of crucial importance in understanding disease states of the channel.

The $Ca^{2+}$ channel-binding and -stabilizing proteins calstabin1 and calstabin2 (also known as FKBP12 and FKBP12.6, respectively) are of critical importance for preventing RyRs from leaking $Ca^{2+}$ and for coupled gating (Marx et al. 1998, 2000) between RyRs (Brillantes et al. 1994a; Timerman et al. 1993; Santulli and Marks 2015; Yuan et al. 2014). Calstabin1 and calstabin2 preferentially bind RyR1 and RyR2, respectively, and help to stabilize the closed state of the channel (Santulli and Marks 2015). Calstabins are the cytosolic targets for the immunosuppressant drugs rapamycin and FK506 (Lombardi et al. 2017a, 2017b). Rapamycin (or sirolimus) coated on coronary artery stents is used to prevent restenosis by inhibiting vascular smooth muscle migration and proliferation (Santulli 2015; Marks 2003; Santulli and Totary-Jain 2013; Santulli et al. 2014). The interaction between calstabins and RyR can regulate the channel and prevent intracellular $Ca^{2+}$ leak that leads to a variety of disease states (Santulli and Marks 2015; Huang et al. 2006; Brillantes et al. 1994a). These proteins are highly specific, with one calstabin bound per RyR protomer, and have been used to isolate RyR from microsomes (Zalk et al. 2015; Xin et al. 1995). Calstabin binds at the N-terminus of the bridging solenoid, possibly rigidifying the interface between BSol and SPRY1/SPRY2, thus stabilizing the link between the pore and cytoplasmic region (des Georges et al. 2016; Zalk et al. 2015; Yan et al. 2015). Reinforcing such hypothesis, a cryo-EM study of RyR2 in the absence of calstabin shows a much greater level of flexibility of the BSol (Peng et al. 2016). This greater flexibility of the BSol may be due to the absence of calstabin, but may also be intrinsic to RyR2.

Additional modulatory proteins associate directly and indirectly with RyR, including calsequestrin, sorcin, triadin, homer, histidine-rich $Ca^{2+}$ binding protein, calmodulin, S100A1, and junctin (Santulli et al. 2017b). RyR function is also regulated by post-translational modifications, including phosphorylation, oxidation and nitrosylation (Santulli et al. 2015a, b, 2017a, b; Marx et al. 2000, 2001b; Bellinger et al. 2008b, 2009; Shan et al. 2010a, b; Andersson et al. 2011; Umanskaya et al. 2014).

The majority of the known post-translational modifications and modulatory protein binding sites are situated on the cytoplasmic shell and influence the cytoplasmic shell dynamics and therefore, indirectly, gating (Gambardella et al. 2017). The shell dynamics could be influenced in several ways: The rigidity of the protomer assembly could be altered, as suggested with calstabins; the strength of interprotomer contacts could be modified, thereby influencing shell movement and gating; the shell movement could be directly constrained, which would either promote (e.g.,

DHPR) or prevent the outward motion necessary for pore opening (Bai et al. 2016; des Georges et al. 2016). It is also possible that other regulatory proteins influence more directly the priming of the core solenoid, which is necessary for gating to occur (des Georges et al. 2016), or influence gating more directly by interacting with the pVSD. For instance, an RyR-specific polyproline segment in the pVSD (des Georges et al. 2016) is a potential binding site for SH3 domain-containing proteins that could have a direct effect on gating.

As discussed above, the movement of the cytoplasmic shell is tightly interconnected with gating. RyRs are known to form paracrystalline arrays in checkerboard patterns (Franzini-Armstrong et al. 1999; Cabra et al. 2016). This feature provides a mechanism by which opening of a single channel can mechanically trigger neighboring channels and greatly amplify $Ca^{2+}$ release via coupled gating (Marx et al. 1998). RyR repeats 1&2, located in the corners of the cytoplasmic shell, is most likely involved in mediating coupled-gating (Lehnart et al. 2003; Marx et al. 1998, 2001a). By triggering neighboring channels both physically and chemically, RyRs act as both signal amplifiers and signal integrators (Fabiato 1983; Endo et al. 1970). This supramolecular allostery and thus the whole dynamics of excitation-contraction coupling is highly sensitive to the binding of protein factors to the shell assembly.

## 11.8 Involvement of RyR in Human Diseases

Over 300 mutations causing human diseases have been mapped to RyRs (Santulli et al. 2017a). Mutations in the cardiac RyR2 are primarily linked to cardiac arrhythmias, including catecholaminergic polymorphic ventricular tachycardia (CPVT) (Lehnart et al. 2008; Santulli et al. 2015a), in which exercise-induced sympathetic activation in conjunction with the mutation causes ventricular tachycardia and sudden cardiac death. Importantly, patients typically do not exhibit prior symptoms or structural modification of the heart, but can experience ventricular arrhythmia and syncope during physical exercise, following stress or acute emotions. The majority of mutations linked to CPVT are located in the pore, pVSD and central domain regions (Santulli et al. 2017b), domains directly implicated in activation and gating (des Georges et al. 2016). Other hotspots are located in the NTD and BSol domains, two domains that form interprotomer contacts and therefore influence the cytoplasmic shell dynamics. The majority of those mutations link to malfunction in the gating mechanism which may be exacerbated under stress and lead to spurious $Ca^{2+}$ sparks and arrhythmia.

Mutations in RyR1 can cause malignant hyperthermia (MH), and RyR1 myopathies previously classified as central core disease (CCD) and multiminicore disease (Santulli et al. 2017a). Additionally, stress-induced post-translational modifications of RyR1 including phosphorylation, oxidation, nitrosylation and depletion of calstabin1 can lead to $Ca^{2+}$ leak, resulting in deleterious effects on muscle function (Matecki et al. 2016; Shan et al. 2010a, b; Lehnart et al. 2005; Bellinger et al. 2009; Fauconnier et al. 2010; Marx et al. 2000; Umanskaya et al. 2014; Santulli et al.

2017a, b). These myopathies include Duchenne muscular dystrophy (Bellinger et al. 2009), sarcoglycanopathies (Andersson et al. 2012) and sarcopenia (Andersson et al. 2011; Santulli et al. 2017a).

MH involves activation of RyR1 induced by a volatile halogenated anesthetic, which causes a rapid rise in core body temperature and can result in organ failure and death if not promptly treated (Rosenberg et al. 2007; Santulli et al. 2017a). MH is a pharmacogenetic disorder, in which the mutation is latent until it is triggered by a drug. In this condition, $Ca^{2+}$ is rapidly released by RyR1, causing uncontrolled muscle contraction. Sarco/endoplasmic reticulum $Ca^{2+}$-ATPase (SERCA) hydrolyzes ATP to pump it back into the SR/ER, consuming ATP and generating the characteristic excessive heat. Although dantrolene is an established therapeutic that resolves MH episodes, mortality from this event remains at approximately 5% (Larach et al. 2014). Despite years of use and studies showing interaction with RyR1, a validated mechanism of action for dantrolene has yet to be reported (Paul-Pletzer et al. 2002; Zhao et al. 2001). A recent study demonstrated that dantrolene efficacy is also affected by the level of $Mg^{2+}$ (Choi et al. 2017). Mutations causing MH are autosomal dominant and typically seen in the central and N-terminal clusters. Another MH mutation hotspot is at the interprotomer contacts between NTD-A and NTD-B, which is disrupted during channel opening (Kimlicka et al. 2013; Santulli et al. 2017a). The location of those mutations, mostly around the N-terminal region and around the Bsol, points to a misregulation of the shell dynamics that would cause uncontrolled pore opening upon the anesthetic binding to RyR1.

CCD is a congenital myopathy characterized by the presence of metabolically inactive tissue cores in muscle fibers, resulting in progressive muscle weakness (Sewry et al. 2002; Santulli et al. 2017a). CCD presents during infancy as delayed motor development and hypotonia. There are no known therapeutics for CCD and it can result in death. Intriguingly, as RyR1 is also found in the brain, one CCD mutation was also discovered to have a neuronal phenotype (De Crescenzo et al. 2012). Mutations that lead to CCD are clustered in the C-terminal region (Quane et al. 1993; Zhang et al. 1993; Santulli et al. 2017b), region directly responsible for $Ca^{2+}$ activation (des Georges et al. 2016; Santulli et al. 2017a).

We can see that in each of these disorders, mutations are clustered in similar hotspots, mostly the interface between protomers (Van Petegem 2015; Tung et al. 2010; Santulli et al. 2017a), but also in the activation domain. Mutations at the interface between protomers are likely to influence gating by affecting the outward movement of the shell necessary for pore opening. Weakening of those interfaces would facilitate pore opening and therefore spurious $Ca^{2+}$ leak (Tateishi et al. 2009; Suetomi et al. 2011). Mutations in the C-terminal region or the core solenoid are more likely to affect the activation mechanism directly, either by facilitating the activated conformation, the binding of the activating ligands $Ca^{2+}$ and ATP, or by preventing inactivation of the channel.

One hotspot is localized in the phosphorylation domain, near the phosphorylation loop, indicating that disease mutations and phosphorylation can affect the same process (Yuchi et al. 2012; Santulli et al. 2017b). Still, the exact role of post-translational modifications on the channel are poorly understood. Cryo-EM struc-

tures of phosphorylated vs dephosphorylated channels showed no differences in the structure and dynamics of the purified receptor (Zalk et al. 2015). These modifications may only be relevant in the context of their interactions with other partners, including DHPR.

## 11.9 Conclusions

The recently published cryo-EM structures of RyR channels in closed and open states represent a breakthrough after years of slow progress in the structural and molecular understanding of disease-causing mutations in RyRs. The new structures have opened the door toward a detailed mechanistic understanding of their function in health and their dysfunction in disease. The improved understanding of the complex mechanisms of ligand binding and activation of the channel also presents opportunities for targeted drug developments addressing many of the known human diseases implicating RyR1 and RyR2.

**Acknowledgements** This work was supported by HHMI (to J.F.) and grants from the National Institutes of Health (R01AR060037 and R01HL061503 to A.R.M., R01GM29169 to J.F., R00DK107895 to G.S.).

**Disclosure** ARM is a consultant and board member and owns shares in ARMGO Pharma, Inc. a biotech startup targeting RyR channels for therapeutic purposes.

## References

Amador FJ, Liu S, Ishiyama N, Plevin MJ, Wilson A, MacLennan DH, Ikura M (2009) Crystal structure of type I ryanodine receptor amino-terminal beta-trefoil domain reveals a disease-associated mutation "hot spot" loop. Proc Natl Acad Sci U S A 106(27):11040–11044. https://doi.org/10.1073/pnas.0905186106

Andersson DC, Betzenhauser MJ, Reiken S, Meli AC, Umanskaya A, Xie W, Shiomi T, Zalk R, Lacampagne A, Marks AR (2011) Ryanodine receptor oxidation causes intracellular calcium leak and muscle weakness in aging. Cell Metab 14(2):196–207. https://doi.org/10.1016/j.cmet.2011.05.014

Andersson DC, Meli AC, Reiken S, Betzenhauser MJ, Umanskaya A, Shiomi T, D'Armiento J, Marks AR (2012) Leaky ryanodine receptors in beta-sarcoglycan deficient mice: a potential common defect in muscular dystrophy. Skelet Muscle 2(1):9. https://doi.org/10.1186/2044-5040-2-9

Bai X-C, Yan Z, Wu J, Li Z, Yan N (2016) The central domain of RyR1 is the transducer for long-range allosteric gating of channel opening. Cell Res. https://doi.org/10.1038/cr.2016.89

Baker MR, Fan G, Serysheva II (2015) Single-particle cryo-EM of the ryanodine receptor channel in an aqueous environment. Eur J Transl Myol 25(1):35–48

Baker RP, Young K, Feng L, Shi Y, Urban S (2007 May 15) Enzymatic analysis of a rhomboid intramembrane protease implicates transmembrane helix 5 as the lateral substrate gate. Proc Natl Acad Sci U S A 104(20):8257–8262

Bellinger AM, Mongillo M, Marks AR (2008a) Stressed out: the skeletal muscle ryanodine receptor as a target of stress. J Clin Invest 118(2):445–453. https://doi.org/10.1172/JCI34006

Bellinger AM, Reiken S, Dura M, Murphy PW, Deng SX, Landry DW, Nieman D, Lehnart SE, Samaru M, LaCampagne A, Marks AR (2008b) Remodeling of ryanodine receptor complex

causes “leaky” channels: a molecular mechanism for decreased exercise capacity. Proc Natl Acad Sci U S A 105(6):2198–2202. https://doi.org/10.1073/pnas.0711074105
Bellinger AM, Reiken S, Carlson C, Mongillo M, Liu X, Rothman L, Matecki S, Lacampagne A, Marks AR (2009) Hypernitrosylated ryanodine receptor calcium release channels are leaky in dystrophic muscle. Nat Med 15(3):325–330. https://doi.org/10.1038/nm.1916
Bezprozvanny I, Watras J, Ehrlich BE (1991) Bell-shaped calcium-response curves of Ins(1,4,5) P3- and calcium-gated channels from endoplasmic reticulum of cerebellum. Nature 351(6329):751–754. https://doi.org/10.1038/351751a0
Brillantes AM, Allen P, Takahashi T, Izumo S, Marks AR (1992) Differences in cardiac calcium release channel (ryanodine receptor) expression in myocardium from patients with end-stage heart failure caused by ischemic versus dilated cardiomyopathy. Circ Res 71(1):18–26
Brillantes AB, Ondrias K, Scott A, Kobrinsky E, Ondriasova E, Moschella MC, Jayaraman T, Landers M, Ehrlich BE, Marks AR (1994a) Stabilization of calcium release channel (ryanodine receptor) function by FK506-binding protein. Cell 77(4):513–523
Brillantes AM, Bezprozvannaya S, Marks AR (1994b) Developmental and tissue-specific regulation of rabbit skeletal and cardiac muscle calcium channels involved in excitation-contraction coupling. Circ Res 75(3):503–510
Brilot AF, Chen JZ, Cheng A, Pan J, Harrison SC, Potter CS, Carragher B, Henderson R, Grigorieff N (2012, March) Beam-induced motion of vitrified specimen on holey carbon film. J Struct Biol 177(3):630–637. https://doi.org/10.1016/j.jsb.2012.02.003
Cabra V, Murayama T, Samsò M (2016) Ultrastructural analysis of self-associated RyR2s. Biophys J 110(12):2651–2662. https://doi.org/10.1016/j.bpj.2016.05.013
Chan WM, Welch W, Sitsapesan R (2000) Structural factors that determine the ability of adenosine and related compounds to activate the cardiac ryanodine receptor. Br J Pharm 130(7):1618–1626. https://doi.org/10.1038/sj.bjp.0703459
Choi RH, Koenig X, Launikonis BS (2017) Dantrolene requires Mg2+ to arrest malignant hyperthermia. Proc Natl Acad Sci U S A. https://doi.org/10.1073/pnas.1619835114
Clarke OB, Hendrickson WA (2016, August) Structures of the colossal RyR1 calcium release channel. Curr Opin Struct Biol 39:144–152. https://doi.org/10.1016/j.sbi.2016.09.002
Dashti A, Schwander P, Langlois R, Fung R, Li W, Hosseinizadeh A, Liao HY, Pallesen J, Sharma G, Stupina VA, Simon AE, Dinman JD, Frank J, Ourmazd A (2014, December 9) Trajectories of the ribosome as a Brownian nanomachine. Proc Natl Acad Sci U S A 111(49):17492–17497. https://doi.org/10.1073/pnas.1419276111
Dashti A, Hail DB, Mashayekhi G, Schwander P, des Georges A, Frank J, Ourmazd A (2017) Conformational Dynamics and Energy Landscapes of Ligand Binding in RyR1. bioRxiv:167080
des Georges A, Clarke OB, Zalk R, Yuan Q, Condon KJ, Grassucci RA, Hendrickson WA, Marks AR, Frank J (2016, September 22) Structural basis for gating and activation of RyR1. Cell 167(1):145–157.e17. https://doi.org/10.1016/j.cell.2016.08.075
De Crescenzo V, Fogarty KE, Lefkowitz JJ, Bellve KD, Zvaritch E, MacLennan DH, Walsh JV Jr (2012) Type 1 ryanodine receptor knock-in mutation causing central core disease of skeletal muscle also displays a neuronal phenotype. Proc Natl Acad Sci U S A 109(2):610–615. https://doi.org/10.1073/pnas.1115111108
Dubochet J, Booy FP, Freeman R, Jones AV, Walter CA (1981) Low temperature electron microscopy. Annu Rev Biophys Bioeng 10:133–149
Dubochet J, Adrian M, Schultz P, Oudet P (1986, March) Cryo-electron microscopy of vitrified SV40 minichromosomes: the liquid drop model. EMBO J 5(3):519–528
Efremov RG, Leitner A, Aebersold R, Raunser S (2015, January 1) Architecture and conformational switch mechanism of the ryanodine receptor. Nature 517(7532):39–43
Endo M (2009) Calcium-induced calcium release in skeletal muscle. Physiol Rev 89(4):1153–1176. https://doi.org/10.1152/physrev.00040.2008
Endo M, Tanaka M, Ogawa Y (1970) Calcium induced release of calcium from the sarcoplasmic reticulum of skinned skeletal muscle fibres. Nature 228(5266):34–36
Fabiato A (1983) Calcium-induced release of calcium from the cardiac sarcoplasmic reticulum. Am J Phys 245(1):C1–14
Fabiato A, Fabiato F (1975) Contractions induced by a calcium-triggered release of calcium from the sarcoplasmic reticulum of single skinned cardiac cells. J Physiol 249(3):469–495

Fan G, Baker ML, Wang Z, Baker MR, Sinyagovskiy PA, Chiu W, Ludtke SJ, Serysheva II (2015) Gating machinery of InsP3R channels revealed by electron cryomicroscopy. Nature 527(7578):336–341. https://doi.org/10.1038/nature15249

Fauconnier J, Thireau J, Reiken S, Cassan C, Richard S, Matecki S, Marks AR, Lacampagne A (2010) Leaky RyR2 trigger ventricular arrhythmias in Duchenne muscular dystrophy. Proc Natl Acad Sci U S A 107(4):1559–1564. https://doi.org/10.1073/pnas.0908540107

Frank J (2016) Generalized single-particle cryo-EM--a historical perspective. Microscopy (Oxf) 65(1):3–8. https://doi.org/10.1093/jmicro/dfv358

Frank J, Ourmazd A (2016, May 1) Continuous changes in structure mapped by manifold embedding of single-particle data in cryo-EM. Methods 100:61–67. https://doi.org/10.1016/j.ymeth.2016.02.007

Frank J, Wagenknecht T, McEwen BF, Marko M, Hsieh CE, Mannella CA (2002, April–May) Three-dimensional imaging of biological complexity. J Struct Biol 138(1-2):85–91

Franzini-Armstrong C, Protasi F, Ramesh V (1999) Shape, size, and distribution of $Ca^{2+}$ release units and couplons in skeletal and cardiac muscles. Biophys J 77(3):1528–1539

Gambardella J, Trimarco B, Iaccarino G, Santulli G (2017) (in press) New insights in cardiac calcium handling and excitation-contraction coupling. Adv Exp Med Biol. https://doi.org/10.1007/5584_2017_106

Gomez AC, Yamaguchi N (2014) Two regions of ryanodine receptor calcium channel are involved in Ca(2+)-dependent inactivation. Biochemistry 53(8):1373–1379. https://doi.org/10.1021/bi401586h

Gomez AC, Holford TW, Yamaguchi N (2016) Malignant hyperthermia-associated mutations in the S2-S3 cytoplasmic loop of type 1 ryanodine receptor calcium channel impair calcium-dependent inactivation. Am J Physiol Cell Physiol 311(5):C749–C757. https://doi.org/10.1152/ajpcell.00134.2016

Grant T, Grigorieff N (2015) Measuring the optimal exposure for single particle cryo-EM using a 2.6 Å reconstruction of rotavirus VP6. Elife 4:e06980

Guo W et al (2016) The EF-hand Ca2+ binding domain is not required for cytosolic $Ca^{2+}$ activation of the cardiac ryanodine receptor. J Biol Chem. https://doi.org/10.1074/jbc.M115.693325

Hakamata Y, Nakai J, Takeshima H, Imoto K (1992) Primary structure and distribution of a novel ryanodine receptor/calcium release channel from rabbit brain. FEBS Lett 312(2–3):229–235

Hamilton SL, Serysheva II (2009, February 13) Ryanodine receptor structure: progress and challenges. J Biol Chem 284(7):4047–4051. https://doi.org/10.1074/jbc.R800054200. Epub 2008 Oct 16

Harnick DJ, Jayaraman T, Ma Y, Mulieri P, Go LO, Marks AR (1995) The human type 1 inositol 1,4,5-trisphosphate receptor from T lymphocytes. Structure, localization, and tyrosine phosphorylation. J Biol Chem 270(6):2833–2840

Hille B (2001) Ion channels of excitable membranes, vol 507. Sinauer, Sunderland

Huang F, Shan J, Reiken S, Wehrens XH, Marks AR (2006) Analysis of calstabin2 (FKBP12.6)-ryanodine receptor interactions: rescue of heart failure by calstabin2 in mice. Proc Natl Acad Sci U S A 103(9):3456–3461. https://doi.org/10.1073/pnas.0511282103

Hwang JH, Zorzato F, Clarke NF, Treves S (2012) Mapping domains and mutations on the skeletal muscle ryanodine receptor channel. Trends Mol Med 18(11):644–657. https://doi.org/10.1016/j.molmed.2012.09.006

Inui M, Saito A, Fleischer S (1987) Purification of the ryanodine receptor and identity with feet structures of junctional terminal cisternae of sarcoplasmic reticulum from fast skeletal muscle. J Biol Chem 262(4):1740–1747

Jiang D, Chen W, Wang R, Zhang L, Chen SR (2007, November 13) Loss of luminal Ca2+ activation in the cardiac ryanodine receptor is associated with ventricular fibrillation and sudden death. Proc Natl Acad Sci U S A 104(46):18309–18314

Kimlicka L, Lau K, Tung CC, Van Petegem F (2013) Disease mutations in the ryanodine receptor N-terminal region couple to a mobile intersubunit interface. Nat Commun 4:1506. https://doi.org/10.1038/ncomms2501

Kushmerick MJ, Moerland TS, Wiseman RW (1992, August 15) Mammalian skeletal muscle fibers distinguished by contents of phosphocreatine, ATP, and Pi. Proc Natl Acad Sci U S A 89(16):7521–7525

Lanner JT, Georgiou DK, Joshi AD, Hamilton SL (2010) Ryanodine receptors: structure, expression, molecular details, and function in calcium release. Cold Spring Harb Perspect Biol 2(11):a003996. https://doi.org/10.1101/cshperspect.a003996

Larach MG, Brandom BW, Allen GC, Gronert GA, Lehman EB (2014) Malignant hyperthermia deaths related to inadequate temperature monitoring, 2007–2012: a report from the North American malignant hyperthermia registry of the malignant hyperthermia association of the United States. Anesth Analg 119(6):1359–1366. https://doi.org/10.1213/ane.0000000000000421

Lau K, Van Petegem F (2014) Crystal structures of wild type and disease mutant forms of the ryanodine receptor SPRY2 domain. Nat Commun 5:5397. https://doi.org/10.1038/ncomms6397

Laver DR, Lenz GK, Lamb GD (2001) Regulation of the calcium release channel from rabbit skeletal muscle by the nucleotides ATP, AMP, IMP and adenosine. J Physiol 537(Pt 3):763–778

Lehnart SE, Huang F, Marx SO, Marks AR (2003) Immunophilins and coupled gating of ryanodine receptors. Cur Top Med Chem 3(12):1383–1391

Lehnart SE, Wehrens XH, Laitinen PJ, Reiken SR, Deng SX, Cheng Z, Landry DW, Kontula K, Swan H, Marks AR (2004) Sudden death in familial polymorphic ventricular tachycardia associated with calcium release channel (ryanodine receptor) leak. Circulation 109(25):3208–3214. https://doi.org/10.1161/01.CIR.0000132472.98675.EC

Lehnart SE, Wehrens XH, Reiken S, Warrier S, Belevych AE, Harvey RD, Richter W, Jin SL, Conti M, Marks AR (2005) Phosphodiesterase 4D deficiency in the ryanodine-receptor complex promotes heart failure and arrhythmias. Cell 123(1):25–35. https://doi.org/10.1016/j.cell.2005.07.030

Lehnart SE, Mongillo M, Bellinger A, Lindegger N, Chen BX, Hsueh W, Reiken S, Wronska A, Drew LJ, Ward CW, Lederer WJ, Kass RS, Morley G, Marks AR (2008) Leaky $Ca^{2+}$ release channel/ryanodine receptor 2 causes seizures and sudden cardiac death in mice. J Clin Invest 118(6):2230–2245. https://doi.org/10.1172/JCI35346

Li X et al (2013) Electron counting and beam-induced motion correction enable near-atomic-resolution single-particle cryo-EM. Nat Methods 10:584–590

Liao M, Cao E, Julius D, Cheng Y (2013) Structure of the TRPV1 ion channel determined by electron cryo-microscopy. Nature 504:107–112

Liu Z, Zhang J, Wang R, Chen SRW, Wagenknecht T (2004) Location of divergent region 2 on the three-dimensional structure of cardiac muscle ryanodine receptor/calcium release channel. J Mol Biol 338:533–545

Liu X, Betzenhauser MJ, Reiken S, Meli AC, Xie W, Chen BX, Arancio O, Marks AR (2012) Role of leaky neuronal ryanodine receptors in stress-induced cognitive dysfunction. Cell 150(5):1055–1067. https://doi.org/10.1016/j.cell.2012.06.052

Lobo PA, Van Petegem F (2009, November 11) Crystal structures of the N-terminal domains of cardiac and skeletal muscle ryanodine receptors: insights into disease mutations. Structure 17(11):1505–1514. https://doi.org/10.1016/j.str.2009.08.016

Lombardi A, Gambardella J, XL D, Sorriento D, Mauro M, Iaccarino G, Trimarco B, Santulli G (2017a, November 20) Sirolimus induces depletion of intracellular calcium stores and mitochondrial dysfunction in pancreatic beta cells. Sci Rep 7(1):15823. https://doi.org/10.1038/s41598-017-15283-y

Lombardi A, Trimarco B, Iaccarino G, Santulli G (2017b, November 13) Impaired mitochondrial calcium uptake caused by tacrolimus underlies beta-cell failure. Cell Commun Signal 15(1):47. https://doi.org/10.1186/s12964-017-0203-0

Ludtke SJ, Serysheva II, Hamilton SL, Chiu W (2005, August) The pore structure of the closed RyR1 channel. Structure 13(8):1203–1211

Maki T, Gruver EJ, Davidoff AJ, Izzo N, Toupin D, Colucci W, Marks AR, Marsh JD (1996) Regulation of calcium channel expression in neonatal myocytes by catecholamines. J Clin Invest 97(3):656–663. https://doi.org/10.1172/JCI118462

Marks AR (2003) Sirolimus for the prevention of in-stent restenosis in a coronary artery. New Engl J Med 349(14):1307–1309. https://doi.org/10.1056/NEJMp038141

Marks AR, Tempst P, Hwang KS, Taubman MB, Inui M, Chadwick C, Fleischer S, Nadal-Ginard B (1989) Molecular cloning and characterization of the ryanodine receptor/junctional chan-

nel complex cDNA from skeletal muscle sarcoplasmic reticulum. Proc Natl Acad Sci U S A 86(22):8683–8687

Marks AR, Priori S, Memmi M, Kontula K, Laitinen PJ (2002) Involvement of the cardiac ryanodine receptor/calcium release channel in catecholaminergic polymorphic ventricular tachycardia. J Cell Physiol 190(1):1–6. https://doi.org/10.1002/jcp.10031

Marx SO, Ondrias K, Marks AR (1998) Coupled gating between individual skeletal muscle $Ca^{2+}$ release channels (ryanodine receptors). Science 281(5378):818–821

Marx SO, Reiken S, Hisamatsu Y, Jayaraman T, Burkhoff D, Rosemblit N, Marks AR (2000) PKA phosphorylation dissociates FKBP12.6 from the calcium release channel (ryanodine receptor): defective regulation in failing hearts. Cell 101(4):365–376

Marx SO, Gaburjakova J, Gaburjakova M, Henrikson C, Ondrias K, Marks AR (2001a) Coupled gating between cardiac calcium release channels (ryanodine receptors). Circ Res 88(11):1151–1158

Marx SO, Reiken S, Hisamatsu Y, Gaburjakova M, Gaburjakova J, Yang YM, Rosemblit N, Marks AR (2001b) Phosphorylation-dependent regulation of ryanodine receptors: a novel role for leucine/isoleucine zippers. J Cell Biol 153(4):699–708

Matecki S, Dridi H, Jung B, Saint N, Reiken SR, Scheuermann V, Mrozek S, Santulli G, Umanskaya A, Petrof BJ, Jaber S, Marks AR, Lacampagne A (2016) Leaky ryanodine receptors contribute to diaphragmatic weakness during mechanical ventilation. Proc Natl Acad Sci U S A 113(32):9069–9074. https://doi.org/10.1073/pnas.1609707113

McMullan G, Chen S, Henderson R, Faruqi AR (2009) Detective quantum efficiency of electron area detectors in electron microscopy. Ultramicroscopy 109:1126–1143

McMullan G, Faruqi AR, Clare D, Henderson R (2014) Comparison of optimal performance at 300keV of three direct electron detectors for use in low dose electron microscopy. Ultramicroscopy 147:156–163

Nakai J, Imagawa T, Hakamat Y, Shigekawa M, Takeshima H, Numa S (1990) Primary structure and functional expression from cDNA of the cardiac ryanodine receptor/calcium release channel. FEBS Lett 271(1–2):169–177

Nakashima Y, Nishimura S, Maeda A, Barsoumian EL, Hakamata Y, Nakai J, Allen PD, Imoto K, Kita T (1997) Molecular cloning and characterization of a human brain ryanodine receptor. FEBS Lett 417(1):157–162

Nelson BR, Wu F, Liu Y, Anderson DM, McAnally J, Lin W, Cannon SC, Bassel-Duby R, Olson EN (2013) Skeletal muscle-specific T-tubule protein STAC3 mediates voltage-induced Ca2+ release and contractility. Proc Natl Acad Sci U S A 110(29):11881–11886. https://doi.org/10.1073/pnas.1310571110

Nogales E (2016, January) The development of cryo-EM into a mainstream structural biology technique. Nat Methods 13(1):24–27

Otsu K, Willard HF, Khanna VK, Zorzato F, Green NM, MacLennan DH (1990) Molecular cloning of cDNA encoding the $Ca^{2+}$ release channel (ryanodine receptor) of rabbit cardiac muscle sarcoplasmic reticulum. J Biol Chem 265(23):13472–13483

Paul-Pletzer K, Yamamoto T, Bhat MB, Ma J, Ikemoto N, Jimenez LS, Morimoto H, Williams PG, Parness J (2002) Identification of a dantrolene-binding sequence on the skeletal muscle ryanodine receptor. J Biol Chem 277(38):34918–34923. https://doi.org/10.1074/jbc.M205487200

Peng W et al (2016) Structural basis for the gating mechanism of the type 2 ryanodine receptor RyR2. Science 354:6310. https://doi.org/10.1126/science.aah5324

Porta M, Zima AV, Nani A, Diaz-Sylvester PL, Copello JA, Ramos-Franco J, Blatter LA, Fill M (2011) Single ryanodine receptor channel basis of caffeine's action on $Ca^{2+}$ sparks. Biophys J 100(4):931–938. https://doi.org/10.1016/j.bpj.2011.01.017

Quane KA, Healy JM, Keating KE, Manning BM, Couch FJ, Palmucci LM, Doriguzzi C, Fagerlund TH, Berg K, Ording H et al (1993) Mutations in the ryanodine receptor gene in central core disease and malignant hyperthermia. Nat Gen 5(1):51–55. https://doi.org/10.1038/ng0993-51

Radermacher M, Wagenknecht T, Grassucci R, Frank J, Inui M, Chadwick C, Fleischer S (1992, April) Cryo-EM of the native structure of the calcium release channel/ryanodine receptor from sarcoplasmic reticulum. Biophys J 61(4):936–940

Radermacher M, Rao V, Grassucci R, Frank J, Timerman AP, Fleischer S, Wagenknecht T (1994a, October) Cryo-electron microscopy and three-dimensional reconstruction of the calcium release channel/ryanodine receptor from skeletal muscle. J Cell Biol 127(2):411–423

Rios E, Brum G (1987) Involvement of dihydropyridine receptors in excitation-contraction coupling in skeletal muscle. Nature 325(6106):717–720. https://doi.org/10.1038/325717a0

Rosemblit N, Moschella MC, Ondriasova E, Gutstein DE, Ondrias K, Marks AR (1999) Intracellular calcium release channel expression during embryogenesis. Dev Biol 206(2):163–177

Rosenberg H, Davis M, James D, Pollock N, Stowell K (2007) Malignant hyperthermia. Orphanet J Rare Dis 2:21–21. https://doi.org/10.1186/1750-1172-2-21

Rullman E, Andersson DC, Melin M, Reiken S, Mancini DM, Marks AR, Lund LH, Gustafsson T (2013) Modifications of skeletal muscle ryanodine receptor type 1 and exercise intolerance in heart failure. J Heart Lung Transplant 32(9):925–929. https://doi.org/10.1016/j.healun.2013.06.026

Saito A, Inui M, Radermacher M, Frank J, Fleischer SJ (1988, July) Ultrastructure of the calcium release channel of sarcoplasmic reticulum. Cell Biol 107(1):211–219

Samsò M, Wagenknecht T, Allen PD (2005, June) Internal structure and visualization of transmembrane domains of the RyR1 calcium release channel by cryo-EM. Nat Struct Mol Biol 12(6):539–544

Samsó M, Feng W, Pessah IN, Allen PD (2009, April 14) Coordinated movement of cytoplasmic and transmembrane domains of RyR1 upon gating. PLoS Biol 7(4):e85. https://doi.org/10.1371/journal.pbio.1000085

Santulli G (2015) microRNAs distinctively regulate vascular smooth muscle and endothelial cells: functional implications in angiogenesis, atherosclerosis, and in-stent restenosis. Adv Exp Med Biol 887:53–77. https://doi.org/10.1007/978-3-319-22380-3_4

Santulli G, Marks AR (2015) Essential roles of intracellular calcium release channels in muscle, brain, metabolism, and aging. Curr Mol Pharmacol 8(2):206–222

Santulli G, Totary-Jain H (2013) Tailoring mTOR-based therapy: molecular evidence and clinical challenges. Pharmacogenomics 14(12):1517–1526. https://doi.org/10.2217/pgs.13.143

Santulli G, Wronska A, Uryu K, Diacovo TG, Gao M, Marx SO, Kitajewski J, Chilton JM, Akat KM, Tuschl T, Marks AR, Totary-Jain H (2014) A selective microRNA-based strategy inhibits restenosis while preserving endothelial function. J Clin Invest 124(9):4102–4114. https://doi.org/10.1172/JCI76069

Santulli G, Pagano G, Sardu C, Xie W, Reiken S, D'Ascia SL, Cannone M, Marziliano N, Trimarco B, Guise TA, Lacampagne A, Marks AR (2015a) Calcium release channel RyR2 regulates insulin release and glucose homeostasis. J Clin Invest 125(5):1968–1978. https://doi.org/10.1172/JCI79273

Santulli G, Xie W, Reiken SR, Marks AR (2015b) Mitochondrial calcium overload is a key determinant in heart failure. Proc Natl Acad Sci U S A 112(36):11389–11394. https://doi.org/10.1073/pnas.1513047112

Santulli G, Lewis D, Marks AR (2017a) Physiology and pathophysiology of excitation–contraction coupling in skeletal muscle: the functional role of ryanodine receptor. J Muscle Res Cell Motil. https://doi.org/10.1007/s10974-017-9470-z

Santulli G, Nakashima R, Yuan Q, Marks AR (2017b) Intracellular calcium release channels: an update. J Physiol. https://doi.org/10.1113/JP272781

Scheres SH (2012, December) RELION: implementation of a Bayesian approach to cryo-EM structure determination. J Struct Biol 180(3):519–530. https://doi.org/10.1016/j.jsb.2012.09.006

Sewry CA, Muller C, Davis M, Dwyer JS, Dove J, Evans G, Schroder R, Furst D, Helliwell T, Laing N, Quinlivan RC (2002) The spectrum of pathology in central core disease. Neuromusc Disord NMD 12(10):930–938

Shan J, Betzenhauser MJ, Kushnir A, Reiken S, Meli AC, Wronska A, Dura M, Chen BX, Marks AR (2010a) Role of chronic ryanodine receptor phosphorylation in heart failure and beta-adrenergic receptor blockade in mice. J Clin Invest 120(12):4375–4387. https://doi.org/10.1172/JCI37649

Shan J, Kushnir A, Betzenhauser MJ, Reiken S, Li J, Lehnart SE, Lindegger N, Mongillo M, Mohler PJ, Marks AR (2010b) Phosphorylation of the ryanodine receptor mediates the cardiac fight or flight response in mice. J Clin Invest 120(12):4388–4398. https://doi.org/10.1172/JCI32726

Sharma MR, Penczek P, Grassucci R, Xin HB, Fleischer S, Wagenknecht T (1998, July 17) Cryoelectron microscopy and image analysis of the cardiac ryanodine receptor. J Biol Chem 273(29):18429–18434

Sharma P, Ishiyama N, Nair U, Li W, Dong A, Miyake T, Wilson A, Ryan T, MacLennan DH, Kislinger T, Ikura M, Dhe-Paganon S, Gramolini AO (2012) Structural determination of the phosphorylation domain of the ryanodine receptor. FEBS J 279(20):3952–3964. https://doi.org/10.1111/j.1742-4658.2012.08755.x

Suetomi T, Yano M, Uchinoumi H, Fukuda M, Hino A, Ono M, Xu X, Tateishi H, Okuda S, Doi M, Kobayashi S, Ikeda Y, Yamamoto T, Ikemoto N, Matsuzaki M (2011) Mutation-linked defective interdomain interactions within ryanodine receptor cause aberrant Ca(2)(+)release leading to catecholaminergic polymorphic ventricular tachycardia. Circulation 124(6):682–694. https://doi.org/10.1161/circulationaha.111.023259

Takeshima H, Nishimura S, Matsumoto T, Ishida H, Kangawa K, Minamino N, Matsuo H, Ueda M, Hanaoka M, Hirose T et al (1989) Primary structure and expression from complementary DNA of skeletal muscle ryanodine receptor. Nature 339(6224):439–445. https://doi.org/10.1038/339439a0

Tateishi H, Yano M, Mochizuki M, Suetomi T, Ono M, Xu X, Uchinoumi H, Okuda S, Oda T, Kobayashi S, Yamamoto T, Ikeda Y, Ohkusa T, Ikemoto N, Matsuzaki M (2009) Defective domain-domain interactions within the ryanodine receptor as a critical cause of diastolic $Ca^{2+}$ leak in failing hearts. Cardiovasc Res 81(3):536–545. https://doi.org/10.1093/cvr/cvn303

Timerman AP, Ogunbumni E, Freund E, Wiederrecht G, Marks AR, Fleischer S (1993) The calcium release channel of sarcoplasmic reticulum is modulated by FK-506-binding protein. Dissociation and reconstitution of FKBP-12 to the calcium release channel of skeletal muscle sarcoplasmic reticulum. J Biol Chem 268(31):22992–22999

Tung CC, Lobo PA, Kimlicka L, Van Petegem F (2010) The amino-terminal disease hotspot of ryanodine receptors forms a cytoplasmic vestibule. Nature 468(7323):585–588. https://doi.org/10.1038/nature09471

Umanskaya A, Santulli G, Xie W, Andersson DC, Reiken SR, Marks AR (2014) Genetically enhancing mitochondrial antioxidant activity improves muscle function in aging. Proc Natl Acad Sci U S A 11(42):15250–15255. https://doi.org/10.1073/pnas.1412754111

Van Petegem F (2015) Ryanodine receptors: allosteric Ion channel giants. J Mol Biol 427(1):31–53. htpps://doi.org/10.1016/j.jmb.2014.08.004

Van Petegem F (2016, October) How to open a ryanodine receptor. Cell Res 26(10):1073–1074

Vest JA, Wehrens XH, Reiken SR, Lehnart SE, Dobrev D, Chandra P, Danilo P, Ravens U, Rosen MR, Marks AR (2005) Defective cardiac ryanodine receptor regulation during atrial fibrillation. Circulation 111(16):2025–2032. https://doi.org/10.1161/01.CIR.0000162461.67140.4C

Wagenknecht T, Grassucci R, Frank J, Saito A, Inui M, Fleischer S (1989, March 9) Three-dimensional architecture of the calcium channel/foot structure of sarcoplasmic reticulum. Nature 338(6211):167–170

Wagenknecht T, Radermacher M (1995, August 1) Three-dimensional architecture of the skeletal muscle ryanodine receptor. FEBS Lett 369(1):43–46, Review

Wei R et al (2016) Structural insights into $Ca^{2+}$-activated long-range allosteric channel gating of RyR1. Cell Res 26:977–994

Xie W, Santulli G, Guo X, Gao M, Chen BX, Marks AR (2013) Imaging atrial arrhythmic intracellular calcium in intact heart. J Mol Cell Cardiol 64:120–123. https://doi.org/10.1016/j.yjmcc.2013.09.003

Xie W, Santulli G, Reiken SR, Yuan Q, Osborne BW, Chen BX, Marks AR (2015) Mitochondrial oxidative stress promotes atrial fibrillation. Sci Rep 5:11427. https://doi.org/10.1038/srep11427

Xin HB, Timerman AP, Onoue H, Wiederrecht GJ, Fleischer S (1995) Affinity purification of the ryanodine receptor/calcium release channel from fast twitch skeletal muscle based on its tight association with FKBP12. Biochem Biophys Res Commun 214(1):263–270. https://doi.org/10.1006/bbrc.1995.2283

Xiong L, Zhang JZ, He R, Hamilton SL (2006) A Ca2+−binding domain in RyR1 that interacts with the calmodulin binding site and modulates channel activity. Biophys J 90(1):173–182. https://doi.org/10.1529/biophysj.105.066092

Yan Z, Bai X-C, Yan C, Wu J, Li Z, Xie T, Peng W, Yin C-C, Li X, Scheres SHW, Shi Y, Yan N (2015) Structure of the rabbit ryanodine receptor RyR1 at near-atomic resolution. Nature 517(7532):50–55. https://doi.org/10.1038/nature14063

Yuan Q, Chen Z, Santulli G, Gu L, Yang ZG, Yuan ZQ, Zhao YT, Xin HB, Deng KY, Wang SQ, Ji G (2014) Functional role of Calstabin2 in age-related cardiac alterations. Sci Rep 4:7425. https://doi.org/10.1038/srep07425

Yuan Q, Yang J, Santulli G, Reiken SR, Wronska A, Kim MM, Osborne BW, Lacampagne A, Yin Y, Marks AR (2016) Maintenance of normal blood pressure is dependent on IP3R1-mediated regulation of eNOS. Proc Natl Acad Sci U S A 113(30):8532–8537. https://doi.org/10.1073/pnas.1608859113

Yuchi Z, Lau K, Van Petegem F (2012) Disease mutations in the ryanodine receptor central region: crystal structures of a phosphorylation hot spot domain. Structure 20(7):1201–1211

Yuchi Z, Yuen SM, Lau K, Underhill AQ, Cornea RL, Fessenden JD, Van Petegem F (2015) Crystal structures of ryanodine receptor SPRY1 and tandem-repeat domains reveal a critical FKBP12 binding determinant. Nat Commun 6:7947. https://doi.org/10.1038/ncomms8947

Zalk R, Clarke OB, des Georges A, Grassucci RA, Reiken S, Mancia F, Hendrickson WA, Frank J, Marks AR (2015, January 1) Structure of a mammalian ryanodine receptor. Nature 517(7532):44–49

Zhang Y, Chen HS, Khanna VK, De Leon S, Phillips MS, Schappert K, Britt BA, Browell AK, MacLennan DH (1993) A mutation in the human ryanodine receptor gene associated with central core disease. Nat Gen 5(1):46–50. https://doi.org/10.1038/ng0993-46

Zhang L, Liu Y, Song F, Zheng H, Hu L, Lu H, Liu P, Hao X, Zhang W, Chen K (2011) Functional SNP in the microRNA-367 binding site in the 3'UTR of the calcium channel ryanodine receptor gene 3 (RYR3) affects breast cancer risk and calcification. Proc Natl Acad Sci U S A 108(33):13653–13658. https://doi.org/10.1073/pnas.1103360108

Zhao F, Li P, Chen SR, Louis CF, Fruen BR (2001) Dantrolene inhibition of ryanodine receptor $Ca^{2+}$ release channels molecular mechanism and isoform selectivity. J Pys Chem 276(17):13810–13816. https://doi.org/10.1074/jbc.M006104200

# Chapter 12
# Conformational Equilibrium of Human Platelet Integrin Investigated by Three-Dimensional Electron Cryo-Microscopy


**Dorit Hanein and Niels Volkmann**

**Abstract** Integrins are bidirectional transmembrane receptors that play central roles in hemostasis and arterial thrombosis. They have been subject to structural studies for many years, in particular using X-ray crystallography, nuclear magnetic resonance spectroscopy, and two-dimensional negative stain electron microscopy. Despite considerable progress, a full consensus on the molecular mechanism of integrin activation is still lacking. Three-dimensional reconstructions of full-length human platelet integrin $\alpha_{IIb}\beta_3$ in lipid-bilayer nanodiscs obtained by electron cryo-microscopy and single-particle reconstruction have shed new light on the activation process. These studies show that integrin $\alpha_{IIb}\beta_3$ exists in a continuous conformational equilibrium ranging from a compact nodular conformation similar to that obtained in crystal structures to a fully extended state with the leg domains separated. This equilibrium is shifted towards the extended conformation when extracellular ligands, cytosolic activators and lipid-bilayer nanodiscs are added. Addition of cytosolic activators and extracellular ligands in the absense of nanodiscs produces significantly less dramatic shifts, emphasizing the importance of the membrane bilayer in the activation process.

**Keywords** Integrin · Electron cryo-microscopy · Image reconstruction · Single-spanning transmembrane receptors · Activation · Conformation · Three-dimensional structure · Talin head domain · RGD peptides · Membrane bilayer · Nanodiscs

D. Hanein · N. Volkmann (✉)
Bioinformatics and Structural Biology Program, Sanford-Burnham-Prebys Medical Discovery Institute, San Diego, CA, USA
e-mail: dorit@burnham.org; niels@burnham.org



J. R. Harris, E. J. Boekema (eds.), *Membrane Protein Complexes: Structure and Function*, Subcellular Biochemistry 87,
https://doi.org/10.1007/978-981-10-7757-9_12

## 12.1 Introduction

Integrins constitute the principal family of extracellular-matrix receptor that transmit bidirectional signals across the plasma membrane. Their binding to the extracellular matrix enables cells to respond to a wide variety of physical and chemical cues (Hynes and Naba 2012) that regulate many biological processes such as hemostasis, differentiation, migration, proliferation, and cell death. Integrins are heterodimeric transmembrane receptors composed of α- and β- subunits, each with a single transmembrane helix, an extracellular ligand-binding domain and a short cytoplasmic tail (Hynes 2002). Integrin receptors are expressed on the cell surface in either an 'on' or an 'off' state with respect to ligand binding. The equilibrium between the two states can be modulated by intra or extracellular cues (Campbell and Humphries 2011) The 'on' state is thought to be stabilized by extracellular ligand binding and binding to scaffolding proteins such as vinculin or talin, ultimately linking integrins to the actin cytoskeleton and thereby mediating mechanotransduction (Sun et al. 2016).

The differences between the two affinity states are essential for regulating cell adhesion, particularly in the case of platelets. Platelets need to be able to circulate freely in a non-adherent state to avoid blood clots. Only stimulation by agonists at the sites of wounds turns on the fibrinogen binding function of $\alpha_{IIb}\beta_3$ integrins, which then leads to aggregation of platelets and the formation of a thrombus, halting the loss of blood. The transition between the 'on' and 'off' affinity states is referred to as activation (for reviews see Banno and Ginsberg 2008; Luo et al. 2007; Bouaouina et al. 2012; Ye et al. 2012; Coller 2015). Many of the current models of integrin's molecular activation mechanism have been primarily inferred from crystal structures of $\beta_3$ integrin extracellular domains (Xiong et al. 2001, 2002, 2009; Zhu et al. 2008, 2009, 2013; Dong et al. 2012) as well as two-dimensional negative-stain electron microscopy (Luo et al. 2007; Nishida et al. 2006; Takagi et al. 2002; Xie et al. 2010; Ye et al. 2010; Zhu et al. 2008; Dai et al. 2015; Su et al. 2016; Eng et al. 2011).

## 12.2 Conformational States of Integrin Receptors

The crystal structures show the receptor in a 'bent' conformation, where the headpiece containing the ligand-binding site is pointed in the same direction as the cytoplasmic tail. The electron microscopy studies indicate that integrins can also adopt upright conformations, which are generally assumed to correspond to high-affinity states (Liddington 2014). Some of the two-dimensional projection images of upright integrins in negative stain show the α- and β-legs separated, other images show the

legs close together even though the β-subunit legs tend to be poorly resolved in either case. In the crystal structures as well as three-dimensional reconstructions of negatively stained bent integrins (Choi et al. 2013; Adair et al. 2005), the legs are always close together.

The bent conformation is generally assumed to correspond to the low-affinity state, in part because the ligand-binding pocket is presumed be close to the membrane, possibly blocking access to the binding site for extracellular ligands. However, three-dimensional negative-stain reconstructions of $\alpha_V\beta_3$ integrins in the absence of membrane show that they can bind relatively bulky fibronectin fragments in the bent conformation (Adair et al. 2005). It is not clear whether the membrane would prevent ligand binding for this integrin type, but a three-dimensional reconstruction of negatively stained $\alpha_{IIb}\beta_3$ integrins in a nanodisc membrane environment (Choi et al. 2013) shows a bent conformation with the ligand-binding site pointing away from the membrane.

## 12.3 Models for Integrin Activation

Attempts to reconcile the bent conformation with the existence of upright conformations have led to the idea that the transition between these two conformations could equate to a biochemical transition in ligand binding affinity. This line of thought suggests that that the bent integrins represent the 'off' state, and that an upward switchblade-like movement of the integrin headpiece turns the integrins to an 'on' state. While this 'switchblade' model of activation is widely discussed (Askari et al. 2009; Takagi et al. 2002; Kinashi 2006; Zhu et al. 2007), it is not the only hypothesis on activation. One alternative, the 'deadbolt' model (Xiong et al. 2003, 2009; Arnaout et al. 2005), proposes that ligand binding induces integrin extension and thus the bent state must already be capable of ligand binding. Others have proposed that activation is controlled by more subtle structural rearrangements involving receptor clustering (Bunch 2010), binding to cytoplasmic proteins (Moser et al. 2009), application of force (Li and Springer 2017) and even the rigidity of the extracellular matrix (Wei et al. 2008).

To transition into the upright conformation with separated legs from the bent crystal structure conformation, the hybrid domain, which connects the β-head with the β-leg, has to swing out. Indeed, different degrees of hybrid domain opening were observed within a crystal lattice, when ligand was soaked into crystals of integrin $\alpha_{IIb}\beta_3$ headpiece (Zhu et al. 2013). Talin binds to the cytoplasmic tails of β integrin subunits (Calderwood et al. 1999). Binding of talin domains to cytoplasmic fragments causes dissociation of integrin $\alpha_{IIb}\beta_3$ transmembrane helices (Wegener et al. 2007; Kim et al. 2009). Association of talin binding with the separation of the α- and β-legs was also shown in living cells for $\alpha_L\beta_2$ integrin (Kim et al. 2003).

However, a direct dissociation effect of talin on the transmembrane helices has not conclusively been shown in the context of the full-length molecule.

Because negative staining approaches involve embedding in a heavy metal stain, absorbing on carbon film support, and dehydration, there is a danger of introducing artifacts into the system (Ye et al. 2010). In addition, the degeneracy of two-dimensional projection images does not allow to distinguish between upright integrins with closed legs and upright integrins with open legs in an orientation that makes the leg appear closed in the projection (Xu et al. 2016). The absence of various domains, especially in the crystal structures, is also a possible source of distortions and artifacts.

## 12.4 Electron Cryo-Microscopy of Full-Length Integrins in Nanodiscs

To overcome these shortcomings, we investigated full-length $\alpha_{IIb}\beta_3$ integrin in a fully hydrated environment using electron cryo-microscopy (Xu et al. 2016). To provide a membrane environment for the receptors, we utilized nanodiscs, which are nanometer-scale phospholipid bilayer membrane islands (Denisov et al. 2004; Xu et al. 2013; Ye et al. 2010; Choi et al. 2013). Nanodiscs match the properties of biological membranes more closely than liposomes (Shaw et al. 2004) and allow access to the receptor for both extracellular ligands and cytosolic binding partners. Sample preparation protocols were adjusted so that only single integrin molecules were incorporated into the nanodiscs to avoid clustering effects.

Reconstructions of platelet integrin $\alpha_{IIb}\beta_3$ were determined in the presence or absence of RGD peptide extracellular ligand, the talin head domain, and nanodiscs. Because the talin head domain was reported to activate integrin $\alpha_{IIb}\beta_3$ for RGD peptide binding, this represents a minimal system for reconstituting potential activation of un-clustered integrin. In all preparations, we found that integrin $\alpha_{IIb}\beta_3$ exists in a continuous conformational equilibrium centered around four main conformational states (Fig. 12.1). These four conformations range from (i) a compact state similar to the bent conformer observed in crystal structures; through (ii, iii) two upright conformers with different degrees of hybrid domain opening and the lower legs close together; to (iv) an upright conformation with the lower legs clearly separated by 8 nm. Like in the three-dimensional negative stain reconstruction in the nanodisc (Choi et al. 2013), the ligand-binding site points away from the membrane and is accessible even to bulky ligands in the bent conformation.

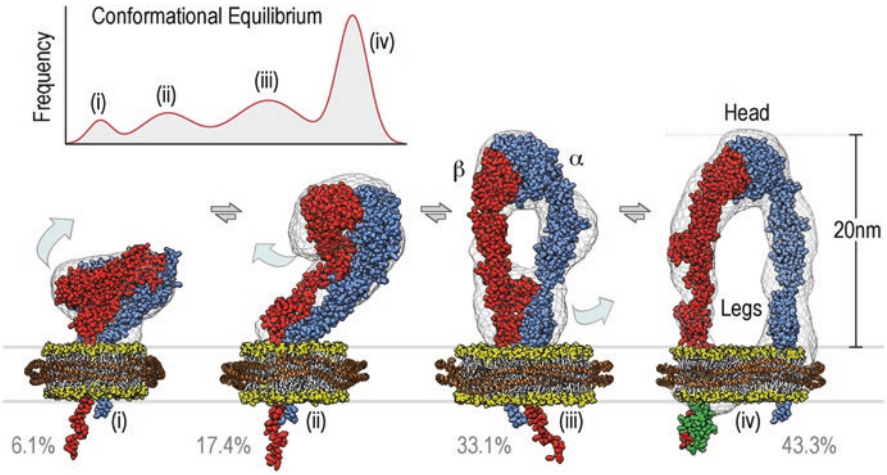


**Fig. 12.1** Integrin $\alpha_{IIb}\beta_3$ exists in a continuous conformational equilibrium centered around four main conformational states. The height of the peaks is given by the percentage of particles assigned to a given conformation, the width was estimated from the structural variability within each group. The equilibrium in the presence of the extracellular ligand RGD, cytosolic binding partner talin head, and lipid bilayers is depicted in the top left corner and centers around the four conformations shown in the lower part of the figure. Space-filling atomic models of $\alpha_{IIb}\beta_3$ integrin (α-subunit in blue, β-subunit in red) embedded in nanodiscs (lipid head groups in yellow, belt protein in orange) are shown fitted into their respective three-dimensional reconstructions (grey wire representation). Required structural transitions are depicted as light blue arrows. In the three-dimensional reconstruction of the upright state (*iv*) density for bound talin head (F3 domain shown in green) was evident

The conformations of integrin were analyzed using unbiased iterative multi-reference single-particle reconstruction techniques (Spahn and Penczek 2009; Scheres 2012). The distribution of the four conformers in the population of integrin samples was compared by tallying the fraction of particles observed in each class of conformers. Integrin $\alpha_{IIb}\beta_3$ by itself is distributed with 12.9% in the bent conformation, 21.1% in the first intermediate, 37.5% in the second intermediate, and 28.5% in the fully upright state. Addition of the RGD peptide ligand or the talin head domain, had a relatively small effect on the distribution of conformers (Fig. 12.2). However, addition of the nanodisc led to a significant shift in the population toward the upright conformation (43.3%).

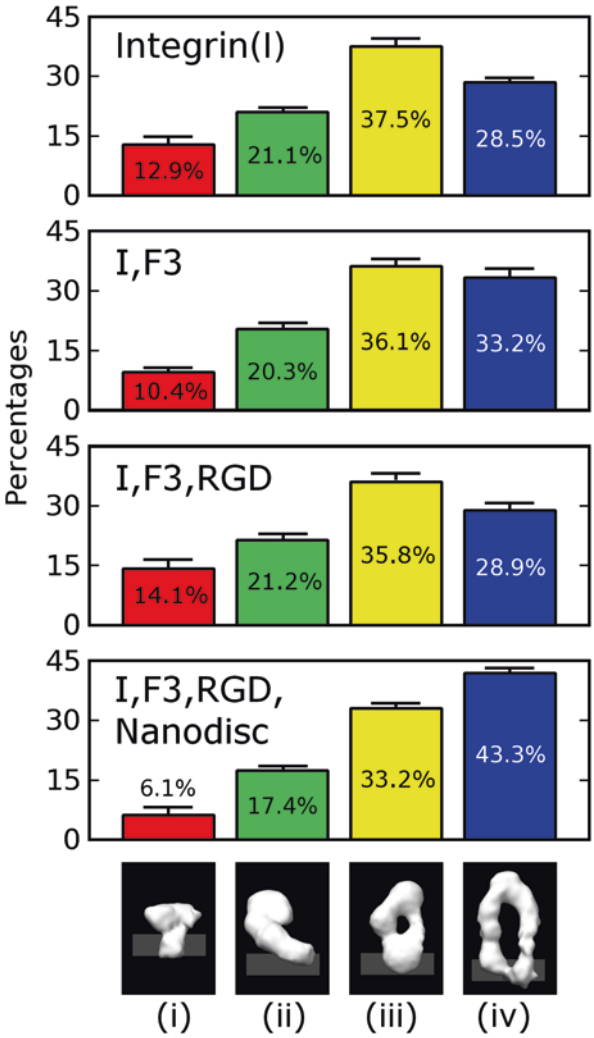


**Fig. 12.2** Distributions of integrin $\alpha_{IIb}\beta_3$ conformers in the presence and absence of extracellular ligands (RGD), cytosolic binding partners (talin head domain F3) and lipid bilayer nanodiscs. Between two and four independent data sets were acquired for each condition. The standard deviation for the percentages was below 2 percentage points for all measurements (see error bars). The presence of talin head domain shifts the equilibrium slightly by 4.7% towards the upright conformation with separated legs. The trend is somewhat reversed if RGD is added as well. When nanodiscs are added, there is a major shift of 14.8% towards the upright (*iv*) conformation

## 12.5 Are Integrin Conformations Tightly Linked to Specific Activation State?

These findings indicate that the activation state of the integrin may not be correlated strongly with any particular global conformation of integrin. Many other lines of evidence support the idea that extension of the integrin to an upright stance is not identical to activation of the ligand binding function. Studies on the hydrodynamics of $\alpha_{IIb}\beta_3$ in the resting state show that it resembles an extended structure rather than a bent conformation (Rocco et al. 2008). Electron cryotomographic studies of $\alpha_{IIb}\beta_3$ in liposomes fail to detect changes in height or orientation with respect to the

membrane in response to activating agents such as $Mn^{2+}$ (Ye et al. 2008) or talin head domain (Ye et al. 2010). Studies on the $\alpha_V\beta_3$ integrin, which shares the same β subunit with $\alpha_{IIb}\beta_3$, show that it can bind an RGD peptide while in the bent conformation (Xiong et al. 2001) and that it remains bent while in complex with a macromolecular ligand (a fragment of fibronectin) (Adair et al. 2005). Results on other integrins are similar. Studies in which FRET was used to study conformational shifts upon activation of integrin $\alpha_4\beta_1$ (Chigaev et al. 2003) and $\alpha_{IIb}\beta_3$ (Coutinho et al. 2007) on the cell surface argue against a mechanistic connection between extension and activation. This conclusion is also supported by studies in which the conformation of $\alpha_4\beta_1$ was probed with antibodies (Chigaev et al. 2009). Finally, rotary shadowed images of constitutively inactive integrin $\alpha_5\beta_1$ reveal extended conformers (Takagi et al. 2003), a finding that also dissociates the connection between activation and extension.

The signal for integrin activation has to be transmitted through the membrane using the transmembrane helices in one way or another. It is well established that talin can disrupt the salt-bridge that holds the transmembrane helices together and simultaneously reorients the transmembrane helix of the β subunit in respect to the membrane (Anthis et al. 2009). Our data indicates that the membrane insertion of the full-length integrin shifts the equilibrium towards the conformation with separated legs with much higher probability than talin alone. Isolated transmembrane helices and the heterodimeric complex of the helices have essentially the same configuration in respect to the membrane and there is apparently no reorientation induced by separation (Lau et al. 2009). Also, the relatively slow transmembrane helix dissociation does not interfere with the much faster activation and there is a fair amount of separated transmembrane helices in membrane environments even if the experimental conditions were tweaked to favor heterodimeric transmembrane helices (Lau et al. 2009).

## 12.6 Conclusions

Together, these findings raise the possibility that integrin leg separation is primarily driven by the membrane insertion while talin's main role would be to reorient the transmembrane helix of the β subunit in the membrane. In this scenario, the reorientation of the transmembrane helix triggers the signal transmission to the ligand-binding site that leads to activation of the ligand-binding capability, not the leg separation (Fig. 12.3). In this model, neither full leg separation nor extension is necessary for activation. All that would be required is breaking the salt bridge that locks the transmembrane helices and a subsequent reorientation of the β subunit helix in the membrane. Because this can be achieved without completely separating the legs and extending the extracelluar domain, it would allow activation of non-extended integrin conformations as well as extended conformations with closed legs.

Switching between signaling modes should carry a reasonable energy expense. The energy expense for separating the legs and to go from bent to extended confor-

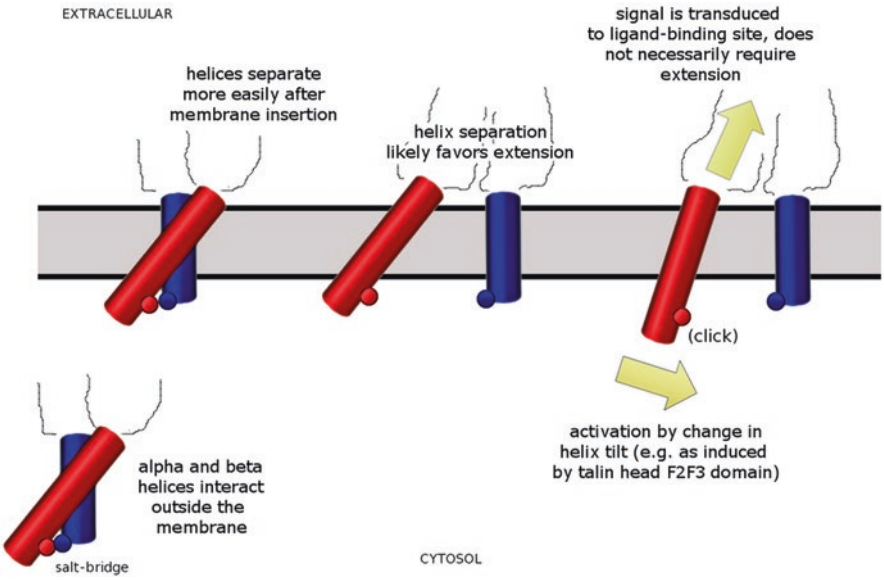


**Fig. 12.3** Possible involvement of helix β-subunit transmembrane helix reorientation in integrin activation. Outside the membrane, the two transmembrane helices (β-subunit red, α-subunit blue) are strongly associated and linked by a salt bridge (lower left corner). Inside the membrane the association is weakened (top left) and the helices can separate (top center) more easily. The separation likely favors extension of the molecule from the bent conformation but does not require or deterministically induce it. Activation could be achieved primarily by a change in helix tilt of the β-subunit transmembrane helix (red) similar to that induced by binding of talin head F2F3 domain. This reorientation triggers the signal transduction to the ligand-binding site (yellow arrows). This action would resemble more a 'light switch' rather than 'switchblade' or a 'deadbolt' mechanism. It would require significantly less energy and could prime the ligand-binding site for binding in all conformational states, including the bent conformation

mation would be much higher than merely breaking the salt bridge and reorienting the transmembrane helix. The talin F2F3 head fragment is a much stronger activator than talin F3 domain alone. Within the framework of the model, this is consistent with the F2 domain being the main factor responsible for reorienting the transmembrane helix (Anthis et al. 2009). The model also explains why other molecules that do not affect the salt-bridge (such as kindlin) can activate integrin. They would induce a reorientation in the transmembrane helix rather than triggering leg separation.

As a consequence of recent hardware and software developments, electron cryo-microscopy has been able to reach near-atomic resolution more frequently than ever before (reviewed in Subramaniam et al. 2016; Fernandez-Leiro and Scheres 2016), including for low-molecular weight assemblies embedded in nanodiscs (Liang et al. 2017). Furthermore, detailed analyses of cellular systems using electron cryo-tomography are becoming more and more feasible (reviewed in Oikonomou and Jensen 2017; Beck and Baumeister 2016). With these technologies in hand, high-resolution electron cryo-microscopy studies of integrin receptors in nanodiscs and detailed analyses of integrins in their cellular context should become possible in the near future.

**Acknowledgments** This work was supported by National Institute of Health research grants CA179087, OD012372 (DH) and GM115972 (NV).

## References

Adair BD, Xiong JP, Maddock C, Goodman SL, Arnaout MA, Yeager M (2005) Three-dimensional EM structure of the ectodomain of integrin {alpha}V{beta}3 in a complex with fibronectin. J Cell Biol 168:1109–1118

Anthis NJ, Wegener KL, Ye F, Kim C, Goult BT, Lowe ED, Vakonakis I, Bate N, Critchley DR, Ginsberg MH, Campbell ID (2009) The structure of an integrin/talin complex reveals the basis of inside-out signal transduction. EMBO J 28:3623–3632

Arnaout MA, Mahalingam B, Xiong JP (2005) Integrin structure, allostery, and bidirectional signaling. Annu Rev Cell Dev Biol 21:381–410

Askari JA, Buckley PA, Mould AP, Humphries MJ (2009) Linking integrin conformation to function. J Cell Sci 122:165–170

Banno A, Ginsberg MH (2008) Integrin activation. Biochem Soc Trans 36:229–229

Beck M, Baumeister W (2016) Cryo-electron tomography: can it reveal the molecular sociology of cells in atomic detail? Trends Cell Biol 26:825–837

Bouaouina M, Harburger DS, Calderwood DA (2012) Talin and signaling through integrins. Methods Mol Biol 757:325–347

Bunch TA (2010) Integrin alphaIIbbeta3 activation in Chinese hamster ovary cells and platelets increases clustering rather than affinity. J Biol Chem 285:1841–1849

Calderwood DA, Zent R, Grant R, Rees DJ, Hynes RO, Ginsberg MH (1999) The Talin head domain binds to integrin beta subunit cytoplasmic tails and regulates integrin activation. J Biol Chem 274:28071–28074

Campbell ID, Humphries MJ (2011) Integrin structure, activation, and interactions. Cold Spring Harb Perspect Biol 3:1–14

Chigaev A, Buranda T, Dwyer DC, Prossnitz ER, Sklar LA (2003) FRET detection of cellular alpha4-integrin conformational activation. Biophys J 85:3951–3962

Chigaev A, Waller A, Amit O, Halip L, Bologa CG, Sklar LA (2009) Real-time analysis of conformation-sensitive antibody binding provides new insights into integrin conformational regulation. J Biol Chem 284:14337–14346

Choi WS, Rice WJ, Stokes DL, Coller BS (2013) Three-dimensional reconstruction of intact human integrin αIIbβ3; new implications for activation-dependent ligand binding. Blood 122:4165–4171

Coller BS (2015) αIIbβ3: structure and function. J Thromb Haemost 13(Suppl 1):S17–S25

Coutinho A, Garcia C, Gonzalez-Rodriguez J, Lillo MP (2007) Conformational changes in human integrin alphaIIbbeta3 after platelet activation, monitored by FRET. Biophys Chem 130:76–87

Dai A, Ye F, Taylor DW, Hu G, Ginsberg MH, Taylor KA (2015) The structure of a full-length membrane-embedded integrin bound to a physiological ligand. J Biol Chem 290:27168–27175

Denisov IG, Grinkova YV, Lazarides AA, Sligar SG (2004) Directed self-assembly of monodisperse phospholipid bilayer Nanodiscs with controlled size. J Am Chem Soc 126:3477–3487

Dong X, Mi LZ, Zhu J, Wang W, Hu P, Luo BH, Springer TA (2012) α(V)β(3) integrin crystal structures and their functional implications. Biochemistry 51:8814–8828

Eng ET, Smagghe BJ, Walz T, Springer TA (2011) Intact (alpha)IIb(beta)3 integrin is extended after activation as measured by solution X-ray scattering and electron microscopy. J Biol Chem 286:35218–35226

Fernandez-Leiro R, Scheres SH (2016) Unravelling biological macromolecules with cryo-electron microscopy. Nature 537:339–346

Hynes RO (2002) Integrins: bidirectional, allosteric signaling machines. Cell 110:673–687

Hynes RO, Naba A (2012) Overview of the matrisome–an inventory of extracellular matrix constituents and functions. Cold Spring Harb Perspect Biol 4:a004903
Kim M, Carman CV, Springer TA (2003) Bidirectional transmembrane signaling by cytoplasmic domain separation in integrins. Science 301:1720–1725
Kim C, Lau TL, Ulmer TS, Ginsberg MH (2009) Interactions of platelet integrin alphaIIb and beta3 transmembrane domains in mammalian cell membranes and their role in integrin activation. Blood 113:4747–4753
Kinashi T (2006) Adhere upright: a switchblade-like extension of beta2 integrins. Immunity 25:521–522
Lau T-L, Kim C, Ginsberg MH, Ulmer TS (2009) The structure of the integrin alphaIIbbeta3 transmembrane complex explains integrin transmembrane signalling. EMBO J 28:1351–1361
Li J, Springer TA (2017) Integrin extension enables ultrasensitive regulation by cytoskeletal force. Proc Natl Acad Sci U S A 114:4685–4690
Liang YL, Khoshouei M, Radjainia M, Zhang Y, Glukhova A, Tarrasch J, Thal DM, Furness SGB, Christopoulos G, Coudrat T, Danev R, Baumeister W, Miller LJ, Christopoulos A, Kobilka BK, Wootten D, Skiniotis G, Sexton PM (2017) Phase-plate cryo-EM structure of a class B GPCR-G-protein complex. Nature 546:118–123
Liddington RC (2014) Structural aspects of integrins. Adv Exp Med Biol 819:111–126
Luo BH, Carman CV, Springer TA (2007) Structural basis of integrin regulation and signaling. Annu Rev Immunol 25:619–647
Moser M, Legate KR, Zent R, Fossler R (2009) The tail of integrins, talin, and kindlins. Science 324:895–899
Nishida N, Xie C, Shimaoka M, Cheng Y, Walz T, Springer TA (2006) Activation of leukocyte beta2 integrins by conversion from bent to extended conformations. Immunity 25:583–594
Oikonomou CM, Jensen GJ (2017) Cellular electron cryotomography: toward structural biology in situ. Annu Rev Biochem 86:873–896
Rocco M, Rosano C, Weisel JW, Horita DA, Hantgan RR (2008) Integrin conformational regulation: uncoupling extension/tail separation from changes in the head region by a multiresolution approach. Structure 16:954–964
Scheres SH (2012) A Bayesian view on cryo-EM structure determination. J Mol Biol 415:406–418
Shaw AW, McLean MA, Sligar SG (2004) Phospholipid phase transitions in homogeneous nanometer scale bilayer discs. FEBS Lett 556:260–264
Spahn CM, Penczek PA (2009) Exploring conformational modes of macromolecular assemblies by multiparticle cryo-EM. Curr Opin Struct Biol 19:623–631
Su Y, Xia W, Li J, Walz T, Humphries MJ, Vestweber D, Cabañas C, Lu C, Springer TA (2016) Relating conformation to function in integrin α5β1. Proc Natl Acad Sci U S A 113:E3872–E3881
Subramaniam S, Earl LA, Falconieri V, Milne JL, Egelman EH (2016) Resolution advances in cryo-EM enable application to drug discovery. Curr Opin Struct Biol 41:194–202
Sun Z, Guo SS, Fässler R (2016) Integrin-mediated mechanotransduction. J Cell Biol 215:445–456
Takagi J, Petre BM, Walz T, Springer TA (2002) Global conformational rearrangements in integrin extracellular domains in outside-in and inside-out signaling. Cell 110:599–511
Takagi J, Strokovich K, Springer TA, Walz T (2003) Structure of integrin alpha5beta1 in complex with fibronectin. EMBO J 22:4607–4615
Wegener KL, Partridge AW, Han J, Pickford AR, Liddington RC, Ginsberg MH, Campbell ID (2007) Structural basis of integrin activation by talin. Cell 128:171–182
Wei W-C, Lin H-H, Shen M-R, Tang M-J (2008) Mechanosensing machinery for cells under low substratum rigidity. Am J Physiol Cell Physiol 295:C1579–C1589
Xie C, Zhu J, Chen X, Mi L, Nishida N, Springer TA (2010) Structure of an integrin with an alphaI domain, complement receptor type 4. EMBO J 29:666–679
Xiong JP, Stehle T, Diefenbach B, Zhang R, Dunker R, Scott DL, Joachimiak A, Goodman SL, Arnaout MA (2001) Crystal structure of the extracellular segment of integrin alpha Vbeta3. Science 294:339–345

Xiong J-P, Stehle T, Zhang R, Joachimiak A, Frech M, Goodman SL, Arnaout MA (2002) Crystal structure of the extracellular segment of integrin alpha Vbeta3 in complex with an Arg-Gly-asp ligand. Science 296:151–155

Xiong J-P, Stehle T, Goodman SL, Arnaout MA (2003) New insights into the structural basis of integrin activation. Blood 102:1155–1159

Xiong J-P, Mahalingham B, Alonso JL, Borrelli LA, Rui X, Anand S, Hyman BT, Rysiok T, Müller-Pompalla D, Goodman SL, Arnaout MA (2009a) Crystal structure of the complete integrin alphaVbeta3 ectodomain plus an alpha/beta transmembrane fragment. J Cell Biol 186:589–600

Xu XP, Zhai D, Kim E, Swift M, Reed C, Volkmann N, Hanein D (2013) Three-dimensional structure of Bax-mediated pores in membrane bilayers. Cell Death Dis 4:e683

Xu XP, Kim E, Swift M, Smith JW, Volkmann N, Hanein D (2016) Three-dimensional structures of full-length, membrane-embedded human αIIbβ3 integrin complexes. Biophys J 110:798–809

Ye F, Liu J, Winkler H, Taylor KA (2008) Integrin alpha IIb beta 3 in a membrane environment remains the same height after Mn2+ activation when observed by cryoelectron tomography. J Mol Biol 378:976–986

Ye F, Hu G, Taylor D, Ratnikov B, Bobkov AA, McLean MA, Sligar SG, Taylor KA, Ginsberg MH (2010) Recreation of the terminal events in physiological integrin activation. J Cell Biol 188:157–173

Ye F, Kim C, Ginsberg MH (2012) Reconstruction of integrin activation. Blood 119:26–33

Zhu J, Boylan B, Luo B-H, Newman PJ, Springer TA (2007) Tests of the extension and deadbolt models of integrin activation. J Biol Chem 282:11914–11920

Zhu J, Luo B-H, Xiao T, Zhang C, Nishida N, Springer TA (2008) Structure of a complete integrin ectodomain in a physiologic resting state and activation and deactivation by applied forces. Mol Cell 32:849–861

Zhu J, Luo B-H, Barth P, Schonbrun J, Baker D, Springer TA (2009) The structure of a receptor with two associating transmembrane domains on the cell surface: integrin alphaIIbbeta3. Mol Cell 34:234–249

Zhu J, Zhu J, Springer TA (2013) Complete integrin headpiece opening in eight steps. J Cell Biol 201:1053–1068

# Chapter 13
# Mitochondrial Proteolipid Complexes of Creatine Kinase


**Uwe Schlattner, Laurence Kay, and Malgorzata Tokarska-Schlattner**

**Abstract** Isoforms of creatine kinase (CK) generate and use phosphocreatine, a concentrated and highly diffusible cellular "high energy" intermediate, for the main purpose of energy buffering and transfer in order to maintain cellular energy homeostasis. The mitochondrial CK isoform (mtCK) localizes to the mitochondrial intermembrane and cristae space, where it assembles into peripherally membrane-bound, large cuboidal homooctamers. These are part of proteolipid complexes wherein mtCK directly interacts with cardiolipin and other anionic phospholipids, as well as with the VDAC channel in the outer membrane. This leads to a stabilization and cross-linking of inner and outer mitochondrial membrane, forming so-called contact sites. Also the adenine nucleotide translocator of the inner membrane can be recruited into these proteolipid complexes, probably mediated by cardiolipin. The complexes have functions mainly in energy transfer to the cytosol and stimulation of oxidative phosphorylation, but also in restraining formation of reactive oxygen species and apoptosis. *In vitro* evidence indicates a putative role of mtCK in mitochondrial phospholipid distribution, and most recently a role in thermogenesis has been proposed. This review summarizes the essential structural and functional data of these mtCK complexes and describes in more detail the more recent advances in phospholipid interaction, thermogenesis, cancer and evolution of mtCK.

**Keywords** Bioenergetics · Cancer · Compartmentalization · Energy transfer · Mitochondria · Oxidative phosphorylation · Thermogenesis

U. Schlattner (✉) · L. Kay · M. Tokarska-Schlattner
Laboratory of Fundamental and Applied Bioenergetics (LBFA), and SFR Environmental and Systems Biology (BEeSy), University Grenoble Alpes, Grenoble, France

Inserm, U1055, Grenoble, France
e-mail: uwe.schlattner@univ-grenoble-alpes.fr



J. R. Harris, E. J. Boekema (eds.), *Membrane Protein Complexes: Structure and Function*, Subcellular Biochemistry 87,
https://doi.org/10.1007/978-981-10-7757-9_13

Cellular functions are mostly carried out by large protein complexes. This is also true for the mitochondrial compartment that contains some of the largest and most intriguing multiprotein complexes in form of the transmembrane respiratory complexes (and supercomplexes formed thereof), as well as the $F_0F_1$-ATPase. Tremendous progress has been made in recent years on their structural elucidation and characterization that is reviewed elsewhere (for a review see Kühlbrandt (2015)). A recurring issue for many of these mitochondrial complexes and membrane proteins is their close interaction with phospholipids, in particular the mitochondria-specific anionic phospholipid cardiolipin (CL), which fulfills multiple structural and functional roles (Planas-Iglesias et al. 2015). Here we will review mitochondrial creatine kinase (mtCK), a peripheral protein complex in mitochondria, which functions in close interaction with CL and some protein partners.

## 13.1 Creatine Kinases: An Overview

Since its discovery by Karl Lohmann in 1935, the enzyme ATP:creatine phosphotransferase (EC 2.7.3.2) or creatine kinase (CK) has attracted much attention for its role in maintaining cellular energy homeostasis, in particular in tissues such as skeletal and heart muscle or brain, which all contain large and polar cells with high and/or fluctuating energy requirements (Jacobus and Lehninger 1973; Bessman and Geiger 1981; Jacobus 1985; Wallimann et al. 1992). The understanding of CK functions rapidly evolved during the last 20 years due to technological advances in mainly three areas: transgenic mouse models with altered CK levels, cellular and reconstituted systems that address subcellular compartmentation, and high resolution X-ray structures (reviewed in Schlattner et al. 2006a; McLeish and Kenyon 2005; Heerschap et al. 2007).

### *13.1.1 Basic CK Functions*

The basic activity of CK is the reversible transfer of the phosphoryl group from the ATP γ-position to the guanidinium group of creatine (Cr) in an equilibrium reaction. However, further specific properties of both CK and its product PCr are crucial for their function at the cellular level, i.e. energy buffering and transfer. PCr serves as an alternative "high energy" carrier with two important advantages as compared to ATP. First, PCr is metabolically inert (except for the CK reaction) and can accumulate to high intracellular concentrations (up to 15–20 mM). This pool can regenerate ATP in the reverse CK reaction, thus serving as a cellular energy buffer during a temporal mismatch between ATP generation and consumption, very similar to a battery function. Second, PCr also diffuses much faster than ATP due to its smaller molecular size. PCr can thus bridge cellular sites of ATP generation and consumption much faster than nucleotides, and more efficiently correct for a spatial

mismatch of ATP availability between these sites. This energy transport function, also called CK/PCr shuttle or circuit, is further supported by the existence of different CK isoforms with precise subcellular localization. In fact, CK isoforms are partially localized at sites of ATP generation, as well as consumption, which drives the transfer of free energy from ATP to PCr at the former sites, and from PCr to ATP at the latter. This energy transfer function or CK/PCr shuttle is particularly important for large and polar cells. Virtually all CK-containing cell types express at least two CK isoforms: a mostly octameric mitochondrial CK (mtCK) localized in the mitochondrial intermembrane space (reviewed in Wyss et al. 1992; Schlattner et al. 2006b), and at least one dimeric cytosolic CK, partially associating with or close to either ATP-producing glycolytic enzymes or different cellular ATPases such as motor proteins and ion pumps (reviewed in Schlattner et al. 2016; Yan 2016). Generally, co-expression occurs with cytosolic muscle-type CK (MCK) and sarcomeric mtCK (smtCK, also called $Mi_bCK$ or CKMT2) in muscle, or cytosolic brain-type CK (BCK) and ubiquitous mtCK (umtCK, also called $Mi_aCK$ or CKMT1) in most brain cells and many other tissues. All these four isoforms are coded by separate genes in the nuclear genome (*Ckm*, *Ckmt2*, *Ckb*, *Ckmt1*); for human umtCK, two almost identical genes (*Ckmt1a*, *Ckmt1b*) encoding the same protein sequence have been identified (Zhang et al. 2007). For further information on these basics of the CK/PCr system, the reader is referred to earlier reviews (Bessman and Carpenter 1985; Wallimann et al. 1992, 2011; Qin et al. 1998; Dzeja and Terzic 2003; Saks et al. 2007).

### *13.1.2 CK Crystallographic Structures*

During the last 20 years, many X-ray crystallographic studies have structurally described the CK family in quite some detail. Understanding molecular functioning of CKs is further supported by the high sequence and structural homology among CK isoforms and even within the entire guanidino (phosphagen) kinase family. The latter includes also enzymes that phosphorylate alternative guanidino substrates like arginine, taurocyamine etc. in lower metazoans (Ellington 2001; Ellington and Suzuki 2007). The crystallographic structure of the large octamer of chicken smtCK solved by Kabsch, Wallimann and colleagues in 1996 has been the first molecular structure of a guanidino kinase (1CRK; (Fritz-Wolf et al. 1996)), and we have later also solved the human umtCK structure (1QK1; (Eder et al. 2000a). However, the inherent flexibility of mtCK was refractive for obtaining very high atomic resolution and true transition state structures. Finally it were the cytosolic CKs that could be solved at higher resolution (rabbit MCK, 2CRK (Rao et al. 1998); human BCK, 1QH4 (Eder et al. 1999); and bovine BCK, 1G0W (Tisi et al. 2001)), and also in the transition state (*Torpedo californica* CK, 1VRP (Lahiri et al. 2002); rabbit MCK, 1U6R (Ohren et al. 2007); and human BCK, 3B6R (Bong et al. 2008)). The latter contain a “dead end” complex of bound substrates, the transition state analog complex (TSAC), consisting of Cr, ADP, $Mg^{2+}$ and nitrate which mimics the transferred

phosphoryl (Milner-White and Watts 1971). However, the best-studied transition state structure within the guanidino kinase family still remains the one of homologous monomeric arginine kinase. First solved by Chapman and colleagues, it has been analyzed in great detail since then (1BG0 (Zhou et al. 1998); 1 M15, (Yousef et al. 2002, 2003); 1P50, (Pruett et al. 2003); 1RL9 and 1SD0 (Gattis et al. 2004; Azzi et al. 2004); 4GVZ (Clark et al. 2012); and 5 J99 (Godsey et al. 2016)). Altogether, with additional crystallographic structures of glycocyamine kinase (3L2F and 3L2G (Lim et al. 2010), lombricine kinase (3JPZ (Bush et al. 2011)), and taurocyamine kinase (4WOE (Merceron et al. 2015)), the whole guanidino kinase family is now structurally very well characterized. Residues involved in substrate binding, catalysis, formation of homooligomers and further CK/protein and CK/lipid interactions are largely known. Throughout this review, amino acids are numbered according to the mature form of human umtCK, if not stated otherwise. Further information on structural aspects can be found in earlier reviews (Kabsch and Fritz-Wolf 1997; Schlattner et al. 1998; McLeish and Kenyon 2005).

## 13.2 Mitochondrial Creatine Kinase

The mitochondrial isoforms of CK differ from their cytosolic counterparts by their specific subcellular localization and their quarternary structure. MtCKs are encoded by separate nuclear genes that contain a classical N-terminal mitochondrial targeting presequence. After their synthesis in the cytosol, the presequence drives mitochondrial import via the TIM/TOM complex before it is cleaved off and localizes the protein into the intermemrane space (IMS). Here, mtCKs first assemble into stable dimers like in case of cytosolic CKs. However, favored by high local concentration and their interaction with mitochondrial membranes (in particular CL and VDAC, see below), the dimers assemble into cuboidal octamers as seen in all EM and crystallographic structures (Fig. 13.1a).

In the following, we will focus on the mitochondrial isoforms of CK, and in particular on the progress in understanding their structure and function. Although direct crystallographic approaches to the flexible mtCK octamer remain a challenge, biochemical and molecular dynamics studies have provided novel insight into the catalytic mechanism and proteolipid complex formation. Progress on mtCK functions has been closely linked to the evolving view of mitochondria as key

**Fig. 13.1** (continued) acids proposed to be involved in electrostatic interactions of umtCK with VDAC and CL are shown in ball-and-stick representation in CPK colors. All molecules have an additional transparent and differently colored van der Waals surface. The structures represented are the substrate-free conformation of homooctameric human umtCK (PDB 1QK1), dimeric human VDAC (PDB 5XDO) and dimeric bovine ANT (PDB 2C3E). The latter is bound to carboxyatractyloside (not shown), fixing ANT in the so-called c-state (open towards IMS, closed towards the matrix), and three molecules of partially ordered cardiolipins located in the inner leaflet of MIM. Figure prepared with UCSF Chimera 1.11

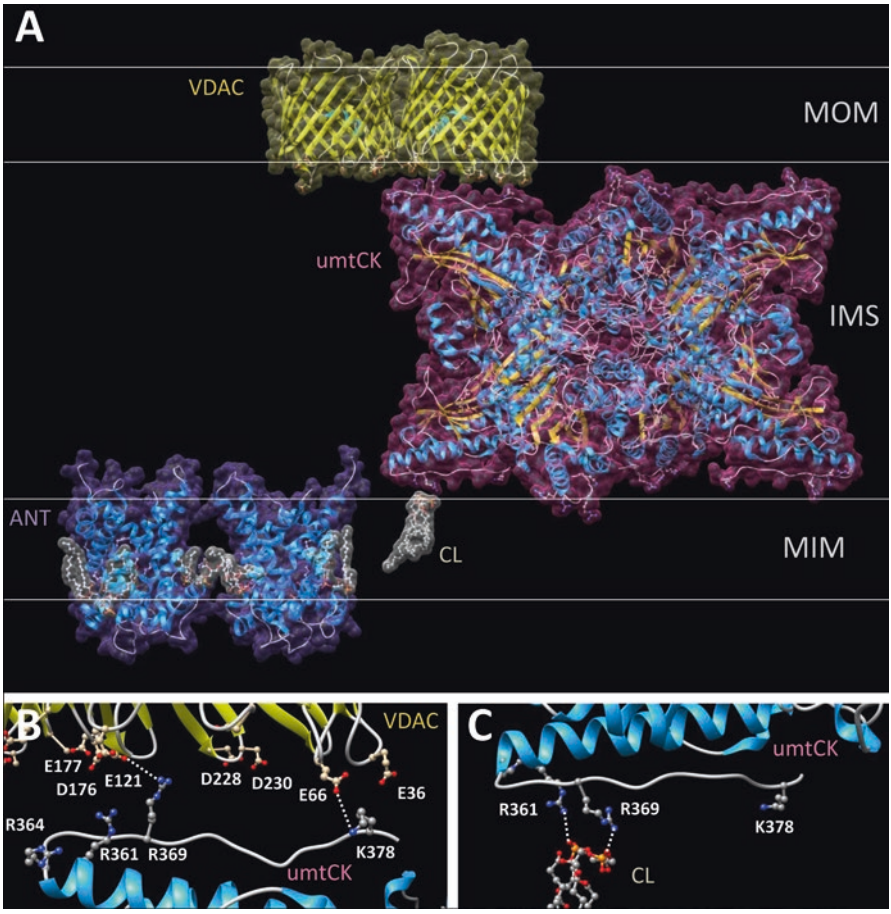


**Fig. 13.1 Proteolipid complex of mtCK.** (**a**) Putative topology of the cuboidal homooctamer of umtCK (red surface) and its direct interaction partners VDAC (yellow surface) in the mitochondrial outer membrane (MOM) and the anionic phospholipid cardiolipin (CL, white surface) in the mitochondrial inner membrane (MIM). ANT (magenta surface) is depicted in MIM near to this complex, based on functional data and co-purification experiments showing close proximity between both and suggesting that they reside in the same MIM cardiolipin patch. Note that only one CL and VDAC dimer are shown, interacting with one dimer in the umtCK octamer; however, every mtCK dimer can engage in these interactions, including additional interactions with CL or other anionic phospholipids in MOM, but probably without achieving exact stoichiometry. Further, since VDAC and ANT most likely form dimers (as shown) or higher oligomers *in vivo,* crystallographic structures representing dimers in the unit cell were chosen. (**b**) Detailed view of the putative mtCK/VDAC interface. Basic residues conserved between mtCK isoforms (R361, R364, R369 K378) and mostly situated in the flexible C-terminal stretch can interact with several acidic residues at the VDAC IMS side. As an example, the both proteins were docked here via two electrostatic interactions (K378-E66, R369-E121). (**c**) Detailed view of the mtCK/CL interface. The same basic C-terminal mtCK residues are involved in electrostatic interactions with CL (e.g. R361 and R369 are perfectly spaced to interact with the two negative charges of the CL head group). All proteins are shown in schematic backbone representation (α-helices blue, β-sheets yellow). Amino

elements at the crossroads of cellular metabolic, regulatory and signaling circuits. For additional information, the reader is referred to earlier reviews on mtCK (Wyss et al. 1992; Schlattner et al. 1998, 2006a, b, 2009; Stachowiak et al. 1998) and on the metabolite channeling and cellular energy units involving mtCK-containing complexes (Saks et al. 2001, 2007; Dzeja and Terzic 2003; Seppet et al. 2005; Schlattner et al. 2013; Zala et al. 2017).

## 13.3 Octameric Structure

### *13.3.1 Fold and Monomer Structure*

The monomer of all CKs and even all guanidino kinases presents a unique and conserved general fold (Fig. 13.2a). It consists of a small all-α N-terminal domain (residues 1–100) and a larger α + β C-terminal domain (residues 113-end) connected by a long linker region without secondary structure (residues 101–112; (Fritz-Wolf et al. 1996). The C-terminal domain is formed by an eight-stranded antiparallel β-sheet, which is flanked by seven α-helices, a fold that is evolutionary related to the C-terminal domain of glutamine synthetase. The saddle-like β-sheet and the only α-helix on its concave side form the highly conserved common core of all CK isoenzymes and largely contributes to the enzyme's active site which is buried in the cleft between the N-and C-terminal domains of CK. Two loops in the region of residues 61–65 and 316–326 are disordered in the X-ray mtCK structures and move during catalysis to shield the active site (Zhou et al. 1998; Lahiri et al. 2002). Additional hinge bending between large and small domain upon substrate binding and during catalysis leads to a more rigid and compact "closed" conformation in the transition state, as opposed to the "open" conformation (Fig. 13.2a).

Mitochondrial and cytosolic CKs present an almost identical, conserved fold, and mainly differ by their primary structure, giving rise to differences in electrostatic surface potential and hydrophobicity. The divergence of the amino acid sequence is particularly pronounced in the N- and C-terminal stretches, which indeed fulfill specific isoenzyme-specific functions stabilizing oligomers and membrane binding, respectively.

### *13.3.2 Dimers and Octamers*

Although CK monomers can be engineered by mutagenesis (Cox et al. 2003), the minimal structural unit of mitochondrial and cytosolic CKs is the dimer. It presents an elongated "banana-like" shape, exposing its two active sites on its concave side. The interaction between the monomers is strong, mostly based on hydrophobic patches including Trp206, and chaotropic conditions with partial unfolding of the

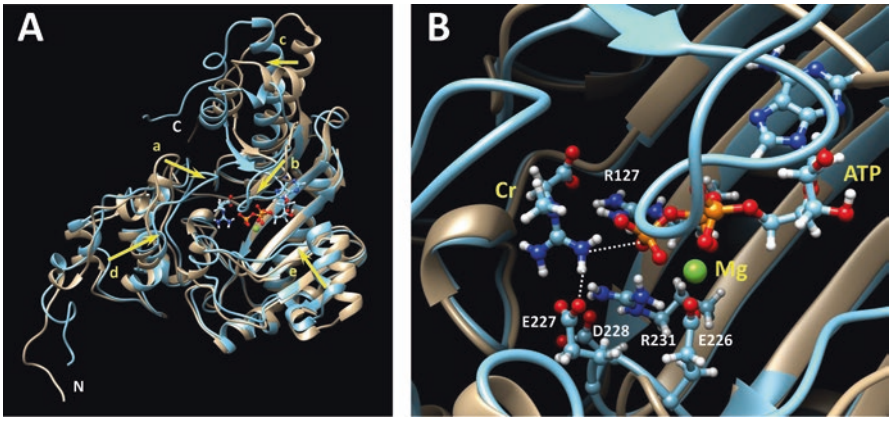


**Fig. 13.2 Phosphotransfer reaction in a mtCK monomer.** A umtCK monomer is shown in schematic backbone representation in absence of substrates (brown) in an "open" conformation (PDB 1QK1, (Eder et al. 2000a) and in presence of Cr and MgATP (blue) in a transition state "closed" conformation (molecular dynamics simulation, (Li et al. 2016)). Both structures were aligned by the β-sheet in the large domain. (**a**) Conformational changes occurring during catalysis indicated by yellow arrows forming a more compact monomer that excludes water from the active site: two loops (a,b) are moving down on the active site, and small (left) and large domains (right) are moving towards each other (c–e). (**b**) Active site of umtCK with bound Cr and MgATP depicted for the "closed" transition state conformation (molecular dynamics simulation, (Li et al. 2016)). In the umtCK active site, only few umtCK residues with a role in phosphoryl transfer are shown as discussed in the text. These include a negatively charged cluster (E226, E227, D228) and two arginines (R127, R129). The plane of the phosphoryl to be transferred and the putative action of E227 as catalytic base are indicated by dotted lines. For further details see (Li et al. 2016). Figure prepared with UCSF Chimera 1.11

monomer are required for their disruption. While all cytosolic CKs remain dimeric, mtCK dimers further associate by their convex sides into large cuboidal octamers with overall dimensions of about 105 × 105 × 86 Å (Schnyder et al. 1991). The four dimers arrange in fourfold rotational symmetry thus generating a central channel, where the N-termini are protruding, and top and bottom faces that are perpendicular to the fourfold octamer axis and each expose the C-termini (Fig. 13.1a). The interaction between dimers is weaker than between monomers and basically involves a hydrophobic patch around Trp264 located in the C-terminal domain, which is strengthened by a number of polar interactions (Fritz-Wolf et al. 1996), which are more pronounced for umtCK than for smtCK (Eder et al. 2000a; Schlattner and Wallimann 2000a). This gives rise to a dynamic equilibrium between dimers and octamers, which depends on the mtCK isoform, protein concentration, oxidation state, and phospholipid interaction, but also on temperature, pH, ionic strength and substrates. Only octamers have high affinity to CL (see below) and are thus able to form larger proteolipid complexes.

## 13.4 Kinase Activity

The general catalytic mechanism of phosphoryl transfer is identical in all CKs and does neither differ between octameric and dimeric mtCK. Since all mtCK structures were solved in absence of substrates (or only ATP present), their catalytic mechanism has not been studied in structural detail. However, given the sequence similarity and the highly preserved general protein fold within the guanidino kinase family, the insight obtained with existing structures can be extrapolated also to mtCK. In addition, more recently, molecular dynamic simulations have been applied to model an umtCK transition state (Li et al. 2016). These data provide insight into the specific fold that CK has acquired in evolution to achieve phosphoryl transfer.

### *13.4.1 Active Site and Substrate Binding*

Each monomer exposes one catalytic site at the surface of the cuboidal mtCK octamer (Fritz-Wolf et al. 1996). The transition state structures have precisely located the active site, with the ATP binding site of CK in a cleft of the large subunit, and the creatine binding site rather between the two CK domains. The residues involved in binding and correct positioning of the substrates have been identified (Zhou et al. 1998; Lahiri et al. 2002) and are not further discussed here.

Binding of substrates switches the CK monomer structure from an "open" to a "closed" conformation. Small and large domains move towards each other, leading to domain-cleft closure, and the two flexible loops act as a lid by closing down on the active site (Fig. 13.2a). This leads to a more compact CK monomer, with the active site protected from water which could lead to non-productive hydrolysis of the activated phosphoryl. These conformational changes seem to depend on binding of Mg-nucleotide alone or both substrates (complete TSAC), with no effects observed with nucleotide or creatine alone. However, in the transition state structure of dimeric *Torpedo* CK with one monomer bound to TSAC and one to MgADP, the Mg-nucleotide does not induce a closed conformation, although it is bound in almost the same position in both monomers (Lahiri et al. 2002). As compared to cytosolic CKs, mtCKs show a much more pronounced substrate binding synergism (Schlattner et al. 2000; Matsushima et al. 2006). That is, binding of the first substrate (binary complex) facilitates binding of the second substrate (ternary complex), indicating a cross-talk between the two substrate binding sites. Such synergism is most pronounced in umtCK and in the direction of PCr production, and involves the flexible elements of the CK structure. Nicking smtCK close to the highly flexible loop 316–326 or co-expressing N- and C-terminal smtCK domains yielded enzymatically active protein, but abolished substrate binding synergism (Wyss et al. 1993; Gross et al. 1996). Besides the more pronounced substrate binding synergism, mtCK isoenzymes may also be more selective in the use of Cr analogues as compared to cytosolic CKs (Boehm et al. 1996).

### *13.4.2 Catalysis*

The catalytic mechanism of CKs has been studied in much detail by physical, chemical, kinetic and spectroscopic techniques, essentially based on cytosolic CKs and related guanidino kinases (for a review see McLeish and Kenyon 2005). The random or ordered bimolecular mechanism, depending on the pH, proceeds via an in-line transfer of a phosphoryl group from ATP to Cr yielding ADP and PCr and *vice versa*, with the equilibrium lying towards PCr generation.

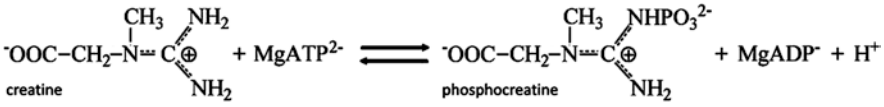


This basic mechanism is the same in all CKs and guanidino kinases. However, some differences exist in the $K_m$, $K_d$ and $V_{max}$ values, e.g. between the two mtCK isoenzymes (Schlattner et al. 2000) or between mtCK octamers and dimers (Kaldis and Wallimann 1995).

Many residues have been implicated in catalysis, but none of them was found to be absolutely essential. This includes Cys278 (Buechter et al. 1992; Hou and Vollmer 1994; Lin et al. 1994) and Trp223 (Messmer and Kagi 1985) in the active site, which were later also shown by site-directed mutagenesis and the transition state structures to play a rather accessory role in binding synergism, correct positioning of the substrates, and stabilization of the transition state (Furter et al. 1993; Gross et al. 1994; Wang et al. 2001; Gattis et al. 2004). A long time controversial issue has been the requirement for a catalytic base, which would favor phosphoryl transfer by accepting the creatine guanidinium proton. Several conserved residues had been proposed as to act as acid-base catalyst, including one of the active site histidines like His61, His92, or His186 (Cook et al. 1981; Rosevear et al. 1981) or two acidic residues, Glu227 and Asp321 (Eder et al. 2000b; Cantwell et al. 2001; Forstner et al. 1997). However, site-directed mutagenesis experiments (Chen et al. 1996; Forstner et al. 1997; Pruett et al. 2003) revealed that although mutating these residues reduces activity, none of them is absolutely essential. Finally, the transition state structures uncovered that only an active site glutamate (Glu227 in umtCK) is correctly positioned to act as a general base catalyst (Zhou et al. 1998; Lahiri et al. 2002). Glutamate functioning as a base is certainly counterintuitive and not an efficient solution, even if its pK may be raised by its environment in the reactive transition state. However, the primary role of the glutamate may be rather the positioning of the guanidinium group than its working as an acid-base catalyst (Zhou et al. 1998). In addition, its role may vary among guanidino kinases. While mutation of the glutamate reduced enzymatic activity by a factor of only 2- to 3000-fold in arginine kinase (Pruett et al. 2003), it was by 25- to 50,000-fold in chicken smtCK (Eder et al. 2000b) and between 200-fold lower to non-detectable activity in human umtCK (Li et al. 2016). Indeed, for human umtCK, a recent molecular dynamics study revealed a two-step dissociative mechanism, in which the Glu227 residue acts as catalytic base (Fig. 13.2b; Li et al. (2016)).

As suggested by all transition state structures of guanidino kinases, the phosphoryl transfer is facilitated by a large number of enzyme-substrate interactions and involves many different mechanisms. These include not only acid-base catalysis, but also correct positioning and perfect alignment of both substrates. The latter mechanism locks the phosphoryl to be transferred in binding distance to the second substrate. In the transition state structures, where a nitrate mimics the transferred phosphoryl, the plane of the anion is perpendicular to a line connecting the guanidinium nitrogen of creatine and the oxygen of the β-phosphate group, passing through the center of the nitrate group. Thus, as suggested earlier by Stroud (1996) for two-substrate reactions, orientation and alignment of substrates in the active site may be more important than any single catalytic residue.

A further controversial issue is the potential non-identical behavior of the monomers within dimeric or octameric complexes. Although this could partially explain why CK has to assemble into larger oligomeric forms, there is contradictory experimental evidence so far concerning differences between monomers (Nevinsky et al. 1982; Wang et al. 1990; Hornemann et al. 2000; Awama et al. 2007). Structural studies showed that at least the catalytic cycle does not proceed synchronously within all monomers in a CK oligomer. In the *Torpedo* transition state structure of dimeric CK, one monomer bound the TSAC, while the other had only Mg-ADP bound (Lahiri et al. 2002). Further, saturating the mtCK octamer with "dead end" TSAC substrates leads to octamer dissociation (Gross and Wallimann 1993), which seems not to occur during normal catalysis. Recently, a dynamic asymmetry between the two monomers of a dimer was found to exist already in the Apo form of dimeric MCK, i.e. in absence of substrate (Londergan et al. 2015). It seems that even after knowing several transition state structures of guanidino kinases, some details of their bisubstrate reaction are still not fully understood.

## 13.5 Proteolipid Complexes

There is a wealth of functional data for a so-called functional coupling or metabolite channeling of mtCK in the intermembrane space, i.e. the preferential use of mitochondrially generated ATP to trigger mitochondrial export of PCr (Schlattner et al. 2006a; Saks et al. 2007). In fact, a close spacial association of mtCK with the ATP-providing adenine nucleotide translocator (ANT or SLC25A4) in the mitochondrial inner membrane (MIM) and Cr-providing mitochondrial porin or voltage dependent anion channel (VDAC) in the mitochondrial outer membrane (MOM) is necessary to drive the mtCK equilibrium reaction towards PCr generation. Lipid and protein interactions have been evidenced that provide the structural basis of this type of metabolite channeling (Schlattner and Wallimann 2013; Zala et al. 2017). The functional unit of mtCK is thus a proteolipid complex, necessary for its multiple roles in efficient energy transfer at the mitochondria/cytosol interface, stimulation of oxidative phosphorylation and further functions related to mitochondrial membranes.

### *13.5.1 Lipid Interactions*

Mitochondrial CK can be isolated together with MIM (Schlegel et al. 1988). This is mainly due to its high affinity electrostatic binding ($K_D \approx 30$ nM) to CL, although binding to other anionic phospholipids can occur, albeit at lower affinity (Schlattner and Wallimann 2000a). CL is particular in having a diacylglycerol structure with a twofold negatively charged head group; it binds to many MIM membrane proteins, including the adenylate translocator and respiratory complexes, and is essential for their active structures (Planas-Iglesias et al. 2015). The CL/phospholipid interaction of mtCK requires several positively charged residues in its exposed and flexible C-terminal stretch that is well suited as a flexible docking domain (residues 362–379, Fig. 13.1c) (Schlattner et al. 2004; Karo et al. 2012), as well as the presence of an intact octameric structure (Fig. 13.1a). The octameric structure has two important consequences for membrane interaction. First, at the faces with fourfold rotational symmetry, it leads to the combined exposure of four C-terminal binding motifs, necessary for high affinity binding not observed with mtCK dimers. Second, by having two such identical binding faces at opposing sides of the cuboidal octamer, it can crosslink two different membranes. By simultaneous binding to CL in MIM as well as other anionic phospholipids or CL in MOM, mtCK induces MIM-MOM contact sites in the IMS (Fig. 13.1a). However, it is important to note that mtCK/membrane interaction is more complex. It shows a biphasic behavior, including high and low affinity binding sites (Schlame and Augustin 1985; Schlattner and Wallimann 2000a, b). Indeed, there are further ionic interactions, possibly within an exposed short internal loop (residues 107–115), and an additional hydrophobic interaction partially resistant to high salt extraction. The latter is probably due to a hydrophobic sequence, which also locates to the flexible C-terminal mtCK stretch. Indeed, mtCK is more hydrophobic than cytosolic CK (Vernoux et al. 2006). Based on these data, a two-step binding model has been proposed for the formation of mtCK/CL complexes (Schlattner et al. 2009), involving electrostatic attraction and absorption, followed by insertion and hydrophobic anchoring in the lipid bilayer (Fig. 13.3c). This model is also consistent with more recent polarographic differential capacity measurements (Maniti et al. 2010). Much of these earlier data is reviewed in more detail elsewhere (Stachowiak et al. 1998; Schlattner et al. 2006a; Schlattner et al. 2009).

More recently, interaction of umtCK with CL-rich membranes has been studied *in silico* by a new coarse-grained molecular dynamics model (Karo et al. 2012). The simulation reproduced umtCK interaction with a model MIM patch, and confirmed the importance of CL and umtCK residues in the C-terminal stretch for high affinity interaction. However, it also revealed that the four C-terminal binding motifs show a different degree of membrane interaction, at a given time, ranging from tight interaction (Fig. 13.3a) to a more loose interaction (Fig. 13.3b) and even transient detachment from the membrane (Karo et al. 2012). In average, only three binding motifs seem to interact simultaneously with the membrane. The strong interaction involved mainly umtCK residues Arg361, Arg364, and Arg369, less Lys378, as well

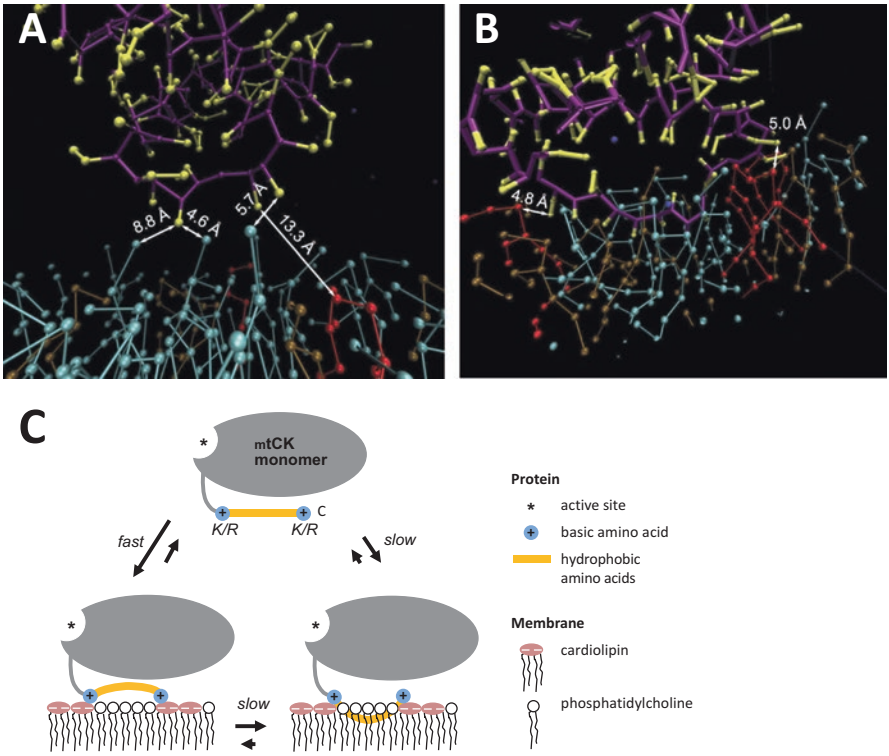


**Fig. 13.3 Membrane interaction of an umtCK monomer.** (**a**,**b**) Molecular dynamics simulation of umtCK octamers interacting with a CL-rich phospholipid bilayer as performed by Vendelin and colleagues (Karo et al. 2012). The simulation shows (**a**) one monomer in a transient situation of binding/detachment from the membrane, and (**b**) another monomer firmly anchored to the membrane throughout the simulation with a C-terminal stretch penetrating the bilayer. Note that the latter is not present in the crystal structure in Fig.13.1. The protein backbone (magenta) carries simplified functional groups (yellow). Phospholipids are represented in ball and stick representation: cardiolipin (CL, red), palmitoyl-oleoyl phosphtidylcholine (POPC, cyan), and palmitoyl-oleoyl phospahtidylethanolamin (POPE, brown). Distances to the closest nitrogen groups of POPC and to head groups of CL are indicated. For further details see (Karo et al. 2012). (**c**) Model of mtCK interaction with a CL-containing phospholipid bilayer. Positive charges (blue) close to the C-terminus (K378 in umtCK) and less distal (K361, K364, and K369 in umtCK) rapidly interact with the twofold negatively charged cardiolipin head group (red), while an unstructured stretch near the C-terminus which is mostly hydrophobic (yellow) more slowly penetrates the lipid bilayer. (**a**) and (**b**) were originally published in (Karo et al. 2012), © the American Society for Biochemistry and Molecular Biology); (**c**) has been modified from Schlattner et al. (2009)

as partial penetration into the lipid bilayer (residues between Gln366 and C-terminus). The weak interaction involved rather residues in the last turn range, i.e. from Arg361 to Ile368 (Karo et al. 2012).

Quite some molecular insight into mtCK/CL complexes was obtained by biophysical analysis of mtCK interactions with CL-rich artificial membranes. Earlier

fluorescence and infrared spectroscopy data clearly indicated that the mtCK/membrane interaction affects the structure of both, the protein and the lipid bilayer. The mtCK octamer undergoes a small conformational change (Granjon et al. 2001; Maniti et al. 2009b), and phospholipid membranes change from a liquid-crystalline state into a more rigid state (Granjon et al. 2001; Schlattner et al. 2004) or, in case of monolayers, from a liquid expanded to a liquid-condensed state (Maniti et al. 2009a; Vernoux et al. 2009). Moreover, when binding to CL-rich membranes, mtCK causes segregation and clustering of CL as first shown by differential scanning calorimetry (Epand et al. 2007b) and later confirmed on monolayers with Brewster angle microscopy for CL (Maniti et al. 2009b) and the likewise anionic CL-precursor phosphatidylglycerol (Vernoux et al. 2009), as well as with two-photon confocal microscopy using CL-rich liposomes (Cheniour et al. 2017). Interestingly, the acyl chain composition of CL seems to determine the clustering effect. While decreased membrane fluidity was observed with any acyl chain composition, highly organized lipid/protein clusters were only induced by unsaturated CL (Maniti et al. 2011). Thus, changes in the CL oxidation state could directly impact mtCK proteolipid complexes.

### *13.5.2 Protein Interactions in Energy Channeling*

There is good functional evidence for a close proximity of mtCK with two transmembrane proteins: ANT (or SLC25A4), an obligatory antiporter for ATP/ADP exchange across MIM, and VDAC, a non-specific, potential-dependent pore in MOM (Wyss et al. 1992). In this topology, the substrates ATP and Cr are preferentially provided to the mtCK active sites by so-called metabolite channeling (Schlattner and Wallimann 2013; Zala et al. 2017), thus driving the mtCK reaction towards PCr generation. Indeed, proteolipid complexes enriched in all these three proteins, albeit still together with some others, could be isolated (Beutner et al. 1996, 1997; Marzo et al. 1998). More recent non-biased interaction studies have identified both, VDAC and ANT, in complexes with the two mtCK isoforms (STRING database: https://string-db.org/; Fig. 13.4).

VDAC is known to engage into many protein/protein interactions (Shoshan-Barmatz et al. 2017). Complex formation between mtCK and VDAC has been observed in independent studies (Brdiczka et al. 1994; Schlattner et al. 2001). First, pure mtCK and VDAC form high $M_r$ complexes as shown by co-sedimentation and gel permeation chromatography. Second, VDAC is able to induce octamerization of a N-terminally truncated mtCK mutant that is unable to octamerize on its own. Third, when reconstituted into "black membranes", VDAC conductance changes after addition of mtCK. Forth, with liposome-reconstituted VDAC, surface plasmon resonance studies confirmed a direct VDAC/mtCK interaction with high affinity ($K_D < 10$ nM) that is predominantly of electrostatic nature and further strengthened by physiological concentrations of calcium. Fifth, all three VDAC isoforms occur in complexes together with mtCK (STRING database; (Datler et al. 2014)). Molecular

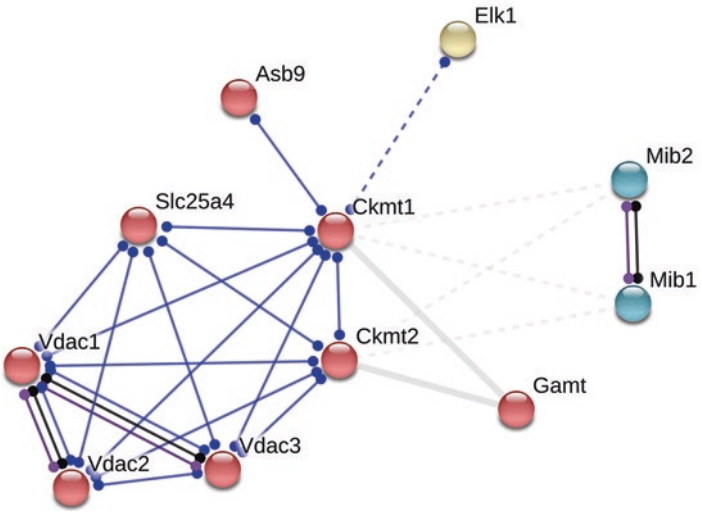


**Fig. 13.4 Protein association network of mtCK**. Functional partners of umtCK in mouse compiled by the STRING database and shown in network representation using k-means clustering (see https://string-db.org/). Nodes represent proteins (identified by gene name), lines represent the type of protein association: interaction (blue), reaction pathway (black), catalysis (magenta), or other (grey). The cluster of red nodes corresponds to high confidence associations (> 0,9). Protein interactions connect umtCK (gene: *Ckmt1*) and smtCK (*Ckmt2*) with ANT (*Slc25a4*) and the three VDAC isfoforms (*Vdac1*, *Vdac2*, Vdac3), as well as umtCK (*Ckmt1*) with the E3 ubiquitin ligase subunit ASB9 (*Asb9*). Interaction with transcription factor ELK1 (gene *Elk1*) is not confirmed. The enzyme GAMT (*Gamt*) is connected to mtCK by biosynthesis of the substrate Cr. A role for E3 ubiquitin-protein ligases Mindbomb homolog 1 and 2 (*Mib1*, *Mib2*) related to mtCK remains to be elucidated. Further mtCK interactors (APP, LRRK2, HSPE1) are not represented. Note that associations in STRING are meant to be specific and meaningful, i.e. proteins jointly contribute to a shared function; this includes but is not limited to physical interaction (direct or in complexes). For references and further details see https://string-db.org/

structures have been solved for VDAC1 by NMR (Hiller et al. 2008; Jaremko et al. 2016) and X-ray crystallography (Bayrhuber et al. 2008; Ujwal et al. 2008; Hosaka et al. 2017), and recently also for zebrafish VDAC2 by X-ray crystallography (Schredelseker et al. 2014). They reveal a 19-standed beta barrel forming the channel, and an N-terminal small alpha helix protruding into the channel (Fig. 13.1a). While the beta-barrel is entirely embedded in the lipid bilayer, only some loops are extending beyond the mitochondrial surface into the cytosol and on the opposite face into the IMS (see http://opm.phar.umich.edu/protein.php?search=2k4t). Within the VDAC1 loops accessible at the IMS side, there is a majority of negative charges, with at least E36, E66, E147, D176/E177 and D230 being very well exposed and thus creating negative surface potential (Fig. 13.1b; numbering according to the alignment in Schredelseker et al. (2014)). These are likely candidates for the electrostatic interaction with umtCK residues R361, R369 and K378 (Fig. 13.1b). All these residues are strictly conserved in VDAC1, and most are also present in

VDAC2. Thus, mtCK binding to MOM involves not only anionic phospholipids, but also VDAC for direct substrate/product exchange with the cytosol.

In case of ANT, no direct interaction with mtCK could be detected so far with targeted techniques like *in vivo* crosslinking or *in vitro* studies with isolated proteins (Muller et al. 1985; Schlattner et al. 2001). This would be consistent with the solved ANT structures (Nury et al. 2006; Pebay-Peyroula et al. 2003). They show only three small ANT loops that are accessible from the IMS side. However, ANT has been found in the same complexes as mtCK by targeted co-immunoprecipitation (Datler et al. 2014) and non-biased screening for protein interaction networks (STRING database; (Fernandez et al. 2009)). The association between these two proteins is therefore most likely mediated by CL (Saks et al. 1987; Vacheron et al. 1997; Schlattner et al. 1998; Schlattner and Wallimann 2000a). ANT and mtCK both show high affinity for CL ($K_D < 100$ nM) (Beyer and Klingenberg 1985; Drees and Beyer 1988; Schlattner and Wallimann 2000a), and mtCK can organize CL-rich membrane patches (Epand et al. 2007b; Maniti et al. 2009b). Both proteins would thus co-localize in such CL patches or rafts. In fact, it is well known that CL-protein interactions are important not only for activity and structural integrity of mitochondrial inner membrane proteins, but also for subunit assembly and complex formation (Planas-Iglesias et al. 2015).

### *13.5.3 Protein Interactions in Targeting and Degrading mtCK*

Other protein interactions occur only at specific moments during the mtCK life cycle. First, the cytosolic preprotein form of umtCK interacts with proteins related to neurodegenerative diseases. Interaction with the C-terminal region of amyloid precursor protein (APP) involved in the pathogenesis of Alzheimer's disease was found *in vitro* and in brain, and shown to stabilize the umtCK preprotein (Li et al. 2006). Similarly, interaction with the leucine-rich repeat kinase 2 (LRRK2), whose mutations are linked to the most common inherited and sporadic Parkinson's disease, suppressed the processing of the immature form of umtCK (Cui et al. 2011). By preventing proper umtCK import into mitochondria, both APP and LRRK2 will impair mitochondrial function and cellular energy levels. Further, a large-scale interaction screen (Wan et al. 2015) identified a mitochondrial 10 kDa heat shock protein (HSPE1) that participates, as a co-chaperonin together with HSP60, in mitochondrial protein import, correct folding and macromolecular assembly. Thus, HSPE1 may assist in mtCK folding and octamer formation in the IMS.

Degradation of mtCK involves another set of protein interactions. An ankyrin repeat and suppressor of cytokine signaling (SOCS) box protein (ASBs), ASB9 (Fig. 13.4), was found to interact with umtCK in a SOCS box-independent manner (Kwon et al. 2010). ASBs function, among others, as substrate-recognition subunit of certain E3 ubiquitin ligases to target these substrates to ubiquitination-mediated proteolysis. The ASB9/umtCK interaction occurs at very high affinity between the active site of umtCK (residues 182–203) and the N-terminal disordered region of

ASB9 plus its first ankyrin repeat domain, with a stoichiometry of one ASB9 per umtCK dimer (Balasubramaniam et al. 2015). Overexpression of ASB9 induces massive ubiquitination of umtCK, leading to mtCK degradation and strongly reduced cellular CK activity (Kwon et al. 2010). This finally generates abnormal mitochondrial structure and decreases mitochondrial membrane potential, similar to the mtCK siRNA knock-down phenotype (Lenz et al. 2007), finally impairing cell growth (Kwon et al. 2010). Other E3 ubiquitin ligases, the Mindbomb homologs (MIB) 1 and 2, were found to interact with CK isoforms in a yeast-two-hybrid (Y2H) screen for zebrafish MIB-binding proteins (STRING database; (Tseng et al. 2014)). However, their role for mtCKs remains to be established.

The transcription factor ELK1 (Fig. 13.4) was found by co-immunprecipitation in complexes with umtCK, ANT and VDAC in brain extracts (Barrett et al. 2006). ELK1 regulates transcription during skeletal and neuronal differentiation (Khurana and Dey 2002; Besnard et al. 2011), but seems to have also extranuclear functions. In the cytosol of neurons, it associates with mitochondria and microtubules and is pro-apoptotic (Barrett et al. 2006; Besnard et al. 2011). Based on its presence in umtCK complexes, it was suggested that ELK1 could activate the pro-apoptotic mitochondrial permeability transition (MPT; (Barrett et al. 2006). However, since mtCK, ANT and VDAC are no longer considered to form the MPT pore but to have mere regulatory roles (Bernardi et al. 2015), a function of ELK1 related to mtCK and/or MPT remains to be shown.

### *13.5.4 Regulation of mtCK Proteolipid Complexes*

Functions of mtCK proteolipid complexes, in particular channeling of energy-rich substrates between the protein partners (outlined further below), are subject to regulation. This is most obvious in tissues with fluctuating energy expenditure like skeletal muscle, where e.g. ADP sensitivity of respiration varies post-exercise (Guerrero et al. 2005; Perry et al. 2012; Ydfors et al. 2016). Molecular mechanisms that could account for such modulation have not been studied systematically. Generally, it is assumed that formation of the mtCK complexes and their protein stoichiometries can vary, thus affecting the efficiency of substrate channeling (Schlattner et al. 2006a, b). However, there are likely also more specific mechanisms operating.

Modulating the permeability of VDAC would be a direct measure to regulate metabolite access to mitochondria in general, and ADP/ATP or Cr/PCr exchange in particular. Although VDAC is the most abundant protein in MOM, modeling approaches suggest that under physiological conditions only very few VDAC channels are freely accessible for cytosolic ADP (Simson et al. 2016). This confirms earlier data showing that permeabilized cells as compared to isolated mitochondria show a higher apparent $K_m$ of respiration for exogenous ADP, i.e. a restricted access of ADP to the matrix, which possibly favors Cr/PCr exchange (Saks et al. 1995, 2001, 2007). Thus, VDAC would constitute a major diffusion limitation for ADP and ATP, together with cytosolic barriers (Alekseev et al. 2016), and the extent of

this limitation could be regulated by VDAC permeability. It had been speculated already earlier that cytoskeleton-MOM interactions could alter MOM permeability, since ADP has increased access to mitochondria (the $K_m$(ADP) decreases) in permeabilized cells subjected to limited proteolysis (Saks et al. 1995). Indeed, cytosolic proteins binding VDAC and reducing its permeability have been identified more recently, including tubulin dimers (Rostovtseva et al. 2008; Noskov et al. 2013), in particular those containing the tubulin ß2 isoform (Kuznetsov et al. 2013), and alpha-synuclein (Rostovtseva et al. 2015). Tubulin, once recruited to the mitochondrial surface via electrostatic interactions with anionic phospholipids (Rostovtseva et al. 2012), further binds to VDAC and penetrates with its tubular N-terminus into the channel. Tubulin ß2 blocks the channel, making it virtually impermeable for adenylates, thus representing a powerful modulator of mitochondrial bioenergetics. Phosphorylation of VDAC may affect its interaction with tubulin (Sheldon et al. 2011) or directly act on VDAC permeability (Martel et al. 2014). Roles of such mechanisms in general regulation of mtCK, respiration and oxidative phosphorylation (Guzun et al. 2012, 2015; Varikmaa et al. 2014) or more in particular in the bioenergetics of cancer cells (Maldonado et al. 2013) have been suggested, but more research will be necessary to solve remaining questions (Rostovtseva and Bezrukov 2012; Noskov et al. 2016). Alternatively, VDAC permeability could be regulated by a membrane potential that, if established across MOM, would afford voltage-dependent regulation of metabolite exchange (Lemeshko 2016).

Posttranslational modifications (PTMs) are another obvious possibility for regulating mtCK proteolipid complexes. As shown more recently, many PTMs are probably widespread among mitochondrial proteins, in particular phosphorylation (Kruse and Hojlund 2017) and acetylation (Baeza et al. 2016), and this may also apply to mtCK and its protein interaction partners. Two studies targeting the mitochondrial phosphoproteome identified putative phosphosites within mtCK, ANT and VDAC. In rat brain mitochondria, immunoaffinity enrichment of phosphotyrosine-containing peptides identified phosphoresidues in ANT and umtCK (Lewandrowski et al. 2008). The ANT residues Tyr190 and Tyr194 are situated in the ATP/ADP binding cavity, and could interfere with transport activity. Tyr115 in umtCK would be strategically exposed to interfere with mtCK/membrane interaction, but experiments with anti-P-Tyr peptide antibodies were inconclusive so far (Schlattner, unpublished data). A more recent study analyzed the phosphoproteome in muscles and liver (Bak et al. 2013), yielding a large number of phosphoresidues in smtCK, ANT, and VDAC1. As much as 18 Ser, Thr and Tyr residues were found phosphorylated in umtCK alone, probably reflecting the increased sensitivity of mass spectrometry-based methods. Unfortunately, the contribution of a low level autophosphorylation in these studies, well described for cytosolic CK (Stolz et al. 2002), remains unknown.

Lysine acetylation was first detected in umtCK (Iwabata et al. 2005) and more recently in smtCK along with MCK, associated with heart failure in mice, thus suggesting a link between acetylation and pathological metabolic changes (Grillon et al. 2012). Here, acetylation was identified by MALDI-TOF/TOF and validated by immunoprecipitation with anti-acetyl-lysine antibody. Further non-biased mass-

spectrometry-based studies confirmed acetylation of both mtCK isoforms (Lundby et al. 2012; Foster et al. 2013; Yang et al. 2011), and many more PTMs were also reported for ANT (Feng et al. 2010; Mielke et al. 2014) and VDAC (Martel et al. 2014). However, whether for phosphorylation or acetylation, stoichiometries of these PTMs are unknown and probably rather low (Baeza et al. 2016), and their functional consequences for the mtCK proteolipid complexes have not yet been elucidated. Further, the modifying enzymes involved in these PTMs are not known. There is some evidence and much speculation about protein kinases acting on and in mitochondria (Lim et al. 2016; Kruse and Hojlund 2017), while acetylation of lysines may occur nonenzymatically, controlled rather by deacetylation via sirtuins, in particular sirtuin 3 (Baeza et al. 2016).

Finally, the very active redox biochemistry in mitochondria, mainly due to their respiratory activity, suggests an important role of redox regulation in mitochondrial proteins (Nietzel et al. 2017). In mtCK, cysteine thiol switches between oxidized and reduced states could occur at the active site Cys278, leading to changes in enzyme activity (Furter et al. 1993), and at Cys358, possibly altering interaction with anionic phospholipids like CL (Wendt et al. 2003). In presence of reactive oxygen and nitrogen species *in vitro* or in pathological situations, rapid oxidation occurs at these cysteines and additional tryptophanes (Soboll et al. 1999; Wendt et al. 2003; Tokarska-Schlattner et al. 2002; Ebermann et al. 2009). This leads to enzymatic inactivation, which can be reversible *in vitro* depending on the oxidant, and dissociation of mtCK proteolipid complexes (Wendt et al. 2003). Interestingly, umtCK emerged to be less prone to oxidation than smtCK (Wendt et al. (2003); Schlattner, unpublished data). In cytosolic BCK and MCK, oxidative conditions induce formation of an intramolecular disulfide bond between Cys74 and Cys146 (MCK numbering; (Hurne et al. 2000; Zhao et al. 2007; Li et al. 2011). While this oxidized form seems to be better protected against further oxidative damage, it is also the preferred substrate for ubiquitination and degradation. In conclusion, all these changes impair mtCK proteolipid complexes and further aggravate energy stress under pathological conditions. Whether the involved cysteines operate as thiol switches also under physiological conditions remains to be shown.

## 13.6 Evolution

The evolution of guanidino kinases has been studied in quite some detail by Ellington, Suzuki and collaborators (Ellington and Roux 1998; Ellington 2001; Ellington and Suzuki 2007; Tanaka et al. 2007). A closer look on phylogenetic relationships within this kinase family allows some interesting conclusions in respect to mtCK functions. The guanidino (phosphagen) kinases all reversibly phosphorylate different guanidino substrates to produce a large pool of “high-energy” phosphates. As mentioned, their similar function is reflected by a high degree of sequence and structural homology. The appearance of guanidino kinases correlates with the emergence of multicellular organisms, indicating that the specialization of cells within

an organism has been the driving force for their evolution. This is probably related to the occurrence of energetically very active cells with a high density of ATP-dependent membrane ion pumps or motor proteins.

According to all available evidence, a hypothetical early CK ancestor gene subsequently diverged into three gene families, cytoplasmic, mitochondrial and flagellar (Ellington and Suzuki 2007). Analysis of CK gene structures revealed that both cytosolic/flagellar and mitochondrial CKs were already present in metazoan evolution before the separation of protostomes (most invertebrates such as arthropods, mollusks, worms) and deuterostomes (echinoderms, protochordates, vertebrates) (Bertin et al. 2007; Ellington and Suzuki 2007). Indeed, homologous genes were found in the oldest, extant metazoan group, the hexactinellid sponges, and thus evolved prior to the divergence of sponges from the metazoan lineage at least 650 million years ago. The oldest known ancestor of the mtCK lineage has been identified in the marine sponge *Tethya aurantia*. One of the three CKs in this sponge displays high homology to vertebrate mtCKs, including a mitochondrial targeting sequence, but forms obligatory dimers, no octamers like all other mtCKs (Sona et al. 2004). The oldest octameric mtCK has been isolated from the marine filter-feeding annelid polychaete worm *Chaetopterus variopedatus*, a protostome invertebrate, where it is present only in the sperm head/midpiece complex where mitochondria are restricted (Ellington and Roux 1998). However, the C-terminal stretch of this mtCK is much shorter than in vertebrates and has additional negative charges (Schlattner et al. 2004), thus more resembling cytosolic CKs which can bind only weakly to CL-containing membranes (Stachowiak et al. 1998). In the more evolved mtCK of the marine chordate *Ciona intestinalis*, the C-terminal stretch is still shorter, but has lost negatively charged residues that could preclude CL interaction. In any case, these ancient octamers would not yet interact with CL in a way vertebrate mtCK is doing.

In conclusion, the capacity for intracellular targeting of CKs, including mtCKs, evolved very early during evolution. It was probably driven by the energy transfer needs of highly polarized cells such as spermatozoa or choanocytes, the water current generating cells in sponges (Ellington 2001; Ellington and Suzuki 2007). Thus, spatial energy buffering may have preceded the general, temporal ATP buffering function. Since the gene data support a common ancestry of all known mtCKs (Bertin et al. 2007), octameric structure and CL interaction of mtCK evolved secondary to mitochondrial localization and possibly successively, resulting in the formation of proteolipid complexes known for vertebrate mtCK. This was probably driven by the advantages of the more efficient metabolite channeling and other mtCK functions described further below.

## 13.7 Physiological Roles

Over the last decade, transgenic mouse models, molecular studies and non-biased screening approaches have confirmed and extended the classical functions of mtCK (which will be treated more briefly here), but also suggest entirely novel ones.

### *13.7.1 Energy Transfer*

The canonical physiological function of CK isoforms is temporal and spatial energy buffering (see introduction). Here, the mtCK constitutes the "providing end" of the CK/PCr shuttle by generating PCr for export into the cytosol and ADP for stimulating ATP resynthesis and oxidative phosphorylation as a whole (Kay et al. 2000) (Fig. 13.5a). As long as sufficient PCr is available, cytosolic CK (at the "receiving" end of the CK/PCr shuttle) continuously regenerates ATP while removing ADP and $H^+$. It thus maintains the high ATP/ADP concentration ratio necessary to release maximal free energy $\Delta G_0$ from ATP hydrolysis. This is required for many ATPases that are highly processive and at the same time require maximal $\Delta G_{0(ATP)}$ for their function.

The CK/PCr system thus plays a crucial role in cellular bioenergetics of skeletal and cardiac muscle, brain and other tissues, where large or polar cells have to deal with high or fluctuating energy demands. Clearly, CK appears not to be essential for viability *per se*, but it provides the necessary energy for situations of maximal performance, high workload or dealing with chronic stress responses and pathological states. Many loss-of-function models support such a role, including many transgenic mouse models developed by Wieringa and colleagues (e.g. (Steeghs et al. 1997)) and cellular siRNA approaches (Lenz et al. 2007; Chang et al. 2008). Mice invalidated for either a cytosolic or a mitochondrial CK (single knockout mice, KO), and in particular those invalidated for both CK isoforms in a given cell type (i.e. cytosolic MCK and smtCK, or cytosolic BCK and umtCK, double KO mice, DKO) showed phenotypes mainly in muscle and brain. While in skeletal muscle, reduced phosphotransfer is associated with impaired repetitive contractions, calcium handling and sarcomere structure (Steeghs et al. 1997; de Groof et al. 2002), heart has reduced contractile reserve and becomes more susceptible to e.g. ischemia-reperfusion injury (Spindler et al. 2004; Lygate et al. 2007), while brain CK deficiency affects spatial learning and memory, as well as hearing loss (Streijger et al. 2004, 2005, 2010; Shin et al. 2007). Single mtCK KO confirmed the essential role of this isoform for maintaining proper PCr and ATP levels in heart (Spindler et al. 2002) and brain (Kekelidze et al. 2001).

Another more recent approach to invalidate the CK/PCr system has been the depletion of the substrate Cr by knocking-out one of the two consecutive enzymes in its biosynthetic pathway: L-arginine:glycine amidinotransferase (AGAT) or guanidinoacetate N-methyltransferase (GAMT). In human, Cr-deficiency occurs as an

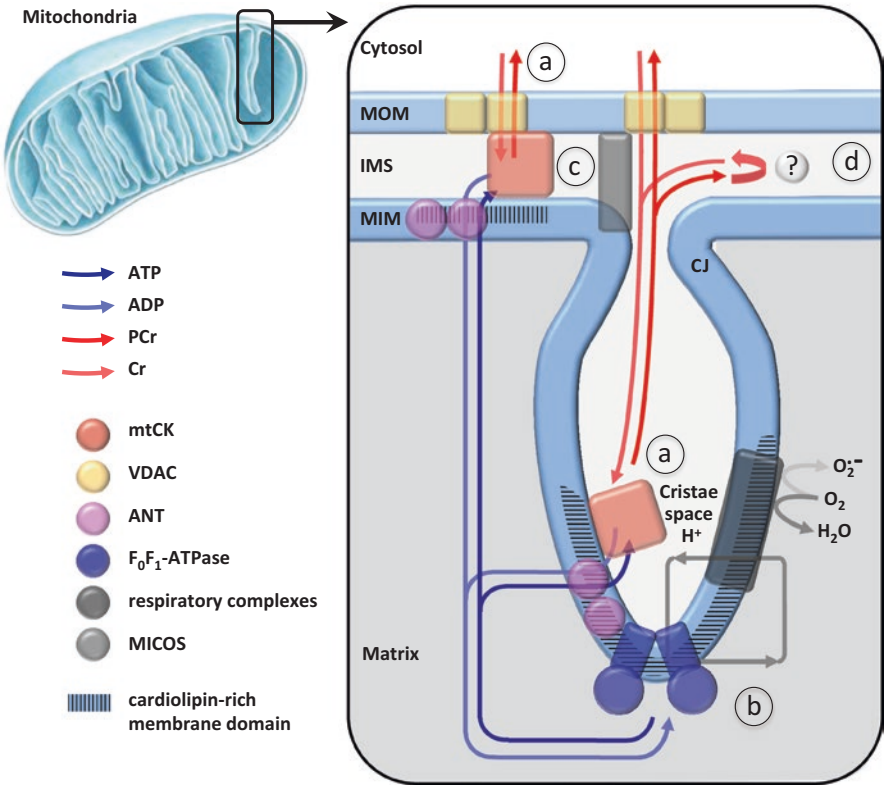


**Fig. 13.5 Overview of mtCK functions**. Schematic representation of a mitochondrial section showing IMS and a cristae, with membranes (blue), membrane proteins involved in generation and transfer of "high energy" phosphoryls (circles and boxes) and metabolite fluxes (arrows). The scheme depicts main four functions of mtCK: (**a**) mtCK converts free energy from ATP into PCr for export out of mitochondria. This occurs at two different locations, IMS and cristae, supported by interaction or close proximity of mtCK with VDAC and ANT (IMS) or ANT alone (cristae). In addition, the high diffusibility of PCr may contribute to efficient export from cristae via cristae junctions and VDAC. Cytosolic CK isoforms, partially co-localizing with ATP-dependent reactions, use PCr to regenerate ATP (not shown). Note that alternative direct ATP/ADP exchange with the cytosol (at a degree dependent on the tissue) and $P_i$ shuttling between cytosol and matrix is not depicted. (**b**) mtCK activity keeps high matrix ADP concentrations, thus supporting ATPase activity and its efficient coupling with respiratory complexes which reduces detrimental side reactions that generate reactive oxygen species (ROS). Matrix ADP and low ROS are also anti-apoptotic, e.g. act against mitochondrial permeability transition. (**c**) mtCK contributes to the formation of contact sites between MIM and MOM, in addition to other protein complexes (e.g. MICOS). This has a stabilizing effect on mitochondrial ultrastructure and leads to intermembrane transfer of anionic phospholipids *in vitro*. (**d**) A mtCK-based futile cycle can be set up by PCr hydrolysis in the IMS (or the cytosol), i.e. without phosphoryl transfer to ADP. This reaction will generate heat, as shown in beige adipocytes (Kazak et al. 2015), but the involved enzyme (see?) is not yet characterized. Abbr.: *MOM* mitochondrial outer membrane, *IMS* intermembrane space; *MIM* mitochondrial inner membrane; *CJ* cristae junction; *MICOS* mitochondrial contact site and cristae organizing system

autosomal recessive disorders that causes a severe, mostly neuronal phenotype (Stockler et al. 2007). In the AGAT KO mouse, systemic Cr depletion also results in a pronounced skeletal muscle phenotype associated with reduced muscle strength and atrophy, mitochondrial dysfunction, intracellular energy deficiency, as well as further structural and physiological abnormalities, that could be reversed by Cr supplementation (Nabuurs et al. 2013). In contrast to all previous loss-of-function models, the GAMT KO mice showed no overt phenotype, except being of much smaller body size and weight (Lygate et al. 2013; Branovets et al. 2013). It remains to be unequivocally shown that this is not due to unrecognized compensatory mechanisms or a consequence of the accumulating guanidinoacetate.

A particularly important role of mtCK and the entire CK/PCr system has been ascribed to the heart that relies on continuous energy supply by oxidative metabolism (Saks et al. 2006, 2012; Guzun et al. 2015). Loss-of-function models clearly established a role of CK under high cardiac workload (Spindler et al. 2004; Lygate et al. 2007). However, its contributions to the contractile phenotype in failing heart remains controversial (Peterzan et al. 2017), and there are some species that survive with very low or even no cardiac mtCK (O'Brien et al. 2014). Likely, there are additional systems for efficient energy transfer at work in the heart, like alternative phosphotransfer circuits (Dzeja et al. 2011) or possibly a mitochondrial reticulum network described for skeletal muscle fibers. This latter network provides a conductive pathway for the proton-motive force, thus replacing diffusion of ATP or PCr (Glancy et al. 2015), and could work together with the CK/PCr system (Wallimann 2015). However, gain-of-function models with increased MCK expression (Akki et al. 2012; Gupta et al. 2012, 2013) or Cr levels (Lygate et al. 2012; Zervou et al. 2016) clearly confirmed direct protective effects of the CK/PCr system in the heart.

More recently, there is increasing interest in the role of the CK/PCr system in brain. Localized ATP generation for cytoskeletal dynamics seems to be one major function. This has been shown for cytosolic BCK and actomyosin in astrocytes and fibroblasts already earlier (Kuiper et al. 2009), but more recently also for mitochondria in developing cerebellar Purkinje cells (Fukumitsu et al. 2015). Here, dendrite-localized, umtCK-containing mitochondria and cytosolic CK act synergistically to support dendritic outgrowth.

### *13.7.2 Regulation of Oxidative Phosphorylation and Apoptosis*

Within mtCK proteolipid complexes, by the close proximity between mtCK, VDAC and ANT, cytosolic Cr and mitochondrial ATP are directly channeled to mtCK, thus shifting the CK reaction towards PCr and ADP generation. An increased flux of Cr, representing a feedback signal for cytosolic energy needs, is thus translated into an increased ADP flux, which has several direct and indirect consequences for mitochondrial function.

The permanent intra-mitochondrial regeneration of ADP keeps the matrix ATP/ADP ratio at low levels, which stimulates the $F_0F_1$-ATPase and the use of the MIM

electrochemical gradient (Fig. 13.5b). This favors coupled respiratory chain function and an electrochemical potential that cause only minimal production of reactive oxygen species (ROS), while hyperpolarization could increase ROS production (Meyer et al. 2006) (Fig. 13.5c). By protecting against increased matrix ATP/ADP ratios and ROS production, which are known inducers of the pro-apoptotic MPT pathway (Bernardi et al. 2015), mtCK activity would have an anti-apoptotic effect (Brdiczka et al. 2006). This is consistent with earlier findings in mitochondria from umtCK-expressing liver, an organ normally devoid of CK. Here, creatine and cyclocreatine, both substrates of mtCK, could inhibit MPT at a similar level as the specific MPT-inhibitor cyclosporine A (Dolder et al. 2003). Conversely, depletion of umtCK in cells by siRNA induces MPT, while reexpression is inhibitory (Datler et al. 2014). The latter effect seemed to be independent of mtCK activity, but the study did not reveal remnant CK activities and cellular Cr levels. An indirect mechanism of mtCK in apoptosis that is based on its enzymatic activity would reconcile the facts that mtCK complexes with ANT and VDAC do not form the MPT pore itself, as assumed earlier (Bernardi et al. 2015), but can regulate MPT, at least concerning mtCK and ANT. Apoptosis-related aspects of mtCK function are discussed in more detail in earlier reviews (Schlattner et al. 2006a, 2009).

### *13.7.3 Cardiolipin Interaction: Structural and Signaling Functions*

The mtCK isoform has the unique property of high affinity interaction with CL and other anionic phospholipids. Since the cuboidal mtCK octamer has a symmetrical structure, there are two opposite binding faces that can interact simultaneously with membrane surfaces, thus forming a sort of crosslinker. This has been shown by cross-linking of liposomes *in vitro* (Stachowiak et al. 1996; Schlattner et al. 2004) and by observation of contact sites between MIM and MOM *in vivo* (Fig. 13.5a top; Kottke et al. 1994). Further, expression of umtCK in mouse livers, normally devoid of CK, increases the number of contact sites between MIM and MOM and stabilizes mitochondria against detergent-induced lysis (Speer et al. 2005). Knocking down umtCK in HeLa and HaCaT cells significantly alters mitochondrial morphology from an elongated towards a more spherical shape with less electron dense matrix (Lenz et al. 2007). Normal cristae membrane topology is lost, showing fewer cristae and an enlarged cristae space, consistent with a loss of contact sites. This morphology impairs overall mitochondrial function, including the MIM membrane potential (Lenz et al. 2007).

Under certain pathological conditions, normal mtCK/CL complexes can turn into large, non-functional mtCK assemblies. For example, smtCK is often found overexpressed in mitochondrial myopathies (e.g. Kitaoka et al. 2013; Stadhouders et al. 1994). In some cases, this smtCK can form long parallel crystalline inclusions that are enveloped or “sandwiched” in-between either MOM and MIM or the cristae

MIM (O'Gorman et al. 1997). More recently, it was shown that mtCK bound to CL-containing monolayers, when oxidized by using 4-hydroxy-2-nonenal (4-HNE), not only looses CK activity, but also aggregates into amyloid-like networks (Maniti et al. 2015).

The simultaneous interaction of the mtCK octamer with two opposite membranes seems to have another consequence. It has been shown *in vitro* that mtCK is able, once bound to two CL-containing membranes, to transfer phospholipids between these membranes, similar to another mitochondrial kinase, the nucleoside diphosphate kinase D (NDPK-D), also called NME4 or NM23-H4 (Epand et al. 2007a). Although NME4/NDPK-D is phylogenetically not related to mtCK, it shares many essential properties. NME4/NDPK-D also localizes to the IMS, has a large symmetrical homooligomeric (hexameric) structure, shows high affinity to CL and some other anionic phospholipids, and can form MIM-MOM contact sites (Tokarska-Schlattner et al. 2008). Importantly, it has been shown for NDPK-D/NME4 that intermembrane transfer of CL between MIM and MOM occurs in living cells, and that exposure of CL at the mitochondrial surface can serve as a signal for mitophagy or apoptosis (Schlattner et al. 2013; Kagan et al. 2016). Given the similarities between NME4/NDPK-D and mtCK, it has been proposed that the latter has a similar mitochondrial CL transfer activity (Schlattner et al. 2009). Interestingly, NME4/NDPK-D and mtCK have quite opposite tissue expression profiles (Schlattner, unpublished data), suggesting that they could replace each other for a CL transfer function (Schlattner et al. 2013). Further research will be necessary to establish an intermembrane CL transfer function of mtCK *in vivo*.

### *13.7.4 Thermogenesis in Adipocytes*

Another novel function of mtCK emerged from studies on the transgenic mice invalidated for both cytosolic BCK and mitochondrial umtCK (DKO) (Streijger et al. 2005). These two isoforms are co-expressed in various cell types of brain and many other tissues, except striated muscle cells. During breeding of these mice, it rapidly became apparent that they also suffer of defective thermoregulation. They are unable to keep their body temperature of 37 °C, develop severe hypothermia during prolonged cold exposure, and need heating lamps or blankets to avoid incidental sudden death and to ascertain reproduction (Streijger et al. 2009). Interestingly, while many brain phenotypic features were also present in the single BCK or umtCK KO mice, albeit much less pronounced (Jost and Van Der Zee 2002; Streijger et al. 2004), defective thermoregulation was only reported for the DKO mice.

Several causative factors for this dysregulation could be discarded, including reduced body weight or physical activity, abnormal food intake/processing, torpor-like hypothermia or dysfunctional brown adipose tissue (BAT), although there was a slight reduction in adipocyte tissue mass and size (Streijger et al. 2009). Inefficient neuronal transmission was thus suggested as the most probable underlying mechanism. A follow-up study identified neuropeptide Y (NPY) as a potential key

component, since upon 12 h cold exposition to 4 °C, NPY levels remained high in CK DKO mice while decreasing in controls (Van der Zee 2013). Indeed, NPY does not only reduce energy expenditure in general, but also decreases BAT thermogenesis, among others by downregulating of UCP1 (Chao et al. 2011; Shi et al. 2013). However, with animals exposed up to 12 h at 4 °C, evolution of UCP1 protein was identical in CK DKO and control mice. Since CK DKO mice suffer of defective thermoregulation already after 6 h at 4 °C, the NPY-UCP1 pathway cannot be the primary cause of this phenotype.

An alternative mechanism could be defective vasoconstriction, which would limit cutaneous vasomotion and thus affect heat exchange between the body and its environment. In support, BCK and umtCK are expressed in endothelial cells and the smooth muscle responsible for vasoconstriction (Payne et al. 1991; Decking et al. 2001; Karamat et al. 2014), and hypertension was associated with high serum CK activity (Brewster et al. 2006). Specifically in high resistance arteries, BCK expression strongly correlates with blood pressure, i.e. smooth muscle contraction (Dillon 2014; Karamat et al. 2014). However, so far, there is no direct experimental support for altered blood pressure or vasoconstriction in either CK DKO or BCK KO mice (Streijger et al. 2009).

Most recently, independent findings have suggested an entirely novel mechanism linking mtCK activity to thermogenesis. Adipocytes have been known to contain few if any umtCK (Streijger et al. 2009). However, more quantitative proteomics identified a strong upregulation of mtCK proteins in thermogenic adipocytes: human BAT as compared to white adipocytes (Svensson et al. 2011; Muller et al. 2016), and mouse beige adipocytes induced by cold exposure (Kazak et al. 2015). Most importantly, the latter study further provided evidence for a mtCK-driven thermogenic futile cycle. In this model, PCr generated by mtCK is not used for cellular work in the cytosol, but instead immediately hydrolyzed, thus increasing energy expenditure and liberating heat energy (Fig. 13.5d). Liberated Cr is then rapidly rephosphorylated by mtCK with mitochondrial ATP, and the generated ADP channeled into the matrix to stimulate respiration, a pathway corresponding to the classical mtCK bioenergetic function (Fig. 13.5a, b). Such PCr futile cycling seems to be present at least in UCP1-positive and -negative beige adipocytes, but not in white adipocytes (Bertholet et al. 2017). Like the futile $Ca^{2+}$-cycling that is well-described for non-shivering thermogenesis in skeletal muscle cells (Bal et al. 2012), the PCr futile cycling could finally explain the long-known UCP1-independent thermogenesis, which can also be observed in UCP1 KO mice (Grimpo et al. 2014). The molecular nature and exact localization of the enzyme(s) catalyzing PCr hydrolysis remain poorly defined so far. However, the model is supported by the phenotype of mice with inducible, adipocyte-specific knockdown of the first and rate-limiting enzyme in Cr-biosynthesis, the arginine glycine amidinotransferase (AGAT or GATM). These animals have reduced adipocyte AGAT and Cr levels, are more cold sensitive, and show impaired adaptive thermogenesis in response to adrenergic stimulation and caloric excess (Kazak et al. 2017). Importantly, they become more obese than controls on a high-fat diet, probably due to reduced diet-induced thermogenesis, and Cr-supplementation can rescue the blunted adrenergic thermogenesis

(Kazak et al. 2017). Thus, the phenotype of these mice supports an important role of adipocyte Cr metabolism and PCr futile cycling in different forms of non-shivering thermogenesis, although a contribution of other metabolic pathways cannot be excluded so far.

Defective thermoregulation observed specifically in the CK DKO mice could therefore be caused by an additive effect of invalidating mtCK-driven PCr futile cycling and a BCK-driven function like vasoconstriction, which individually may be insufficient to produce an obvious thermoregulation phenotype in the single CK KO animals. Increasing the mtCK-driven PCr futile cycling by drugs or nutritional supplementation could open novel possibilities for treating obesity and metabolic disease in general.

### *13.7.5 Cancer*

There is a broad body of literature on CK expression in cancer. The large majority concerns cytosolic BCK, and in most types of malignant solid tumors and cancer cell lines this enzyme was found overexpressed (e.g. (Zeng et al. 2012)). Mechanistically, BCK overexpression can be controlled by the adenovirus oncogene E1a (Kaddurah-Daouk et al. 1990) or inactivation of the p53 tumor suppressor (Zhao et al. 1994; Tamir and Bengal 1998). In general, this is considered as an adaptation of cancer cells to sustain their high energy turnover rates. However, there may be also more specific functions for ATP regeneration at particular cellular sites, e.g. supporting cell cycle and mitotic spindle elongation or inhibiting apoptosis (Yan 2016). Interestingly, also BCK released from cancer cells into the extracellular space was found to contribute to the high energetic needs of these cells (Loo et al. 2015). Although BCK upregulation was suggested by numerous studies as a potential biomarker for early diagnosis (e.g. more recently by (Huddleston et al. 2005; Zeng et al. 2012; Chang et al. 2015)), its diagnostic value is not widely accepted so far.

More recently, genetic and proteomic screens shifted the focus to specific overexpression of umtCK in cancer. Importantly, in most studies reported so far, such upregulation is closely associated with proliferation, metastasis, or overall poor prognosis for cancer patients. We reported such a correlation first for an aggressive Hodgkin-derived cell line (Kornacker et al. 2001), and later umtCK overexpression was also observed in breast cancer as a negative prognostic marker (Cimino et al. 2008; Qian et al. 2012), in sporadic gastric cancers (D'Errico et al. 2009), in prostate cancer facilitating progression (Pang et al. 2009), in hepatocellular carcinoma linked to poor prognosis (Uranbileg et al. 2014), and in acute myeloid leukemia, necessary to promote survival of EVI1-positive myeloma cells (Fenouille et al. 2017). In prostate cancer, umtCK overexpression seems to decline with cancer progression (Amamoto et al. 2016). Only in squamous cell carcinoma, oral or advanced-stage head and neck, inverse pattern was observed, with downregulation of umtCK and higher expression associated with lower risk of local recurrence or metastasis (Onda et al. 2006; Pavon et al. 2016).

The mechanism by which umtCK could favor cancer cell proliferation and spreading in carcinomas is not entirely clear. More efficient mitochondrial ATP generation and energy transduction may not be the major beneficial effect, since cancer cells rely much less on mitochondrial energy supply. However, mtCK activity could be important to drive respiration for the various biosynthetic needs of cancer cells. Alternatively, other less characterized mtCK functions could play a role, like regulation of cell signaling via ROS and Akt (Meyer et al. 2006; Pang et al. 2009) or phospholipid transfer (Schlattner et al. 2009). This issue certainly needs to be addressed by more mechanistic studies.

In sarcomas, regulation of mtCK is different. Sarcomas induced by carcinogens in mouse skeletal muscle, which expresses MCK and smtCK, show downregulation of both CK isoforms and reduced creatine levels (Patra et al. 2008). This downregulation continued with progression of the malignancy, leading finally to a total loss of CK, linked to a deficiency of the relevant transcription factors MyoD and myogenin (Bera and Ray 2009).

Another issue relating mtCK to cancer is the cardiotoxicity of many anti-cancer treatments. Inhibition of cardiac bioenergetics is one of the hallmarks of such cardiotoxicity, induced in particular by the anthracycline anti-cancer drugs like doxorubicin (reviewed in Tokarska-Schlattner et al. 2006). These cardiotoxic side effects remain a challenge in terms of involved mechanisms and prevention. We have shown with purified mtCK *in vitro* and in the perfused rat heart model that doxorubicin impairs structure and function of mtCK by oxidative modification of key residues (Tokarska-Schlattner et al. 2002, 2005). Ultimately, this leads to mtCK kinase inactivation, octamer dissociation into dimers, and inhibited mtCK interaction with CL, which impedes membrane binding (Tokarska-Schlattner et al. 2002), thus affecting mitochondrial respiration and inducing bioenergetics stress (Tokarska-Schlattner et al. 2005, 2007). Cardiac smtCK occurred to be more sensitive to such damage than umtCK, consistent with selective cardiac toxicity of the drug and different molecular properties and structures of these two isoforms (Schlattner, unpublished data).

### *13.7.6 Serum*

CK released by necrotic cells into the serum is of diagnostic interest. Heart-specific MBCK, a heterodimer of cytosolic MCK and BCK, appearing in human serum after myocardial infarction, has been used in clinical diagnostics for decades before being mostly replaced by cardiac-specific troponins (Saenger and Jaffe 2008; Antman 2017). Further, serum CK activity is associated with blood pressure (Brewster et al. 2006) and the occurrence of serum BCK in cancer patients has been suggested as a putative marker for early diagnosis of malignancies (Huddleston et al. 2005; Ishikawa et al. 2005).

Another type of CK occurring in serum is known as macroenzyme creatine kinase type 2 (macroCK2). It was first detected in the serum of patients suffering of cancer (Koven et al. 1983) and later also in HIV-infected patients treated with the anti-viral

drug tenofovir (Schmid et al. 2006). In the latter case, we could show that the macroCK2 is identical to umtCK (Schmid et al. 2006), stabilized by tenofovir in its octameric form, and probably released by kidney epithelium (Schmid et al. 2013) due to low-level mitochondrial toxicity specific to tenofovir (Watanabe et al. 2012). This may involve oxidation of umtCK and/or CL, which would reduce umtCK membrane affinity and favor release the enzyme from severely damaged mitochondria.

However, does serum umtCK have diagnostic value? Its occurrence was not predictive for tenofovir-induced cell damage and HIV-related malignancies (Schmid et al. 2013). Earlier studies suggested a similar absence of prognostic value in case of neoplastic diseases (Castaldo et al. 1990). However, the availability of novel isoform-specific anti-human mtCK monoclonal antibodies for immunoinhibition assays (Hoshino et al. 2009) led to the detection of umtCK in the serum of patients with hepatocellular carcinoma (Soroida et al. 2012) and this had prognostic value as a risk factor (Enooku et al. 2014). Given the emerging link between umtCK overexpression in cancer and poor prognosis, there is eventually a role for serum umtCK to serve as a prognostic marker, an issue that deserves further investigation.

## 13.8 Conclusions and Perspectives

Although CK is certainly one of the best-studied metabolic enzymes, it is far from being over-studied. Much is known about its molecular structure, cellular function, and physiological roles, but there are still some issues to be clarified. It is unclear whether the mtCK proteolipid complexes in mitochondria are stable or rather transient structures, how composition is altered depending on the physiological state of the cell, and what is their share in contact site formation relative to other complexes like NME4/NDPK-D or MICOS. Concerning molecular functions of mtCK proteolipid complexes, their exact role in phospholipid transfer, thermogenesis and cancer still awaits a definite answer. Further, the CK/PCr system as a whole has been well studied in muscle, also due to the anatomical homogeneity of this tissue, but fewer work has been done in brain and other tissues, despite the phenotypes observed in loss-of-function models. Finally, is there a chance for pharmacological intervention, taking advantage of the many positive effects of the CK/PCr system? This may include supplementing creatine or manipulating endogenous Cr-synthesis, Cr-uptake or CK expression (see also a recent conference report by Wallimann and Harris (2016)). Thus, it seems that quite some parts of the puzzle are still missing, and that yet some surprises may be ahead.

**Acknowledgments** The authors thank all present and former members of the groups at the Univ. Grenoble Alpes (formerly Université Joseph Fourier) and at ETH Zurich, in particular Prof. emer. Theo Wallimann for his continued interest in our work and valuable comments on the present chapter. More recent work by the authors has been funded by the French Agence Nationale de Recherche (chair of excellence to U.S.), the EU 7th framework program (ANTHRAWES no.041870 and ANTHRAPLUS no.249202 to M.T.S.).

## Literature


Akki A, Su J, Yano T, Gupta A, Wang Y, Leppo MK, Chacko VP, Steenbergen C, Weiss RG (2012) Creatine kinase overexpression improves ATP kinetics and contractile function in postischemic myocardium. Am J Physiol Heart Circ Physiol 303(7):H844–H852. https://doi.org/10.1152/ajpheart.00268.2012

Alekseev AE, Guzun R, Reyes S, Pison C, Schlattner U, Selivanov VA, Cascante M (2016) Restrictions in ATP diffusion within sarcomeres can provoke ATP-depleted zones impairing exercise capacity in chronic obstructive pulmonary disease. Biochim Biophys Acta 1860(10):2269–2278. https://doi.org/10.1016/j.bbagen.2016.04.018

Amamoto R, Uchiumi T, Yagi M, Monji K, Song Y, Oda Y, Shiota M, Yokomizo A, Naito S, Kang D (2016) The expression of ubiquitous mitochondrial creatine kinase is downregulated as prostate cancer progression. J Cancer 7(1):50–59. https://doi.org/10.7150/jca.13207

Antman EM (2017) The introduction and clinical use of cardiac-specific troponin assays. Clin Pharmacol Ther. https://doi.org/10.1002/cpt.773

Awama AM, Mazon H, Vial C, Marcillat O (2007) Despite its high similarity with monomeric arginine kinase, muscle creatine kinase is only enzymatically active as a dimer. Arch Biochem Biophys 458(2):158–166. https://doi.org/10.1016/j.abb.2006.09.001

Azzi A, Clark SA, Ellington WR, Chapman MS (2004) The role of phosphagen specificity loops in arginine kinase. Protein Sci 13(3):575–585. https://doi.org/10.1110/ps.03428304

Baeza J, Smallegan MJ, Denu JM (2016) Mechanisms and dynamics of protein acetylation in mitochondria. Trends Biochem Sci 41(3):231–244. https://doi.org/10.1016/j.tibs.2015.12.006

Bak S, Leon IR, Jensen ON, Hojlund K (2013) Tissue specific phosphorylation of mitochondrial proteins isolated from rat liver, heart muscle, and skeletal muscle. J Proteome Res 12(10):4327–4339. https://doi.org/10.1021/pr400281r

Bal NC, Maurya SK, Sopariwala DH, Sahoo SK, Gupta SC, Shaikh SA, Pant M, Rowland LA, Bombardier E, Goonasekera SA, Tupling AR, Molkentin JD, Periasamy M (2012) Sarcolipin is a newly identified regulator of muscle-based thermogenesis in mammals. Nat Med 18(10):1575–1579. https://doi.org/10.1038/nm.2897

Balasubramaniam D, Schiffer J, Parnell J, Mir SP, Amaro RE, Komives EA (2015) How the ankyrin and SOCS box protein, ASB9, binds to creatine kinase. Biochemistry 54(8):1673–1680. https://doi.org/10.1021/bi501420n

Barrett LE, Van Bockstaele EJ, Sul JY, Takano H, Haydon PG, Eberwine JH (2006) Elk-1 associates with the mitochondrial permeability transition pore complex in neurons. Proc Natl Acad Sci U S A 103(13):5155–5160. https://doi.org/10.1073/pnas.0510477103

Bayrhuber M, Meins T, Habeck M, Becker S, Giller K, Villinger S, Vonrhein C, Griesinger C, Zweckstetter M, Zeth K (2008) Structure of the human voltage-dependent anion channel. Proc Natl Acad Sci U S A 105(40):15370–15375. https://doi.org/10.1073/pnas.0808115105

Bera S, Ray M (2009) The transcriptional cascade associated with creatine kinase down-regulation and mitochondrial biogenesis in mice sarcoma. Cell Mol Biol Lett 14(3):481–496. https://doi.org/10.2478/s11658-009-0014-4

Bernardi P, Rasola A, Forte M, Lippe G (2015) The mitochondrial permeability transition pore: channel formation by F-ATP synthase, integration in signal transduction, and role in pathophysiology. Physiol Rev 95(4):1111–1155. https://doi.org/10.1152/physrev.00001.2015

Bertholet AM, Kazak L, Chouchani ET, Bogaczynska MG, Paranjpe I, Wainwright GL, Betourne A, Kajimura S, Spiegelman BM, Kirichok Y (2017) Mitochondrial patch clamp of beige adipocytes reveals UCP1-positive and UCP1-negative cells both exhibiting futile Creatine cycling. Cell Metab 25(4):811–822. e814. https://doi.org/10.1016/j.cmet.2017.03.002

Bertin M, Pomponi SM, Kokuhuta C, Iwasaki N, Suzuki T, Ellington WR (2007) Origin of the genes for the isoforms of creatine kinase. Gene 392(1–2):273–282. https://doi.org/10.1016/j.gene.2007.01.007

Besnard A, Galan-Rodriguez B, Vanhoutte P, Caboche J (2011) Elk-1 a transcription factor with multiple facets in the brain. Front Neurosci 5:35. https://doi.org/10.3389/fnins.2011.00035

Bessman SP, Carpenter CL (1985) The creatine-creatine phosphate energy shuttle. Annu Rev Biochem 54:831–862. https://doi.org/10.1146/annurev.bi.54.070185.004151

Bessman SP, Geiger PJ (1981) Transport of energy in muscle: the phosphorylcreatine shuttle. Science 211(4481):448–452

Beutner G, Ruck A, Riede B, Welte W, Brdiczka D (1996) Complexes between kinases, mitochondrial porin and adenylate translocator in rat brain resemble the permeability transition pore. FEBS Lett 396(2–3):189–195

Beutner G, Ruck A, Riede B, Brdiczka D (1997) Complexes between hexokinase, mitochondrial porin and adenylate translocator in brain: regulation of hexokinase, oxidative phosphorylation and permeability transition pore. Biochem Soc Trans 25(1):151–157

Beyer K, Klingenberg M (1985) ADP/ATP carrier protein from beef heart mitochondria has high amounts of tightly bound cardiolipin, as revealed by 31P nuclear magnetic resonance. Biochemistry 24(15):3821–3826

Boehm EA, Radda GK, Tomlin H, Clark JF (1996) The utilisation of creatine and its analogues by cytosolic and mitochondrial creatine kinase. Biochim Biophys Acta 1274(3):119–128

Bong SM, Moon JH, Nam KH, Lee KS, Chi YM, Hwang KY (2008) Structural studies of human brain-type creatine kinase complexed with the ADP-Mg2+-NO3- -creatine transition-state analogue complex. FEBS Lett 582(28):3959–3965. https://doi.org/10.1016/j.febslet.2008.10.039

Branovets J, Sepp M, Kotlyarova S, Jepihhina N, Sokolova N, Aksentijevic D, Lygate CA, Neubauer S, Vendelin M, Birkedal R (2013) Unchanged mitochondrial organization and compartmentation of high-energy phosphates in creatine-deficient GAMT−/− mouse hearts. Am J Physiol Heart Circ Physiol 305(4):H506–H520. https://doi.org/10.1152/ajpheart.00919.2012

Brdiczka D, Kaldis P, Wallimann T (1994) In vitro complex formation between the octamer of mitochondrial creatine kinase and porin. J Biol Chem 269(44):27640–27644

Brdiczka DG, Zorov DB, Sheu SS (2006) Mitochondrial contact sites: their role in energy metabolism and apoptosis. Biochim Biophys Acta 1762(2):148–163. https://doi.org/10.1016/j.bbadis.2005.09.007

Brewster LM, Mairuhu G, Bindraban NR, Koopmans RP, Clark JF, van Montfrans GA (2006) Creatine kinase activity is associated with blood pressure. Circulation 114(19):2034–2039. https://doi.org/10.1161/CIRCULATIONAHA.105.584490

Buechter DD, Medzihradszky KF, Burlingame AL, Kenyon GL (1992) The active site of creatine kinase. Affinity labeling of cysteine 282 with N-(2,3-epoxypropyl)-N-amidinoglycine. J Biol Chem 267(4):2173–2178

Bush DJ, Kirillova O, Clark SA, Davulcu O, Fabiola F, Xie Q, Somasundaram T, Ellington WR, Chapman MS (2011) The structure of lombricine kinase: implications for phosphagen kinase conformational changes. J Biol Chem 286(11):9338–9350. https://doi.org/10.1074/jbc.M110.202796

Cantwell JS, Novak WR, Wang PF, McLeish MJ, Kenyon GL, Babbitt PC (2001) Mutagenesis of two acidic active site residues in human muscle creatine kinase: implications for the catalytic mechanism. Biochemistry 40(10):3056–3061

Castaldo G, Salvatore F, Sacchetti L (1990) Serum type-2 macro-creatine kinase isoenzyme is not a useful marker of severe liver diseases or neoplasia. Clin Biochem 23(6):523–527

Chang EJ, Ha J, Oerlemans F, Lee YJ, Lee SW, Ryu J, Kim HJ, Lee Y, Kim HM, Choi JY, Kim JY, Shin CS, Pak YK, Tanaka S, Wieringa B, Lee ZH, Kim HH (2008) Brain-type creatine kinase has a crucial role in osteoclast-mediated bone resorption. Nat Med 14(9):966–972. https://doi.org/10.1038/nm.1860

Chang CC, Liou CB, MJ S, Lee YC, Liang CT, Ho JL, Tsai HW, Yen TH, Chu FY (2015) Creatine kinase (CK)-MB-to-Total-CK ratio: a laboratory indicator for primary cancer screening. Asian Pac J Cancer Prev 16(15):6599–6603

Chao PT, Yang L, Aja S, Moran TH, Bi S (2011) Knockdown of NPY expression in the dorsomedial hypothalamus promotes development of brown adipocytes and prevents diet-induced obesity. Cell Metab 13(5):573–583. https://doi.org/10.1016/j.cmet.2011.02.019

Chen LH, Borders CL Jr, Vasquez JR, Kenyon GL (1996) Rabbit muscle creatine kinase: consequences of the mutagenesis of conserved histidine residues. Biochemistry 35(24):7895–7902. https://doi.org/10.1021/bi952798i

Cheniour M, Brewer J, Bagatolli L, Marcillat O, Granjon T (2017) Evidence of proteolipid domain formation in an inner mitochondrial membrane mimicking model. Biochim Biophys Acta 1861(5 Pt A):969–976. https://doi.org/10.1016/j.bbagen.2017.02.001

Cimino D, Fuso L, Sfiligoi C, Biglia N, Ponzone R, Maggiorotto F, Russo G, Cicatiello L, Weisz A, Taverna D, Sismondi P, De Bortoli M (2008) Identification of new genes associated with breast cancer progression by gene expression analysis of predefined sets of neoplastic tissues. Int J Cancer 123(6):1327–1338. https://doi.org/10.1002/ijc.23660

Clark SA, Davulcu O, Chapman MS (2012) Crystal structures of arginine kinase in complex with ADP, nitrate, and various phosphagen analogs. Biochem Biophys Res Commun 427(1):212–217. https://doi.org/10.1016/j.bbrc.2012.09.053

Cook PF, Kenyon GL, Cleland WW (1981) Use of pH studies to elucidate the catalytic mechanism of rabbit muscle creatine kinase. Biochemistry 20(5):1204–1210

Cox JM, Davis CA, Chan C, Jourden MJ, Jorjorian AD, Brym MJ, Snider MJ, Borders CL Jr, Edmiston PL (2003) Generation of an active monomer of rabbit muscle creatine kinase by site-directed mutagenesis: the effect of quaternary structure on catalysis and stability. Biochemistry 42(7):1863–1871. https://doi.org/10.1021/bi027083b

Cui J, Yu M, Niu J, Yue Z, Xu Z (2011) Expression of leucine-rich repeat kinase 2 (LRRK2) inhibits the processing of uMtCK to induce cell death in a cell culture model system. Biosci Rep 31(5):429–437. https://doi.org/10.1042/BSR20100127

D'Errico M, de Rinaldis E, Blasi MF, Viti V, Falchetti M, Calcagnile A, Sera F, Saieva C, Ottini L, Palli D, Palombo F, Giuliani A, Dogliotti E (2009) Genome-wide expression profile of sporadic gastric cancers with microsatellite instability. Eur J Cancer 45(3):461–469. https://doi.org/10.1016/j.ejca.2008.10.032

Datler C, Pazarentzos E, Mahul-Mellier AL, Chaisaklert W, Hwang MS, Osborne F, Grimm S (2014) CKMT1 regulates the mitochondrial permeability transition pore in a process that provides evidence for alternative forms of the complex. J Cell Sci 127(Pt 8):1816–1828. https://doi.org/10.1242/jcs.140467

de Groof AJ, Fransen JA, Errington RJ, Willems PH, Wieringa B, Koopman WJ (2002) The creatine kinase system is essential for optimal refill of the sarcoplasmic reticulum $Ca^{2+}$ store in skeletal muscle. J Biol Chem 277(7):5275–5284. https://doi.org/10.1074/jbc.M108157200

Decking UK, Alves C, Wallimann T, Wyss M, Schrader J (2001) Functional aspects of creatine kinase isoenzymes in endothelial cells. Am J Physiol Cell Physiol 281(1):C320–C328

Dillon PF (2014) Equilibrium enzymes in regulatory systems: a problem in scalar-vector transition. Hypertension 63(1):27–28. https://doi.org/10.1161/HYPERTENSIONAHA.113.02251

Dolder M, Walzel B, Speer O, Schlattner U, Wallimann T (2003) Inhibition of the mitochondrial permeability transition by creatine kinase substrates. Requirement for microcompartmentation. J Biol Chem 278(20):17760–17766. https://doi.org/10.1074/jbc.M208705200

Drees M, Beyer K (1988) Interaction of phospholipids with the detergent-solubilized ADP/ATP carrier protein as studied by spin-label electron spin resonance. Biochemistry 27(23):8584–8591

Dzeja PP, Terzic A (2003) Phosphotransfer networks and cellular energetics. J Exp Biol 206(Pt 12):2039–2047

Dzeja PP, Hoyer K, Tian R, Zhang S, Nemutlu E, Spindler M, Ingwall JS (2011) Rearrangement of energetic and substrate utilization networks compensate for chronic myocardial creatine kinase deficiency. J Physiol 589(Pt 21):5193–5211. https://doi.org/10.1113/jphysiol.2011.212829

Ebermann L, Piper C, Kuhl U, Klingel K, Schlattner U, Siafarikas N, Zeichhardt H, Schultheiss HP, Dorner A (2009) Impact of myocardial inflammation on cytosolic and mitochondrial creatine kinase activity and expression. Basic Res Cardiol 104(3):247–257. https://doi.org/10.1007/s00395-008-0773-5

Eder M, Schlattner U, Becker A, Wallimann T, Kabsch W, Fritz-Wolf K (1999) Crystal structure of brain-type creatine kinase at 1.41 Å resolution. Protein Sci 8(11):2258–2269. https://doi.org/10.1110/ps.8.11.2258

Eder M, Fritz-Wolf K, Kabsch W, Wallimann T, Schlattner U (2000a) Crystal structure of human ubiquitous mitochondrial creatine kinase. Proteins 39(3):216–225

Eder M, Stolz M, Wallimann T, Schlattner U (2000b) A conserved negatively charged cluster in the active site of creatine kinase is critical for enzymatic activity. J Biol Chem 275(35):27094–27099. https://doi.org/10.1074/jbc.M004071200

Ellington WR (2001) Evolution and physiological roles of phosphagen systems. Annu Rev Physiol 63:289–325

Ellington WR, Suzuki T (2007) Early evolution of the creatine kinase gene family and the capacity for creatine biosynthesis and membrane transport. Subcell Biochem 46:17–26

Ellington WR, Roux K, Pineda AO Jr (1998) Origin of octameric creatine kinases. FEBS Lett 425(1):75–78

Enooku K, Nakagawa H, Soroida Y, Ohkawa R, Kageyama Y, Uranbileg B, Watanabe N, Tateishi R, Yoshida H, Koike K, Yatomi Y, Ikeda H (2014) Increased serum mitochondrial creatine kinase activity as a risk for hepatocarcinogenesis in chronic hepatitis C patients. Int J Cancer 135(4):871–879. https://doi.org/10.1002/ijc.28720

Epand RF, Schlattner U, Wallimann T, Lacombe ML, Epand RM (2007a) Novel lipid transfer property of two mitochondrial proteins that bridge the inner and outer membranes. Biophys J 92(1):126–137

Epand RF, Tokarska-Schlattner M, Schlattner U, Wallimann T, Epand RM (2007b) Cardiolipin clusters and membrane domain formation induced by mitochondrial proteins. J Mol Biol 365(4):968–980

Feng J, Lucchinetti E, Enkavi G, Wang Y, Gehrig P, Roschitzki B, Schaub MC, Tajkhorshid E, Zaugg K, Zaugg M (2010) Tyrosine phosphorylation by Src within the cavity of the adenine nucleotide translocase 1 regulates ADP/ATP exchange in mitochondria. Am J Physiol Cell Physiol 298(3):C740–C748. https://doi.org/10.1152/ajpcell.00310.2009

Fenouille N, Bassil CF, Ben-Sahra I, Benajiba L, Alexe G, Ramos A, Pikman Y, Conway AS, Burgess MR, Li Q, Luciano F, Auberger P, Galinsky I, DeAngelo DJ, Stone RM, Zhang Y, Perkins AS, Shannon K, Hemann MT, Puissant A, Stegmaier K (2017) The creatine kinase pathway is a metabolic vulnerability in EVI1-positive acute myeloid leukemia. Nat Med 23(3):301–313. https://doi.org/10.1038/nm.4283

Fernandez E, Collins MO, Uren RT, Kopanitsa MV, Komiyama NH, Croning MD, Zografos L, Armstrong JD, Choudhary JS, Grant SG (2009) Targeted tandem affinity purification of PSD-95 recovers core postsynaptic complexes and schizophrenia susceptibility proteins. Mol Syst Biol 5:269. https://doi.org/10.1038/msb.2009.27

Forstner M, Muller A, Stolz M, Wallimann T (1997) The active site histidines of creatine kinase. A critical role of his 61 situated on a flexible loop. Protein Sci 6(2):331–339. https://doi.org/10.1002/pro.5560060208

Foster DB, Liu T, Rucker J, O'Meally RN, Devine LR, Cole RN, O'Rourke B (2013) The cardiac acetyl-lysine proteome. PLoS One 8(7):e67513. https://doi.org/10.1371/journal.pone.0067513

Fritz-Wolf K, Schnyder T, Wallimann T, Kabsch W (1996) Structure of mitochondrial creatine kinase. Nature 381(6580):341–345. https://doi.org/10.1038/381341a0

Fukumitsu K, Fujishima K, Yoshimura A, YK W, Heuser J, Kengaku M (2015) Synergistic action of dendritic mitochondria and creatine kinase maintains ATP homeostasis and actin dynamics in growing neuronal dendrites. J Neurosci 35(14):5707–5723. https://doi.org/10.1523/JNEUROSCI.4115-14.2015

Furter R, Furter-Graves EM, Wallimann T (1993) Creatine kinase: the reactive cysteine is required for synergism but is nonessential for catalysis. Biochemistry 32(27):7022–7029

Gattis JL, Ruben E, Fenley MO, Ellington WR, Chapman MS (2004) The active site cysteine of arginine kinase: structural and functional analysis of partially active mutants. Biochemistry 43(27):8680–8689. https://doi.org/10.1021/bi049793i

Glancy B, Hartnell LM, Malide D, ZX Y, Combs CA, Connelly PS, Subramaniam S, Balaban RS (2015) Mitochondrial reticulum for cellular energy distribution in muscle. Nature 523(7562):617–620. https://doi.org/10.1038/nature14614

Godsey MH, Davulcu O, Nix JC, Skalicky JJ, Bruschweiler RP, Chapman MS (2016) The sampling of conformational dynamics in ambient-temperature crystal structures of arginine kinase. Structure 24(10):1658–1667. https://doi.org/10.1016/j.str.2016.07.013

Granjon T, Vacheron MJ, Vial C, Buchet R (2001) Mitochondrial creatine kinase binding to phospholipids decreases fluidity of membranes and promotes new lipid-induced beta structures as monitored by red edge excitation shift, laurdan fluorescence, and FTIR. Biochemistry 40(20):6016–6026

Grillon JM, Johnson KR, Kotlo K, Danziger RS (2012) Non-histone lysine acetylated proteins in heart failure. Biochim Biophys Acta 1822(4):607–614. https://doi.org/10.1016/j.bbadis.2011.11.016

Grimpo K, Volker MN, Heppe EN, Braun S, Heverhagen JT, Heldmaier G (2014) Brown adipose tissue dynamics in wild-type and UCP1-knockout mice: in vivo insights with magnetic resonance. J Lipid Res 55(3):398–409. https://doi.org/10.1194/jlr.M042895

Gross M, Wallimann T (1993) Kinetics of assembly and dissociation of the mitochondrial creatine kinase octamer. A fluorescence study. Biochemistry 32(50):13933–13940

Gross M, Furter-Graves EM, Wallimann T, Eppenberger HM, Furter R (1994) The tryptophan residues of mitochondrial creatine kinase: roles of Trp-223, Trp-206, and Trp-264 in active-site and quaternary structure formation. Protein Sci 3(7):1058–1068. https://doi.org/10.1002/pro.5560030708

Gross M, Wyss M, Furter-Graves EM, Wallimann T, Furter R (1996) Reconstitution of active octameric mitochondrial creatine kinase from two genetically engineered fragments. Protein Sci 5(2):320–330. https://doi.org/10.1002/pro.5560050216

Guerrero K, Wuyam B, Mezin P, Vivodtzev I, Vendelin M, Borel JC, Hacini R, Chavanon O, Imbeaud S, Saks V, Pison C (2005) Functional coupling of adenine nucleotide translocase and mitochondrial creatine kinase is enhanced after exercise training in lung transplant skeletal muscle. Am J Physiol Regul Integr Comp Physiol 289(4):R1144–R1154. https://doi.org/10.1152/ajpregu.00229.2005

Gupta A, Akki A, Wang Y, Leppo MK, Chacko VP, Foster DB, Caceres V, Shi S, Kirk JA, Su J, Lai S, Paolocci N, Steenbergen C, Gerstenblith G, Weiss RG (2012) Creatine kinase-mediated improvement of function in failing mouse hearts provides causal evidence the failing heart is energy starved. J Clin Invest 122(1):291–302. https://doi.org/10.1172/JCI57426

Gupta A, Rohlfsen C, Leppo MK, Chacko VP, Wang Y, Steenbergen C, Weiss RG (2013) Creatine kinase-overexpression improves myocardial energetics, contractile dysfunction and survival in murine doxorubicin cardiotoxicity. PLoS One 8(10):e74675. https://doi.org/10.1371/journal.pone.0074675

Guzun R, Gonzalez-Granillo M, Karu-Varikmaa M, Grichine A, Usson Y, Kaambre T, Guerrero-Roesch K, Kuznetsov A, Schlattner U, Saks V (2012) Regulation of respiration in muscle cells in vivo by VDAC through interaction with the cytoskeleton and MtCK within mitochondrial Interactosome. Biochim Biophys Acta 1818(6):1545–1554. https://doi.org/10.1016/j.bbamem.2011.12.034

Guzun R, Kaambre T, Bagur R, Grichine A, Usson Y, Varikmaa M, Anmann T, Tepp K, Timohhina N, Shevchuk I, Chekulayev V, Boucher F, Dos Santos P, Schlattner U, Wallimann T, Kuznetsov AV, Dzeja P, Aliev M, Saks V (2015) Modular organization of cardiac energy metabolism: energy conversion, transfer and feedback regulation. Acta Physiol (Oxf) 213(1):84–106. https://doi.org/10.1111/apha.12287

Heerschap A, Kan HE, Nabuurs CI, Renema WK, Isbrandt D, Wieringa B (2007) In vivo magnetic resonance spectroscopy of transgenic mice with altered expression of guanidinoacetate methyltransferase and creatine kinase isoenzymes. Subcell Biochem 46:119–148

Hiller S, Garces RG, Malia TJ, Orekhov VY, Colombini M, Wagner G (2008) Solution structure of the integral human membrane protein VDAC-1 in detergent micelles. Science 321(5893):1206–1210. https://doi.org/10.1126/science.1161302

Hornemann T, Rutishauser D, Wallimann T (2000) Why is creatine kinase a dimer? Evidence for cooperativity between the two subunits. Biochim Biophys Acta 1480(1–2):365–373

Hosaka T, Okazaki M, Kimura-Someya T, Ishizuka-Katsura Y, Ito K, Yokoyama S, Dodo K, Sodeoka M, Shirouzu M (2017) Crystal structural characterization reveals novel oligomeric interactions of human voltage-dependent anion channel 1. Protein Sci 26(9):1749–1758. https://doi.org/10.1002/pro.3211

Hoshino T, Sakai Y, Yamashita K, Shirahase Y, Sakaguchi K, Asaeda A, Kishi K, Schlattner U, Wallimann T, Yanai M, Kumasaka K (2009) Development and performance of an enzyme immunoassay to detect creatine kinase isoenzyme MB activity using anti-mitochondrial creatine kinase monoclonal antibodies. Scand J Clin Lab Invest 69(6):687–695. https://doi.org/10.3109/00365510902981171

Hou LX, Vollmer S (1994) The activity of S-thiomethyl modified creatine kinase is due to the regeneration of free thiol at the active site. Biochim Biophys Acta 1205(1):83–88

Huddleston HG, Wong KK, Welch WR, Berkowitz RS, Mok SC (2005) Clinical applications of microarray technology: creatine kinase B is an up-regulated gene in epithelial ovarian cancer and shows promise as a serum marker. Gynecol Oncol 96(1):77–83. https://doi.org/10.1016/j.ygyno.2004.08.047

Hurne AM, Chai CL, Waring P (2000) Inactivation of rabbit muscle creatine kinase by reversible formation of an internal disulfide bond induced by the fungal toxin gliotoxin. J Biol Chem 275(33):25202–25206. https://doi.org/10.1074/jbc.M002278200

Ishikawa J, Taniguchi T, Takeshita A, Maekawa M (2005) Increased creatine kinase BB activity and CKB mRNA expression in patients with hematologic disorders: relation to methylation status of the CKB promoter. Clin Chim Acta 361(1–2):135–140. https://doi.org/10.1016/j.cccn.2005.05.028

Iwabata H, Yoshida M, Komatsu Y (2005) Proteomic analysis of organ-specific post-translational lysine-acetylation and -methylation in mice by use of anti-acetyllysine and -methyllysine mouse monoclonal antibodies. Proteomics 5(18):4653–4664. https://doi.org/10.1002/pmic.200500042

Jacobus WE (1985) Respiratory control and the integration of heart high-energy phosphate metabolism by mitochondrial creatine kinase. Annu Rev Physiol 47:707–725

Jacobus WE, Lehninger AL (1973) Creatine kinase of rat heart mitochondria. Coupling of creatine phosphorylation to electron transport. J Biol Chem 248(13):4803–4810

Jaremko M, Jaremko L, Villinger S, Schmidt CD, Griesinger C, Becker S, Zweckstetter M (2016) High-resolution NMR determination of the dynamic structure of membrane proteins. Angew Chem Int Ed Engl 55(35):10518–10521. https://doi.org/10.1002/anie.201602639

Jost CR, Van Der Zee CE, In 't Zandt HJ, Oerlemans F, Verheij M, Streijger F, Fransen J, Heerschap A, Cools AR, Wieringa B (2002) Creatine kinase B-driven energy transfer in the brain is important for habituation and spatial learning behaviour, mossy fibre field size and determination of seizure susceptibility. Eur J Neurosci 15(10):1692–1706

Kabsch W, Fritz-Wolf K (1997) Mitochondrial creatine kinase--a square protein. Curr Opin Struct Biol 7(6):811–818

Kaddurah-Daouk R, Lillie JW, Daouk GH, Green MR, Kingston R, Schimmel P (1990) Induction of a cellular enzyme for energy metabolism by transforming domains of adenovirus E1a. Mol Cell Biol 10(4):1476–1483

Kagan VE, Jiang J, Huang Z, Tyurina YY, Desbourdes C, Cottet-Rousselle C, Dar HH, Verma M, Tyurin VA, Kapralov AA, Cheikhi A, Mao G, Stolz D, St Croix CM, Watkins S, Shen Z, Li Y, Greenberg ML, Tokarska-Schlattner M, Boissan M, Lacombe ML, Epand RM, Chu CT, Mallampalli RK, Bayir H, Schlattner U (2016) NDPK-D (NM23-H4)-mediated externalization of cardiolipin enables elimination of depolarized mitochondria by mitophagy. Cell Death Differ 23(7):1140–1151. https://doi.org/10.1038/cdd.2015.160

Kaldis P, Wallimann T (1995) Functional differences between dimeric and octameric mitochondrial creatine kinase. Biochem J 308(Pt 2):623–627

Karamat FA, Oudman I, Ris-Stalpers C, Afink GB, Keijser R, Clark JF, van Montfrans GA, Brewster LM (2014) Resistance artery creatine kinase mRNA and blood pressure in humans. Hypertension 63(1):68–73. https://doi.org/10.1161/HYPERTENSIONAHA.113.01352

Karo J, Peterson P, Vendelin M (2012) Molecular dynamics simulations of creatine kinase and adenine nucleotide translocase in mitochondrial membrane patch. J Biol Chem 287(10):7467–7476. https://doi.org/10.1074/jbc.M111.332320

Kay L, Nicolay K, Wieringa B, Saks V, Wallimann T (2000) Direct evidence for the control of mitochondrial respiration by mitochondrial creatine kinase in oxidative muscle cells in situ. J Biol Chem 275(10):6937–6944

Kazak L, Chouchani ET, Jedrychowski MP, Erickson BK, Shinoda K, Cohen P, Vetrivelan R, GZ L, Laznik-Bogoslavski D, Hasenfuss SC, Kajimura S, Gygi SP, Spiegelman BM (2015) A creatine-driven substrate cycle enhances energy expenditure and thermogenesis in beige fat. Cell 163(3):643–655. https://doi.org/10.1016/j.cell.2015.09.035

Kazak L, Chouchani ET, Lu GZ, Jedrychowski MP, Bare CJ, Mina AI, Kumari M, Zhang S, Vuckovic I, Laznik-Bogoslavski D, Dzeja P, Banks AS, Rosen ED, Spiegelman BM (2017) Genetic depletion of adipocyte creatine metabolism inhibits diet-induced thermogenesis and drives obesity. Cell Metab 26(4):660–671. e663. https://doi.org/10.1016/j.cmet.2017.08.009

Kekelidze T, Khait I, Togliatti A, Benzecry JM, Wieringa B, Holtzman D (2001) Altered brain phosphocreatine and ATP regulation when mitochondrial creatine kinase is absent. J Neurosci Res 66(5):866–872. https://doi.org/10.1002/jnr.10060

Khurana A, Dey CS (2002) Involvement of Elk-1 in L6E9 skeletal muscle differentiation. FEBS Lett 527(1–3):119–124

Kitaoka Y, Ogborn DI, Mocellin NJ, Schlattner U, Tarnopolsky MA (2013) Monocarboxylate transporters and mitochondrial creatine kinase protein content in McArdle disease. Mol Genet Metab 108(4):259–262. https://doi.org/10.1016/j.ymgme.2013.01.005

Kornacker M, Schlattner U, Wallimann T, Verneris MR, Negrin RS, Kornacker B, Staratschek-Jox A, Diehl V, Wolf J (2001) Hodgkin disease-derived cell lines expressing ubiquitous mitochondrial creatine kinase show growth inhibition by cyclocreatine treatment independent of apoptosis. Int J Cancer 94(4):513–519

Kottke M, Wallimann T, Brdiczka D (1994) Dual electron microscopic localization of mitochondrial creatine kinase in brain mitochondria. Biochem Med Metab Biol 51(2):105–117

Koven IH, Freedman M, Miller D, Reece S, Maitland A, Sigurdson E, Blackstein ME (1983) Macro--creatine kinase 2: a possible marker of gastrointestinal cancer? Surgery 94(4):631–635

Kruse R, Hojlund K (2017) Mitochondrial phosphoproteomics of mammalian tissues. Mitochondrion 33:45–57. https://doi.org/10.1016/j.mito.2016.08.004

Kühlbrandt W (2015) Structure and function of mitochondrial membrane protein complexes. BMC Biol 13:89. https://doi.org/10.1186/s12915-015-0201-x

Kuiper JW, van Horssen R, Oerlemans F, Peters W, van Dommelen MM, te Lindert MM, ten Hagen TL, Janssen E, Fransen JA, Wieringa B (2009) Local ATP generation by brain-type creatine kinase (CK-B) facilitates cell motility. PLoS One 4(3):e5030. https://doi.org/10.1371/journal.pone.0005030

Kuznetsov AV, Javadov S, Guzun R, Grimm M, Saks V (2013) Cytoskeleton and regulation of mitochondrial function: the role of beta-tubulin II. Front Physiol 4:82. https://doi.org/10.3389/fphys.2013.00082

Kwon S, Kim D, Rhee JW, Park JA, Kim DW, Kim DS, Lee Y, Kwon HJ (2010) ASB9 interacts with ubiquitous mitochondrial creatine kinase and inhibits mitochondrial function. BMC Biol 8:23. https://doi.org/10.1186/1741-7007-8-23

Lahiri SD, Wang PF, Babbitt PC, McLeish MJ, Kenyon GL, Allen KN (2002) The 2.1 a structure of Torpedo Californica creatine kinase complexed with the ADP-mg(2+)-NO(3)(−)-creatine transition-state analogue complex. Biochemistry 41(47):13861–13867

Lemeshko VV (2016) VDAC electronics: 3. VDAC-creatine kinase-dependent generation of the outer membrane potential in respiring mitochondria. Biochim Biophys Acta 1858(7 Pt A):1411–1418. https://doi.org/10.1016/j.bbamem.2016.04.005

Lenz H, Schmidt M, Welge V, Kueper T, Schlattner U, Wallimann T, Elsasser HP, Wittern KP, Wenck H, Staeb F, Blatt T (2007) Inhibition of cytosolic and mitochondrial creatine kinase by siRNA in HaCaT- and HeLaS3-cells affects cell viability and mitochondrial morphology. Mol Cell Biochem 306(1–2):153–162

Lewandrowski U, Sickmann A, Cesaro L, Brunati AM, Toninello A, Salvi M (2008) Identification of new tyrosine phosphorylated proteins in rat brain mitochondria. FEBS Lett 582(7):1104–1110. https://doi.org/10.1016/j.febslet.2008.02.077

Li X, Burklen T, Yuan X, Schlattner U, Desiderio DM, Wallimann T, Homayouni R (2006) Stabilization of ubiquitous mitochondrial creatine kinase preprotein by APP family proteins. Mol Cell Neurosci 31(2):263–272. https://doi.org/10.1016/j.mcn.2005.09.015

Li XH, Chen Z, Gao YS, Yan YB, Zhang F, Meng FG, Zhou HM (2011) Generation of the oxidized form protects human brain type creatine kinase against cystine-induced inactivation. Int J Biol Macromol 48(2):239–242. https://doi.org/10.1016/j.ijbiomac.2010.09.018

Li Q, Fan S, Li X, Jin Y, He W, Zhou J, Cen S, Yang Z (2016) Insights into the phosphoryl transfer mechanism of human ubiquitous mitochondrial creatine kinase. Sci Rep 6:38088. https://doi.org/10.1038/srep38088

Lim K, Pullalarevu S, Surabian KT, Howard A, Suzuki T, Moult J, Herzberg O (2010) Structural basis for the mechanism and substrate specificity of glycocyamine kinase, a phosphagen kinase family member. Biochemistry 49(9):2031–2041. https://doi.org/10.1021/bi9020988

Lim S, Smith KR, Lim ST, Tian R, Lu J, Tan M (2016) Regulation of mitochondrial functions by protein phosphorylation and dephosphorylation. Cell Biosci 6:25. https://doi.org/10.1186/s13578-016-0089-3

Lin L, Perryman MB, Friedman D, Roberts R, Ma TS (1994) Determination of the catalytic site of creatine kinase by site-directed mutagenesis. Biochim Biophys Acta 1206(1):97–104

Londergan CH, Baskin R, Bischak CG, Hoffman KW, Snead DM, Reynoso C (2015) Dynamic asymmetry and the role of the conserved active-site thiol in rabbit muscle creatine kinase. Biochemistry 54(1):83–95. https://doi.org/10.1021/bi5008063

Loo JM, Scherl A, Nguyen A, Man FY, Weinberg E, Zeng Z, Saltz L, Paty PB, Tavazoie SF (2015) Extracellular metabolic energetics can promote cancer progression. Cell 160(3):393–406. https://doi.org/10.1016/j.cell.2014.12.018

Lundby A, Lage K, Weinert BT, Bekker-Jensen DB, Secher A, Skovgaard T, Kelstrup CD, Dmytriyev A, Choudhary C, Lundby C, Olsen JV (2012) Proteomic analysis of lysine acetylation sites in rat tissues reveals organ specificity and subcellular patterns. Cell Rep 2(2):419–431. https://doi.org/10.1016/j.celrep.2012.07.006

Lygate CA, Fischer A, Sebag-Montefiore L, Wallis J, ten Hove M, Neubauer S (2007) The creatine kinase energy transport system in the failing mouse heart. J Mol Cell Cardiol 42(6):1129–1136. https://doi.org/10.1016/j.yjmcc.2007.03.899

Lygate CA, Bohl S, ten Hove M, Faller KM, Ostrowski PJ, Zervou S, Medway DJ, Aksentijevic D, Sebag-Montefiore L, Wallis J, Clarke K, Watkins H, Schneider JE, Neubauer S (2012) Moderate elevation of intracellular creatine by targeting the creatine transporter protects mice from acute myocardial infarction. Cardiovasc Res 96(3):466–475. https://doi.org/10.1093/cvr/cvs272

Lygate CA, Aksentijevic D, Dawson D, ten Hove M, Phillips D, de Bono JP, Medway DJ, Sebag-Montefiore L, Hunyor I, Channon KM, Clarke K, Zervou S, Watkins H, Balaban RS, Neubauer S (2013) Living without creatine: unchanged exercise capacity and response to chronic myocardial infarction in creatine-deficient mice. Circ Res 112(6):945–955. https://doi.org/10.1161/CIRCRESAHA.112.300725

Maldonado EN, Sheldon KL, DeHart DN, Patnaik J, Manevich Y, Townsend DM, Bezrukov SM, Rostovtseva TK, Lemasters JJ (2013) Voltage-dependent anion channels modulate mitochondrial metabolism in cancer cells: regulation by free tubulin and erastin. J Biol Chem 288(17):11920–11929. https://doi.org/10.1074/jbc.M112.433847

Maniti O, Cheniour M, Marcillat O, Vial C, Granjon T (2009a) Morphology modifications in negatively charged lipid monolayers upon mitochondrial creatine kinase binding. Mol Membr Biol 26(3):171–185. https://doi.org/10.1080/09687680802698639

Maniti O, Lecompte MF, Marcillat O, Desbat B, Buchet R, Vial C, Granjon T (2009b) Mitochondrial creatine kinase binding to phospholipid monolayers induces cardiolipin segregation. Biophys J 96(6):2428–2438. https://doi.org/10.1016/j.bpj.2008.12.3911

Maniti O, Lecompte MF, Marcillat O, Vial C, Granjon T (2010) Mitochondrial creatine kinase interaction with cardiolipin-containing biomimetic membranes is a two-step process involving adsorption and insertion. Eur Biophys J 39(12):1649–1655. https://doi.org/10.1007/s00249-010-0600-4

Maniti O, Cheniour M, Lecompte MF, Marcillat O, Buchet R, Vial C, Granjon T (2011) Acyl chain composition determines cardiolipin clustering induced by mitochondrial creatine kinase binding to monolayers. Biochim Biophys Acta 1808(4):1129–1139. https://doi.org/10.1016/j.bbamem.2011.01.005

Maniti O, Francois-Moutal L, Lecompte MF, Vial C, Lagarde M, Guichardant M, Marcillat O, Granjon T (2015) Protein "amyloid-like" networks at the phospholipid membrane formed by 4-hydroxy-2-nonenal-modified mitochondrial creatine kinase. Mol Membr Biol 32(1):1–10. https://doi.org/10.3109/09687688.2015.1023376

Martel C, Wang Z, Brenner C (2014) VDAC phosphorylation, a lipid sensor influencing the cell fate. Mitochondrion 19(Pt A):69–77. https://doi.org/10.1016/j.mito.2014.07.009

Marzo I, Brenner C, Zamzami N, Susin SA, Beutner G, Brdiczka D, Remy R, Xie ZH, Reed JC, Kroemer G (1998) The permeability transition pore complex: a target for apoptosis regulation by caspases and bcl-2-related proteins. J Exp Med 187(8):1261–1271

Matsushima K, Uda K, Ishida K, Kokufuta C, Iwasaki N, Suzuki T (2006) Comparison of kinetic constants of creatine kinase isoforms. Int J Biol Macromol 38(2):83–88. https://doi.org/10.1016/j.ijbiomac.2005.12.023

McLeish MJ, Kenyon GL (2005) Relating structure to mechanism in creatine kinase. Crit Rev Biochem Mol Biol 40(1):1–20. https://doi.org/L8629333257560X6 [pii] 1080/10409230590918577

Merceron R, Awama AM, Montserret R, Marcillat O, Gouet P (2015) The substrate-free and -bound crystal structures of the duplicated taurocyamine kinase from the human parasite Schistosoma mansoni. J Biol Chem 290(20):12951–12963. https://doi.org/10.1074/jbc.M114.628909

Messmer CH, Kagi JH (1985) Tryptophan residues of creatine kinase: a fluorescence study. Biochemistry 24(25):7172–7178

Meyer LE, Machado LB, Santiago AP, da-Silva WS, De Felice FG, Holub O, Oliveira MF, Galina A (2006) Mitochondrial creatine kinase activity prevents reactive oxygen species generation: antioxidant role of mitochondrial kinase-dependent ADP re-cycling activity. J Biol Chem 281(49):37361–37371. https://doi.org/10.1074/jbc.M604123200

Mielke C, Lefort N, McLean CG, Cordova JM, Langlais PR, Bordner AJ, Te JA, Ozkan SB, Willis WT, Mandarino LJ (2014) Adenine nucleotide translocase is acetylated in vivo in human muscle: modeling predicts a decreased ADP affinity and altered control of oxidative phosphorylation. Biochemistry 53(23):3817–3829. https://doi.org/10.1021/bi401651e

Milner-White EJ, Watts DC (1971) Inhibition of adenosine 5′-triphosphate-creatine phosphotransferase by substrate-anion complexes. Evidence for the transition-state organization of the catalytic site. Biochem J 122(5):727–740

Muller M, Moser R, Cheneval D, Carafoli E (1985) Cardiolipin is the membrane receptor for mitochondrial creatine phosphokinase. J Biol Chem 260(6):3839–3843

Muller S, Balaz M, Stefanicka P, Varga L, Amri EZ, Ukropec J, Wollscheid B, Wolfrum C (2016) Proteomic analysis of human brown adipose tissue reveals utilization of coupled and uncoupled energy expenditure pathways. Sci Rep 6:30030. https://doi.org/10.1038/srep30030

Nabuurs CI, Choe CU, Veltien A, Kan HE, van Loon LJ, Rodenburg RJ, Matschke J, Wieringa B, Kemp GJ, Isbrandt D, Heerschap A (2013) Disturbed energy metabolism and muscular dystrophy caused by pure creatine deficiency are reversible by creatine intake. J Physiol 591(2):571–592. https://doi.org/10.1113/jphysiol.2012.241760

Nevinsky GA, Ankilova VN, Lavrik OI, Mkrtchyan ZS, Nersesova LS, Akopyan JI (1982) Functional non-identity of creatine kinase subunits of rabbit skeletal muscle. FEBS Lett 149(1):36–40

Nietzel T, Mostertz J, Hochgrafe F, Schwarzlander M (2017) Redox regulation of mitochondrial proteins and proteomes by cysteine thiol switches. Mitochondrion 33:72–83. https://doi.org/10.1016/j.mito.2016.07.010

Noskov SY, Rostovtseva TK, Bezrukov SM (2013) ATP transport through VDAC and the VDAC-tubulin complex probed by equilibrium and nonequilibrium MD simulations. Biochemistry 52(51):9246–9256. https://doi.org/10.1021/bi4011495

Noskov SY, Rostovtseva TK, Chamberlin AC, Teijido O, Jiang W, Bezrukov SM (2016) Current state of theoretical and experimental studies of the voltage-dependent anion channel (VDAC). Biochim Biophys Acta 1858(7 Pt B):1778–1790. https://doi.org/10.1016/j.bbamem.2016.02.026

Nury H, Dahout-Gonzalez C, Trezeguet V, Lauquin GJ, Brandolin G, Pebay-Peyroula E (2006) Relations between structure and function of the mitochondrial ADP/ATP carrier. Annu Rev Biochem 75:713–741. https://doi.org/10.1146/annurev.biochem.75.103004.142747

O'Brien KM, Mueller IA, Orczewska JI, Dullen KR, Ortego M (2014) Hearts of some Antarctic fishes lack mitochondrial creatine kinase. Comp Biochem Physiol A Mol Integr Physiol 178:30–36. https://doi.org/10.1016/j.cbpa.2014.08.003

O'Gorman E, Piendl T, Muller M, Brdiczka D, Wallimann T (1997) Mitochondrial intermembrane inclusion bodies: the common denominator between human mitochondrial myopathies and creatine depletion, due to impairment of cellular energetics. Mol Cell Biochem 174(1–2):283–289

Ohren JF, Kundracik ML, Borders CL Jr, Edmiston P, Viola RE (2007) Structural asymmetry and intersubunit communication in muscle creatine kinase. Acta Crystallogr D Biol Crystallogr 63(Pt 3):381–389. https://doi.org/10.1107/S0907444906056204

Onda T, Uzawa K, Endo Y, Bukawa H, Yokoe H, Shibahara T, Tanzawa H (2006) Ubiquitous mitochondrial creatine kinase downregulated in oral squamous cell carcinoma. Br J Cancer 94(5):698–709. https://doi.org/10.1038/sj.bjc.6602986

Pang B, Zhang H, Wang J, Chen WZ, Li SH, Shi QG, Liang RX, Xie BX, Wu RQ, Qian XL, Yu L, Li QM, Huang CF, Zhou JG (2009) Ubiquitous mitochondrial creatine kinase is overexpressed in the conditioned medium and the extract of LNCaP lineaged androgen independent cell lines and facilitates prostate cancer progression. Prostate 69(11):1176–1187. https://doi.org/10.1002/pros.20969

Patra S, Bera S, SinhaRoy S, Ghoshal S, Ray S, Basu A, Schlattner U, Wallimann T, Ray M (2008) Progressive decrease of phosphocreatine, creatine and creatine kinase in skeletal muscle upon transformation to sarcoma. FEBS J 275(12):3236–3247. https://doi.org/10.1111/j.1742-4658.2008.06475.x

Pavon MA, Parreno M, Tellez-Gabriel M, Leon X, Arroyo-Solera I, Lopez M, Cespedes MV, Casanova I, Gallardo A, Lopez-Pousa A, Mangues MA, Quer M, Barnadas A, Mangues R (2016) CKMT1 and NCOA1 expression as a predictor of clinical outcome in patients with advanced-stage head and neck squamous cell carcinoma. Head Neck 38(Suppl 1):E1392–E1403. https://doi.org/10.1002/hed.24232

Payne RM, Haas RC, Strauss AW (1991) Structural characterization and tissue-specific expression of the mRNAs encoding isoenzymes from two rat mitochondrial creatine kinase genes. Biochim Biophys Acta 1089(3):352–361

Pebay-Peyroula E, Dahout-Gonzalez C, Kahn R, Trezeguet V, Lauquin GJ, Brandolin G (2003) Structure of mitochondrial ADP/ATP carrier in complex with carboxyatractyloside. Nature 426(6962):39–44. https://doi.org/10.1038/nature02056

Perry CG, Kane DA, Herbst EA, Mukai K, Lark DS, Wright DC, Heigenhauser GJ, Neufer PD, Spriet LL, Holloway GP (2012) Mitochondrial creatine kinase activity and phosphate shuttling are acutely regulated by exercise in human skeletal muscle. J Physiol 590(21):5475–5486. https://doi.org/10.1113/jphysiol.2012.234682

Peterzan MA, Lygate CA, Neubauer S, Rider O (2017) Metabolic remodelling in hypertrophied and failing myocardium: a review. Am J Physiol Heart Circ Physiol 00731:02016. https://doi.org/10.1152/ajpheart.00731.2016

Planas-Iglesias J, Dwarakanath H, Mohammadyani D, Yanamala N, Kagan VE, Klein-Seetharaman J (2015) Cardiolipin interactions with proteins. Biophys J 109(6):1282–1294. https://doi.org/10.1016/j.bpj.2015.07.034

Pruett PS, Azzi A, Clark SA, Yousef MS, Gattis JL, Somasundaram T, Ellington WR, Chapman MS (2003) The putative catalytic bases have, at most, an accessory role in the mechanism of arginine kinase. J Biol Chem 278(29):26952–26957. https://doi.org/10.1074/jbc.M212931200

Qian XL, Li YQ, Gu F, Liu FF, Li WD, Zhang XM, Fu L (2012) Overexpression of ubiquitous mitochondrial creatine kinase (uMtCK) accelerates tumor growth by inhibiting apoptosis of breast cancer cells and is associated with a poor prognosis in breast cancer patients. Biochem Biophys Res Commun 427(1):60–66. https://doi.org/10.1016/j.bbrc.2012.08.147

Qin W, Khuchua Z, Cheng J, Boero J, Payne RM, Strauss AW (1998) Molecular characterization of the creatine kinases and some historical perspectives. Mol Cell Biochem 184(1–2):153–167

Rao JK, Bujacz G, Wlodawer A (1998) Crystal structure of rabbit muscle creatine kinase. FEBS Lett 439(1–2):133–137

Rosevear PR, Desmeules P, Kenyon GL, Mildvan AS (1981) Nuclear magnetic resonance studies of the role of histidine residues at the active site of rabbit muscle creatine kinase. Biochemistry 20(21):6155–6164

Rostovtseva TK, Bezrukov SM (2012) VDAC inhibition by tubulin and its physiological implications. Biochim Biophys Acta 1818(6):1526–1535. https://doi.org/10.1016/j.bbamem.2011.11.004

Rostovtseva TK, Sheldon KL, Hassanzadeh E, Monge C, Saks V, Bezrukov SM, Sackett DL (2008) Tubulin binding blocks mitochondrial voltage-dependent anion channel and regulates respiration. Proc Natl Acad Sci U S A 105(48):18746–18751. https://doi.org/10.1073/pnas.0806303105

Rostovtseva TK, Gurnev PA, Chen MY, Bezrukov SM (2012) Membrane lipid composition regulates tubulin interaction with mitochondrial voltage-dependent anion channel. J Biol Chem 287(35):29589–29598. https://doi.org/10.1074/jbc.M112.378778

Rostovtseva TK, Gurnev PA, Protchenko O, Hoogerheide DP, Yap TL, Philpott CC, Lee JC, Bezrukov SM (2015) Alpha-Synuclein shows high affinity interaction with voltage-dependent anion channel, suggesting mechanisms of mitochondrial regulation and toxicity in Parkinson disease. J Biol Chem 290(30):18467–18477. https://doi.org/10.1074/jbc.M115.641746

Saenger AK, Jaffe AS (2008) Requiem for a heavyweight: the demise of creatine kinase-MB. Circulation 118(21):2200–2206. https://doi.org/10.1161/CIRCULATIONAHA.108.773218

Saks VA, Khuchua ZA, Kuznetsov AV (1987) Specific inhibition of ATP-ADP translocase in cardiac mitoplasts by antibodies against mitochondrial creatine kinase. Biochim Biophys Acta 891(2):138–144

Saks VA, Kuznetsov AV, Khuchua ZA, Vasilyeva EV, Belikova JO, Kesvatera T, Tiivel T (1995) Control of cellular respiration in vivo by mitochondrial outer membrane and by creatine kinase. A new speculative hypothesis: possible involvement of mitochondrial-cytoskeleton interactions. J Mol Cell Cardiol 27(1):625–645

Saks VA, Kaambre T, Sikk P, Eimre M, Orlova E, Paju K, Piirsoo A, Appaix F, Kay L, Regitz-Zagrosek V, Fleck E, Seppet E (2001) Intracellular energetic units in red muscle cells. Biochem J 356(Pt 2):643–657

Saks V, Dzeja P, Schlattner U, Vendelin M, Terzic A, Wallimann T (2006) Cardiac system bioenergetics: metabolic basis of the Frank-Starling law. J Physiol 571(Pt 2):253–273. https://doi.org/10.1113/jphysiol.2005.101444

Saks V, Kaambre T, Guzun R, Anmann T, Sikk P, Schlattner U, Wallimann T, Aliev M, Vendelin M (2007) The creatine kinase phosphotransfer network: thermodynamic and kinetic considerations, the impact of the mitochondrial outer membrane and modelling approaches. Subcell Biochem 46:27–65

Saks V, Kuznetsov AV, Gonzalez-Granillo M, Tepp K, Timohhina N, Karu-Varikmaa M, Kaambre T, Dos Santos P, Boucher F, Guzun R (2012) Intracellular energetic units regulate metabolism in cardiac cells. J Mol Cell Cardiol 52(2):419–436. https://doi.org/10.1016/j.yjmcc.2011.07.015

Schlame M, Augustin W (1985) Association of creatine kinase with rat heart mitochondria: high and low affinity binding sites and the involvement of phospholipids. Biomed Biochim Acta 44(7–8):1083–1088

Schlattner U, Wallimann T (2000a) Octamers of mitochondrial creatine kinase isoenzymes differ in stability and membrane binding. J Biol Chem 275(23):17314–17320

Schlattner U, Wallimann T (2000b) A quantitative approach to membrane binding of human ubiquitous mitochondrial creatine kinase using surface plasmon resonance. J Bioenerg Biomembr 32(1):123–131

Schlattner U, Wallimann T (2013) Metabolite channeling. In: Lennarz WJ, Lane MD (eds) Encyclopedia of biological chemistry, 2nd edn. Academic Press, New York, pp 80–85

Schlattner U, Forstner M, Eder M, Stachowiak O, Fritz-Wolf K, Wallimann T (1998) Functional aspects of the X-ray structure of mitochondrial creatine kinase: a molecular physiology approach. Mol Cell Biochem 184(1–2):125–140

Schlattner U, Eder M, Dolder M, Khuchua ZA, Strauss AW, Wallimann T (2000) Divergent enzyme kinetics and structural properties of the two human mitochondrial creatine kinase isoenzymes. Biol Chem 381(11):1063–1070

Schlattner U, Dolder M, Wallimann T, Tokarska-Schlattner M (2001) Mitochondrial creatine kinase and mitochondrial outer membrane porin show a direct interaction that is modulated by calcium. J Biol Chem 276(51):48027–48030

Schlattner U, Gehring F, Vernoux N, Tokarska-Schlattner M, Neumann D, Marcillat O, Vial C, Wallimann T (2004) C-terminal lysines determine phospholipid interaction of sarcomeric mitochondrial creatine kinase. J Biol Chem 279(23):24334–24342

Schlattner U, Tokarska-Schlattner M, Wallimann T (2006a) Mitochondrial creatine kinase in human health and disease. Biochim Biophys Acta 1762(2):164–180

Schlattner U, Tokarska-Schlattner M, Wallimann T (2006b) Molecular structure and function of mitochondrial creatine kinases. In: Vial C (ed) Creatine kinase. Nova Science Publishers, New York, pp 123–170

Schlattner U, Tokarska-Schlattner M, Ramirez S, Bruckner A, Kay L, Polge C, Epand RF, Lee RM, Lacombe ML, Epand RM (2009) Mitochondrial kinases and their molecular interaction with cardiolipin. Biochim Biophys Acta 1788(10):2032–2047. https://doi.org/10.1016/j.bbamem.2009.04.018

Schlattner U, Tokarska-Schlattner M, Ramirez S, Tyurina YY, Amoscato AA, Mohammadyani D, Huang Z, Jiang J, Yanamala N, Seffouh A, Boissan M, Epand RF, Epand RM, Klein-Seetharaman J, Lacombe ML, Kagan VE (2013) Dual function of mitochondrial Nm23-H4 protein in phosphotransfer and intermembrane lipid transfer: a cardiolipin-dependent switch. J Biol Chem 288(1):111–121. https://doi.org/10.1074/jbc.M112.408633

Schlattner U, Klaus A, Ramirez Rios S, Guzun R, Kay L, Tokarska-Schlattner M (2016) Cellular compartmentation of energy metabolism: creatine kinase microcompartments and recruitment of B-type creatine kinase to specific subcellular sites. Amino Acids 48(8):1751–1774. https://doi.org/10.1007/s00726-016-2267-3

Schlegel J, Zurbriggen B, Wegmann G, Wyss M, Eppenberger HM, Wallimann T (1988) Native mitochondrial creatine kinase forms octameric structures. I. Isolation of two interconvertible mitochondrial creatine kinase forms, dimeric and octameric mitochondrial creatine kinase: characterization, localization, and structure-function relationships. J Biol Chem 263(32):16942–16953

Schmid H, Muhlbayer D, Roling J, Sternfeld T, Julg B, Schlattner U, Nelson PJ, Bogner JR, Wallimann T, Goebel FD (2006) Macroenzyme creatine kinase (CK) type 2 in HIV-infected patients is significantly associated with TDF and consists of ubiquitous mitochondrial CK. Antivir Ther 11(8):1071–1080

Schmid H, Tokarska-Schlattner M, Fuessl B, Roder M, Kay L, Attia S, Lederer SR, Goebel FD, Schlattner U, Bogner JR (2013) Macro CK2 accumulation in tenofovir-treated HIV patients is facilitated by CK oligomer stabilization but is not predictive for pathology. Antivir Ther 18(2):193–204. https://doi.org/10.3851/IMP2313

Schnyder T, Gross H, Winkler H, Eppenberger HM, Wallimann T (1991) Structure of the mitochondrial creatine kinase octamer: high-resolution shadowing and image averaging of single molecules and formation of linear filaments under specific staining conditions. J Cell Biol 112(1):95–101

Schredelseker J, Paz A, Lopez CJ, Altenbach C, Leung CS, Drexler MK, Chen JN, Hubbell WL, Abramson J (2014) High resolution structure and double electron-electron resonance of the zebrafish voltage-dependent anion channel 2 reveal an oligomeric population. J Biol Chem 289(18):12566–12577. https://doi.org/10.1074/jbc.M113.497438

Seppet EK, Eimre M, Anmann T, Seppet E, Peet N, Kaambre T, Paju K, Piirsoo A, Kuznetsov AV, Vendelin M, Gellerich FN, Zierz S, Saks VA (2005) Intracellular energetic units in healthy and diseased hearts. Exp Clin Cardiol 10(3):173–183

Sheldon KL, Maldonado EN, Lemasters JJ, Rostovtseva TK, Bezrukov SM (2011) Phosphorylation of voltage-dependent anion channel by serine/threonine kinases governs its interaction with tubulin. PLoS One 6(10):e25539. https://doi.org/10.1371/journal.pone.0025539

Shi YC, Lau J, Lin Z, Zhang H, Zhai L, Sperk G, Heilbronn R, Mietzsch M, Weger S, Huang XF, Enriquez RF, Baldock PA, Zhang L, Sainsbury A, Herzog H, Lin S (2013) Arcuate NPY controls sympathetic output and BAT function via a relay of tyrosine hydroxylase neurons in the PVN. Cell Metab 17(2):236–248. https://doi.org/10.1016/j.cmet.2013.01.006

Shin JB, Streijger F, Beynon A, Peters T, Gadzala L, McMillen D, Bystrom C, Van der Zee CE, Wallimann T, Gillespie PG (2007) Hair bundles are specialized for ATP delivery via creatine kinase. Neuron 53(3):371–386. https://doi.org/10.1016/j.neuron.2006.12.021

Shoshan-Barmatz V, Krelin Y, Shteinfer-Kuzmine A (2017) VDAC1 functions in $Ca^{2+}$ homeostasis and cell life and death in health and disease. Cell Calcium. https://doi.org/10.1016/j.ceca.2017.06.007

Simson P, Jepihhina N, Laasmaa M, Peterson P, Birkedal R, Vendelin M (2016) Restricted ADP movement in cardiomyocytes: cytosolic diffusion obstacles are complemented with a small number of open mitochondrial voltage-dependent anion channels. J Mol Cell Cardiol 97:197–203. https://doi.org/10.1016/j.yjmcc.2016.04.012

Soboll S, Brdiczka D, Jahnke D, Schmidt A, Schlattner U, Wendt S, Wyss M, Wallimann T (1999) Octamer-dimer transitions of mitochondrial creatine kinase in heart disease. J Mol Cell Cardiol 31(4):857–866. https://doi.org/10.1006/jmcc.1998.0925

Sona S, Suzuki T, Ellington WR (2004) Cloning and expression of mitochondrial and protoflagellar creatine kinases from a marine sponge: implications for the origin of intracellular energy transport systems. Biochem Biophys Res Commun 317(4):1207–1214. https://doi.org/10.1016/j.bbrc.2004.03.176

Soroida Y, Ohkawa R, Nakagawa H, Satoh Y, Yoshida H, Kinoshita H, Tateishi R, Masuzaki R, Enooku K, Shiina S, Sato T, Obi S, Hoshino T, Nagatomo R, Okubo S, Yokota H, Koike K, Yatomi Y, Ikeda H (2012) Increased activity of serum mitochondrial isoenzyme of creatine kinase in hepatocellular carcinoma patients predominantly with recurrence. J Hepatol 57(2):330–336. https://doi.org/10.1016/j.jhep.2012.03.012

Speer O, Back N, Buerklen T, Brdiczka D, Koretsky A, Wallimann T, Eriksson O (2005) Octameric mitochondrial creatine kinase induces and stabilizes contact sites between the inner and outer membrane. Biochem J 385(Pt 2):445–450

Spindler M, Niebler R, Remkes H, Horn M, Lanz T, Neubauer S (2002) Mitochondrial creatine kinase is critically necessary for normal myocardial high-energy phosphate metabolism. Am J Physiol Heart Circ Physiol 283(2):H680–H687. https://doi.org/10.1152/ajpheart.00800.2001

Spindler M, Meyer K, Stromer H, Leupold A, Boehm E, Wagner H, Neubauer S (2004) Creatine kinase-deficient hearts exhibit increased susceptibility to ischemia-reperfusion injury and impaired calcium homeostasis. Am J Physiol Heart Circ Physiol 287(3):H1039–H1045. https://doi.org/10.1152/ajpheart.01016.2003

Stachowiak O, Dolder M, Wallimann T (1996) Membrane-binding and lipid vesicle cross-linking kinetics of the mitochondrial creatine kinase octamer. Biochemistry 35(48):15522–15528. https://doi.org/10.1021/bi961838v

Stachowiak O, Schlattner U, Dolder M, Wallimann T (1998) Oligomeric state and membrane binding behaviour of creatine kinase isoenzymes: implications for cellular function and mitochondrial structure. Mol Cell Biochem 184(1–2):141–151

Stadhouders AM, Jap PH, Winkler HP, Eppenberger HM, Wallimann T (1994) Mitochondrial creatine kinase: a major constituent of pathological inclusions seen in mitochondrial myopathies. Proc Natl Acad Sci U S A 91(11):5089–5093

Steeghs K, Benders A, Oerlemans F, de Haan A, Heerschap A, Ruitenbeek W, Jost C, van Deursen J, Perryman B, Pette D, Bruckwilder M, Koudijs J, Jap P, Veerkamp J, Wieringa B (1997) Altered $Ca^{2+}$ responses in muscles with combined mitochondrial and cytosolic creatine kinase deficiencies. Cell 89(1):93–103

Stockler S, Schutz PW, Salomons GS (2007) Cerebral creatine deficiency syndromes: clinical aspects, treatment and pathophysiology. Subcell Biochem 46:149–166

Stolz M, Hornemann T, Schlattner U, Wallimann T (2002) Mutation of conserved active-site threonine residues in creatine kinase affects autophosphorylation and enzyme kinetics. Biochem J 363(Pt 3):785–792

Streijger F, Jost CR, Oerlemans F, Ellenbroek BA, Cools AR, Wieringa B, Van der Zee CE (2004) Mice lacking the UbCKmit isoform of creatine kinase reveal slower spatial learning acquisition, diminished exploration and habituation, and reduced acoustic startle reflex responses. Mol Cell Biochem 256–257(1–2):305–318

Streijger F, Oerlemans F, Ellenbroek BA, Jost CR, Wieringa B, Van der Zee CE (2005) Structural and behavioural consequences of double deficiency for creatine kinases BCK and UbCKmit. Behav Brain Res 157(2):219–234. https://doi.org/10.1016/j.bbr.2004.07.002

Streijger F, Pluk H, Oerlemans F, Beckers G, Bianco AC, Ribeiro MO, Wieringa B, Van der Zee CE (2009) Mice lacking brain-type creatine kinase activity show defective thermoregulation. Physiol Behav 97(1):76–86. https://doi.org/10.1016/j.physbeh.2009.02.003

Streijger F, Scheenen WJ, van Luijtelaar G, Oerlemans F, Wieringa B, Van der Zee CE (2010) Complete brain-type creatine kinase deficiency in mice blocks seizure activity and affects intracellular calcium kinetics. Epilepsia 51(1):79–88. https://doi.org/10.1111/j.1528-1167.2009.02182.x

Stroud RM (1996) Balancing ATP in the cell. Nat Struct Biol 3(7):567–569

Svensson PA, Jernas M, Sjoholm K, Hoffmann JM, Nilsson BE, Hansson M, Carlsson LM (2011) Gene expression in human brown adipose tissue. Int J Mol Med 27(2):227–232. https://doi.org/10.3892/ijmm.2010.566

Tamir Y, Bengal E (1998) p53 protein is activated during muscle differentiation and participates with MyoD in the transcription of muscle creatine kinase gene. Oncogene 17(3):347–356. https://doi.org/10.1038/sj.onc.1201929

Tanaka K, Uda K, Shimada M, Takahashi K, Gamou S, Ellington WR, Suzuki T (2007) Evolution of the cytoplasmic and mitochondrial phosphagen kinases unique to annelid groups. J Mol Evol 65(5):616–625. https://doi.org/10.1007/s00239-007-9046-4

Tisi D, Bax B, Loew A (2001) The three-dimensional structure of cytosolic bovine retinal creatine kinase. Acta Crystallogr D Biol Crystallogr 57(Pt 2):187–193

Tokarska-Schlattner M, Wallimann T, Schlattner U (2002) Multiple interference of anthracyclines with mitochondrial creatine kinases: preferential damage of the cardiac isoenzyme and its implications for drug cardiotoxicity. Mol Pharmacol 61(3):516–523

Tokarska-Schlattner M, Zaugg M, da Silva R, Lucchinetti E, Schaub MC, Wallimann T, Schlattner U (2005) Acute toxicity of doxorubicin on isolated perfused heart: response of kinases regulating energy supply. Am J Physiol Heart Circ Physiol 289(1):H37–H47. https://doi.org/10.1152/ajpheart.01057.2004

Tokarska-Schlattner M, Zaugg M, Zuppinger C, Wallimann T, Schlattner U (2006) New insights into doxorubicin-induced cardiotoxicity: the critical role of cellular energetics. J Mol Cell Cardiol 41(3):389–405. https://doi.org/10.1016/j.yjmcc.2006.06.009

Tokarska-Schlattner M, Dolder M, Gerber I, Speer O, Wallimann T, Schlattner U (2007) Reduced creatine-stimulated respiration in doxorubicin challenged mitochondria: particular sensitivity of the heart. Biochim Biophys Acta 1767(11):1276–1284. https://doi.org/10.1016/j.bbabio.2007.08.006

Tokarska-Schlattner M, Boissan M, Munier A, Borot C, Mailleau C, Speer O, Schlattner U, Lacombe ML (2008) The nucleoside diphosphate kinase D (NM23-H4) binds the inner mitochondrial membrane with high affinity to cardiolipin and couples nucleotide transfer with respiration. J Biol Chem 283(38):26198–26207. https://doi.org/10.1074/jbc.M803132200

Tseng LC, Zhang C, Cheng CM, Xu H, Hsu CH, Jiang YJ (2014) New classes of mind bomb-interacting proteins identified from yeast two-hybrid screens. PLoS One 9(4):e93394. https://doi.org/10.1371/journal.pone.0093394

Ujwal R, Cascio D, Colletier JP, Faham S, Zhang J, Toro L, Ping P, Abramson J (2008) The crystal structure of mouse VDAC1 at 2.3 a resolution reveals mechanistic insights into metabolite gating. Proc Natl Acad Sci U S A 105(46):17742–17747. https://doi.org/10.1073/pnas.0809634105

Uranbileg B, Enooku K, Soroida Y, Ohkawa R, Kudo Y, Nakagawa H, Tateishi R, Yoshida H, Shinzawa S, Moriya K, Ohtomo N, Nishikawa T, Inoue Y, Tomiya T, Kojima S, Matsuura T, Koike K, Yatomi Y, Ikeda H (2014) High ubiquitous mitochondrial creatine kinase expression in hepatocellular carcinoma denotes a poor prognosis with highly malignant potential. Int J Cancer 134(9):2189–2198. https://doi.org/10.1002/ijc.28547

Vacheron MJ, Clottes E, Chautard C, Vial C (1997) Mitochondrial creatine kinase interaction with phospholipid vesicles. Arch Biochem Biophys 344(2):316–324. https://doi.org/10.1006/abbi.1997.0181

Van der Zee CE (2013) Hypothalamic plasticity of neuropeptide Y is lacking in brain-type creatine kinase double knockout mice with defective thermoregulation. Eur J Pharmacol 719(1–3):137–144. https://doi.org/10.1016/j.ejphar.2013.07.027

Varikmaa M, Bagur R, Kaambre T, Grichine A, Timohhina N, Tepp K, Shevchuk I, Chekulayev V, Metsis M, Boucher F, Saks V, Kuznetsov AV, Guzun R (2014) Role of mitochondria-cytoskeleton interactions in respiration regulation and mitochondrial organization in striated muscles. Biochim Biophys Acta 1837(2):232–245. https://doi.org/10.1016/j.bbabio.2013.10.011

Vernoux N, Granjon T, Marcillat O, Besson F, Vial C (2006) Interfacial behavior of cytoplasmic and mitochondrial creatine kinase oligomeric states. Biopolymers 81(4):270–281. https://doi.org/10.1002/bip.20412

Vernoux N, Maniti O, Marcillat O, Vial C, Granjon T (2009) Mitochondrial creatine kinase interaction with heterogeneous monolayers: effect on lipid lateral organization. Biochimie 91(6):752–764. https://doi.org/10.1016/j.biochi.2009.03.014

Wallimann T (2015) The extended, dynamic mitochondrial reticulum in skeletal muscle and the creatine kinase (CK)/phosphocreatine (PCr) shuttle are working hand in hand for optimal energy provision. J Muscle Res Cell Motil 36(4–5):297–300. https://doi.org/10.1007/s10974-015-9427-z

Wallimann T, Harris R (2016) Creatine: a miserable life without it. Amino Acids 48(8):1739–1750. https://doi.org/10.1007/s00726-016-2297-x

Wallimann T, Wyss M, Brdiczka D, Nicolay K, Eppenberger HM (1992) Intracellular compartmentation, structure and function of creatine kinase isoenzymes in tissues with high and fluctuating energy demands: the 'phosphocreatine circuit' for cellular energy homeostasis. Biochem J 281(Pt 1):21–40

Wallimann T, Tokarska-Schlattner M, Schlattner U (2011) The creatine kinase system and pleiotropic effects of creatine. Amino Acids 40(5):1271–1296. https://doi.org/10.1007/s00726-011-0877-3

Wan C, Borgeson B, Phanse S, Tu F, Drew K, Clark G, Xiong X, Kagan O, Kwan J, Bezginov A, Chessman K, Pal S, Cromar G, Papoulas O, Ni Z, Boutz DR, Stoilova S, Havugimana PC, Guo X, Malty RH, Sarov M, Greenblatt J, Babu M, Derry WB, Tillier ER, Wallingford JB, Parkinson J, Marcotte EM, Emili A (2015) Panorama of ancient metazoan macromolecular complexes. Nature 525(7569):339–344. https://doi.org/10.1038/nature14877

Wang XC, Zhou HM, Wang ZX, Tsou CL (1990) Is the subunit the minimal function unit of creatine kinase? Biochim Biophys Acta 1039(3):313–317

Wang PF, McLeish MJ, Kneen MM, Lee G, Kenyon GL (2001) An unusually low pK(a) for Cys282 in the active site of human muscle creatine kinase. Biochemistry 40(39):11698–11705

Watanabe D, Yoshino M, Yagura H, Hirota K, Yonemoto H, Bando H, Yajima K, Koizumi Y, Otera H, Tominari S, Nishida Y, Kuwahara T, Uehira T, Shirasaka T (2012) Increase in serum mitochondrial creatine kinase levels induced by tenofovir administration. J Infect Chemother 18(5):675–682. https://doi.org/10.1007/s10156-012-0393-8

Wendt S, Schlattner U, Wallimann T (2003) Differential effects of peroxynitrite on human mitochondrial creatine kinase isoenzymes. Inactivation, octamer destabilization, and identification of involved residues. J Biol Chem 278(2):1125–1130. https://doi.org/10.1074/jbc.M208572200

Wyss M, Smeitink J, Wevers RA, Wallimann T (1992) Mitochondrial creatine kinase: a key enzyme of aerobic energy metabolism. Biochim Biophys Acta 1102(2):119–166

Wyss M, James P, Schlegel J, Wallimann T (1993) Limited proteolysis of creatine kinase. Implications for three-dimensional structure and for conformational substrates. Biochemistry 32(40):10727–10735

Yan YB (2016) Creatine kinase in cell cycle regulation and cancer. Amino Acids 48(8):1775–1784. https://doi.org/10.1007/s00726-016-2217-0

Yang L, Vaitheesvaran B, Hartil K, Robinson AJ, Hoopmann MR, Eng JK, Kurland IJ, Bruce JE (2011) The fasted/fed mouse metabolic acetylome: N6-acetylation differences suggest acetylation coordinates organ-specific fuel switching. J Proteome Res 10(9):4134–4149. https://doi.org/10.1021/pr200313x

Ydfors M, Hughes MC, Laham R, Schlattner U, Norrbom J, Perry CG (2016) Modelling in vivo creatine/phosphocreatine in vitro reveals divergent adaptations in human muscle mitochondrial respiratory control by ADP after acute and chronic exercise. J Physiol 594(11):3127–3140. https://doi.org/10.1113/JP271259

Yousef MS, Fabiola F, Gattis JL, Somasundaram T, Chapman MS (2002) Refinement of the arginine kinase transition-state analogue complex at 1.2 a resolution: mechanistic insights. Acta Crystallogr D Biol Crystallogr 58(Pt 12):2009–2017

Yousef MS, Clark SA, Pruett PK, Somasundaram T, Ellington WR, Chapman MS (2003) Induced fit in guanidino kinases--comparison of substrate-free and transition state analog structures of arginine kinase. Protein Sci 12(1):103–111. https://doi.org/10.1110/ps.0226303

Zala D, Schlattner U, Desvignes T, Bobe J, Roux A, Chavrier P, Boissan M (2017) The advantage of channeling nucleotides for very processive functions. F1000Res 6:724. https://doi.org/10.12688/f1000research.11561.1

Zeng GQ, Zhang PF, Deng X, Yu FL, Li C, Xu Y, Yi H, Li MY, Hu R, Zuo JH, Li XH, Wan XX, Qu JQ, He QY, Li JH, Ye X, Chen Y, Li JY, Xiao ZQ (2012) Identification of candidate biomarkers for early detection of human lung squamous cell cancer by quantitative proteomics. Mol Cell Proteomics 11(6):M111 013946. https://doi.org/10.1074/mcp.M111.013946

Zervou S, Yin X, Nabeebaccus AA, O'Brien BA, Cross RL, McAndrew DJ, Atkinson RA, Eykyn TR, Mayr M, Neubauer S, Lygate CA (2016) Proteomic and metabolomic changes driven by elevating myocardial creatine suggest novel metabolic feedback mechanisms. Amino Acids 48(8):1969–1981. https://doi.org/10.1007/s00726-016-2236-x

Zhang Y, Malekpour M, Al-Madani N, Kahrizi K, Zanganeh M, Lohr NJ, Mohseni M, Mojahedi F, Daneshi A, Najmabadi H, Smith RJ (2007) Sensorineural deafness and male infertility: a contiguous gene deletion syndrome. J Med Genet 44(4):233–240. https://doi.org/10.1136/jmg.2006.045765

Zhao J, Schmieg FI, Simmons DT, Molloy GR (1994) Mouse p53 represses the rat brain creatine kinase gene but activates the rat muscle creatine kinase gene. Mol Cell Biol 14(12):8483–8492

Zhao TJ, Yan YB, Liu Y, Zhou HM (2007) The generation of the oxidized form of creatine kinase is a negative regulation on muscle creatine kinase. J Biol Chem 282(16):12022–12029. https://doi.org/10.1074/jbc.M610363200

Zhou G, Somasundaram T, Blanc E, Parthasarathy G, Ellington WR, Chapman MS (1998) Transition state structure of arginine kinase: implications for catalysis of bimolecular reactions. Proc Natl Acad Sci U S A 95(15):8449–8454

# Chapter 14
# The Vacuolar ATPase – A Nano-scale Motor That Drives Cell Biology


**Michael A. Harrison and Steven P. Muench**

**Abstract** The vacuolar $H^+$-ATPase (V-ATPase) is a ~1 MDa membrane protein complex that couples the hydrolysis of cytosolic ATP to the transmembrane movement of protons. In essentially all eukaryotic cells, this acid pumping function plays critical roles in the acidification of endosomal/lysosomal compartments and hence in transport, recycling and degradative pathways. It is also important in acid extrusion across the plasma membrane of some cells, contributing to homeostatic control of cytoplasmic pH and maintenance of appropriate extracellular acidity. The complex, assembled from up to 30 individual polypeptides, operates as a molecular motor with rotary mechanics. Historically, structural inferences about the eukaryotic V-ATPase and its subunits have been made by comparison to the structures of bacterial homologues. However, more recently, we have developed a much better understanding of the complete structure of the eukaryotic complex, in particular through advances in cryo-electron microscopy. This chapter explores these recent developments, and examines what they now reveal about the catalytic mechanism of this essential proton pump and how its activity might be regulated in response to cellular signals.

**Keywords** Vacuolar H+-ATPase (V-ATPase) · Acidification · Proton pump · Cryo-electron microscopy · Endosomal compartment · Lysosomal compartment · Molecular motor

M. A. Harrison (✉) · S. P. Muench
School of Biomedical Sciences, Faculty of Biological Sciences, The University of Leeds, Leeds, UK
e-mail: m.a.harrison@leeds.ac.uk; s.p.muench@leeds.ac.uk



J. R. Harris, E. J. Boekema (eds.), *Membrane Protein Complexes: Structure and Function*, Subcellular Biochemistry 87,
https://doi.org/10.1007/978-981-10-7757-9_14

## 14.1 The V-ATPase Plays a Central Role in Eukaryotic Cell Physiology

The vacuolar ATPases are membrane-bound protein complexes that use the free energy released when ATP is hydrolysed to drive the transmembrane movement of protons. They can therefore be described essentially as ATP-driven acid pumps. The name originates from their discovery in the membranes surrounding the vacuolar compartments found within yeast and plant cells, but now also describes pumps found in the endomembranes of essentially all eukaryotic cells. Despite the 'vacuolar' designation, V-ATPase can also play physiologically critical roles at the plasma membrane of some cells. Assembling a V-ATPase requires as many as 30 individual polypeptide subunits encoded by up to 14 different genes, with many subunits also represented as multiple isoforms and splice variants. Underlining the diverse but critical roles of the V-ATPase in cell physiology, mutations in many of the subunit-encoding genes lead to pathology: osteopetrosis, distal renal tubule acidosis, forms of hereditary deafness and the disease cutix laxa are all associated with loss of V-ATPase activity. The discussion below provides only the most superficial overview of V-ATPase function in eukaryotic cells. For greater in-depth analysis, the reader is directed to some of the excellent recent reviews that examine the cell biology (Maxson and Grinstein 2014), structure/function (Marshansky et al. 2014) and physiological roles of the V-ATPase (Breton and Brown 2013) in much greater detail than can be covered here.

The V-ATPase belongs to a family of membrane protein complexes that operate as rotary molecular motors for the purpose of energy transformation. This family includes the $F_1F_o$-ATPase, or ATP synthase, that couples proton motive force to ATP synthesis and the A-ATPases that act as ATP synthases in archaea. It also includes eubacterial 'A-ATPases' that share similarity with the archaeal enzymes but which are, like the eukaryotic V-ATPases, ATP-driven ion pumps. These are sometimes referred to as 'bacterial V-ATPases' or V/A-ATPases. In functional terms, the V-ATPase rotary motor can be divided into two parts, each comprising multiple subunits that move with respect to each other during the catalytic cycle of the complex. The part designated the *stator* includes a motor that converts the free energy of ATP hydrolysis into mechanical movement of a *rotor*. Concerted movement of the rotor (that includes part of the proton pump) relative to a membrane-embedded part of the stator leads to proton movement. Exactly how this process occurs is one of the major unanswered questions in molecular bioenergetics, but with increasingly detailed structural information about the V-ATPase complex, we are moving closer to answering it.

The endomembrane function of the V-ATPase has several facets. The acidic interior of late endosomal/lysosomal compartments generated by the V-ATPase is required for the activity of hydrolases that have a low pH optimum, hence V-ATPase activity supports degradative processes in the cell. Acidification of early and recycling endosomes is required for dissociation of ligand from receptor, the classic example being separation of low density lipoprotein from its plasma membrane

receptor. Recycling of receptor back to the plasma membrane and the consigning of ligand to breakdown in the lysosome are therefore also dependent on V-ATPase activity. In the broader context of membrane transport, distribution from the trans-Golgi network of proteins destined for the lysosome is also V-ATPase dependent, the resulting vesicular acidification being required to trigger dissociation of glycosylated protein from the mannose-6-phosphate receptors. Defective glycosylation in the Golgi as a consequence of V-ATPase dysfunction resulting from natural mutations in genes for V-ATPase subunits also has Acidification of endosomal compartments also plays a role in viral pathogenesis, with release of the viral genetic material into the cytoplasm facilitated by low pH conditions.

One of the first vertebrate V-ATPase activities to be characterised was that found in chromaffin granules of the adrenal medulla. V-ATPase activity in specialised secretory compartments such as this underlines its second major function in endomembranes, supporting the uptake of small molecules into secretory vesicles by secondary active transport. This function is particularly important in the brain, where neurotransmitter loading into synaptic vesicles can be driven either by the proton concentration gradient ($\Delta pH$) or electrical ($\Delta\psi$) components of the electrochemical membrane potential established by the V-ATPase. Proteolytic processing and secretion of peptidic hormones such as insulin also require the acidic conditions generated by the V-ATPase in secretory vesicles, linking V-ATPase dysfunction to disorder such as diabetes mellitus (see (Maxson and Grinstein 2014) and references therein for a more detailed discussion of these topics).

V-ATPases are also found at the plasma membrane of some cell types, where their activity leads to net acid efflux. This may be required for the specialised function of that particular cell, as is the case for bone-resorbing osteoclasts and epididymal clear cells. As part of the natural cycle of bone repair, osteoclasts adhere to bone and form a sealed extracellular compartment (the resorptive lacuna) into which the V-ATPase pumps $H^+$. The resulting acidic conditions contribute to the dissolution of the mineral component of bone and support the activity of proteolytic enzymes that break down its collagenous part. Naturally occurring mutations in the genes for V-ATPase subunits also have implications for this process: loss of V-ATPase activity leads to defects in bone development and remodelling, manifesting as osteopetrosis. V-ATPase activity also has a major role to play in male fertility, generating the low pH in the lumen of the male reproductive tract necessary for sperm maturation. In renal intercalated cells, V-ATPase activity at the apical membrane is an important factor in urinary acidification, contributing to acid-base balance and systemic pH homeostasis. A similar homeostatic function in tumour cells has been proposed, with plasma membrane V-ATPases contributing to the maintenance of a stable cytoplasmic pH even as the cell produces excess organic acids such as lactate as fall-out from high rates of glycolysis in a hypoxic environment. As a side-effect of this process, the low pH around the tumour cell supports proteolytic breakdown of the extracellular matrix, promoting the invasiveness that can lead to formation of secondary metastatic tumours.

It is clear from even an outline description of its functions that the V-ATPase plays a central and fundamental role in eukaryotic cells. Because of this importance,

the complex has continued to stimulate interest as a potential therapeutic target. To fully realise this potential a more complete and detailed understanding of its structure is required, in particular mapping out any changes in conformation that reflect different catalytic states, and any changes that can be correlated with a response to a regulatory signal. The focus of this chapter is on the most recent advances in our understanding of the structure of the eukaryotic V-ATPase, exploring the insights that these advances provide into the processes that control this essential enzyme. Structural biology has made major contributions to our understanding of V-ATPase organisation, in particular through the crystallographic analysis of homologous bacterial ATPase subunits and sub-complexes (see Table 14.1). However, it is electron microscopy that has arguably had the biggest impact in recent years, in particular the use of methods for 3-D reconstruction from 2-D images of single particles. Low resolution models generated using data collected from specimens negatively stained with heavy metals provided the first insights into the architecture of the eukaryotic V-ATPase (Wilkens et al. 1999; Bernal and Stock 2004; Coskun et al. 2004; Diepholz et al. 2008a), but data from cryo-electron microscopy of single particles in their native state in ice are now providing structural information at a resolution rivalling that achievable with x-ray crystallography. Advances in electron microscope instrumentation, in particular the more widespread use of cameras that incorporate direct electron detectors, allow more usable information to be collected before radiation damage occurs. A second key area of development has been in image processing software, with the programme RELION capable of dissecting out related structures with subtly different conformations from a single dataset (see (Bai et al. 2015; Fernandez-Leiro and Scheres 2016) for a discussion of this topic). Because the V-ATPase is a large, dynamic and flexible molecular motor able to adopt a range of conformations as part of its natural catalytic cycle, application of this approach is particularly suited to its analysis. Complete structural models are now emerging that allow not only accurate fitting of crystal structures but are sufficiently well resolved to allow different catalytic states to be seen. In some instances it has also been possible to see the extent to which the conformation of a crystallographic subunit structure differs from that of the same polypeptide integrated into the functional V-ATPase complex. The sections that follow explore these new structural models in detail.

## 14.2 Structure of the V-ATPase

Our earliest understanding of the basic organisation of the V-ATPase stemmed from its fundamental similarity to the much better characterised $F_1F_o$ATPase ('ATP synthase'). A combination of low resolution electron microscopy and protein biochemistry approaches pointed to a similar bi-domain structure, with conditions such as cold shock in the presence of Mg.ATP able to strip the $V_1$ catalytic domain from the membrane. Similar to the situation with F-ATPase, a DCCD-reactive 'proteolipid' component remained in the membrane. Clearly, there are also broad parallels between the two ATPases in terms of their activity: the V-ATPase is essentially the

**Table 14.1** Crystallographic structures of V-ATPase complexes and subunits

| Subunit/ complex | PDB code | Species | Resolution (Å) | Comment | References |
|---|---|---|---|---|---|
| $(AB)_3(EG)_3DFH$ | 5D80 | *S. cerevisiae* | 6.2 | The auto-inhibited yeast $V_1$ domain | Oot et al. (2016) |
| $(AB)_3DF$ | 3A5C | *Th. thermophilus* | 4.51 | Bacterial homologue of $V_1$ with 2 catalytic sites occupied by nucleotide, one site empty | Numoto et al. (2009) |
| $(AB)_3DF$ | 3W3A | *Th. thermophilus* | 3.9 | Bacterial homologue of $V_1$: conformational differences between AB units around 'occupied' and 'empty' catalytic sites implies rigid body rearrangement, not inter-domain movement. | Nagamatsu et al. (2013) |
| $(AB)_3DF$ | 5KNB/C/D | *E. hirae* | 2.89–3.25 | Bacterial $V_1$ homologue in different nucleotide occupancy states correlating with steps in the ATPase catalytic cycle. | Suzuki et al. (2016) |
| $(AB)_3DF$ | 3VR2/3/4/5 | *E. hirae* | 2.17–3.9 | Nucleotide-free and AMP-PNP-bound forms of a bacterial $V_1$ homologue. | Arai et al. (2013) |
| C | 1U7L | *S. cerevisiae* | 1.75 | | Drory et al. (2004) |
| DF | 3AON | *E. hirae* | 2.0 | Bacterial homologue of the rotor shaft heterodimer | Saijo et al. (2011) |
| DF | 4RND | *S. cerevisiae* | 3.18 | Yeast rotor shaft heterodimer | Balakrishna et al. (2015) |
| EG | 3K5B | *Th. thermophilus* | 3.1 | Bacterial homologue of the stator peripheral stalk | Lee et al. (2010) |
| EG | 3V6I | *Th. thermophilus* | 2.25 | | Stewart et al. (2012) |
| $EGC_{head}$ | 4DL0/4EFA | *S. cerevisiae* | 2.82–2.9 | Two forms of a segment of the eukaryotic V-ATPase stator, part of C linked to peripheral stalk S3. | Oot et al. (2012) |

(continued)

**Table 14.1** (continued)

| Subunit/ complex | PDB code | Species | Resolution (Å) | Comment | References |
|---|---|---|---|---|---|
| F | 2D00 | | 2.2 | Bacterial homologue. Two conformations, 'retracted' and 'extended' in the presence of ATP are proposed. | Makyio et al. (2005) |
| H | 1HO8 | *S. cerevisiae* | 2.95 | The first crystal structure of a eukaryotic V-ATPase subunit | Sagermann et al. (2001) |
| $a_{CT}$ | 5TJ5 | *S. cerevisiae* | 3.9 | Computational model based on cryo-EM data | Mazhab-Jafari et al. (2016) |
| $a_{NT}$ | 3RRK | *Meiothermus ruber* | 2.64 | Bacterial homologue of the subunit *a* soluble domain (residues 1-301) | Srinivasan et al. (2011) |
| *c*-ring | 2BL2 | *E. hirae* | 2.1 | Bacterial homologue, the NtpK decameric ring from *E. hirae* | Murata et al. (2005) |
| *d* | 1R5Z | *Th. thermophilus* | 1.95 | Bacterial homologue, previously called subunit C in bacteria | Iwata et al. (2004) |

same as the F-ATPase operating in reverse as an ATP-driven ion pump, and although each ATPase has a distinctive inhibitor sensitivity profile (discussed in Sect. 14.3), fundamentally similar catalytic mechanisms could be inferred. Cloning and sequencing of genes for the V-ATPase (the genetically pliable *Saccharomyces cerevisiae* system has proven particularly useful in this regard) underlined the similarity of many core subunits of the V-ATPase to those of the F-ATPase, hence pointing to shared evolutionary origins (this topic is reviewed in (Nelson 1992)).

Some subunits of the V-ATPase have subsequently proved amenable to expression in bacterial systems, facilitating the solving of their individual structures to high resolution using x-ray crystallography (see Table 14.1). Where detailed structures of V-ATPase components have not been available, the crystallographic structures of bacterial homologues have proven to be very effective surrogates for their eukaryotic counterparts. In parallel with structural biology, biochemical methods aimed at understanding protein-protein interactions in the V-ATPase have provided a map of subunit contacts (see, allowing the 3-D jigsaw puzzle of its fully assembled structure to be pieced together. More recently, 3-D reconstructions from electron microscopy of single V-ATPase particles have provided an insight into the architecture of the complex and provided a framework into which individual high resolution structures can be fitted, with subunit contacts arranged in line with the constraints generated by protein biochemistry experiments. In the last 3 years, with significant

advances in both electron microscope instrumentation and image analysis algorithms, it has been possible to push resolution of these EM-generated models to sub-nanometre levels, to the extent that distinct conformational states indicative of specific steps in the catalytic state of the V-ATPase can now be resolved. In this section, the focus is on how evidence from x-ray crystallography, protein biochemistry and from recent advances in cryo-electron microscopy have converged to provide a detailed, robust and reliable model of the V-ATPase.

### *14.2.1 Overview of the V-ATPase Structure: Domain Architecture and Subunit Arrangement*

The mature, fully active V-ATPase is a ≈ 1 MDa complex containing as many as 30 individual polypeptides assembled from a pool of 12-16 different gene products (Fig. 14.1). The full complex is ≈250 Å along its long axis and projects ≈180 Å from the membrane, giving it the classical 'mushroom' appearance in low resolution electron microscopy images that is similar to early observations of the $F_1F_o$-ATPase (ATP synthase, or F-ATPase) in mitochondrial inner membrane vesicles (Dschida and Bowman 1992). By analogy to F-ATPase, the cytoplasmic and membrane-bound domains of the V-ATPase are referred to as $V_1$ and $V_o$ ("vee-oh"), respectively. The $V_1$ domain that projects into the cytoplasm contains subunits designated A-H in an $A_3B_3CDE_3FG_3H$ stoichiometry. Three copies each of the A and B subunits alternate in a pseudo-hexameric arrangement, with each AB unit forming an ATP-hydrolysing catalytic site. At the centre of $V_1$, the D subunit extends ~140 Å through the $(AB)_3$ complex to contact the integral membrane domain $V_o$ (Fig. 14.1a, c; magenta). This subunit, in association with subunit F attached to its membrane-proximal end (Fig. 14.1a, c; orange), appears in EM images as a central stalk that connects $V_1$ to $V_o$ and can be thought of as the 'axle' of the V-ATPase rotary motor, transmitting rotational movement generated by catalysis to the proton pump that resides in $V_o$. EM-generated 3-D models of the V-ATPase also show the presence of three peripheral stalks ((Zhang et al. 2008; Diepholz et al. 2008a; Muench et al. 2009), shown as S1-S3 in Fig. 14.1a, each of which is a heterodimer of the E and G subunits (Kitagawa et al. 2008). Each E subunit is anchored to the end of a B subunit furthest from the membrane (see Fig. 14.1a, c; cyan) and extends, in combination with subunit G, as an ~150 Å-long helical coiled-coil across the surface of B, finally projecting towards the membrane domain (Fig. 14.1a, c; yellow). The projecting ends of all three EG peripheral stalks connect to a remarkable feature – a horizontal collar that largely surrounds the mid-region of the complex. This feature is unique to the eukaryotic V-ATPase, a much shorter version being found in the bacterial and archaeal A-ATPase that has peripheral stalks equivalent only to S1 and S2 (discussed in (Muench et al. 2011). The collar consists of subunit C that links S2 to S3 (Fig. 14.1a right panel, dark green) and the N-terminal domain of subunit *a* ($a_{NT}$ in Fig. 14.1c; grey), a 100 kDa polypeptide that also constitutes a major part of the

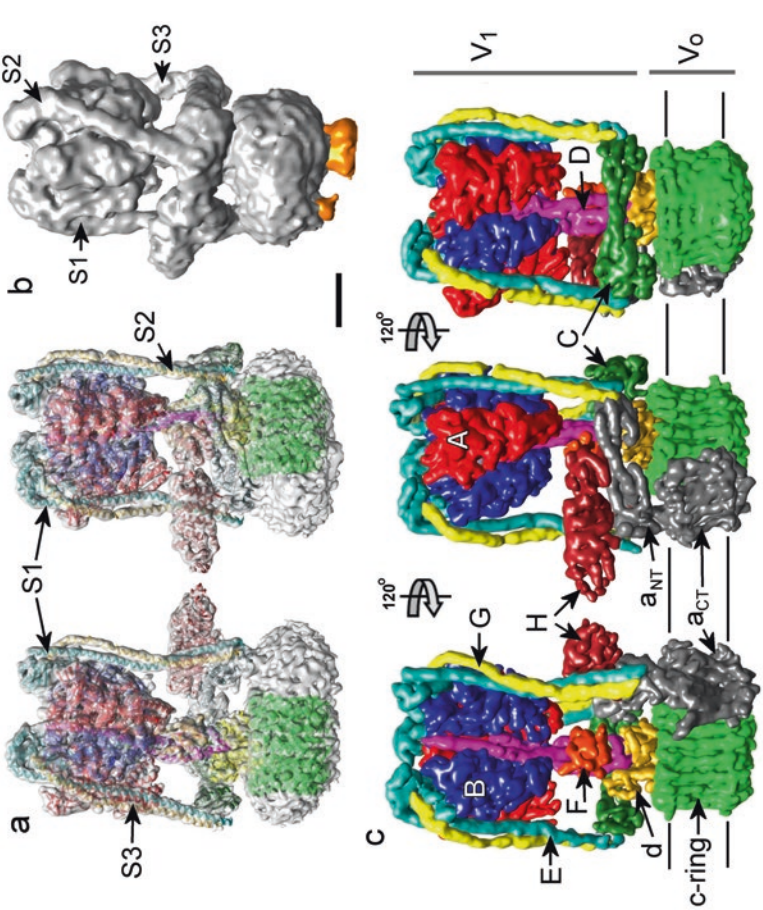


**Fig. 14.1** Macromolecular structure of the V-ATPase. (**a**) Electron density map of the *S. cerevisiae* V-ATPase at 6.9 Å resolution generated by cryo-electron microscopy of single particles (EMD-6284 (Zhao et al. 2015) with crystal structures of individual subunits fitted. The peripheral stalks that constitute part of the stator of the V-ATPase rotary motor are labeled S1-S3. (**b**) Electron density map of the plasma membrane V-ATPase from *Manduca sexta* (EMD-2781) at ~10 Å resolution. Densities observed specifically in the plasma membrane complex are coloured orange. Glycosylation makes a significant contribution to the major density. (**c**) Three views of the segmented map of the *Saccharomyces cerevisiae* V-ATPase The $V_1$ domain contains subunits in a $(AB)_3(EG)_3CDFH$ stoichiometry. $V_o$ contains *a* and *d* subunits and a ring of *c* subunits that in yeast is a 10-mer containing a combination of *c*, *c′* and *c″* subunits. Subunit *a* contains an N-terminal soluble domain ($a_{NT}$) and C-terminal integral membrane domain ($a_{CT}$). Horizontal lines represent approximate limits of the membrane bilayer. In the left-hand image, an A subunit has been removed to reveal the D subunit. Scale bar is 35 Å

membrane domain $V_o$, discussed below. This $a_{NT}$ region links S1 to S2, and also binds the H subunit (Fig. 14.1a, c; brown), a polypeptide that plays a major role in regulating ATPase activity in $V_1$ (discussed in Sect. 14.4).

The C-terminal part of subunit *a* ($a_{CT}$ in Fig. 14.1) is an integral membrane domain involved in proton transport across the membrane, constituting the membrane-embedded end of the stator. Adjacent to $a_{CT}$, $V_o$ also contains a ring of *c* subunits (Fig. 14.1a, c; light green) that, as part of the rotor of the V-ATPase motor, also plays a central role in proton transport (discussed in detail in Section 14.2.3). The *c*-ring in *Saccharomyces* V-ATPase appears to be decameric, based on fitting the four transmembrane helices of each 16 kDa subunit *c* polypeptide into the highest resolution electron density maps from cryo-EM data (Zhao et al. 2015; Mazhab-Jafari et al. 2016). However, subunit *c* from other organisms may form rings with varying stoichiometries, for example in arthropods where it may be hexameric (Clare et al. 2006). The linkage between the *c*-ring and the D subunit is made by the *d* subunit, a polypeptide that adopts a cone-like fold that partially plugs the cavity at the centre of the *c*-ring (Fig. 14.1; gold). In the intact V-ATPase, it projects ≈25 Å from the *c*-ring to make the contact with the foot of the D subunit that is critical in coupling ATP hydrolysis to proton pumping (Fig. 14.1c, right panel). High resolution cryo-EM data for the *Saccharomyces* $V_o$ also show that the central cavity of the c-ring also contains the additional N-terminal helix of the subunit *c* homologue *c*" (Vma16p in *S. cerevisiae*) (Mazhab-Jafari et al. 2016). It is also likely to contain lipid, as detected in the bacterial A-ATPase (Zhou et al. 2011).

V-ATPases that spend time at the plasma membrane, such as the enzyme isolated from the apical membrane of *Manduca sexta* midgut epithelium (Fig. 14.1b) and the enzyme from bovine brain coated vesicles (Wilkens et al. 1999) also show a prominent density in EM-derived images on the extracellular/lumenal side of the *c*-ring (Fig. 14.1b; orange). This density is at least partially a result of glycosylation (Rawson et al. 2015), although it is unclear to which protein component the sugar residues are attached. A potential candidate is the 'accessory protein' Ac45, the product of the atp6ap1 gene in humans that is heavily glycosylated and known to play a role in navigating the V-ATPase to and from the plasma membrane (Jansen et al. 2008; Smith et al. 2016). However, although Ac45 is expressed in some insect species, it has not been identified as a component of the *Manduca* V-ATPase and its location within $V_o$ remains uncertain. A second small integral membrane subunit of $V_o$, the ≈10 kDa *e* subunit (Merzendorfer et al. 1999; Blake-Palmer et al. 2007) is also heavily glycosylated in *Manduca sexta*. However, cryo-EM data indicate that the yeast homologue of this helical hairpin polypeptide (Vma9p) is located at the interface between the membrane and the C-terminal domain of subunit *a*, far away from the centre of the *c*-ring (see Fig. 14.3a) (Mazhab-Jafari et al. 2016). A smaller density projecting on the extracellular side of the $V_o$ region containing $a_{CT}$ in 3-D reconstructions of the *Manduca* V-ATPase could represent the glycosylation carried by this subunit (Fig. 14.1b). Alternatively, it could reflect the glycosylation of $a_{CT}$ itself (Esmail et al. 2017).

Although historically the V-ATPase organisation has been described in terms of $V_1$ soluble and $V_o$ membrane domains, we can now also define its parts in terms of

their contributions to the *stator* and *rotor* functions of this molecular motor. The $(AB)_3$ catalytic hexamer is the ATP-powered torque generator, driving a rotor comprising D, F, *d* and the *c*-ring. The current model of ATP-dependent proton movement requires the relative movement of the *c*-ring with respect to subunit *a* (discussed in Sect. 14.2.3), hence *a* must be fixed to $(AB)_3$ as part of a *stator* structure. This is achieved by connecting $(AB)_3$ to $a_{NT}$ via the three EG peripheral stalks, either directly in the case of S1, at the $a_{NT}$-C junction in the case of S2 or at the end of C for S3 (compare the locations in Fig.14.1a, c). Interesting corollaries of this subunit network is that it must (a) contain sufficiently strong protein-protein contacts to resist the torque generated by the catalytic activity of the complex (assuming some resistance at the $a_{CT}$-*c*-ring interface), whilst (b) being sufficiently flexible to accommodate the significant conformational changes that occur in $V_1$ during the catalytic cycle. These aspects are discussed later in this chapter.

In higher eukaryotes, many of the V-ATPase subunits are encoded by multiple genes, giving rise to distinct subunit isoforms (covered in greater depth than is possible here in (Sun-Wada and Wada 2010; Toei et al. 2010)). Subunits that could be considered to be 'core' to V-ATPase activity, such as A, D, F and *c* are represented by single gene products, whereas others exist as two or more forms. Typically, one ubiquitously expressed isoform predominates in the majority of cells types, with an alternative form expressed at high levels only in particular tissues. The best characterised example of this is the $B_1$ subunit (atp6v1b1), which is highly expressed in kidney, olfactory epithelium and epididymis, the corresponding $B_2$ isoform being ubiquitous. Because of its predominance in renal cells, naturally-occurring mutations in atp6v1b1 can lead to distal renal tubular acidosis (Karet et al. 1999). Similarly, the $C_1$, $E_2$, $G_1$ and $d_1$ isoforms are ubiquitous, whereas their related isoforms are preferentially expressed. $C_2$, $d_2$ and $G_3$ in kidney and epididymis, $E_1$ in testis and olfactory epithelium, $G_2$ in brain (Toei et al. 2010). Whereas the soluble subunits of the vertebrate V-ATPase are represented by only two isoforms (the exception being the three isoform G subunit), there are as many as four subunit *a* isoforms (encoded by the atp6v0a1-4 genes), with diversity further increased by the expression of additional splice variants (Nishi and Forgac 2000; Toyomura et al. 2000; Karet 2005; Toei et al. 2010; Sun-Wada and Wada 2010). Although sequence conservation between these isoforms appears modest at 47–61%, specific regions such as the transmembrane helices directly involved in proton transport (discussed below) show almost complete conservation, and it is most likely that all isoforms share fundamentally similar secondary and tertiary structures.

Particular subunit *a* isoforms are highly expressed in certain cell types. Some variants of the $a_1$ isoform may be ubiquitous, localised to early endosomes and exocytotic vesicles. In tumour cells of epithelial origin, $a_1$ transits through the plasma membrane and recycles through the endosomal system in parallel with the transferrin receptor (Smith et al. 2016). Some $a_1$ variants are however particularly abundant in neuronal and neuroendocrine tissue, where they locate to synaptic and secretory vesicles respectively (Morel et al. 2003; Saw et al. 2011). Intriguingly, the $a_1$ isoform appears to play two quite distinct and different roles in synaptic vesicles. The first is linked to its core function as part of an ATP-driven proton pump, the resulting

proton gradient energising neurotransmitter uptake into vesicles. The second role is in $Ca^{2+}$-regulated vesicle fusion with the plasma membrane via $V_o$ interaction with the SNARE protein synaptobrevin, leading to neurotransmitter release (Hiesinger et al. 2005; Di Giovanni et al. 2010; Wang et al. 2014). A similar membrane fusion function proposed for $V_o$ in *Saccharomyces cerevisiae* (Peters et al. 2001) is disputed, with the process subsequently reported to be dependent only on vesicle acidification and not on the physical presence of the V-ATPase (Coonrod et al. 2013). The $a_2$ isoform has been detected in early endosomes (Hurtado-Lorenzo et al. 2006) and in the Golgi complex (Toyomura et al. 2003; Saw et al. 2011), with mutations in atp6v0a2 causing the glycosylation defects and dysfunctional trafficking that are associated with the disease *cutis laxa* (Kornak et al. 2008). However, this may not be solely an $a_2$-dependent effect, with mutations in atp6v1a and atp6v1e1 also causing *cutis laxa* with varying degrees of severity (Van Damme et al. 2017).

The $a_3$ isoform predominates in late endosomes/lysosomes (Toyomura et al. 2003; Sun-Wada et al. 2009), and is particularly highly expressed in cell types for which the associated degradative function is especially important, such as active osteoclasts and macrophages. In osteoclasts, the $a_3$-containing V-ATPase is recruited to the bone-resorbing 'ruffled border' of the plasma membrane, and in macrophages the same isoform acidifies the maturing phagosome (Toyomura et al. 2003; Sun-Wada et al. 2009). The $a_3$ isoform is also highly expressed in pancreatic β-cells, being found in the membranes of insulin secretory granules (Sun-Wada et al. 2006). The $a_4$ isoform is most highly expressed in renal tissue (Smith et al. 2000; Oka et al. 2001; Breton and Brown 2013), and although the $a_1$, $a_3$ and $a_4$ forms may all feature at the plasma membrane of kidney proximal tubule cells (Hurtado-Lorenzo et al. 2006), it is the V-ATPase containing $a_4$ that appears to be a specialist plasma membrane version of the complex. Not just in renal intercalated cells but also in epididymal clear cells, $a_4$ is targeted to the apical membrane (Pietrement et al. 2006). Accumulation at the apical membrane is regulated by a bicarbonate-sensitive soluble adenylate cyclase (sAC) activity (Pastor-Soler et al. 2003), with actin depolymerisation by gelsolin activity regulated by sAC apparently a key factor in retaining high levels of V-ATPase (Beaulieu et al. 2005). In some lower eukaryotes there can be an extraordinary variety of *a* subunits. In *Paramecium tetraurelia* for example there are 17 genes for subunit *a* isoforms, each one with the potential to produce a polypeptide with its own distinctive functional characteristics (Wassmer et al. 2006).

With such a variety of subunit isoforms, there is clearly the potential for a large number of different V-ATPases, each of which could have a unique set of functional characteristics. Currently, little is known about the potential functional differences between subunit isoforms. It is unclear whether or not inclusion of different subunit isoform alters, for example, the catalytic function of the V-ATPase (for example by changing the ATP/$H^+$ coupling ratio, for which there is evidence in yeast (Kawasaki-Nishi et al. 2001b)). Further, in Saccharomyces cerevisiae, targeting appears to be a function of the cytoplasmic N-terminal domain of the a subunit, as it is in the budding yeast *Saccharomyces cerevisiae* (Kawasaki-Nishi et al. 2001a). In vertebrate systems, targeting of the assembled V-ATPase to different compartments appears to

be an intrinsic property of the subunit *a* polypeptide. Although glycosylation is reported to be a key factor (Esmail et al. 2017), the details of this targeting process remain uncertain. What does seem to be emerging is that variations in subunit composition in different cell types can alter the so-called 'interactome' of that particular enzyme, such that the contacts it makes for example within a regulatory/sensing network are tuned to the physiological signals specifically within that cell type. For example, the renal $B_1$ subunit isoform binds the PDZ protein NHERF ($Na^+/H^+$ exchanger regulatory factor) in B-intercalated cells, and interaction that could play a role in modulating plasma membrane V-ATPase activity in those cells (Breton et al. 2000). Similarly, the $a_4$ subunit isoform uniquely interacts with the glycolytic enzyme phosphofructokinase-1, potentially linking V-ATPase activity to the broader energetic status of the cell.

Although historically the V-ATPase organisation has been described in terms of $V_1$ soluble and $V_o$ membrane domains, we can now also define its parts in terms of their contributions to the *stator* and *rotor* functions of this molecular motor. The $(AB)_3$ catalytic hexamer is the ATP-powered torque generator, driving a rotor comprising D, F, *d* and the *c*-ring. The current model of ATP-dependent proton movement requires the relative movement of the *c*-ring with respect to subunit *a* (discussed in Sect. 14.2.3), hence *a* must be fixed to $(AB)_3$ as part of a *stator* structure. This is achieved by connecting $(AB)_3$ to $a_{NT}$ via the three EG peripheral stalks, either directly in the case of S1, at the $a_{NT}$-C junction in the case of S2 or at the end of C for S3 (compare the locations in Fig.14.1a, c). Interesting corollaries of this subunit network is that it must (a) contain sufficiently strong protein-protein contacts to resist the torque generated by the catalytic activity of the complex (assuming some resistance at the $a_{CT}$-*c*-ring interface), whilst (b) being sufficiently flexible to accommodate the significant conformational changes that occur in $V_1$ during the catalytic cycle. These aspects are discussed later in this chapter.

### *14.2.2 Structural Features of the V-ATPase Subunits*

Although in recent years there have of course been significant advances in both the resolution and reliability of 3-D V-ATPase reconstructions from cryo-EM data, resolution is not yet at the point where precise orientations of individual side chains can be determined. The quality is however sufficiently high that crystal structures of individual subunits or sub-complexes (listed in Table 14.1) can be precisely fitted with enough confidence to allow detailed inferences to be drawn regarding the properties of interacting surfaces. In some instances, adjustments to crystal structures have proven necessary for optimal fitting to the cryo-EM reconstructions, indicating that their conformations in situ within the V-ATPase differ from those in the crystal. This in turn implies some intrinsic flexibility, a not unexpected quality for components of such a dynamic, mobile molecule. Although crystal structures of an increasing number of bona fide eukaryotic V-ATPase subunits are becoming available (see

Table 14.1), many of those available are for bacterial forms. What is clear is that despite often very little similarity at the sequence level, the folds of prokaryotic and eukaryotic homologues can be essentially indistinguishable, the prokaryotic forms generally providing a very accurate and precise fit to the 3-D maps of eukaryotic V-ATPase. Some V-ATPase subunits form very stable sub-complexes that have proven amenable to crystallisation (Table 14.1), providing more precise insights into the chemistry of the subunit interactions.

The A and B subunits share a similar fold with each other and to a lesser extent with the β and α subunits of the F-ATPase, underlining their common evolutionary origin (Nelson and Taiz 1989). In broad terms, each can be considered to have three distinct regions: a β-barrel region at the N-terminus, a central mixed α-helical/β--sheet region that contains the active site, and a C-terminal helical bundle closest to the membrane (Maher et al. 2009; Numoto et al. 2009; Oot et al. 2016). The β-barrel regions from A and B alternate to form a six-membered ring at the top of $V_1$ that encircles the top of the D subunit that forms the central 'axle' of the V-ATPase rotary motor. Comparison of A/B dimers with different catalytic site nucleotide occupancy states shows that the C-terminal α-helical region moves position according to catalytic state, being displaced in directions outwards from the midline of the complex and away from the corresponding subunit B component of the catalytic unit when the active site is empty (Nagamatsu et al. 2013; Oot et al. 2016). In particular, this C-terminal region includes a helix-loop-helix motif that forms structure analogous to a 'lever' that can interact directly with the D subunit rotor. Movement of this 'lever', linked to conformational changes around the active site that are driven by ATP turnover and hydrolysis product release, applies torque to the D subunit 'axle' of the V-ATPase rotary motor, spinning the rotor and energising the proton pump (discussed in Sect. 14.2.3). The D subunit itself is an α-helical coiled-coil that passes through the centre of $V_1$ (see Fig. 14.1c). The N-terminus of the subunit is close to the position occupied by the active sites in the $(AB)_3$ complex, at a depth of ~45 Å from the top of $V_1$. The N-terminus precedes a ~90 Å α-helix that reaches the membrane domain, before folding as a short β-strand section that leads into a curved ~150 Å α-helix that extends the full distance from membrane domain to the β-barrel ring of $(AB)_3$ (Saijo et al. 2011; Balakrishna et al. 2015; Oot et al. 2016). The small F subunit, with which D forms a stable heterodimer, may have a regulatory function (Imamura et al. 2004). In the bacterial homologue of the V-ATPase (called A-ATPase by some authors to differentiate it from the eukaryotic complex), a ~40 residue the C-terminal region of F can adopt an extended conformation that contacts the 'lever' of subunit A (Makyio et al. 2005; Numoto et al. 2009). In this way subunit F may be able to form a ratchet-like structure that prevents adverse movement of the subunit D rotor. There are functional parallels with the epsilon subunit of the bacterial F-ATPase, which occupies a similar position on the rotor of the F-type complex. The fold of F is reminiscent of CheY, a chemotaxis response protein that regulates the direction of rotation of another motor, the bacterial flagellum (Makyio et al. 2005).

The E subunit that forms part of the three stator filaments of the V-ATPase consists of two distinct regions: from the N-terminal end that associates with the collar

region of the stator, a single ~120 Å α-helix extends to a C-terminal cap that associates with the β-barrel region at the top of each B subunit. The long helix of E associates with the G subunit, a polypeptide comprising a single α-helix, to form parallel right-handed coiled-coil (Lee et al. 2010; Stewart et al. 2012). E and G form a stable heterodimer even in heterologous expression systems, and pre-assembly of this sub-complex presumably precedes integration into the V-ATPase. Interaction is mediated via hendecad and quindecad repeats of hydrophobic residues in both G and E, effectively zipping up the two parallel helices to make a strong interaction capable of resisting the dynamic flexing evident in the active V-ATPase (Lee et al. 2010). Interestingly, crystal structures of the both eukaryotic and bacterial EG stalks show conformational variability. The bacterial form shows a degree of flexion in the helical coiled-coil (Stewart et al. 2012), and the eukaryotic form (as part of a sub-complex with a segment of the C subunit, discussed below) can adopt two configurations. The first has a relatively high degree of curvature in the helical coiled-coil, the second form being quite straight (Oot et al. 2012). Both forms can be fitted to 3-D reconstructions of the V-ATPase, the curved form being the best fit for stator stalks S2 and S3, and the straighter form optimal for S1 (as in Fig. 14.1a, c). The S1 stalk uniquely is adjacent to an AB catalytic unit in the 'open' state (unoccupied by nucleotide phosphate), hence the presumption is that the catalytic state (and hence conformation) of the AB unit dictates the conformation of the adjacent EG stalk (Oot et al. 2012, 2016). In other words, the inherent flexibility of the EG heterodimer is able to accommodate the significant conformational changes that occur in the $(AB)_3$ hexamer during catalysis. The property of EG to behave like a flexible rod suggests another potential function in the V-ATPase: acting to buffer energy transfer between the symmetry-mismatched ATPase and proton pumps, allowing the 3-phase motor to apply constant torque to the rotor.

The collar region of the V-ATPase stator contains elements of both $V_1$ (the C and H subunits) and $V_o$ ($a_{NT}$). The H subunit of *Saccharomyces* expresses as a fully-folded protein in *E. coli*, and it was the first V-ATPase subunit to have its structure solved by x-ray crystallography (Sagermann et al. 2001). It has a very unusual fold, with its large N-terminal domain linked to the smaller C-terminal region by a flexible coupling. The conformation of the 'natural' form of subunit H fitted to cryo-EM-derived structural models differs from the crystallographic form, requiring movement of the C-terminal domain about the flexible coupling to achieve optimal fitting. The fold of H contains a large number of *armadillo* repeats (short helical hairpins), forming an α-solenoid protein reminiscent of β-catenin that is involved in WNT signalling during development. Why this specific fold has been adapted as a eukaryotic V-ATPase component is unclear. Subunit H does plays a central role in regulation of V-ATPase activity via controlled domain dissociation (see Sect. 14.4.1).

Subunit C, which has no bacterial homologues, provides the connection between stator stalks S2 and S3 (Fig. 14.1). The crystallographic structure (Drory et al. 2004; Oot et al. 2012) shows two long and one short α-helical segments separate a 'foot' domain that binds S2 and a 'head' domain that links to S3 (Fig. 14.2a). The 'head' and 'foot' share similar fold comprising 3 short α-helical regions and 3 β-strands

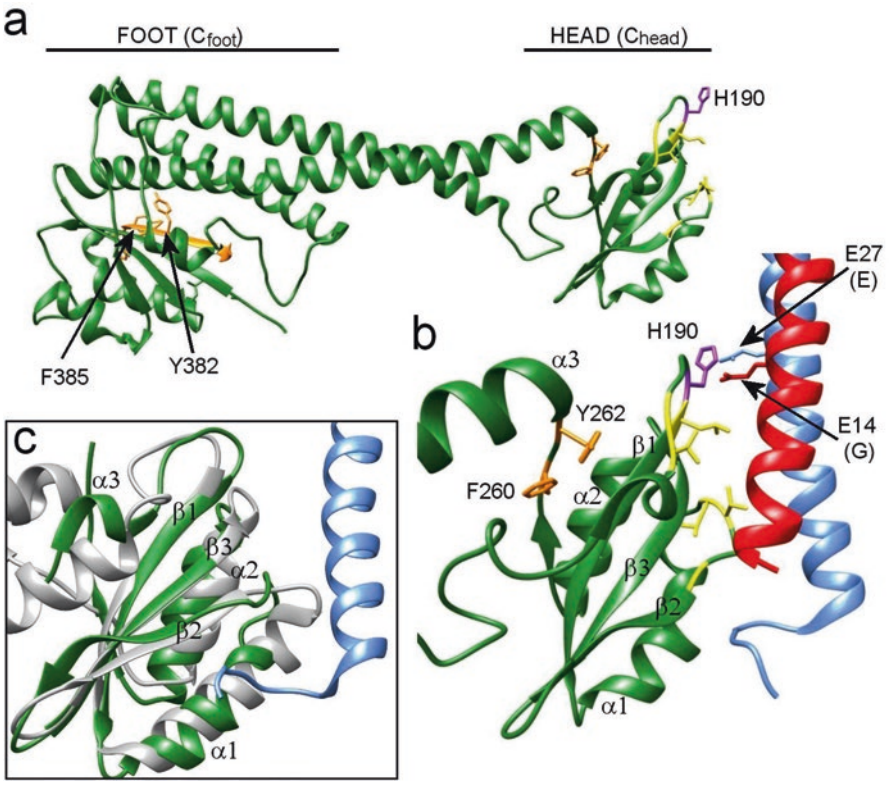


**Fig. 14.2** Subunit C structure and interactions. (**a**) The overall fold of the C subunit from *Saccharomyces cerevisiae* (PDB 1U7L (Drory et al. 2004) shows 'foot' and 'head' regions that contact peripheral stator stalks S2 and S3, respectively (see Fig. 14.1a). The 'head' and 'foot' regions have similar folds, comprising a 3-strand β-sheet adjacent to two short α-helical segments. Aromatic residues and β-strand in the 'foot' that are mutationally sensitive are shown orange. (**b**) Detail of the interaction between $C_{head}$ and subunit E in the EG peripheral stalk S3 (modelled on the $C_{head}EG$ crystal structure, PDB 4EFA (Oot et al. 2012)). Contacts between C-His190 (magenta), E-Glu27 (blue) and G-Glu14 (red) and between subunit E and a cluster of hydrophobic residues on C (yellow) are proposed to underpin the strong interaction between subunit C and the S3 stalk (see text for details). (**c**) Subunit C and the N-terminal domain of subunit *a* share similar folds. The end of $a_N$ predicted to interact with the S2 peripheral stalk (see Fig. 14.1) adopts a 3 β-strand/2 α-helix fold that is remarkably coincident with that of the $C_{head}$ region (green). Similar modes of interaction with subunit E (blue) are therefore plausible. Model constructed by superimposing the crystal structure of bacterial $a_{NT}$ (PDB 3RRK (Srinivasan et al. 2011)) on the $C_{head}EG$ structure (PDB 4EFA)

(Fig. 14.2a, b). Mutagenesis of the yeast *VMA5* gene encoding subunit C has shown that aromatic residues adjacent to these regions (and in the sequence comprising a β-strand in the 'foot': orange in Fig. 14.2) are required for stability of the subunit and hence for V-ATPase assembly (Curtis et al. 2002). Work from the Stephan Wilkens' lab on an $EGC_{head}$ complex (Fig. 14.2b) has given the most detailed picture of the contacts that hold together the collar of the stator network (Oot et al. 2012).

At the junction of subunit C with subunit E the $C_{head}$ region presents a surface of hydrophobic residues to the E subunit, suggesting extensive hydrophobic interactions drive subunit assocation (Fig. 14.2b). A histidine residue (His190) on the loop that precedes the first β-strand of $C_{head}$ (β1; Fig. 14.2b) is also implicated in EG binding, being in close proximity to glutamate residues contributed by E and G (Fig. 14.2b).

The region of the collar that links S1 and S2 is $a_{NT}$, technically part of $V_o$ that remains associated with the membrane when any peripheral subunits are stripped away. Curiously, the fold of the bacterial homologue of $a_{NT}$ shares a similar fold overall to subunit C (Srinivasan et al. 2011), with a similar bundle of extended α-helices forming the major part of the collar linking stator stalks S1 and S2. This implies a common genetic origin for C and $a_{NT}$. The fold of the region of $a_{NT}$ that connects to subunit E of S2 in particular closely mirrors that of the subunit C head region (Fig. 14.2c), hence this region can be thought of as a conserved subunit E-binding module represented in both E-binding subunits. By analogy, it acts like a hydrophobic 'sticky pad' to connect the core α-helices of the collar to the respective stator stalks. Comparison of the shapes of the CEG heterotrimer in solution and in situ in cryo-EM-based V-ATPase models suggests that the linkage between $C_{head}$ and the core α-helices of C may be intrinsically flexible, permitting the angle between EG and C to change whilst maintaining strong subunit contacts (Diepholz et al. 2008b; Oot et al. 2012). This could be another physical characteristic that allows the structure of the complex to accommodate large conformational changes during catalysis. It is worth noting that subunit connections within the stator network must be relatively strong, at least equal in energetic terms to the torque generated by ATP hydrolysis that drives the proton pump.

In the $V_o$ domain, the foot of the subunit D/F rotor connects to subunit *d*, the fold of which resembles an inverted cone that plugs the cavity at the centre of the *c*-ring (Fig. 14.3). As the adaptor that connects the D/F rotor 'axle' to the *c*-ring, *d* plays a crucial role in transmitting the torque generated by ATP hydrolysis to the *c*-ring that is a key part of the proton pump. As alluded to above for connections within the stator, the D/*d* and *d*/*c*-ring connections in the rotor must be sufficiently strong to resist the rotational forces generated in the system that would otherwise force their separation (the mechanics of the system are discussed further below). The only available crystal structure for *d* is that from *Thermus thermophilus* (Table 14.1), but is a remarkably good fit to the subunit *d* density in the best resolved electron density maps from cryo-EM. The individual subunit *c* polypeptides in the *c*-ring to which *d* is connected fold as four-helical bundles, with a highly conserved glutamate residue located on the fourth helix, positioned mid-way across the membrane and accessible from the lipid phase of the membrane. Sequence analysis indicates that the V-ATPase *c* subunit is a tandem repeat of the two-helix *c*-subunit of the F-ATPase, a result of gene duplication but with the loss of the corresponding acidic residue from the first part of the repeat (Mandel et al. 1988). In 3-D reconstructions of the V-ATPase from cryo-EM data, the *c*-ring effectively appears as two concentric rings of 20 transmembrane helices (best evidence indicates a 10-mer ring (Benlekbir et al. 2012)).

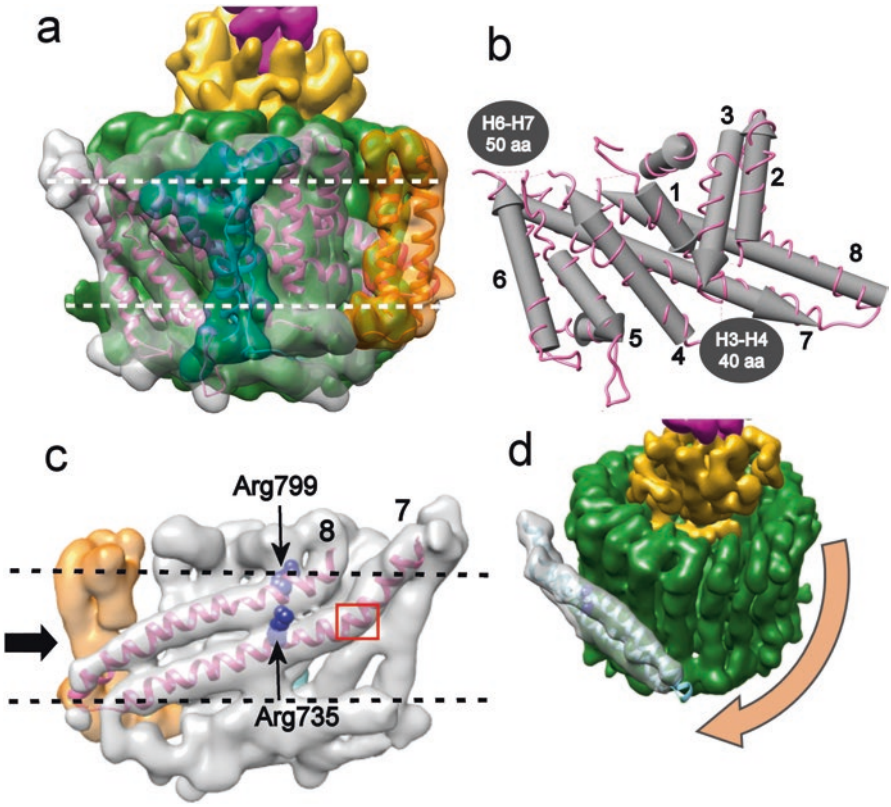


**Fig. 14.3** Organisation of the $V_o$ membrane domain. (**a**) Segmented electron density map of the *S. cerevisiae* $V_o$ (EMD-6284 (Zhao et al. 2015), showing the foot of the D subunit (magenta), *d* subunit (gold), *c*-ring (green) and C-terminal domain of the *a* subunit (grey). The $a_{NT}$ region has been removed for clarity. Densities assigned to the *e* subunit (Vma9p) and an uncharacterised *f* subunit (Mazhab-Jafari et al. 2016) are shown in cyan and orange, respectively. The model of Mazhab-Jafari et al. of the *a*-*e*-*f* fold (PDB 5tjf) is shown fitted to the density map ($a_{CT}$: pink; *e*: cyan; *f*: orange). Dashed lines indicate the approximate boundaries of the membrane bilayer. (**b**) The 8-helical model of $a_{CT}$ by Mazhab-Jafari et al. The approximate positions of the large helix 3–4 and helix 6–7 loops of uncertain fold that were not modelled in PDB 5tjf are shown. Helix 1 links to $a_{NT}$. (**c**) Surface of $a_{CT}$ at the interface with the *c*-ring. Helices 7 and 8 contain conserved arginine residues Arg735 and Arg799, respectively (*Saccharomyces* residue numbering). Arg735 is known to be required for proton translocation. The red box shows the presumed location of a cluster of residues implicated in binding of the inhibitor bafilomycin. Rotational movement would cause the c-ring to step in from the left hand side, as shown by the arrow. (**d**) Interaction of the *c*-ring with the $a_{CT}$ helix 7–8 hairpin. The direction of rotation of the D-*d*-*c*-ring rotor is indicated by the arrow

In the inner ring, with alternating Helices 1 and 3 of subunit *c*, tight packing is facilitated by a strip of conserved glycine residues occurring with helical periodicity along Helix 3. The outer ring, alternating Helix 2 and Helix 4, forms the external surface of the *c*-ring that forms an interface either with the lipid phase or with $a_{CT}$ that is the membrane-embedded end of the stator (see Fig. 14.1c).

The exact fold of $a_{CT}$ proved difficult to pin down for many years. Both biochemical labeling experiments aimed at identifying residues exposed to the soluble and lipid phases (Leng et al. 1999) and predictive algorithms provided somewhat ambiguous results, suggesting as many as nine transmembrane helices. More recent biochemical experiments favoured a model with 8 TMHs (Toei et al. 2011; Wang et al. 2008), a figure that fits the most recent cryo-EM data (Mazhab-Jafari et al. 2016), where 6 regions of density have been allocated to 'classical' transmembrane regions that traverse the membrane at angles close to perpendicular to the membrane plane (Fig. 14.3a, b). In addition to these 6 α-helices, $a_{CT}$ also has the striking feature of two additional extended helices (Helices 7 and 8) that form a helical hairpin that sits at an acute angle with respect to the membrane. The start of Helix 7 and end of Helix 8 are close the cytoplasmic surface of the membrane, whereas the loop that connects these helices is close to the lumenal/extracellular side of the membrane on the other side of $a_{CT}$ (Fig. 14.3c). This remarkable feature is common to other rotary ATPases, being seen in the subunit *a* homologue of F-ATPases (Allegretti et al. 2015; Zhou et al. 2015), and must represent an essential part of the proton translocation apparatus. It contains arginine residues (Arg735 and Arg799 in *Saccharomyces*; (Fig. 14.3c)) within conserved 'Leu-Arg-Leu' motifs, with the former at least known to be essential for proton pumping. This helical hairpin essentially then forms the principal interface between the surface of the *c*-ring and the stator, acting as a rail across which the *c*-ring slides (Fig. 14.3d).

Improved resolution of cryo-EM data for $V_o$ components has allowed John Rubinstein and colleagues (Mazhab-Jafari et al. 2016) to construct a robust computational model of $a_{CT}$ based on their ~6 Å reconstruction of the *Saccharomyces cerevisiae* V-ATPase (Fig. 14.3a, b). This model, that accommodates both the structural and biochemical data, consists of six helical segments that form the interface with the lipid phase and effectively sequester the Helix 7–8 hairpin from the hydrophobic environment. The model does not include two extended loop regions that are not well resolved in the cryo-EM-derived 3-D reconstruction: a 40 residue section between Helices 3 and 4 on the luminal/extracellular side, and a 50 residue section on the cytoplasmic side between Helices 6 and 7 (Fig. 14.3b). This latter region, which sits at the end of the Helix 7–8 hairpin at the point at which pump is proposed to acquire protons for translocation, is unusually enriched in acidic residues. It is interesting to speculate that it represents some form of 'proton trap' that supplies $H^+$ to the pump. Even more speculatively, it could allow the pump to respond to changes in cytoplasmic pH. Altered hydrogen bonding within a cluster of acidic residues is postulated to change the open state of the ASIC-1 channel in response to altered pH (Jasti et al. 2007). The EM-derived reconstruction of $V_o$ also shows two additional polypeptides, each comprising two α-helices. One is identified as subunit *e* (Vma9p in *Saccharomyces*; orange in Fig. 14.3a), the other remains unidentified at the time of writing, but could be a polypeptide involved in assembly of the complex.

### *14.2.3 Organisation of the Rotary Proton Pump – Mechanistic Insights from Structural Biology*

While the majority of complete, cryo-EM-derived structural models of the V-ATPase have been obtained using eukaryotic sources (*Saccharomyces cerevisiae* and the insect *Manduca sexta*), most of the data relating to the mechanism of have been obtained with bacteria enzymes, often referred to as A-ATPases. We have argued that the designation 'V-type' should be reserved for eukaryotic proton pumps that have three stator filaments and the C and H subunits (Muench et al. 2011). Others have argued perfectly logically that 'V-ATPase' should allude to function, hence should include ATP-driven rotary ion pumps from both prokaryotes and eukaryotes, regardless of any structural variations. This is a reasonable argument, since enzymes are after all generally named according to their activity and not their structural characteristics, but is complicated by the fact that some bacterial A/V-ATPases are primarily ATP synthases. What is clear is that the structural similarity between 'core' bacterial and eukaryotic subunits means that observations regarding the basic enzymology and mechanics of bacterial forms are highly likely to be valid for the eukaryotic pumps too. The same argument also applies to the F-ATPases (ATP synthases), in which the fundamental biochemistry that couples the proton motive force to ATP synthesis is in most respects simply the reverse of what the V-ATPase does. Below, we discuss how key features of the V-ATPase relate to its function as a rotary ion pump.

The V-ATPase rotary pump can be divided into the two functional sub-complexes that move relative to each other during the catalytic cycle: the stator (Fig. 14.4a; grey) that contains the ATPase motor that induces movement of the D-F-*d*-*c*-ring rotor (Fig. 14.4a; coloured by subunit). Sequential hydrolysis of ATP occurs at each of the three equivalent active sites in the complex in turn, with each site in a different state of nucleotide occupancy at any time, hence each site cycles through 'open' (empty), ADP/phosphate-bound and ATP-bound states. Structural models that correlate with these three distinct conformational states have been obtained by cryo-EM (Zhao et al. 2015). In the ATPase motor, each catalytic step is linked to a 120° step of the rotor. In the most recent catalytic model of Suzuki and colleagues (Suzuki et al. 2016) that amalgamates observations from single molecule dynamics experiments and crystallographic studies of different nucleotide-bound states, a conformational change in the $(AB)_3$ complex is induced by ATP binding to the 'open' site. This in turn alters the conformation of the ADP-bound site, triggering ADP release. It is this release that is associated with each 120° step of the rotor, hence the conformational change associated with ADP release must include the 'power stroke' that produces torque. It is also proposed to induce changes in the third, ATP-bound site that causes ATP hydrolysis and immediate release of inorganic phosphate. In this way each catalytic site has progressed to the next state, and the cycle continues for as long as the system is fed by ATP.

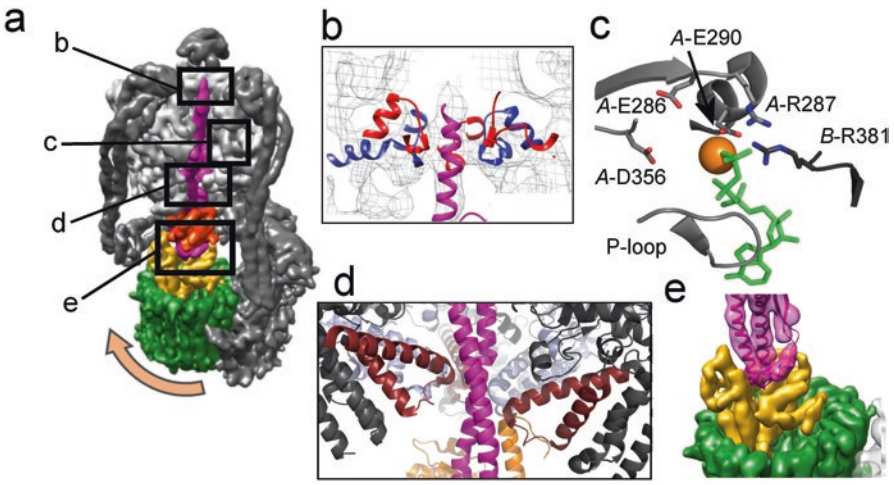


**Fig. 14.4** Motor functions in the V-ATPase. (**a**) Map of the *Saccharomyces* V-ATPase (EMD-6284) with the D-F-*d*-*c*-ring 'rotor' coloured as in Fig. 14.1. (**b**) The 'bearing' region in $V_1$ containing loops contributed by A (red) and B (blue). (**c**) Active site modelled on the crystal structure from *T. thermophilus* (PDB 3GQB (Maher et al. 2009). The positions of AMP-PNP (green) and $Mg^{2+}$ are inferred from their positions in the active site in the homologous $F_1$-ATPase. (**d**) Interaction between 'lever' loops in subunit A (brown) and the subunit D rotor shaft (magenta). (**e**) The 'screwdriver' interaction of the rotor shaft D subunit (magenta) with the *d* subunit (gold)

If we examine the cryo-EM derived structures of the eukaryotic V-ATPase, we can see some interesting features of the rotor-stator interactions. For greatest mechanical efficiency, the D/F part of the rotor must make minimal interaction with the $(AB)_3$ complex in the centre of which it sits (in essence, it must be frictionless). At the same time, the rotor must be maintained in the correct position to engage with the ATPase torque-generating motor. We have proposed that a ring of density around the top of the D subunit to which all six A and B subunits contribute a helix-loop-helix feature (Fig. 14.4b) acts as a type of bearing to maintain the rotor in the correct position, and that electrostatic effects may play a role in ensuring that this bearing is frictionless (Rawson et al. 2015). This feature may also compress the D subunit to maintain its engagement with *d* in the membrane domain (discussed below).

The geometry of amino acid side chains in the active sites of the V-, A(V)- and even F-type ATPases are remarkably conserved, indicating fundamental similarities in reaction chemistry. By analogy to the chemistry of the F-ATPase, a glutamate residue in the eukaryotic V-ATPase active site (*A*-E290 in Fig. 14.4c, *Saccharomyces* residue numbering) is proposed to activate a bound water molecule, facilitating ATP hydrolysis by nucleophilic attack on the γ-phosphate. An arginine residue (*B*-R381; Fig. 14.4c) acts as an 'arginine finger' that stabilises the penta-coordinate transition state of the γ-phosphate, occupying different position in 'open' and 'closed' (i.e. occupied) active site conformations. Another feature found in the active sites of all the rotary ATPases is a section of the catalytic subunit designated the 'P-loop' that

contains a Walker A motif and is involved in nucleotide binding (Fig. 14.4c). Crystal structures of *Enterococcus hirae* $A_1$ ($V_1$) domains indicate that a conserved lysine residue at the C-terminal end of the P-loop in the A subunit is also directly involved in co-ordinating the γ-phosphate (Suzuki et al. 2016). In F-ATPase, the P-loop is found in both the catalytic β subunit (equivalent and related to V-ATPase A subunit (Bowman et al. 1988c) and the α subunit (equivalent and related to V-ATPase B (Bowman et al. 1988a), with the three α subunit copies involved in non-catalytic ADP binding (Abrahams et al. 1994). The B subunit in V-ATPase lacks the P-loop equivalent, hence the non-catalytic A-B interfaces in $A_1$ ($V_1$) do not bind ADP (Numoto et al. 2009). How this impacts on the catalytic cycle of the V(A)-ATPases is uncertain, but single molecule biophysical analysis of the rotational stepping that occurs during the catalytic cycle certainly indicates that the V/A-type enzymes do differ from the $F_1$ ATPase operating in ATP hydrolysis mode (Imamura et al. 2005; Suzuki et al. 2016).

The conformational changes triggered by the cycle of ATP binding/hydrolysis/ADP release must ultimately be translated into the torque generation that results in rotor movement. Again, much of our understanding of this process comes from study of the $F_1$-ATPase operating in the ATP hydrolysing direction, and from the prokaryotic A(V)-ATPases. In F-ATPase, extended helix-loop-helix segments at the bottom of the catalytic β subunit (containing the conserved DELSEED motif) effectively act as levers, undergoing sequential movements (linked to the conformational changes in the active site) that apply a turning force to the central rotor. The V/A--ATPases have a very similar structure (Fig. 14.4d), and although the nature of the movements of the A subunit may differ from those in the F-ATPase (Suzuki et al. 2016), the fundamental principles behind torque generation appear to be conserved.

The increasing resolution of 3-D reconstruction from cryo-EM data is also provided greater insight into the coupling between the DF rotor axle and *d*-*c*-ring of the proton pump. The functions of this coupling appear to demand contradictory physical properties. Firstly, it must be strong enough to resist the torque generated during catalysis, hence a very strong protein-protein interaction between the foot of D and the 'plug' of subunit *d* is inferred. However, at least in the *Saccharomyces cerevisiae* and *Manduca sexta* V-ATPases, this contact can be rapidly but reversibly broken as part of a process of regulated domain dissocation in response to physiological signals (discussed in Sect. 14.4.1). Under such low energy conditions, the $V_1$ domain that includes the D subunit detaches from the membrane and becomes inactive for ATP hydrolysis. Whilst it is possible to speculate that the cellular signals that drive this process could lead to conformational changes in D, F or *d* to cause a break in the subunit contact, a more plausible explanation is that the foot of D is in fact not tightly bound to *d*. Instead, cryo-EM reconstructions of the yeast V-ATPase suggest that the foot of the D subunit fits into *d* in a way more analogous to a screwdriver (subunit D) engaging with a screw (subunit *d*) (Fig. 14.4e), held in place by the stator structure of the V-ATPase. Consistent with this idea, we have observed that spontaneous decomposition of the *Manduca* V-ATPase into its individual domains can lead to loss of the D subunit from $V_1$ (unpublished). The stator of the V-ATPase then

assumes an important function in maintaining the structure of the rotor, not only orienting the D subunit precisely so it engages with the *d* subunit, but also compressing it to ensure that that engagement is maintained. The closest macroscopic equivalent of this is in the engineering concept of 'tensegrity', in which a network under tension (here, the stator) compresses a strut (here, the D/F dimer), in this example maintaining contact between D and the *d*/*c*-ring membrane complex.

What do we know about the mechanism of proton pumping across the membrane? Mutagenesis studies certainly show that the conserved glutamate residue on subunit c is necessary, as is the arginine residue on Helix 7 of subunit a (and likely also the arginine on Helix 8 of a). Both residues are positioned at the mid-point of the membrane, and hence can come into close proximity at the a-c interface (Fig. 14.5a). At the lipid/c-ring interface, the subunit c glutamate must be protonated, since the thermodynamic cost of exposing a charged residue to this environment is too high. This is underlined by the sensitivity of these glutamates to modification by the lipid-soluble reagent dicyclohexylcarbodiimide (DCCD), which reacts only with protonated carboxylic acids. How do these components interact to link proton movement to rotational movement? Current models are based on the concept of 'half-channels' in $a_{CT}$ within the membrane that connect to the *c*-ring but that are not continuous with each other (Vik and Antonio 1994; Junge and Nelson 2005) (Fig. 14.5). According to this model, torque applied to the *c*-ring by the ATPase motor forces a *c*-subunit with protonated glutamate to make a rotational step away from the lipid environment and into the interface with $a_{CT}$. It then releases the proton into a half-channel that allows it to exit on the lumenal side of the membrane. The low pH of this exit channel should favour retention of the proton, but a role for the arginine residue(s) has been proposed such that the positive charge induces a decrease in the $pK_a$ for the glutamate residue, making it more likely to relinquish its proton (Gräbe et al. 2000). A similar half-channel functions to connect the cytoplasmic side of the membrane to the deprotonated *c*-subunits at the *a*-*c* interface. By acquiring a proton through this channel, the now neutralised *c*-subunit can make the rotation step away from the *a*-*c* interface towards the hydrophobic environment of the membrane. Thus, each proton boards the *c*-ring rotor on the cytoplasmic side of subunit *a*, is carried by one complete rotation of the *c*-ring, before exiting on the lumenal side of subunit *a* (Fig. 14.5b).

What is the experimental evidence for the existence of the half-channels? In the homologous subunit *a* of F-ATPase, modification of mutagenically introduced cysteine residues by a water-soluble silver reagent suggests penetration into the fold of the subunit via a pore or channel, consistent with a water-filled half-channel on the cytoplasmic side (Angevine and Fillingame 2003). In the most recent, more highly resolved 3-D reconstructions of the V-ATPase, regions of low density are becoming evident that could fulfil the role of half-channel (Fig. 14.5c). In particular, there is clear evidence of a pore that is open to the cytoplasmic side that penetrates the subunit *a* density towards the region at which the subunit *c* glutamate and subunit *a* arginine(s) would come into close proximity, a possible conduit through which a cytoplasmic proton could access the *c*-ring (Zhao et al. 2015). Although the story remains incomplete, certainly needed more detailed, higher resolution structural models of $V_o$, current evidence appears to be supportive of the half-channel model.

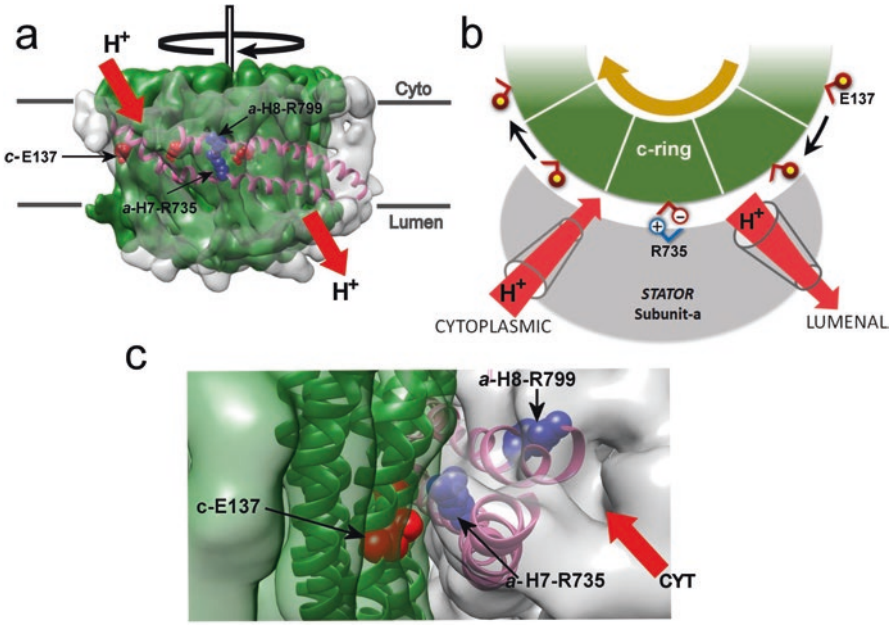


**Fig. 14.5** Proton translocation through the membrane domain. (**a**) Proton movement energised by ATP-fuelled rotation of the *c*-ring (green) requires a highly conserved glutamate residue (E137; red spacefill) on subunit *c*, positioned mid-way across the lipid bilayer and exposed at the *c*-ring/lipid interface. Arg735 on Helix 7 of subunit *a* (*a*-H7-R735; blue spacefill) (and potentially Arg790 (*a*-H8-R790)) is also essential and can come into close proximity to *c*-E137 at the *a*-*c*-ring interface. Protons access E137 at the *a*-*c* interface via a hypothetical 'half-channel' from the cytoplasm (red arrow), and exit via a 'half-channel' on the lumenal side. Black arrow indicates the direction of c-ring rotation relative to the subunit a stator. Structures are from the cryo-EM-generated map of the yeast V-ATPase (EMD-6284 (Zhao et al. 2015)) fitted with segments of the $ac_8c'c''def$ model (PDB 5tj5) (Mazhab-Jafari et al. 2016). Residue numbers are for the *Saccharomyces* subunits throughout. (**b**) The side chain of the *c*-subunit glutamate (*c*-E137) residue can only locate to the non-polar lipid environment if in the neutral, protonated state (indicated by yellow spheres). When the rotational movement brings the protonated residue into the *a*-*c* interface, it sheds its proton into the 'half-channel' that opens to the lumenal (low pH) side. This deprotonation may be facilitated by the arginine residue(s) on subunit *a* (see text for details). To exit the *a*-*c* interface and become re-exposed to the hydrophobic environment, the glutamate residue must become neutralised by acquiring a proton from the cytoplasmic side of the membrane via a second 'half-channel. Sequential rotational stepping of the *c*-ring then brings the protonated residue back to the lumenal 'exit' channel at the *a*-*c* interface. (**c**) Detail of the theorised *c*-E137/*a*-R735 interaction. Models were generated as in (**a**). Higher resolution cryo-EM data (such as in EMD-6284) allow structural features that could represent the cytoplasmic 'half-channel' (CYT) to be visualised

## 14.3 Molecular Pharmacology of the V-ATPase

### *14.3.1 Is the V-ATPase a Viable Target for Drug Development?*

Because of its central role in cellular physiology, the V-ATPase has long been regarded as a potential therapeutic target. The discovery of the bafilomycin/concanamycin family of compounds as highly potent and specific V-ATPase inhibitors (Bowman et al. 1988b; Drose et al. 1993) at least suggested that this this potential could be realised, either by directly exploiting these naturally occurring plecomacrolide antibiotics or using them as templates from which new small molecules could be fashioned (Gagliardi et al. 1998; Farina and Gagliardi 1999). Inhibition of the rotary ATPases by this type of macrolide antibiotic is common to both the F- and V-ATPases, with the F-type enzyme sensitive to oligomycin. Although there is no overlap in the sensitivity of each ATPase type to its specific inhibitor, the similar chemistry of the compounds and (as we will see below) some common ground regarding their binding sites implies a similar mechanism of action. Since the discovery of the bafilomycin family as specific V-ATPase inhibitors, a number of other compounds with similar specificity and potency (reviewed in more detail than is possible here by (Huss and Wieczorek 2009). Some, such as the benzolactone enamide apicularen (Boyd et al. 2001; Osteresch et al. 2012) and the macrolactone archazolid (Sasse et al. 2003; Bockelmann et al. 2010), are natural molecules produced by myxobacteria, while others such as the indole pentadieneamides are synthetic small molecule mimetics of pharmacologically active parts of the bafilomycin molecule (Gagliardi et al. 1998).

Two areas of clinical importance have to date been the focus of efforts to develop V-ATPase-targeted therapeutics: osteoporosis and cancer. Because of the essential role the V-ATPase plays in bone resorption by osteoclasts, the initial focus was on developing inhibitors that specifically targeted the V-ATPase at the resorptive 'ruffled membrane' of active osteoclasts. Although some success has been reported in achieving a 'tissue-specific' effect in both cell-based and animal models of osteoporosis (see for example (Mattson and Keeling 1996; Keeling et al. 1998; Gagliardi et al. 1998; Visentin et al. 2000)), to date these studies have been unable to progress into humans. The presumption is that because of the ubiquitous nature of the V-ATPase in human cells, it would be very difficult to achieve a sufficiently large therapeutic window to make V-ATPase targeted anti-osteoporotic drugs viable.

A second area of interest in the development of V-ATPase inhibitors as potential therapeutics is cancer (reviewed in (Sennoune et al. 2004b; Fais et al. 2007; Neri and Supuran 2011), where two functions of the V-ATPase could be targeted. The first relates to the involvement of the V-ATPase in the acidification of endosomal compartments, where sequestration and accelerated efflux of weakly basic chemotherapeutic drugs contributes to multi-drug resistance (Raghunand et al. 1999; Luciani et al. 2004; De Milito and Fais 2005). Co-treatment with V-ATPase inhibitors therefore has the potential to improve the efficacy of this type of chemotherapy drug. The second area relates to the unique physiology of cancer cells. Solid tumours

support unusually high levels or glycolysis (the Warburg effect), but the resulting high levels of organic acid metabolites such as lactate present the cancer cell with the problem of maintaining a stable cytoplasmic pH. The V-ATPase appears to play a direct role in this pH homeostasis, with loss of activity either through chemical inhibition or genetic knock-down leading to intracellular acidosis and cell death (Ohta et al. 1998; Ishisaki et al. 1999; Lu et al. 2005; Morimura et al. 2008; Sasazawa et al. 2009). If targeted inhibition of tumour cell V-ATPase activity were possible it could therefore specifically induce apoptosis in cancer cells. The low pH environment of solid tumours also support the activities of proteolytic enzymes that degrade the extracellular matrix, facilitating tumour cells migration and invasion during the process of metastasis (see for example (Rozhin et al. 1994; Kubota and Seyama 2000; Chung et al. 2010). Inhibiting the acid efflux capacity tumour cells specifically could therefore have the added benefit of limiting the systemic spread of cancer (Rofstad et al. 2006; Niikura 2007; Supino et al. 2008). Some studies have found that invasive cancer cell lines (representing models of high metastatic potential) express intrinsically higher levels of plasma membrane V-ATPase activity than do related non-invasive cells (Sennoune et al. 2004a). Other studies have found little difference between invasive and non-invasive cells (Smith et al. 2016). The correlation purely linking plasma membrane V-ATPase activity and metastatic potential may therefore be inconclusive, but what is clear is that metastatic tumour cells do require this activity to express their invasive phenotype. There is also evidence that invasive cells have a specific 'fingerprint' of subunit *a* isoforms (Hinton et al. 2009; Folkers and Hinton 2012), suggesting that these cells could be targeted if isoform-specific inhibitors could be developed. Notwithstanding potential issues with toxicity, all of these avenues for drug development rely on the premise that specific, targeted inhibitors can be developed, a key to which is greater understanding of the structures of binding sites for existing inhibitor compounds. Our current knowledge of these sites is discussed in the next section.

### *14.3.2 A More Detailed Knowledge of Inhibitor Binding from Structural Biology*

It is clear that the great majority of V-ATPase inhibitors (including the plecomacrolides, macrolactones and indoles) bind to the membrane domain of the V-ATPase. All are capable of partitioning into the bilayer, where they intercalate between the membrane lipids and access the external surface of $V_o$ at its protein/lipid interface (Pali et al. 2004a, b). A number of experimental approaches have all indicated that the *c*-ring contains the binding sites for these lipid-soluble inhibitors, including photochemical cross-linking (Huss et al. 2002; Bockelmann et al. 2010; Osteresch et al. 2012), biophysical methods (Pali et al. 2004b; Whyteside et al. 2005) and identification of mutations leading to resistance (Bowman and Bowman 2002; Bowman et al. 2004). In the case of oligomycin binding to the F-ATPase, this latter

genetic approach has also identified residues on the F-type subunit *a* homologue that confer resistance if mutated. A similar strategy applied to the *Saccharomyces cerevisiae* V-ATPase has implicated a cluster of sites on helix 7 of Vph1p (the yeast subunit *a* homologue) in bafilomycin binding (Wang et al. 2005) (see Fig. 14.3c). Interestingly, this region is at the 'exit' end of the aCT Helix 7-8 hairpin (discussed in Sect. 14.2.2), the point at which the *c*-ring should acquire a cytoplasmic proton to allow rotational stepping into the hydrophobic environment. We can speculate therefore about the inhibitory mechanism of bafilomycin: it could block loading of protons onto the crucial glutamate residue of subunit *c*, either directly or more subtly by altering the conformation of *c* and/or *a*. Stepping of the proton pump rotor cannot occur if the subunit *c* glutamate is not neutralised by acquisition of a proton (discussed in Sect. 14.2.3), hence proton pumping would be blocked. More broadly, the direct involvement of subunit *a* in inhibitor binding at least offers the promise that compounds specific to the four vertebrate *a* isoforms could be developed, although the implicated region is highly conserved.

Although a high resolution structure of the *c*-ring of $V_o$ is not currently available, the high degree of conservation in the sequences of *c* polypeptides means that the *Saccharomyces* subunit can be confidently modelled using the crystallographic structure of the decameric ring of NtpK, the $Na^+$-translocating subunit *c* homologue from *Enterococcus hirae* (Murata et al. 2005). Mapping the residues identified by Bowman and colleagues as being involved in concanamycin binding (Bowman et al. 2004) onto this type of homology-based model (Fig. 14.6a, b) shows that they are predominantly located at, or near, the lipid-exposed surface of the *c*-ring, consistent with biophysical data (Pali et al. 2004b). These residues are clustered mostly around helices 2 and 4 contributed by different *c* subunits at an inter-molecular interface (Fig. 14.6a, b; blue residues). The region of helix 4 involved extends from the cytoplasmic end of the helix to a point close to the middle of the bilayer, and includes Glu137 that is essential for proton translocation. Residues involved in binding the macrolactone archazolid overlap the concanamycin binding region to some extent and include Glu137 (Bockelmann et al. 2010), they are more clustered around a region of helix 4 towards the mid-point of the bilayer (Fig. 14.6a, b; green residues). There is also overlap between the binding sites for bafilomycin and the indole pentadieneamides (Whyteside et al. 2005). Based on the broad overlap in binding sites for a variety of V-ATPase inhibitors, a common mechanism by which the compounds bind and exert their inhibitory effect seems likely. By partitioning into the bilayer, the concentration of inhibitor can be effectively much higher than in the bulk aqueous phase, promoting binding to the surface of the *c*-ring. The most obvious possible mechanism of inhibiting proton pumping is if inhibitor binding simply obstructs entrance of the proton-loaded *c*-ring into the subunit *a* interface, preventing unloading of its proton into the lumenal 'half-channel (as outlined in Sect. 14.2.3). However, it is worth noting that assuming the highly plausible model of Mazhab-Jafari et al. (2016) shown in Fig. 14.3 is accurate, the region of subunit *a* implicated in bafilomycin binding by Wang et al. (2005) is at the exit side of subunit *a* (see Fig. 14.3c). The implication is therefore that bafilomycin prevents proton translocation not by blocking rotational stepping of proton-loaded subunit *c* into

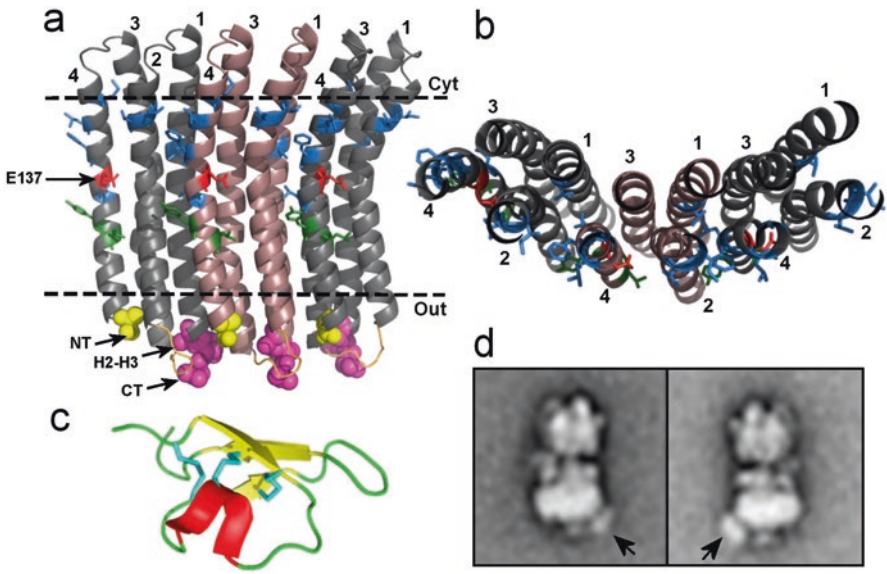


**Fig. 14.6** Inhibitor binding to the c-ring. (**a**) Section of the subunit *c* (Vma3p) ring from *Saccharomyces cerevisiae* modelled using the structure of the homologous NtpK polypeptide from *Enterococcus hirae* as template. Three subunits are shown with alternating colours with the lipid-facing surface towards the viewer. Each subunit comprises 4 transmembrane helices, with helices 2 and 4 positioned at the interface with the membrane lipid. E137 is the glutamate residue involved in transmembrane proton movement. Residues implicated in the binding of the macrolide antibiotics bafilomycin and concanamycin (blue) and archazolid (green, along with E137) are shown with stick representation. Residues at the N-terminus (NT; yellow), C-terminus (CT; magenta) and in the extracellular loop between helices 2 and 3 (H2-H3; orange) are involved in binding the insecticidal peptide inhibitor PAb1. Dashed lines indicate the approximate boundary of the membrane. (**b**) Section of the c-ring as in (**a**), viewed perpendicular to the plane of the membrane, from the cytoplasmic side. Alternating helices 2 and 4 constitute the lipid-facing surface. (**c**) Fold of the seed polypeptide PA1b, a potent and specific inhibitor of insect V-ATPases. (**d**) Negative stain electron microscopy of the *Manduca sexta* V-ATPase with PA1b-biotin-streptavidin complex bound (density indicated by arrows). Two class averages are shown, different views

contact with the subunit *a* 'unloading zone', but rather by preventing rotational stepping away from the 'loading zone'. This could perhaps occur through stabilisation of the rotor-stator interaction, or alternatively by directly preventing subunit *c* from re-acquiring a proton and becoming neutralised, a prerequisite for rotational stepping towards contact with the lipid phase.

### *14.3.3 A New Generation of V-ATPase Inhibitors*

In addition to the plecomacrolides and macrolactones produced by soil bacteria presumably to help them compete against fungi, molecules that are effective V-ATPase inhibitors are also produced by pathogenic bacteria. Yersinia

pseudotuberculosis inhibits V-ATPase-dependent phagosomal acidification via a mechanism that remains uncharacterised but presumably involves secretion of a V-ATPase-specific toxin (Tsukano et al. 1999), and the SidK protein of *Legionella pneumophila* is reported to target the catalytic subunit A (Xu et al. 2010). Further characterisation of these effects could provide a foundation for new V-ATPase inhibitors. In their evolutionary drive to counter predation by insects, plants have also developed effective V-ATPase inhibitors. The small seed protein pea albumin1 b-subunit (PA1b; Fig. 14.6c), a member of the knottin protein family, is a highly potent V-ATPase inhibitor that is also uniquely specific for insect V-ATPases (Chouabe et al. 2011). In electron microscopy studies in which the *Manduca sexta* V-ATPase was tagged with PA1b (Muench et al. 2014), the labeled inhibitor protein could be seen bound to the region corresponding to the extracellular surface of $V_o$ (Fig. 14.6d). Photochemical cross linking also identified subunit *c* and potentially subunit *e* as contributors to the PA1b binding site (Muench et al. 2014). Identification of resistance mutations furthermore points specifically to the N-terminal, C-terminal and extracellular loop regions of subunit *c* as being involved in PA1b binding (Fig. 14.6a; yellow, pink and orange highlighted regions). Typical of many membrane proteins, these regions are the least conserved parts of the subunit, a characteristic that allows for the unique specificity of this inhibitory protein. A remarkable feature of PA1b inhibition is therefore its ability to block V-ATPase activity by binding only to the extracellular part of the complex without ever entering the cell, presumably by preventing rotational movement of the *c*-ring.

## 14.4 The V-ATPase As a Component of Cellular Sensing Networks

Intuitively, it makes sense for a membrane complex that consumes significant amounts of the cellular ATP budget to be tightly regulated. In particular, linking this regulation to the energy status of the cell would allow its activity to be tuned up or down according to the prevailing physiological priorities. Although this type of regulatory mechanism was initially observed in only a few eukaryotic systems such as the insect *Manduca sexta* (Sumner et al. 1995) and the yeast *Saccharomyces* (Kane 1995; Parra and Kane 1998), it is now becoming more evident that the V-ATPase may also be part of a wider sensing nexus within the cells of higher eukaryotes (Maxson and Grinstein 2014; Cotter et al. 2015; Marshansky et al. 2014). Single molecule electron microscopy, and more recently x-ray crystallography, have begun to provide structural explanations of the regulatory phenomena that have been mapped out using cell biological and biochemical approaches. In this section, we examine progress made towards understanding the structural changes that accompany regulation of the V-ATPase, and discuss evidence for specific signalling mechanism that could trigger these changes. We also explore emerging ideas about wider functions of the V-ATPase in sensing.

### *14.4.1 Physiological Signals Can Trigger Reversible Inactivation of the V-ATPase*

In Tobacco hornworm (the larval stage of the Tobacco Hawkmoth), the activity of the V-ATPase at the apical membrane of goblet cells lining the midgut account for as much as 10% of the total ATP generated by the insect (Dow and Peacock 1989). The electrogenic $H^+$ transport supported by this activity is coupled to an $H^+/K^+$ antiporter, with the resulting alkalinisation of the midgut lumen supporting the digestive function of the animal and the $K^+$ potential driving nutrient uptake in the form of amino acid/$K^+$ symport (Wieczorek et al. 1999). It was initially observed that during the moulting stage of the larva, the transepithelial voltage dissipates and that this correlates with the loss of most of the ATP hydrolysing and $H^+$ transport activities of the goblet cell membrane (Sumner et al. 1995; Merzendorfer et al. 1997). Although the animal is unable to eat during moulting, resulting in major energetic stress on the cells during this period, the regulatory mechanism that has evolved can mitigate this to some extent by switching off the coupled transport process that has become temporarily redundant. The molecular basis for this deactivation process is the reversible, transient dissociation of the $V_1$ catalytic domain from the membrane domain (Fig. 14.7a). $V_1$ remains essentially complete, with only subunit C detaching from the complex (Graf et al. 1996), but with its ATPase activity silenced to prevent what would be futile ATP turnover in the detached $V_1$ (Sumner et al. 1995). There are very clear parallels between this system and the one at work in *Saccharomyces*, in which glucose deprivation also leads to rapid dissociation of $V_1$ from the membrane (Kane 1995; Parra and Kane 1998), accompanied by release of subunit C. More recent evidence relating to the reversible inactivation phenomenon *in vivo* in *Saccharomyces* suggests that domain dissociation does not necessarily mean pronounced movement of $V_1$ away from the vacuolar membrane, but rather a more subtle uncoupling, with only subunit C diffusing into the cytoplasm (Tabke et al. 2014). It is easy to see how a more limited physical separation would support the rapid restoration of activity that is observed once favourable physiological conditions are restored, with binding of subunit C likely to be the rate-limiting factor. In yeast, stable assembly of the V-ATPase and re-association of $V_1$ with the membrane domain both require the Regulator of ATPase of Vacuoles and Endosomes (RAVE) complex (Seol et al. 2001; Smardon et al. 2002), with this complex playing a specific role in bringing subunit C back into the functional complex (Smardon and Kane 2007). In *Manduca*, purified inactive $V_1$ domain can bind recombinant subunit C with 1:1 stoichiometry (Muench et al. 2013). Although this reconstitution was performed at non-physiological concentrations of both proteins, it does imply that re-association of subunit C in this system may not require any functional equivalent of RAVE.

Early models of the inactive $V_1$ domain from *Saccharomyces* generated by electron microscopy of single particles in negative stain showed an asymmetric density at the base of the complex in contact with the region containing the subunit D/F ‘axle’ of the rotary motor (Zhang et al. 2003). A very similar model was generated for the *Manduca* $V_1$ using the same approach (Muench et al. 2013). With the loss of

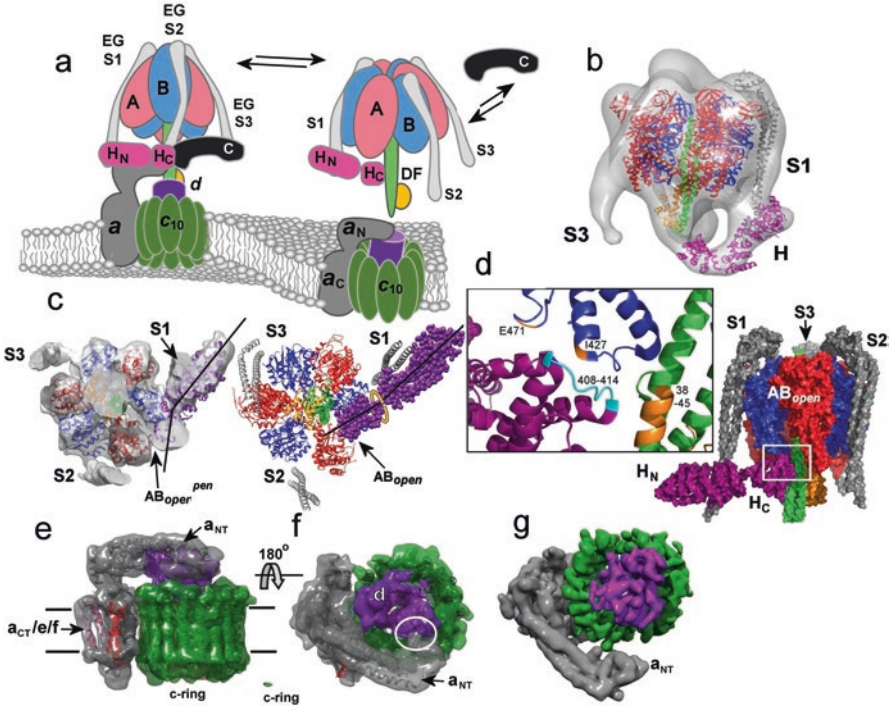


**Fig. 14.7** Auto-inhibition of the V-ATPase. (**a**) Model for domain dissociation leading to auto-inhibition in the *S. cerevisiae* and *M. sexta* V-ATPases. Uncoupling of $V_1$ from $V_o$ involves rearrangement of the H subunit C-terminal domain ($H_C$) and detachment of subunit C. (**b**) 3-D reconstruction of the auto-inhibited *M. sexta* $V_1$ from cryo-electron microscopy (EMD-2317) fitted with the crystal structures of the *T. thermophilus* $(AB)_3DF$ (PDB 3W3A (Nagamatsu et al. 2013)), EG (PDB 3K5B (Stewart et al. 2012)) and *Saccharomyces cerevisiae* H (PDB 1HO8 (Sagermann et al. 2001)). (**c**) Comparison of the positions of H in the active V-ATPase (left: PDB 3W3A and 1HO8 fitted to EMD-6284) and in the crystal structure of the auto-inhibited *Saccharomyces* $V_1$ (right: PDB 5D80 (Oot et al. 2016)). (**d**) The C-terminal domain of H plays a key role in auto-inhibition. In the crystal structure of the auto-inhibited yeast $V_1$ (PDB 5D80), $H_N$ remains fixed to peripheral stator stalk S1 but $H_C$ relocates to contact both B (adjacent to the 'open' catalytic site) and the rotor shaft subunit D. A loop region comprising residues 408-414 in $H_C$ (box) is in contact with loops of B containing Glu471 and Ile427 and with D residues 38-45. Colouring as in (**a**). (**e–g**) Comparison of auto-inhibited (**e** and **f**) and active (**g**) *Saccharomyces* $V_o$ membrane domains. In the auto-inhibited complex (EMD-8364 fitted with a $ac_8c'c''def$ model (PDB 5tj5) (Mazhab-Jafari et al. 2016), the *d* subunit (magenta) is shifted closer towards $a_{CT}$. (**f**) The N-terminal domain of a ($a_{NT}$) is closer to (and in contact with) *d*, compared to its position in the active complex (**g**). Colouring as in (**a**)

subunit C upon domain dissociation, the H subunit remains as the only likely candidate for this density, which does in fact accommodate the crystal structure of Vma13p very well. Consistent with the observation that subunit H is necessary for silencing ATP hydrolysis in $V_1$ (Parra et al. 2000), these data provided direct structural evidence that the H subunit changes position during regulated domain

dissociation, moving to contact rotor components and prevent the rotational stepping that would permit ATP turnover. Further biochemical support for this model has come from a chemical cross-linking study that identified a contact between the C-terminal domain of H and subunit F in the rotor (Jefferies and Forgac 2008). Further supporting a direct role in silencing $V_1$ activity, addition of recombinantly-expressed HCT significantly inhibits Mg.ATP hydrolysis by the detached $V_1$ domain (Diab et al. 2009; Benlekbir et al. 2012)

Because of the inherently low resolution of negative stain EM data, stator stalks in the inactive $V_1$ complexes could not be seen, limiting information about stator re-organisation during the domain dissociation process. These features were, however, resolved in a model of the inactive $V_1$ domain isolated from starved Manduca larvae, generated by 3-D reconstruction from cryo-EM of single particles (Fig. 14.7b). This model showed a density linking the S1 stator filament to the central rotor that contains subunits D and F. In the intact complex, the S1 filament interacts with H and the *a* subunit N-terminal domain ($a_N$: see Fig. 14.1), hence the model suggests that H can rotate about S1 once released from its contact with $a_N$, allowing it to bind to the rotor. It follows that prevention of futile ATP hydrolysis by $V_1$ in the insect system closely parallels the mechanism proposed to occur in *Saccharomyces*. It should be noted however that there are limitations to the *Manduca* $V_1$ model: Firstly, the 'H density' in the 3-D reconstructions is relatively weak, implying heterogeneity in the particles. If H does not adopt this position in all detached $V_1$ domains, does this undermine confidence in its role in the inactivation model? Secondly, it is difficult to see how the H subunit could carry out such a dramatic movement whilst retaining its contact with S1 without introducing significant twisting (and hence distortion) into S1. Further work at higher resolution is needed to resolve these issues and to perhaps shed more light on the process of V-ATPase re-activation in this system.

A more recent model of the 'auto-inhibited' $V_1$ from *Saccharomyces*, generated by x-ray crystallography and with resolution down to 6.2 Å, has shed more light on the molecular basis for inactivation (Oot et al. 2016). In this model (Fig. 14.7c–d), the N-terminal domain of H maintains essentially the same position in the auto-inhibited $V_1$ as it does in the complete, fully active V-ATPase (compare Fig. 14.7c left and right images), making the same stable contact with the S1 stator component. The position of the $H_{CT}$ domain is, however, dramatically different from its position in the intact V-ATPase: with the flexible linker region between the subunit H domains acting as a 'universal joint', $H_{CT}$ swings through an angle of ~90° relative to its position of optimal fit to electron density maps of the intact V-ATPase (see Fig. 14.1). Even more strikingly, $H_{CT}$ rotates ~150° around the long axis of the subunit (Fig. 14.7c right). As a consequence, $H_{CT}$ comes into direct contact with both the C-terminal domain of the B subunit that contributes to the 'open' catalytic site and to a region of the N-terminal segment of rotor axle subunit D. The requirement for such a high degree of flexibility explains why mutagenic replacement of the flexible linker with a rigid Pro-Pro-Pro sequence abolishes a significant proportion of the inhibitory effect of $H_{CT}$ ((Benlekbir et al. 2012)). A non-conserved loop region in $H_{CT}$ between Asn408 and Lys414 forms the crucial inhibitory interface, contacting

loop structures around residues Glu471 and Ile427 of B and a region encompassing residues 38-45 of D (Fig. 14.7d). It is clear from these data that a simple brake on the rotation of the D subunit is not the sole, or perhaps even the principal mechanism of auto-inhibition in the yeast $V_1$. The catalytic cycle of the V-ATPase involves a sequence of major conformational changes within the AB hexamer, possibly also including some rotor-independent changes propagated directly between AB units, as seen in F-ATPase (Uchihashi et al. 2011). Consequently, fixing the position of loops in the C-terminal region of one B subunit by binding the $H_{CT}$ 'inhibitory loop' can be assumed to prevent the transition between catalytic states, resulting in inhibition.

The H subunit of *Manduca* lacks the 'inhibitory loop' sequence found in the yeast polypeptide, hence auto-inhibition in the insect system cannot be dependent on exactly the same protein-protein contacts observed in yeast. This does not exclude the possibility that the basic principles of the mechanisms in the two systems are broadly similar, and they do have a number of other common features: in both the cryo-EM-derived reconstruction of auto-inhibited V1 from *Manduca* and the equivalent *Saccharomyces* crystal structure, the H subunit is adjacent to the AB unit in the 'open' catalytic state ((Oot et al. 2016; Muench et al. 2013)). Both complexes also retain ADP, with the yeast and insect complexes containing ~1.3 and ~1.7 ADP molecules per complex respectively (Huss and Wieczorek 2007; Oot et al. 2016). ADP is a potent inhibitor of V-ATPase activity (Moriyama and Nelson 1989; David and Baron 1994; Webster and Apps 1996; Huss and Wieczorek 2007; Obrdlik et al. 2010), has been proposed to contribute to auto-inhibition of $V_1$ (Parra et al. 2000) and promotes at least partial domain dissociation (Moriyama and Nelson 1989). In the crystal structure of the auto-inhibited yeast V1, the catalytic sites adjacent to peripheral stalks S2 and S3 are conformationally distinct (i.e. non-equivalent) closed sites, with the S2 site fully occupied by ADP, the S3 site partially so, based on the presence of unassigned electron density (Oot et al. 2016). This arrangement of catalytic states most resembles the 'State 2' described by Zhao et al. for the *Saccharomyces* V-ATPase, in which the AB units adjacent to S2 and S3 are in the 'tight' and 'loose' configurations respectively, as described for the *binding change mechanism* operating in ATP hydrolysis mode (Zhao et al. 2015). Because of the low resolution of the cryo-EM data in the *Manduca* $V_1$ model, the conformations of these sites are indistinguishable. The other area where the two structures have some similarity is in the conformation of their peripheral stalks. In the crystal structure of the yeast $V_1$, S1 (in contact with $H_{NT}$) and S2 are extended, adopting essentially the same conformation as in the holoenzyme (Oot et al. 2016). S3, however, adopts a much more curved conformation, coming into contact with an A subunit at the base of the complex (Fig. 14.7c, right). Oot et al. (2016) propose that this may be part of a mechanism to minimise re-assembly when auto-inhibition is favoured. Although limited by much lower resolution, it appears that the same 'curved' conformation may also occur in the *Manduca* $V_1$, but in this case it is S2, with S3 more extended (but with a pronounced kink at its free end) (Muench et al. 2013).

How does the $V_1$ complex arrive at the auto-inhibited state? According to one model (Huss and Wieczorek 2007), the V-ATPase in effect 'senses' an unfavourable

ADP/ATP ratio and responds by dissociating its domains and switching off Mg.ATP hydrolysis. During its normal catalytic cycle, the enzyme is proposed to transiently pass through an unstable state (we could presume that this occurs when the active site next to S1 is in the 'open' state and ADP remains tightly bound to at least one other site). Under normal physiological conditions (high ATP availability), the open site can bind ATP and the catalytic cycle simply continues. However, under conditions of high ADP/ATP ratio, after binding and hydrolysis of ATP, inhibitory ADP remains bound and the open site is unable to acquire ATP. As a result, the enzyme stalls in the unstable state, allowing domain dissociation to occur. This model explains why the ATPase must be active for auto-inhibition to occur: the *Manduca* enzyme turns over (on average) one ATP per $V_1V_o$ complex before de-activiating (Huss and Wieczorek 2007), and active yeast V-ATPase is also required for auto-inhibition (Parra and Kane 1998). Huss and Wieczorek also propose how this mechanism can account for the very early (but still largely unexplained) observation that incubation with Mg.ATP at low temperature more effectively dissociates the V-ATPase domains than does physiological temperature (Moriyama and Nelson 1989). By slowing catalysis, the ADP-bound unstable state should persist for longer, favouring domain separation.

Rather than being mediated directly through effects on the catalytic cycle of the complex, the signals triggering reversible dissociation and auto-inhibition could instead act more remotely through non-catalytic subunits. Fluctuations in metabolite levels or pH, second messengers or protein kinase activities are all plausible signal mediators, and are discussed below. Generically, the effect of these signals can be thought of in terms of a 'stator destabilisation' model, whereby the signal affects the conformation of one of the stator subunits (subunit C is emerging as the preferred candidate, discussed in the next section). Sequential conformational changes then follow that break the protein-protein contacts that physically couple the $V_1$ and $V_o$ domains. In the example proposed by Oot et al. (2016), a signal could target the low affinity interaction between C and S2, triggering the release of C from the complex. This in turn would destabilise the contact between S2 and $a_{NT}$, causing $a_{NT}$ to let go of H and adopt a new position in $V_o$ (see below). Since the rotor shaft D appears not to be fixed to the membrane domain, $V_1$ can uncouple from $V_o$ with minimal physical separation. Once unconstrained by $a_{NT}$, $H_{CT}$ can adopt the auto-inhibitory conformation seen in the yeast $V_1$ crystal structure (Oot et al. 2016). This type of model also provides a relatively simple pathway to re-assembly, with removal of the inhibitory signal allowing the stator components to return to their 'active' conformations and be re-integrated into an active enzyme, perhaps facilitated by a chaperone such as RAVE in a process that recapitulates *de novo* assembly of active V-ATPase.

In addition to switching off Mg.ATP hydrolysis, the $V_o$ domain that remains otherwise intact within the membrane after $V_1$ detachment becomes impermeable to protons (Beltran and Nelson 1992; Zhang et al. 1992; Crider et al. 1994; Couoh-Cardel et al. 2015). This contrasts with the $F_o$ domain of the related F-ATPase (ATP synthase), which allows the free movement of protons after removal of the corresponding catalytic domain $F_1$, preventing establishment of any proton motive force.

In the case of V-ATPase, experiments examining the properties of $V_o$ in isolation have typically relied on forced removal of $V_1$ by cold shock in the presence of Mg.ATP (Beltran and Nelson 1992), isolation of naturally occurring free $V_o$ (Zhang et al. 1992) or prevention of $V_1$ assembly by genetic deletion of a $V_1$ subunit (Couoh-Cardel et al. 2015). Influx of protons can be measured by loading membrane vesicles with a protonation-sensitive fluorescent dye and high concentrations of $K^+$, followed by dilution into low $K^+$ buffer. Introduction of valinomycin allows $K^+$ ion efflux, imposing an electrochemical potential (inside negative) sufficient to drive $H^+$ into the vesicle through any open channel or pore. Any increase in $H^+$ concentration is detected as apparent pH-dependent quenching of fluorescence. Using this type of approach, $V_o$ from sources as diverse as brain coated vesicles and adrenal chromaffin granules (potentially containing different subunit *a* isoforms), and from yeast vacuolar membranes have consistently shown resistance to passive proton movement. Only the isolated yeast *c*-ring reconstituted into planar lipid bilayers shows properties of a passive channel, permitting over 8 nS of conductance in single channel recordings (Couoh-Cardel et al. 2016). This conductance is presumed to occur through the centre of the *c*-ring and not through the canonical $H^+$ translocation pathway, despite the presence of density likely to originate from the N-terminal helices of the *c*" isoform (Vma16p) (Mazhab-Jafari et al. 2016)and potentially also from bound lipid as occurs in other rotary ATPases (Zhou et al. 2011). Intriguingly, this channel property is reminiscent of the cell-cell communication function previously proposed for the *c*-ring from arthropod species (Finbow et al. 1995). Removal of the *d* subunit from yeast $V_o$ by detergent treatment is not sufficient to introduce passive proton flux, hence it is clear that subunit *a* (perhaps in combination with subunit *e*) is responsible for controlling proton movement through the membrane domain. In this context, it is worth also noting that early experiments with solvent-extracted subunit *c* reconstituted into lipid vesicles also showed passive proton movement that was inhibited by DCCD (Sun et al. 1987), implying direct involvement of the Helix 4 glutamate residue that is an essential component in the mechanism of ATP-driven proton transport.

Recent electron microscopic analyses of 'closed' $V_o$ isolated from yeast with defective $V_1$ assembly (Couoh-Cardel et al. 2015) or after glucose deprivation (Mazhab-Jafari et al. 2016) show significant structural re-organisation when compared to the membrane domain of active complex (Fig. 14.7e–g). In particular, the $a_{NT}$ 'arm' that forms the stator linkage between S1 and S2 (and with H) in the holoenzyme moves position, swinging closer to the centre of the complex and making contact with the *d* subunit density (compare Fig. 14.7f, g). The *d* subunit itself sits more deeply in the *c*-ring and is significantly more offset from the central axis of the complex than is observed in the holoenzyme, being closer to (and tilted towards) the $a_{CT}$ domain (Mazhab-Jafari et al. 2016) (Fig. 14.7e–f). The most simplistic model for blocking proton movement is one in which this contact prevents rotation of the *d*-*c*-ring rotor, but can be excluded on the basis that inhibition of proton movement in the 'locked' $V_o$ is dependent on neither subunit *d* (Couoh-Cardel et al. 2015) nor $a_{NT}$ (Qi and Forgac 2008). Perhaps a more subtle structural

rearrangement within $a_{CT}$ that occludes the putative proton channels is responsible for blocking transport. An early investigation into the transport properties of isolated $V_o$ showed that treatment at pH 4 could initiate passive proton translocation activity that remained sensitive to bafilomycin (Crider et al. 1994). This is unlikely to simply occur as a result $a_{CT}$ detachment from the *c*-ring, which could then operate as a passive channel: subunit *a* is also implicated in bafilomycin binding (Wang et al. 2005), hence retained sensitivity this inhibitor implies retained contact between *a* and the *c*-ring. It would certainly be interesting to see any impact of this treatment on $V_o$ structure. What the observed changes do suggest is that $a_{NT}$ may be 'spring-loaded' in the intact complex in a way similar to that suggested for the C subunit (Oot et al. 2012), perhaps an important feature that facilitates domain dissociation?

The cryo-EM reconstruction of $V_o$ from the auto-inhibited V-ATPase also appears to show proximity between subunit *c*" (Vma16p) and subunit *a*. Resolution of this interaction from cryo-EM data indicates a very high degree of homogeneity in the $V_o$ particles, leading to the conclusion that (as observed in auto-inhibited $V_1$), $V_o$ also adopts a uniform 'dissociation sensitive' state in which c" is locked onto subunit a (Mazhab-Jafari et al. 2016). Disulphide cross-linking experiments on the intact *Saccharomyces* V-ATPase *in situ* in the vacuolar membrane but in the absence of substrate indicate that subunit *c′* (Vma11p) can be in close alignment with the functionally critical Arg735 residue of subunit *a* (Kawasaki-Nishi et al. 2003). Although these data do not exclude *a*-*c″* interaction in the intact complex, they do exclude this contact as the uniform 'resting state' in the absence of Mg.ATP. Hence, it seems probable that the *a*-*c″* 'locked' state is specifically required for controlled domain dissociation in yeast. Perhaps (as postulated for $V_1$ (Huss and Wieczorek 2007)) it represents a low stability state that facilitates subunit separation. Alternatively, because the proton-translocating Glu residue located on transmembrane Helix 4 of *c* and *c′* is found instead on Helix 2 in *c″*, this residue is presented in a different way at the *a*-*c″* interface compared to the equivalent contact the other *c-ring* members. This could also be a factor in preventing passive $H^+$ movement in auto-inhibited $V_o$.

Although the intracellular signals that lead to auto-inhibition in *Saccharomyces cerevisiae* and *Manduca sexta* remain incompletely resolved (see Sect. 14.4.2), the physiological states that trigger these signals and the molecular basis for silencing both ATPase activity and proton transport are now becoming established. An important question that does remain unanswered is whether this type of transient, reversible dissociation process as a means of controlling V-ATPase activity is ubiquitous in eukaryotes. It is certainly the case that high glucose status promotes V-ATPase activity in some mammalian cells in a way that parallels the situation in *Saccharomyces* when auto-inhibition is reversed by restoration of normal glucose (Sautin et al. 2005; Kuzinski et al. 2010; Kohio and Adamson 2013). For example, in renal epithelial cells, glucose promotes V-ATPase assembly, increased activity and trafficking between compartments via a phosphatidylinositol 3-kinase (PI3K) mediated process (Sautin et al. 2005). Glucose also increased V-ATPase-dependent

acidification of secretory granules in insulin-secreting cells, with cAMP/PKA signalling implicated in this instance (Tompkins et al. 2002). Although perhaps implied, it remains unclear whether or not reciprocal processes in which V-ATPase activity is down-regulated mirror the rapid domain dissociation seen in yeast. Relevant to this, $V_1$ subunit detachment from the membrane has been correlated with the significant loss of V-ATPase-dependent acidification that occurs when bovine rumen epithelial cells are treated with the metabolic inhibitor deoxyglucose (Kuzinski et al. 2010), clearly resembling the effect of glucose deprivation in *Saccharomyces*. The modulation of V-ATPase activity via PI3K signalling alluded to above may be conserved throughout the eukaryota, with the same signalling process reported to be responsible for controlling tonoplast acidification in plant stomatal guard cells (Liu et al. 2016). PI3K signalling also affects V-ATPase function in bone-resorbing osteoclasts by modulating the interaction between the proton pump and microfilaments. Specifically, PI3K inhibition promotes association between F-actin and both B subunit isoforms (Chen et al. 2004) (see Fig. 14.8). There is also a positive requirement for PI3K activity in stimulating the fusion of V-ATPase-containing vesicles with the ruffled membrane in osteoclasts, an important step in the process of activating bone resorption (Nakamura et al. 1997). This suggests a model in which these acidic vesicles are bound by microfilaments via the V-ATPase before becoming committed to fusion with the resorptive membrane as the osteoclast becomes activated. From a somewhat broader perspective, the V-ATPase activity in *Saccharomyces cerevisiae* also appears to be modulated by phosphatidylinositol

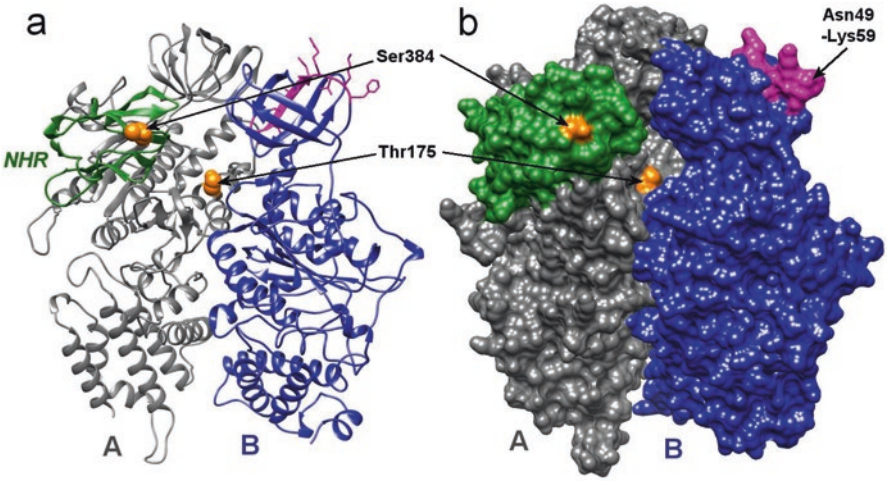


**Fig. 14.8** Phosphorylation of subunit A by AMPK and PKA. Model of human subunits A (grey) and $B_1$ (blue) constructed using the yeast homologues as template, in (**a**) ribbon and (**b**) space-filling formats. The site formed by the junction of the subunits is non-catalytic. The 'non-homologous region' (NHR) of subunit A is coloured green and the putative actin binding region of $B_1$ (Asn49-Lys59) is magenta. Reported kinase modification sites Ser384 (AMPK) and Thr175 (equivalent to the PKA target residue in the mouse protein) are coloured orange

kinase activity. The signalling lipid phosphatidylinositol 3,5-bisphosphate (PI(3,5)$P_2$), a recognised regulator of endosomal function, is reported to bind to the subunit *a* homologue Vph1p and to stabilise $V_1$-$V_o$ interaction, hence promoting V-ATPase activity in response to kinase-mediated signalling (Li et al. 2014).

### *14.4.2 The V-ATPase: A Protein Kinase Substrate?*

The effects of PI3K activity on V-ATPase function suggest short time-frame signalling via the master kinase PDK1 (phosphoinositide-dependent kinase-1), with subsequent direct modification by activated PKC, or longer-term effects mediated via MAPK/ERK1/2 or Akt pathways. Both of these processes have been implicated in the increased V-ATPase activity observed in renal type A intercalated cells when stimulated by angiotensin II (Rothenberger et al. 2007). In *Saccharomyces*, however, auto-inhibition caused by glucose depletion occurs even in strains deleted for the yeast PKC homologue Pkc1p (Parra and Kane 1998), indicating that a different process is at work in these cells. This same study proposed that auto-inhibition required sensing of a glucose metabolite downstream of glucose-6-phosphate by catalytically active V-ATPase. Using a genetic approach, Bond and Forgac identified the Ras regulators IRA1/2 in the yeast auto-inhibition process (Bond and Forgac 2008). Since Ras modulates adenylate cyclase activity and hence cAMP levels, the trail of evidence leads to cAMP-dependent protein kinase (protein kinase A, PKA) as a potential regulator of V-ATPase activity (Bond and Forgac 2008).

There is now a considerable body of evidence that V-ATPase function in vertebrates is also regulated by protein kinases, including both PKA and AMP-activated protein kinase (AMPK). V-ATPase activity can therefore be linked to extracellular signals via adenylate cyclase/cAMP and to cellular energy status. In an early study of insulinoma cells, PKA modulators were observed to have significant effects on a glucose-induced increase in secretory granule acidification (Tompkins et al. 2002). However, it was unclear at that time whether this effect was direct (mediated via PKA-catalysed phosphorylation of V-ATPase subunits) or indirect, mediated via an unidentified regulator that was itself the PKA substrate. A proteomic screen of kinase substrates in mouse brain did however show that subunit A is phosphorylated by AMPK (Tuerk et al. 2007), direct evidence that at least one V-ATPase subunit can be directly modified by a regulatory kinase. Subsequently, activation of PKA via the action of a bicarbonate-sensitive soluble adenylate cyclase (sAC) was linked to increased levels of V-ATPase at the apical membranes of both epididymal clear cells (Hallows et al. 2009; Pastor-Soler et al. 2009) and renal type A intercalated cells (Gong et al. 2010). In a further twist, this positive effect of PKA activity was found to be strongly opposed by AMPK, suggesting reciprocal control of the V-ATPase by the two kinases (Hallows et al. 2009; Gong et al. 2010). The clear implication is that increased acid efflux mediated via cAMP/PKA in response to physiological signals can be overridden by AMPK when conserving energy is the highest imperative. More detailed biochemical analyses of kinase action on the V-ATPase identified

residue Ser175 in mouse subunit A as the target for PKA and Ser384 in the same polypeptide as the AMPK substrate (Alzamora et al. 2010; Alzamora et al. 2013) (Fig. 14.8). Ser175 (which is a threonine residue in human A) is located at the non-catalytic interface between A and B subunits in the assembled V-ATPase (Fig. 14.8). Although this site is not hidden behind a subunit E/G peripheral stator stalk (see Fig. 14.1), its accessibility to a protein kinase in a pre-assembled AB heterodimer would still be expected to be severely restricted. Rather than directly modulating V-ATPase enzyme activity, it seems possible that phosphorylation of Ser173 by PKA increases apical membrane V-ATPase activity instead by promoting assembly of cytosolic subunits into an active, membrane-bound complex. This would be consistent with the observed shift of $V_1$ subunit immunofluorescence staining from cytosol to apical membrane in response to PKA activation (Hallows et al. 2009; Pastor-Soler et al. 2009).

The Ser384 site of subunit A phosphorylation is highly conserved and located within the 90-residue 'non-homologous region' (Fig. 14.8), a segment that distinguishes subunit A from its evolutionary relative the β subunit of F-ATPase. Although mutations to this region in Vma1p, the yeast A homologue, are known to adversely affect ATPase activity, coupling between ATP hydrolysis and $H^+$ transport and auto-inhibition (Shao et al. 2003; Shao and Forgac 2004), it is unclear how introduction of a phosphate group to this region could bring about major changes in V-ATPase activity, relatively remote as it is from either the active site or the interface with other subunits. It would certainly be intriguing to see the impact of phosphorylation of either site on the conformation of subunit A.

In insects, cAMP/PKA signalling plays diverse and important roles, for example in regulating fluid secretion in response to hormones. In these invertebrates, it is subunit C rather than subunit A that has emerged as the substrate for PKA. In *Manduca sexta* for example, C can be phosphorylated by PKA either as the unbound polypeptide or as part of the $V_1$ domain, but not as part of the holoenzyme (Voss et al. 2007). In the salivary gland of the blowfly *Calliphora vicina*, serotonin signalling via cAMP/PKA induced phosphorylation of a polypeptide of the same mass as subunit C, the observed phosphorylation being inhibited by antibodies to subunit C (Voss et al. 2007). Based on these observations, a role for PKA in assembly of the V-ATPase (analogous to the effects seen in mammalian cells) seems highly likely. Conversely, because subunit C does not appear to be phosphorylated whilst part of the fully assembled V-ATPase (Voss et al. 2007), a role in the auto-inhibition process appears less likely.

Subunit C is also reported to be a substrate for a plant protein kinase, being phosphorylated *in vitro* by the kinase WNK (*with no lysine*) from *Arabidopsis thaliana* (Hong-Hermesdorf et al. 2006). The mammalian homologues of WNK are involved in processes such as regulation of ion transport across epithelial membranes. Serine and threonine residues within the phospho-peptides derived from subunit C that were identified in that study coincided with those scoring highly using the phosphorylation site prediction algorithm NetPhos (Blom et al. 1999). These sites, spread across both the 'head' and 'foot' regions of C, suggest that phosphorylation could influence the ability of C to interact with subunit E in peripheral stalks 2 and

3 within the V-ATPase stator. Are the C subunits of other species also potential phosphorylation sites? Using this bioinformatics approach, and applying a high stringency score for probability, we have examined potential phosphorylation sites in *Saccharomyces*, *Manduca sexta* and the human $C_1$ and $C_2$ isoforms (Fig. 14.9). The yeast C (Vma5p) contains 7 high-probability phosphorylation sites (Fig. 14.9a), with residues at positions 126, 279 and 332 being equivalent to those identified as targets of WNK activity by Hong-Hermesdorf et al. The polypeptide from *Manduca sexta* has only one high scoring potential phosphorylation site, Ser326, which coincides with Ser338 in yeast (Fig. 14.9b, d). This same residue is also identified as a

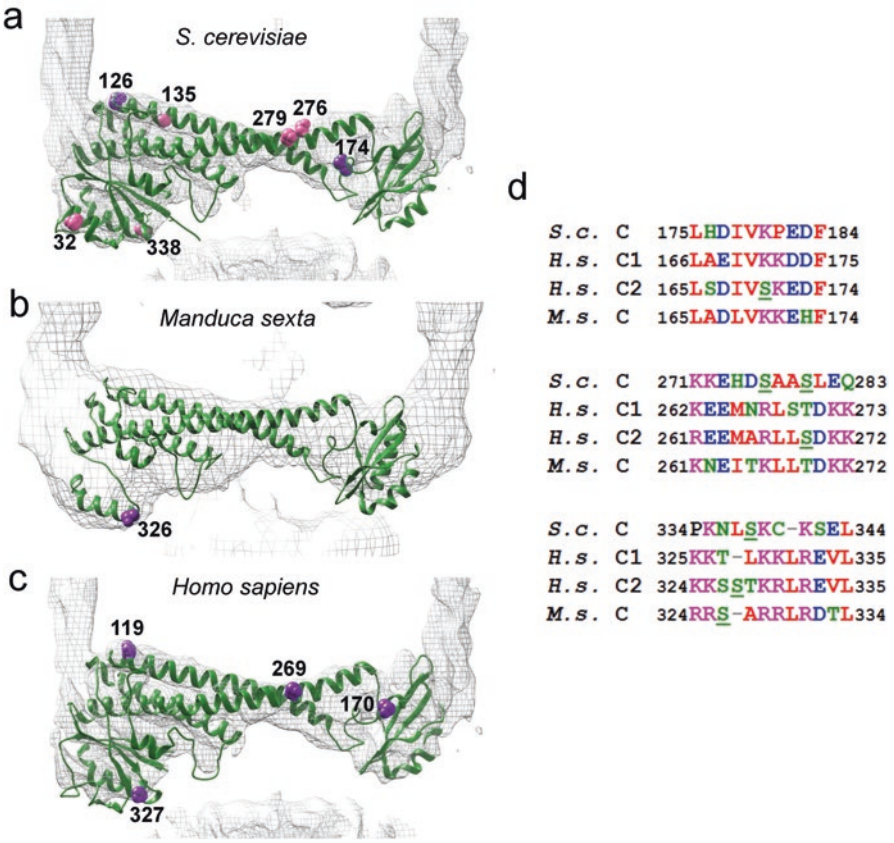


**Fig. 14.9** Potential phosphorylation sites on subunit C. Serine and threonine residues were scored for potential modification by protein kinases using NetPhos (magenta) and NetPhosYeast (pink). Only residues scoring ≥0.990 are shown. (**a**) *Saccharomyces cerevisiae* subunit C (Vma5p: PDB 1U7L) fitted to the cryo-EM generated electron density map of the V-ATPase from the same species. Models of the (**b**) *Manduca sexta* subunit C and (**c**) human C subunit isoform 2 generated using the Vma5p crystal structure as template. The *M. sexta* model is fitted to the cryo-EM V-ATPase map from the same species. (**d**) Example sequence alignments for regions containing potential phosphorylation sites in *Saccharomyces cerevisiae* (*S.c.*), human (*H.s.*) isoforms 1 and 2, and *M. sexta* C subunits. Alignments were generated using CLUSTAL

high probability phosphorylation site in the human $C_2$ isoform (Fig. 14.9c), along with residues 119, 170 and 269 that are also equivalent to potential sites in Vma5p. We can speculate therefore that C subunits across a range of eukaryotic kingdoms have at least one potential PKA modification site, although this remains to be tested experimentally. As with phosphorylation of subunit A, the likely impact of covalent modification on the function of subunit C is unclear: in general terms, effects could range from relatively large to quite small conformational changes or changes to the electrostatics of the polypeptide (Johnson and Lewis 2001), any of which could impact on subunit interactions and hence on assembly of the V-ATPase complex.

Another fascinating link between the V-ATPase and cellular signalling has also come to light, connecting the V-ATPase at the lysosomal membrane to activation of mTORC1 (mammalian (or mechanistic) target of rapamycin complex 1). This pentameric complex is a master regulator that responds to nutrient and energy status, growth factor and stress signals to control autophagy and cell growth, in particular acting as a strong repressor of autophagy when amino acid availability is high (see (Jewell et al. 2013) for a detailed discussion of the topic). Activation of mTORC1 involves its recruitment to the lysosomal membrane, where it associates with the Rag GTPase complex that is itself bound to the membrane by its association with a scaffold protein, the Ragulator complex. Ragulator acts as a guanine exchange factor (GEF) for the Rag GTPases, activating them for mTORC1 recruitment. Crucially, Ragulator makes an amino acid-dependent association directly with the active lysosomal V-ATPase (Zoncu et al. 2011), presumably the complex containing the $a_3$ subunit isoform. In a further fascinating twist, the V-ATPase is also able to sense amino acids in the lumen of the lysosome (Zoncu et al. 2011), transferring that information to Ragulator on the external surface of the lysosome via an unknown mechanism. This switches on the GEF activity of Ragulator, switching on the Rag GTPase complex for mTORC1 binding. The net effect therefore is to transmit information about lysosomal amino acid status from the V-ATPase to mTORC1.

## 14.5 Future Directions

Through the combination of single particle cryo-electron microscopy, x-ray crystallography and single molecule biophysics, our understanding of the structure and mechanism of the V-ATPase has advanced significantly from where it was 15 years ago. A clear picture is emerging of the architecture of the complex, and how specifically rotational movement is generated in $V_1$ and transmitted to the proton pump in the membrane. Until relatively recently, we had little real insight into the structure of the membrane domain of any rotary ATPase. Resistant to both 3-D and 2-D crystallisation, single particle cryo-EM has provided the breakthrough in our understanding of how components involved in moving the proton across the membrane are organised. We also now have a greater appreciation of the V-ATPase as a component of cellular signalling networks, and how its activity can respond to these

signals. So what are the outstanding questions still to be addressed? We speculate that these fall into four broad areas:

1. *Structures of V-ATPase signalling supercomplexes.* The molecular basis for amino acid sensing by the lysosomal V-ATPase, and how it transmits information to Ragulator, are unknown, but clearly these have significant implications for our understanding of nutrient sensing by the cell. The same argument applies to V-ATPase interaction with the important metabolic enzymes aldolase and phosphofructokinase-1: do these interactions result in mutual changes in conformation that impact on their functions? Here, it may be possible to simply reconstitute the V-ATPase with recombinant enzyme prior to cryo-EM. A similar approach has recently been successfully used to analyse binding of the bacterial toxin protein SidK to the ATPase (EMD-8724) (Zhao et al. 2017).
2. *Dissecting out the stages in RAVE-mediated assembly.* The problem faced by the yeast cell in assembling the V-ATPase are similar to those experienced during auto-inhibition: stopping wasteful ATP hydrolysis by $V_1$ prior to it being coupled to $V_o$, and at the same time preventing passive proton movement through the membrane domain. Dissecting out the structures of different assembly intermediates associated with RAVE would significantly aid in our understanding of how (and in what order) subunits are integrated as part of assembly and 'powering up' of the complex.
3. *Determining the structural impact of regulatory signals.* Can structural models of the V-ATPase provide a description of how phenomena such as protein phosphorylation or pH sensing affect conformation and function? These potentially quite subtle changes in conformation are likely to require significant advances in the resolution of the models.
4. *The mechanism of proton translocation.* With recent higher resolution models of both the V-ATPase and F-ATPase we are moving towards a better understanding of the proton translocation pathway, but higher resolution models are needed so that side chain geometry can be visualised. It could also be very informative to see in detail how compounds such as bafilomycin exert their inhibitory effects on proton movement, presumably acting at the subunit *a*/*c*-ring interface.

A potential problem is that many of these interesting subjects for study are potentially low abundance complexes, and there is a clear need for resolution at a level where side chain geometry can be seen. However, if these complexes can be isolated in stable and monodisperse form, single particle cryo-EM is arguably the best approach to addressing their structures. Only microgram amounts of protein are required, and absolute purity is not essential because of the capacity of currently used image analysis software to accommodate particle heterogeneity. Mixed populations in different conformations may even be advantageous: different conformers may be resolved from a single dataset. The hope is that in the next few years we will gain a detailed and complete understanding not only of the steps in the energy transforming process in the V-ATPase, but also how it receives and transmits signals that are essential for cell function.

## References


Abrahams JP, Leslie AG, Lutter R, Walker JE (1994) Structure at 2.8 Å resolution of $F_1$-ATPase from bovine heart mitochondria. Nature 370:621–628

Allegretti M, Klusch N, Mills DJ, Vonck J, Kuhlbrandt W, Davies KM (2015) Horizontal membrane-intrinsic α-helices in the stator a-subunit of an F-type ATP synthase. Nature 521:237–240

Alzamora R, Thali RF, Gong F, Smolak C, Li H, Baty CJ, Bertrand CA, Auchli Y, Brunisholz RA, Neumann D, Hallows KR, Pastor-Soler NMPKA (2010) Regulates vacuolar H(+)-ATPase localization and activity via direct phosphorylation of the A subunit in kidney cells. J Biol Chem 285:24676–24685

Alzamora R, Al-Bataineh MM, Liu W, Gong F, Li H, Thali RF, Joho-Auchli Y, Brunisholz RA, Satlin LM, Neumann D, Hallows KR, Pastor-Soler NM (2013) AMP-activated protein kinase regulates the vacuolar $H^+$-ATPase via direct phosphorylation of the A subunit (ATP6V1A) in the kidney. Am J Physiol Ren Physiol 305:F943

Angevine CM, Fillingame RH (2003) Aqueous access channels in subunit a of rotary ATP synthase. J Biol Chem 278:6066–6074

Arai S, Saijo S, Suzuki K, Mizutani K, Kakinuma Y, Ishizuka-Katsura Y, Ohsawa N, Terada T, Shirouzu M, Yokoyama S, Iwata S, Yamato I, Murata T (2013) Rotation mechanism of *Enterococcus hirae* $V_1$-ATPase based on asymmetric crystal structures. Nature 493:703–707

Bai XC, McMullan G, Scheres SHW (2015) How cryo-EM is revolutionizing structural biology. Trends Biochem Sci 40:49–57

Balakrishna AM, Basak S, Manimekalai MSS, Grüber G (2015) Crystal structure of subunits D and F in complex gives insight into energy transmission of the eukaryotic V-ATPase from *Saccharomyces cerevisiae*. J Biol Chem 290:3183–3196

Beaulieu V, Da Silva N, Pastor-Soler N, Brown CR, Smith PJS, Brown D, Breton S (2005) Modulation of the actin cytoskeleton via gelsolin regulates vacuolar $H^+$-ATPase recycling. J Biol Chem 280:8452–8463

Beltran C, Nelson N (1992) The membrane sector of vacuolar H(+)-ATPase by itself is impermeable to protons. Acta Physiol Scand 607(Supplementum):41–47

Benlekbir S, Bueler SA, Rubinstein JL (2012) Structure of the vacuolar-type ATPase from *Saccharomyces cerevisiae* at 11Å resolution. Nat Struct Mol Biol 19:1356–1362

Bernal RA, Stock D (2004) Three-dimensional structure of the intact *Thermus thermophilus* $H^+$-ATPase/synthase by electron microscopy. Structure 12:1789–1798

Blake-Palmer KG, Su Y, Smith AN, Karet FE (2007) Molecular cloning and characterization of a novel form of the human vacuolar $H^+$-ATPase e-subunit: an essential proton pump component. Gene 393:94–100

Blom N, Gammeltoft S, Brunak S (1999) Sequence- and structure-based prediction of eukaryotic protein phosphorylation sites. J Mol Biol 294:1351–1362

Bockelmann S, Menche D, Rudolph S, Bender T, Grond S, von Zezschwitz P, Muench SP, Wieczorek H, Huss M, Archazolid A (2010) Binds to the equatorial region of the c-ring of the vacuolar $H^+$-ATPase. J Biol Chem 285:38304–38314

Bond A, Forgac M (2008) The Ras/cAMP/protein kinase A pathway regulates glucose-dependent assembly of the vacuolar ($H^+$)-ATPase in yeast. J Biol Chem 283:36513–36521

Bowman BJ, Bowman EJ (2002) Mutations in subunit c of the vacuolar ATPase confer resistance to bafilomycin and identify a conserved antibiotic binding site. J Biol Chem 277:3965–3972

Bowman BJ, Allen R, Wechser MA, Bowman EJ (1988a) Isolation of genes encoding the Neurospora vacuolar ATPase: analysis of *VMA2* encoding the 57 kDa polypeptide and comparison to *VMA1*. J Biol Chem 263:14002–14007

Bowman EJ, Siebers A, Altendorf K (1988b) Bafilomycins: a class of inhibitors of membrane ATPases from microorganisms, animal cells, and plant cells. Proc Natl Acad Sci U S A 85:7972–7976

Bowman EJ, Tenney K, Bowman BJ (1988c) Isolation of genes encoding the *Neurospora* vacuolar ATPase: analysis of *VMA1* encoding the 67 kDa subunit reveals homology to the other ATPases. J Biol Chem 263:13994–14001

Bowman EJ, Graham LA, Stevens TH, Bowman BJ (2004) The bafilomycin/concanamycin binding site in subunit c of the V-ATPases from *Neurospora crassa* and *Saccharomyces cerevisiae*. J Biol Chem 279:33131–33138

Boyd MR, Farina C, Belfiore P, Gagliardi S, Kim JW, Hayakawa Y, Beutler JA, McKee TC, Bowman BJ, Bowman EJ (2001) Discovery of a novel antitumor benzolactone enamide class that selectively inhibits mammalian vacuolar-type ($H^+$)-atpases. J Pharmacol Exp Ther 297:114–120

Breton S, Brown D (2013) Regulation of luminal acidification by V-ATPase. Physiology 28:318–329

Breton S, Wiederhold T, Marshansky V, Nsumu N, Ramesh V, Brown D (2000) The B1 subunit of the $H^+$ATPase is a PDZ domain-binding protein. Colocalization with NHE-RF in renal B-intercalated cells. J Biol Chem 275:18219–18224

Chen SH, Bubb MR, Yarmola EG, Zuo J, Jiang J, Lee BS, Lu M, Gluck SL, Hurst IR, Holliday LS, Vacuolar H (2004) $^+$-ATPase binding to microfilaments: regulation in response to phosphatidylinositol 3-kinase activity and detailed characterization of the actin-binding site in subunit B. J Biol Chem 279:7988–7998

Chouabe C, Eyraud V, Da Silva P, Rahioui I, Royer C, Soulage C, Bonvallet R, Huss M, Gressent F (2011) New mode of action for a knottin protein bioinsecticide pea albumin 1 subunit b (PA1b) is the first peptidic inhibitor of V-ATPase. J Biol Chem 286:36291–36296

Chung C, Mader C, Protiva P, Schmitz J, Koleske A, Crawford S, Gorelick F (2010) The vacuolar-ATPase (v-ATPase) confers invasive properties to human pancreatic cancer by modulating MMPs. Pancreas 39:1315

Clare DK, Orlova EV, Finbow ME, Harrison MA, Findlay JBC, Saibil HR (2006) An expanded and flexible form of the vacuolar ATPase membrane sector. Structure 14:1149–1156

Coonrod EM, Graham LA, Carpp LN, Carr TM, Stirrat L, Bowers K, Bryant NJ, Stevens TH (2013) Homotypic vacuole fusion in yeast requires organelle acidification and not the V-ATPase membrane domain. Dev Cell 27:462–468

Coskun Ü, Chaban YL, Lingl A, Müller V, Keegstra W, Boekema EJ, Grüber G (2004) Structure and subunit arrangement of the A-type ATP synthase complex from the archaeon *Methanococcus jannaschii* visualized by electron microscopy. J Biol Chem 279:38644–38648

Cotter K, Stransky L, McGuire C, Forgac M (2015) Recent insights into the structure, regulation and function of the V-ATPases. Trends Biochem Sci 40:611–622

Couoh-Cardel S, Milgrom E, Wilkens S (2015) Affinity purification and structural features of the yeast vacuolar ATPase $V_o$ membrane sector. J Biol Chem 290:27959–27971

Couoh-Cardel S, Hsueh YC, Wilkens S, Movileanu L (2016) Yeast V-ATPase proteolipid ring acts as a large-conductance transmembrane protein pore. Sci Rep 6:24774

Crider BP, Xie X-S, Stone DK (1994) Bafilomycin inhibits proton flow through the $H^+$ channel of vacuolar proton pumps. J Biol Chem 269:17379–17381

Curtis KK, Francis SA, Oluwatosin Y, Kane PM (2002) Mutational analysis of the subunit C (Vma5p) of the yeast vacuolar H+-ATPase. J Biol Chem 277:8979–8988

David P, Baron R (1994) The catalytic cycle of the vacuolar $H^+$-ATPase. Comparison of proton transport in kidney and osteoclast-derived membranes. J Biol Chem 269:30158–30163

De Milito A, Fais S (2005) Tumor acidity, chemoresistance and proton pump inhibitors. Future Oncol 1:779–786

Di Giovanni J, Boudkkazi S, Mochida S, Bialowas A, Samari N, Leveque C, Youssouf F, Brechet A, Iborra C, Maulet Y, Moutot N, Debanne D, Seagar M, El Far O (2010) V-ATPase membrane sector associates with synaptobrevin to modulate neurotransmitter release. Neuron 67:268–279

Diab H, Ohira M, Liu M, Cobb E, Kane PM (2009) Subunit interactions and requirements for inhibition of the yeast $V_1$-ATPase. J Biol Chem 284:13316–13325

Diepholz M, Börsch M, Böttcher B (2008a) Structural organization of the V-ATPase and its implications for regulatory assembly and disassembly. Biochem Soc Trans 36:1027–1031

Diepholz M, Venzke D, Prinz S, Batisse C, Flörchinger B, Rössle M, Svergun DI, Böttcher B, Féthière J (2008b) A different conformation for EGC stator subcomplex in solution and in the assembled yeast V-ATPase: possible implications for regulatory disassembly. Structure 16:1789–1798

Dow JA, Peacock JM (1989) Microelectrode evidence for the electrical isolation of goblet cell cavities in *Manduca sexta* middle midgut. J Exp Biol 143:101–114

Drory O, Frolow F, Nelson N (2004) Crystal structure of yeast V-ATPase subunit C reveals its stator function. EMBO Rep 5:1148–1152

Drose S, Bindseil KU, Bowman EJ, Siebers A, Zeeck A, Altendorf K (1993) Inhibitory effects of modified bafilomycins and concanamycins on P- and V-type adenosinetriphosphatases. Biochemistry 32:3902–3906

Dschida WJ, Bowman BJ (1992) Structure of the vacuolar atpase from neurospora-crassa as determined by electron-microscopy. J Biol Chem 267:18783–18789

Esmail S, Kartner N, Yao Y, Kim JW, Reithmeier RAF, Manolson MF (2017) N-linked glycosylation of a subunit isoforms is critical for vertebrate vacuolar H -ATPase (V-ATPase) biosynthesis. J Cell Biochem 119:861–875

Fais S, De Milito S, You H, Qin W (2007) Targeting vacuolar $H^+$-ATPases as a new strategy against cancer. Cancer Res 67:10627–10630

Farina C, Gagliardi S (1999) Selective inhibitors of the osteoclast vacuolar proton atpase as novel bone antiresorptive agents. Drug Discov Today 4:163–172

Fernandez-Leiro R, Scheres SHW (2016) Unravelling biological macromolecules with cryo-electron microscopy. Nature 537:339–346

Finbow ME, Harrison MA, Jones PC (1995) Ductin – a proton pump component, a gap junction channel and a neurotransmitter release channel. BioEssays 17:247–255

Folkers KM, Hinton AM (2012) The role of the vacuolar $H^+$-ATPase subunit a isoforms in secretion and activation of cathepsin L in human breast cancer cells. FASEB J 26:956.5

Gagliardi S, Nadler G, Consolandi E, Parini C, Morvan M, Legave MN, Belfiore P, Zocchetti A, Clarke GD, James I, Nambi P, Gowen M, Farina C (1998) 5-(5,6-Dichloro-2-indolyl)-2-methoxy-2,4-pentadienamides: novel and selective inhibitors of the vacuolar H+-ATPase of osteoclasts with bone antiresorptive activity. J Med Chem 41:1568–1573

Gong F, Alzamora R, Smolak C, Li H, Naveed S, Neumann D, Hallows KR, Pastor-Soler NM, Vacuolar H (2010) +-ATPase apical accumulation in kidney intercalated cells is regulated by PKA and AMP-activated protein kinase. Am J Physiol Ren Physiol 298:F1162–F1169

Gräbe M, Wang H, Oster G (2000) The mechanochemistry of V-ATPase proton pumps. Biophys J 78:2798–2813

Graf R, Harvey WR, Wieczorek H (1996) Purification and properties of a cytosolic V-1 ATPase. J Biol Chem 271:20908–20913

Hallows KR, Alzamora R, Li H, Gong F, Smolak C, Neumann D, Pastor-Soler NM (2009) AMP-activated protein kinase inhibits alkaline pH- and PKA-induced apical vacuolar H+-ATPase accumulation in epididymal clear cells. Am J Physiol Cell Ph 296:C672–C681

Hiesinger PR, Fayyazuddin A, Mehta SQ, Rosenmund T, Schulze KL, Zhai RG, Verstreken P, Cao Y, Zhou Y, Kunz J, Bellen HJ (2005) The v-ATPase V-0 subunit a1 is required for a late step in synaptic vesicle exocytosis in Drosophila. Cell 121:607–620

Hinton A, Sennoune SR, Bond S, Fang M, Reuveni M, Sahagian GG, Jay D, Martinez-Zaguilan R, Forgac M (2009) Function of a subunit isoforms of the V-ATPase in pH homeostasis and in vitro invasion of MDA-MB231 human breast cancer cells. J Biol Chem 284:16400–16408

Hong-Hermesdorf A, Brux A, Gruber A, Gruber G, Schumacher K (2006) A WNK kinase binds and phosphorylates V-ATPase subunit C. FEBS Lett 580:932–939

Hurtado-Lorenzo A, Skinner M, El Annan J, Futai M, Sun-Wada GH, Bourgoin S, Casanova J, Wildeman A, Bechoua S, Ausiello DA, Brown D, Marshansky V (2006) V-ATPase interacts with ARNO and Arf6 in early endosomes and regulates the protein degradative pathway. Nat Cell Biol 8:124–1U8

Huss M, Wieczorek H (2007) Influence of ATP and ADP on dissociation of the V-ATPase into its $V_1$ and $V_o$ complexes. FEBS Lett 581:5566–5572

Huss M, Wieczorek H (2009) Inhibitors of V-ATPases: old and new players. J Exp Biol 212:341–346

Huss M, Ingenhorst G, Konig S, Gassel M, Drose S, Zeeck A, Altendorf K, Wieczorek H (2002) Concanamycin A, the specific inhibitor of V-ATPases, binds to the $V_o$ subunit c. J Biol Chem 277:40544–40548

Imamura H, Ikeda C, Yoshida M, Yokoyama K (2004) The F subunit of *Thermus thermophilus* $V_1$-ATPase promotes ATPase activity but is not necessary for rotation. J Biol Chem 279:18085–18090

Imamura H, Takeda M, Funamoto S, Shimabukuro K, Yoshida M, Yokoyama K (2005) Rotation scheme of $V_1$-motor is different from that of $F_1$-motor. Proc Natl Acad Sci U S A 102:17929–17933

Ishisaki A, Hashimoto S, Amagasa T, Nishihara T (1999) Caspase-3 activation during the process of apoptosis induced by a vacuolar type $H^+$-ATPase inhibitor. Biol Cell 91:507–513

Iwata M, Imamura H, Stambouli E, Ikeda C, Tamakoshi M, Nagata K, Makyio H, Hankamer B, Barber J, Yoshida M, Yokoyama K, Iwata S (2004) Crystal structure of a central stalk subunit C and reversible association/dissociation of vacuole-type ATPase. Proc Natl Acad Sci U S A 101:59–64

Jansen EJR, Scheenen WJJM, Hafmans TGM, Martens GJM (2008) Accessory subunit Ac45 controls the V-ATPase in the regulated secretory pathway. Biochim Biophys Acta 1783:2301–2310

Jasti J, Furukawa H, Gonzales EB, Gouaux E (2007) Structure of acid-sensing ion channel 1 at 1.9Å resolution and low pH. Nature 449:316–323

Jefferies KC, Forgac M (2008) Subunit H of the vacuolar ($H^+$) ATPase inhibits ATP hydrolysis by the free $V_1$ domain by interaction with the rotary subunit F. J Biol Chem 283:4512–4519

Jewell JL, Russell RC, Guan KL (2013) Amino acid signalling upstream of mTOR. Nat Rev Mol Cell Biol 14:133–139

Johnson LN, Lewis RJ (2001) Structural basis for control by phosphorylation. Chem Rev 101:2209–2242

Junge W, Nelson N (2005) Nature's rotary electromotors. Science 308:642–644

Kane PM (1995) Disassembly and reassembly of the yeast vacuolar H(+)-ATPase in vivo. J Biol Chem 270:17025–17032

Karet FE (2005) Physiological and metabolic implications of V-ATPase isoforms in the kidney. J Bioenerg Biomembr 37:425–429

Karet FE, Finberg KE, Nelson RD, Nayir A, Mocan H, Sanjad SA, Rodriguez-Soriano J, Santos F, Cremers CWRJ, Pietro AD, Hoffbrand BI, Winiarski J, Bakkaloglu A, Ozen S, Dusunsel R, Goodyer P, Hulton SA, DK W, Skvorak AB, Morton CC, Cunningham MJ, Jha V, Lifton RP (1999) Mutations in the gene encoding B1 subunit of $H^+$-ATPase cause renal tubular acidosis with sensorineural deafness. Nat Genet 21:84–90

Kawasaki-Nishi S, Bowers K, Nishi T, Forgac M, Stevens TH (2001a) The amino-terminal domain of the vacuolar proton-translocating ATPase a-subunit controls targeting and in vivo dissociation, and the carboxyl-terminal domain affects coupling of proton transport and ATP hydrolysis. J Biol Chem 276:47411–47420

Kawasaki-Nishi S, Nishi T, Forgac M (2001b) Yeast V-ATPase complexes containing different isoforms of the 100-kDa a-subunit differ in coupling efficiency and in vivo dissociation. J Biol Chem 276:17941–17948

Kawasaki-Nishi S, Nishi T, Forgac M (2003) Interacting helical surfaces of the transmembrane segments of subunits a and c' of the yeast V-ATPase defined by disulfide-mediated cross-linking. J Biol Chem 278:41908–41913

Keeling DJ, Herslof M, Mattson JP, Ryberg B (1998) Tissue-selective inhibition of vacuolar acid pumps. Acta Physiol Scand 163:195–201

Kitagawa N, Mazon H, Heck AJR, Wilkens S (2008) Stoichiometry of the peripheral stalk subunits E and G of yeast V1-ATPase determined by mass spectrometry. J Biol Chem 283:3329–3337

Kohio HP, Adamson AL (2013) Glycolytic control of vacuolar-type ATPase activity: a mechanism to regulate influenza viral infection. Virology 444:301–309

Kornak U, Reynders E, Dimopoulou A, van Reeuwijk J, Fischer B, Rajab A, Budde B, Nurnberg P, Foulquier F, Lefeber D, Urban Z, Gruenewald S, Annaert W, Brunner HG, van Bokhoven H, Wevers R, Morava E, Matthijs G, Van Maldergem L, Mundlos S (2008) Impaired glycosylation and cutis laxa caused by mutations in the vesicular $H^+$-ATPase subunit ATP6V0A2. Nat Genet 40:32–34

Kubota S, Seyama Y (2000) Overexpression of vacuolar ATPase 16-kDa subunit in 10T1/2 fibroblasts enhances invasion with concomitant induction of matrix metalloproteinase-2. Biochem Biophys Res Commun 278:390–394

Kuzinski J, Zitnan R, Warnke-Gurgel C, Schweigel M (2010) The vacuolar-type $H^+$-ATPase in ovine rumen epithelium is regulated by metabolic signals. J Biomed Biotechnol 2010:525034

Lee LK, Stewart AG, Donohoe M, Bernal RA, Stock D (2010) The structure of the peripheral stalk of *Thermus thermophilus* $H^+$-ATPase/synthase. Nat Struct Mol Biol 17:373–379

Leng XH, Nishi T, Forgac M (1999) Transmembrane topography of the 100-kDa a subunit (Vph1p) of the yeast vacuolar proton translocating ATPase. J Biol Chem 274:14655–14661

Li SC, Diakov TT, Xu T, Tarsio M, Zhu W, Couoh-Cardel S, Weisman LS, Kane PM (2014) The signaling lipid $PI(3,5)P_2$ stabilizes $V_1$-$V_o$ sector interactions and activates the V-ATPase. Mol Biol Cell 25:1251–1262

Liu J, Ji Y, Zhou J, Xing D (2016) Phosphatidylinositol 3-kinase promotes V-ATPase activation and vacuolar acidification and delays methyl jasmonate-induced leaf senescence. Plant Physiol 170:1714–1731

Lu X, Qin W, Li J, Tan N, Pan D, Zhang H, Xie L, Yao G, Shu H, Yao M, Wan D, Gu J, Yang S (2005) The growth and metastasis of human hepatocellular carcinoma xenografts are inhibited by small interfering RNA targeting to the subunit ATP6L of proton pump. Cancer Res 65:6843–6849

Luciani F, Spada M, De Milito A, Molinari A, Rivoltini L, Montinaro A, Marra M, Lugini L, Logozzi M, Lozupone F, Federici C, Lessi E, Parmiani G, Arancia G, Belardelli F, Fais S (2004) Effect of proton pump inhibitor pretreatment on resistance of solid tumors to cytotoxic drugs. J Natl Cancer Inst 96:1702–1713

Maher MJ, Akimoto S, Iwata M, Nagata K, Hori Y, Yoshida M, Yokoyama S, Iwata S, Yokoyama K (2009) Crystal structure of $A_3B_3$ complex of V-ATPase from *Thermus thermophilus*. EMBO J 28:3771–3779

Makyio H, Iino R, Ikeda C, Imamura H, Tamakoshi M, Iwata M, Stock D, Bernal RA, Carpenter EP, Yoshida M, Yokoyama K, Iwata S (2005) Structure of a central stalk subunit F of prokaryotic V-type ATPase/synthase from *Thermus thermophilus*. EMBO J 24:3974–3983

Mandel M, Moriyama Y, Hulmes JD (1988) Pan Y-CE, Nelson H, Nelson N. cDNA sequence encoding the 16-kDa proteolipid of chromaffin granules implies gene duplication in the evolution of $H^+$-ATPases. Proc Natl Acad Sci U S A 85:5521–5524

Marshansky V, Rubinstein JL, Grüber G (2014) Eukaryotic V-ATPase: novel structural findings and functional insights. Biochim Biophys Acta 1837:857–879

Mattson JP, Keeling DJ (1996) [3-H]Bafilomycin as a probe for the transmembrane proton channel of the osteoclast vacuolar $H^+$-ATPase. Biochim Biophys Acta 1280:98–106

Maxson ME, Grinstein S (2014) The vacuolar-type $H^+$-ATPase at a glance – more than a proton pump. J Cell Sci 127:4987–4993

Mazhab-Jafari MT, Rohou A, Schmidt C, Bueler SA, Benlekbir S, Robinson CV, Rubinstein JL (2016) Atomic model for the membrane-embedded $V_o$ motor of a eukaryotic V-ATPase. Nature 539:118–124

Merzendorfer H, Graf R, Huss M, Harvery WR, Wieczorek H (1997) Regulation of proton-translocating V-ATPases. J Exp Biol 200:225–235

Merzendorfer H, Huss M, Schmid R, Harvey WR, Wieczorek H (1999) A novel insect V-ATPase subunit M9.7 is glycosylated extensively. J Biol Chem 274:17372–17378

Morel N, Dedieu JC, Philippe JM (2003) Specific sorting of the a1 isoform of the V-H(+)ATPase a subunit to nerve terminals where it associates with both synaptic vesicles and the presynaptic plasma membrane. J Cell Sci 116:4751–4762

Morimura T, Fujita K, Akita M, Nagashima M, Satomi A (2008) The proton pump inhibitor inhibits cell growth and induces apoptosis in human hepatoblastoma. Pediatr Surg Int 24:1087–1094

Moriyama Y, Nelson N (1989) Cold inactivation of vacuolar proton-ATPases. J Biol Chem 264:3577–3582

Muench SP, Huss M, Song CF, Phillips C, Wieczorek H, Trinick J, Harrison MA (2009) Cryo-electron microscopy of the vacuolar ATPase motor reveals its mechanical and regulatory complexity. J Mol Biol 386:389–399

Muench SP, Trinick J, Harrison MA (2011) Structural divergence of the rotary ATPases. Q Rev Biophys 44:311–356

Muench SP, Scheres SHW, Huss M, Phillips C, Vitavska O, Wieczorek H, Trinick J, Harrison MA (2013) Subunit positioning and stator filament stiffness in regulation and power transmission in the $V_1$ motor of the *Manduca sexta* V-ATPase. J Mol Biol 426:286–300

Muench SP, Rawson S, Eyraud V, AsF D, Da Silva P, Phillips C, Trinick J, Harrison MA, Fdr G, Huss M (2014) PA1b inhibitor binding to subunits c and e of the vacuolar ATPase reveals its insecticidal mechanism. J Biol Chem 289:16399–16408

Murata T, Yamato I, Kakinuma Y, Leslie AGW, Walker JE (2005) Structure of the rotor of the V-type Na+-ATPase from *Enterococcus hirae*. Science 308:654–659

Nagamatsu Y, Takeda K, Kuranaga T, Numoto N, Miki K (2013) Origin of asymmetry at the intersubunit interfaces of $V_1$-ATPase from *Thermus thermophilus*. J Mol Biol 425:2699–2708

Nakamura I, Sasaki T, Tanaka S, Takahashi N, Jimi E, Kurokawa T, Kita Y, Ihara S, Suda T, Fukui Y (1997) Phosphatidylinositol-3 kinase is involved in ruffled border formation in osteoclasts. J Cell Physiol 172:230–239

Nelson N (1992) Evolution of organellar proton-ATPases. Biochim Biophys Acta 1100:109–124

Nelson N, Taiz L (1989) The evolution of $H^+$ ATPases. Trends Biochem Sci 14:113–116

Neri D, Supuran CT (2011) Interfering with pH regulation in tumours as a therapeutic strategy. Nat Rev Drug Discov 10:767–777

Niikura K (2007) Effect of a V-ATPase inhibitor, FR202126, in syngeneic mouse model of experimental bone metastasis. Cancer Chemother Pharmacol 60:555–562

Nishi T, Forgac M (2000) Molecular cloning and expression of three isoforms of the 100-kDa a subunit of the mouse vacuolar proton-translocating ATPase. J Biol Chem 275:6824–6830

Numoto N, Hasegawa Y, Takeda K, Miki K (2009) Inter-subunit interaction and quaternary rearrangement defined by the central stalk of prokaryotic $V_1$-ATPase. EMBO Rep 10:1228–1234

Obrdlik P, Diekert K, Watzke N, Keipert C, Pehl U, Brosch C, Boehm N, Bick I, Ruitenberg M, Volknandt W, Kelety B (2010) Electrophysiological characterization of ATPases in native synaptic vesicles and synaptic plasma membranes. Biochem J 427:151–159

Ohta T, Arakawa H, Futagami F, Fushida S, Kitagawa H, Kayahara M, Nagakawa T, Miwa K, Kurashima K, Numata M, Kitamura Y, Terada T, Ohkuma S, Bafilomycin A (1998) (1) induces apoptosis in the human pancreatic cancer cell line Capan-1. J Pathol 185:324–330

Oka T, Murata Y, Namba M, Yoshimizu T, Toyomura T, Yamamoto A, Sun-Wada GH, Hamasaki N, Wada Y, Futai M (2001) alpha 4, a unique kidney-specific isoform of mouse vacuolar $H^+$-ATPase subunit a. J Biol Chem 276:40050–40054

Oot RA, Huang LS, Berry EA, Wilkens S (2012) Crystal structure of the yeast vacuolar ATPase heterotrimeric $EGC_{head}$ peripheral stalk complex. Structure 20:1881–1892

Oot RA, Kane PM, Berry EA, Wilkens S (2016) Crystal structure of yeast $V_1$-ATPase in the autoinhibited state. EMBO J 35:1694–1706

Osteresch C, Bender T, Grond S, von Zezschwitz P, Kunze B, Jansen R, Huss M, Wieczorek H (2012) The binding site of the V-ATPase inhibitor apicularen is in the vicinity of those for bafilomycin and archazolid. J Biol Chem 287:31866–31876

Pali T, Dixon N, Kee TP, Marsh D (2004a) Incorporation of the V-ATPase inhibitors concanamycin and indole pentadiene in lipid membranes. Spin-label EPR studies. Biochim Biophys Acta 1663:14–18

Pali T, Whyteside G, Dixon N, Kee TP, Ball S, Harrison MA, Findlay JBC, Finbow ME, Marsh D (2004b) Interaction of inhibitors of the vacuolar $H^+$-ATPase with the transmembrane V-o-sector. Biochemistry 43:12297–12305

Parra KJ, Kane PM (1998) Reversible association between the $V_1$ and $V_o$ domains of yeast vacuolar $H^+$-ATPase is an unconventional glucose-induced effect. Mol Cell Biol 18:7064–7074

Parra KJ, Keenan KL, Kane PM (2000) The H subunit (Vma13p) of the yeast V-ATPase inhibits the ATPase activity of cytosolic $V_1$ complexes. J Biol Chem 275:21761–21767

Pastor-Soler N, Beaulieu V, Litvin TN, Silva ND, Chen Y, Brown D, Buck J, Levin LR, Breton S (2003) Bicarbonate-regulated adenylyl cyclase (sAC) is a sensor that regulates pH-dependent V-ATPase recycling. J Biol Chem 278:49523–49529

Pastor-Soler N, Alzamora R, Naveed S, Smolak C, Gong F, Hallows KR (2009) Novel regulation of V-ATPase by PKA and AMPK in kidney intercalated cells. FASEB J 23:602

Peters C, Bayer MJ, Buhler S, Andersen JS, Mann M, Mayer A (2001) Trans-complex formation by proteolipid channels in the terminal phase of membrane fusion. Nature 409:581–588

Pietrement C, Sun-Wada GH, Da Silva N, Mckee M, Marshansky V, Brown D, Futai M, Breton S (2006) Distinct expression patterns of different subunit isoforms of the V-ATPase in the rat epididymis. Biol Reprod 74:185–194

Qi J, Forgac M (2008) Function and subunit interactions of the N-terminal domain of subunit a (Vph1p) of the yeast V-ATPase. J Biol Chem 283:19274–19282

Raghunand N, Martinez-Zaguilan R, Wright SH, Gillies RJ (1999) pH and drug resistance. II. Turnover of acidic vesicles and resistance to weakly basic chemotherapeutic drugs. Biochem Pharmacol 57:1047–1058

Rawson S, Phillips C, Huss M, Tiburcy F, Wieczorek H, Trinick J, Harrison MA, Muench SP (2015) Structure of the vacuolar $H^+$-ATPase rotary motor reveals new mechanistic insights. Structure 23:461–471

Rofstad EK, Mathiesen B, Kindem K, Galappathi K (2006) Acidic extracellular pH promotes experimental metastasis of human melanoma cells in athymic nude mice. Cancer Res 66:6699–6707

Rothenberger F, Velic A, Stehberger PA, Kovacikova J, Wagner CA (2007) Angiotensin II stimulates vacuolar $H^+$-ATPase activity in renal acid-secretory intercalated cells from the outer medullary collecting duct. J Am Soc Nephrol 18:2085–2093

Rozhin J, Sameni M, Ziegler G, Sloane BF (1994) Pericellular pH affects distribution and secretion of cathepsin-B in malignant cells. Cancer Res 54:6517–6525

Sagermann M, Stevens TH, Matthews BW (2001) Crystal structure of the regulatory subunit H of the V-type ATPase of *Saccharomyces cerevisiae*. Proc Natl Acad Sci U S A 98:7134–7139

Saijo S, Arai S, Hossain KMM, Yamato I, Suzuki K, Kakinuma Y, Ishizuka-Katsura Y, Ohsawa N, Terada T, Shirouzu M, Yokoyama S, Iwata S, Murata T (2011) Crystal structure of the central axis DF complex of the prokaryotic V-ATPase. Proc Natl Acad Sci U S A 108:19955–19960

Sasazawa Y, Futamura Y, Tashiro E, Imoto M (2009) Vacuolar H+-ATPase inhibitors overcome Bcl-xL-mediated chemoresistance through restoration of a caspase-independent apoptotic pathway. Cancer Sci 100:1460–1467

Sasse F, Steinmetz H, Höfle G, Reichenbach H (2003) Archazolids, new cytotoxic macrolactones from Archangium gephyra (Myxobacteria). Production, isolation, physico-chemical and biological properties. J Antibiot (Tokyo) 56:520–525

Sautin YY, Lu M, Gaugler A, Zhang L, Gluck SL (2005) Phosphatidylinositol 3-kinase-mediated effects of glucose on vacuolar $H^+$-ATPase assembly, translocation, and acidification of intracellular compartments in renal epithelial cells. Mol Cell Biol 25:575–589

Saw NMN, Kang SYA, Parsaud L, Han GA, Jiang TD, Grzegorczyk K, Surkont M, Sun-Wada GH, Wada Y, Li LJ, Sugita S (2011) Vacuolar $H^+$-ATPase subunits $V_o$a1 and $V_o$a2 cooperatively regulate secretory vesicle acidification, transmitter uptake, and storage. Mol Biol Cell 22:3394–3409

Sennoune SR, Bakunts K, Martinez GM, Chua-Tuan JL, Kebir Y, Attaya MN, Martinez-Zaguilan R (2004a) Vacuolar $H^+$-ATPase in human breast cancer cells with distinct metastatic potential: distribution and functional activity. Am J Physiol Cell Ph 286:C1443–C1452

Sennoune SR, Luo DF, Martinez-Zaguilan R (2004b) Plasmalemmal vacuolar-type $H^+$-ATPase in cancer biology. Cell Biochem Biophys 40:185–206

Seol J, Shevchenko A, Shevchenko A, Deshaies R (2001) Skp1 forms multiple protein complexes, including RAVE, a regulator of V-ATPase assembly. Nat Cell Biol 3:384–391

Shao E, Forgac M (2004) Involvement of the nonhomologous region of subunit a of the yeast V-ATPase in coupling and in vivo dissociation. J Biol Chem 279:48663–48670

Shao E, Nishi T, Kawasaki-Nishi S, Forgac M (2003) Mutational analysis of the non-homologous region of subunit a of the yeast V-ATPase. J Biol Chem 278:12985–12991

Smardon AM, Kane PM (2007) RAVE is essential for the efficient assembly of the C subunit with the vacuolar $H^+$-ATPase. J Biol Chem 282:26185–26194

Smardon AM, Tarsio M, Kane PM (2002) The RAVE complex is essential for stable assembly of the yeast V-ATPase. J Biol Chem 277:13831–13839

Smith AN, Skaug J, Choate KA, Nayir A, Bakkaloglu A, Ozen S, Hulton SA, Sanjad SA, Al-Sabban EA, Lifton RP, Scherer SW, Karet FE (2000) Mutations in ATP6N1B, encoding a new kidney vacuolar proton pump 116-kD subunit, cause recessive distal renal tubular acidosis with preserved hearing. Nat Genet 26:71–75

Smith GA, Howell GJ, Phillips C, Muench SP, Ponnambalam S, Harrison MA (2016) Extracellular and luminal pH regulation by vacuolar $H^+$-ATPase isoform expression and targeting to the plasma membrane and endosomes. J Biol Chem 291:8500–8515

Srinivasan S, Vyas NK, Baker ML, Quiocho FA (2011) Crystal structure of the cytoplasmic N-terminal domain of subunit I, a homolog of subunit a, of V-ATPase. J Mol Biol 412:14–21

Stewart AG, Lee LK, Donohoe M, Chaston JJ, Stock D (2012) The dynamic stator stalk of rotary ATPases. Nat Commun 3:687

Sumner JP, Dow JA, Earley FG, Klein U, Jager D, Wieczorek H (1995) Regulation of plasma membrane V-ATPase activity by dissociation of peripheral subunits. J Biol Chem 270:5649–5653

Sun S-X, Xie X-S, Stone DK (1987) Isolation and reconstitution of the dicyclohexylcarbodiimid-sensitive proton pore of the clathrin coated vesicle proton translocating complex. J Biol Chem 262:14790–14794

Sun-Wada GH, Wada Y (2010) Vacuolar-type proton pump ATPases: roles of subunit isoforms in physiology and pathology. Histol Histopathol 25:1611–1620

Sun-Wada GH, Toyomura T, Murata Y, Yamamoto A, Futai M, Wada Y (2006) The a3 isoform of V-ATPase regulates insulin secretion from pancreatic beta-cells. J Cell Sci 119:4531–4540

Sun-Wada GH, Tabata H, Kawamura N, Aoyama M, Wada Y (2009) Direct recruitment of $H^+$-ATPase from lysosomes for phagosomal acidification. J Cell Sci 122:2504–2513

Supino R, Petrangolini G, Pratesi G, Tortoreto M, Favini E, Dal Bo L, Casalini P, Radaelli E, Croce AC, Bottiroli G, Misiano P, Farina C, Zunino F (2008) Antimetastatic effect of a small-molecule vacuolar $H^+$-ATPase inhibitor in in vitro and in vivo preclinical studies. J Pharmacol Exp Ther 324:15–22

Suzuki K, Mizutani K, Maruyama S, Shimono K, Imai FL, Muneyuki E, Kakinuma Y, Ishizuka-Katsura Y, Shirouzu M, Yokoyama S, Yamato I, Murata T (2016) Crystal structures of the ATP-binding and ADP-release dwells of the $V_1$ rotary motor. Nat Commun 7:13235

Tabke K, Albertmelcher A, Vitavska O, Huss M, Schmitz H-P, Wieczorek H (2014) Reversible disassembly of the yeast V-ATPase revisited under in vivo conditions. Biochem J 462:185–197

Toei M, Saum R, Forgac M (2010) Regulation and isoform function of the V-ATPases. Biochemistry 49:4715–4723

Toei M, Toei S, Forgac M (2011) Definition of membrane topology and identification of residues important for transport in subunit a of the vacuolar ATPase. J Biol Chem 286:35176–35186

Tompkins LS, Nullmeyer KD, Murphy SM, Weber CS, Lynch RM (2002) Regulation of secretory granule pH in insulin-secreting cells. Am J Physiol Cell Ph 283:C429–C437

Toyomura T, Oka T, Yamaguchi C, Wada Y, Futai M (2000) Three subunit a isoforms of mouse vacuolar $H^+$-ATPase. Preferential expression of the a3 isoform during osteoclast differentiation. J Biol Chem 275:8760–8765

Toyomura T, Murata Y, Yamamoto A, Oka T, Sun-Wada GH, Wada Y, Futai M (2003) From lysosomes to the plasma membrane: localization of vacuolar type $H^+$-ATPase with the a3 isoform during osteoclast differentiation. J Biol Chem 278:22023–22030

Tsukano H, Kura F, Inoue S, Sato S, Izumiya H, Yasuda T, Watanabe H (1999) *Yersinia pseudotuberculosis* blocks the phagosomal acidification of B10.A mouse macrophages through the inhibition of vacuolar $H^+$-ATPase activity. Microb Pathog 27:253–263

Tuerk RD, Thali RF, Auchli Y, Rechsteiner H, Brunisholz RA, Schlattner U, Wallimann T, Neumann D (2007) New candidate targets of AMP-activated protein kinase in murine brain revealed by a novel multidimensional substrate-screen for protein kinases. J Proteome Res 6:3266–3277

Uchihashi T, Iino R, Ando T, Noji H (2011) High-speed atomic force microscopy reveals rotary catalysis of rotorless $F_1$-ATPase. Science 333:755–758

Van Damme T, Gardeitchik T, Mohamed M, Guerrero-Castillo S, Freisinger P, Guillemyn B, Kariminejad A, Dalloyaux D, van Kraaij S, Lefeber DJ, Syx D, Steyaert W, De Rycke R, Hoischen A, Kamsteeg EJ, Wong SY, van Scherpenzeel M, Jamali P, Brandt U, Nijtmans L, Korenke GC, BHY C, CCY M, Hausser I, Kornak U, Fischer-Zirnsak B, Strom TM, Meitinger T, Alanay Y, Utine GE, PKC L, Ghaderi-Sohi S, Coucke P, Symoens S, De Paepe A, Thiel C, Haack TB, Malfait F, Morava E, Callewaert B, Wevers RA (2017) Mutations in ATP6V1E1 or ATP6V1A cause autosomal-recessive cutis laxa. Am J Hum Genet 100:216–227

Vik SB, Antonio BJ (1994) A mechanism of proton translocation by $F_1F_0$ ATP synthases; suggested by double mutants of the *a* subunit. J Biol Chem 269:30364–30369

Visentin L, Dodds RA, Valente M, Misiano P, Bradbeer JN, Oneta S, Liang X, Gowen M, Farina C (2000) A selective inhibitor of the osteoclastic V-$H^+$-ATPase prevents bone loss in both thyroparathyroidectomized and ovariectomized rats. J Clin Invest 106:309–318

Voss M, Vitavska O, Walz B, Wieczorek H, Baumann O (2007) Stimulus-induced phosphorylation of vacuolar $H^+$-ATPase by protein kinase a. J Biol Chem 282:33735–33742

Wang Y, Inoue T, Forgac M (2005) Subunit a of the yeast V-ATPase participates in binding of bafilomycin. J Biol Chem 280:40481–40488

Wang Y, Toei M, Forgac M (2008) Analysis of the membrane topology of transmembrane segments in the C-terminal hydrophobic domain of the yeast vacuolar ATPase subunit a (Vph1p) by chemical modification. J Biol Chem 283:20696–20702

Wang D, Epstein D, Khalaf O, Srinivasan S, Williamson WR, Fayyazuddin A, Quiocho FA, Hiesinger PR (2014) $Ca^{2+}$-Calmodulin regulates SNARE assembly and spontaneous neurotransmitter release via v-ATPase subunit V0a1. J Cell Biol 205:21–31

Wassmer T, Kissmehl R, Cohen J, Plattner H (2006) Seventeen a-subunit isoforms of *Paramecium* V-ATPase provide high specialization and function. Mol Biol Cell 17:917–930

Webster LC, Apps DK (1996) Analysis of nucleotide-binding by a vacuolar proton- translocating adenosine-triphosphatase. Eur J Biochem 240:156–164

Whyteside G, Meek PJ, Ball SK, Dixon N, Finbow ME, Kee TP, Findlay JBC, Harrison MA (2005) Concanamycin and indolyl pentadieneamide inhibitors of the vacuolar $H^+$-ATPase bind with high affinity to the purified proteolipid subunit of the membrane domain. Biochemistry 44:15024–15031

Wieczorek H, Brown D, Grinstein S, Ehrenfeld J, Harvey WR (1999) Animal plasma membrane energization by proton motive v-atpases. BioEssays 21:637–648

Wilkens S, Vasilyeva E, Forgac M (1999) Structure of the vacuolar ATPase by electron microscopy. J Biol Chem 274:31804–31810

Xu L, Shen X, Bryan A, Banga S, Swanson MS, Luo ZQ (2010) Inhibition of host vacuolar $H^+$-ATPase activity by a *Legionella pneumophila* effector. PLoS Pathog 6:e1000822

Zhang J, Myers M, Forgac M (1992) Characterization of the $V_0$ domain of the coated vesicle ($H^+$)-ATPase. J Biol Chem 267:9773–9778

Zhang Z, Charsky C, Kane PM, Wilkens S (2003) Yeast $V_1$-ATPase: affinity purification and structural features by electron microscopy. J Biol Chem 278:47299–47306

Zhang Z, Zheng Y, Mazon H, Milgrom E, Kitagawa N, Kish-Trier E, Heck AJR, Kane PM, Wilkens S (2008) Structure of the yeast vacuolar ATPase. J Biol Chem 283:35983–35995

Zhao J, Benlekbir S, Rubinstein JL (2015) Electron cryomicroscopy observation of rotational states in a eukaryotic V-ATPase. Nature 521:241–245

Zhao J, Beyrakhova K, Lui Y, Alvarez CP, Bueler SA, Xu L, Xu C, Boniecki MT, Kanelis V, Luo Z-Q, Cygler M, Rubinstein JL (2017) Molecular basis for the binding and modulation of V-ATPase by a bacterial effector protein. PLoS Pathog 13:e1006394

Zhou M, Morgner N, Barrera NP, Politis A, Isaacson SC, Matak-Vinkovi-ç D, Murata T, Bernal RA, Stock D, Robinson CV (2011) Mass spectrometry of intact V-type ATPases reveals bound lipids and the effects of nucleotide binding. Science 334:380–385

Zhou A, Rohou A, Schep DG, Bason JV, Montgomery MG, Walker JE, Grigorieff N, Rubinstein JL (2015) Structure and conformational states of the bovine mitochondrial ATP synthase by cryo-EM. eLife 4:e10180

Zoncu R, Bar-Peled L, Efeyan A, Wang S, Sancak Y, Sabatini DM (2011) mTORC1 senses lysosomal amino acids through an inside-out mechanism that requires the vacuolar $H^+$-ATPase. Science 334:678